Gunnar Seemann

Modeling of Electrophysiology and Tension Development in the Human Heart

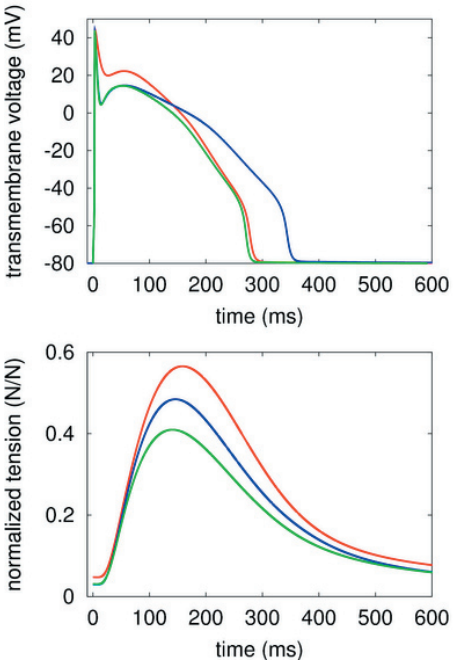

universitätsverlag karlsruhe

Gunnar Seemann

Modeling of Electrophysiology and Tension Development in the Human Heart

Modeling of Electrophysiology and Tension Development in the Human Heart

von
Gunnar Seemann

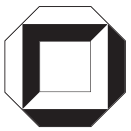

universitätsverlag karlsruhe

Dissertation, Universität Karlsruhe (TH)
Fakultät für Elektrotechnik und Informationstechnik, 2005
Referenten: Prof. Dr. rer. nat. Olaf Dössel, Prof. Dr.-Ing. Rüdiger Dillmann

Impressum

Universitätsverlag Karlsruhe
c/o Universitätsbibliothek
Straße am Forum 2
D-76131 Karlsruhe
www.uvka.de

Universitätsverlag Karlsruhe 2005
Print on Demand

ISBN 3-937300-66-X

Modeling of Electrophysiology and Tension Development in the Human Heart

Zur Erlangung des akademischen Grades eines

DOKTOR-INGENIEURS

von der Fakultät für
Elektrotechnik und Informationstechnik
der Universität Fridericiana Karlsruhe

genehmigte

DISSERTATION

von

Dipl.-Ing. Gunnar Seemann
aus Hamburg

Tag der mündlichen Prüfung:	27. April 2005
Hauptreferent:	Prof. Dr. rer. nat. Olaf Dössel
Korreferent:	Prof. Dr.-Ing. Rüdiger Dillmann

Contents

1

Introduction

The heart is a physiologically and anatomically complex organ. It is mainly composed of four cavities surrounded by muscles. These muscles are constructed of discrete cells, so-called myocytes. The myocytes are enclosed by a membrane in which proteins are inserted allowing selective ion transportation. This transport of ions leads to the electrical activation of the myocytes, which is expressed by the action potential. The membrane separates intra- from extracellular space. A large fraction of the intracellular volume is filled with force generating units. In tissue, the myocytes are coupled electrically. By this coupling, the electrical activation of one cell is conducted to the neighboring myocytes.
The electrical excitation of cardiac cells causes mechanical contraction during a heart cycle. This electro-mechanical coupling is controlled by intracellular calcium. The cardiac electrical activity depends on tissue type and distribution, geometry of the heart, and heart rate. Furthermore, fiber orientation, distribution of gap junctions and pathologies influence the activity of the heart.
The electromechanical properties of the heart are not homogeneously distributed. Experimental measurements of atrial tissue from different anatomical regions show electrophysiological differences. These variations are due to different ion channel expression throughout the atrium. In the ventricular myocardium an electrophysiological heterogeneity is also present caused by transmurally changing ion channel density and kinetics. This influences mainly the plateau and repolarization phase of the action potential and the development of tension.
Some pathologies are caused by defects mainly influencing the heterogeneous balance by changing electrophysiological characteristics only in parts of the tissue. E.g. long QT syndrome, familial atrial fibrillation, and the genesis of torsades de pointes were assigned to the disarrangement of the heterogeneity. A large group of pathologies lead to cardiac arrhythmia. Atrial fibrillation for example is the most common arrhythmia diagnosed for more than 2 million patients in Europe and America annually. The occurrence of atrial fibrillation increases with age, with a prevalence rising from 0.5 % of people in their fifties to nearly 10 % of the octogenarians.
Animal experiments and clinical studies produced significant insights into cellular electrophysiology in the last decades. The mechanisms underlying the complex interaction of cells and the initiation and perpetuation of arrhythmia is up to now not completely understood. The clinical treatment of various pathologies is often based on empirical knowledge.
Mathematical models form a basis to understand the mechanisms and interactions in the heart. Commonly, these models consist of coupled ordinary differential equations. The scope of modeling reaches from reconstruction of the genetic functioning to organ modeling. The gene models reconstruct the expression of proteins. Protein models can be integrated into e.g. a cell membrane to characterize the properties of a cell. These cells were coupled to describe

tissue or even an organ. Application of these models can be found in biomedical science e.g. for education and training purposes, for development and tests of pharmaceuticals, and to develop new medical devices and therapeutic strategies.
Modeling of cardiac electromechanics provides knowledge of physiological and pathological phenomena. The models are based on measurement data of protein, cell, tissue, or organ properties and thus help to integrate different scales of measured data. An important purpose of the models is to support the understanding of the mechanisms between these scales and of physiological as well as pathological interactions. A detailed model of the human heart will provide a useful and complimentary tool to investigate the dynamical behavior in a detailed way that cannot be achieved experimentally at present. All electrophysiological parameters during normal and abnormal excitation can be traced and analyzed. A further advantage of the model is that no ethical restrictions with respect to patient and animal experiments exist. On the other hand, models are always simplified descriptions of the real process and thus the results need to be validated by experimental work.
The modeling of cardiac electromechanics includes several different research topics, i.e. anatomy, electrophysiology, excitation conduction, tension development, passive mechanics, and fluid dynamics (fig. 1.1). The anatomical model builds the basis to describe the individual heart. The electrophysiological model reproduces the activity of a single cardiac myocytes. The conduction is determined by models of the electrical current flow in tissue. Partial differential equations have to be solved for these models. The tension model describes the tension development process in the contractile unit of myocardial cells dependent on the calcium concentration within the cell. The passive mechanical models utilze the generated tension as input to describe the deformation of the myocardium. Finally, the contraction of the heart initiates the flow of blood, which is described by fluid dynamical models.
These models are coupled by e.g. electromechanical, biomechanical, and mechanoelectrical feedback. Electromechanical feedback is a process describing the tension development initiated by the cellular electrical activity. Biomechanical feedback explains coupling between cellular tension and deformation. Mechanoelectrical coupling is the influence of tissue deformation on the electrophysiology by stretch sensitive membrane proteins. The tissue strain is also influencing the tension development. Furthermore, the ejection of blood is caused by the flow and thus fluid dynamics change the shape of the heart.
The active electromechanical behavior of the human heart is the subject of this work. Thus, the modeling of anatomy, electrophysiology and tension development will be described. Passive deformation and fluid dynamics were not detailed in this work.

1.1 Objectives of the Thesis

The focus of this work was directed to the mathematical modeling of the anatomy, electrophysiology and tension development in the human heart. In order to achieve quantitative simulations in the scope of this focus, new models were developed and existing models were enhanced. A main objective of this thesis was to reconstruct human electromechanical heterogeneity in schematic and realistic anatomical models. An anatomical highly detailed data set of the heart was utilized to extract different geometries or to describe inhomogeneity in the atrium. The fiber orientation is inserted in the ventricular model with a new technique based on measurement data. These inhomogeneous and anisotropic anatomical models were used to simulate the excitation conduction in the human heart.

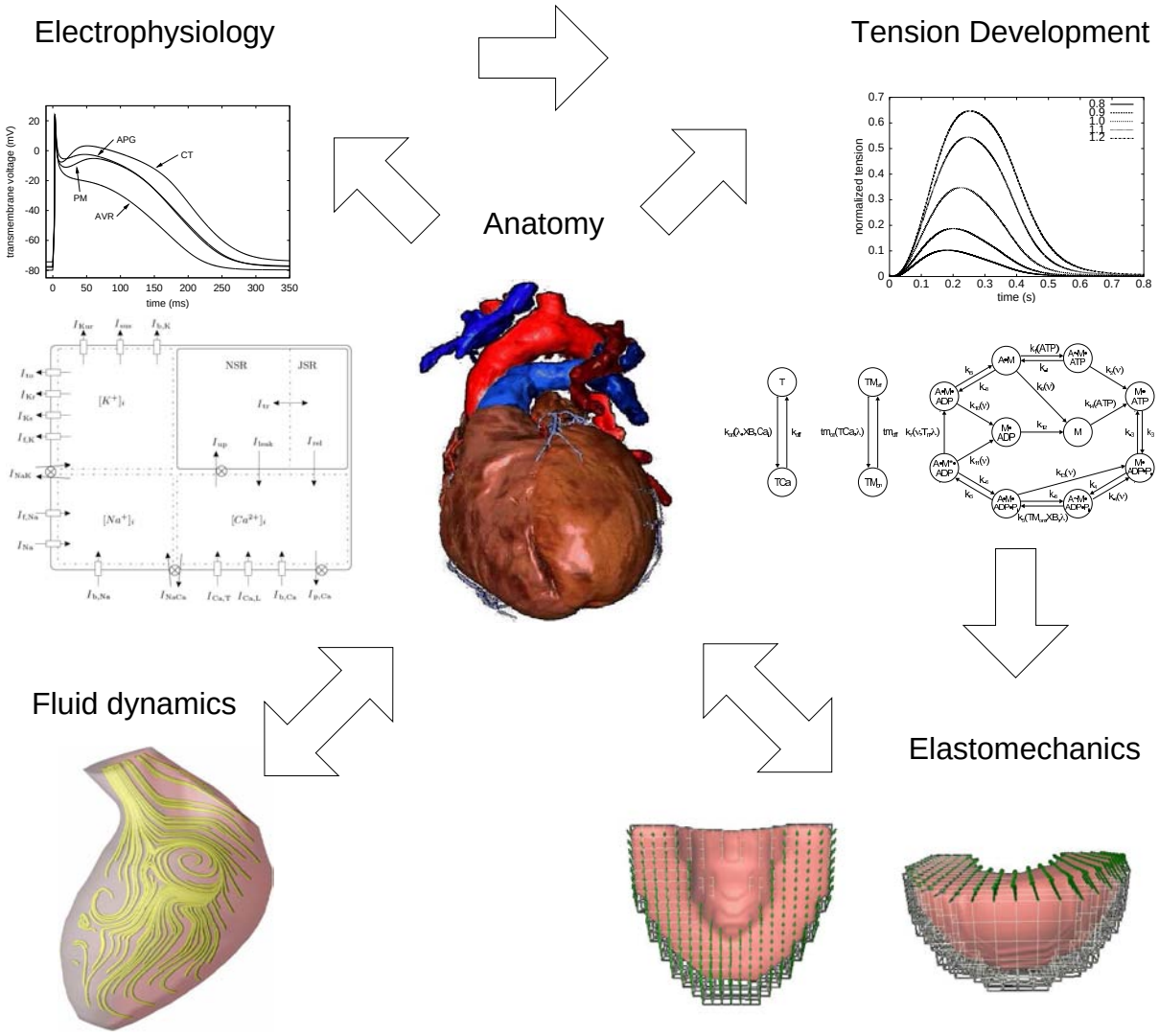

Fig. 1.1. Heart modeling overview. The arrows depict interaction of different models. Anatomy influences every other part of the modeling process. The electrophysiology triggers the tension development (excitation contraction coupling). The tension is input for the elastomechanical approach. The deformation of the heart influences the anatomy and all other components. The contraction is interacting with the fluid dynamics.

The heterogeneous electrophysiology is reconstructed implementing new or adapting existing models. The developed human sinoatrial node model is based on combining a human atrial with a rabbit sinoatrial model. Heterogeneous atrial electrophysiology is achieved by incorporating measurement data of different atrial regions. A transmural varying ventricular model was designed in corporation with a new model of tension development to investigate the electromechanical heterogeneity. Furthermore, several different pathological states were modeled to depict the capacity of the models reconstructing cardiac dysfunction.
The designed anatomical, electrophysiological, and tension development models were used to simulate and investigate the interplay for either physiological or pathological cases. The results help to gain new insights into the heart's function not elaborated to date or to support the understanding of pathologies e.g. cardiac arrhythmias.

1.2 Organization of the Thesis

The thesis is divided into three parts. The first seven chapters describe the state of the art, one chapter the methodology and two chapters the results of this work.
Chapter 2 and 3 describe the anatomy of the heart and its modeling. The microscopic as well as the macroscopic anatomy of the heart is illustrated with the involved structures. Furthermore, medical imaging systems are discussed briefly and an overview of digital image processing and anatomical model generation is given.
The electrophysiological properties in cardiac cells are detailed in chapter 4. The different involved membrane proteins are described and the role of calcium for the excitation contraction coupling is explained. Furthermore, the atrial and ventricular electrophysiology is illustrated. Chapter 5 describes the transfer of electrophysiology into mathematical models. Several existing electrophysiological models are discussed.
The physiological part ends with chapter 6 and 7 were tension development and its modeling are introduced. The interaction of the proteins troponin, tropomyosin, actin, and myosin during constant and dynamic calcium transients are discussed for both physiology and modeling. Existing models of tension development are described.
The mathematical and physical foundations of this work are described in chapter 8. These include ordinary and partial differential equations and their solution methods as well as minimization approaches and basic knowledge about the theory of electrical fields that are important for the methodology of this work.
Chapter 9 illustrates how the described methods and mathematical approaches are combined to a simulation environment, in which models can be designed or adapted. The excitation conduction is calculated and visualized within this simulation environment.
Chapter 10 and 11 address the results of this work. The new approaches are detailed and compared to measurement data and other models in chapter 10. Chapter 11 describes the electromechanical simulation including the excitation conduction in the tissue. Pathological simulations are outlined in both chapters.
The last chapter of this thesis summarizes the results and provides the perspectives for further research.

2

Anatomy and Physiology of the Heart

The human heart is a muscular organ with a weight of 230 to 350 g and the size of a persons fist [1, 2, 3]. Its function is to maintain the blood flow through the vessels by periodic contractions and relaxations. In this way the body is supplied with oxygen and nutrients. Also, the end products of the metabolism are carried away from the cells. The heart is separated by the septum into two separate but functionally and anatomically similar subsystems: the right and the left half. They represent the division of the blood circulation system into two different systems (fig. 2.1). Both halves are separated into an upper part (atrium) and a lower part (ventricle) [4, 5].
The heart is located in between the lungs in the mediastinum of the thorax and is surrounded by the pericardium, which is a closed sac of connective tissue. The main axis of the heart is normally oriented from back-top-right to front-bottom-left with the base at the upper and the apex at the lower end.
The deoxygenated blood from the body is collected in the right atrium through the Vena cava inferior and the Vena cava superior (fig. 2.1) [6, 7, 8]. The blood is transported through the tricuspid valve to the right ventricle during the relaxation phase of the heart, which is called diastole, due to the shifting of the valve plane. Furthermore, the right ventricular filling is supported by the pumping mechanism of the atrium during the atrial contraction (systole). The following contraction of the right ventricle pumps the blood through the pulmonary valve into the truncus pulmonalis and further on to the lungs where the blood is oxygenated.
Then, the blood is collected through the four pulmonary veins into the left atrium. The blood reaches the left ventricle through the mitral valve. During the contraction of the left ventricle the blood is ejected via the aortis valve into the aorta and further on into the body circulation. The heart itself is supplied with oxygenated blood through coronary arteries, which spread from the aorta all over the heart.
The four valves of the heart determine the direction of the blood flow due to their unidirectional characteristics. The valves are located in the heart skeleton, which separates the atria from the ventricles and which is build of connective tissue.
The walls of the different parts of the heart have different thicknesses due to the pressure the muscle has to work against. The walls of the atria are thin ($<2\ mm$), because they have to build a pressure difference of only 20 $mmHg$ [9]. The walls of the ventricles are thicker (right: ca. 10 mm, left: ca. 20 mm), since the ventricles have to produce about 30 $mmHg$ pressure difference in the right and approximately 50 $mmHg$ in the left ventricle.

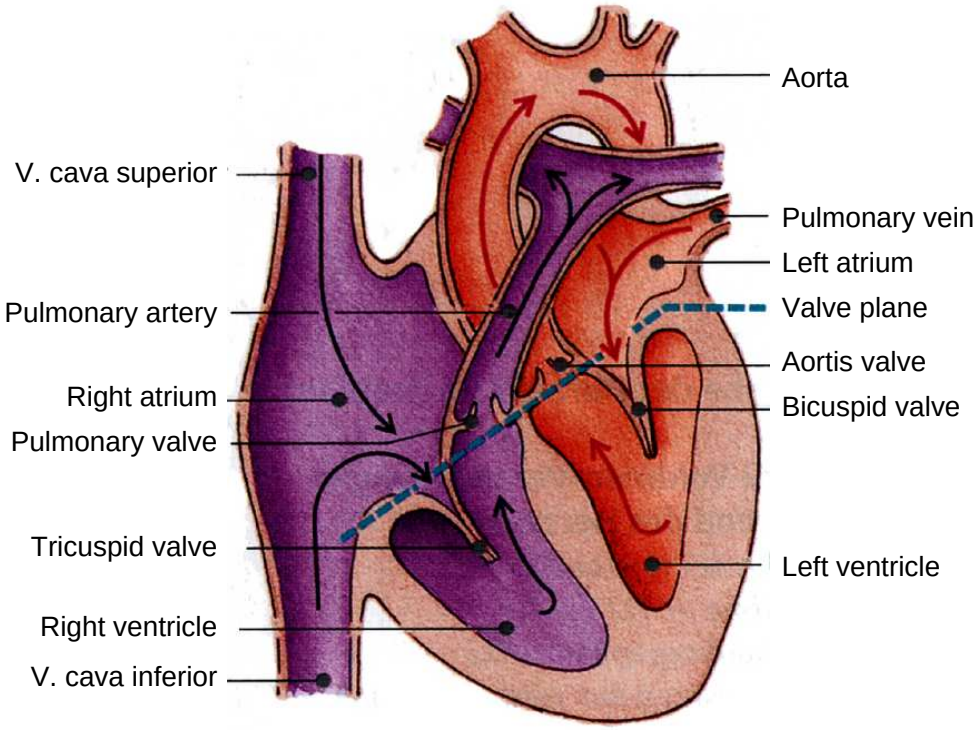

Fig. 2.1. Geometry of the heart and blood flow. The right and the left atrium are located at the upper part of the heart. At the lower part, the two ventricles are visible. Deoxygenated blood reaches the right atrium through the V. cava superior and inferior. Oxygenated blood flows through the four pulmonary veins into the left atrium. During the contraction of the atria, the blood is transported through the tricuspid and the bicuspid valve into the right and the left ventricle, respectively. During the next contraction of the ventricles the blood is pumped from the right ventricle through the pulmonary valve into the lung circulation and from the left ventricle through the aortis valve into the body circulation. Fig. adapted from [6].

2.1 Cardiomyocyte

The myocardium consists mostly of muscle cells (cardiomyocytes). These have commonly a cylindrical shape, particularly in the working myocardium. The cardiomyocytes are arranged in the myocardium in such way that they are electrically and mechanically coupled via the intercalated discs mainly at the long end of the cells [1]. The volume, surface area and distribution of intracellular components can vary due to different function of different cardiomyocytes. Myocytes of the working myocardium produce mainly mechanical tension. Thus the contractile elements of the working myocardium consume a larger fraction of intracellular space than those of e.g. the sinoatrial node. Cardiac cells from the excitation initiation and conduction system, e.g. the sinoatrial node, have the function to initiate the excitation. The length of a cardiomyocyte of the working myocardium ranges from 50 to 120 μm, its diameter between 5 and 25 μm [1].
Every myocyte is linked to one or more capillary for the support with oxygen and nutrients needed for the metabolism (fig. 2.2). The cell's interior is surrounded by the cell membrane to separate the intracellular space from the extracellular space. Specific membrane proteins, which form pores in the membrane, enable the transport of e.g. ions and metabolites. The intracellular space of a cardiomyocyte consists mainly of the nucleus, mitochondria, the sarcoplasmic reticulum and some thousands myofibrills.

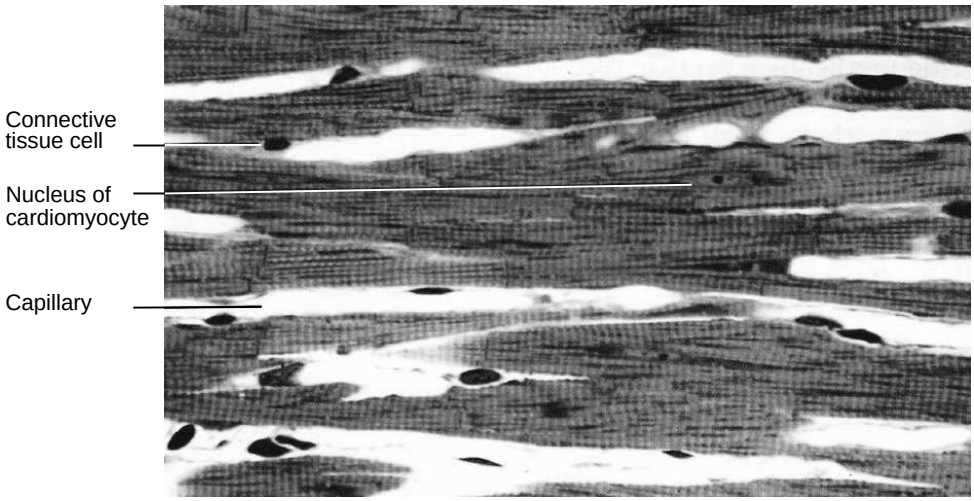

Fig. 2.2. Cross-section through the left ventricular myocardium. The branched muscle fibers build a net-like structure. Connective tissue is located between layers of muscle bundles. Each cell has one nucleus and is supplied by capillaries. Fig. adapted from [10].

2.1.1 Cell Membrane

The cell membrane of a cardiomyocyte (sarcolemma) consists of a selective permeable phospholipid bilayer. The lipids of the membrane halves are oriented in such a way that the hydrophobic tails are connected to each other. The hydrophilic heads are grouped to the outer side and are in contact with the aqueous solution of the intracellular and the extracellular space. The thickness of the sarcolemma ranges between 4 and 5 nm [12].
The cell membrane of most cardiomyocytes forms intrusions at certain distances spreading at the z-discs along the junctional part of the sarcoplasmic reticulum into the cell (fig. 2.3). The activation of the cell can be conducted near to the sarcoplasmic reticulum through these

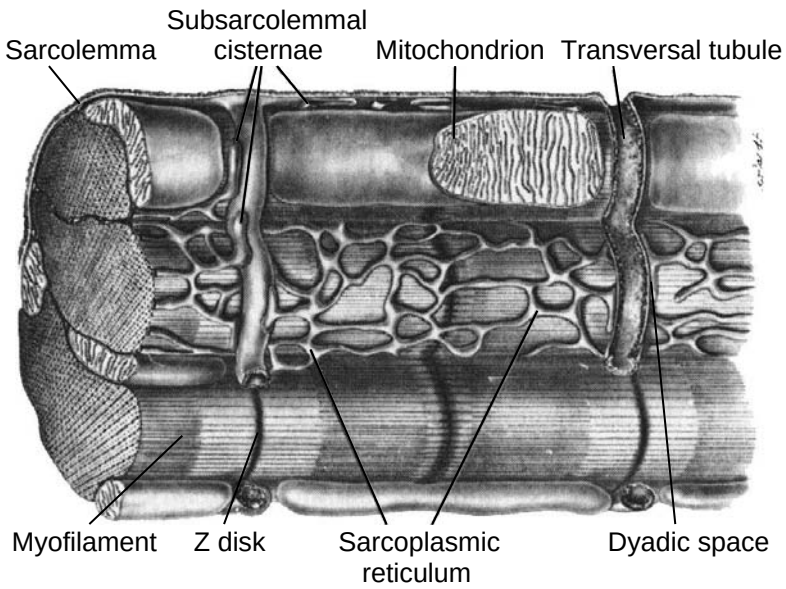

Fig. 2.3. Schematic description of the intracellular structures of a cardiomyocyte. The sarcolemma surrounds the cells interior. Important intracellular structures are e.g. the mitochondria as the generator of the cell's chemical energy carrier, the sarcoplasmic reticulum as a large calcium buffer and the myofilaments as the tension generating unit. Fig. adapted from [11].

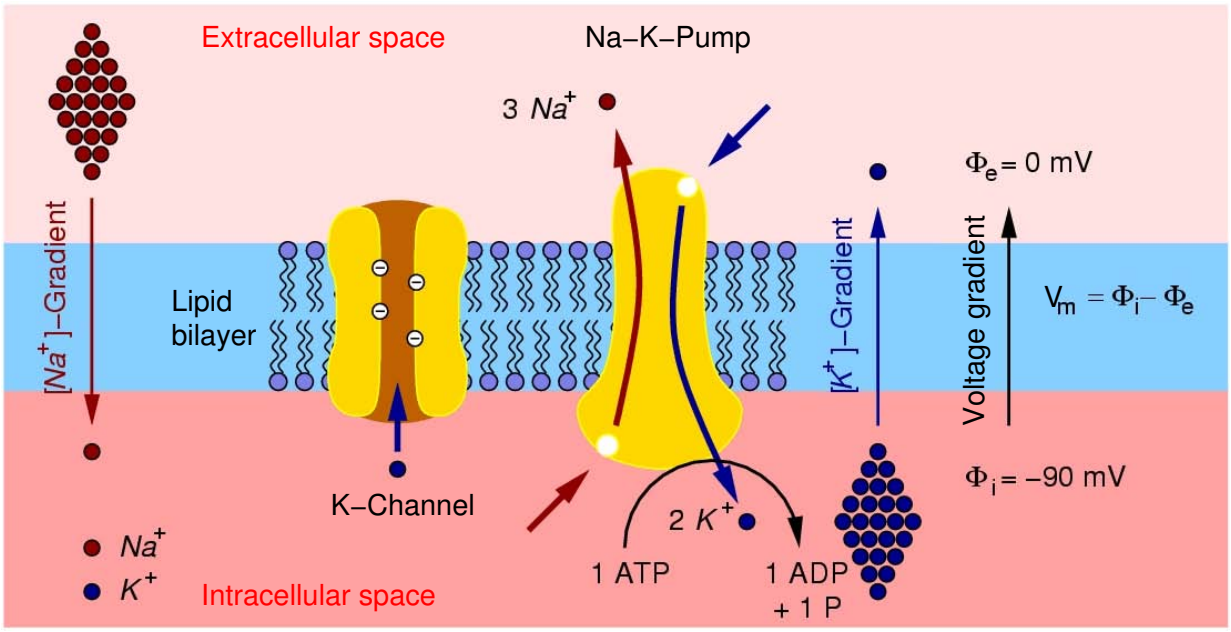

Fig. 2.4. Schematic description of the cell membrane including membrane proteins and ionic concentrations for K^+ and Na^+. Red and blue circles characterize Na^+ and K^+ ions, respectively. The Na-K pump and one exemplary K^+ channel as transmembrane proteins are marked in yellow. The binding sites of the K^+ channel are displayed with a minus sign. The thin arrows across the membrane depict the direction of concentration and voltage gradients. The thick arrows show the direction of the ion flow through the membrane proteins. Fig. adapted from [12].

so-called transversal tubuli (T tubules). The fraction of the T tubule surface of the whole sarcolemmal area is between 10 % and 50 % [13].
Various pore forming proteins are included in the sarcolemma. These pores are mainly specific to distinct ion types e.g. sodium, potassium and calcium. Also exchanger and pump proteins are located in the membrane. Specific calcium channels are located in the membrane of the transversal tubuli to trigger the calcium release of the sarcoplasmic reticulum into the intracellular domain (myoplasm). In contrast to membrane ion channels, the low resistance ohmic coupling pores between adjacent cells, so-called gap junctions, do not show ion selectivity. The structure of the ionic channels, exchangers, and pumps as well as of the gap junctions is described in detail below.

2.1.1.1 Ionic Channels, Exchanger and Pumps

Various pore forming proteins are inserted in the sarcolemma (fig. 2.4). They normally have a cylindrically shaped form with a diameter of approximately 1 nm [12]. These proteins function as ionic transport, exchange or pumping mechanisms, specified by the ion type, which can pass through, e.g. the sodium channel, calcium channels, potassium channels, the sodium-calcium exchanger and the sodium-potassium pump. All these proteins define the selective sarcolemmal permeability to the specific ion type. Their molecular structure and electrophysiology can vary under a subdivision group of each channel type. Their gating characteristics is described by an opening and closing behavior (section 4.3).
All functional channels consist of several subunits coded by different genes (fig. 2.5). Additionally to the channel building α-subunits, several coexisting subunits, i.e. β- and γ-subunits, can modulate the channels function. Thus, a wide range of channel function is possible with species, organ or even tissue specific expression.

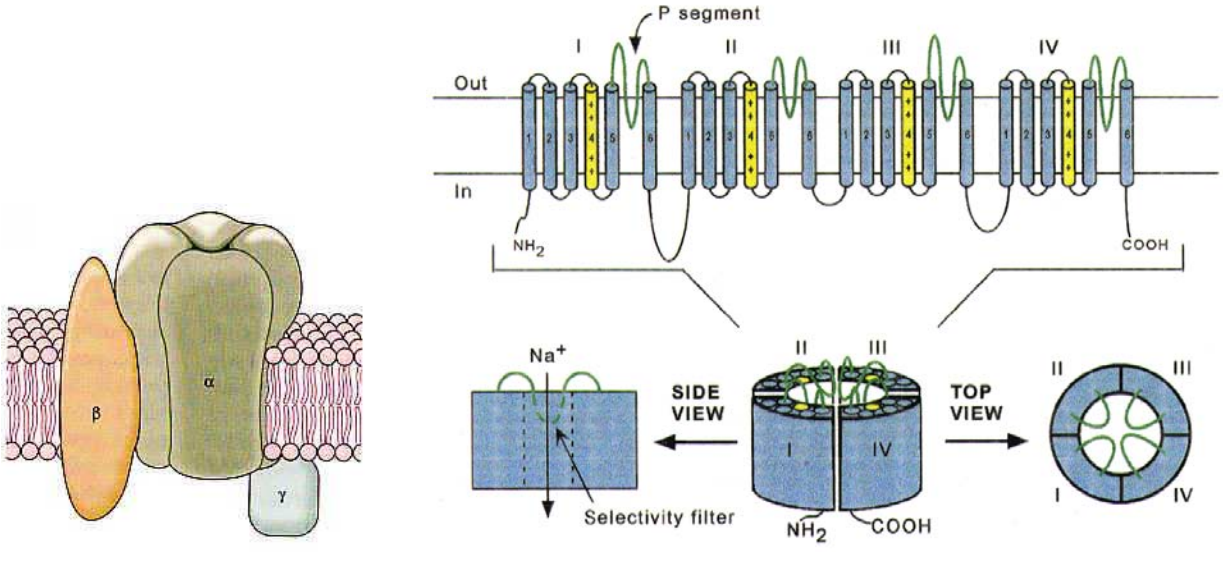

(a) (b)

Fig. 2.5. Construction of ion channels I. (a) Schematic description of the structure of an ion channel. The characteristics of the channel building α-subunits is modulated by further (β, γ)-subunits. (b) Structure of the Na^+ channel. Four equal elements consisting of six transmembrane segments form the pore with the P segment as the selectivity filter. Figs. from [14].

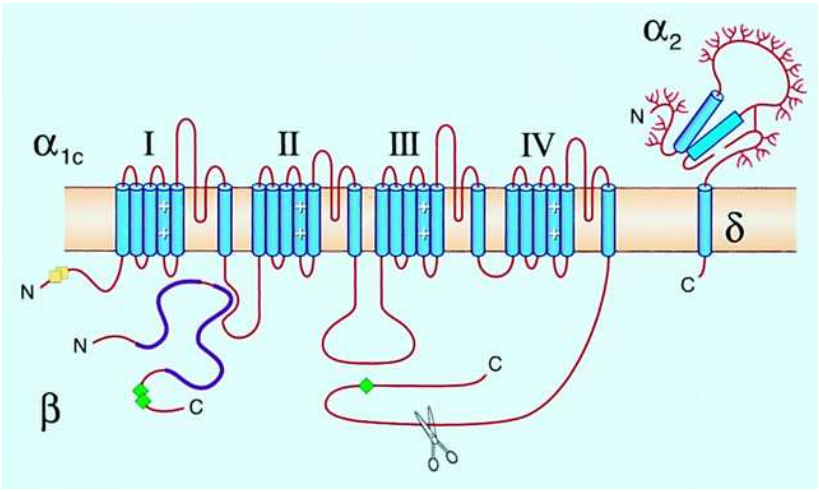

(a)

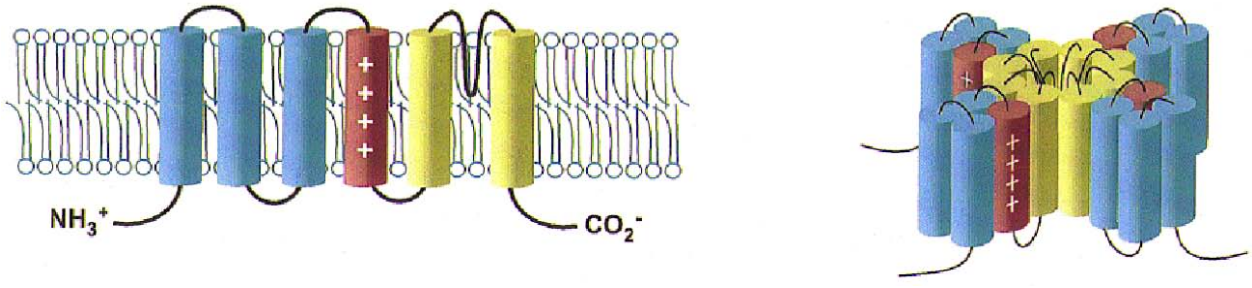

(b)

Fig. 2.6. Construction of ion channels II. (a) Structure of the L-type Ca^{2+} channel [15]. (b) Structure of voltage gated K^+ channel α-subunits [16].

Different proteins exist for carrying different ion types. One specific type of Na^+ channel is predominantly expressed in cardiac myocytes (fig. 2.5b). In the group of calcium and potassium channels, several different variations exist. Two calcium channels are predominant in cardiac sarcolemma [17, 18, 19, 20]. One is the L-type Ca^{2+} channel or so-called dihydropyridine receptor (DHPR), which is located in the sarcolemmal membrane of the T tubules (fig. 2.6a). The other is the T-type Ca^{2+} channel, which is a channel with less expression in ventricular cells but prominent in most other excitable cells of the heart.
A large variety of potassium channels are expressed in the heart [21, 22, 23, 24]. The potassium channels can be divided into two classes: One class with two transmembrane segments and one pore in-between (2Tm–1P channels) and the other with six transmembrane segments and a pore (6Tm–1P channels). The 2Tm–1P K^+ channels have inward rectifying characteristics. The characteristics of the 6Tm–1P class are the voltage-dependent activation, inactivation and deactivation of the channels (fig. 2.6b).

2.1.1.2 Gap Junctions

At the coupling region of neighboring cells, the so-called intercalated discs, specialized proteins of adjacent cells form in a bundled manner a low electrical resistance pore called gap junction (fig. 2.7) [25, 26, 27]. Near this area, the adjacent cells are mechanically glued together [28]. The intercalated discs are mainly located near to the ends of cardiomyocytes [29]. A gap junction is a cylinder or barrel shaped construction with a length of 2 – 12 nm and a channel diameter of 1.5 – 2 nm (fig. 2.7c). It is an intercellular channel, composed of two connexons, each belonging to another cell. They build a gap of 2 – 3 nm (fig. 2.7b). A connexon is a hexamer of six proteins called connexins. The hydrophilic channel is surrounded by the hexamer of both connexons. Molecules of an atomic weight up to 1 kD can pass the gap junction e.g. ions, nutrients and metabolites [33, 34].

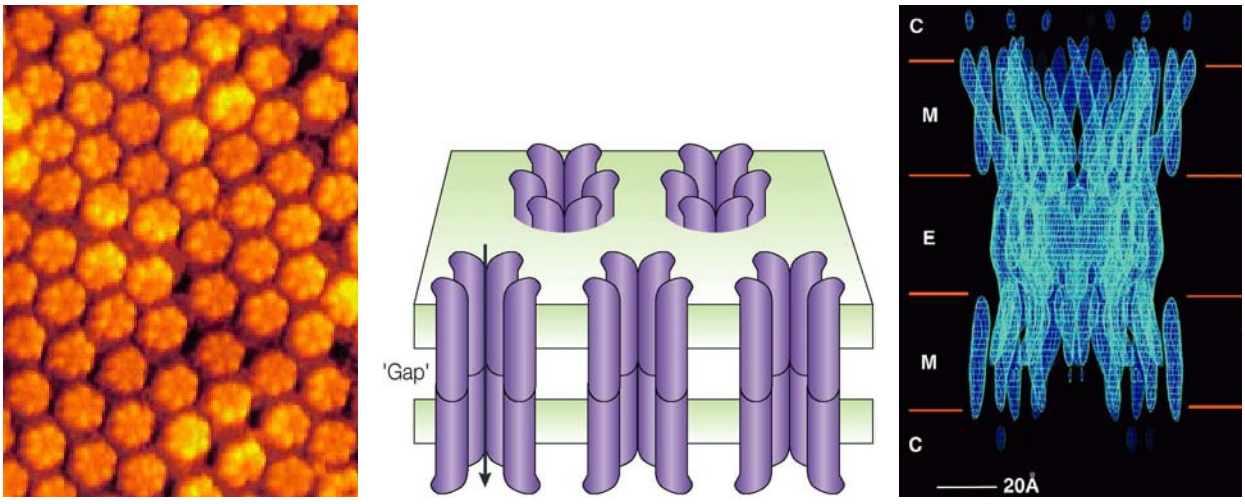

(a) (b) (c)

Fig. 2.7. Construction of a gap junction. (a) Extracellular connexon surface and arrangement of connexons in atomic force microscopy. Each connexon has an average diameter of 8 nm [30]. (b) Schematic description. Two connexons, each build of six connexins, join at the gap of two adjacent cells and form the gap junction. The axial channel (marked by the arrow) provides a direct connection between two cells [31]. (c) Side view of the molecular organization of a gap junction with "E" the extracellular gap, "M" the membrane area and "C" the cytoplasmic space [32].

The density and distribution of gap junctions differ depending on the tissue type [35]. As the density of gap junctions in e.g. the sinoatrial node is much less than in ventricular myocardium, excitation velocity in the sinoatrial node is much slower than in ventricular myocardium. Also, the arrangement of the intercalated discs play an important role in the anisotropic electrical properties of the coupling. The ratio of longitudinal to transverse conduction velocity e.g. in the crista terminalis is 10:1 compared with 3:1 in the ventricles [35].

2.1.2 Intracellular Components

The nucleus, mitochondria, myofibrils, sarcoplasmic reticulum and cytoskeleton are located in the intracellular space of the cardiomyocytes (fig. 2.3). The remaining volume of the intracellular space is filled with a liquid solution containing lipids, carbon hydrates, salts and proteins. The important structures for the electromechanical function of the intracellular space of a cardiomyocyte are explained below.

2.1.2.1 Mitochondria

Mitochondria are cellular organelles with a length of 0.3 – 1.7 μm and a diameter of 0.2 – 1 μm. They are surrounded by a bilayer membrane also containing membrane channels. Mitochondria supply the cell and other cellular components with energy by metabolism. This function is performed by its internal components. The ribosomes generate adenosine triphosphate (ATP) via oxygenation of nutrients. About 14 – 20 % of the volume of atrial and 25 – 36 % of ventricular myocytes is occupied by mitochondria. As a cellular energy provider, mitochondria are located near to the energy recipients such as the myofilaments and the ATP consuming membrane pumps. Mitochondria are also the structures where the oxidative phosphorylation and the tricarboxylic acid cycle take place [36].

2.1.2.2 Myofibrils

Myofibrils are tube shaped fibers in which the mechanical tension of the cells is generated. They are build up of connected sequences of the contractile functional units called sarcomeres. Each sarcomere is packed with bundles of myofilaments. The myofilaments comprise actin and myosin filaments. Approximately 41 – 53 % of the volume of atrial and 45 – 54 % of ventricular working myocytes are filled with myofibrils. The thickness of a myofibril is in the range between 1 and 3 μm [37].

Sarcomere Alternating light and dark bands appear along cardiomyocytes in the microscope. That is the reason why the cardiac muscle is called striated. The structure of the sarcomere is shown in figs. 2.8 and 2.9. The larger dark A bands are bisected by a dark narrow strip, the H zone. M discs are found in the center line of the H zone. The narrow light I bands are bisected by the Z disc appearing like a black line. The Z discs function as an anchor point for the actin filaments. The segment between two Z discs is the sarcomere.
Each sarcomere has a resting length of 1.6 – 2.2 μm with the mean resting length of 2 μm. The sarcomere can be shortened to about 80 % of the resting length. Besides mechanical active myofilaments, the sarcomere contains of passive mechanical structures like titin and nebulin. Titin binds the myosin filament elastically to the Z discs [39]. Nebulin is coupled closely to the whole actin filament and is important for the regular appearance of actin.

Myofilaments The myofilament as the tension generating unit is build up of two types of filaments: thin filaments and thick filaments (fig. 2.10). The two lightly stained sides of the

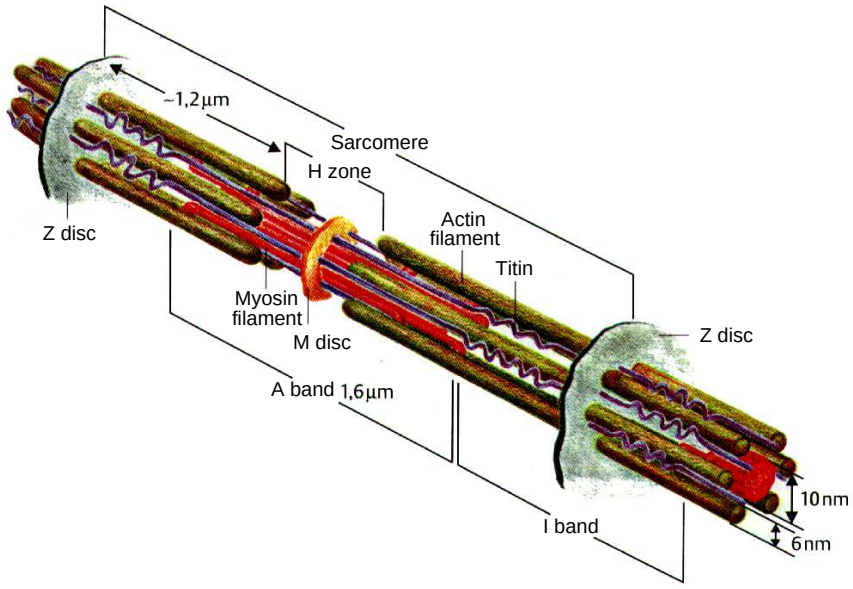

Fig. 2.8. Schematic description of a sarcomere of a cardiomyocyte. The sarcomere is located between two Z discs. The actin filaments of the sarcomere are fixed in their central area to the Z discs i.e. the actin chain extends into two adjacent sarcomeres. The myosin filament is located in the middle of the sarcomere and bound to the Z discs via the flexible titin filament. The area with myosin is called A band. The area where only actin is visible is called I band. The H zone is the area where only myosin is visible. In the middle of the H zone is a thin membrane called M disc. Fig. adapted from [38].

Z disc are composed of thin filaments, the so-called actin filaments. Myosin filaments can be exclusively seen in the H zone. The myosin filaments are neighbored to each other in a triagonal lattice with an actin filament within. The array of neighbored actin filaments builds a hexagonal lattice surrounding a myosin filament. Besides actin and myosin, myofilaments also include associated components like troponin and tropomyosin.

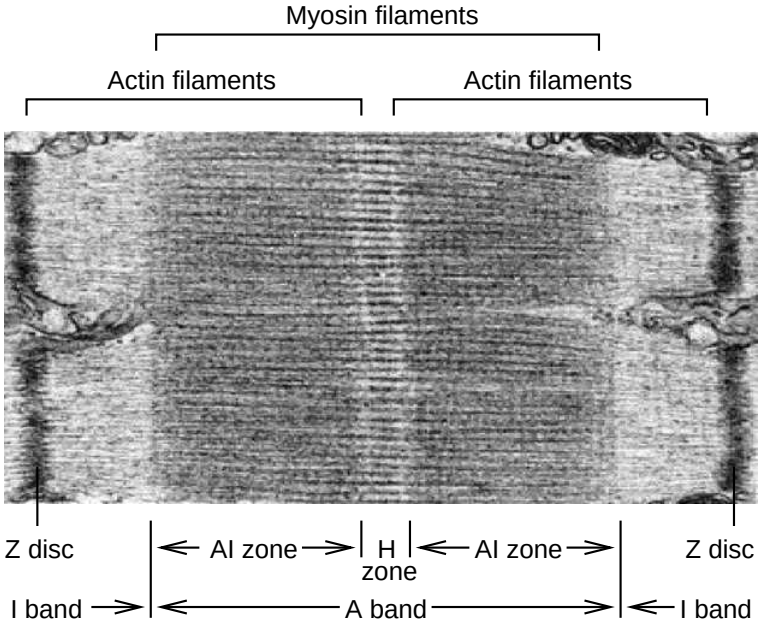

Fig. 2.9. Electron micrography of a sarcomere of a cardiomyocyte. Fig. adapted from [37].

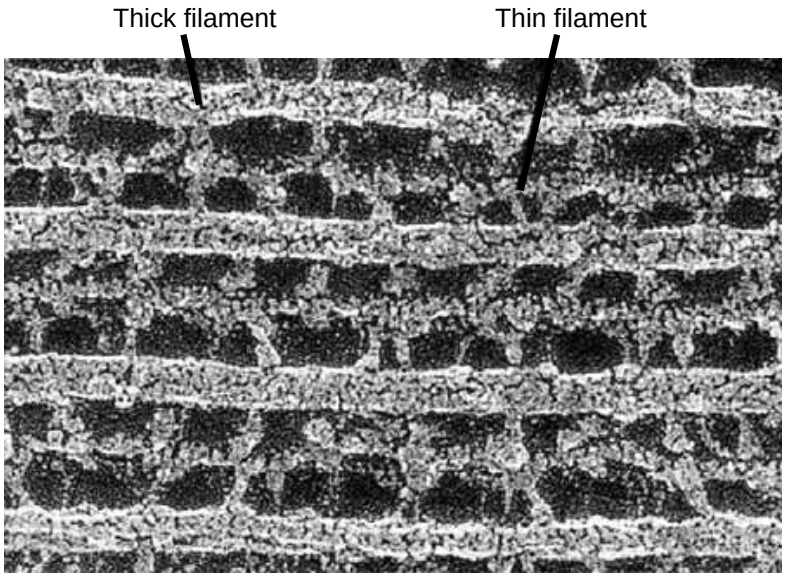

Fig. 2.10. Electron micrography shows actin myosin cross-bridges in the AI zone of a striated flight muscle of an insect. This image shows a nearly crystalline array of thick myosin and thin actin filaments. The muscle was in rigor state at preparation. The myosin heads, protruding from the thick filaments, connect with the actin filaments at regular intervals. Fig. adopted from [37].

Thin filament The thin filament is build up of the three components actin, tropomyosin (Tm) and troponin (Tn) with three subunits (fig. 2.11). Actin is a polymer consisting of approximately 350 spherical G actin monomers that are build together to a long strip called F actin. Bound to the Z disc, two actin strips build in a double helix form the main component of the thin filament. In the gap between the actin filaments lies the rope-like protein chain of several tropomyosins where the heads and tails of the tropomyosins are connected to each other [40]. Every tropomyosin protein extends along seven actin monomers. The tropomyosin is located between the two actin filaments in the resting position and the binding site for myosin is hidden.
The troponin complex with its three components troponin C (TnC), troponin I (TnI) and troponin T (TnT) is located at the end of each tropomyosin (fig. 2.11). TnC is the Ca^{2+} binding subunit, TnI is the actin bound and actin-myosin ATPase inhibiting part, and TnT the tropomyosin binding site, having a head and a tail part. Due to the binding of Ca^{2+}

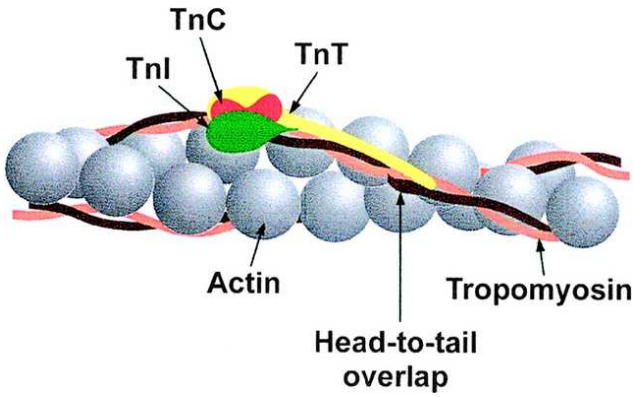

Fig. 2.11. The thin filament is constructed of three proteins: actin, tropomyosin and troponin. Troponin contains the three functional subunits: troponin C (TnC), troponin I (TnI) and troponin T (TnT). Fig. adapted from [40].

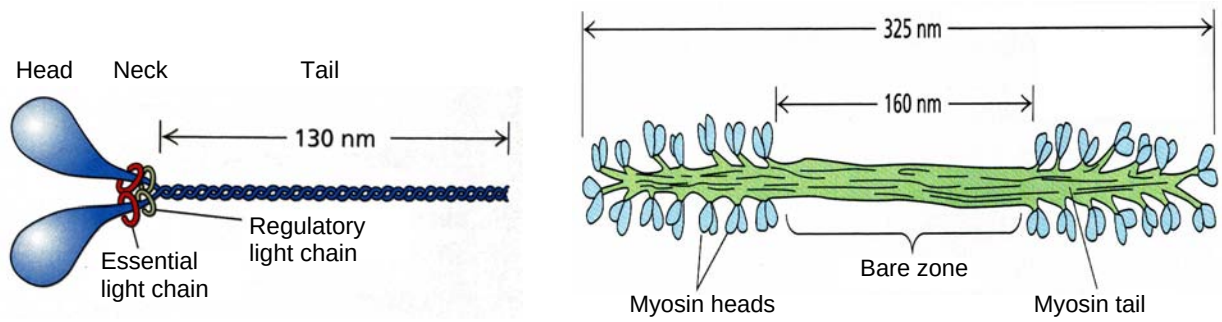

(a) (b)

Fig. 2.12. Structure of a thick filament. (a) The myosin II protein is organized into head, neck, and tail domains. (b) The thick filaments are polymers of myosin II. The heads are located at both ends of the bare zone of the thick filament. Figs. adapted from [39].

to troponin C the troponin-tropomyosin complex is shifted and the myosin binding site of actin is exposed. Only in this state, the cross-bridge cycle of actin and myosin is enabled (section 6.1).

Thick filament The thick filament is composed of several myosin II molecules, which are all approximately 150 *nm* long (fig. 2.12). The thick filament has a diameter of 15 *nm* and a length of approximately 325 *nm*. Each myosin filament consists of two ball shaped heads, a neck region, and a tail domain, which are build of coiled coil molecules. The head group, which is also called the motor domain, contains a binding site for actin and a pocket for the binding and hydrolysis of ATP. The conformation changes in the head group, which is closely coupled with the binding and hydrolysis of ATP, are responsible for the binding with actin and the development of tension during a contraction. Two light chains are located at the neck region, which influences the stiffness of the neck region and the activity of the head group. The tail domains of several hundred myosin molecules couple to each other forming the thick filament. The thick filament has head groups at both ends, organized in opposite directions. The area where no head groups are located is called bare zone.

2.1.2.3 Sarcoplasmic Reticulum

The sarcoplasmic reticulum (SR, fig. 2.3) is an intracellular organelle and is entirely separated from the myoplasm by a membrane. The SR acts as a high capacitance reservoir for calcium. The volume of the SR takes 0.83 – 9.93 % of the whole cell volume [13]. The SR can be divided into two parts: the network SR, also called longitudinal tubule, forming a mesh throughout the inner space of the cell along the sarcomeres and the junctional SR mostly building an immediate neighborhood to the T tubules.
Several ionic channels are inserted in the membrane of the SR regulating the myoplasmic concentration of calcium. Thus they are mainly supporting the excitation contraction coupling. Sarcoplasmic proteins are e.g. the ryanodine receptor, phospholamban, triadin and junctin.

Network sarcoplasmic reticulum The network SR (NSR) is usually wrapped around a sarcomere. The NSR can also spread out into neighboring sarcomeres. The NSR of cardiomyocytes is not as organized as the NSR of skeletal myocytes. Mainly Ca^{2+} pumps are found in a constant density along the membrane of the NSR.
A membrane protein located in the NSR is phospholamban. Depending on the phosphorylation state, phospholamban binds to and regulates the activity of the SR Ca^{2+} pump [41].

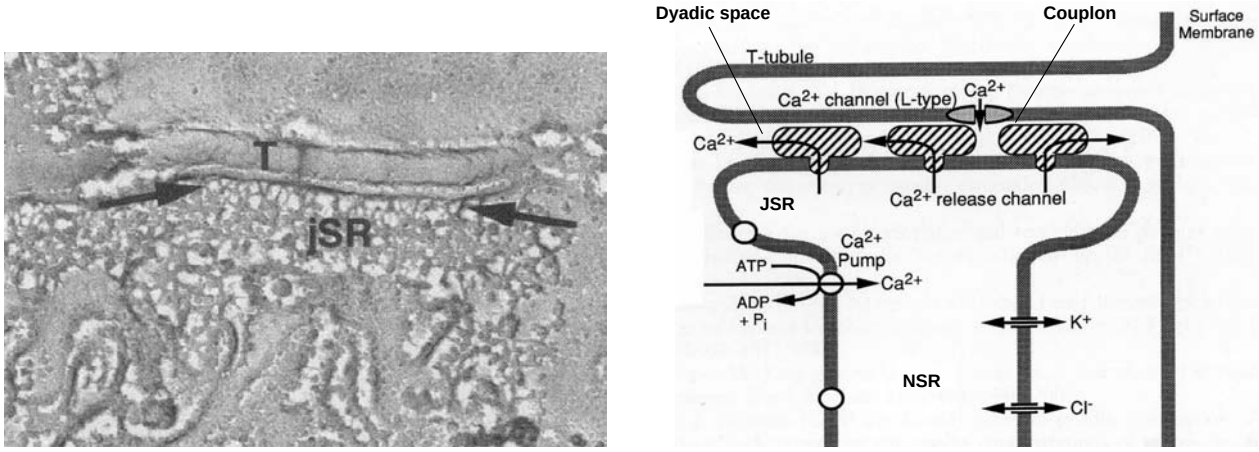

(a) (b)

Fig. 2.13. Junction between T tubule and sarcoplasmic reticulum (SR). (a) At the T tubule (marked with T) is a dyad with the terminal cisternae part of the SR (marked with jSR). The lumen of the junctional SR (JSR) is filled with a network of calsequestrin. Linking structures connect calsequestrin protein groups to the junctional side of the terminal cisternae (marked by two arrows). Fig. from [44]. (b) Schematic representation with the JSR, the network SR (NSR), the dyadic space and a couplon between sarcolemmal Ca^{2+} channels and SR Ca^{2+} release channels. Fig. adapted from [45].

Thus, phospholamban is an important modulator in the excitation contraction coupling. An over-expression of phospholamban can e.g. cause contractile failure [42, 43].

Junctional sarcoplasmic reticulum The main part of the junctional SR (JSR) is located close to the T tubules (fig. 2.13). The JSR has sac-like vesicles called terminal cisternae. A single contact between a terminal cisternae and the T tubule is called dyad, the space inside this cleft is named dyadic space.
Specific proteins are inserted in the membrane of the JSR, which are called ryanodine receptors (RyR). The RyRs are 12 *nm* long and are organized as large arrays. One array can have a diameter of up to 200 *nm* consisting of up to 100 RyRs [46].
The RyRs of the JSR and the DHPRs of the T tubules form a functional unit at the dyads called couplon. The function of the couplon determines the cellular excitation contraction coupling as it controls mainly the release of calcium from the SR into the myoplasm [47].
Several proteins are located inside the JSR involved in the excitation contraction coupling process. These proteins include calsequestrin, which is a SR resident protein and are connected to the RyRs [48, 49]. The regulatory effect of calsequestrin is mediated by the membrane anchoring proteins triadin and junctin.

2.2 Tissue Types of the Myocardium

The heart mainly consists of myocytes of the atrial and ventricular working myocardium. Other cardiac tissues are blood vessels that are attached to the heart, valves that control the blood flow direction, and the system of excitation initiation and conduction. Furthermore, connective tissue in the skeleton of the heart and in-between myocytes as mechanical connections as well as nerves of the autonomous nervous system modulating the properties of the myocytes especially the ones of the initiation and conduction system exist [50].

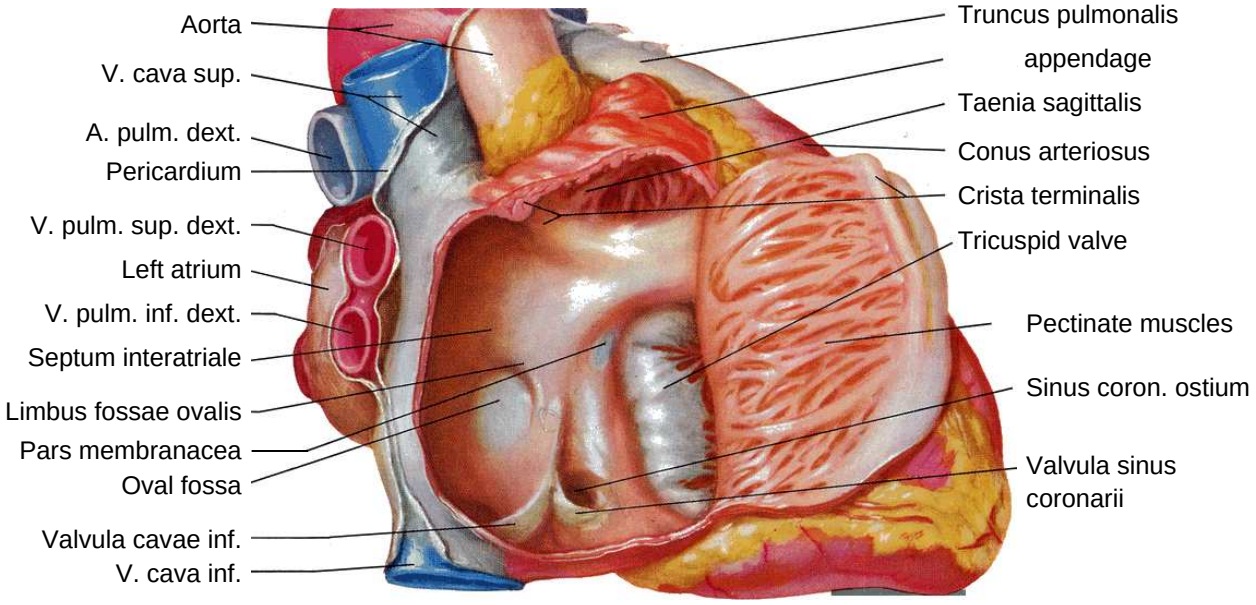

Fig. 2.14. Opened right atrium. Important structures for describing atrial electrophysiology are the right and left atrium, the crista terminalis, pectinate muscles, the oval fossa, and the atrial appandages. Fig. adapted from [51].

2.2.1 Atria

The two atria form the upper part of the heart (fig. 2.14). Right and left atrium are separated by the septum interatriale. The atrial septum consists of myocardium with exception of a central region, named oval fossa, where connective tissue is located. The inferior and superior vena cavae as well as the sinus coronarius are connected to the right atrium. The vessels connected to the left atrium are the four pulmonary veins (fig. 2.15). The myocardium of the atria has an average thickness of less than 2 mm.
Both atria have an appendage, which is capable to store blood and thus enlarge the capacity of the atria. The right appendage is nearly triangular and is located near the Aorta ascendens. The left appendage lies lateral of the truncus pulmonalis.
A distinct muscle bundle called crista terminalis (CT) is located at the inner side of the right atrium. The CT has a thickness of 5 – 8 mm and is spreading from the anterior side of the atrial septum along the orifice of the superior vena cava towards the inferior vena cava and vanishes near the orifice of the sinus coronarius [52]. Adjoining from the crista terminalis, smaller muscular structures i.e. pectinate muscles spread over the rest of the right atrium towards the tricuspid valve.
The sinoatrial node (SAN) is located at the orifice of the superior vena cava adjacent to the CT [53]. The SAN has a length of 10 – 30 mm, nearly the thickness of the atrial wall and spreads along the CT towards the inferior vena cava. The size, shape and location of the SAN can vary. The normal length is 20 mm, the width is 5 mm. In the physiological case, the SAN is the primary pacemaker of the heart.
The Bachmann bundle starts near to the SAN as interatrial connection and spreads near to the left atrial appendage. A further interatrial connection is related to the coronary sinus and the limb of the oval fossa. The left atrium has also pectinate muscles starting from the Bachmann bundle but they are not as strongly developed as in the right atrium.

2.2.2 Ventricles

The two ventricles form the lower part of the heart (fig. 2.15). The right and left ventricle are also separated by a septum. The ventricular septum is consisting only of myocardium. The ventricular walls are enclosed by the epicardium and the endocardium. The thickness of the left ventricular structures is larger than of the right ventricle due to the different pressure it works against. The ventricles are electrophysiologically inhomogeneous in transmural as well as in apico-basal direction. No large morphological distinctions of the myocytes can be seen in different regions of the ventricle.
The connections to the atria and the descending vessels are located at the upper part of the ventricles called ostia [54]. In the left ventricle, the mitral and the aortic ostium are found where the mitral and the aortic valves are located. The right ventricle has the tricuspid and the pulmonary ostium also associated to the corresponding valves.
At the inner side of the ventricles, structured muscles are attached (fig. 2.15), the papillary muscles and trabeculae. Papillary muscles are connected at the one end to the subendocardial myocardium and at the other end via tendons at the atrioventricular valves. Trabeculae are muscular bundles that pervade the ventricle at the endocardium.

2.2.3 Excitation Initiation and Conduction System

The sinoatrial node (SAN) as the primary pacemaker of the heart and the atrioventricular node (AVN) as the secondary pacemaker (fig. 2.16, section 4.7.2) are belonging to the excitation initiation system (fig. 2.17). The AVN is only a pacemaker if the SAN is not depolarizing or if the excitation is not conducted towards the AVN. Deeper structures like the His bundle,

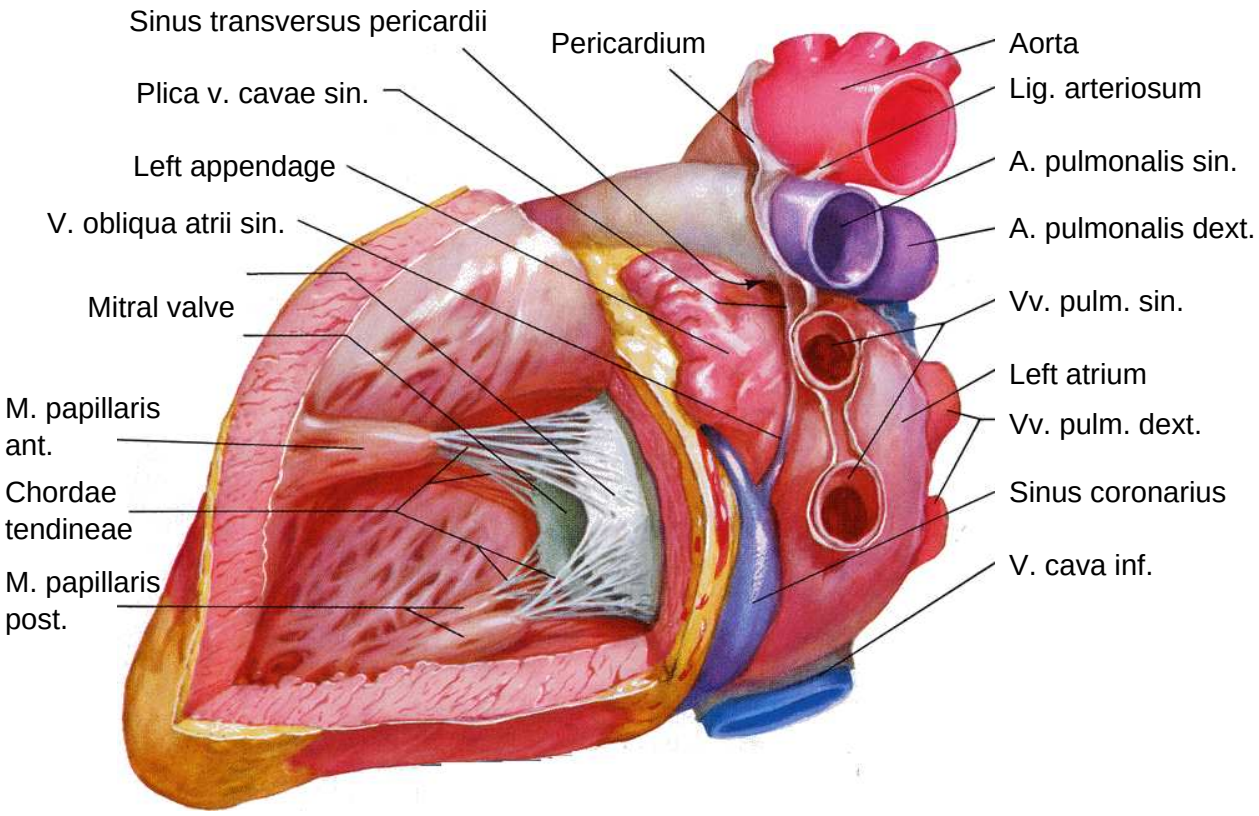

Fig. 2.15. View in the opened left ventricle and on the left atrium. The thicknes of the left ventricular wall is approx. 2 *cm*. Fig. adapted from [51].

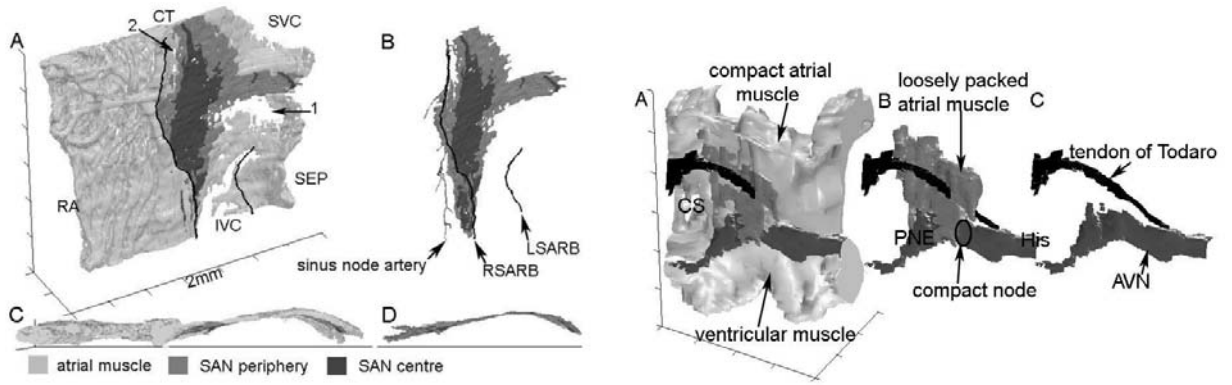

(a) (b)

Fig. 2.16. Anatomical model of the SA and the AV node. (a): 3D SAN model with (A), and without surrounding tissue (B), and in top-down view (C) and (D), respectively. (b): 3D AVN model with surrounding tissue (A), with loosely packed atrial muscle (B), and with tendon of Todaro (C). Figs. from [55].

the Tawara branches, and the Purkinje fibers can also depolarize spontaneously. This will happen, if the excitation is not conducted by the AVN e.g. III. degree bundle block. This initiation system is called tertiary.

Two different types of cells were observed in the SAN [56]: central cells, acting as primary pacemaker cells and having a spindle-like shape as well as peripheral cells, conducting the excitation towards the CT having a spider-like shape. Central cells have a length of 115 –

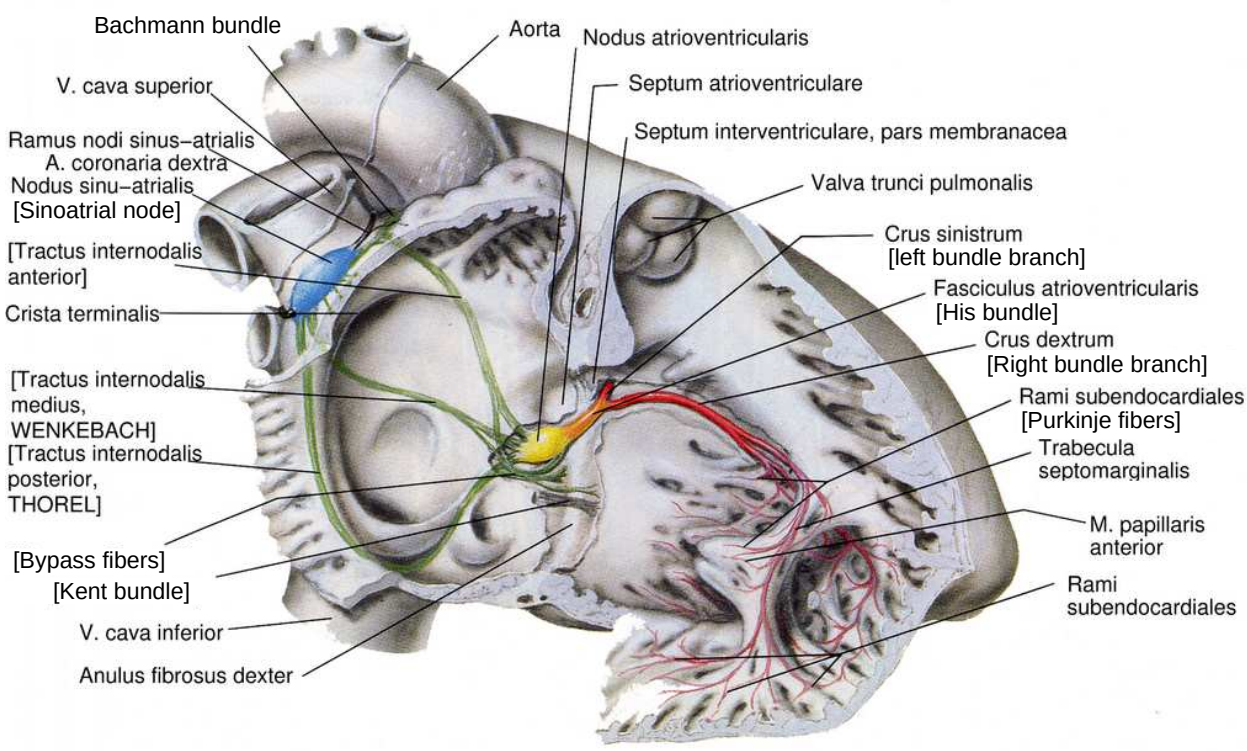

Fig. 2.17. Cardiac excitation initiation and conduction system. The primary pacemaker is the sinoatrial node. Fast bundles in the right atrium are the crista terminalis, pectinate muscles, and the internodal bundles. Interatrial connections are the Bachmann bundle, the limbus of the oval fossa and a connection located by the coronary sinus. The AV node is the secondary pacemaker. The excitation conduction system consists of the His bundle, the Tawara branches, and the Purkinje fibers, which spread network-like into the subendocardial myocardium. Fig. from [51].

130 μm and a diameter of 5 – 7 μm whereas peripheral cells extend to 92 – 102 μm with a diameter of 7 – 9 μm. 45 – 50 % of the SAN consists of a matrix of connective tissue where the SAN cells are packed in [57]. Sympathetic and parasympathetic innervation influences mainly the frequency of the SAN and thus of the heart [58].
The AVN is located in the lower atrial septum close to the orifice of the coronary sinus within the triangular area described by Koch (fig. 2.16 b) [59]. The AV junctional area can be divided into atrial approaches to the AVN, the AVN itself, and the AV bundle [60]. Different cell types can be distinguished in the AVN: transitional, mid-nodal, and low-nodal cells. The distal part of the AVN is surrounded by elastic and collagen connective tissue and descends into the His bundle.
The excitation conduction system is located in-between the AVN and the working myocardium of the ventricles. It consists of the His bundle, the Tawara bundle branches and the extended network-like Purkinje fibers. The His bundle is isolated by fibrous tissue and is the only physiological electrical pathway between atria and ventricles. The His bundle merges into the left and right Tawara bundle branches [53]. The end of the branches are connected to Purkinje fibers, which build a dense network and are finally connected to the subendocardial ventricular working myocardium via gap junctions.

2.3 Muscle Fiber Orientation

The macroscopic anisotropy of the electrical excitation conduction as well as of the contraction is strongly influenced by the shape of the cardiomyocytes, the anisotropy of mechanical and electrical coupling at the intercalated discs and the orientation of the muscle fibers and layers inside the myocardium. The ventricular myocardium has an oriented and laminated structure. Large differences in the structuring between atria and ventricles exist [2].

2.3.1 Atria

The atrial fiber orientation is not as structured as in the ventricle (section 2.3.2). Only the conduction pathways i.e. crista terminalis and Bachmann bundle, the pectinate muscles and the tissue near the mitral and tricuspidal ostia, near the superior and inferior vena cavae and near the pulmonary veins have an organized orientation. The fiber orientation of the atrial working myocardium has a complex and nearly unstructured fashion [61]. Also, an unstructured fiber orientation is reported inside the sinoatrial node [53].

2.3.2 Ventricles

The muscle fiber orientation in the ventricles is oriented and laminated in an organized manner [63, 64, 65, 66, 67]. The measurements of Streeter in human left ventricular tissue showed a continuos transmural rotation of the main helix angle, which is the angle of the fiber parallel to the local endocardial surface [66]. An angle of 0° is the equatorial direction and an angle of ±90° is the orientation from apex to base.
In the human left ventricle the helix angle is 55° in the subendocardial border and −75° in the subepicardial layer (fig. 2.18). The change of the helix angle in-between is nearly linear with 0° in the middle of the wall. A linear change of the helix angle is reported for the right ventricle. The fiber orientation at the apex and in the middle of the septum is oriented more complex. Papillary muscles have a fiber orientation longitudinal to their first principal axis.

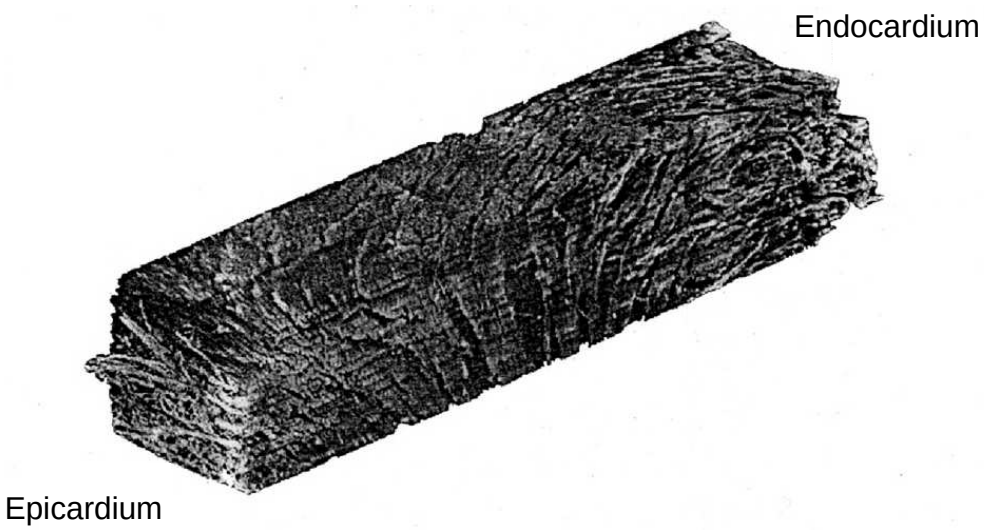

Fig. 2.18. Fiber orientation in a ventricular wall of rat. The rotation of the fiber orientation from endocardium to epicardium is clearly visible. The direction of the main axis of the myocytes vary transmurally in all three planes. Fig. adapted from [62].

Three to ten cardiomyocytes are grouped in the ventricle and surrounded by a network of connective tissue. These bundles of myocytes are loosely coupled by sparse and long collagen fibers building layers of tissue (fig. 2.19). Gaps between these layers can exist, known as cleavage planes. Branches of the bundled layers can connect adjacent layers intersecting the cleavage planes [68]. This complex microscopic and macroscopic arrangement of cardiomyocytes plays an important role for the mechanical function of the ventricles.

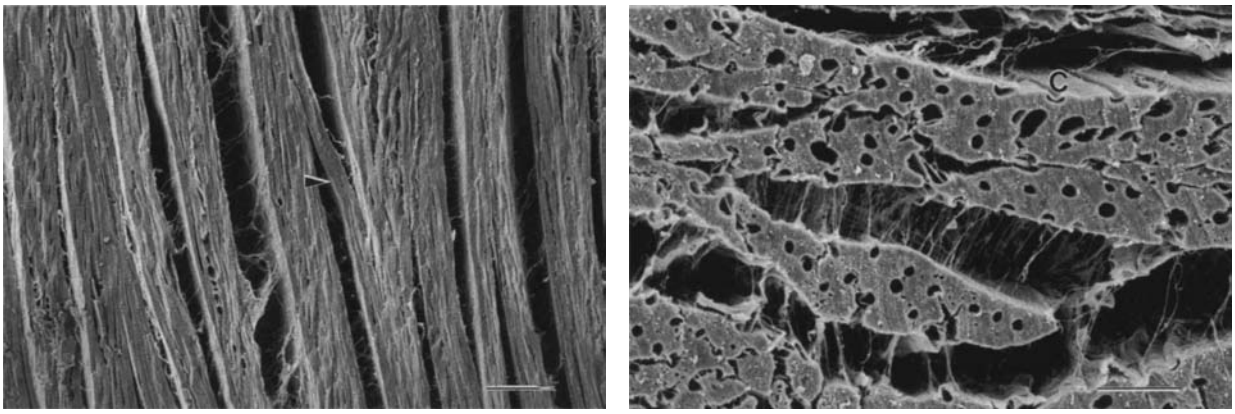

(a) (b)

Fig. 2.19. Micrography of fiber orientation and lamination. (a) The myocytes are organized in layers with branches (arrow) and collagen fibers between adjacent sheets. Scale bar: 100 μm. (b) Myocardial sheets are surrounded by connective tissue, which supports cappilaries (C). Scale bar: 25 μm. Fig. adopted from [68].

3

Modeling Cardiac Anatomy

Digital images together with digital image processing techniques form a base to create models of cardiac anatomy. The process of generating a three-dimensional model using raw image data can be subdivided into several steps [69]. The first step is the generation of the raw morphological image data using medical image devices like magnetic resonance tomography (MR), computed tomography (CT), ultrasonic (US) systems, and color images of cryosections. The next step is the pre-processing of the generated data set to enhance the quality of the data for further processing. The following process is called segmentation, where groups of elements are joined into a region. Then, certain features are extracted from these regions, which is the base for the so-called classification step. During the classification step, equivalent regions are assigned e.g. to a specific tissue class. The whole process of generating models of cardiac anatomy is enhanced by including a priori knowledge.

3.1 Data Material

Most of the data used for anatomical modeling of the human body are provided by data of medical imaging systems. Additionally, available models of the human body can be used, which mostly base in this work on the data provided by the Visible Human Project [70, 71].

3.1.1 Medical Imaging Systems

Medical imaging systems use the interaction of external electromagnetic fields, ionizing radiation, or ultrasonic fields with biological tissue to determine geometrical information. Most of the medical imaging systems used to get three-dimensional information of the body are tomographical or ultrasonic systems. These systems produce one or more slices of an object in one cycle or even full 3D data. Afterwards, the location and orientation of the object or the sensor is changed to get further information from different areas of the body. The data can then be merged into a full three-dimensional data set.

3.1.1.1 Computed Tomography

The computed tomography system is an X-ray based system [72, 73, 74, 75]. The system creates an image of the tissue dependent attenuation coefficient for X-ray. This information is used to get information about the tissue distribution (fig. 3.1a). The CT image is e.g. a transversal slice of the body. The image is reconstructed using projections of several angles around the body.

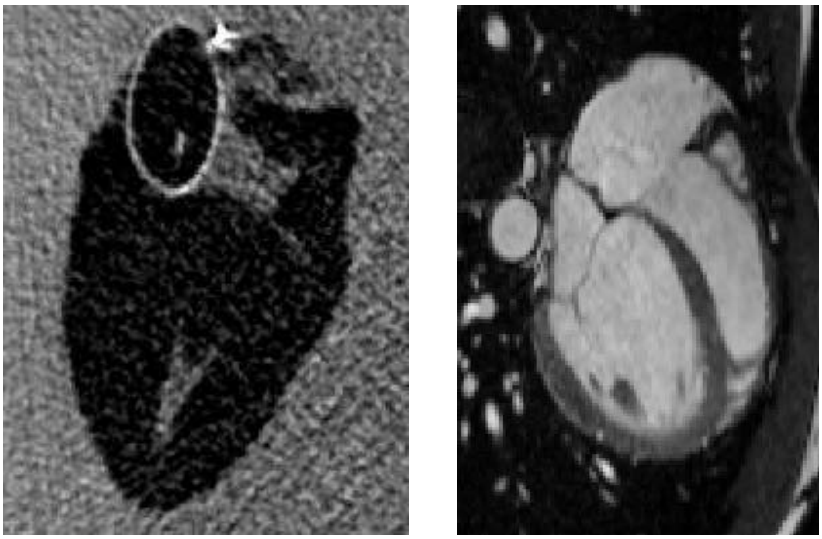

(a) (b)

Fig. 3.1. Images from CT and MRI of the heart. (a) CT image of a Langendorff pig heart in a longitudinal view. The attenuation coefficient of muscle is higher than the one of the aqueous solution making the muscle appear darker. Data from [76]. (b) In vivo MRI image of a human heart in a trans-thoracic view. Data from [77].

3.1.1.2 Magnetic Resonance Tomography

The resonance behavior of nuclei is used for magnetic resonance tomography to determine the distribution of tissue in the body. An additional static magnetic field is applied to achieve sharp resonance absorption. The magnetic field interacts mainly with the hydrogen atomic nucleus, which is present in different densities according to a specific tissue. After application of the nucleus magnetization, the relaxation is measured to determine tissue specific differences (fig. 3.1b). For more information about MRI see e.g. [72, 79, 80, 81].

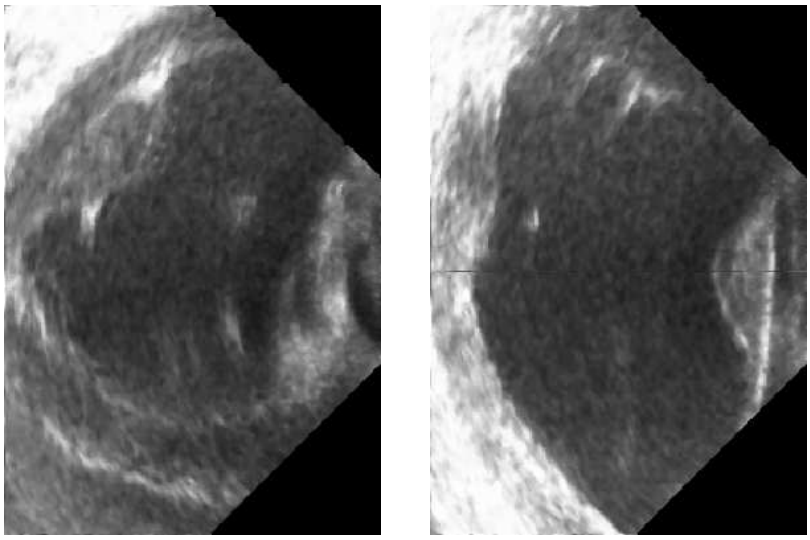

(a) (b)

Fig. 3.2. Images of a pig heart from a 3D ultrasonic device. The US transducer is placed at the epicardium of the right ventricle through the opened chest. (a) Transversal and (b) longitudinal view through the left ventricle of the same animal. Darker areas indicate blood as a homogeneous medium with only few reflections. Data from [78].

3.1.1.3 3D Ultrasonic Devices

Ultrasonic (US) systems are based on measuring the absorption, reflection, refraction, and scattering of ultrasonic waves at the boundaries between two areas with different ultrasonic impedance [72, 82, 83, 84]. The US transducer is build to date of a ceramic piezo element and acts as actor and sensor. An array of piezo elements can be used to achieve two-dimensional images (fig. 3.2). A rotating array of transducers is normally used for a 3D US data set. Today, first piezo element matrix transducers are in the market for full 3D imaging.

3.1.2 Visible Human Project

The National Library of Medicine of the National Institute of Health in Bethesda, Maryland, USA, initiated a project to put a high-resolution anatomical data set of a male and a female at the science disposal [70, 71]. The data was taken from corpses of a 38 year old man and a 59 year old woman. The given data quality and spatial resolution is very high compared to the data of medical imaging systems. CT and MR images were taken from both complete bodies. Afterwards, the corpses were frozen and again CT data was aquired (male body only). The most important data for the Visible Human Project were taken after the freezing. The frozen corpses were sliced and photographical images were taken, the so-called cryosection images.

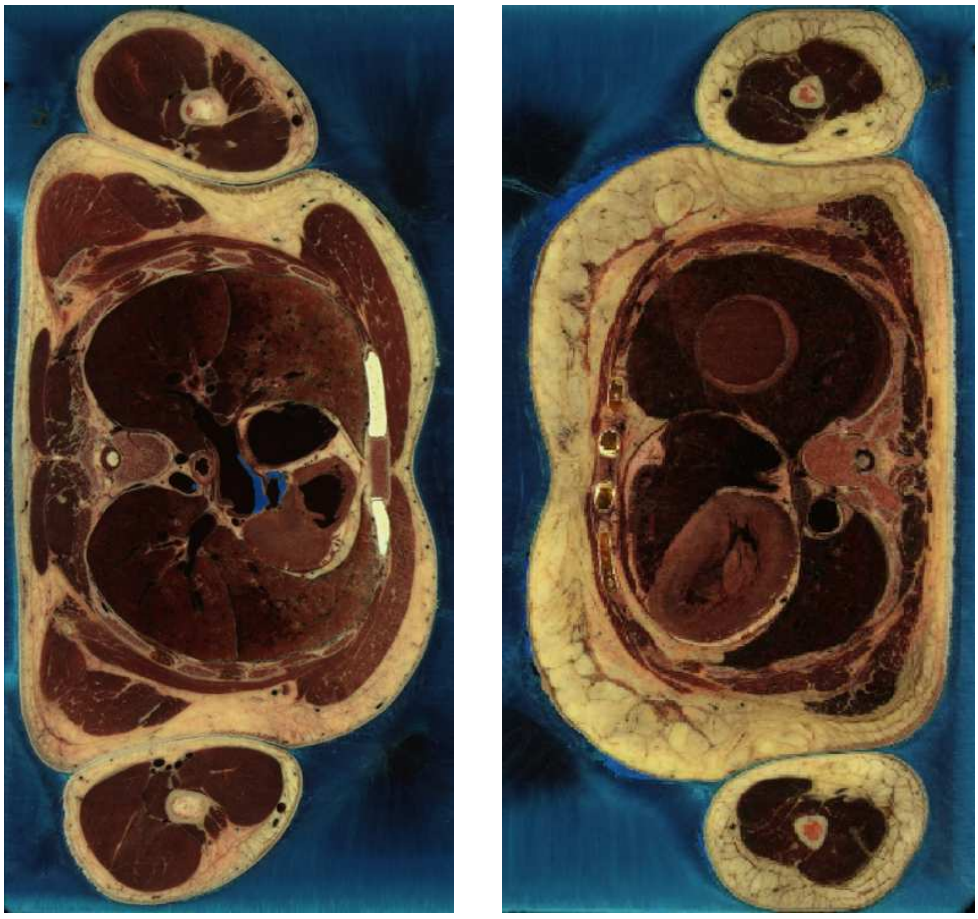

(a) (b)

Fig. 3.3. Exemplary cryosection photography of (a) the Visible Man and (b) the Visible Female data set in a transversal view through the heart. Brown parts are mainly muscles, white are bones, light brown is fat, and blue is the frozen filling liquid.

3.1.2.1 Visible Man Data Set

The Visible Man data set is based on the corpse of a 38 year old, 93 kg in weight, and 1.80 m tall male. The cryosections have a distance of 1 mm leading to 1878 photographic images. Each of the photos consists of 2048 $\times$ 1216 pixels, with each pixel having a size of 0.33 mm $\times$ 0.33 mm. Each image was digitized with 24 bits leading to a total data volume of approximately 15 GB of data for the cryosections for the whole body. Figure 3.3a shows an exemplary cryosection in a transversal view.

3.1.2.2 Visible Female Data Set

The Visible Female data set originated from the corpse of a 59 year old woman. The in-slice resolution and pixel size were equivalent to the Visible Man data set. The distance between two slices of the corpse of the woman was 0.33 mm, which was three times higher than the distance in the Visible Man data set. This led to 5189 image slices with a total amount of memory consumption of approximately 40 GB for the whole female body. Figure 3.3b displays an exemplary cryosection in a transversal view in the plane of the heart.

3.2 Digital Image Processing

Digital image processing can be divided into pre-processing, feature extraction, segmentation, and classification. The digital image processing techniques used to derive the anatomical models presented in this work are introduced briefly. A model derived with these techniques in a previous work is shown in fig. 3.4 [85]. The opened body of the Visible Man data set including several tissue classes with the original colors of the cryosection images is illustrated. For further information about digital image processing techniques refer to e.g. [69, 86, 87, 88, 89, 90, 91].

3.2.1 Preprocessing

Aim of image pre-processing is to reduce the complexity of further image processing steps. The common pre-processing steps are transformation of coordinates e.g. to translate or scale images, filtering e.g. to enhance borders and to suppress noise, and matching of image data of e.g. two different slices and two different systems.

3.2.1.1 Coordinate Transformation

Transformation of coordinates might be necessary to correct geometrical errors in the data, or to scale, translate and rotate images to fit to neighboring images. Commonly, affine, homogeneous and radial basis function transformations are used in digital image processing.

Affine transformations are able to scale, translate, shear and rotate data. The affine transformation T_{aff} returning the transformed vector x' is defined by:

$$x' = T_{aff}(x) = A_{aff}x + b_{aff}$$

with the scaling and rotation matrix A_{aff}, the translation vector b_{aff}, and the data vector x. A sequence of affine transformations is itself an affine transformation. Parallel lines will always be transformed into parallel lines using affine transformations.

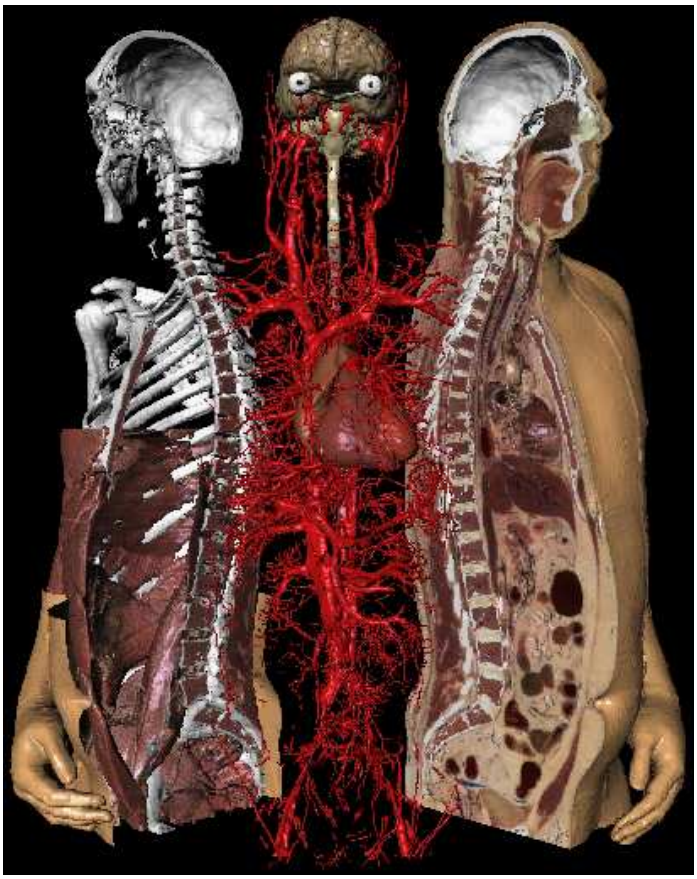

Fig. 3.4. Segmented Visible Man data set. The body including several tissue classes is illustrated with the original colors of the cryosection images. Fig. from [85].

A rigid transformation is a special case of the affine transformation, which consists only of translation and rotation, i.e. the distance between two points and the angles between two lines are preserved.

Homogeneous transformations are similar to affine transformations: The translation vector b and the transformation matrix A of the affine transformation are combined to one single matrix. Additionally, it is possible to carry out perspective transformations using homogeneous transformations, i.e. parallel lines do not necessarily have to be transformed to parallel lines.
The point $x = (x_1, x_2, x_3)^T$ is transfered in a four-dimensional point $x_{hom} = (x_1, x_2, x_3, 1)^T$ when using homogeneous transformations. The homogeneous transformation T_{hom} returning the transformed vector x'_{hom} is defined by:

$$x'_{hom} = T_{hom}(x_{hom}) = A_{hom} x_{hom}$$

with the 4×4 transformation matrix A_{hom} consisting of:

$$A_{hom} = \begin{pmatrix} a_{11} & a_{12} & a_{13} & b_1 \\ a_{21} & a_{22} & a_{23} & b_2 \\ a_{31} & a_{32} & a_{33} & b_3 \\ \lambda_1 & \lambda_2 & \lambda_3 & 1 \end{pmatrix}$$

with the elements $a_{11} \ldots a_{33}$ of the transformation matrix A_{aff} of the affine transformation, the elements $b_1 \ldots b_3$ of the translation vector b_{aff}, and the perspective transformation vector $\lambda = (\lambda_1, \lambda_2, \lambda_3)$.

The final three-dimensional vector x' is gained by transferring the four-dimensional vector $x'_{hom} = (x'_{hom,1}, x'_{hom,2}, x'_{hom,3}, x'_{hom,4})^T$ using:

$$x' = \frac{1}{x'_{hom,4}} \begin{pmatrix} x'_{hom,1} \\ x'_{hom,2} \\ x'_{hom,3} \end{pmatrix}$$

Radial basis function transformations are used to warp images. The transformation T_{RBF} is a combined transformation consisting of an affine transformation T_A and a radial transformation T_R:

$$T_{RBF}(x) = T_A(x) + T_R(x)$$

The radial transformation T_R is made of a local radial function for each direction in the three-dimensional space given by:

$$R(x) = \sum_{i=1}^{N} a_i g(|x - x_i|)$$

with the anchor point x_i, the scalar parameter a_i, and the radial basis function g. The norm $|x - x_i|$ is the distance between two points. The radial basis function g can be of different characteristic, e.g. local or global [92].

3.2.1.2 Filtering

The main purposes of the filtering process is to reduce artifacts and noise, enhance or extract image features, and therefore reduce errors in the following segmentation step. Two main groups of filter can be distinguished: linear and non-linear filter. A sequence of filter can be applied to construct hybrid filter.

Linear filter transfer the original image into a transformed image by using a filter mask. Main applications of linear filter are low-pass and high-pass filtering. Low-pass filtering is achieved by average filter reducing the noise but blurring the image. Gradient and Laplacian filter are used for high-pass filtering. High-pass filter are used to enhance the edges of an image. Linear filter fulfill the criteria linearity, additivity, commutativity, and associativity.

Non-linear filter do not fulfill linearity, additivity, commutativity, and associativity. The result of the filtering can be different if several filter were applied in another sequence or with other scaling factors of each filter. A typical group of non-linear filter are the so-called morphological or rank-order filter, where the value of the central element of the filter mask is replaced by a value of a specific element of the filter area. The elements of the filter area are transfered into a list sorted by the value of the elements.
Three important morphological operators are median, erosion, and dilation filter. Median filter have a smoothing characteristic by using the middle value of the sorted list of values. Erosion uses the smallest value of the sorted list to replace the central value of the filter area. Thus, the filter erases small areas with high values. Small areas with low values are erased with the dilation filter, which uses the largest value in the list.

Hybrid filter are achieved by subsequent application of linear and/or non-linear filter. Important hybrid filter for image processing of medical data are opening and closing. Opening is the subsequent application of n-times erosion and n-times dilation, while closing works vice versa. Opening erases small roughness areas and breaks small junctions between adjacent objects. Closing erases small spaces and connects tight adjacent objects.

3.2.1.3 Matching

Matching is used to combine data of the same object in such a way that all parts of the data have the same coordinate system. To generate a 3D anatomical model, the images of several slices and different imaging techniques have to be combined to apply digital image processing methods. The transformation of coordinates is mainly used to match the data.

3.2.2 Segmentation

Segmentation is called the image processing step where image data of homogeneous areas are joined to a region. Different anatomical data can be segmented by usage of automatic, semi-automatic and manual digital image processing techniques [69]. Furthermore, the segmentation techniques can be distinguished by point, region and edge based methods. The point based methods use only the information of the local element for the decision, to which region this element is assigned. Region based methods consider local and neighboring features for this decision. Edge based methods use extracted edges in the image data to apply homogeneous regions. Some of the common techniques, which are also used in this work, are described below.

3.2.2.1 Threshold Method

The threshold method is a simple approach to segment independent pixels using a histogram analysis. In the case of medical images, mainly the gray values of the pixels are observed. If a gray value is below some range, it belongs to one group, if it is above, it is segmented into the other. This method is a point based approach and creates often non-contiguous segments.

3.2.2.2 Region Growing Technique

Region growing is a region based technique. In this approach, a set of seed points is defined. The following steps decide whether the neighboring points have the same features, e.g. the same gray value range, compared to the set of seed points. If this is true, the neighboring point is included into the list of seed points. This process is repeated iteratively until no new neighbors were found. The definiteness of the segmented object is the main advantage of the region growing compared to the threshold method.

3.2.2.3 Watershed Algorithm

The edge based watershed algorithm unites voxels to a region based on an approach using the magnitude of the image data gradient. Voxels are assigned to the same region, if they all have a continuous descending path to the same local minimum. Local minima are found, where the gradient of the image data is zero. The results achieved with the watershed method lead often to a data set with a large number of segments due to the high probability of many local minima. Thus, the regions have to be fused manually or automatically.

3.2.2.4 Active Contours

Active contour methods are edge based techniques for automatic and semi-automatic segmentation. A-priori knowledge about initial position and shape of the object is of great significance for the correct solution of this method. An initial contour in 2D (snake) or in 3D

(surface) is iteratively adapted to the edges of the data. The contour is modified under consideration of weighted energy terms, until the energy of the system is minimized. The energy E of the system can be described by the sum of internal E_{int} and external E_{ext} energies:

$$E(v) = E_{int}(v) + E_{ext}(v)$$

with the function $v(s)$ describing the contour with the parameter s, which is $s \in [0, 1]$ in 2D and $s \in [0, 1][0, 1]$ in 3D. The internal energy is composed of the stretching and the bending energy, each weighted with a factor controlling the tension and bending of the contour, respectively. The external energy can be composed of several energies e.g. describing the ballon energy, the data energy, the attractor energy, and the gravity energy.
The energy of the data D, as an example, is defined with the potential function p in 2D as:

$$E_{data}(v) = \int_0^1 p(v(s))ds$$

The potential function p uses the negative magnitude of the data gradient:

$$p(x) = -\omega_p |\nabla D(x)|$$

The weighting factors and energy functions have to be adapted for each segmentation problem. Traditional active contours have a constant topology. An extension of the traditional active contour are the topologically adaptive active contours, which allow the merging and splitting of contours during each iteration step [93, 94].

3.2.2.5 Manual Methods

Manual methods are applied for segmentation mainly if automatic or semi-automatic approaches fail due to low quality of the data and if expert knowledge is needed for segmentation. Other manual methods are tightly coupled to automatic methods in such a way that the user can interact with the automatic method (semi-automatic approach).
An important manual method is the interactively deformable mesh, which is an approach in combination with the active contour model. The user can pick one node of the automatic segmented contour and modify its location. The movement of the elements influence also the position of adjacent elements using the radial basis function transformation.

3.2.3 Classification

Classification is defined as the assignment of segmented regions in the data into classes. These classes correspond to tissue types in an anatomical model. Numerical and non-numerical approaches exist besides manual classification [69, 88]. Features are extracted to classify the data in the numerical classification procedures. Most important numerical classificators are the minimum-distance approach and the nearest-neighbor method, which belong to the class of geometrical classification methods. Geometrical approaches classify the data on estimating the distances in a feature space.
The non-numerical classification methods use more complex features of the data. Typical methods are rule based approaches and neural networks.

4

Cardiac Electrophysiology

The myocardium consists of several different types of cardiomyocytes. Specialized cells are responsible mainly for the initiation of the electrical activity, others mainly for the fast conduction of excitation. The majority of cells are myocytes of the working myocardium generating the contraction of the heart. This is performed by electro-mechanical coupling mechanisms, which transfer the electrical signal into a mechanical tension. But also myocytes from the working myocardium conduct excitation.
Both atria and ventricles build a syncytium, which means that the cells are electrically coupled. Gap junctions (section 2.1.1.2) have a low electrical resistance and provide this electrical connection. The density and distribution of gap junctions lead to an anisotropic electrical intracellular conductivity depending on the tissue type. The electrical impulse is mainly transferred through gap junctions to adjacent cells leading to a macroscopic excitation conduction. The atria and ventricles are isolated from each other by the heart skeleton which is build of connective tissue. Conduction of the excitation from the atrium to the ventricles is commonly only possible through the excitation conduction system. This has been described in chapter 2 and shall be briefly summarized before cellular cardiac electrophysiology is described in detail in this section.
The sequence of activation of the heart is well organized to synchronize the pumping function (fig. 4.1). The physiological electrical excitation starts in the sinoatrial node (SAN), which is the primary pacemaker. It is composed of self-depolarizing cells (auto-rhythmicity). Then, the fast right atrial conduction pathways, i.e. the crista terminalis (CT) and pectinate muscles (PM) transmit the excitation. During that phase, the right atrial working myocardium gets depolarized. At the same time, the Bachmann bundle (BB) transmits the activation towards the left atrium and the whole atrium is activated. All conduction pathways are characterized by a large electrical conductivity along the fiber direction. The excitation reaches the atrioventricular (AV) node, which is the only electrical path between atria and ventricles in the physiological case. The activation is delayed in the AV node to synchronize the temporal sequence of contraction between atria and ventricles. The His bundle is located adjacent to the AV node. It transmits the excitation to the Tawara bundle, which consists of three branches: one to the right and two to the left ventricle. The excitation is then conducted via the network-like Purkinje fibers to the subendocardial myocardium of the ventricles. From there, the whole ventricle gets activated from endocardium to epicardium as well as from apex to base. A possible re-excitation of the conduction system by the ventricular myocardium is prevented by longer refractory periods in the conduction system. The excitation velocities, conduction delays, refractory periods and auto-rhythmic frequencies of different cardiomyocytes in the physiological case are presented in tab. 4.1.

Table 4.1. Physiologic parameters of cardiac tissue. The excitation velocity v, conduction delay t_{cond}, absolute refractory period t_{ref}, and auto-rhythmic frequency f for different cardiomyocytes are depicted [95].

Tissue type	v (m/s)	t_{cond} (ms)	t_{ref} (ms)	f $(1/min)$
Sinoatrial node	0.05	0	130	70
Atria	0.8	60 – 100	130	0
Atrioventricular node	0.05	70	140	50 – 60
His bundle	1.75	5	280	40 – 50
Tawara branches	1.5	10	380	40 – 50
Purkinje fibers	3	5	380	30 – 40
Ventricle (subendocardial)	1.5	100	300	0
Ventricle (subepicardial)	1	100	300	0

The phenomena of cell activation and spreading of excitation is based on ionic flow through the cell membrane and between adjacent cells. The characteristic course of action potential (AP) of cardiomyocytes is achieved by passage of specific ions in a suitably temporal sequence through the cell membrane. This behavior is nonlinear and is based on the change in conformation of protein pores that are inserted in the sarcolemma forming a selective permeable membrane. The cell membrane encloses the intracellular space from the liquid solution of the extracellular space (section 2.1). The pores in the sarcolemma are mainly ion specific. One can distinguish between passive channels, pumps and exchangers.
Ionic channels transport ions like sodium, potassium and calcium along electro-chemical gradients. Pumps like the Na/K ATPase actively carry ions. Energy delivered by the hydrolysis of adenosine triphosphate (ATP) is required for the active transport. Exchangers like the Na/Ca transporter transfer two different types of ions in the same or opposite direction. The sarcoplasmic reticulum (SR) is surrounded by its own membrane with specific channels and is an intracellular reservoir for Ca^{2+}. The ion channels, pumps and exchangers are classified by the ion type, which can pass the protein, and by the protein's characteristics.

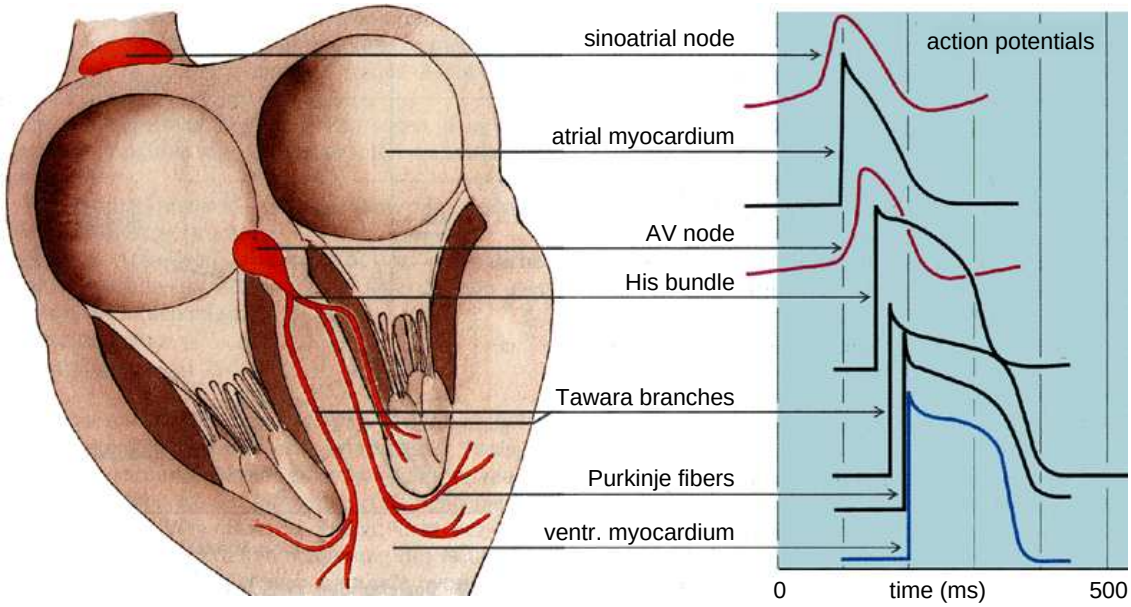

Fig. 4.1. Cardiac myocardium including excitation initiation and conduction system with corresponding action potentials and temporal delay. The cells of the sinoatrial node, atrioventricular node and conduction system are cells with auto-rhythmic properties. The longest temporal delay of the excitation is located in the AV node. Fig. adapted from [6].

Most of the ion channels have a high ion selectivity and can only stay in a conducting or a non-conducting state. The characteristics of the currents depend on the properties of activation, inactivation and deactivation of the channels. Activation is called the increase in the probability of a channel to open. Some channels can get into a state after activation where they close time-dependently even with further stimulation. This transition is called inactivation. The channel recovery into the excitable state is called deactivation. All these processes are due to conformational changes in the ion channel protein. The maximum amplitude of the current of a type of channels is dependent on the channel density.
Important sarcolemmal channels for the electro-mechanical coupling are the L-type Ca^{2+} channels located at the end of the transversal tubuli [17]. Opening of these voltage-gated channels lead to an increase of Ca^{2+} concentration in the dyadic space, which lies between the T-tubule and the SR. This concentration triggers the opening of calcium induced calcium release channels (ryanodine receptors, RyR) of the SR [96], which provokes calcium sparks as a positive feedback mechanism. Summing of several sparks leads to an increase of the free myoplasmic calcium concentration. Finally, calcium is transported by Ca^{2+} specific pumps back into the SR [96] and transported extracellularly by the sarcolemmal Na/Ca exchangers [97].

4.1 Measurement Systems

One can distinguish between single cell and excitation conduction measurement systems. The voltage clamp technique is a method to measure single cell activity. For measurements of single channel properties the so-called patch clamp technique was developed [98]. The underlying principle of the patch clamp technique relies on a high-resistance seal in the order of 60 $G\Omega$ between a glass micropipette and a membrane [99]. The seal is usually attained by gentle suction, gained by pressing a very fine, fluid-filled pipette tip with an opening of about 0.5 μm against the membrane of an intact cell. A small patch of the membrane is drawn into the pipette tip. One electrode lies inside the pipette, the other in the bathing solution. The patch clamp amplifier measures current through or voltage across the membrane.
The most widely used mode of patch clamp method is the control of voltage across the membrane and the measurement of current flow. This technique allows the investigation of each channel's behavior with respect to the whole cell or a membrane patch. It even allows to investigate the behavior of a single channel by using a suitable pipette size.
A variation of the voltage clamp method, the so-called double cell voltage clamp technique, is used to determine the electrophysiological behavior of gap junctions. The intercellular voltage is controlled by two voltage sources with common reference potential. The voltages are registered in conjunction with the applied current, which offers the possibility to calculate the conductivity. The potential difference is the voltage across the gap junction.
To examine the excitation conduction in tissue, electrocardiographic and optical systems can be used. Electrocardiographic setups measure the extracellular potential produced by the membrane currents of cardiomyocytes. Commonly, multi-electrode socks at the epicardial border [100], multi-electrode catheters at the endocardial border [101, 102], or electrodes placed by motorized micro-manipulators in an experimental setup [103] are used to determine excitation conduction velocities by detecting activation times.
Optical systems record the light signal of fluorescent dyes that are inserted in the cell membrane. These dyes relax after activation with a light source in dependence of the voltage across the membrane [104, 105]. The excitation conduction is traced by video recordings using image processing techniques.

4.2 Diffusion of Ions

The transport mechanisms of proteins in the membranes of cells can be either active or passive. Active transport requires energy, passive transport is due to electrical and/or chemical gradients. The transport of ions can be through the cell membrane, intracellularly or intercellularly [106]. Active transport is described in section 4.3.2 and 4.3.3.
Passive transport by diffusion is a "down hill transport" mechanism. It is the transport of particles due to the stochastic Brownian movement of the molecules [38]. This transport is not directed and a diffusion in one direction can only be obtained if the substance at one location is more concentrated than in another. The diffusion coefficient D is defined according to the Stokes-Einstein equation as:

$$D = \frac{RT}{6\pi r\eta}$$

with the absolute temperature T, the viscosity of the fluid η, the radius r of the diffusing particles, and the gas constant $R = 8.3144\frac{J}{K\ mol}$. The rate of diffusion J_d of a volume filled with uncharged particles dissected by a semi-permeable membrane is defined according to Fick's diffusion law:

$$J_d = A\ D\ \frac{\Delta C}{\Delta x} \tag{4.1}$$

with the surface area A of the semi-permeable membrane, the concentration gradient ΔC between the two subspaces, and the thickness of membrane Δx. The transport of substances via diffusion is only applicable if the membrane is thin and permeable only for these substances. If the substances are electrically charged particles, e.g. ions, the concentration gradient leads to a potential gradient U, which provides a directed diffusion through the membrane with the force F_m and the valence z_X of the ion X:

$$F_m = z_X\ \frac{U}{\Delta x}$$

The total flux $\boldsymbol{j}_X = \boldsymbol{j}_{D,X} + \boldsymbol{j}_{E,X}$ is composed of a part caused by diffusion $\boldsymbol{j}_{D,X}$ and a part due to electrical forces $\boldsymbol{j}_{E,X}$. The two flux components are described by:

$$\boldsymbol{j}_{D,X} = -D_X \nabla[X], \quad \boldsymbol{j}_{E,X} = -D_X \frac{[X] z_X F}{RT} \nabla\phi$$

with the concentration of the ion type $[X]$, the electrical potential ϕ, and the diffusion constant D_X:

$$D_X = \frac{u_X RT}{|z_X| F} \tag{4.2}$$

with the ionic mobility u_X. This leads to the Nernst-Planck equation describing the total flux $\boldsymbol{j}_X$:

$$\boldsymbol{j}_X = \boldsymbol{j}_{D,X} + \boldsymbol{j}_{E,X} = -D_X \left(\nabla[X] + \frac{[X] z_X F}{RT} \nabla\phi \right)$$

An electrochemical equilibrium is achieved if $\boldsymbol{j}_X$ through the membrane is zero. A concentration difference of ion type X between inner side i and outer side o exists across the membrane in this electrochemical equilibrium. The concentration difference leads to an electrical voltage across the membrane, the so-called equilibrium voltage E_X. E_X is defined by the Nernst equation [107] as:

$$E_x = \frac{RT}{z_X F}\ \ln \frac{[X]_o}{[X]_i} \tag{4.3}$$

Table 4.2. Valence of ions, ion concentrations and Nernst voltages in myocytes at room temperature [108].

Ion type	Valence z_X	Extracellular concentration $[X]_o$ $(mmol/kg\,H_2O)$	Intracellular concentration $[X]_i$ $(mmol/kg\,H_2O)$	Nernst voltage (mV)
K^+	1	4.5	160	–95.4
Na^+	1	144	10	80.8
Ca^{2+}	2	1.3	0.00001 – 0.0001	126.5 – 157.3
Cl^-	1	114	4	–74.5

with the effective ion concentration $[X]$ of ion type X, the absolute temperature T, and Faraday's constant $F = 9.65 \cdot 10^4 \frac{As}{mol}$. Table 4.2 depicts ionic concentrations and Nernst voltages for several ion types.

4.3 Electrical Properties of Cellular Membranes

The cellular membranes are constructed of a phospholipid bilayer, in which proteins are inserted forming pores (section 2.1.1). The cell membrane (sarcolemma) separates the intra- and extracellular spaces having different concentrations of various ions (tab. 4.2). Also, intracellular membranes like the membrane of the sarcoplasmic reticulum separate two spaces with differing ionic concentrations. The concentration gradients across membranes are resulting from transport proteins i.e. ionic pumps and determine the driving force of passive ionic channels and ionic exchangers.

4.3.1 Ionic Channels

Ion channels can take different configurations. In the conducting state ions pass through, in the non-conducting not. Ion channels regulate the selective permeability of the membrane due to their state and thus the transmembrane voltage. "Gating" is called the process of back and forth switching of closed and opened state. Gating is controlled in different ways. For one group of channels the transmembrane voltage controls gating [109, 110]. For other channels binding of extracellular neurotransmitters like ACh and adrenaline as well as intracellular ligands like ATP and cyclic adenosine monophosphate (cAMP) trigger gating [111, 112]. Mechanical stimulation also activates the gating process in some proteins [113].
Voltage sensitive channels have an electrical sensor that transfers the transmembrane voltage change into a change of the conformation of the ion channel (fig. 4.2). This change opens or closes the channel. For a ligand controlled channel, a specialized binding site exists. If the ligand is bound, the ion channel is opened. The ligand binding site is located either on the extracellular side of the channel to react on e.g. neurotransmitters or in the intracellular domain to react on ligands like ATP or cAMP [114].
Ions are not isolated in a liquid solution but have an environment, being a complex of water molecules. The dipoles of the water are electrostatically bound to the ion. These hydrated ions can not pass through ion channels. Thus, dehydration of the ion is necessary to allow an ion flow through the cell membrane. The energy of hydration, i.e. the energy of the interaction between ion and water, has to be replaced by the binding energy of the ion channel. The energy difference between these two reactions determines if a specific ion can pass through the channel. The differences in the hydration energy between different ions is one reason for the ion selectivity of ion channels in addition to the size and the charge of the ions [115].
The electrophysiological behavior of ion channels can be examined with patch clamp techniques. One single channel can be either in a conducting or non-conducting state. The probability for one channel to open or close can be estimated by measuring the conductivity

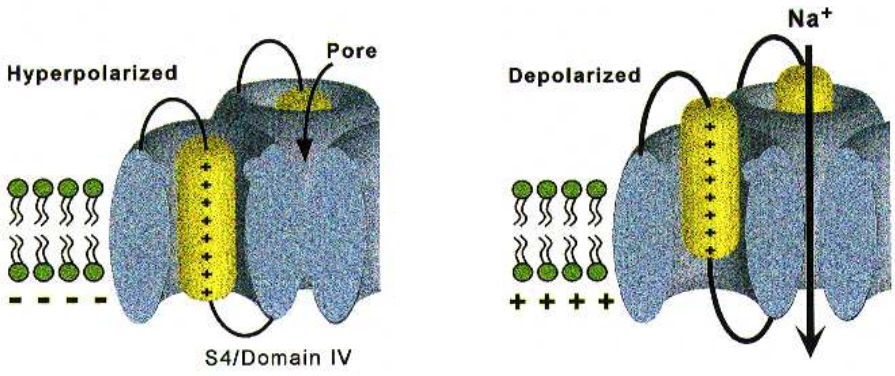

(a) (b)

Fig. 4.2. Functional description of Na^+ channel. The α-subunit with the S4 activation sensor is shown. Ion flow is facilitated or prevented due to conformation changes [14]. (a) Closed channel. (b) Opened channel.

over a time period. As described, the conformation changes leading to opening and closing of the channel is driven by the voltage, ion concentrations, or ligands. Also the time is an important factor since the transition from one state to another is time dependent. The total current through the cell membrane of one specific channel type is determined by summing the randomly distributed fluxes of single channels.

Mainly three ion specific channel types exist in cardiomyocytes, i.e. Na^+, K^+, and Ca^{2+} channels, with a variety of sub-classes. The Na^+ channel is responsible for the fast upstroke of the transmembrane voltage after exceeding a certain threshold [109, 118]. The pores of the Na^+ channels open very fast, but close after approximately 0.1 ms with a transition into an inactive state. Some studies also report late components of the Na^+ channel especially in ventricular cells that are located in the mid-myocardium. These lead to a prolongation of the plateau phase [119, 120]. Steady state features of the Na^+ channel are exemplary depicted in fig. 4.3a.

Potassium channels are the group of channels with the largest variety of electrophysiological differences. Voltage-gated K^+ channels have a 6Tm-1P structure (section 2.1.1.1). This group

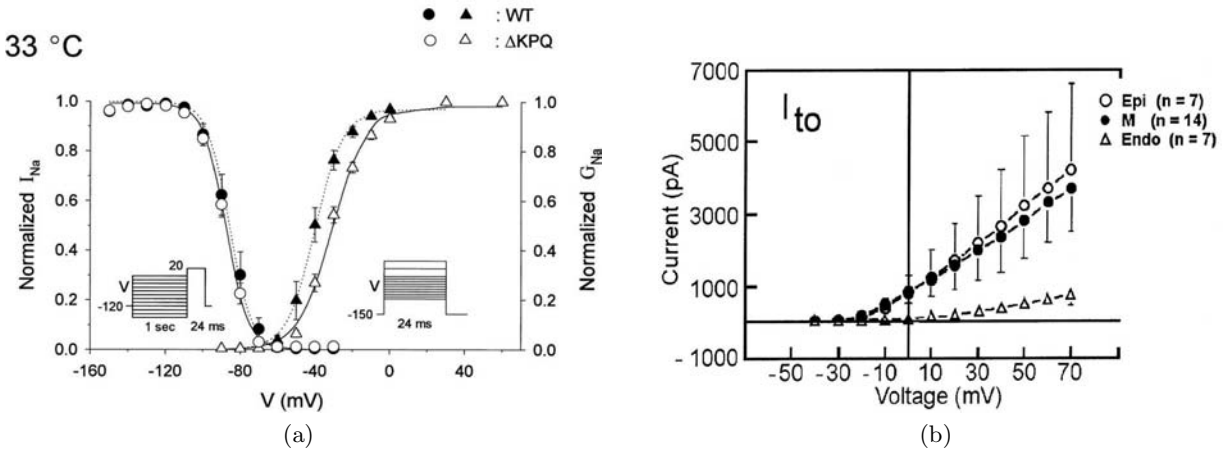

(a) (b)

Fig. 4.3. Characteristics of Na^+ ion channel and transient outward K^+ channel. (a) Steady state inactivation and activation relationships for a physiological (wild type, WT) and a mutant (ΔKPQ) Na^+ channel. The corresponding clamp protocols are shown in the insets. The lines indicate fits to Boltzmann functions [116]. (b) Heterogeneous I-V plot of transient outward K^+ current in subendocardial (Endo), subepicardial (Epi) and midmyocardial (M) cells [117].

includes the transient outward current I_{to}, the sustained outward current I_{sus}, the slow and rapid delayed rectifier K^+ current I_{Ks} and I_{Kr}, respectively, the ultra rapid K^+ current I_{Kur}, and the K^+ component of the so-called funny current I_f [16, 21, 110, 122, 123]. I_{to} is responsible for the notch in the AP directly after the depolarization, which is also termed "spike-and-dome" morphology. It has a fast and a slow activation component also termed $I_{to,1}$ and $I_{to,2}$, respectively. The I_{to} channel is mainly open during positive transmembrane voltages (fig. 4.3b). The sustained outward K^+ current I_{sus} was measured in cells of atrial working myocardium and of the sinoatrial node [124]. Up to now, it is not clarified if I_{to} and I_{sus} belong to different pore proteins or are just two different phases of the same one. I_{Kr} and I_{Ks} are the main contributors for the repolarization, especially the late repolarization. Figure 4.4 illustrates the voltage protocol behavior of the two delayed rectifier K^+ currents. I_{Ks} has a linear current-voltage relationship during activation (fig. 4.4c) and is faster in steady state of activation (fig. 4.4a) compared to I_{Kr} activation (fig. 4.4b). The steady state activation current-voltage relationship is nonlinear for I_{Kr}, having the largest value at 10 mV (fig. 4.4c). The inactivation of both I_{Kr} and I_{Ks} is faster compared to their activation. I_{Kur} is only found in the atria and is a rapidly activating, non-inactivating K^+ current [125]. Its main function is to keep the duration of the atrial action potential short. I_f is the so-called pacemaker current and only activates during hyperpolarization. It has a K^+ and a Na^+ component, with the Na^+ component being more dominant. I_f can increase the resting voltage of a cell towards the activation voltage of the fast Na^+ current. Thus, I_f is a contributor for pacemaker cells. It is less expressed in atrial cells and nearly missing in ventricular myocytes.

The other class of K^+ selective channels are those with the 2Tm-1P structure. They all have inward rectifying characteristics. They are distinguished between the "classic" inward rectifying K^+ current I_{K1}, the acetylcholine-sensitive current $I_{K,ACh}$, and the adenosine triphosphate-sensitive current $I_{K,ATP}$ [21, 110, 122]. I_{K1} is responsible for the maintenance of the resting voltage and also supports the late repolarization phase. It is closed during activation of the cells but opens at negative voltages (fig. 4.5a) leading to a constant flow of K^+ ions out of the cell during the resting phase. The influence of this current is dependent on

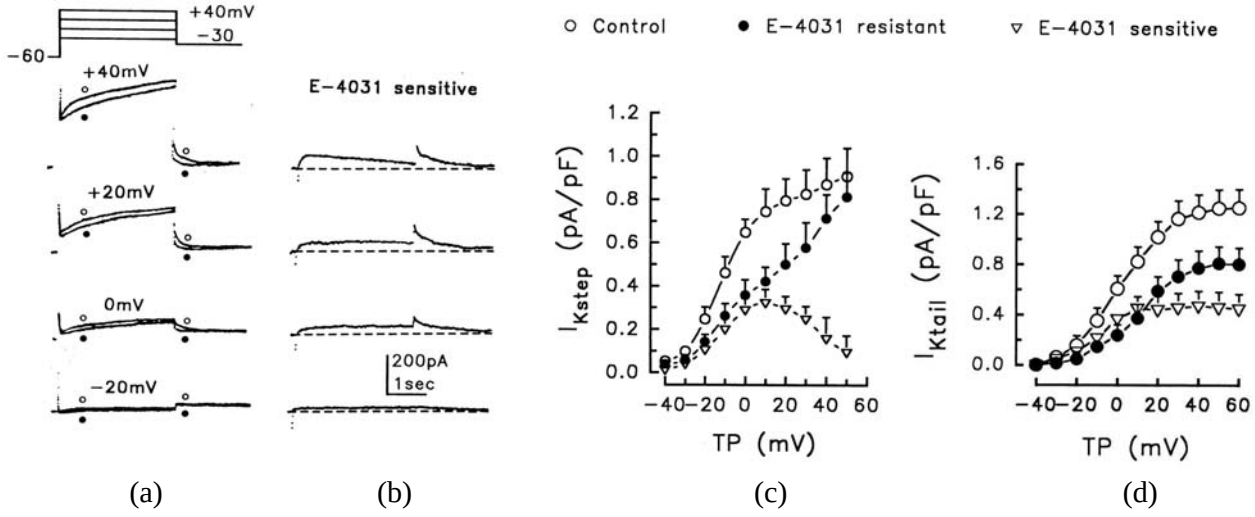

Fig. 4.4. Characteristics of slow and rapid delayed rectifier K^+ channel [121]. I_{Ks} is named E-4031 resistant, I_{Kr} E-4031 sensitive. Control is $I_{Ks} + I_{Kr}$. (a) Control and I_{Ks} current during voltage protocol followed by repolarization pulse (inset). (b) Course of I_{Kr} by subtracting I_{Ks} from control. (c) Maximum steady state current $I_{K_{step}}$ during test potential. (d) Maximum steady state current $I_{K_{tail}}$ during repolarization pulse.

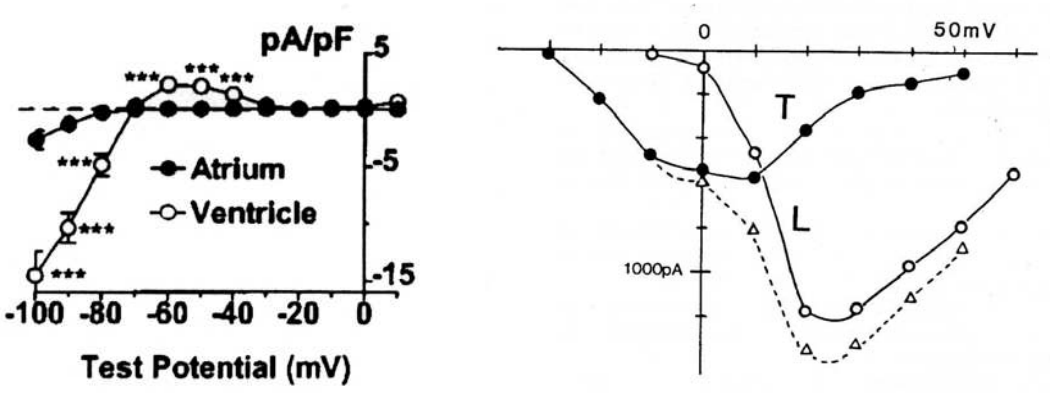

(a) (b)

Fig. 4.5. Characteristics of the K^+ rectifier channel and the L-type and T-type Ca^{2+} channel. (a) Maximum steady state amplitude of I_{K1} in the human atrium and ventricle [126]. (b) Peak I-V plots for T-type (closed circle), L-type (opened circle), and summary Ca^{2+} current (rectangles) from cardiac Purkinje cells [18].

the extracellular K^+ concentration. $I_{K,ACh}$ is opened when ACh attaches to the extracellular binding site of this channel. In this way, the transmitter ACh can reduce the duration of an action potential. $I_{K,ATP}$ is active during low concentration of intracellular ATP. A reduced ATP concentration leads to an unbinding of ATP from the intracellular binding site of the $I_{K,ATP}$ channel. The AP is shortened and contractility i.e. the energy consumption is reduced to avoid cellular damage.

The third group of ion-specific membrane proteins are Ca^{2+} channels. At least four types are expressed in the heart [17]. Two of them are located in the sarcolemma: L-type (long-lasting) and T-type (tiny) Ca^{2+} channels [18]. The other two are expressed in internal membranes: The SR Ca^{2+} release channel, also called ryanodine receptor, and the so-called IP_3 receptor of the SR. The T-type Ca^{2+} channel is highly expressed in SAN and AVN cells and has only a minor function in myocytes of the working myocardium [127]. T-type Ca^{2+} channels open at more negative potentials but also inactivate faster compared to the L-type Ca^{2+} channel (fig. 4.5b). The L-type Ca^{2+} channel and the SR Ca^{2+} release channel are detailed in section 4.6.1. The functional role of the IP_3 receptor is nearly unknown in cardiac tissue.

4.3.2 Ionic Pumps

Ions are transported under transformation of energy against the electrochemical gradient at several locations of the cell. This so-called primary active transport mechanism is achieved by specific membrane proteins, termed ion pumps. The energy needed is provided by hydrolysis of adenosine triphosphate (ATP) into adenosine diphosphate (ADP) and phosphate. This form of energy can be used directly by the cells [128]. Thus, the ion pumps are also called ATPases. Ion pumps generate an electrochemical gradient. This gradient is used for passive fast ionic currents through ion channels [106].

Three different pumping proteins are the main contributors for translocating ions in the human heart: The Na/K and the Ca^{2+} pump, both expressed in the sarcolemma, and the Ca^{2+}-ATPase in the sarcoplasmic reticulum. Both Ca^{2+} pumping proteins are described in more detail in section 4.6.1.

The Na/K pump is the most prominent ATPase in the sarcolemma. In every transport process three Na^+ ions are transported out of and two K^+ ions into the cell. Thus, an ion concentra-

tion gradient between intra- and extracellular space is achieved, which is very important to maintain the resting transmembrane voltage and for the excitability of the cells. One ATP molecule is hydrolyzed during one transport process to achieve the conformation changes of the protein and the following affinity changes of the binding sites of Na^+ and K^+. The rate of pumping depends on the intra- and extracellular concentration of Na^+ and K^+ as well as on the transmembrane voltage (fig. 4.6a) [106].

4.3.3 Ionic Exchangers

Ionic exchangers are membrane proteins that are able to interchange ions and other substances located near the protein in the liquid solution. The kinetics are described by conformation and affinity changes. The exchangers are transport proteins, which transport specific ions through the membrane using electrical and chemical gradients. The activity of the exchangers is modulated by nervous influence or signaling substances.
An exchanger is termed symport if the involved molecules are transported in the same direction, otherwise antiport. If the transported molecule are ions, the exchange causes a current through the membrane. The electrochemical gradient of one of the involved ion types is the driving force of the exchange process. This electrochemical gradient is achieved with a primary active transport mechanism, i.e. with the ion pumps. An ionic exchanger is a secondary active transport, since the "up hill transport" of one ion type is coupled to a passive transport of the forcing ion.
One of the most important exchangers in the heart is the Na/Ca exchanger in the sarcolemma (fig. 4.6b). It has a stoichiometry of 3 Na^+:1 Ca^{2+} and thus is an important Ca^{2+}-transporter due to the high concentration gradient of Na^+. In cardiac myocytes, the Na/Ca exchanger commonly operates in the forward mode, i.e. three Na^+ enter the cell and one Ca^{2+} is extruded at each transaction. During depolarization, $[Ca^{2+}]_i$ increase is mediated also by the sarcolemmal Na/Ca exchanger. This is the so-called reverse mode. The sarcolemmal Na/Ca exchanger in cardiac myocytes functions in both forward (Ca^{2+} efflux) and reverse (Ca^{2+} influx) modes of operation [131, 132]. During one exchange cycle the protein undergoes a series of molecular rearrangements [97].

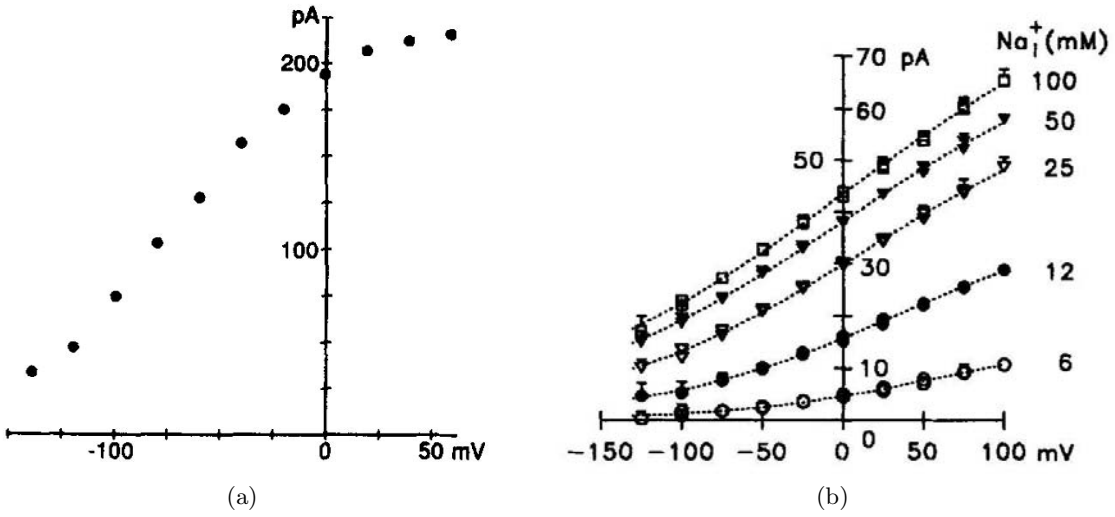

(a) (b)

Fig. 4.6. Characteristics of ion pumps and exchanger. (a) Current-voltage relationship of the Na/K pump [129]. (b) I-V plot of Na/Ca exchanger at different extracellular Na^+ concentrations [130].

4.4 Transmembrane Voltage

As described in section 4.3, ions are passing the sarcolemma from intracellular to extracellular space and vice versa through membrane proteins. The transport of charges through the cell membrane leads to a change in the ion concentration difference between intra- and extracellular space. The electrochemical gradient causes a potential difference across the membrane, which is called transmembrane voltage V_m:

$$V_m = \Phi_i - \Phi_e$$

with the intracellular potential Φ_i and the extracellular potential Φ_e.

4.4.1 Resting Voltage

The Nernst equation (eq. 4.3) describes the equilibrium voltage of a membrane, which is only permeable by one ion type. An extension of the Nernst equation to many types of ions is the Goldman-Hodgkin-Katz equation. It allows the consideration of several ions i.e. K^+, Na^+, and Cl^- [133, 134]:

$$E = \frac{RT}{F} \ln \frac{P_{K^+}[K^+]_e + P_{Na^+}[Na^+]_e + P_{Cl^-}[Cl^-]_i}{P_{K^+}[K^+]_i + P_{Na^+}[Na^+]_i + P_{Cl^-}[Cl^-]_e} \tag{4.4}$$

with the gas constant R, the absolute temperature T and the Faraday constant F. $[X]_i$ and $[X]_e$ are the effective intra- and extracellular concentrations of the ion type X, respectively. The permeability P_K, P_{Na}, and P_{Cl} of K^+, Na^+, and Cl^- ions, respectively, is given by:

$$P_X = \frac{D_X \beta_X}{\Delta x} \tag{4.5}$$

with the diffusion coefficient D_X of the ion X (eq. 4.2), the water-membrane partition coefficient β_X, and the thickness Δx of the membrane.
Cells can have different transmembrane voltage but only the equilibrium voltage of excitable cells is called resting voltage. To describe the resting voltage of a cell membrane, the Goldman-Hodgkin-Katz equation has to be enhanced by the permeability of Ca^{2+} and the charge transport of the sarcolemmal pumps and exchangers. The resting voltage is in the range between –30 mV and –100 mV for different cardiac cell types [135].
Concentration gradients, the low permeability for Na^+ ions, and high permeability for K^+ ions are responsible for the resting membrane voltage. The K^+ concentration in the intracellular space is 35-fold larger than in the extracellular space, the Na^+ concentration 25-fold smaller [108]. As the sarcolemma has a low permeability for Na^+ ions during the resting phase, the Na^+ concentration gradient is not neutralized by a passive diffusion. Furthermore, the high permeability of K^+ ions during the resting phase causes a constant diffusion of K^+ ions outside of the cell. The Na/K pump transports these K^+ ions back into the cell. Thus, the resting voltage of cardiomyocytes is nearly the equilibrium voltage of K^+. As the sarcolemma is also permeable for Cl^- ions, the electrochemical gradient of Cl^- contributes for the shifting of the resting voltage towards less negative voltages.

4.4.2 Action Potential

In excitable cells, e.g. nerve and muscle cells, the ion permeability of the cell membrane can vary due to an electrical stimulus. If V_m exceeds some certain threshold an action potential

(AP) is initiated in an "all-or-nothing" fashion [38]. The AP shape is varying for different cell types and stimulus frequencies. The reason for the initiation of the depolarization is a change in the electrical gradient between intra- and extracellular space. Until the threshold is reached the cell tries to counteract the rise of V_m.
After exceeding the threshold, fast Na^+ channels get activated avalanche-like and the Na^+ current depolarizes the cell until a positive transmembrane voltage can be recognized, the so-called overshoot (fig 4.7a). Na^+ channels get inactive after approximately 0.1 ms, which is the end of the overshoot and they stay closed for a certain time. Ca^{2+} channels and early K^+

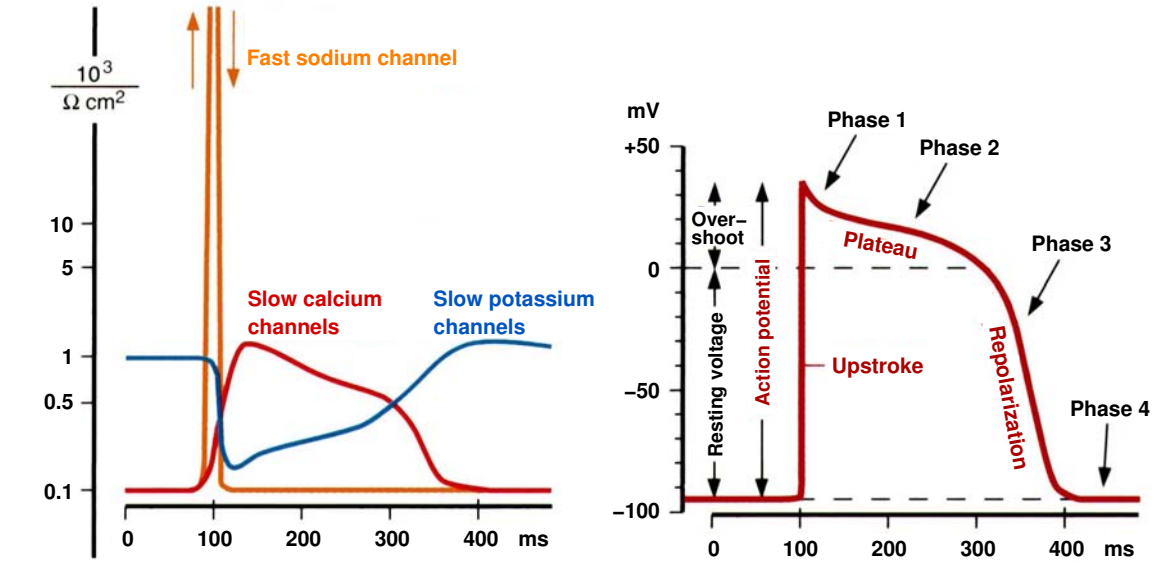

(a)

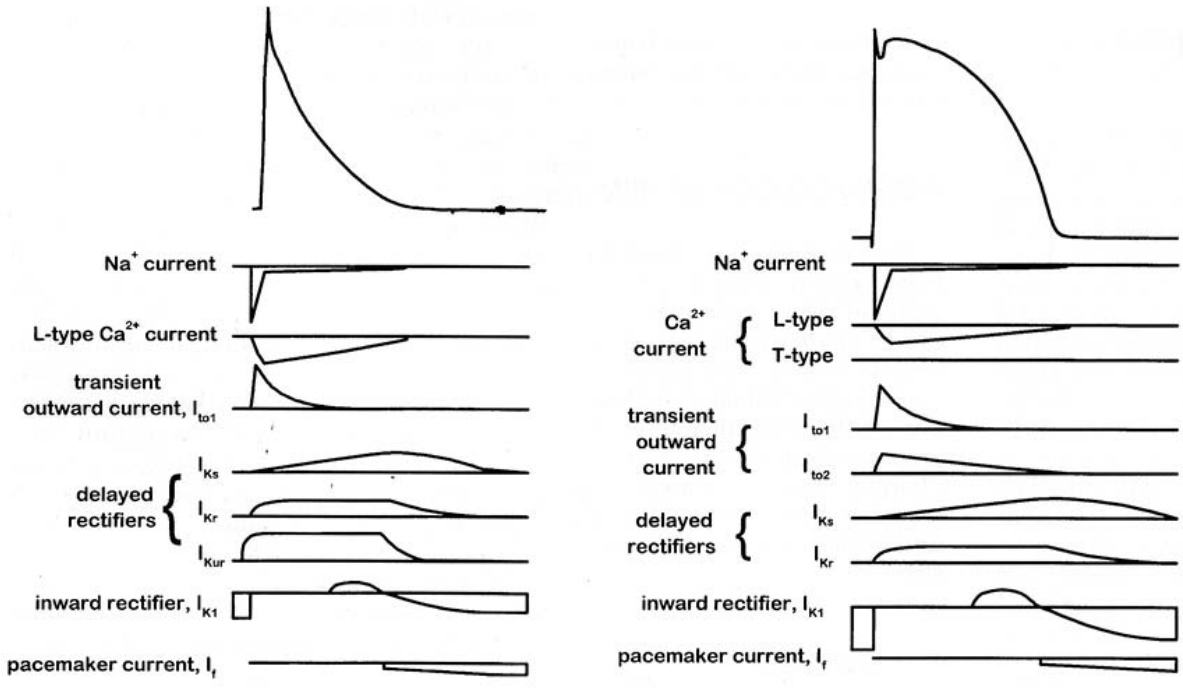

(b)

Fig. 4.7. Schematic representation of APs and underlying ionic currents. (a) Principal description of the phenomena, (b) Atrial (left) and ventricular (right) myocytes. Figs. adapted from [136, 137].

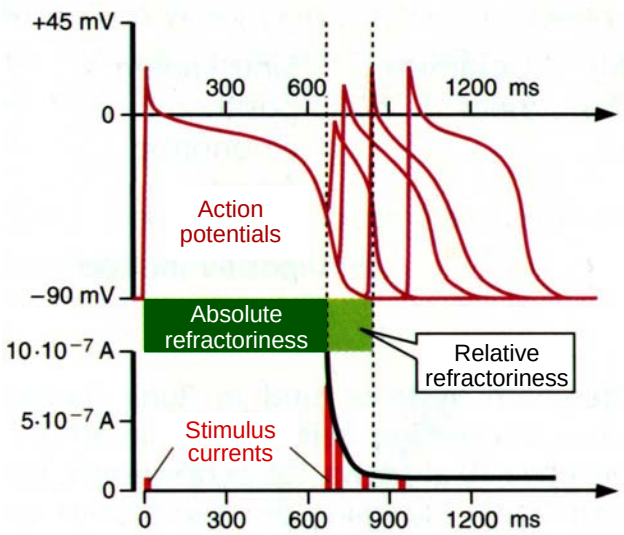

Fig. 4.8. Schematic description of the refractoriness of cardiomyocytes. The influence of stimulation intervals and amplitudes to excite a cell is shown. During the resting phase only a small stimulus current is needed to depolarize the cell. The cell is not re-excitable during the absolute refractory period. In the relative refractory period only high amplitude currents lead to an activation of the cell but with a less long action potential duration. Fig. adapted from [136].

channels open during the depolarization with much less speed compared to Na^+ channels. A transient outward K^+ flux (I_{to}) is responsible for the "spike-and-dome" morphology of the AP in the early repolarization phase, which is called repolarization phase 1 (fig 4.7a). The Ca^{2+} influx is a main contributor to the nearly constant V_m during the plateau phase (repolarization phase 2). The length of the plateau phase differs depending on e.g. the cell type and the basic cycle length. The outflow of K^+ ions mainly through delayed voltage dependent K^+ channels repolarizes the cell (fig 4.7a). This period is termed repolarization phase 3. The early resting phase including hyperpolarizations where I_{K1} opens and the other K^+ channels close is called repolarization phase 4. Figure 4.7b shows APs and the corresponding activity of selected currents for atrial and ventricular cells.

4.4.3 Refractory Periods

After the cell is activated it is not re-excitable for a certain time even when applying large stimulus currents. This is due to the inactivated state of the fast Na^+ channels. Na^+ channels deactivate depending on the transmembrane voltage i.e. if V_m is below –50 mV again [108]. Thus, the cell is not re-excitable during the inactive phase of Na^+ channels, called absolute refractory period. It is followed by the relative refractory period, where Na^+ channels can partly re-activate but where V_m as well as the K^+ and Ca^{2+} channels are still not resting. Thus, APs with a shorter duration and lower amplitude are evoked in this phase (fig. 4.8). Furthermore, the amplitude of the stimulus needs to be larger during that phase to exceed the cell's threshold. The end of the refractory period is defined as the time where V_m is resting and where the overshoot of the subsequent depolarization is at normal values. The length of the refractory period correlates with the AP duration (APD) and is 100 – 200 ms for atrial and 200 – 300 ms for ventricular myocytes [137].
The refractory period is an important physiological factor for the heart. It restricts the frequency of depolarizations and thus prevents the heart from a premature re-excitation, which could occur during rotating electrical waves [138]. Another important role of the refractory

period in the heart can be found in the AV-node where it realizes a low-pass filter between atria and ventricles, which is known as the Wenckebach effect [139]. A fast re-excitation of the atria, e.g. due to atrial fibrillation, is not conducted to the ventricle with the same frequency but only every 1 – 4 excitations.

4.5 Excitation Conduction

The myocardium is build mainly of discrete cardiomyocytes. These myocytes are surrounded by the extracellular space and coupled electrically by gap junctions. The discrete structure influences e.g. the electrophysiological properties of the tissue [140, 141]. The conduction of excitation is driven by electrical coupling of the cardiomyocytes. If one cell gets activated, V_m rises and a voltage gradient between adjacent cells can be measured. Due to this gradient a current through gap junctions and through the extracellular space flows into the neighboring resting cell and this cell gets activated. The intercellular electrical coupling leads to a functional electrical syncytium of the myocardium. Since the conductivity of the gap junctions is larger than the conductivity between adjacent cells via the extracellular space, the activation sequence is mainly influenced by the anisotropic electrical properties of gap junctions.

4.5.1 Gap Junctions

Gap junctions (section 2.1.1.2) behave primarily like low resistance ohmic resistors, which vary the conductivity depending on the trans-junctional voltage [33, 142]. In contrast to membrane channels they do not show ion selectivity, but allow passage of both cations and anions with a slightly preference for cations. They also provide intercellular metabolic coupling [32].
The conductance of a gap junction depends on ionic factors such as the intracellular concentrations of H^+, Ca^{2+}, Na^+, and Mg^{2+} [143]. Thus, gap junction conductance is influenced by application of drugs, which alters the concentration of these ions. Pathologies like myocardial ischemia varies gap junction conductance, because the pH value of the extracellular fluid is changed and that influences the concentration of intracellular H^+ [26].
Alteration of gap junctional conductance effects the overall electrical interaction between cardiac myocytes. Because connexins form the gap junction, they are important determinants of myocardial coupling properties. Changing genetic expression of connexins causes changed overall electrical conductance. Computer simulations and experimental studies showed that a reduction in gap junctional conductance results in reduced excitation conduction velocity [144]. Measurements showed that the density of gap junctions of the SAN and the AVN is less than in atrial and ventricular tissue [145].

4.6 Excitation Contraction Coupling

The process, in which electrical excitation enables the myocyte to contract is called excitation contraction coupling (ECC). The Ca^{2+} current through the membrane of T tubules plays an important role for ECC. It triggers the so-called Ca^{2+}-induced Ca^{2+}-release (CICR) from the sarcoplasmic reticulum (SR). The increase of free myoplasmic calcium is the main reason for the development of tension in the contractile unit. Since many transmembrane proteins are involved in the ECC process, intensive research on their properties is crucial in order to understand their individual electrophysiological behavior and conclusively the whole functionality of ECC.

Calcium is considered to be the most important ion involved in the cardiac ECC [146]. The inward Ca^{2+} current contributes to the AP plateau, increases intracellular calcium, and induces the activation of the contraction (fig. 4.9 inset). Measurements with the patch clamp technique revealed that Ca^{2+} current reaches its peak value in approximately $2 - 3\ ms$ after begin of the depolarization. The combination of Ca^{2+} influx from extracellular space and Ca^{2+} release from SR raises the free intracellular Ca^{2+} concentration ($[Ca^{2+}]_i$) and allows Ca^{2+} to bind to the thin filament protein TnC. The TnC-Ca^{2+} complex enables the contraction process of the myofilaments. However, contraction depends not solely on $[Ca^{2+}]_i$, but also on other indispensable factors.

4.6.1 Involved Ionic Channels

Several calcium specific proteins are involved in cardiac ECC and the calcium removal procedure (fig. 4.9). They are located in the sarcolemma and intracellular organelles, e.g. the SR and mitochondria. This section describes channels that contribute to the increasing of $[Ca^{2+}]_i$, i.e. the L-type Ca^{2+} channel (DHPR) and the SR Ca^{2+} release channel (RyR). Four pathways involved in Ca^{2+} transport out of the myoplasm are known, i.e. the SR Ca^{2+}-ATPase, the sarcolemmal Ca^{2+}-ATPase, and the mitochondrial Ca^{2+} uniport. The Na/Ca exchanger was already explained in section 4.3.3.

Dihydropyridine Receptors (DHPR) are voltage-dependent L-type Ca^{2+} channels. They are sensitive to dihydropyridines and are activated by depolarization of the cell membrane. DHPRs are found mostly adjacent to the junctional segment of the SR (section 2.1.2.3).

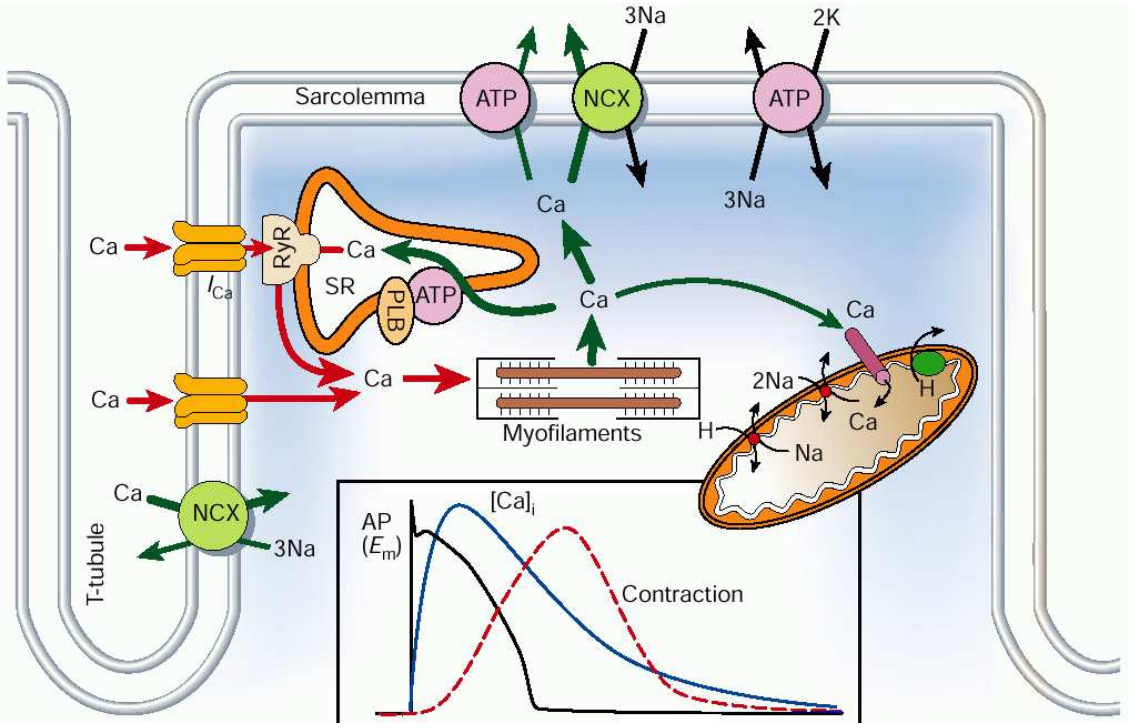

Fig. 4.9. Transmembrane channels for calcium fluxes can be divided into two groups, i.e. channels which increase (red-colored) and decrease (green-colored) $[Ca^{2+}]_i$. Increasing $[Ca^{2+}]_i$ proteins are DHPR (denoted as I_{Ca}) and RyR. Decreasing $[Ca^{2+}]_i$ proteins are SR Ca^{2+}-ATPase, sarcolemmal Na^+/Ca^{2+} exchanger (NCX), sarcolemmal Ca^{2+}-ATPase (ATP), and mitochondrial uniport (The mitochodrion is the ellipsoid shaped part). Calcium binds to proteins of the myofilament during high $[Ca^{2+}]_i$. (Inset) Time course of transmembrane voltage, intracellular concentration of calcium, and contraction. Fig. from [147].

Studies showed that the Ca^{2+}-induced Ca^{2+}-release mechanism is initiated and mediated by the L-type Ca^{2+} channel current [147]. The selectivity of L-type Ca^{2+} channel in ion transport is mediated by preferential binding of two principal competitors, i.e. Ca^{2+} over Na^{+} [148].

Ryanodine Receptors (RyR) are channels that releases Ca^{2+} from the SR. RyRs are located at the junctional SR (JSR). The Ca^{2+} buffer calsequestrin participates in the active Ca^{2+} release process by modulating and inhibiting the function of RyRs [48, 49, 149].

SR Ca^{2+}-ATPase: The free myoplasmic Ca^{2+} concentration is kept below 0.1 μM during the resting phase, primarily by Ca^{2+} pumps [150, 151]. Ca^{2+} pumps are mainly located along the membrane of the network SR (NSR) moving Ca^{2+} continually from the myoplasm into the SR. Because of this activity, the SR acts as an intracellular reservoir for calcium. The transport mechanism starts with the reaction of two calcium ions and one ATP molecule, binding with high affinity to the myoplasmic sites of the pump. The phosphate terminal of ATP is transferred to a receptor and ATP gets hydrolyzed. Calcium ions are adsorbed and obstructed in the pump. The hydrolysis reduces the affinity of calcium ions, which can be released to the lumen of the SR. The cardiac SR Ca^{2+}-ATPase is endogenously inhibited by the integral membrane protein phospholamban [152].

Sarcolemmal Ca^{2+}-ATPases function as a maintainer of low $[Ca^{2+}]_i$ during the resting phase [153]. Transport of one Ca^{2+} is driven by the hydrolysis of one ATP. Sarcolemmal Ca^{2+}-ATPase possesses a high affinity to Ca^{2+}, but its transport rate is very slow. A sole removal of intracellular calcium through this pump would take about $20-40\,s$ for the myocyte to relax [13]. In comparison to the SR Ca^{2+}-ATPase, the number of sarcolemmal Ca^{2+}-ATPases in the cell membrane represents only a minor portion of the total membrane proteins. The sarcolemmal Ca^{2+}-ATPase has a higher affinity for Ca^{2+} than the sarcolemmal Na/Ca exchanger, but the sarcolemmal exchanger has a higher maximal throughput of Ca^{2+}.

Mitochondrial Ca^{2+} uniport: The mitochondria feature Ca^{2+} removal channels, the so-called mitochondrial Ca^{2+} uniports. They remove myoplasmic Ca^{2+} into the mitochondria, but the removal rate is very slow. The required energy is mostly replenished by mitochondrial oxidative phosphorylation. Slow cumulative changes in intra-mitochondrial calcium ions can increase the production of ATP to match increased energetic demands [154]. Since both, ATP and changes of $[Ca^{2+}]_i$ are important for the cardiac contraction and relaxation, mitochondrial calcium dynamic plays an important role during ECC.

4.6.2 Intracellular Calcium Transients

The transsarcolemmal Ca^{2+} influx through the DHPR channels does not activate the myofilaments directly, but through the CICR from the SR. This process describes how a small elevation of the dyadic calcium concentration leads to a larger Ca^{2+} release from the SR [13]. CICR does not occur in an all-or-none fashion and can be graded with the magnitude of Ca^{2+} influx current through the sarcolemma i.e. modulated by DHPR [155]. The amplitude of CICR also depends on the rate at which the calcium concentration near to the SR changes. A high concentration of Ca^{2+} in the dyadic space inactivates CICR.

4.6.2.1 Ca^{2+} Sparks

Ca^{2+} sparks are spontaneous local Ca^{2+} transients from RyRs (fig. 4.10), which are located at the junctional couplon, thus mostly at the dyadic spaces along the T-tubules (section 2.1.2.3) [147]. Ca^{2+} sparks are occuring nearly synchronous in a cluster of about 6 – 20

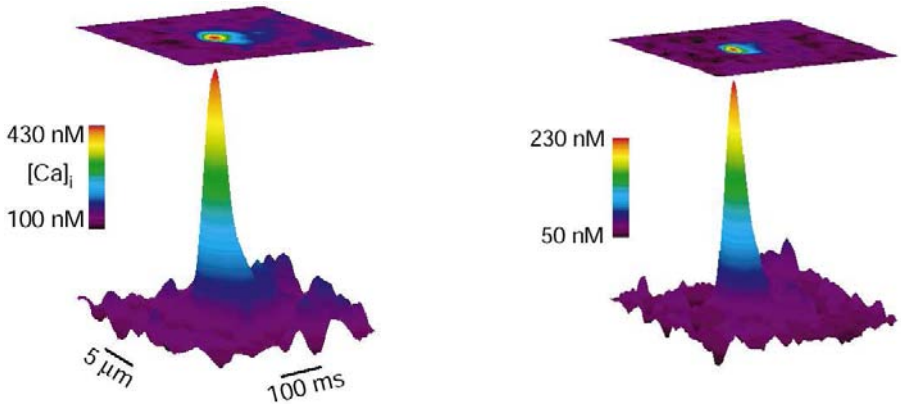

(a) (b)

Fig. 4.10. Ca^{2+} sparks occur at certain locations and rise to a peak in about 10 ms. Ca^{2+} sparks decline in about 20 ms. They have a spatial diameter of 2.5 μm. (a) Recorded in intact mouse ventricular myocytes. (b) Permeabilized cells. Fig. from [147].

RyRs. They can be recorded with a rising time to their peak of about 10 ms and a declining time of about 20 ms. In a resting myocyte, Ca^{2+} sparks are rare stochastic events, which are distributed equally to all RyRs. If the Ca^{2+} concentration in the dyadic space or the SR is high enough, stochastic releases of Ca^{2+} at a couplon can activate a neighboring couplon.
During the activation of the cell, sparks of all participating RyRs are synchronously evoked in time by depolarization [156]. The sychronization leads to an overlap in time and space of the Ca^{2+} transients and $[Ca^{2+}]_i$ raises [157]. Since the number of involved RyRs is high, the measured Ca^{2+} transients appear spatially uniform and of high amplitude.

4.6.2.2 Activation and Deactivation of Calcium Release

Usually, a cluster of L-type Ca^{2+} channels is involved synchronizing RyR clusters. But even one single opened local L-type Ca^{2+} channel in one couplon can trigger synchronous sparks of the involved RyRs. This single opened DHPR is sufficient to fully activate the release process at that couplon. Other neighboring RyRs can be activated either by high local Ca^{2+} (> 10 μM) or by coupling mechanisms between RyRs.
Figure 4.11 describes the gating mechanism of RyRs in presence of Ca^{2+}. A RyR is equipped with two Ca^{2+} binding sites including a coupling channel key, which functions as a release valve. One of the Ca^{2+} binding sites has a low affinity, the other a higher affinity. When $[Ca^{2+}]_i$ in the dyadic space increases, Ca^{2+} binds to the lower affinity site. This site has a

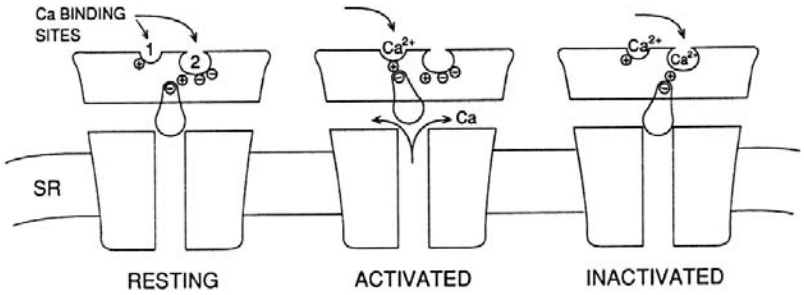

Fig. 4.11. Schematic diagram of the activation and inactivation mechanism of RyR. The binding of Ca^{2+} to the low affinity activation site (1) leads to a rapid activation of RyR. Binding of Ca^{2+} to the high affinity site (2) inactivates RyR. Fig. from [13].

very high triggering rate, causing the valve to open the release channel. If the dyadic Ca^{2+} concentration increases further on, Ca^{2+} binds also to the high affinity sites having a slower triggering rate leading to the inactivation of RyRs.
Since the cardiac myocytes have to relax during the diastolic phase, the CICR has to recline. Three potential mechanisms describe the turn-off process [13, 158]:

Local depletion of JSR Ca^{2+} is a long lasting procedure, since Ca^{2+} sparks do not decline within 200 ms. Ionic diffusion from the NSR prevents local Ca^{2+} depletion at the JSR. This causes the reduction of the whole Ca^{2+} concentration of the SR, which modulates RyR gating and contributes to turning-off SR Ca^{2+} release during a contraction.

RyR inactivation is a mechanism depending on $[Ca^{2+}]_i$ and has two types. The first mechanism is the inactivation state of RyR itself. The RyR is unavailable for reopening until it recovers (fig. 4.11). The second is called adaptation mechanism. After the activation, RyRs relax and adapt their behavior to a lower triggering probability.

Stochastic attrition describes the very rapid local fall of $[Ca^{2+}]_i$ and the interruption of the otherwise positive feedback release. The reason could be the simultaneous stochastic closing of L-type Ca^{2+} channels and all RyRs in a junctional area.

4.6.3 Calcium Removal and Balance

After contraction, Ca^{2+} must be removed from the myoplasm to allow cellular relaxation. The SR Ca^{2+} ATPase is the major removal mechanism [147]. The sarcolemmal Ca^{2+}-ATPase and mitochondrial Ca^{2+} uniporter contribute together only approximately 2 % to the calcium removal. Furthermore, they are slow systems. The average amount of Ca^{2+} removed from the myoplasm during relaxation and dilatation must be the same as the amount of Ca^{2+} influx. If the calcium balance was not attained, the cell would gain or lose Ca^{2+} and is not in steady state.
Several buffering mechanisms are involved in balancing the intracellular calcium dynamics. Calsequestrin is a SR Ca^{2+} binding protein, which is closely related to RyRs. The primary function of calsequestrin is to sequester Ca^{2+} into the lumen of the SR during the relaxation phase and accumulate Ca^{2+} there. It binds Ca^{2+} with high capacity (40 – 50 Ca^{2+} ions per calsequestrin), but with moderate affinity. Two predominant buffers of Ca^{2+} exist in the myoplasm: calmodulin and troponin. Calmodulin is a signaling protein, which reacts on long-term variations of $[Ca^{2+}]_i$ to modulate the expression of proteins in the cell. Troponin is the Ca^{2+} binding protein of the myofilaments and will be detailed in chapter 6.

4.7 Tissue Specific Electrophysiology

Electrophysiological heterogeneity is a well known property of the heart, although, the effects of the heterogeneity and the reason why "evolution has created" it are poorly understood. In the atria, several bundles and regions have different electrophysiological properties than the cells of the atrial working myocardium. Furthermore, the electrical coupling, i.e. the density and distribution of gap junction varies between the different structures. In the ventricles, a strong transmural heterogeneity was identified leading to a dispersion of repolarization. The depolarization propagates commonly from endocardium towards epicardium, while the repolarization propagates mainly in the other direction.
The excitation of the heart is initiated in the sinoatrial node (SAN), the so-called primary pacemaker. Further cells towards the ventricle also have self-depolarizing properties. These

are the atrioventricular (AV) node as the secondary pacemaker, and distal parts of the conduction system as tertiary pacemaker (tab. 4.1). The frequency of the secondary pacemaker is lower than the frequency of the SAN. Hence, the AV node develops autorhythmic depolarizations only, if the primary pacemaker fails or if the excitation is not conducted from SAN to AV node. The tertiary pacemaker has an even lower frequency than the AV node. The electrophysiological differences of auto-rhythmic cells compared to working myocytes are explained in this section exemplary by the properties of the SAN.

4.7.1 Pacemaker Activity of the Sinoatrial Node

The physiological excitation of the heart driven by the SAN is called sinus rhythm. The frequency adaptation of the SAN is controlled by the autonomous nerve system and by hormones in the blood [50, 58]. Voltage clamp experiments have gained knowledge of the influence of different ionic channels on the morphology of the pacemaker potential [127]. A significant difference of SAN cells compared to cells of e.g. the atrial working myocardium (AWM) is the lack of the inward rectifier current I_{K1} [127]. This already leads to a slowly increasing resting voltage, which finally exceeds the threshold and the cell begins to depolarize spontaneously.
There are additional changes in ionic channels of SAN cells compared to other myocytes. The maximum conductance $g_{Na,max}$ of the fast sodium channel is reduced or zero in SAN cells leading to a prominent reduction in the upstroke velocity of the AP of SAN cells compared to AWM [160]. The maximum diastolic potential (MDP) of pacemaker cells is determined mainly by the amplitude of I_{Kr}. The maximum conductance $g_{Kr,max}$ of this current is increased in SAN cells. Also, I_{Ks} is larger in SAN cells leading to an increased total delayed rectifier K^+ current, which decreases the MDP [161]. The potential in the phase where the cells activate slowly towards depolarization is called pacemaker potential (fig. 4.12a). It is influenced by enlarged current $I_{Ca,L}$. The same holds for the MDP and thus the frequency. $I_{Ca,L}$ is mainly responsible for the upstroke of the AP in central SAN cells [162]. The presence of $I_{Ca,T}$ was proved in cardiac SAN cells by experiments [127]. If this current is blocked, a negative chronotropic effect is present in SAN. The sustained outward K^+ current I_{sus} was measured in SAN cells [124].
The hyperpolarization activated current I_f is also a current mainly expressed in pacemaker cells. This current was measured in human [163] and rabbit [164]. It is carried by both Na^+ and K^+. Na^+ has the predominant fraction during diastolic potentials. The current I_f activates from voltages larger than –50 mV. Its current is increased by an increased $[K^+]_o$ [165].
The SAN is functionally, structurally, and electrophysiologically heterogeneous. The excitation of the SAN starts in its central cells and activates the periphery towards the crista

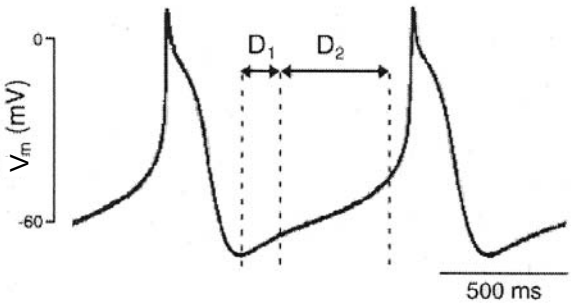

Fig. 4.12. Transmembrane voltage of an isolated sinoatrial node cell. First (D1) and second (D2) phase of the pacemaker potential. Fig. from [159].

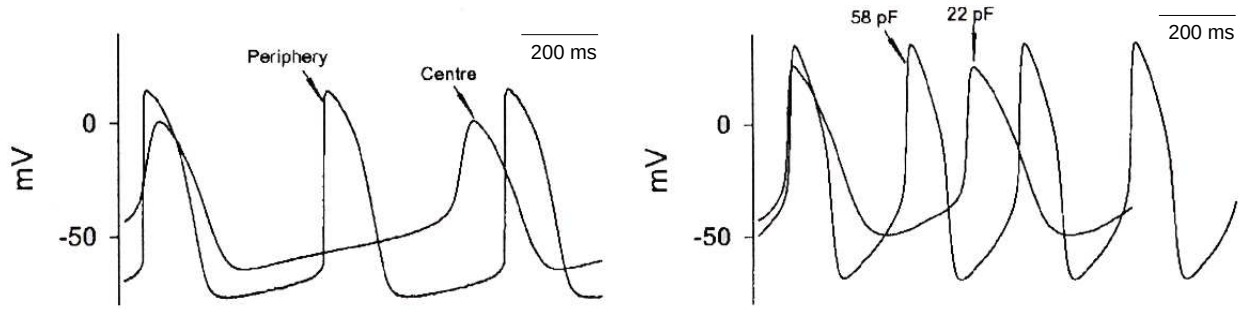

(a) (b)

Fig. 4.13. Heterogeneous transmembrane voltages of isolated sinoatrial node cells measured in rabbit. (a) Recorded in tissue of central and peripheral SAN cells [169]. (b) Measured in SAN cells of different size, thus different membrane capacitance [167].

terminalis and the atrial working myocardium [166]. The cells in the center of the SAN are smaller and thus the membrane capacitance is lower. This and additionally varying ion channel densities lead to a difference of AP morphology in the heterogeneous SAN (fig. 4.13a). The AP upstroke in central cells is smaller than of peripheral cells and the frequency is lower. Also, the maximum diastolic potential is lower, the maximum systolic potential is less negative, and the APD is longer in central cells. The relation between capacitance and AP was reported in rabbit experiments [167] illustrated in fig. 4.13b.
Since the single cell frequency of central cells is lower than the frequency of isolated peripheral cells, there must be a mechanism to let the center of the SAN be the primary region of activation. This mechanism is the gradient electrotonic effect due to varying gap junction densities. Peripheral cells are neighbored by atrial working myocytes. Since these cells have a more negative resting voltage than the SAN cells, the transmembrane voltage of peripheral cells is shifted also towards more negative voltages and thus the frequency is reduced. As the volume of central cells is small, heterogeneous distribution of gap junctions allows the sinoatrial node to drive the activation of the atrial muscle. The density of gap junctions decreases from periphery towards center of the SAN leading to a partly less coupling in the central cells [168]. Thus, central cells can depolarize even without the fast sodium current and can still activate the neighboring regions. Besides the density dependence of gap junctions, a cell-size dependence in pattern of connexin expression is existing in SAN cells of different regions. Central cells express one type of connexin, peripheral cells express two types.
Most of the measurement data to describe the behavior of SAN cells are gained by animal experiments, mainly from rabbits. Measurements of the electrophysiological properties in the human SAN are rare. They showed that the maximum diastolic potential is $-62.5 \pm 4.7\ mV$ and the overshoot $9.8 \pm 2.7\ mV$ [170]. The depolarization of the AP is initiated in human at $-48.5 \pm 6.0\ mV$. Furthermore, it was shown that the electrophysiological properties of human sinoatrial node are comparable to canine and rabbit [170]. Mainly the autorhythmic frequency of the different species show large variations.

4.7.2 Atrial Electrophysiology

Important anatomical structures in the atria for excitation initiation and conduction are the sinoatrial node, the crista terminalis (CT), the pectinate muscles (PM), and the interatrial connections, e.g. Bachmann's bundle (BB). The left and right atrial working myocardium (AWM) is also conducting the electrical excitation but its main function is mechanical contraction.

Table 4.3. APD_{50} and APD_{90} of different regions of the canine right atrium at different stimulus frequencies [174]. CT: crista terminalis; APG: appendage; PM: pectinate muscles; AVR: atrioventricular ring.

f	CT	APG	PM	AVR
APD_{50}				
0.1 Hz	186±8 ms	120±2 ms	103±3 ms	58±2 ms
1.0 Hz	157±5 ms	118±2 ms	98±2 ms	49±3 ms
2.0 Hz	120±4 ms	85±2 ms	49±2 ms	45±3 ms
APD_{95}				
0.1 Hz	328±13 ms	210±7 ms	245±4 ms	181±4 ms
1.0 Hz	270±10 ms	180±3 ms	190±3 ms	160±4 ms
2.0 Hz	219±7 ms	155±2 ms	152±3 ms	140±3 ms

Physiological excitation of the heart is initiated in the SAN. Then, the fast right atrial pathways, i.e. CT and PM, conduct excitation preferentially towards the atrioventricular region. During that phase the right atrium (RA) becomes depolarized. At the same time, BB conducts the excitation towards left atrium (LA). Further connections between both atria are the limbus of the fossa ovalis [171] and an area at the coronary sinus [172]. Finally, the whole atrium gets excited after approximately 120 ms [173]. All conduction pathways are characterised by a large conductivity along the fiber direction leading to a fast conduction velocity along the main fiber axis.

Recent simultaneous bi-atrial measurement from humans by non-contact mapping systems investigated interatrial coupling [173]. They showed that the earliest activation of the left atrium is via BB during sinus rhythm. Furthermore, the time to activation after SAN activation is 19 ms for right atrial part of the BB and 24 ms for the right atrial septum. In left atrial measurements, the first activation was after 41 ms near BB and after 43 ms in septal regions. The total endocardial activation time, which is the time when all of the tissue gets depolarized, is: 23 ms for BB, 81 ms for RA, 80 ms for LA, and 120 ms for the whole atrium. The atrium is electrophysiologically inhomogeneous. The APD in different regions of the atrium varies significantly (tab. 4.3). Experimental measurements of atrial tissue from different anatomical regions of canine show these electrophysiological differences (fig. 4.14) [174]. Myocytes from CT have the most prominent "spike-and-dome" morphology and the longest APD. Myocytes from PM and those from the APG show intermediate APDs compared to those from the crista terminalis. Myocytes from the atrioventricular ring have the shortest APD and no "spike-and-dome" morphology. The differences in ionic channel density of I_{to}, I_{Kr}, and $I_{Ca,L}$ were identified to produce these varying AP morphologies.

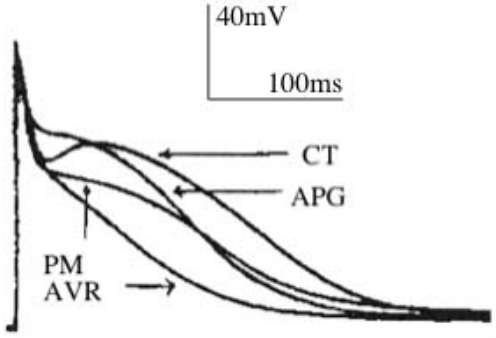

Fig. 4.14. Heterogeneous atrial courses of the action potential of crista terminalis (CT), pectinate muscles (PM), appendage (APG), and atrioventricular ring (AVR) in measurement data of Feng et al. in canine atrium. Fig from [174].

Table 4.4. Measurements concerning heterogeneity of ion channel characteristics in human and canine ventricular tissue. Only the mean values are listed.

Current	Author	Species	Subendocardium	M cells	Subepicardium
I_{to}	Li et al. [175]	Human	2.2 pA/pF	6.0 pA/pF	6.9 pA/pF
	Wettwer et al. [177]	Human	2.3 pA/pF		7.9 pA/pF
	Opthof et al. [178]	Canine	25%	87%	100%
	Liu et al. [176]	Canine	714 pA	3638 pA	4203 pA
I_{Ks}	Opthof et al. [178]	Canine	92%	46%	100%
	Liu et al. [179]	Canine	1.83 pA/pF	0.92 pA/pF	1.99 pA/pF
I_{K1}	Li et al. [175]	Human	–8.2 pA/pF	–8.3 pA/pF	–10 pA/pF
	Opthof et al. [178]	Canine	89%	74%	100%
	Liu et al. [176]	Canine	348 pA	289 pA	392 pA
I_{NaCa}	Zygmunt et al. [180]	Canine	–0.21 pC/pF	–0.316 pC/pF	–0.293 pC/pF

4.7.3 Ventricular Electrophysiology

The ventricles of the mammalian heart are relatively thick walled compared to the atria and also show regional heterogeneity, i.e. myocytes isolated from different transmural and apico-basal regions have non-equal electrical properties characterized by varying APDs. Three principal cell types can be distinguished: subendocardial, subepicardial, and midmyocardial (M) cells. They differ in electrophysiology, in respond to pharmacological agents, and in their expression of pathologies.

A "spike-and-dome" morphology of the AP is present in subepicardial cells and vanishes throughout the wall towards the endocardium (fig. 4.15). The APD is varying in measurements concerning 50 % (APD_{50}) and 90 % (APD_{90}) repolarization [176]. The mean human APD_{90} in endocardial cells is 263 ms, in mid-myocardial 390 ms and in epicardial 271 ms [175]. The underlying mechanisms of these differences are defined by the heterogeneous distribution of ion channel characteristics, mainly the change of ion channel densities. Altogether, the differences between transmural transmembrane voltages are important factors for generating the upright monophasic T wave in transmural electrocardiograms (ECG). Up to now, four different currents are known to have physiological transmural differences in human and canine ventricles (tab. 4.4): I_{to}, I_{Ks}, I_{K1} and I_{NaCa}.

I_{to} is primarily forming the early phase of the AP, i.e. generation of notch [122]. It furthermore influences APD and refractoriness. I_{to} is largest (100 %) in epicardial cells, decreases to about 90 % in M cells, and to about 25 % endocardially [175, 176, 177, 178].

I_{Ks} mainly influences the plateau phase and late repolarization [110, 122]. The slow deactivation process causes the rate-dependent shortening of APD. A decreasing density of I_{Ks}

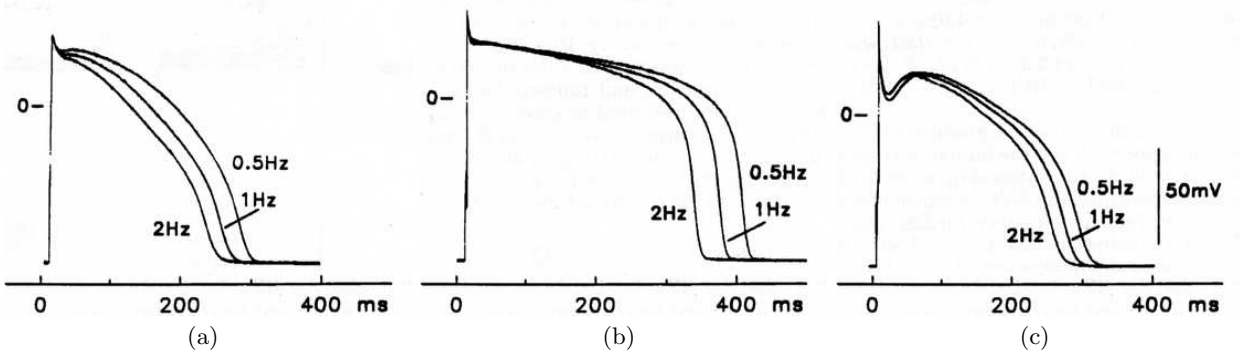

Fig. 4.15. APs recorded from myocytes isolated from (a) subendocardial, (b) midmyocardial, and (c) subepicardial regions of the canine left ventricle during different stimulation frequencies. Figs from [175].

channels lead to a prolongation of APD. While I_{Ks} is nearly the same in endo- and epicardial cells, it is reduced to approximately 50 % in M cells [178, 179].
I_{K1} plays an important role during negative transmembrane voltages, especially for maintaining a stable resting potential [110, 122]. I_{K1} is largest in epicardial cells and smaller in endocardial and M cells [175, 176, 178].
The main function of I_{NaCa} is to support the calcium pump of the SR to quickly reduce the myoplasmic calcium concentration after activation [97]. While I_{NaCa} is nearly the same in epicardial and M cells, it is reduced about 30 % in endocardial cells [180]. These changes are reported to date only in canine [180] and guinea-pig [181] ventricular cells.
It is not finally clarified if other ion channels have transmural heterogeneous characteristics in larger mammalian hearts. Late I_{Na} is expected to be enlarged in M cells [117, 182]. Cordeiro et al. reported recently heterogeneity in unloaded cell shortening, Ca^{2+} transients, and L-type Ca^{2+} current of epicardial, endocardial, and midmyocardial cells that were isolated from canine left ventricle [183]. Peak $I_{Ca,L}$ and total charge is declining from epicardium towards endocardium. Furthermore, time to peak $[Ca^{2+}]_i$ was shortest in subepicardial cells.
The location of M cells varies within the ventricular wall [117]. In the canine heart, M cells can be found in more subepicardial regions within the lateral wall, more subendocardial areas in the anterior wall and throughout the wall near the valves. A recent study supports the existence of M cells in a third of the distance between endocardium and epicardium with a smooth transition between the three cell groups [184].
A substantial electrophysiological gradient was also measured along the apico-basal axis [185]. In epicardial muscle layers of the apex the effective refractory period (ERP) was longer than in the base in in-vivo experiments of intact canine heart using 10 needle electrodes inserted into basal, midwall and apical regions of the left ventricular wall. Apico-basal disparity of repolarization varies between individual muscle layers.

4.8 Pathoelectrophysiology

A large variety of different pathologies of the heart exists influencing electrical excitation and mechanical function. Pathologies with an anatomical origin for example could be either atrial or ventricular hypertrophy. Electrophysiological pathologies, which will not be described in detail in this section are e.g. blocks of the excitation initiation and conduction system (sick sinus syndrome, atrioventricular blocks of diversity degrees, bundle branch blocks, Morgagni-Adams-Stokes syndrom, etc.), pathological excitation of the ventricle via e.g. the bundle of Kent (Wolff-Parkinson-White syndrom), extrasystoles of the atria and ventricles, and infarction induced pathoelectrophysiology. A main focus in this work is given on tachyarrhythmias like atrial fibrillation and genetic defects like long QT syndromes.

4.8.1 Tachyarrhythmia

The human heart is excited periodically with a frequency of 60 to 70 beats per minute (bpm) in rest. Arrhythmia is called any excitation of the heart with an unphysiological frequency. If the heart beats too slow, e.g. due to the sick sinus syndrome [186], the arrhythmia is called bradycardia. If it beats faster than normal during rest it is called tachyarrhythmia. A frequency of faster than 100 bpm is a tachycardia. Even faster excitations are called flutter and fibrillation e.g. due to re-entry mechanisms and spiral wave breakup [187]. Flutter is a monomorphic tachyarrhythmia, hence it appears with regular rate and rhythm. Polymorphic

tachyarrhythmias are irregular in rate and rhythm. The most dangerous rhythm is a form of polymorphic tachyarrhythmia i.e. fibrillation.
The wavelength of excitable tissue is an important determinant for the generation of tachyarrhythmias. The wavelength is the distance travelled by the electrical impulse in one refractory period. The wavelength is the product of the refractory period and the conduction velocity. According to the prevalent hypotheses, the wavelets of fibrillation circulate randomly across the myocardium. When a wavefront encounters tissue islands in the absolute refractory state, it can become fractionated, creating new daughter wavelets. The wavelength plays an important role to sustain the multiple wavelets [188]. If the pathlength of the reentrant circuit is smaller than the wavelength, the impulse will traverse the circuit and return to its starting point, forcing the wave to impinge on still-refractory tissue and die out. Thus, the pathlength is always longer as compared to the wavelength to sustain a re-entry (fig. 4.16).

4.8.1.1 Flutter

Atrial and ventricular tachycardia is an arrhythmia where the myocardium is excited with an unphysiological frequency of 100 to 160 bpm during rest. If this frequency rises to between 200 and 250 bpm the arrhythmia is called flutter [190].
Atrial flutter is very often based on the influence of a self-activating zone in the atrium or initiated by a rotating wave (re-entry). This is possible due to the shortened refractory period and the reduced excitation conduction velocity during higher frequencies leading to a reduced wavelength. Atrial flutter can be addressed to e.g. arteriosclerotic or rheumatic heart disease [191].
Atrial flutter is mainly driven by a reentrant activation of the right atrium alone, including atrial septum and right atrial free wall [192]. The central area of block around which the reentrant wave circulates includes normally an anatomical component e.g. the vena cavae and the tricuspid valve ring. In this case, the anatomical obstacle is the center of the rotor.
As in the atrium, ventricular tachycardia is due to fast re-excitation of the tissue without control of a pacemaker system [193]. The excitation patterns are pathologic but have a rhythmic periodicity. Ventricular tachycardia (VT) could be initiated by the pathological electrical excitation of an physical damaged region like the focal activation in long QT syndrome (section 4.8.2.2) or in the ischemic border zone of an infarction. Several other mechanisms have been addressed to initiate and maintain VT e.g. unidirectional block of conduction or spiral waves and three-dimensional rotors. VT is closely related to pathologies like coronary

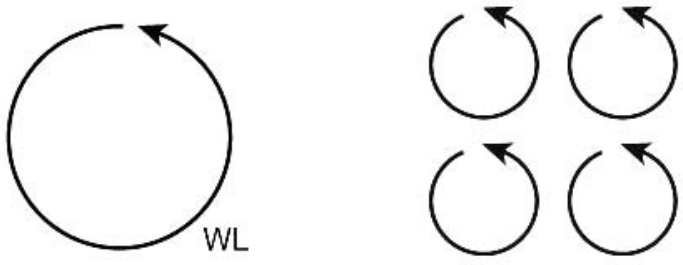

(a) (b)

Fig. 4.16. Role of wavelength (WL) in the stability of arrhythmia. The size of functional re-entry circuits depends on the wavelength. (a) Arrhythmia is not sustained because of normal wavelength and normal geometrical size. (b) Short wavelengths allow several simultaneous circuits to be maintained in the tissue. Figs. from [189].

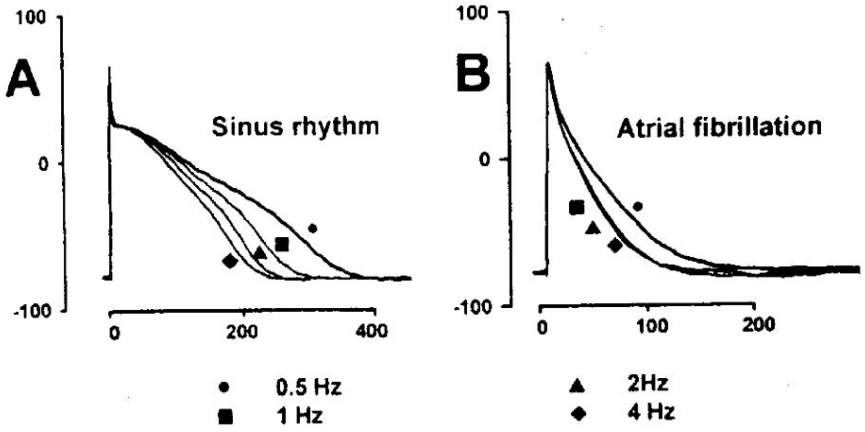

Fig. 4.17. Representative APs from healthy atrial myocytes (sinus rhythm) and a myocyte in persistent atrial fibrillation after cardioversion. The differences are assigned to the electrophysiological remodeling process initiated by AF. Fig. from [199].

artery disease [194], dilated cardiomyopathy [195], Brugada syndrome [196], and long QT syndrome. Many pathologies destabilize the electrophysiological balance of the heart. The patient suffering VT are of high risk to fall into ventricular fibrillation (section 4.8.1.2).

4.8.1.2 Fibrillation

Atrial fibrillation (AF) is an abnormal rapid activation of the atrial muscle, which results in the massive reduction of contractility in the atria. The atrial frequency is fastened from sinus rhythm (SR) to 400 – 600 bpm due to e.g. re-entry mechanisms [189]. The effects of sustained AF can be e.g. severe congestive heart failure, thromboembolism, cardiomyopathy, ventricular arrhythmia, and electrical remodeling of the atria, which supports persistence of AF [189]. The occurence of AF rises with age. 0.5% of the 50 years old and over 5% of the 70 years old are effected [197]. AF can be classified by:

Paroxysmal AF: These episodes of AF self-terminate within 48 hours to less than 7 days [189]. The heart changes from SR to AF for episodes lasting from seconds to days. The essential feature of paroxysmal AF is that the episodes terminate spontaneously.

Persistent AF: When an episode of AF has lasted longer than 7 days, AF is called persistent [189]. It may be the first time of arrhythmia or be preceeded by recurrent episodes of paroxysmal AF. Termination using electrical cardioversion is required.

Permanent AF: When AF was present for some time and fails to terminate using cardioversion or is terminated but replaced within 24 hours, it is called permanent [198].

Recent clinical research suggested that AF causes electrophysiological modifications that may contribute to the abnormal electrophysiological substrate, which facilitates the progression of AF i.e. electrophysiological remodeling. In SR, the APD is much longer at all frequencies and the cells display a clear frequency dependent adaptation of the APD with shortening at higher stimulation rates. In contrast, the APD in electrophysiologically remodeled atrial tissue is already very short at slow rates and there is almost no further shortening as the stimulation frequency is increased (fig. 4.17) [199, 200].
The reduced APD is a consequence of electrophysiological changes, which are induced by AF itself. The abbreviated APD causes a decreased wavelength. This decreases the minimum

reentrant circuit size. The number of circuits is increased, favouring multiple-circuit re-entry and tending to perpetuate AF [189]. If AF lasts for a while, a Ca^{2+} overload is recognized in the cells due to the higher release level of the sarcoplasmic reticulum [201]. Cellular proteases and kinases react on this overload and the changed expression of various channels in the membrane leads to a permanent reduction in APD. Thus, AF itself causes progressive electrophysiological changes, which induce shortening of the EPR and promote the initiation or perpetuation of AF ("AF begets AF") [202].
Ventricular fibrillation (VF) is a rapid, disorganized, and asynchronous contraction of the ventricular muscle [203]. This arrhythmia may lead to death due to reduced blood flow if it is not treated by defibrillation. VF is the leading cause of sudden cardiac death in the industrialized world, accounting for nearly 300.000 deaths annually in the United States [187]. It most often occurs in patients with structural cardiac abnormalities. Also, genetic defects may cause VF. The mechanisms and dynamics of VF are similar to atrial fibrillation.

4.8.2 Genetic Defects

Dysfunction of ion channels that lead to diseases i.e. ion channelopathies can result from inherited or acquired defects of ion channel genes. Inherited abnormalities could be caused by genetic defects, acquired ones could be due to poisons or toxins. The dysfunction may lead to an increased or decreased channel activity or even to a changed characteristics of the proteins function. The complex interaction of the heterogeneous characteristics can be disturbed by genetic defects, diseases, or drugs. In this section, only genetic defects, which are important to understand the modeling aims of this work, are explained.

4.8.2.1 Familial Atrial Fibrillation

Atrial fibrillation can have its origin in a genetic defect, which occurs on a familial basis. By sequence analysis in a four-generation family, Chen et al. identified a missense mutation S140G, which alters the normal α-subunit encoding *KCNQ1* gene of the slow delayed outward rectifier potassium current I_{Ks} channel [204]. The mutant channel function was recorded by whole cell patch clamping in transfected COS-7 cells. The current-voltage relationship was measured by a step protocol. Starting from the holding potential of $-80\,mV$, the potential was stepped for each 3 seconds between $-130\,mV$ and $50\,mV$ in a $10\,mV$ increment. The current density of I_{Ks} in COS-7 cells was increased significantly (gain-of-function effect). The current and the voltage had a nearly linear dependency and activation and deactivation were instantaneous. The mutation led to a shortened APD and reduced effective refractory period (ERP), which support the initiation and perpetuation of AF [189].

4.8.2.2 Long QT Syndrome

Some pathologies are based on defects mainly influencing the interaction of the transmural heterogeneous properties. For example the long QT syndrome [205], Brugada syndrome [196], and in some cases the genesis of Torsades de Points [206] were assigned to the disarrangement of the transmural heterogeneity.
One of the most investigated pathologies due to genetic defect are the long QT (LQT) syndromes (tab. 4.5). They cause changes in the dispersion of ventricular repolarization and are characterized by changes in the morphology of the ECG during the QT interval and T wave [117]. The QT interval is always prolonged and the T wave is broadened and enlarged

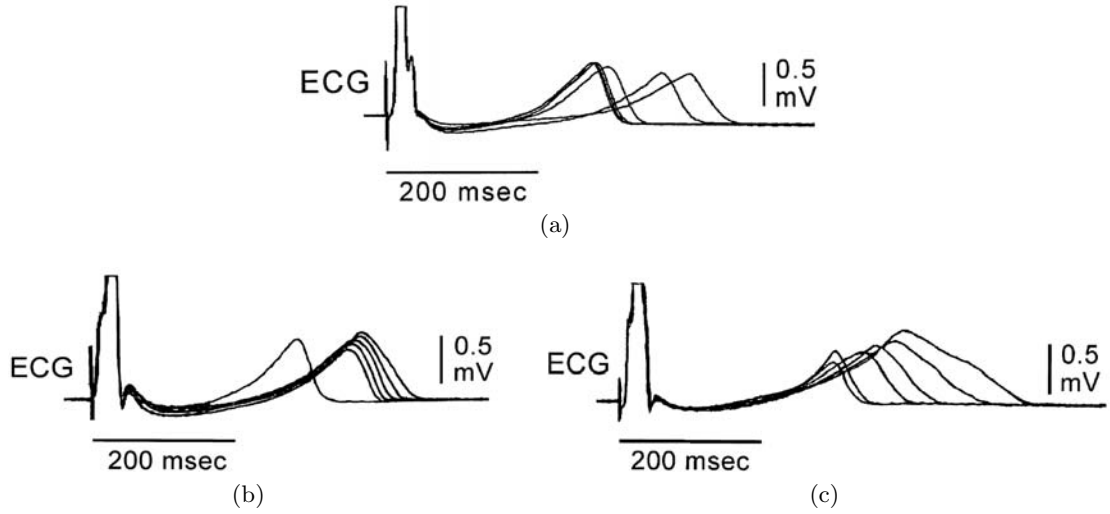

Fig. 4.18. Measured transmural ECGs of (a) LQT1 [210], (b) LQT2 [211], and (c) LQT3 [211]. The three LQT syndromes of canine myocytes are modeled pharmacologically.

in amplitude in some cases. The most common types of LQT syndromes are LQT1, LQT2, and LQT3, where the genes encoding the subunits of the proteins forming the currents I_{Ks}, I_{Kr}, and $I_{Na,L}$ are mutant, respectively [120, 121, 207, 208, 209].
Cause of the LQT1 syndrome is the loss of I_{Ks} channel function due to a defect of channel gene *KCNQ1* [210, 211]. This loss increased the APD in all cell types, since I_{Kr} is distributed nearly homogeneously inside the ventricular wall. Besides the prolongation of the QT interval, only small changes of the T wave morphology are visible in the transmural ECG (fig. 4.18a).
In case of the LQT2 syndrome a defect in gene *KCNH2* is responsible for the I_{Kr} channel to lose its capability to let K^+ ions pass [211]. Due to the heterogeneous distribution of the remaining repolarization current I_{Ks} the APD of the M cells is more prolonged than the APD of endo- or epicardial cells. Additionally to the QT interval prolongation, this results in larger amplitudes and widened shape of the T wave (fig. 4.18b).
A disturbance of the inactivating process of the I_{Na} channel due to a defect in channel gene *SCN5A* is the reason for LQT3 [211]. During repolarization phase 2 the mutant I_{Na} channel re-opens partly, which does not happen in physiological cases in this extend. The APD of all cell types is prolonged but largest in M cells because of the already longer plateau phase. This leads to the prolongation of the QT interval and a widening of the T wave. Furthermore, the amplitude of the T wave is enlarged (fig. 4.18c).

Table 4.5. Overview of the most common long-QT syndromes including effects. Data from [117, 212, 213].

Syndrome	Gene	Protein	Effect
LQT1	*KCNQ1*	KvLQT1	I_{Ks} reduced
LQT2	*KCNH2*	HERG	I_{Kr} reduced or blocked
LQT3	*SCN5A*	Nav 1.5	Late sustained I_{Na}, slowed inactivation
LQT4	*ANK2*	Ankyrin B	unknown
LQT5	*KCNE1*	MinK	I_{Ks} reduced
LQT6	*KCNE2*	MiRP1	Faster deactivation of I_{Kr}

5

Modeling Cardiac Electrophysiology

The computational reconstruction of cellular electrophysiology started in 1949 by Hodgkin and Huxley, who described the dynamic electrophysiology of a giant squid axon. They measured the active and passive electrical behavior and found a set of equations reconstructing the measured data [214].
The formalisms of Hodgkin and Huxley and also most of the models of cardiac electrophysiology using the same type of equations describe the channel gating kinetics on the molecular level that produce the ionic currents. The protein descriptions are included into a model of the cell membrane, where the contribution of each ionic current is summed up. The currents furthermore effect the ionic concentrations in intra- and extracellular space. For modeling the conduction of excitation, these cells are electrically coupled on the tissue level describing the anatomical shape of the organ and also considering the flow of ions between adjacent cells.
Most of the cardiac electrophysiological models are based on the Hodgkin-Huxley formalisms. They consist of mathematical reconstructions of currents through ionic channels, pumps, and exchangers. These currents are dependent on time, on transmembrane voltage, and on the concentration of ions and other substances. The currents represent the ionic flow through the pores of the sarcolemma and membranes of intracellular structures. One important intracellular structure for cardiac electrophysiology is the sarcoplasmic reticulum (section 2.1.2.3). The mathematical reconstruction of the ion channels, pumps, and exchangers is described in the first part of this chapter. The gating mechanism is introduced to describe the kinetics of these pores.
The sarcolemma can be represented with an electrical equivalent circuit consisting of a capacitance, variable and static conductances, and voltage sources. The capacitance represents the sarcolemma. The variable conductances depict the different ion channels. The voltage sources are the Nernst voltages. The parameters of the circuit are adjusted due to measurement data. The protein descriptions in conjunction with the membrane properties form a model, which reconstructs the electrophysiology of excitable cells. To understand the mechanisms of these models, the Hodgkin-Huxley model is introduced. Cardiac electrophysiological models are described, mainly those of human atrial and ventricular myocytes.
The coupling of cardiac myocytes in a mathematical sense is represented by models of current flow in the tissue. Some of these excitation conduction models consider the discrete nature of the cells in the tissue, others describe the conduction of excitation in a more macroscopic and continuos manner. At least the current flowing through the intracellular space and through the coupling protein of adjacent cells, i.e. gap junctions, is reconstructed in both approaches to consider the anisotropic electrical properties of the tissue. If the electrical field of the extracellular space is also considered for the calculation of the intercellular current, the description includes the properties of cardiac tissue more precisely. In the last physiological part of this

chapter, the so-called monodomain and bidomain model of electrical current flow is described in detail.
Since the modeling of cardiac tissue is based on enhancing the knowledge about the physiological as well as the pathological states of the heart, large efforts in the area of computational cardiology were spent in investigating the mechanisms and effects of pathoelectrophysiology, which is explained at the end of this chapter.

5.1 Models of the Membrane Protein Kinetics

As described in section 4.3.1 the sarcolemma and other intracellular membranes are bridged by membrane proteins building a selective permeable membrane. Some of them are ionic channels opening and closing in a time and voltage dependent manner. They are influenced by the concentration gradient of ions between the intra- and extracellular space or the concentration of ligands, and do not consume directly energy. Also, the properties of ionic pumps, which depend on the concentration of ATP, and exchangers are inserted in the membranes. For each of the proteins, different mathematical approaches were developed to reconstruct their kinetics.
A simple model to describe the movement of charge through a membrane protein, which is selective for only the ion type X, is given by an ohmic conductor:

$$I_X = g_X(V_m - E_{rev}) \tag{5.1}$$

The net current I_X due to the movement of ion X through the protein depends on the variable conductance of the channel g_X to ion X and the effective voltage for this ion type across the membrane $(V_m - E_{rev})$, with the reversal potential E_{rev}, where no net ion flux through the pore is present. E_{rev} is normally given by the Nernst voltage (eq. 4.3). The driving force of the current is $V_m - E_{rev}$. Sometimes, the proteins are not perfectly selective for only one ion type. Thus, the reversal potential is not the same as the Nernst voltage, but is given by an enhanced Goldman-Hodgkin-Katz equation (eq. 4.4) considering also calcium.

5.1.1 Gating Kinetics

The gating kinetics describes the protein configuration that is important for its ions conductance. One single protein in the membrane can be either opened or closed. There may be several configurations where the protein is in a closed state. Furthermore, the protein can get into one or more inactive states. Altogether, this behavior can be considered mathematically with states and functions describing the transition between these states using a Markov model.
In the simplest case, the description consists of only one open and one closed state. The transition between the two states is rapid and there is a negligible number of channels in transition. Therefore, if the fraction of all channels of the same type in the open state is γ, the fraction of closed channels must be $(1 - \gamma)$:

$$\begin{array}{ccc} & \alpha_\gamma & \\ 1-\gamma & \rightleftharpoons & \gamma \\ \text{closed} & \beta_\gamma & \text{open} \end{array}$$

with the voltage dependent rate constant α_γ describing the transition from the closed to the open state. The rate constant β_γ is related to the opposite transition. The gate describing this process can be modeled by a differential equation:

$$\frac{\mathrm{d}\gamma}{\mathrm{d}t} = \alpha_\gamma(1-\gamma) - \beta_\gamma\gamma \tag{5.2}$$

γ is the so-called gating variable. The change in the amount of open channels in the steady state equals to zero ($\frac{\mathrm{d}\gamma}{\mathrm{d}t} = 0$). Thus, the amount of open channels in the steady state γ_∞ is:

$$\gamma_\infty = \frac{1}{1+\beta_\gamma/\alpha_\gamma}$$

Including this, eq. 5.2 can be re-written in the form:

$$\frac{\mathrm{d}\gamma}{\mathrm{d}t} = \frac{\gamma_\infty - \gamma}{\tau_\gamma} \qquad \text{with} \qquad \tau_\gamma = \frac{1}{\alpha_\gamma + \beta_\gamma}$$

as the relaxation time constant for the voltage clamp experiment. In the following, the dependence of the rate constants on the transmembrane voltage will be discussed.
The ratio between the fraction of channels in the open state during equilibrium γ_∞ and the fraction of channels in the closed state $1-\gamma_\infty$ is given by a Boltzmann distribution [215]:

$$\frac{\gamma_\infty}{1-\gamma_\infty} = \exp\left(\frac{\Delta G_\gamma}{RT}\right) \tag{5.3}$$

with the gas constant R, the absolute temperature T, and the free energy difference between the open and the closed state ΔG_γ given by [216]:

$$\Delta G_\gamma = \Delta G_\gamma^0 + z_\gamma F V_m$$

where ΔG_γ^0 represents the conformation energy and the entropy change as well as $z_\gamma F V_m$ being assigned to the redistribution charge during the transition. z_γ is the valence of the ion, F the Faraday's constant, and V_m the transmembrane voltage. Equation 5.3 can be re-written giving the voltage dependence of the channels in the open state γ_∞ during equilibrium:

$$\gamma_\infty = \frac{1}{1+\lambda_\gamma \exp(-b_\gamma V_m)} \tag{5.4}$$

with the constants $\lambda_\gamma = \exp(-\Delta G_\gamma^0/RT)$ and $b_\gamma = z_\gamma F/RT$.
The relaxation time constant τ_γ and also the rate constants α_γ and β_γ can be modeled with different approaches. One approach is based on the conventional transition-state theory [217]. The voltage dependence of the rate constants in a membrane can be described by:

$$k = k_0 \exp\left(-\eta\frac{zFV_m}{RT}\right) \tag{5.5}$$

with the so-called electrical distance η and the voltage independent constant k_0. Complex kinetics are not reconstructible with this mono-exponential voltage dependence. They can be considered with composite reactions $A \rightleftharpoons B$. Two exemplary composite reactions are the so-called competition between two routes for the transition [216] and the so-called transition through an intermediate step [218]. The first describes e.g. two different pathways for the folding of a membrane protein. In this case, the reaction kinetics is given by a linear combination of rates:

$$\frac{\mathrm{d}[A]}{\mathrm{d}t} = (p_1 k_{-1} + p_2 k_{-2})[B] - (p_1 k_1 + p_2 k_2)[A] \tag{5.6}$$

where k_i and k_{-i} denotes the forward and backward reaction of the routes $i = 1, 2$, respectively, and p_i is the probability of route i given by:

$$p_1 = \frac{1}{1 + \exp(-\Delta G_b / RT)}, \qquad p_2 = 1 - p_1$$

with ΔG_b as the difference between the activation free energies of the routes. The second composite reaction (transition through an intermediate step) is given by:

$$\frac{\mathrm{d}[A]}{\mathrm{d}t} = \frac{k_{-1}k_{-2}}{k_{-1} + k_2}[B] - \frac{k_1 k_2}{k_{-1} + k_2}[A] \tag{5.7}$$

with the reaction rate k_1 and k_{-1} associated with the transitions between state $[A]$ and the intermediate step as well as k_2 and k_{-2} for the transitions between the intermediate step and state $[B]$. In both composite reactions (eqs. 5.6 and 5.7), the rates k_i and k_{-i} are expressed by exponential functions given by eq. 5.5. This leads to a general description of the voltage dependence as a rational function of exponentials.
A more complex approach for the gating process is needed if the channel cannot only switch between closed and open state, but further protein configurations are possible e.g. further closed states and inactive states. This can be solved by incorporating a Markov chain model describing every protein configuration by one state with transitions between all states. In the scope of this work, only simple Markov chain models are introduced, but an ionic model based on this approach is described in section 5.5.7 and a sodium channel defect is described with a Markov chain model in section 5.7.2. Another method for incorporating several protein configurations is to combine gates in series. The common choice is combining gates because the number of states and transitions is smaller than in the Markov chain models. Thus, the computational cost of combining gates in series is smaller.
If a number of i gates are combined in series, one single channel is only open if all gates γ_i are in the open state. Hence, the probability for all channels of the same type to be in the open state is $\prod \gamma_i$. Assuming that i gates have the same characteristics and that one gate is open with the probability γ, the probability of the channel population being in the open state is equal to γ^i.

5.1.2 Ionic Channels

The conductivity of the cell membrane is mainly dependent on the density and state of ionic channels since these kinds of membrane proteins build the largest population of membrane spanning pores. Most of the ion channels are selective to one specific ion type. As shown before, the single ion channel can be either open or closed. If it is open, the channel is conducting ions with an intrinsic current-voltage relation $I_{pore}(V)$. V is the effective voltage normally given by $V_m - E_{rev}$. Furthermore, the intra- and extracellular environment determines the activity of the channel. If a large number of equal ion channels N are inserted in the cell membrane, the channel current I_{ch} is given by:

$$I_{ch} = N P_o P_{ni} I_{pore}(V)$$

with the probability for one channel being in the open state P_o and the probability of not being inactivated P_{ni}. Similar to the activation, inactivation is a time and voltage dependent process. Also, receptors for e.g. ligands can lead to a channel inactivation. The probabilities P_o and P_{ni} are determined by the gating kinetics described in section 5.1.1.

The pore specific current $I_{pore}(V)$ can be determined by incorporating Ohm's law, classical electrodiffusion or barrier models. In the simplest and most common descriptions for ionic channels, Ohm's law is used to calculate the current-voltage relationship:

$$I_{pore} = g_{pore}(V_m - E_{rev})$$

with the reversal potential E_{rev}, and the pore conductance g_{pore}. The reversal potential is given by the Nernst equation (eq. 4.3) if the ion channel is only selective for one specific ion type. If the pore is permeable to several ions, the reversal potential is given by an enhanced Goldman-Hodgkin-Katz equation (eq. 4.4) considering also calcium.
For some models of ion channels, the pore specific current $I_{pore}(V)$ is determined under consideration of the electrodiffusion theory. Based on this theory, Goldman, Hodgkin, and Katz developed a model describing the selectivity and permeability of the protein. The electrodiffusion current through the pore is described as [219]:

$$I_{pore} = P_X z_X^2 \frac{F^2 V_m}{RT} \frac{\gamma_i [X]_i - \gamma_o [X]_o \exp(-z_X F V_m / RT)}{1 - \exp(-z_X F V_m / RT)}$$

with the ion type X, the membrane permeability for this ion type P_X, and the concentration at the entrance and the exit of the pore $[X]_i$ and $[X]_o$, respectively, with the corresponding partition coefficients γ_i and γ_o.
A third way to describe the pore specific current $I_{pore}(V)$ is to consider the energy barrier characteristics of some ion channels. A pore has one or more internal binding sites. At these sites the ion has to bind to get through the pore. The detailed current-voltage relationship is explained in [219]. The common approximation of the energy barrier approach is given by:

$$I_{pore} = \frac{g_X}{1 + \lambda \exp(b V_m)} (V_m - E_X)$$

with the conductance of the pore g_X for ion type X, the constants b and λ, and the Nernst voltage E_X. This equation is a combination of eq. 5.1 and eq. 5.3. Thus, this current is described as an ohmic conductor having a gate that is immediately in steady state.

5.1.3 Ionic Pumps

If the ionic movement by passive diffusion through the ionic channel is not reversed, the gradients in ion concentration and the transmembrane voltage would disappear after some minutes. To maintain those gradients, ion pumps are included in the membrane to transport ions up their concentration gradient under consumption of energy (ATP). The pump is usually described as a binding process. The pump current I_{pump} in the kinetic models of the transporters have the characteristics [220]:

$$I_{pump} = N P_{sites} I_{trans}(V)$$

with the number of equal ion pumps N, the probability of having occupied entrance sites P_{sites}, and the averaged single pump current $I_{trans}(V)$ through the transporter pore. P_{sites} is given using a Hill's equation [219]:

$$P_{sites} = \frac{1}{1 + (K_{m,X}/[X])^n} \tag{5.8}$$

with the equilibrium constant of the reaction $K_{m,X}$ of ion X describing the concentration at half saturation, the concentration of the ion $[X]$, and the number n of ions of type X that can bind to the receptor, also called Hill's coefficient.
If the ionic pump has only voltage independent characteristics and only one type of ion can pass through the transport protein at a time, the pump current $I_{p,X}$ is described by:

$$I_{p,X} = \frac{I_{p,X,max}}{1 + (K_{m,X}/[X])} \tag{5.9}$$

where $I_{p,X,max}$ is the maximum current flowing through the transporter. The sarcolemmal and SR Ca^{2+} ATPases show this kind of charcteristic. More complex ionic pumps like the Na/K pump carry two or more ion types. Furthermore, they are able to transport more than one ion per protein reconfiguration and they may also be working transmembrane voltage dependent. In this case, the equation for the pump current I_{p,X_i} is more complex:

$$I_{p,X_i} = I_{X_i,max}(V_m) \prod P_{sites,i} \tag{5.10}$$

with the maximum voltage dependent current $I_{X_i,max}(V_m)$ and the product of all probabilities having occupied entrance sites $\prod P_{sites,i}$. Each probability is described by eq. 5.8.

5.1.4 Ionic Exchangers

Ionic exchangers do not need metabolic energy to perform the translocation of ions directly. Instead, they use the energy available in one given ion's electrochemical gradient to transport another ion against its gradient. Since ionic exchangers can work in both forward and backward mode, the total exchanger current I_x is given by the superposition of the currents for the forward reaction $I_{x,forw}$ and for the backward reaction $I_{x,back}$:

$$I_x = I_{x,forw} - I_{x,back}$$

Both current components follow a description of binding processes denoted in eq. 5.8. Since two ion types, each with two binding sites are involved, the current components are:

$$I_{x,\mu} = NFk_{\mu}(V)P_{sites,X_o}P_{sites,Y_i}(1 - P_{sites,X_i})(1 - P_{sites,Y_o})$$

with μ being either forward or backward mode, the number of ionic exchangers N, the forward and backward reaction rate k_{forw} and k_{back}, respectively, and the probabilities of having occupied entrance sites P_{sites} for the ion types X and Y for either intracellular i and extracellular o binding site. The probabilities P_{sites} are each described by the formula of eq. 5.8. If some of the intra- or extracellular concentrations are low, the saturation effect can be neglected:

$$P_{sites,X} = \frac{1}{1 + (K_{m,X}/[X])^n} \approx ([X]/K_{m,X})^n$$

and the probability of having free entrance sites $(1 - P_{sites})$ is assumed to be 1. Furthermore, the balance relation between forward and backward reaction rate

$$\frac{k_{back}}{k_{forw}} = \exp(-FV_m/RT)$$

allows to consider only one of the reaction rates. This reduces the complexity of the equations describing ionic exchangers. The Na/Ca exchanger for example is mathematically described in section 5.5.2.

5.1.5 Intracellular Calcium Dynamics

Calcium is the mediator of the excitation contraction coupling (ECC) as described in section 4.6. The L-type Ca^{2+} channel triggers the Ca^{2+} induced Ca^{2+} release (CICR) current from the sarcoplasmic reticulum (SR) during one heart cycle. Ca^{2+} is uptaken again by the SR Ca^{2+}ATPase and extruded outside of the cell by the Na/Ca exchanger as well as the sarcolemmal Ca^{2+} ATPase. In the SR, Ca^{2+} is translocated between the network (NSR) and the junctional SR (JSR). Furthermore, Ca^{2+} binds to proteins such as troponin, calmodulin, and calsequestrin. In sum, the amount of free intracellular Ca^{2+} in the myoplasm is determined by many processes.
The ionic flow between the Ca^{2+} compartments, i.e. intracellular, NSR, JSR, and dyadic space, is determined by channels, pumps, exchangers, and diffusion. The electrical field in the membrane of the SR is very small. Thus, the ionic current $I_{Ca,SR}$ through the proteins of the SR membrane is only determined by the ion concentration gradient:

$$I_{Ca,SR} = kP([Ca^{2+}]_a - [Ca^{2+}]_b)$$

with k as the flow rate, P as the probability for a gate being in the open state (eq. 5.8), and the concentration of Ca^{2+} in the compartment a and b, $[Ca^{2+}]_a$ and $[Ca^{2+}]_b$, respectively.
Additionally to the translocation, calcium is also buffered in the intracellular space of the cells and the SR. In this way, Ca^{2+} can play an important role as secondary messenger that regulates intracellular processes by binding to intracellular proteins. These Ca^{2+} binding proteins are troponin and calmodulin in the myoplasm and calsequestrin in the JSR.
The kinetics of buffering can be modeled by:

$$\frac{\mathrm{d}[BCa]}{\mathrm{d}t} = \alpha_B[B][Ca^{2+}] - \beta_B[BCa]$$

with the concentration of Ca^{2+} bound to the buffer $[BCa]$, the concentration of free buffers $[B]$ and the rate constants α_B and β_B dependent on the calcium concentration $[Ca^{2+}]$. The occupancy number O_B is defined considering the concentration of binding sites $[B]_{max}$:

$$O_B = [BCa]/[B]_{max}$$

This leads to an equation, which is only describing the kinetics of the buffering process by $[Ca^{2+}]$ and O_B:

$$\frac{\mathrm{d}O_B}{\mathrm{d}t} = \alpha_B[Ca^{2+}](1 - O_B) - \beta_B O_B \tag{5.11}$$

The flux of ions, which is reduced in a compartment due to a buffering process is then

$$J_{Ca,B} = -[B]_{max}\frac{\mathrm{d}O_B}{\mathrm{d}t}$$

If the buffer is assumed to be instantaneously in equilibrium with its surrounding compartment eq. 5.11 is set to zero. The equilibrium occupancy number $O_{B,\infty}$ and the flux of ions between the buffer and the compartment is then defined as:

$$O_{B,\infty} = \frac{[Ca^{2+}]}{[Ca^{2+}] + K_{m,B}} \quad \text{and} \tag{5.12}$$
$$J_{Ca,B} = -\frac{[B]_{max}K_{m,B}}{([Ca^{2+}] + K_{m,B})^2}\frac{\mathrm{d}[Ca^{2+}]}{\mathrm{d}t}$$

with the equilibrium constant of the buffering $K_{m,B}$ given by β_B/α_B. In section 5.5.3 a description of the intracellular calcium buffering is presented for the buffering mechanism of eq. 5.12.

5.2 The Capacitance of the Cell Membrane

The electrical equivalent of the cell membrane without conducting membrane proteins is a capacitor. The electric charge Q accumulated at the membrane surface is proportional to the voltage across the membrane (transmembrane voltage V_m):

$$Q = C_m V_m$$

with the proportional factor C_m being the capacitance of the cell membrane. The sum of the membrane ionic currents through ionic channels, pumps, and exchangers I_{mem} is responsible for the variation of V_m. The intercellular stimulus current I_{inter} combined with I_{mem} determines the temporal derivative of V_m:

$$\frac{\mathrm{d}V_m}{\mathrm{d}t} = -\frac{1}{C_m}(I_{mem} - I_{inter}) \tag{5.13}$$

5.3 Ionic Concentrations

The ion concentration in the intra- and extracellular space is varying for each involved ion type. The change in the concentration is determined by active ion pumps and passive transport through channels and secondary active transport through exchangers. The temporal variation of the ion concentration depends on the specific ion currents I_X:

$$\frac{\mathrm{d}[X]}{\mathrm{d}t} = -\frac{I_X A}{z_X F V} \tag{5.14}$$

with the ion type X, the membrane surface area A, the valence of the ion z_X, and the volume V of the region, where X is distributed. The specific ion current I_X consists of all ionic currents where the ion type X is involved.
The concentration of ions (mainly Na^+, K^+, and Ca^{2+}) are defined in several domains, which can be divided into compartments. These domains are the extracellular space, the cleft space (the extracellular region close to the membrane), and the intracellular space including e.g. the dyadic space, NSR, and JSR.

5.4 Hodgkin-Huxley Model

The model by Hodgkin and Huxley of 1952 is the basis for most of the currently developed mathematical descriptions of the electrophysiological behavior of cardiac myocytes. As such, it will be described in this section.
Hodgkin and Huxley developed a mathematical model of a giant axon based on voltage clamp measurements [214]. The cell membrane is reconstructed as an electrical equivalent circuit (fig. 5.1), which considers variable resistors, voltage sources, and a capacitor. The variable resistors are the ion channels, the voltage sources are determined by the Nernst voltages, and the capacitor represents the cell membrane itself. The model allows the calculation of ionic fluxes of Na^+ and K^+ through the membrane to determine the change in transmembrane voltage (eq. 5.13). The total transmembrane current I_{mem} consists of:

$$I_{mem} = I_{Na} + I_K + I_L$$

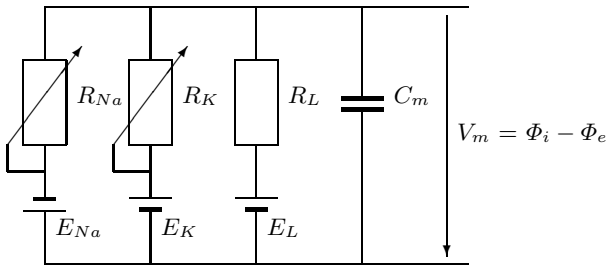

Fig. 5.1. Electrical equivalent circuit of the cell membrane of the Hodgkin-Huxley model describing the electrophysiology of a giant squid axon. The resistors R_X describe the conductivity of the channels of type X and E_X are the voltage sources.

with the sodium current I_{Na}, the potassium current I_K, and the sum of the leakage currents of other ions I_L, mainly Cl^-. Each of these currents is described similar to eq. 5.1:

$$I_{Na} = g_{Na}(V_m - E_{Na}), \quad I_K = g_K(V_m - E_K), \quad I_L = g_L(V_m - E_L)$$

with the variable conductances g_{Na} and g_K, the constant conductance g_L, and the reversal potentials E_{Na}, E_K, and E_L. The reversal potentials are determined by the Nernst voltages and are fixed to:

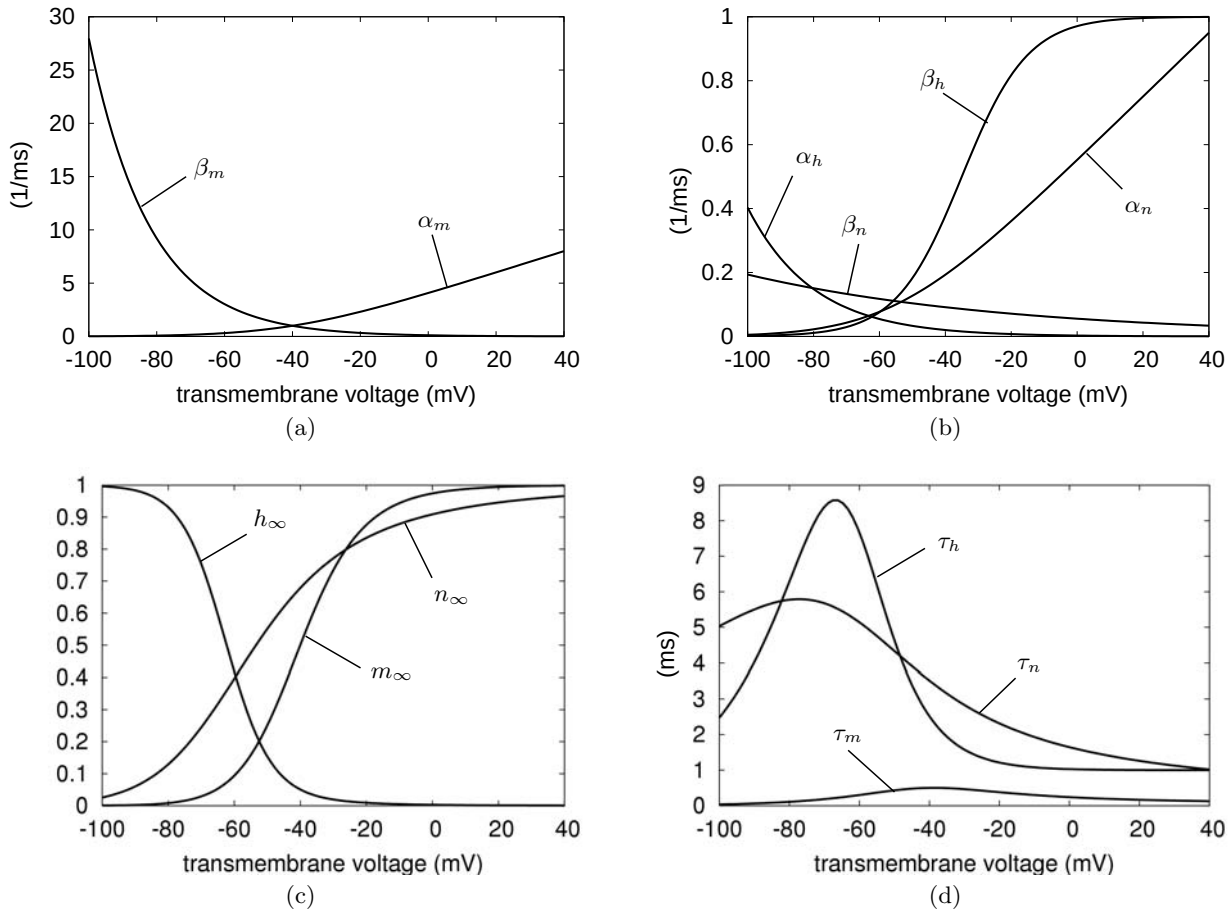

Fig. 5.2. Voltage dependent gating kinetics of the Hodgkin-Huxley I_{Na} and I_K channel. (a) Rate constants of the activation gating variable m of the I_{Na} channel α_m and β_m. (b) Rate constants of the inactivation gating variable h of the I_{Na} channel α_h and β_h and of the activation gating variable n of the I_K channel α_n and β_n. (c) Fraction of gates in steady state m_∞, h_∞, and n_∞ for the gating variables m, h, and n, respectively. (d) Relaxation time constants τ_m, τ_h, and τ_n for the three gating variables.

$$E_{Na} = +50\ mV, \qquad E_K = -77\ mV, \qquad E_L = -54.6\ mV$$

In the model of Hudgkin-Huxley, the maximum conductances of the channels are:

$$g_{Na,max} = 120\ mS/cm^2, \quad g_{K,max} = 36\ mS/cm^2, \quad g_L = 0.3\ mS/cm^2$$

The kinetics of ion currents in the model of Hodgkin and Huxley is described by gating variables. The time and voltage dependent sodium conductivity g_{Na} is modeled by:

$$g_{Na} = g_{Na,max} m^3 h$$

with the activation gating variable m and the inactivation gating variable h. The activation process considers three independent, but same gates leading to m^3. The voltage dependent rate constants of these gating variables are (V_m in mV):

$$\alpha_m = 0.1 \left(-\frac{V_m + 40}{\exp\left(-\frac{V_m+40}{10}\right) - 1} \right), \quad \beta_m = 4 \exp\left(-\frac{V_m + 65}{18} \right)$$
$$\alpha_h = 0.07 \exp\left(-\frac{V_m + 65}{20} \right), \quad \beta_h = \frac{1}{\exp\left(-\frac{V_m+35}{10}\right) + 1}$$

A model for K^+ channel with four gating particles fits best to the measurement data. Thus, the time and voltage dependent potassium conductivity g_K is given by:

$$g_K = g_{K,max} n^4$$

with the activation gating variable n. The rate constants of this gating variable are:

$$\alpha_n = 0.01 \left(-\frac{V_m + 55}{\exp\left(-\frac{V_m+55}{10}\right) - 1} \right), \quad \beta_n = 0.125 \exp\left(-\frac{V_m + 65}{80} \right)$$

The time course of m, h, n, and V_m follow the differential equation after defining some initial values:

$$\frac{\mathrm{d}m}{\mathrm{d}t} = \alpha_m(1-m) - \beta_m m, \qquad \frac{\mathrm{d}h}{\mathrm{d}t} = \alpha_h(1-h) - \beta_h h, \qquad \frac{\mathrm{d}n}{\mathrm{d}t} = \alpha_n(1-n) - \beta_n n$$

Figure 5.2 a,b depicts the rate constants of the gating variables m, h, and n in dependence of V_m. Figure 5.2 c,d shows the corresponding steady state values and relaxation time constants (section 5.1.1).

5.5 Models of Cardiomyocytes

The properties of excitable cells are investigated mathematically for more than 50 years. Noble created the first cardiac electrophysiological model, which reconstructs the properties of Purkinje fibers based on early measurement data and consists of four channels [221]. The techniques for measuring the membrane protein properties were enhanced in the following years and several models were built describing the cell in more and more detail (tab. 5.1). The models of Beeler and Reuter (1977) [223] as well as Luo and Rudy (1991) [231] were important approaches until the mid 90s. Most of the recently developed human cardiac electrophysiological models are based on these two models. The newer models consist of up to approximately

Table 5.1. Ionic models describing cardiac electrophysiology.

Year	Author	Specimen	Species
1962	Noble [221]	Purkinje fiber	-
1975	McAllister, Noble, Tsien [222]	Purkinje fiber	-
1977	Beeler, Reuter [223]	Ventricular myocardium	Mammalian
1980	Yanagihara, Noma, Irisawa [224]	Sinoatrial node	Rabbit
1982	Bristow, Clark [225]	Sinoatrial node	Rabbit
1983	Bristow, Clark [226]	Sinoatrial node	Rabbit
1984	Noble, Noble [227]	Sinoatrial node	Rabbit
1985	DiFrancesco, Noble [228]	Purkinje fiber	Mammalian
1987	Hilgemann, Noble [229]	Atrial working myocardium	Rabbit
1990	Earm, Noble [230]	Atrial working myocardium	Rabbit
1991	Luo, Rudy [231]	Ventricular myocardium	Mammalian
1994	Luo, Rudy [232, 233]	Ventricular myocardium	Guinea-pig
1994	Demir, Clark, Murphey, Giles [234]	Sinoatrial node	Rabbit
1996	Dokos, Celler, Lovell [235]	Sinoatrial node	Mammalian
1996	Lindblad, Murphey, Clark, Giles [236]	Atrial working myocardium	Rabbit
1996	Demir, O'Rourke, Tomaselli, Marban, Winslow [237]	Ventricular myocardium	Rabbit
1998	Courtemanche, Ramirez, Nattel [238]	Atrial working myocardium	Human
1998	Nygren, Fiset, Firek, Clark, Lindblad, Clark, Giles [239]	Atrial working myocardium	Human
1998	Jafri, Rice, Winslow [240]	Ventricular myocardium	Guinea-pig
1998	Noble, Varghese, Kohl, Noble [241]	Ventricular myocardium	Guinea-pig
1998	Priebe, Beuckelmann [242]	Ventricular myocardium	Human
1999	Demir, Clark, Giles [243]	Sinoatrial node	Rabbit
1999	Winslow, Rice, Jafri, Marbán, O'Rourke [244, 245]	Ventricular myocardium	Canine
2000	Ramirez, Nattel, Courtemanche [246]	Atrial working myocardium	Canine
2000	Zhang, Holden, Kodoma, Honjo, Lei, Varghese, Boyett [247]	Sinoatrial node	Rabbit
2001	Boyett, Zhang, Garny, Holden [248]	Sinoatrial node	Rabbit
2001	Pandit, Clark, Giles, Demir [249]	Ventricular myocardium	Rat
2001	Puglisi, Bers [250]	Ventricular myocardium	Rabbit
2002	Kneller, Ramirez, Chartier, Courtemanche, Nattel [251]	Atrial working myocardium	Canine
2002	Kurata, Hisatome, Imanishi, Shibamoto [252]	Sinoatrial node	Rabbit
2002	Bernus, Wilders, Zemlin, Verschelde, Panfilov [253]	Ventricular myocardium	Human
2004	Lovell, Cloherty, Celler, Dokos [254]	Sinoatrial node	Rabbit
2004	Ten Tusscher, Noble, Noble, Panfilov [255]	Ventricular myocardium	Human
2004	Iyer, Mazhari, Winslow [256]	Ventricular myocardium	Human

60 equations describing the properties of the cell membrane, ionic concentrations, intracellular structures like the sarcoplasmic reticulum, and calcium buffering mechanisms and also consider the effects of mechanical stretch to the cell.

Models describing human electrophysiology are the Courtemanche et al. model (1998) [238] and the Nygren et al. model (1998) [239] for atrial activity as well as as the models of Priebe and Beuckelmann (1998) [242], of Bernus et al. (2002) [253], of Ten Tusscher et al. (2004) [255], and of Iyer et al. (2004) [256] for ventricular activity. The action potentials (AP) and the course of the intracellular calcium concentration $[Ca^{2+}]_i$ of the first five human ionic models are displayed in fig. 5.3. Furthermore, fig. 5.3 depicts the APs and the course of $[Ca^{2+}]_i$ for the Beeler-Reuter model and for the Luo-Rudy model of ventricular characteristics and of the rabbit sinoatrial node model of Zhang and coworkers (2000) [247]. The differences in the morphology are mainly due to different measurements underlying the models and inclusion of

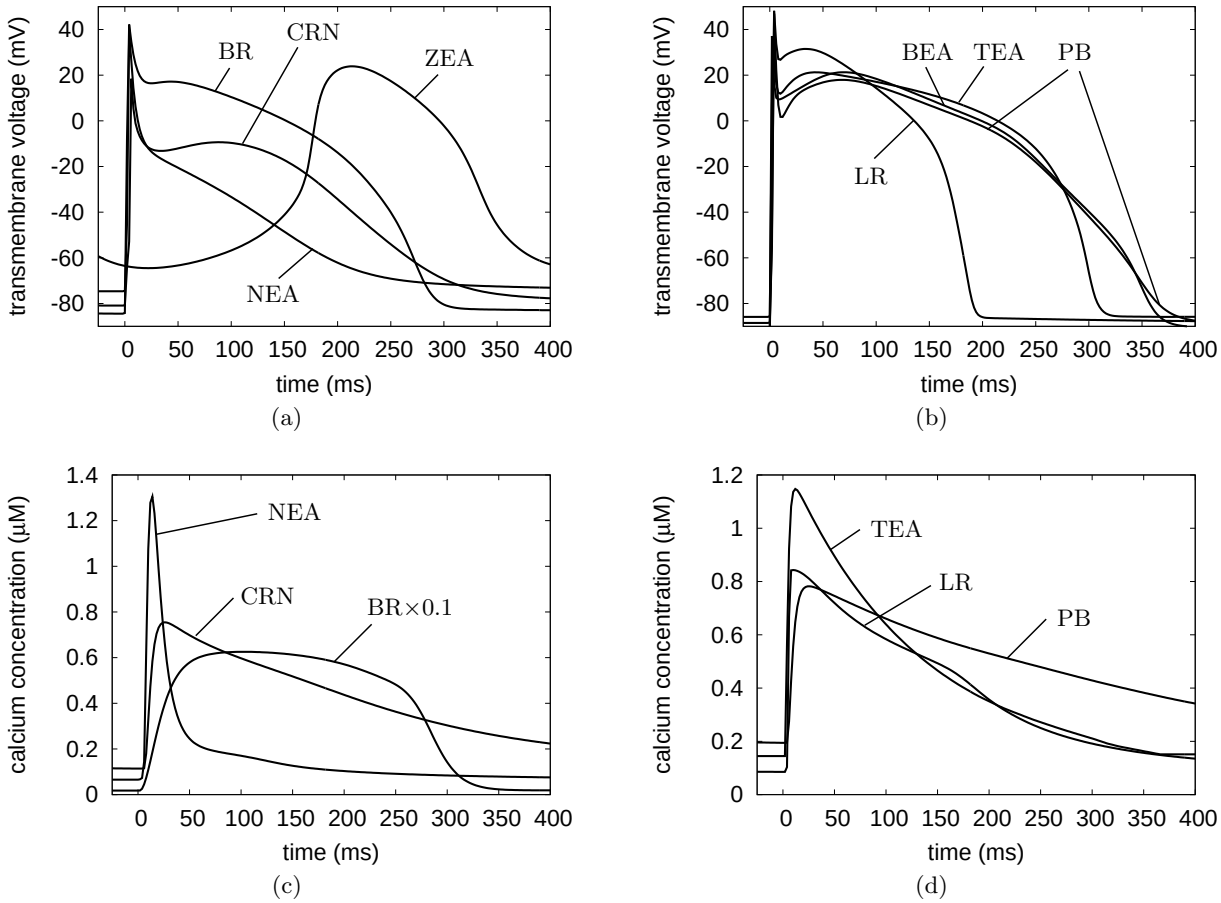

Fig. 5.3. Action potentials and courses of intracellular calcium concentration $[Ca^{2+}]_i$ of models of different cardiomyocytes stimulated with a basic cycle length of 1000 ms. (a) Atrial models of Nygren et al. (NEA) [239] and of Courtemanche, Ramirez, and Nattel (CRN) [238] as well as the ventricular models of Beeler and Reuter (BR) [223] and the self-depolarizing rabbit sinoatrial node model of Zhang et al. (ZEA) [247]. (b) Ventricular models Luo and Rudy (LR) [232, 233], of Priebe and Beuckelmann (PB) [242], of Bernus et al. (BEA) [253], and of Ten Tusscher et al. (TEA) [255]. (c) Calcium variation in the intracellular space during an AP of the models of (a). The $[Ca^{2+}]_i$ of the BR model is scaled. (d) Courses of $[Ca^{2+}]_i$ for the models during an AP described in (b).

different descriptions of the equations. Another reason is that the measurements are obtained from different regions of the heart with different properties.
The models of Beeler and Reuter and Luo and Rudy as well as the six human ionic models are described below. Additionally, the rabbit sinoatrial node model of Zhang et al. is presented as an auto-rhythmic cell. Each additional ionic current due to channels, pumps, and exchangers is explained to give examples for the theoretical description of section 5.1.

5.5.1 Beeler-Reuter Model

The Beeler-Reuter model was the first electrophysiological model describing the behavior of a mammalian ventricular myocyte (fig. 5.5 a) [223]. The model was based on the equations by Hodgkin and Huxley. The transmembrane current I_{mem} is given by:

$$I_{mem} = I_{Na} + I_{b,Na} + I_{K1} + I_{X1} + I_S$$

with the currents: I_{Na} = fast Na^+; $I_{b,Na}$ = background Na^+; I_{K1} = rectifier K^+; I_{X1} = non-specific outward; and I_S = non-specific inward shown in fig. 5.4 a determining the course of the transmembrane voltage and of the intracellular calcium concentration (fig. 5.3 a,c).
I_{Na} was modeled in the same way as in the Hodgkin-Huxley model apart from including a second inactivation gating variable j:

$$I_{Na} = g_{Na,max} m^3 h j (V_m - E_{Na})$$

A background current is commonly defined by eq. 5.1 without having a gate. In the Beeler-Reuter model, the background Na^+ current is thus given by:

$$I_{b,Na} = g_{b,Na,max}(V_m - E_{Na})$$

The voltage dependent classical rectifier potassium current I_{K1} is based on the formulae of McAllister et al. [222] (V_m in mV):

$$I_{K1} = 0.35 \left(\frac{4 \exp[0.04(V_m + 85) - 1]}{\exp[0.08(V_m + 53)] + \exp[0.04(V_m + 53)]} + \frac{0.2(V_m + 23)}{1 - \exp[-0.04(V_m + 23)]} \right)$$

The construction of this equation is not biophysically motivated but fits a function, which describes best the measured properties. Also, the time and voltage dependent outward current I_{X1}, which is mainly due to potassium ions, is only partly given by eq 5.1:

$$I_{X1} = 0.8\, X1 \frac{\exp[0.04(V_m + 77)] - 1}{\exp[0.04(V_m + 35)]}$$

with the gating variable $X1$ following the processes explained in section 5.1.1.
The time and voltage dependent inward current I_S is assumed to be mainly due to the flow of Ca^{2+} ions. The description follows eq 5.1:

$$I_S = g_{S,max}\, d\, f\, (V_m - E_S)$$

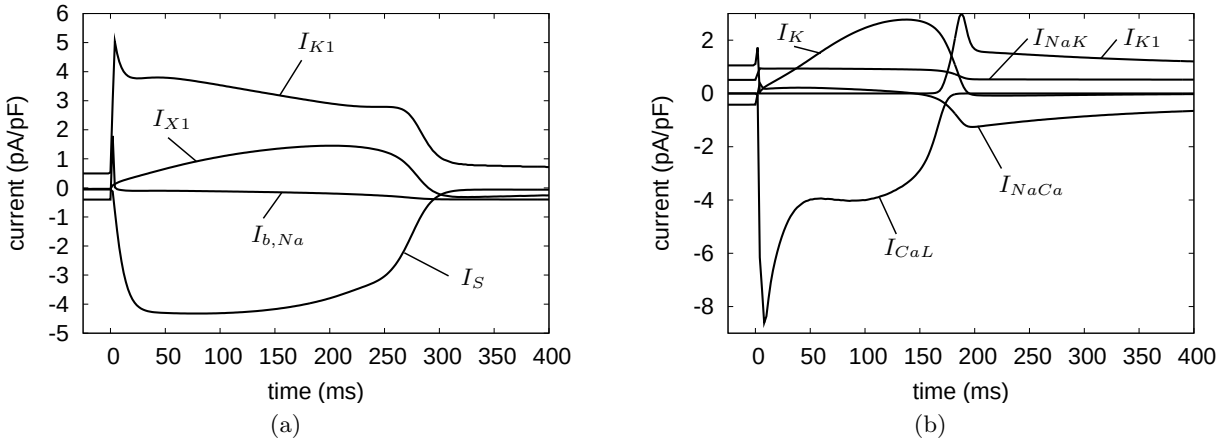

(a) (b)

Fig. 5.4. Ionic currents of the Beeler-Reuter and the Luo-Rudy model. (a) Background Na^+ current $I_{b,Na}$, rectifier K^+ current I_{K1}, non-specific outward current I_{X1}, and non-specific inward current I_S of the Beeler-Reuter model [223]. (b) L-type Ca^{2+} current $I_{Ca,L}$, delayed rectifier K^+ current I_K, classical rectifier K^+ current I_{K1}, Na/Ca exchange current I_{NaCa}, and Na/K pump current I_{NaK} of the Luo-Rudy model [232, 233].

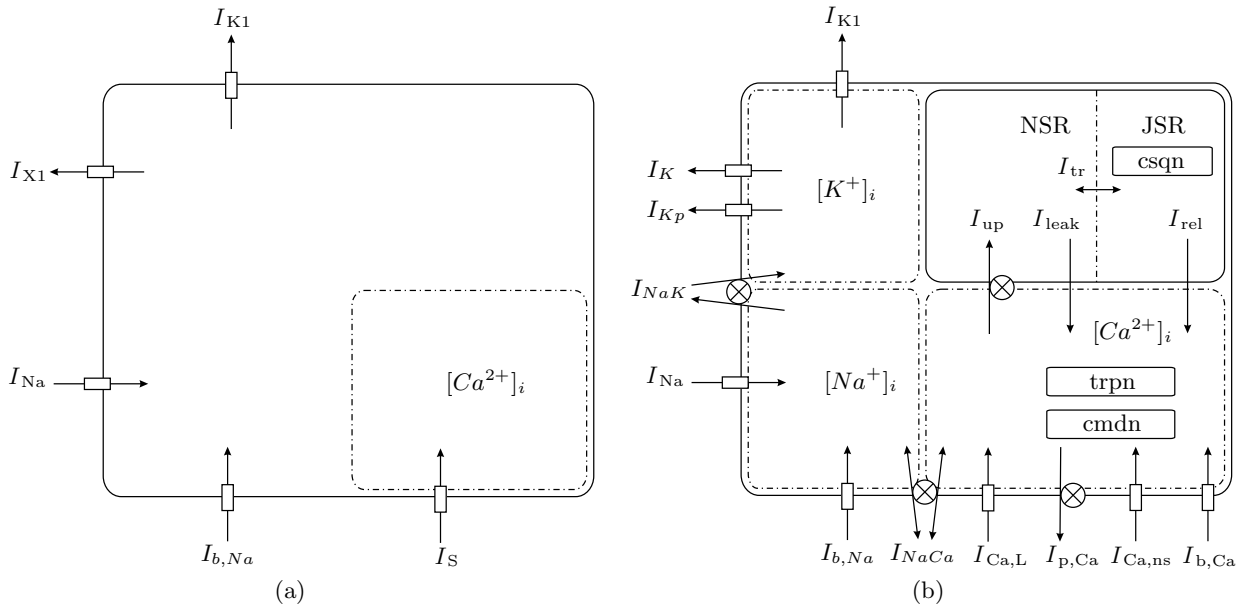

Fig. 5.5. Schematic description of the ionic model of (a) Beeler-Reuter and (b) Luo-Rudy with the implemented currents, pumps, exchangers and the intracellular Ca^{2+}, K^+, and Na^+ concentrations. The Luo-Rudy model contains a detailed description of the intracellular Ca^{2+} dynamics including the sarcoplasmic reticulum consisting of network SR (NSR) and junctional SR (JSR) and the buffering of Ca^{2+} to troponin (trpn), calmodulin (cmdn), and calsequestrin (csqn). The currents are described in the text.

with the activation gating variable d, the inactivation gating variable f, and the reversal potential $E_S = -82.3 - 13.0287 \ln [Ca^{2+}]_i$. The variation of the intracellular calcium concentration $[Ca^{2+}]_i$ is given by:

$$\frac{\mathrm{d}[Ca^{2+}]_i}{\mathrm{d}t} = -10^{-7} I_S + 0.07(10^{-7} - [Ca^{2+}]_i)$$

5.5.2 Luo-Rudy Models

The models of Luo-Rudy were developed in several stages [231, 232, 233, 257, 258, 259] and were used and developed further on [260, 261, 262, 208]. The dynamic version of 1994 [232, 233] is the most widely used model. This will be explained in detail.
The dynamic Luo-Rudy model describes the electrophysiology of a guinea-pig ventricular myocyte. This model is based in the Luo-Rudy model of 1991 [231]. The dynamic Luo-Rudy model of 1994 includes formulations for most of the sarcolemmal channels, pumps and exchangers and for the Ca^{2+} handling in the sarcoplasmic reticulum (SR). Furthermore, compartments were considered for myoplasm, network SR (NSR) and junctional SR (JSR), and Ca^{2+} buffers in the myoplasm (troponin, calmodulin) and in the JSR (calsequestrin) were defined. It takes into account myoplasmic concentration variations of Na^+ and K^+ as well as Ca^{2+}. The total transmembrane current I_{mem} is given by (fig. 5.5 b):

$$\begin{aligned} I_{mem} = I_{Na} + I_{Ca,L} + I_K + I_{K1} + I_{Kp} + I_{NaCa} \\ + I_{NaK} + I_{Ca,ns} + I_{p,Ca} + I_{b,Ca} + I_{b,Na} \end{aligned}$$

with the currents: I_{Na} = fast Na^+; $I_{Ca,L}$ = L-type Ca^{2+}; I_K = delayed rectifier K^+; I_{K1} = rectifier K^+; I_{Kp} = plateau K^+; I_{NaCa} = Na/Ca exchanger; I_{NaK} = Na/K pump; $I_{Ca,ns}$ =

non-specific Ca^{2+} activated; $I_{p,Ca}$ = sarcolemmal Ca^{2+} pump; $I_{b,Ca}$ = background Ca^{2+}; and $I_{b,Na}$ = background Na^+. Some of these currents are depicted in fig. 5.4 b.
Furthermore, the Luo-Rudy model incorporates Ca^{2+} currents in the intracellular space between the myoplasm, the NSR and the JSR with I_{up} as the SR Ca^{2+} pump current from myoplasm to NSR, I_{leak} as the leakage Ca^{2+} current from NSR to myoplasm, I_{tr} as Ca^{2+} translocation current between NSR and JSR, and I_{rel} as the Ca^{2+} release current from JSR to myoplasm (Ca^{2+} induced Ca^{2+} release). The equations are explained in section 5.5.3.
I_{Na} and the background currents $I_{b,Ca}$ and $I_{b,Na}$ are described as in the Beeler-Reuter model.
The L-type Ca^{2+} channel is assumed to be permeable for Ca^{2+}, Na^+, and K^+ with the highest permeability for Ca^{2+}:

$$I_{Ca,L} = g_{Ca,L,max}\, d\, f\, f_{Ca}\, (I_{Ca} + I_{Ca,Na} + I_{Ca,K}) \quad \text{with}$$
$$I_X = P_X\, z_X^2 \frac{V_m F^2}{RT} \frac{\gamma_{X_i}\,[X]_i\, \exp(z_X V_m F/RT) - \gamma_{X_o}[X]_o}{\exp(z_X V_m F/RT)} \tag{5.15}$$

I_X is either I_{Ca}, or $I_{Ca,Na}$, or $I_{Ca,K}$ for the Ca^{2+}, Na^+, and K^+ component of the L-type Ca^{2+} channel, respectively. P_X are the permeabilities for the ion types X and the corresponding partition coefficients γ_i and γ_o for intra- and extracellular space, respectively. $[X]_i$ and $[X]_o$ are the concentrations of the ion type X at the entrance and the exit of the pore. d and f are activation and inactivation gating variables, respectively, and f_{Ca} is the $[Ca^{2+}]_i$ dependent gate given by:

$$f_{Ca} = \frac{1}{1 + ([Ca^{2+}]_i + K_{m,Ca})^2}$$

with the equilibrium constant of the reaction $K_{m,Ca}$. The time and voltage dependent current I_K, the current I_{K1}, and the plateau current I_{Kp} are defined following eq. 5.1:

$$I_K = g_{K,max} x^2 x_i (V_m - E_K), \quad I_{K1} = g_{K1,max} K1 (V_m - E_{K1}), \quad I_{Kp} = g_{Kp,max} Kp (V_m - E_{Kp})$$

with the activation gates x and Kp and the inactivation gates x_i and $K1$. $K1$ is asssumed to be always in steady state and thus described by eq. 5.4. E_{K1} and E_{Kp} are given by the Nernst voltage and E_K by a modified Goldman-Hodgkin-Katz equation, since I_K is assumed also to be permeable to Na^+:

$$E_K = \frac{RT}{F} \ln\left(\frac{[K^+]_o + P_{Na,K}\,[Na^+]_i}{[K^+]_i + P_{Na,K}\,[Na^+]_o}\right)$$

with P_{NaK} as the Na/K permeability ratio.
The Na/Ca exchanger is given by the equations described in section 5.1.4:

$$I_{NaCa} = k_{NaCa} \frac{1}{K_{m,Na}^3 + [Na^+]_o^3} \cdot \frac{1}{K_{m,Ca} + [Ca^{2+}]_o} \cdot \frac{1}{1 + k_{sat} \exp[(\eta - 1) V_m F/RT]}$$
$$\cdot \left(\exp[\eta V_m F/RT][Na^+]_i^3 [Ca^{2+}]_o - \exp[(\eta - 1) V_m F/RT][Na^+]_o^3 [Ca^{2+}]_i\right)$$

with η as the position of the energy barrier that controls the voltage dependence and k_{sat} as the saturation factor that ensures saturation at very negative potentials.
The Na/K pump is reconstructed taking care of eq. 5.10. It has two independent binding sites for Na^+ and K^+. This leads to the form considering two probability functions (eq. 5.8):

$$I_{NaK} = I_{NaK,max} f_{NaK} \frac{1}{1 + (K_{m,Nai}/[Na^+]_i)^{\frac{3}{2}}} \frac{1}{1 + K_{m,Ko}/[K^+]_o}$$

with the transmembrane voltage dependent function f_{NaK} of $[Na^+]_o$.
The non-specific Ca^{2+} activated current $I_{Ca,ns}$ has a Na^+ and K^+ component each described by a Hill's equation approach presented in eq. 5.9 considering that the maximum current is given in the same form like eq. 5.15. The sarcolemmal Ca^{2+} pump current $I_{p,Ca}$ is defined by the voltage independent pump characteristics of eq. 5.9. The intracellular calcium dynamics is described in the next section since it is not defined in a closed mathematical formula in the Luo-Rudy model, but has a trigger. Also, the variation of the concentrations is explained later (section 5.5.4). The resulting action potential and $[Ca^{2+}]_i$ transient of the Luo-Rudy model is presented in fig. 5.3 b,d.

5.5.3 Courtemanche et al. Model

The model of Courtemanche, Ramirez, and Nattel (CRN) is describing the electrophysiological properties of a cell of the human atrial working myocardium [238]. The schematic description of the currents representing the selective permeability of the membrane is depicted in fig. 5.6 a. The temporal evolution of the transmembrane voltage (fig. 5.3 a) is described using eq. 5.13 with I_{mem} as the sum of the membrane currents:

$$\begin{aligned} I_{mem} = I_{Na} + I_{K1} + I_{to} + I_{Kur} + I_{Kr} + I_{Ks} + I_{Ca,L} \\ + I_{p,Ca} + I_{NaK} + I_{NaCa} + I_{b,Na} + I_{b,Ca} \end{aligned}$$

with the currents: I_{Na} = fast Na^+; I_{K1} = rectifier outward K^+; I_{to} = transient outward K^+; I_{Kur} = ultra rapid delayed outward K^+; I_{Kr} = rapid delayed outward K^+; I_{Ks} = slow delayed outward K^+; $I_{Ca,L}$ = L-type inward Ca^{2+}; $I_{p,Ca}$ = Ca^{2+} pump outward; I_{NaK} = Na/K pump; I_{NaCa} = Na/Ca exchanger; $I_{b,Na}$ = background Na^+; and $I_{b,Ca}$ = background Ca^{2+}. Some of these currents during an AP are depicted in fig. 5.7 a.

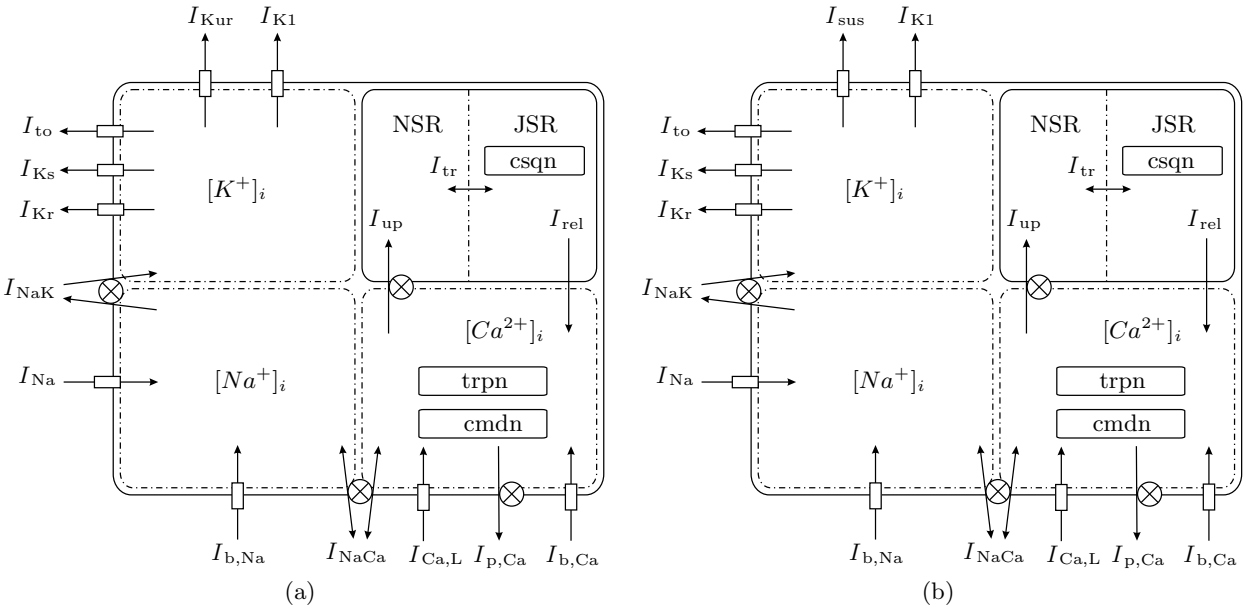

Fig. 5.6. Schematic description of (a) the Courtemanche et al. and (b) the Nygren et al. electrophysiological model. Both models are structurally similar, different only in I_{Kur} in the one and I_{sus} in the other model. The properties differ largely (fig. 5.3 a and fig. 5.7). The symbols and ionic currents are explained in previous figures or in the text.

This model includes two additional currents, which were not described in the previous sections: I_{to} and I_{Kur}. Both currents share similar activation kinetics but differ in their inactivation properties:

$$I_{to} = g_{to,max} o_a^3 o_i \left(V_m - E_K\right)$$
$$I_{Kur} = g_{Kur,max} u_a^3 u_i \left(V_m - E_K\right)$$
$$g_{Kur,max} = 0.005 + \frac{0.05}{1 + \exp\left[\frac{V_m - 15}{-13}\right]}$$

with the activation gating variables o_a and u_a, the inactivation gating variables o_i and u_i, and the voltage dependent maximum conductances $g_{to,max}$ and $g_{Kur,max}$. As an example, the rate constants for the activation o_a and the inactivation o_i gating variable are described by:

$$\alpha_{o_a} = \frac{0.65}{\exp\left(-\frac{V_m+10}{8.5}\right) + \exp\left(-\frac{V_m-30}{59.0}\right)}, \quad \beta_{o_a} = \frac{0.65}{2.5 + \exp\left(\frac{V_m+82}{17}\right)}$$
$$\tau_{o_a} = \frac{1}{\left(\alpha_{o(a)} + \beta_{o(a)}\right) K_{Q_{10}}}, \quad o_{a\infty} = \frac{1}{1 + \exp\left(-\frac{V_m+20.47}{17.54}\right)}$$
$$\alpha_{o_i} = \frac{1}{18.53 + \exp\left(\frac{V_m+113.7}{10.95}\right)}, \quad \beta_{o_i} = \frac{1}{35.56 + \exp\left(-\frac{V_m+1.26}{7.44}\right)}$$
$$\tau_{o_i} = \frac{1}{(\alpha_{o(i)} + \beta_{o(i)}) K_{Q_{10}}}, \quad o_{i\infty} = \frac{1}{1 + \exp\left(\frac{V_m+43.1}{5.3}\right)}$$

$K_{Q_{10}} = Q_{10}^{\frac{T-T_0}{10}}$ with $Q_{10} = 2.2$. $K_{Q_{10}}$ is a temperature factor that permits the adjustment of the relaxation time constant of the process to be adapted to a given temperature when the measured data is gained at e.g. room temperature.
The intracellular calcium dynamics are expressed in the CRN model using a two compartment model for the SR. This considers the ionic flow between the NSR, the JSR, and the myoplasm with three currents:

$$I_{up} = \frac{I_{up,max}}{1 + (K_{up}/[Ca^{2+}]_i)}, \qquad I_{tr} = \frac{[Ca^{2+}]_{JSR} - [Ca^{2+}]_{NSR}}{\tau_{tr}},$$
$$I_{rel} = k_{rel} u^2 v\, w \left([Ca^{2+}]_{NSR} - [Ca^{2+}]_i\right)$$

with the concentration of Ca^{2+} in the NSR and the JSR, $[Ca^{2+}]_{NSR}$ and $[Ca^{2+}]_{JSR}$, repectively, the time constant τ_{tr}, the two Ca^{2+} flux dependent activation and inactivation gating variables u and v, respectively, and the voltage dependent inactivation w. u and v are functions depending on the release current I_{rel}, the L-type Ca^{2+} current, and the Na/Ca exchange current I_{NaCa}. The three buffers of Ca^{2+} in the cell are given by:

$$[Ca^{2+}]_{cmdn} = [cmdn]_{max} \frac{[Ca^{2+}]_i}{[Ca^{2+}]_i + K_{m,cmdn}}, \quad [Ca^{2+}]_{trpn} = [trpn]_{max} \frac{[Ca^{2+}]_i}{[Ca^{2+}]_i + K_{m,trpn}}$$
$$[Ca^{2+}]_{csqn} = [csqn]_{max} \frac{[Ca^{2+}]_{JSR}}{[Ca^{2+}]_{JSR} + K_{m,csqn}}$$

with the concentrations of bound calcium to calmodulin ($[Ca^{2+}]_{cmdn}$), troponin ($[Ca^{2+}]_{trpn}$), and calsequestrin ($[Ca^{2+}]_{csqn}$), and the corresponding maximum concentrations $[cmdn]_{max}$, $[trpn]_{max}$, and $[csqn]_{max}$.

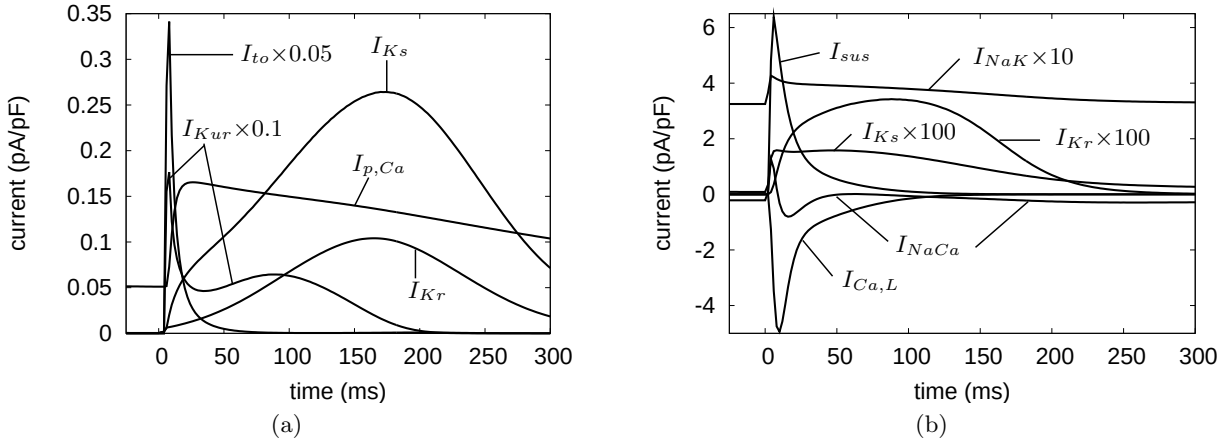

(a) (b)

Fig. 5.7. Ionic curents of the Courtemanche et al. and the Nygren et al. model. Some of the currents are scaled. The ionic currents are expressed in previous figures or in the text.

5.5.4 Nygren et al. Model

The ionic model of Nygren, Fiset, Firek, Clark, Lindblad, Clark, and Giles is defining the electrophysiological properties of human atrial myocytes [239]. The set of membrane currents is nearly the same as in the CRN model:

$$I_{mem} = I_{Na} + I_{Ca,L} + I_{K1} + I_{to} + I_{sus} + I_{Kr} + I_{Ks} \\ + I_{p,Ca} + I_{NaK} + I_{NaCa} + I_{b,Na} + I_{b,Ca}$$

with the currents: I_{Na} = fast Na^+; I_{K1} = rectifier outward K^+; I_{to} = transient outward K^+; I_{sus} = sustained outward K^+; I_{Kr} = rapid delayed outward K^+; I_{Ks} = slow delayed outward K^+; $I_{Ca,L}$ = L-type inward Ca^{2+}; $I_{p,Ca}$ = Ca^{2+} pump outward; I_{NaK} = Na/K pump; I_{NaCa} = Na/Ca exchanger; $I_{b,Na}$ = background Na^+; and $I_{b,Ca}$ = background Ca^{2+}.
The main difference to the CRN model is that I_{Kur} was replaced by the sustained K^+ outward current I_{sus}. But the kinetics of both currents are described by the same set of equations. Further differences are variable bulk concentrations, and that Nygren et al. assumed buffers not to be instantaneously in equilibrium with their surrounding compartments. This behavior is described by eq. 5.11 for each Ca^{2+} buffer.
An exemplary amplitude of some currents during the AP is illustrated in fig. 5.6 b. The course of the transmembrane voltage and of the intracellular calcium concentration are depicted in fig. 5.3 a and c. The variation of the intracellular concentration of the three main ion types is given in this and the other models following eq. 5.14:

$$\frac{\mathrm{d}[Ca^{2+}]_i}{\mathrm{d}t} = -I_{Ca,tot}\frac{A}{2\,V_i F}, \qquad \frac{\mathrm{d}[K^+]_i}{\mathrm{d}t} = -I_{K,tot}\frac{A}{V_i F}, \qquad \frac{\mathrm{d}[Na^+]_i}{\mathrm{d}t} = -I_{Na,tot}\frac{A}{V_i F}$$

with the total calcium current $I_{Ca,tot} = I_{Ca,L} + I_{b,Ca} + I_{p,Ca} - 2\cdot I_{NaCa} + I_{up} - I_{rel}$, the total potassium current $I_{K,tot} = I_{K1} + I_{Kr} + I_{Ks} + I_{sus} + I_{to} - 2\cdot I_{NaK}$, and the total sodium current $I_{Na,tot} = I_{Na} + I_{b,Na} + 3\cdot I_{NaK} + 3\cdot I_{NaCa}$.

5.5.5 Priebe-Beuckelmann Model

The Priebe-Beuckelmann model [242] is based on the second phase dynamical Luo-Rudy model (LRd) [232, 233] and reproduces the electrophysiology of a human ventricular cell

(fig. 5.3 b,d). The LRd model was enhanced in the Priebe-Beuckelmann model by considering new human ventricular voltage-clamp measurements. I_{Kr}, I_{Ks}, I_{to}, I_{K1}, and I_{Ca} were adapted to these measurements. The model consists of two parameter sets describing on one hand a physiological cell and on the other hand a heart failure cell. The model is constructed of equations for currents, concentrations, and buffers (fig. 5.8) with the sum of the transmembrane currents I_{mem} given by:

$$I_{mem} = I_{Na} + I_{K1} + I_{to} + I_{Kr} + I_{Ks} + I_{Ca} + I_{NaK} + I_{NaCa} + I_{b,Na} + I_{b,Ca}$$

Exemplary currents of the Priebe-Beuckelmann model are depicted in fig. 5.9 a during a stimulation of the cell with a frequency of 1 Hz.

5.5.6 Bernus et al. Model

The model of Bernus, Wilders, Zemlin, Verschelde, and Panfilov [253] is primarily based on a reformulation and numerical simplification of the Priebe-Beuckelmann model. They restricted the set of gating variables from 12 in the Priebe-Beuckelmann model to six in their model. The involved currents are basically the same (fig. 5.8 b):

$$I_{mem} = I_{Na} + I_{K1} + I_{to} + I_{K} + I_{Ca} + I_{NaK} + I_{NaCa} + I_{b,Na} + I_{b,Ca}$$

This model handles the delayed rectifier current $I_K = I_{Kr} + I_{Ks}$ as one single current with one single activation gating variable X:

$$I_K = g_{K,max} X^2 \, (V_m - E_K)$$

Further simplifications decreased the computational cost. Since the variation of $[Na^+]_i$ and $[K^+]_i$ is very small, they were set to a constant value. Furthermore, $[Ca^{2+}]_i$ was set constant with the aim of neglecting the whole intracellular calcium handling. This also leads to a

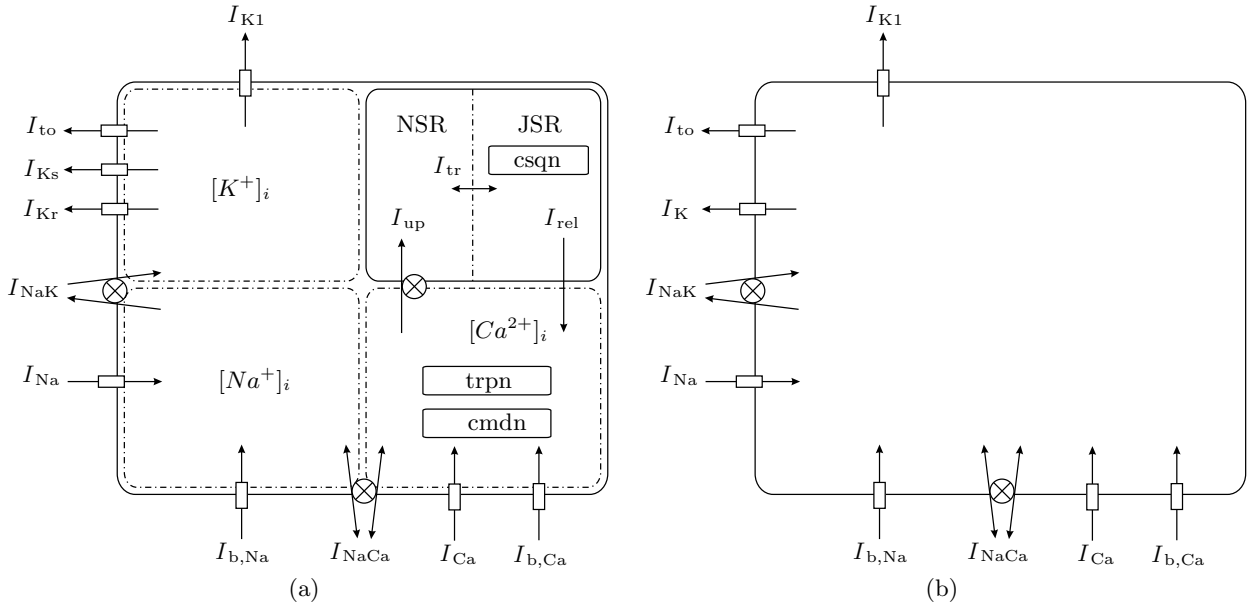

Fig. 5.8. Schematic description of the ionic model (a) of Priebe and Beuckelmann as well as (b) of Bernus et al. with the implemented currents, pumps, exchangers and other components. The Bernus et al. model has no dynamic ion concentration handling.

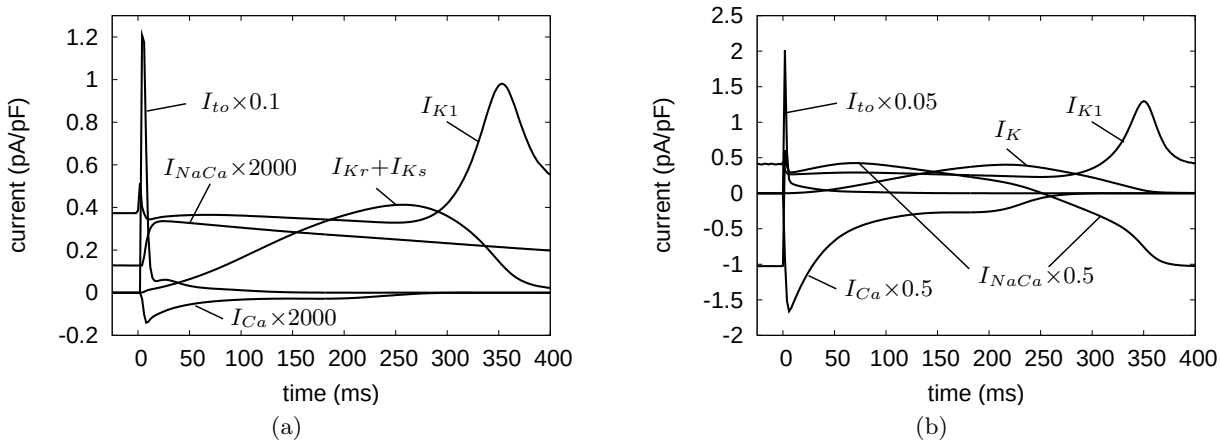

Fig. 5.9. Exemplary ionic curents of (a) the Priebe-Beuckelmann and (b) the Bernus et al. model. Some of the currents are scaled. Interestingly, I_{Ca} and I_{NaCa} are differing by a factor of approximatly 5000 between the models. The ionic currents are expressed in previous figures or in the text.

simplification of the equation for I_{Ca}, since f_{Ca} is a constant and the activation gating variable d is assumed to be instantaneous in steady state, thus is only described by the steady state function d_∞. The same strategy was performed for the transient outward current I_{to}: r is replaced by r_∞. A further simplification was the combination of the two inactivation gating variables (h and j) of the I_{Na} current into one inactivation gating variable v having a quadratic inactivation dependence (v^2).
Figure 5.3 b shows the AP of the Bernus et al. model with some corresponding currents presented in fig. 5.9 b.

5.5.7 Ten Tusscher et al. Model

Ten Tusscher, Noble, Noble, and Panfilov introduced a model of human ventricular characteristics to study ventricular arrhythmia in long-term simulations (fig. 5.10 a) [255]. The model is based on recent measurement data of most of the major ionic currents. The set of transmembrane currents is given by:

$$I_{mem} = I_{Na} + I_{K1} + I_{to} + I_{Kr} + I_{Ks} + I_{Ca,L} + I_{NaK} + I_{NaCa} + I_{p,Ca} + I_{b,Na} + I_{b,Ca}$$

where the currents are described in the same way as in other models, but the kinetics are adapted to human measurement data. Some currents are depicted in fig. 5.11 a corresponding to the course of transmembrane voltage and of the calcium concentration given in fig. 5.3 b and d, respectively. The calcium dynamics are reconstructed with a more simple approach compared to e.g. the Nygren et al. model. A feature of the ten Tusscher et al. model is that it has two different parameter sets to reconstruct subendo- and subepicardial cell properties.

5.5.8 Iyer et al. Model

The model of Iyer, Mazhari, and Winslow reconstructs the electrophysiological properties of human ventricular myocytes and is primarly based on the earlier canine model of Winslow et al. [244]. The channels are mainly defined by Markov chain models. The total membrane current is defined as:

$$\begin{aligned} I_{mem} = {} & I_{Na} + I_{K1} + I_{Kr} + I_{Ks} + I_{Kv1.4} + I_{Kv4.3} + I_{K,p} \\ & + I_{Ca} + I_{Ca,K} + I_{NaK} + I_{NaCa} + I_{Ca,p} + I_{b,Na} + I_{b,Ca} \end{aligned}$$

with the two components of the transient outward current $I_{Kv1.4}$ and $I_{Kv4.3}$, and the plateau Ca^{2+} and K^+ currents $I_{Ca,p}$ and $I_{K,p}$, respectively. $I_{Kv1.4}$ is encoded by gene $KCND3$ and exhibits fast recovery from inactivation. $I_{Kv4.3}$ is encoded by gene $KCNA4$ and exhibits slow recovery from inactivation. Some gates are still defined familiar to the Hodgkin-Huxley formulation. For I_{Na}, I_{Kr}, I_{Ks}, the two components of I_{to}, $I_{Ca,L}$, and the Ca^{2+} induced Ca^{2+} release (CICR) current of the sarcoplasmic reticulum I_{rel}, Markov chain models for describing the gating process are used. A further speciality of this model is the consideration of the concentration of Ca^{2+} in the region between the JSR and the T tubule (dyadic space) as in the model of Noble et al. [241]. This additional compartment is necessary to describe the calcium dynamics of the couplon consisting of L-type Ca^{2+} channels and CICR channels. As this model includes Markov chains, the computational cost to solve the equations is much larger than in other ionic models.

5.5.9 Zhang et al. Model

The electrophysiological model of Zhang, Holden, Kodama, Honjo, Lei, Varghese, and Boyett is describing the properties of the rabbit sinoatrial node (SAN) in central and peripheral cells (fig. 5.10 b) [247]. It is based on rabbit SAN experimental data and is constructed of 14 currents constructing the AP shown in fig. 5.3 a:

$$\begin{aligned} I_{mem} = {} & I_{Na} + I_{\mathrm{Ca,L}} + I_{\mathrm{Ca,T}} + I_{\mathrm{to}} + I_{sus} + I_{Kr} + I_{Ks} \\ & + I_{f,Na} + I_{f,K} + I_{b,Na} + I_{b,Ca} + I_{b,K} + I_{NaCa} + I_{pCa} \end{aligned}$$

with the T-type Ca^{2+} current $I_{Ca,T}$ and the so-called funny current I_f, a hyperpolarization activated pacemaker current carried by Na^+ and K^+. Both current components ($I_{f,Na}$ and $I_{f,K}$) have the same activation gating variable y:

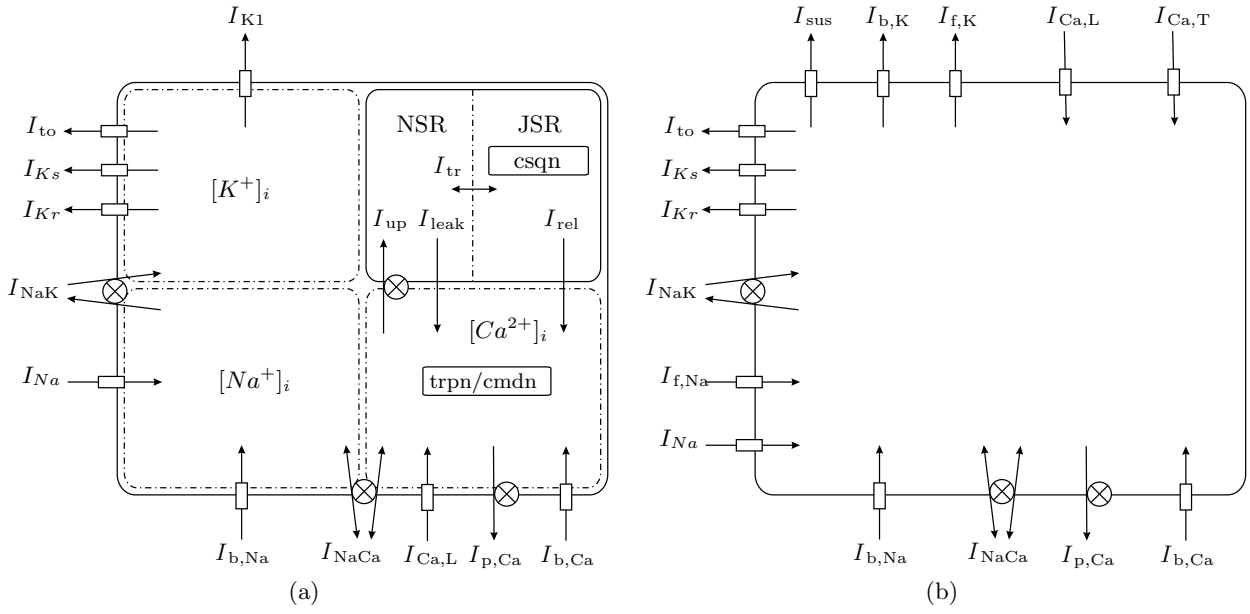

Fig. 5.10. Schematic description of (a) the Ten Tusscher et al. [255] and (b) the Zhang et al. [247] model. The Zhang et al. model has no dynamic ion concentration handling.

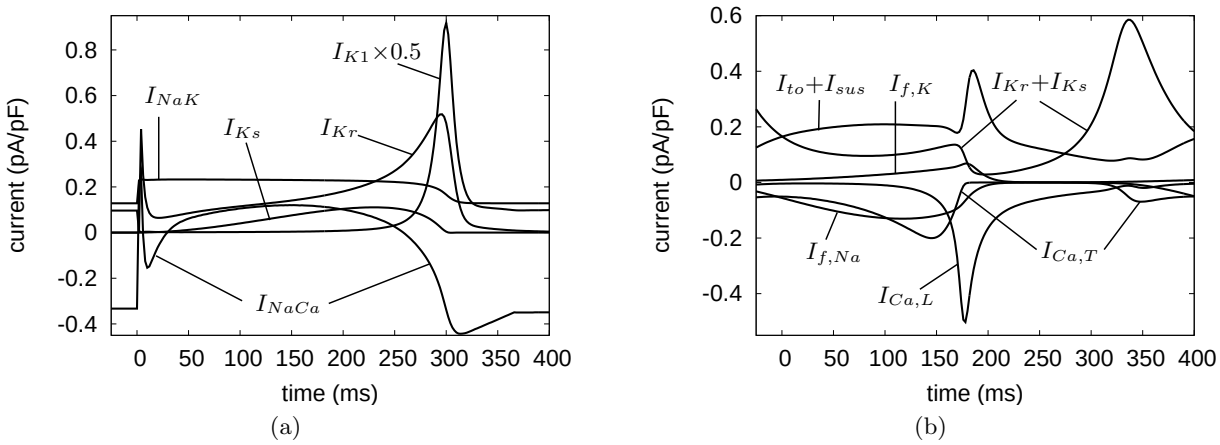

(a) (b)

Fig. 5.11. Ionic curents of (a) the ten Tusscher et al. and (b) the central Zhang et al. model.

$$I_{\mathrm{f}} = I_{f,K} + I_{f,Na}$$
$$I_{f,K} = g_{f,K,max}\, y\,(V_m - E_K)\,, \quad I_{f,Na} = g_{f,Na,max}\, y\,(V_m - E_{Na})$$
$$\alpha_y = \exp\left(-\frac{V_m + 78.91}{26.62}\right), \quad \beta_y = \exp\left(\frac{V_m + 75.13}{21.25}\right)$$

The T-type Ca^{2+} current was proven to have an important contribution in SAN cells (fig. 5.11 b) [127]. If this current is blocked, a negative chronotropic effect is present in the SAN. $I_{Ca,T}$ is implemented in the Zhang et al. model in a similar way than the L-type Ca^{2+} currents in other models.
Some of the maximum conductances of the model were differing to describe the cells from central and peripheral regions. Mainly the maximum conductance of the channels depicting the currents $I_{Ca,L}$, I_{to}, I_{sus}, I_{Kr}, I_{Ks}, and I_f are reduced for the central cell compared to the peripheral cell. I_{Na} is not expressed in the central SAN myocytes and the membrane capacitance is reduced since central cells are smaller than peripheral.

5.6 Excitation Conduction

The conduction of the excitation in the heart is based on the electrical coupling between cells (section 4.5). Commonly, excitation conduction is calculated in tissue with two different approaches. The first method is macroscopic and the tissue is described as a continuum. One computational node is reproducing the properties of several real myocytes. The macroscopic methods can be divided into three different types: Cellular automata being rule based systems, simplified reaction-diffusion systems neglecting mainly the complex flow of ions through the cell membrane and through gap junctions, and models of the electrical flow combined with detailed electrophysiological descriptions, i.e. monodomain and bidomain models. In the macroscopic models, the discrete structure and thus the inhomogeneous microscopic excitation conduction due to geometric variations of the cells and different densities and expressions of gap junctions is neglected.
The second method is a microscopic description of the discrete structure of the cells in the tissue. Each myocyte is divided into several mathematical nodes leading to a more detailed description of the electrophysiological behavior of the cell compared to the macroscopic approach, but commonly with a much higher mathematical and therefore computational effort.

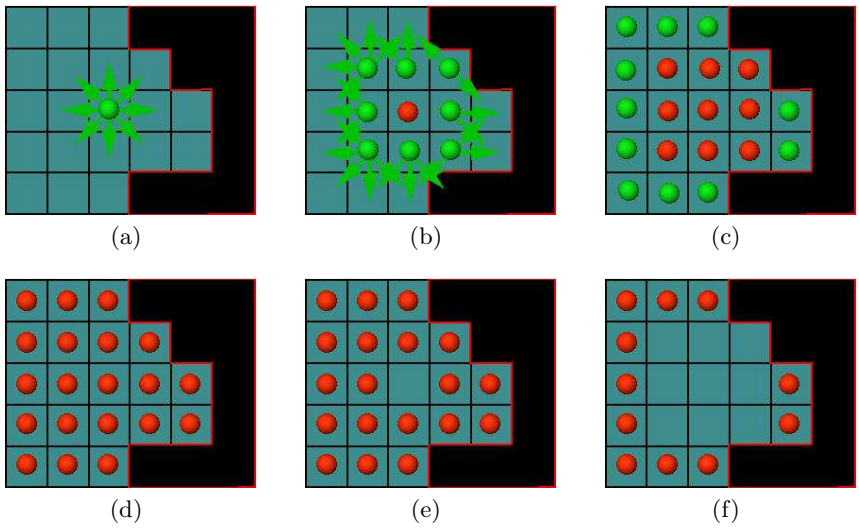

Fig. 5.12. Schematic functioning of a cellular automaton. The green dots are active elements, red dots represent the refractory state. After an initial stimulus (a) the excitation is conducted to neighboring cells (b). The elements are refractory during the plateau phase (c,d). After repolarization (e,f) the cells are again excitable. Fig. from [264].

Microscopic models allow the individual modeling of myocytes with several elements considering different ionic mechanisms and gap junction densities in each node [140, 263]. As microscopic modeling is not in the scope of this work, it is not further detailed in this section.

5.6.1 Cellular Automata

The application of rule based models of the excitation conduction like cellular automata allows the efficient simulation of the cardiac electrophysiology [265, 266, 267, 268, 269, 270]. The geometrical information of the model usually considers the anisotropic and heterogeneous anatomical features of the heart. Furthermore, tissue dependent electrophysiological parameters like refractory periods, action potential courses, excitation conduction velocities, and autorhythmic properties are considered, which are taken from literature.
A cellular automaton can be divided into two components [271, 272]: A regular, discrete, finite network representing the underlying spatial structure and a finite automaton working at each node of the network. The network consists e.g. of an anatomical model of the human heart. The tissue specific excitation conduction velocity and the anisotropy of the myocardium can be considered based on myocyte orientation data. The finite automaton at each node point represents the physiological state by modeling the course of the transmembrane voltage depending on tissue type, stimulation frequency and refractory periods. The scheme of a cellular automaton is depicted in fig. 5.12.

5.6.2 Simplified Reactions-Diffusion Systems

Modeling of excitation conduction with simplified reaction-diffusion systems can reconstruct the physiological and pathological excitation on tissue and organ level [138, 273, 274]. The reaction-diffusion systems consists of two components: One represents the membrane activity (reaction part), and the other describes the electrical interaction of the tissue (diffusion part). An early representative is the two state FitzHugh-Nagumo model [275]:

$$\frac{\partial u}{\partial t} = \frac{u - \frac{u^3}{3} - v}{\epsilon} + D\nabla^2 u, \qquad \frac{\partial v}{\partial t} = \epsilon(u + \beta - \gamma v)$$

with the state variable u for the activation of transmembrane voltage and the state variable v for inactivation. The diffusion term is formulated for isotropic media with the scalar diffusion coefficient D. The parameters β, γ, and ϵ are the so-called membrane parameters and are influencing the course of the AP. The diffusion coefficient and the membrane parameters are time dependent.
Modifications of the FitzHugh-Nagumo equations allow a more realistic description of the conduction in the myocardium [276, 277]. This model considers the anisotropic features of the tissue by using a diffusion tensor. It includes more membrane parameters to adapt the AP course to measured data.

5.6.3 Models of the Electrical Flow

A common approach to reproduce the activity of cardiac tissue consists of a model describing the anisotropic excitation conduction in combination with an electrophysiologically accurate ionic model. The ionic models are explained in section 5.5. The excitation conduction model could be either based on resistor networks or can consider the electrical flow of ions between adjacent cells using Poisson's equation. The advantage of resistor networks to describe electrical coupling of cardiac cells is the lower computational cost compared to approaches based on Poisson's equation. The most important disadvantage is that varying anisotropic conductivities in the tissue are not reproducible with the resistor network approaches.
A further distinction is made between models considering the extracellular space to be on constant potential and thus calculating the current flow through the intracellular space and through gap junctions (monodomain model) and approaches taking the current flow in intra- and extracellular space as well as through gap junctions into account (bidomain model). Both, monodomain and bidomain model can be represented by resistor network or Poisson's equation based approaches. As the implemented method in this work is based on the calculation of Poisson's equation, this approach is detailed further.

5.6.3.1 Bidomain Model

The discrete electrical interaction of the tissue can be approximated by the continuous approach of the bidomain model [278, 279, 280, 281, 282]. The bidomain model considers the current flow in the intra- and the extracellular domain independently. The two domains are separated by the cell membrane (fig. 5.13) through which currents flow between the domains. Hence, the intercellular stimulus current, which drives the conduction of excitation is constructed with the influences of both domains.
Conductivity tensors for both domains are defined to consider the anisotropic electrical properties of cardiac tissue and the surrounding medium e.g. blood, bath, and air. The extracel-

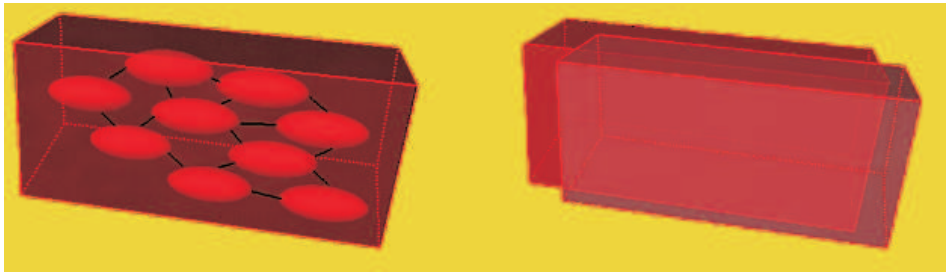

Fig. 5.13. The two domains of the bidomain model. The intracellular space is separated from the extracellular space by a membrane. Fig. from [270].

Table 5.2. Intra- and extracellular conductivities (S/m) [281, 283]. σ_{il} and σ_{el} are the longitudinal intra- and extracellular conductivities. σ_{it} and σ_{et} are the transversal intra- and extracellular conductivities.

	Clerc (1976)	Roberts and Scher (1982)	Colli-Franzone (1993)
σ_{il}	0.174	0.344	0.3
σ_{it}	0.0193	0.0596	0.031525
σ_{el}	0.625	0.117	0.2
σ_{et}	0.236	0.0802	0.13514

lular anisotropy is determined by the cylindrical shape of the cells in combination with the fiber orientation of the cells and the sheet orientation of a myocardial layer. The intracellular anisotropic conductivity tensor represents density and distribution of gap junctions and also the oriented intracellular structures of the cell with respect to the orientation of the myocytes. As the microscopic intra- and extracellular conductivities vary between adjacent cells the bidomain model uses a mean conductivity tensor to describe the macroscopic anisotropy in both domains.
For each domain, Poisson's equation is defined with index e for the extracellular domain and index i for the intracellular domain:

$$\nabla \left(\sigma_e \nabla \Phi_e\right) = -\beta I_m - I_{se} \tag{5.16}$$

$$\nabla \left(\sigma_i \nabla \Phi_i\right) = \beta I_m - I_{si} \tag{5.17}$$

with the intra- and extracellular potentials Φ_i and Φ_e, respectively, the corresponding conductivity tensors σ_i and σ_e, the transmembrane current density I_m, the membrane surface to cell volume ratio β, and externally applied current sources I_{si} and I_{se} in the intra- and extracellular domain, respectively.
The conductivity tensors σ_i and σ_e represent the anisotropic electrical properties of the tissue and depend on the tissue type and the orientation of the main axis of the myocytes. Table 5.2 depicts an overview of commonly used values for the conductivities.
Based on the assumption of orthotropic conductivity distribution in cardiac myocytes and thus the rotational symmetry, the conductivity tensors σ_i and σ_e can be constructed with only the longitudinal and transversal conductivities of the intracellular (σ_{il} and σ_{it}, respectively) and the extracellular space (σ_{el} and σ_{et}, respectively):

$$\sigma_{i,e} = \mathbf{R} \begin{pmatrix} \sigma_{(i,e)l} & 0 & 0 \\ 0 & \sigma_{(i,e)t} & 0 \\ 0 & 0 & \sigma_{(i,e)t} \end{pmatrix} \mathbf{R}^T$$

whereas the rotation matrix $\mathbf{R}$ is constructed of the two components $\mathbf{R}_{xy}$ and $\mathbf{R}_{xz}$ with $\mathbf{R} = \mathbf{R}_{xz}\mathbf{R}_{xy}$:

$$\mathbf{R}_{xy} = \begin{pmatrix} \cos\varphi & \sin\varphi & 0 \\ -\sin\varphi & \cos\varphi & 0 \\ 0 & 0 & 1 \end{pmatrix}, \qquad \mathbf{R}_{xz} = \begin{pmatrix} \cos\vartheta & 0 & \sin\vartheta \\ 0 & 1 & 0 \\ -\sin\vartheta & 0 & \cos\vartheta \end{pmatrix}$$

φ and ϑ describe the orientation of the fiber's main axis in the global space with φ being the angle in the (x,y)-plane and ϑ being the angle in the (x,z)-plane.
A mathematically useful reformulation of the two Poisson's equations (eqs. 5.16 and 5.17) is performed to achieve the bidomain equations. The two domains are coupled via the transmembrane voltage V_m, which is defined by:

$$V_m = \Phi_i - \Phi_e \tag{5.18}$$

Furthermore, the transmembrane current density I_m, which flows into one domain must come from the other. Thus, in the summation of the two Poisson's equations (eqs. 5.16 and 5.17) I_m vanishes:

$$\nabla (\sigma_i \nabla \Phi_i) + \nabla (\sigma_e \nabla \Phi_e) = -I_{si} - I_{se}$$

Under the assumption that no externally applied current sources are present and with $V_m = \Phi_i - \Phi_e$, this can be transfered into:

$$\begin{aligned} \nabla (\sigma_i \nabla \Phi_i) &= -\nabla (\sigma_e \nabla \Phi_e) \\ \nabla (\sigma_i \nabla (V_m + \Phi_e)) &= -\nabla (\sigma_e \nabla \Phi_e) \\ \nabla ((\sigma_i + \sigma_e) \nabla \Phi_e) &= -\nabla (\sigma_i \nabla V_m) \end{aligned} \tag{5.19}$$

Equation 5.19 is the first part of the bidomain model describing the influence of the transmembrane voltage on the extracellular potential. V_m is commonly calculated with the ionic models presented in section 5.5. The second part of the bidomain equations is constructed based on eq. 5.17 under consideration of eq. 5.18:

$$\begin{aligned} \nabla (\sigma_i \nabla \Phi_i) &= \nabla (\sigma_i \nabla (V_m + \Phi_e)) = \nabla (\sigma_i \nabla V_m) + \nabla (\sigma_i \nabla \Phi_e) \\ &= \beta I_m - I_{si} = \beta \left(C_m \frac{\mathrm{d}V_m}{\mathrm{d}t} + I_{mem} \right) - I_{si} \end{aligned}$$

since the current I_m describes the summed up flow through the membrane given by the electrophysiological models:

$$I_m = \left(C_m \frac{\mathrm{d}V_m}{\mathrm{d}t} + I_{mem} \right)$$

Thus to conclude, the second part of the bidomain equations is given by:

$$\nabla (\sigma_i \nabla V_m) + \nabla (\sigma_i \nabla \Phi_e) = \beta \left(C_m \frac{\mathrm{d}V_m}{\mathrm{d}t} + I_{mem} \right) - I_{si} \tag{5.20}$$

It describes in which way the currents in intra and extracellular space are determining the intercellular stimulus current as an input for the electrophysiological models.
The tissue is normally surrounded by a bath medium. In the heart, this bath is equivalent to the blood at the endocardial boundary and the pericardium at the epicardial boundary. The bath and the extracellular space of the tissue build a continuous domain in the bidomain model but with different conductivity tensors. The conductivity in the isotropic bath is assumed to be a scalar value. The intracellular domain is only defined in the active tissue since the bath has no coupled intracellular space. To consider different media, boundary conditions need to be included. The first boundary condition is a grounded potential in the bathing medium to provide a reference potential. A further boundary condition is the continuity of the normal current at the tissue-bath interface in the extracellular domain:

$$\mathbf{n}^{\mathbf{T}} \sigma_e \nabla \Phi_e = \mathbf{n}^{\mathbf{T}} \sigma_b \nabla \Phi_e$$

with σ_b being the scalar conductivity of the bath and $\mathbf{n}$ is the unit vector normal to the boundary surface between the two media.
As the intracellular space is only defined in the tissue, the intracellular current density is zero at the tissue-bath interface:

$$\mathbf{n}^{\mathbf{T}} \sigma_i \nabla \Phi_i = 0$$

5.6.3.2 Monodomain Model

The bidomain model can be translated into the monodomain model under the assumption, that the extracellular space has the same longitudinal to transversal conductivity ratio than the intracellular space. This means, that the conductivity tensors differ only by a multiplication with a scalar value $\sigma_i = \kappa\sigma_e$. This can be inserted into eq. 5.19:

$$\begin{aligned}\nabla\left(\sigma_i \nabla V_m\right) &= -\nabla\left(\left(\sigma_i + \frac{\sigma_i}{\kappa}\right)\nabla\Phi_e\right) = -\left(1 + \frac{1}{\kappa}\right)\nabla\left(\sigma_i\nabla\Phi_e\right) \\ &= (\kappa+1)\beta\left(C_m\frac{\mathrm{d}V_m}{\mathrm{d}t} + I_{mem}\right)\end{aligned} \tag{5.21}$$

The monodomain model contains only one unknown potential, namely $V_m(x, y, z)$ that directly describes the intercellular current.

5.7 Pathoelectrophysiology

A reasonable amount of mathematical descriptions for pathological behavior of cardiac cells and of cardiac tissue has been developed in the last decades, e.g. [242, 255, 259, 262, 284, 285, 286, 287, 288, 289]. Most of these models describe the tissue in an arrhythmic state and the authors are investigating the genesis, mechanisms and effects of flutter or fibrillation in either atrium or ventricle. On the other hand, some groups have worked on modeling the electrophysiological basics for the pathological states based on measurement data on the single cell level.
Additionally to these two main areas of interest, several other work was carried out to understand the heart's function in pathological states. As an example, Faber and Rudy investigated intracellular sodium overload of cardiac cells [259] and Priebe and Beuckelmann designed their model of human ventricular electrophysiology (section 5.5.5) to understand the mechanisms of heart failure [242].

5.7.1 Arrhythmia

Arrhythmias are the most common reason for sudden cardiac death. Their mechanisms are still not understood well. Thus, the area of reconstruction of atrial and ventricular arrhythmia is one of the most interesting investigations in computational cardiology.
The knowledge about cardiac anatomy, electrophysiology and its interaction in physiological as well as patholgical cases has increased dramatically in the last years. For the simulation of cardiac electrophysiology, these findings have improved the level of reality but also complexity. As an example, Harrild and Henriquez investigated the complex interplay between structure and anisotropy in the human atrium in sinus rhythm and also during atrial flutter [284]. Sampson and Henriquez had a look on the influence of inhomogeneities in myocardial structure and ionic properties on excitation and repolarization [285]. They estimated the likelihood of premature stimuli in this heterogeneous approach to produce functional block, which may initiate ventricular arrhythmias. Xie and coworkers have investigated the influence of ventricular geometry on the genesis of ventricular fibrillation due to wave breakup mechanisms [287]. Clayton and Holden simulated the conduction and repolarization of both normal beats and arrhythmias in the case of transmural heterogeneous electrophysiological properties [289]. Ten Tusscher et al. created their model of human ventricular electrophysiology (section 5.5.7) to

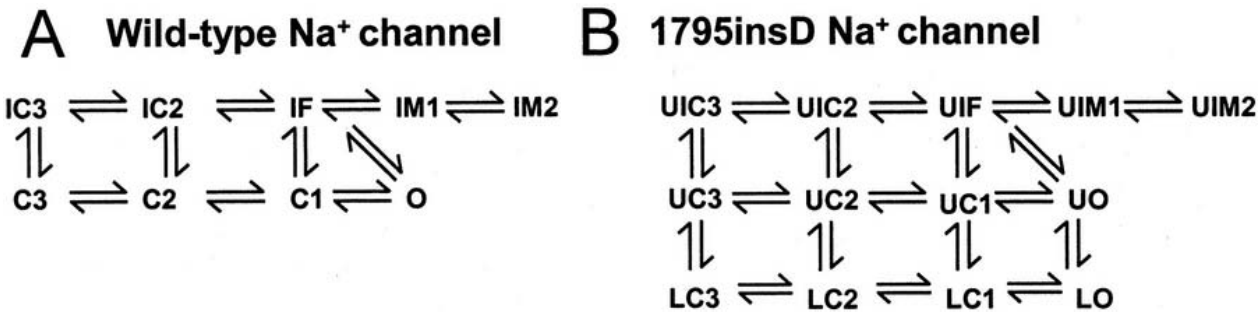

Fig. 5.14. Markov models for normal (wild-type) (A) and mutant 1795insD (B) cardiac Na^+ channels. The mutant model contains two gating modes. U (upper) indicates background mode of gating; L (lower), a small population of bursting channels that fail to inactivate [286].

understand the dynamics of spiral wave rotation in heterogeneous human tissue [255]. Also, the mechanical induction of ventricular arrhythmias following a mechanical impact due to mechano-electrical feedback mechanisms has been simulated by Li and colleagues [288].

5.7.2 Long QT Syndrome

Genetic defects are of great interest for the modeling of cellular pathoelectrophysiology, since the mechanisms of these pathologies are well understood and the electrophysiological changes of the defects can be measured in transfected cells. Up to now, the main focus concerning genetic defects in computational cardiology is given on the long QT syndrome.
For example Gima and Rudy identified the relation between the electrophysiological changes due to the LQT1, LQT2, and LQT3 syndrome and the changed electrocardiographic waveforms [262]. As in the measurment data (section 4.8.2.2) LQT1 prolongs the QT interval in their simulations without widening the T wave. Clancy and Rudy have developed a model describing the physiological and the mutant I_{Na} channel with a Markov chain model (fig. 5.14) [286]. The mutation is located in the C terminus of the cardiac Na^+ channel, 1795insD. It causes two distinct clinical syndromes, LQT3 and Brugada, by differentially disrupting cellular electrical behavior in epicardial and midmyocardial cell types.

6

Cardiac Tension Development

The mechanical function of a cardiomyocyte is initiated by electrical excitation. This process is called excitation contraction coupling (ECC). The electrical activation of the muscle cell is responsible for the increasing concentration of intracellular calcium, which, in turn, triggers the tension development in the force generating units. Thus, tension onset follows nearly the same spatiotemporal sequence as the electrical excitation conduction.
The muscle contraction is initiated by an increase of the free myoplasmic Ca^{2+} concentration $[Ca^{2+}]_i$ from 0.01 μM to over 1 μM as a consequence of the Ca^{2+}-induced Ca^{2+} release from the JSR at the dyadic space [108]. In the presence of high $[Ca^{2+}]_i$, Ca^{2+} is bound to troponin and tropomyosin is shifted. Tropomyosin and troponin complexes act as mediator and the position of these proteins on the thin filaments controls actin-myosin interaction. If tropomyosin is shifted, the myosin binding sites of actin are exposed.
The troponin complex is bound with coiled-coil tropomyosin along the actin filament in the resting state with low $[Ca^{2+}]_i$. Troponin I (TnI) overlays the myosin binding site of the actin filament and hence inhibits the actin-myosin interaction [13]. The inhibition is caused by a strong chemical connection between TnI and myosin binding sites of the actin filament.
Once calcium is bound to troponin C (TnC), the binding configuration between TnI and TnC is strengthened. This stronger bond destabilizes the link between TnI and actin. Also, the binding between troponin T (TnT) and tropomyosin becomes stronger according to the chemical re-configuration. Both strong chemical bonds result in the shifting of tropomyosin and the release of TnI from the myosin binding site. This allows the myosin head to build the so-called cross-bridge (XB) interaction. The hydrolysis of ATP releases energy, which is necessary for the XB interaction.

6.1 Interaction of Actin and Myosin

The contraction of the muscle is based on the shortening of millions of sarcomeres bundled in the myofibrils parallelly and serially. The sarcomeres are shortened by interaction of actin and myosin filaments as shown in fig. 6.1. The myosin heads are not connected to the actin filament in the resting state. The XB cycle of actin and myosin is activated if calcium is bound to TnC and the myosin binding site is opened due to the shift of TnI.
Myosin filaments move over a field of actin filaments, which are bound to the Z discs at their tails [37]. This movement is caused by the myosin head sliding along the actin filament. The reason for this movement is that the actin filament has a polarity. The operation direction of the myosin head is mainly towards the plus end of the actin filament [290].

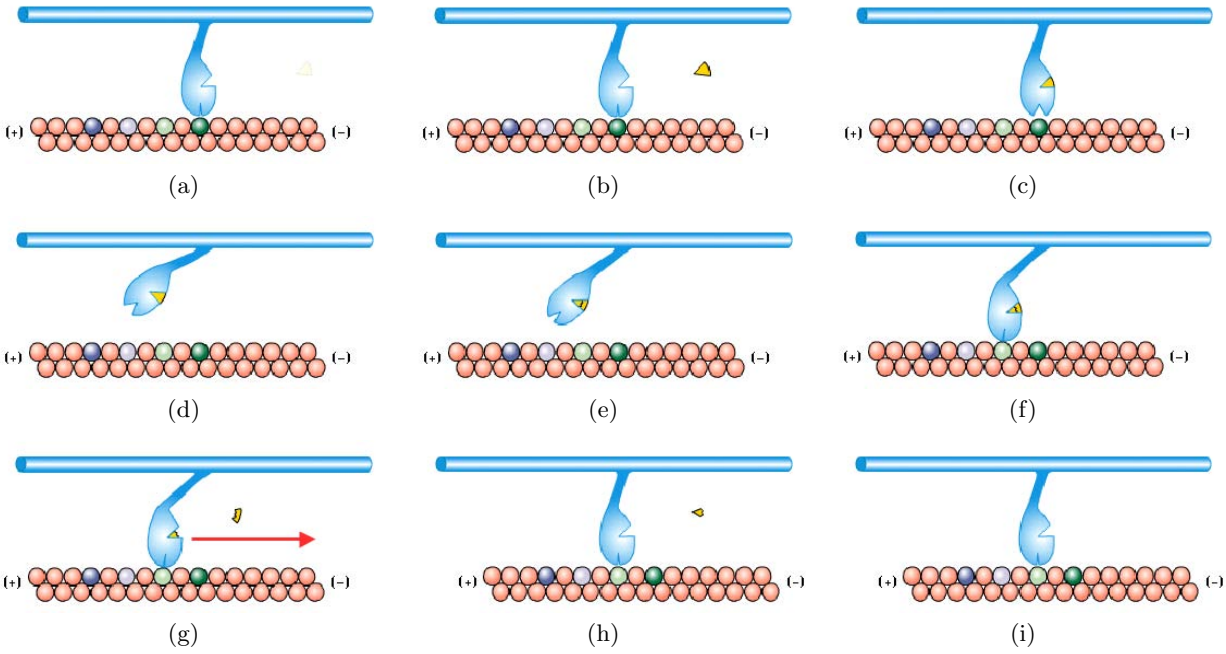

Fig. 6.1. Cross-bridge cycle during tension development including ATP (shown as a small triangle) hydrolysis. (a): Myosin head binds actin tightly in a rigor state. (b),(c): Bound ATP causes a dissociation of the actin-myosin binding through a conformation change. (d): The myosin head moves toward the plus end of the actin filament. (e),(f): During the binding between the myosin head and actin, ATP is hydrolyzed to ADP (a smaller triangle) and P_i (a small quadrad segment), but they are still bound together. (g): Dissociation of P_i occurs, while the myosin head uses freed energy to execute the power stroke. (h),(i): Release of ADP restores the attached myosin head in the rigor state. Figs. from [37].

The tension generated in each XB interaction are amplified by the multitude of thick filaments in a sarcomere and the multitude of sarcomeres in a myofibril. The movement of myosin heads at both ends of the thick filament draws the thin filaments toward the center of the sarcomere. As long as the concentration of intracellular calcium and ATP is high enough, the shortening of the sarcomere is terminated, only if either the ends of the thick filaments reach the Z disc or the minus ends of the thin filaments overlap each other at the center of the A band.
During the cross-bridge cycle, binding and hydrolysis of ATP is required for tension development of myocytes. The hydrolysis of one ATP molecule leads to a one-step movement of myosin. Figure 6.1 shows the whole XB cycle.
The actin binding site and ATP binding pocket in the head domain of a myosin molecule are located opposite and distant from each other, but connected by a surface cleft. The presence of this cleft provides an obvious mechanism for generating large movements of the head motor domain [37]. Starting with the rigor state, in which a myosin head binds actin tightly, the opposite actin binding site is opened, if ATP is bound to the myosin head through a nucleotide binding. A large change in the molecular conformation of the head domain couples the functional interaction between the ATP and actin binding site.
The binding between the myosin head and actin is now weakened and allows the pivoting motion of the myosin head. Due to the polarity of the actin filament and the selectivity of the myosin head, the dissociated myosin head moves to the plus end of the actin filament. During this movement, ATP hydrolyzes to ADP, phosphate (P_i), hydrogen (H^+) and $-7.3\frac{kcal}{mol}$ of energy is freed:

$$ATP + H_2O \longrightarrow ADP + P_i + H^+ \tag{6.1}$$

The hydrolysis causes a second conformational change in the myosin head, which allows the myosin head to rebind to the next possible myosin binding site having a weak bond. If enough intracellular Ca^{2+} is present, TnI is not overlapping the myosin binding site. At this state, the actin binding site of the myosin head is closed partially. As phosphate dissociates from the ATP binding pocket, the myosin head undergoes a third conformational change. This step is called the power stroke, which causes the myosin head to move. The myosin head moves in discrete steps of approximately 5 – 10 nm. During each power stroke, a myosin head generates a tension of 1 – 5 pN [37, 291]. The fourth molecular conformational change, which is called isomerisation, restores myosin to its rigor state by releasing the remaining ADP. The transition velocity of this process is dependent on the tension, which acts on the XB. The transition rate is slowed with rising tension.

6.2 Calcium Tension Relationship

Calcium sensitivity of tension can be determined by least square regressions using the Hill transformation to approximate the linear function of the sigmoid calcium tension relations (fig. 6.2a):

$$\log\left(\frac{T_{\%}}{1-T_{\%}}\right) = n_H\left(\log\left[Ca^{2+}\right]_i + \log\left[Ca^{2+}\right]_{50}\right), \tag{6.2}$$

with active tension as a fraction of maximal Ca^{2+}-activated tension $T_{\%}$, the concentration of intracellular calcium at half maximum of the developed tension $[Ca^{2+}]_{50}$, and the Hill parameter n_H, representing the steepness of the function.
The Ca^{2+} concentration is quantified in $\mu molar$ (μM), which is equal to $\mu mol/l$. The Ca^{2+} concentrations is usually displayed in the logarithmic unit pCa:

$$pCa = -\log\left[Ca^{2+}\right]_i \quad , \quad pCa_{50} = -\log\left[Ca^{2+}\right]_{50} \tag{6.3}$$

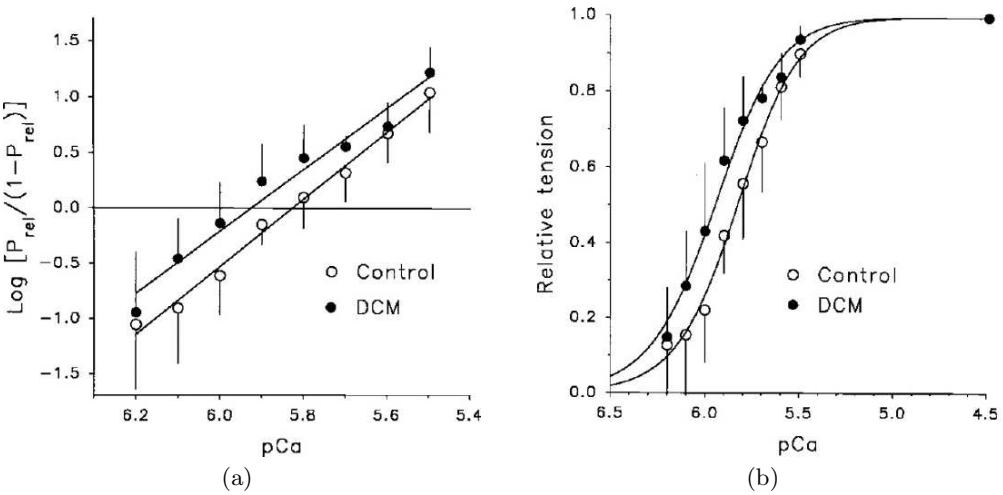

Fig. 6.2. Calcium tension relationship. An augmented Ca^{2+} sensitivity of canine myocytes with dilated cardiomyopathy (DCM) was observed in contrast to a control group. (a) Linear function of the sigmoid calcium tension relations. P_{rel} refers to tension as a fraction of maximum tension. The steepness was reduced in the DCM case, but the relative tension was larger. (b) Hill curve of the calcium tension relation. Tensions are normalized to the maximal Ca^{2+}-activated tension for each group. pCa is defined as $-\log\left[Ca^{2+}\right]_i$. Figs. from [292].

Mean calcium tension curves were fitted to the sigmoid Hill equation for the purpose of data representation and data analysis. The quantitative description of typical relationships between intracellular Ca^{2+} concentration and tension is represented by the Hill equation (fig. 6.2b):

$$T = T_0 \frac{[Ca^{2+}]_i^{n_H}}{[Ca^{2+}]_i^{n_H} + [Ca^{2+}]_{50}^{n_H}}, \tag{6.4}$$

with a measured active tension T, and the maximum tension T_0 in saturated calcium steady state. The fraction of T by T_0 results in the relative tension $T_{\%}$, which is also called the normalized tension.

$$T_{\%} = \frac{T}{T_0} = \frac{[Ca^{2+}]_i^{n_H}}{[Ca^{2+}]_i^{n_H} + [Ca^{2+}]_{50}^{n_H}}, \tag{6.5}$$

6.3 Length Tension Relationship

Since tension development in each sarcomere depends on the occurrence of XB cycles, the maximal tension at any sarcomere length is determined by the degree of overlap of the actin and myosin filaments (fig. 6.3) [13]. All myosin heads are able to interact with the actin filament at the optimal overlap with the sarcomere length between 2 and 2.2 μm. If the sarcomere is stretched and leaves its optimal overlap zone, the potentially developable tension declines gradually, until it is not possible to create XBs. The final tension is zero at the point where no overlap is present, with a sarcomere length of approximately 3.6 μm.
The actin filaments from both sides of the sarcomere begin to overlap each other at a shorter sarcomere length of approximately 1.9 μm. The overlapping of the thin filaments causes the compensation of tension, which is generated by XB cycles. The thick filament is maximally

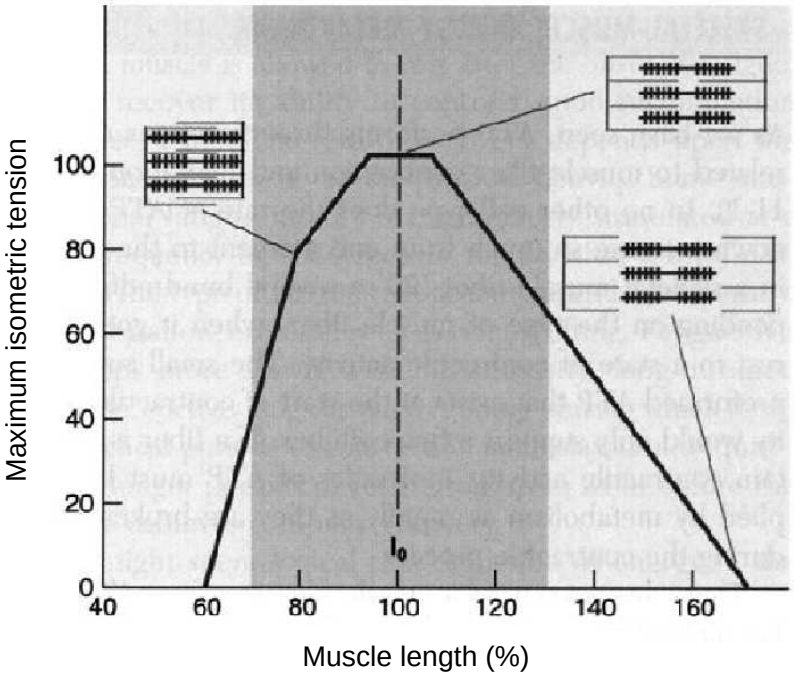

Fig. 6.3. Length tension relationship of the overlapping actin and myosin in cardiomyocytes. Inset shows the degree of overlap between actin and myosin filaments. Tension reaches its maximum at the optimal overlap. Fig. from [293].

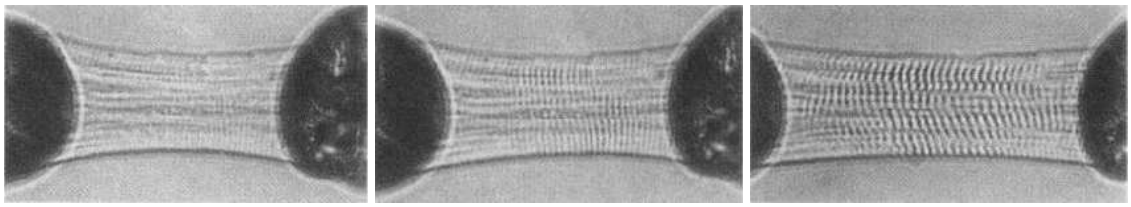

(a) (b) (c)

Fig. 6.4. Photomicrographs show a skinned rat left ventricular myocyte stored in relaxing solution at different sarcomere lengths, ranging from (a) 2.0 μm, (b) 2.2 μm, to c) 3.0 μm. Figs. from [299].

compressed and no effective tension can be generated at a sarcomere length below approximately 1.4 μm.
Myocytes have a special characteristic to prevent sarcomeres from being stretched over the optimal overlap degree. This characteristic is due to strong parallel elastic structures, i.e. nebulin and titin, and prevents in consequence the progressive decrease in contraction and finally the failure of cardiac output [294]. The maximal reachable sarcomere length of a myocyte is approximately 2.3 μm.
The normal function length of a cardiac sarcomere lies between 1.8 and 2.2 μm, the so-called ascending limb of the length tension curve. Since the increase of sarcomere length leads to increasing tension, the increase of diastolic volume can lead to an increasing systolic contraction. That is the reason why the undisturbed relaxation of cardiac myocyte is very important for maintaining a healthy heart [13].

6.4 Isometric Tension Development

Isometric tension development is defined by measuring the tension during fixed length of the cell. Isometric tension measurements are performed by usage of e.g. an inverted microscope [295, 296, 297, 298] usually at room temperature in order to preserve the structural integrity of the tissue during activation. The pH value is 6.7 – 7.1 and a sarcomere length of e.g. 2.2 μm in relaxing solution is set (fig. 6.4). The myocytes are then clamped between an isometric force transducer and a piezoelectric length driver. Two exemplary methods of steady-state stimulation are (fig. 6.5):

Twitch by electrical stimulation: The specimen is stimulated electrically by two tipping microelectrodes. Stimulation frequency of e.g. 0.8 – 1 Hz allows diastolic tension to return to resting levels before the onset of the next contraction and production of stable contractions.

Tetanus by increasing calcium concentration: Preparation is first exposed to low calcium concentration. To determine the relation between Ca^{2+} concentration and tension, a series of calcium solutions with a certain concentration is generated by cyclical injection at fixed intervals. The preparation is then loaded with a Ca^{2+}-regulated bioluminescent indicator by a modified chemical loading procedure. Steady-state tension in tetanized muscles is measured.

Tension and preparation length during experiments are recorded. Sarcomere length is monitored by photomicroscopy. Calcium concentration is monitored by bioluminescent substances. The light emitted by the Ca^{2+}-aequorin interaction is detected by a photomultiplier.
In order to compare tension generation between cells of different sizes, total tension has to be normalized to myocyte cross-sectional area. Active tension is calculated as the difference

Fig. 6.5. Experiments with human myocytes show different durations of tension by twitch and tetanus activation at given $[Ca^{2+}]_e$ of 16 mM (15 Hz frequency, 50 ms pulse duration). In the upper graph, L represents the luminescence signal, which corresponds to $[Ca^{2+}]_i$. In the lower graph, tension is presented in g/mm^2. Absolute tension during tetanus is larger than during twitch activation. Fig. from [300].

between the total tension, developed at any given calcium concentration, and passive tension, measured in relaxing solution.
Experiments show that increase of given extracellular Ca^{2+} concentration leads to the increase of developed tension, both with twitch and tetanus steady-state stimulations [300]. For an overview about measurement results concerning calcium-tension relationship and Hill parameters during isometric tension development, see [301].

6.5 Dynamic Tension Development

Dynamical tension development can be measured during excitation of the cell. The upstroke and relaxation times were measured for the tension development after an electrical excitation of the cell.
Tension development after fast changes of the sarcomere length was measured in experiments (fig. 6.6). The preparations were first bathed in a solution with constant calcium concentration. Then, the preparation were stimulated and the XBs were broken by a fast cell stretch at maximum tension development. The fraction of troponin bound calcium is only influenced a little due to the influence of XB bindings on the calcium affinity of troponin [303]. The re-development of tension is described by the exponential function:

$$T(t) = T_{max}(1 - e^{-k_{tr}t}) + T_0 \tag{6.6}$$

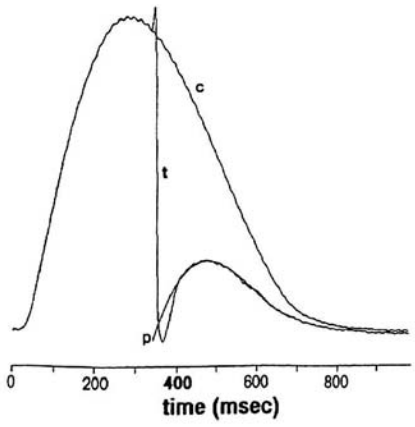

Fig. 6.6. Tension development after fast sarcomere length changes. c is the control curve and t the breakup experiment. XB bindings were broken by a fast length change and the tension declines. The re-development of tension is marked with p. Fig. from [302].

The re-developed tension is given by the coefficient k_{tr}, the maximum tension T_{max}, and the resting tension T_0. The coefficient k_{tr} determines how fast the tension returns to the initial value. The re-developed tension is slowed if the calcium concentration is lower i.e. k_{tr} is smaller for lower maximum tension. A resting tension T_0 is present due to the resulting cross-bridges after the cell stretching. The resting tension is not influencing the coefficient k_{tr}, which was shown by different experiments where similar values were measured [304, 305, 306]. For an overview about measurement results concerning calcium-tension relationship and Hill parameters during dynamic tension development, see [301].

6.6 Cooperativity Mechanisms

Each cross-bridge cycle does not work as a stand-alone functional unit during the contraction. There are interactions, which effect the functionality of each participating protein, e.g. tropomyosin and the troponin complex. Generally, working proteins or proteins in motion cannot function without interfering with the neighboring proteins. This effect can be particularly observed between those proteins, which possess binding sites. Interferences, which cause functional positive feedback between them, are called cooperativity mechanisms.
Three major cooperativity mechanisms between tropomyosin, the troponin complex, and the cross-bridge cycle itself are reported, i.e. cross-bridge–troponin, cross-bridge–cross-bridge, and tropomyosin–tropomyosin feedback [307].

Cross-bridge–Troponin (XB–Tn): The strong binding between actin and myosin leads to an enhanced affinity of the troponin complex to calcium [303, 308, 309, 310, 311]. To date, there is no description explaining the details of the mechanism functionality. Experiments showed that a sudden increase of intracellular calcium can be caused by a rapid prolongation of myocytes [310, 312, 313]. This phenomenon can be explained using the XB–Tn cooperativity mechanism, since the number of cross-bridges is inverse proportional to the prolongation of the myocyte. Thus, the amount of bound calcium is also reduced, and consequently the number of free intracellular calcium increases.

Cross-bridge–Cross-bridge (XB–XB): Occurrence of cross-bridge binding supports the building of cross-bridges in the vicinity [314]. Once a cross-bridge occurs and the pivoting myosin head leaves the opened myosin binding site of actin filament, the tropomyosin still stays shifted. This enhances the possibility for another myosin head to build a cross-bridge with this opened myosin-binding site.

Tropomyosin–Tropomyosin (Tm–Tm): This mechanism describes that neighboring tropomyosin molecules tend to change their molecular state according to the state of the immediate neighboring molecules [315]. The reason for this mechanism is based on the molecular structures of the coil-coiled strings of each neighboring tropomyosin, which overlap in the configuration head to tail (section 2.1.2.2). The Tm–Tm cooperativity mechanism describes the serial and rapid shifting procedures of neighboring tropomyosin molecules along the thin filaments and is also the reason for the coupled activation of the myosin binding sites of an actin filament.

7

Modeling Cardiac Tension Development

The tension development in cardiomyocytes can be reconstructed with the aid of several models published in the last decades (tab. 7.1). The first model was proposed in 1938 by A. V. Hill [316]. His model describes the tension-velocity relationship of tetanized skeletal muscle. The theory of the sliding filament was presented in 1953. A. F. Huxley and N. Niedergerke as well as H. E. Huxley and J. Janson developed this theory with the help of new measurement techniques describing the tension development by the interlocking of two different filaments in striated muscles. This theory was confirmed in the following years by several experiments. A. F. Huxley created a model of skeletal muscle based on the sliding filament theory in 1957 [317]. Up to now, several mathematical tension development models were presented reconstructing the properties of cardiac cells (tab. 7.1).
Tension development is described in the models by different states, which are derived by physiological interactions between troponin, tropomyosin, actin, and myosin. The transition rates between these states are influenced by several parameters, e.g. the intracellular calcium concentration $[Ca^{2+}]_i$ and the extend of stretch of the sarcomeres. $[Ca^{2+}]_i$ acts as an input for the models and is the mediator between electrophysiology and tension development.

7.1 Hill Model

A. V. Hill investigated the relationship between contraction speed and heat production under varying loads. The skeletal muscle of frogs was adjusted at both ends and was tetanized by electrical stimulations. The contraction velocity v was measured after release of the muscle in dependence of the tension P. The dependancy is given by:

$$(v + b)(P + a) = b(P_0 + a)$$

with the maximum isometric tension P_0, and the constants a and b. The mechanical work W is given by the product of P and v:

$$W = Pv = \frac{Pb(P_0 - P)}{(P + a)}$$

7.2 Hunter-McCulloch-ter Keurs Model

The Hunter-McCulloch-ter Keurs model is based on the principle of four mathematical equations for reconstructing cross-bridge kinetics, length dependency of tension development, passive elasticity of the myocardium, and velocity of the processes [323].

Table 7.1. Mathematical models of tension development.

Year	Author	Specimen	Species
1938	Hill [316]	skeletal muscle	frog
1957	Huxley [317]	skeletal muscle	–
1980	Panerai [318]	papillary muscle	mammalian
1991	Peterson, Hunter, Berman [302]	papillary muscle	New Zealand white rabbit
1994	Landesberg, Sideman [319]	skinned cardiomyocyte	–
1994	Landesberg, Sideman [320, 321]	cardiac muscle	–
1997	Hunter, Nash, Sands [322]	cardiac muscle	mammalian
1998	Hunter, McCulloch, ter Keurs [323]	cardiac myocyte	–
1998	Guccione, Motabar-Zadeh, Zahalak [324]	cardiac myocyte	–
1999	Rice, Winslow, Hunter [325]	papillary muscle	New Zealand white rabbit
2000	Rice, Jafri, Winslow [326]	cardiac muscle	ferret
2001	Mlcek, Neumann, Kittnar, Novak [327]	cardiac myocyte	–
2001	Nickerson, Smith, Hunter [328]	cardiac myocyte	–

The first state of the model is described by the availability of cross-bridge binding sites. The availability of myosin binding sites of actin relates to the binding of calcium to TnC and is the number of possible occurrences of cross-bridges. A maximal amount of bound calcium $Ca_{b,max}$ and a maximum generated tension T_0 is defined. The temporal course of the amount of bound calcium Ca_b is described by the differential equation:

$$\frac{\mathrm{d}Ca_b}{\mathrm{d}t} = \rho_0 Ca_i(Ca_{b,max} - Ca_b) - \rho_1(1 - \frac{T}{\gamma T_0})Ca_b$$

with the amount of intracellular calcium Ca_i, ρ_0 and ρ_1 as transition parameters, the tension parameter γ, and the tension T. The second term of the equation represents the dissociation rate depending on the tension T.
The number of free myosin binding sites of actin z is given by:

$$\frac{\mathrm{d}z}{\mathrm{d}t} = \alpha_0((\frac{Ca_b}{Ca_{z,50}})^{n_z}(1 - z) - z)$$

with the transition rate of tropomyosin α_0, and the Hill parameters $Ca_{z,50}$ and n_z. $Ca_{z,50}$ describes the calcium concentration, when half of available myosin binding sites are opened similar to the Hill parameter from eq. 6.4 for tension development. The parameters $Ca_{z,50}$ and n_z depend on the sarcomere length λ. λ is measured in μm at resting length relative to the values of $Ca_{z,50,ref}$ and $n_{z,ref}$:

$$C_{z,50} = 10^{6+(\log_{10} Ca_{z,50,ref})(1+\beta_2(\lambda-1))}, \quad n_z = n_{z,ref}(1 + \beta_1(\lambda - 1))$$

with β_1 and β_2 as stretch dependent constants for n_z and $Ca_{z,50}$, respectively.
The second state concerning the developed tension T_0, which is relative to the value at resting length T_{ref}, is calculated depending on the sarcomere length λ, the number of free myosin binding sites of actin z, and a stretch dependent tension constant β_0:

$$T_0 = T_{ref}(1 + \beta_0(\lambda - 1))z \tag{7.1}$$

The Hunter-McCulloch-ter Keurs model also integrates the passive elasticity of the myocardium and the velocity of the processes. Both variables are represented by:

$$T = T_0 \frac{1 + aQ}{1 - Q}$$

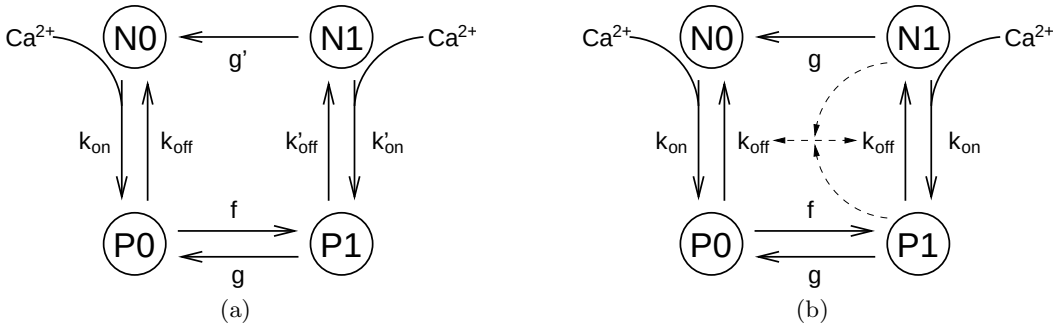

Fig. 7.1. (a) Schematic description of the Peterson-Hunter-Berman model. (b) State diagram of the Landesberg-Sideman model. In both models, N depicts the state where tropomyosin is blocking the myosin binding site of actin ("off"-position). Troponin switches in the "on"-position with the binding of calcium (state P). The number behind the states (0 or 1) expresses the ability of building cross-bridges. The dashed lines in (b) represent the XB-Tn cooperativity mechanism.

with the parameter for the tension velocity relationship a, and the function Q:

$$Q = \sum_{i=1}^{3} A_i \int_{-\infty}^{t} e^{\alpha_i (t-\tau)} \dot{\lambda}(\tau) d\tau \tag{7.2}$$

which calculates the integration of the temporal derivative of sarcomere length $\lambda(t)$. The temporal weighting factor $e^{\alpha_i(t)}$ suppresses older events. Further parameters for the function Q are A_1 as the factor for slow tension reclination, A_2 and A_3 as the factors for fast tension reclination, α_1 as an exponential factor for slow tension reclination, as well as α_2 and α_3 as exponential factors for fast tension reclination.

7.3 Peterson-Hunter-Berman Model

The model of Peterson, Hunter, and Berman is based on the recognition that actin and myosin can interact without calcium bound to troponin [302]. If calcium is bound to troponin, tropomyosin is not connected to the myosin binding site of the actin filament and tropomyosin is in the so-called "on"-position. Cross-bridge (XB) interaction between actin and myosin can exist in this tropomyosin position. Furthermore, if calcium is dissociated from troponin and tropomyosin is in the so-called "off"-position, the XB bonds need not to be detached.
This model consists of four states, describing the position of tropomyosin and the appearance of cross-bridges (fig. 7.1a). State $N0$ is the resting state without XB and with closed myosin

Table 7.2. Coefficients of the Peterson-Berman-Hunter model and of the Landesberg-Sideman model.

Coefficient	Peterson et al.	Landesberg et al.
k_{on}	$39\mu M^{-1}s^{-1}$	$39\mu M^{-1}s^{-1}$
k'_{on}	$40k_{on}$	k_{on}
k_{off}	$19,6s^{-1}$ $(= k'_{off})$	$k_{on}/K_{app}(T_n)$
$K_{app}(T_n)$	—	$0,0174 + 0.173T_n +$ $1,54T_n^2 + 0,282T_n^3$
f	$0,95s^{-1}$	$40s^{-1}$
g	2,04 s^{-1}	$12s^{-1}$
g'	15 s^{-1}	—
T_n	α(P1+N1)/T_{max}	α(P1+N1)/T_{max}
T_{max}	f/(f+g)	f/(f+g)

binding site ("off"-position). If a certain amount of intracellular calcium is prominent, it is bound to troponin and tropomyosin is shifted opening the myosin binding site ("on"-position of tropomyosin). This state corresponds to $P0$. The two states $P1$ and $N1$ are the tension developing states, i.e. strong XB interactions between actin and myosin exist. The states do not depict absolute values but rather represent the configuration portion of actin and myosin. If $N0$, $N1$, $P0$, and $P1$ are the fraction of systems that are in the corresponding state, than all numbers sum up to give the value of one:

$$N0 + N1 + P0 + P1 = 1$$

The transitions between the states are given by a system of first order differential equations:

$$\frac{\mathrm{d}}{\mathrm{d}t}\begin{pmatrix} N0 \\ P0 \\ P1 \\ N1 \end{pmatrix} = \boldsymbol{M}\begin{pmatrix} N0 \\ P0 \\ P1 \\ N1 \end{pmatrix}$$

with the 4×4 matrix $\boldsymbol{M}$ consisting of the transition coefficient between the states $k_{on}([Ca]_i^{2+})$, $k'_{on}([Ca]_i^{2+})$, k_{off}, k'_{off}, g, g', and f:

$$\boldsymbol{M} = \begin{pmatrix} -k_{on}[Ca^{2+}]_i & k_{off} & 0 & g' \\ k_{on}[Ca^{2+}]_i & -k_{off} - f & g & 0 \\ 0 & f & -g - k'_{off} & k'_{on}[Ca^{2+}]_i \\ 0 & 0 & k'_{off} & -k'_{on}[Ca^{2+}]_i - g' \end{pmatrix}$$

with $k_{on}([Ca]_i^{2+})$ and $k'_{on}([Ca]_i^{2+})$ as the shifting probability of tropomyosin in the "on"-position without and with XBs, respectively, k_{off} and k'_{off} as the back-shifting probability without and with XBs, respectively, as well as the transition between week and strong cross-bridges f and vice versa for tropomyosin in "off"-position g' and in "on"-position g. A transition between $N0$ and $N1$ does not exist because no XBs can be achieved if tropomyosin is in the "off"-position. The values of the transition coefficients are summarized in tab. 7.2.
The normalized developed tension T_n results from the overlap function α, the tension developing states $N1$ and $P1$, and the maximum tension T_{max}:

$$T_n = \frac{\alpha(P1 + N1)}{T_{max}} \tag{7.3}$$

The overlap function α (fig. 7.2) depicts the overlapping of actin and myosin (section 6.3) with the sarcomere length SL given by:

$$\alpha = \begin{cases} 1 - 0.7333(2 - SL) & SL \leq 2 \\ 1 & 2 < SL \leq 2.2 \\ 1 - 0.7333(SL - 2.2) & 2.2 < SL \end{cases} \tag{7.4}$$

The correlation of cross-bridges and the binding of calcium to troponin (XB-Tn cooperativity mechanism) is included in this model by setting k'_{on} to the 40-fold value of k_{on}.

7.4 Landesberg-Sideman Model

The first version of the model of Landesberg and Sideman [319] consists of four states (fig. 7.1b) and is comparable in structure to the Peterson-Hunter-Berman model. The used

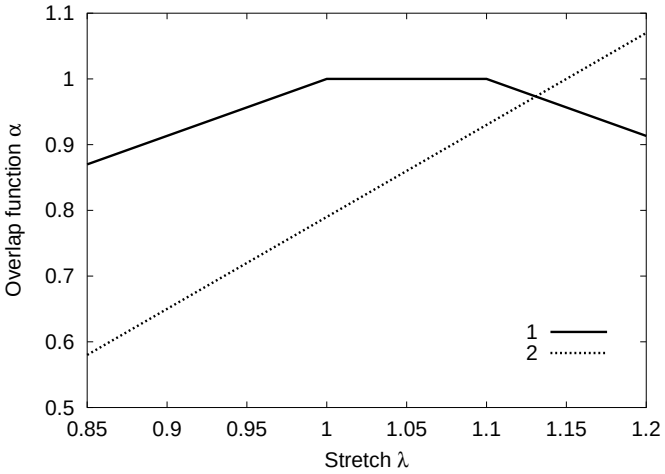

Fig. 7.2. The overlap function α in solid line is used for the Peterson-Hunter-Bermann and the Rice-Winslow-Hunter models. Landesberg-Sideman uses a monotonously raising overlap function (dashed line).

parameters are presented in tab. 7.2. An extension of this model was presented by Landesberg and Sideman including the velocity dependent building of XBs [320, 321].
The extended model of Landesberg and Sideman is based on the cycle of cross-bridges. Several physiologically motivated assumptions were included e.g. that calcium can dissociate from troponin during the interaction of actin and myosin. The model is described by a system of coupled differential equations:

$$\frac{\mathrm{d}}{\mathrm{d}t}\begin{pmatrix} N0 \\ P0 \\ P1 \\ N0 \end{pmatrix} = \boldsymbol{M}\begin{pmatrix} N0 \\ P0 \\ P1 \\ N0 \end{pmatrix}$$

The transition matrix $\boldsymbol{M}$ depends on $[Ca^{2+}]_i$ and the contraction velocity ν:

$$\boldsymbol{M} = \begin{pmatrix} -k_{on}[Ca^{2+}]_i & k_{off} & 0 & g_0 + g_1\nu \\ k_{on}[Ca^{2+}]_i & -f - k_{off} & g_0 + g_1\nu & 0 \\ 0 & f & -g_0 - g_1\nu - k_{off} & k_{on}[Ca^{2+}]_i \\ 0 & 0 & k_{off} & -k_{on}[Ca^{2+}]_i - g_0 - g_1\nu \end{pmatrix}$$

The coefficients k_{on}, k_{off}, f, g_0, and g_1 are the transition parameters. The feedback mechanism of the cross-bridge bindings to the affinity of calcium to troponin, i.e. the XB-Tn cooperativity mechanism, is implemented by including a tension dependent dissociation rate k_{off}. The velocity component ν is given by:

$$\nu = \frac{1}{L_m}\frac{\mathrm{d}L_s}{\mathrm{d}t}$$

with the relative change in the total overlap length L_s and the length of the thick filament L_m.
The resulting tension T of this model is the combination of the tension T_{XB}, which is generated by the cross-bridges, and the tension T_{PE}, which results from the passive elastic properties of the myocardium:

$$T = T_{XB} + T_{PE}$$

The developed tension T_{XB} is given by:

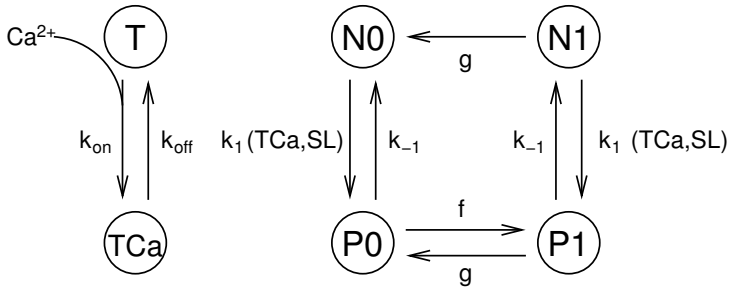

Fig. 7.3. State diagram of the 3^{rd} Rice-Winslow-Hunter model. It shows the separation between the activity of troponin (left) and the activity of tropomyosin (right), which is coupled with the occurrence of cross-bridges. The activities are coupled by the fraction of calcium bound to troponin (TCa).

$$T_{XB} = (\bar{T} - \eta\nu)XBB$$

with the tension developed by each cross-bridge $\bar{T}$, the viscosity of the cross-bridge η, the contraction velocity ν, and the amount of effective cross-bridge bindings XBB, which is proportional to $N1 + P1$.

7.5 Rice-Winslow-Hunter Models

Rice, Winslow, and Hunter developed three further tension development models to evaluate cooperativity mechanisms [325]. The model of Peterson-Hunter-Berman and Landesberg-Sideman were named model 1 and model 2, respectively. The three new models of Rice-Winslow-Hunter were named model 3, 4, and 5. These models include the dependency of tension development by $[Ca^{2+}]_i$ and the sarcomere length SL. Moreover, they include in each model a different number of cooperativity mechanisms. Model 3 considers the binding of calcium to troponin and the subsequent shifting of tropomyosin. Model 4 and 5 extend this feature by adding more cross-bridge binding states per troponin-tropomyosin complex.

7.5.1 Model 3

This model including the Tm–Tm cooperativity mechanism describes the actin myosin interaction with six states divided into two groups: T and TCa as well as N0, N1, P0, P1 (fig. 7.3). T and TCa express the binding of calcium to troponin, the other four states are the same as the ones from the Peterson-Hunter-Berman model. TCa represents the binding between troponin and calcium for the troponin group, whereas the symbol T describes unbound troponin. The influence of XBs on the affinity of calcium for troponin is neglected in this model. The Tm–Tm cooperativity mechanism, which considers the overlapping of tropomyosin strands, is incorporated by changing the dependency rate of troponin to the shifting of tropomyosin. The mathematical equation describing the relation between the states are:

$$T + TCa = 1$$
$$N0 + N1 + P0 + P1 = 1$$

The transition rates from unbound troponin T to bound troponin TCa and vice versa are represented by the coefficient k_{on} and k_{off}, respectively. The transition is described by a first order differential equation, considering $[Ca^{2+}]_i$:

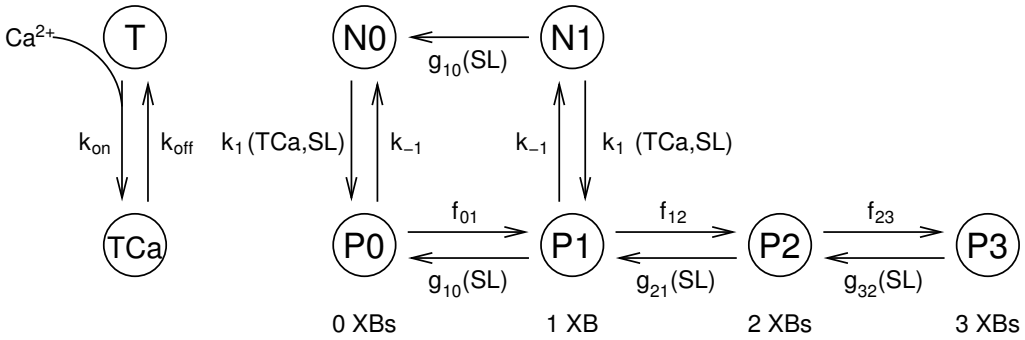

Fig. 7.4. State diagram of the 4^{th} Rice-Winslow-Hunter model with Tm–Tm and XB–XB cooperativity mechanisms. The diagram shows the extension of the former model with two additional states, which represents the number of cross-bridges. Iterative coupling between XBs indicates the support of an existing cross-bridge on the occurrence of further XBs.

$$\frac{\mathrm{d}}{\mathrm{d}t}\begin{pmatrix} T \\ TCa \end{pmatrix} = \begin{pmatrix} -k_{on}([Ca^{2+}]_i) & k_{off} \\ k_{on}([Ca^{2+}]_i) & -k_{off} \end{pmatrix}\begin{pmatrix} T \\ TCa \end{pmatrix}$$

The transition rates between N0 and P0 as well as between N1 and P1 are described with the coefficients k_1 and k_{-1}, respectively, which depend on sarcomere length and TCa as the integration of the Tm–Tm cooperativity mechanism (fig. 7.3). For the transition from P0 to P1 and vice versa, the coefficients f and g, respectively, are used, whereas for the transiton from N1 to N0 solely g is present. The coupling between tropomyosin states can be described by the first order differential equation:

$$\frac{\mathrm{d}}{\mathrm{d}t}\begin{pmatrix} N0 \\ P0 \\ P1 \\ N1 \end{pmatrix} = \boldsymbol{M}\begin{pmatrix} N0 \\ P0 \\ P1 \\ N1 \end{pmatrix}$$

with the 4×4 transition matrix $\boldsymbol{M}$:

$$\boldsymbol{M} = \begin{pmatrix} -k_1 & k_{-1} & 0 & g \\ k_1 & -k_{-1} - f & g & 0 \\ 0 & f & -g - k_{-1} & k_1 \\ 0 & 0 & k_{-1} & -k_1 - g \end{pmatrix}$$

k_1 is a function of the sarcomere length and bound troponin. The parameters are detailed in tab. 7.3. The resulting normalized tension T_n is calculated by eqs. 7.3 and 7.4.

7.5.2 Model 4

This model is an extension to model 3 considering the Tm–Tm and the XB–XB cooperativity mechanism. The XB–XB cooperativity mechanism is integrated into the model by adding two further XB states P2 and P3, which describe the number of possible interacted XBs per functional troponin-tropomyosin complex. The second and the third XB depends iteratively on the first XB with shifted tropomyosin (fig. 7.4).
The changes of the maximum tension during fixed calcium concentration but varying sarcomere lengths is reproducible using model 4 compared to model 3. A sarcomere length dependent unbinding rate of the cross-bridges $g(SL)$ is incorporated to consider these findings.

The slowing of the relaxation due to several XB bindings (1–3) is prevented by an increasing unbinding rate (g_{10}, g_{21}, g_{32}). Another effect of the addition of two further states is the possibility that tropomyosin can be held in the opened state by several cross-bridges. This is implemented in the model by preventing any transitions from $P2$ or $P3$ directly to the N states.
The rising probability of building cross-bridges due to cross-bridges, i.e. the XB-XB cooperativity mechanism, is realized in this model by a rising building rate (f_{01} – f_{23}) in dependance of the amount of already existing and possible XBs.
The first order differential equation for this model is:

$$\frac{\mathrm{d}}{\mathrm{d}t}\begin{pmatrix} N0 \\ P0 \\ P1 \\ N1 \\ P2 \\ P3 \end{pmatrix} = \boldsymbol{M}\begin{pmatrix} N0 \\ P0 \\ P1 \\ N1 \\ P2 \\ P3 \end{pmatrix}$$

with the 6×6 transition matrix $\boldsymbol{M}$, which is dependent on the bound troponin and the sarcomere length:

$$\boldsymbol{M} = \begin{pmatrix} -k_1 & k_{-1} & 0 & g_{10} & 0 & 0 \\ k_1 & -k_{-1} - f_{01} & g_{10} & 0 & 0 & 0 \\ 0 & f_{01} & -g_{10} - k_{-1} - f_{12} & k_1 & g_{12} & 0 \\ 0 & 0 & k_{-1} & -k_1 - g_{01} & 0 & 0 \\ 0 & 0 & f_{12} & 0 & -g_{21} - f_{23} & g_{32} \\ 0 & 0 & 0 & 0 & f_{23} & -g_{32} \end{pmatrix}$$

The factors of the transition matrix are depicted in tab. 7.3. The binding of calcium to troponin is described equivalent to model 3. The developed normalized tension of this model is weighted with the additional cross-bridge states:

$$T_n = \frac{\alpha(P1 + N1 + 2P2 + 3P3)}{T_{max}}$$

with the overlap function α of the Peterson-Hunter-Berman model (eq. 7.4).

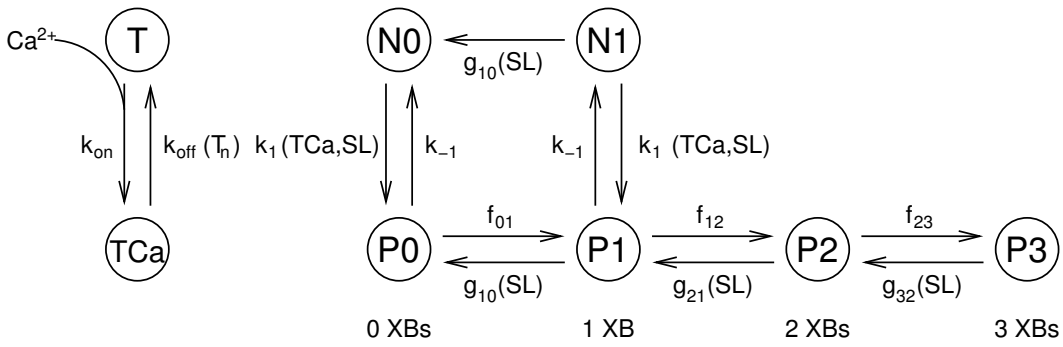

Fig. 7.5. The state diagram of the 5^{th} Rice-Winslow-Hunter model with Tm–Tm, XB–XB, and XB–Tn cooperativity mechanism includes the influence of cross-bridge on the troponin interaction with calcium, as the XB–Tn cooperativity mechanism.

7.5.3 Model 5

The fifth model is a modification of model 4. No changes in the amount of states is found (fig. 7.5). This model including the Tm–Tm and XB–XB cooperativity mechanisms integrates the XB–Tn cooperativity mechanism by including a feedback of the tension generating states $N1$, $P1$, $P2$, and $P3$ to the unbinding rate of calcium from troponin. With this feature the new calcium release coefficient k'_{off} is defined as:

$$k'_{off} = k_{off}(1 - T_n/2)$$

This causes a strong feedback effect of tension on the binding rate between troponin and calcium.
The system of equations describing the model is the same as in model 4 (eqs. 7.5.2 – 7.5.2) using the parameters listed in tab. 7.3. Two slightly different versions of the 5^{th} model are described.

Table 7.3. Transition coefficients of the three Rice-Winslow-Hunter models.

	Rice 3	**Rice 4**	**Rice 5**
k_{on}	40 $\mu M^{-1}s^{-1}$	20 $\mu M^{-1}s^{-1}$	20 $\mu M^{-1}s^{-1}$
k_{off}	20 s^{-1}	40 s^{-1}	40 s^{-1} 1. vers.: k_{off}'=k_{off}(1–T/2) 2. vers.: k_{off}'=k_{off}(1–3T/4)
k_1	$k_{-1}(TCa/K_{1/2})^N$	$k_{-1}(TCa/K_{1/2})^N$	$k_{-1}(TCa/K_{1/2})^N$
k_{-1}	45 s^{-1}	45 s^{-1}	45 s^{-1}
f	10 s^{-1}	10 s^{-1} 1 XB: f_{01}=2f 2 XB: f_{01}=2f, f_{12}=7f 3 XB: f_{01}=3f, f_{12}=10f, f_{23}=7f	10 s^{-1} f_{01}=3f, f_{12}=10f, f_{23}=7f
g	20 s^{-1}	g_{01}(SL)=g(SL) g_{12}(SL)=2g(SL) g_{23}(SL)=2g(SL)	g_{01}(SL)=g(SL) g_{12}(SL)=3g(SL) g_{23}(SL)=3g(SL)
g(SL)		$g^*[1+(1–SL_{norm})^{1,6}]$ 1 XB: g*=25 s^{-1} 2 XB: g*=27,5 s^{-1} 3 XB: g*=30 s^{-1}	$g^*[1+(1–SL_{norm})^{1,6}]$ 1 XB: g*=25 s^{-1} 2 XB: g*=27,5 s^{-1} 3 XB: g*=30 s^{-1}
F F_{max}	α(P1+N1)/F_{max} f/(f+g)	α(P1+N1+2P2+3P3)/F_{max} $P1_{max}$+2$P2_{max}$+3$P3_{max}$ $P1_{max}$=$f_{01}g_{2,1}$'$g_{3,2}$'/$\sum$ $P2_{max}$=$f_{01}f_{12}$'$g_{3,2}$'/$\sum$ $P3_{max}$=$f_{01}f_{12}$'f_{23}'/$\sum$	α(P1+N1+2P2+3P3)/F_{max} $P1_{max}$+2$P2_{max}$+3$P3_{max}$ $P1_{max}$=$f_{01}g_{2,1}$'$g_{3,2}$'/$\sum$ $P2_{max}$=$f_{01}f_{12}$'$g_{3,2}$'/$\sum$ $P2_{max}$=$f_{01}f_{12}$'$g_{3,2}$'/$\sum$
$\sum$		$g^*_{1,0}g^*_{2,1}g^*_{3,2}$+$f_{01}g^*_{2,1}g^*_{3,2}$+ $f_{01}f_{12}g^*_{3,2}$+ $f_{01}f_{12}f_{23}$	$g^*_{1,0}g^*_{2,1}g^*_{3,2}$+$f_{01}g^*_{2,1}g^*_{3,2}$+ $f_{01}f_{12}g^*_{3,2}$+$f_{01}f_{12}f_{23}$
$g^*_{i,j}$		$g_{i,j}g^*$	$g_{i,j}g^*$
$K_{1/2}$	(1+K_{Ca}/(1,5 μM– SL_{norm} 1,0 μM))$^{-1}$	(1+K_{Ca}/(1,5 μM– SL_{norm} 1,0 μM))$^{-1}$	(1+K_{Ca}/(1,8 μM– SL_{norm} 1,0 μM))$^{-1}$
N	7+3 SL_{norm}	5+3 SL_{norm}	1. vers.: 3,4+1,4 SL_{norm} 2. vers.: : 2,6+SL_{norm}
SL_{norm}	(SL–1,7 μM) /(23 μM–1,7 μM)	(SL–1,7 μM) /(23 μM–1,7 μM)	(SL–1,7 μM) /(23 μM–1,7 μM)
K_{Ca}	k_{off}/k_{on}=0,5 μM	k_{off}/k_{on}=2 μM	k_{off}/k_{on}=2 μM

8

Mathematical and Physical Basics

Modeling of the electromechanical behavior of the human heart requires knowledge of several mathematical and physical basics as well as numerical methods. They are detailed in this chapter as far as they are used to model the anatomical, electrophysiological, and tension development properties of the heart, or since they are necessary for understanding the results achieved using the simulations.
Most of the biophysical models describing the electrophysiological behavior as well as the tension development are based on so-called Markov models, which describe the process of transition between discrete states of a system. These processes are time dependent and thus necessitate the numerical solution of ordinary differential equations describing the properties of the cells. Coupling of several cells into a net describing the tissue as an electrically coupled system requires knowledge of the theory of electrical fields and the electrical properties of the tissue. The bidomain model, which is used in this work to describe the electrical coupling of cells, is based on the generalized Poisson's equation for stationary electrical fields. This kind of approach delivers partial differential equations for the excitation conduction. The partial differential equations describing the electrical activity of the cells in combination with the conduction of excitation are discretized with the finite difference or the finite element method and a system of linear algebraic equations is achieved. This linear equation system is solved directly or iteratively. The mathematics behind this modeling is explained in the first part of this chapter.
Recently published measurement data has to be considered in order to generate new or to adapt available electrophysiological and tension development models. The finding of the correct parameters of the model is achieved by comparing the simulated behavior of e.g. an ionic channel to the measured equivalent. In order to optimize the parameters of the model, minimization techniques are utilized as explained in this chapter.
The last section of this chapter deals with the matrix diagonalization method. It is used in this work for determining the first principal axis of anatomical structures whose fibers are arranged in bundles. These structures, e.g. fast conducting pathways in the atrium, have strong anisotropic features. The matrix diagonalization method is used to define the local longitudinal direction of the fibers in a region of interest.

8.1 Markov Chain Models

Continuous-time Markov models are known from statistical signal processing and are used to describe a system when a signal in a multi-state process is fluctuating randomly between a few discrete levels [329, 330]. As an example, single channels of the cell membrane (section 5.1.2)

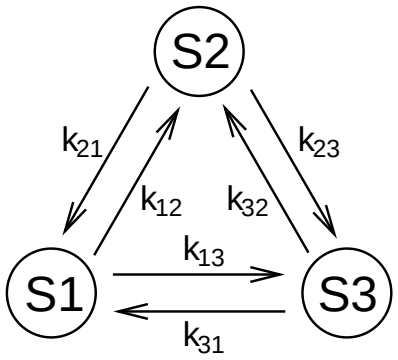

Fig. 8.1. Three-state Markov model. s_i are the states and k_{ij} are the transition rates between the states.

and the interaction of actin and myosin in the myofilament of the cells (chapter 7) have randomly fluctuating properties. The Markov model describes the signal $I(t)$ depending on the so-called internal hidden state. The value I_i of the signal is associated for each possible discrete state s_i $(i = 1, \ldots, n)$. The probability $p(s_i, t)$ for the system to be in state s_i at time t is given by the ordinary differential equation:

$$\frac{\mathrm{d}p(s_i,t)}{\mathrm{d}t} = \sum_{j=1}^{n} k_{ji} p(s_j,t) - p(s_i,t) \sum_{j=1}^{n} k_{ij} \tag{8.1}$$

with the transition rate k_{ij} from state s_i to state s_j and the rate k_{ji} for the opposite transition. The transition rates are probabilities of transitions per unit time. The first term of eq. 8.1 represents an evolution towards state s_i, the second one away from state s_i. If several equal states are present in the system, the ensemble-averaged value $I_{ea}(t)$ of the signal $I(t)$ is:

$$I_{ea}(t) = \sum_{i=1}^{n} p(s_i,t) I_i$$

In the case of channel gating for example, I_i can be either 1 if the channel is open or 0 if it is closed. $I_{ea}(t)$ can be compared to the corresponding measured data and the state signal I_i, the transition rates k_{ji}, and the state probabilities $p(s_i, t)$ have to be adapted to fit both measured and reconstructed signal. The parameter estimation can be performed by Bayesian estimation from a set of measured data [331] or by using the minimization methods described in section 8.6.
The number of states n to describe a randomly fluctuating process has to be chosen to be as small as possible, since the number of possible transitions increases as $2\sum_{i=1}^{n-1} i$. An example for a three-state Markov chain model with six possible transitions is given in fig. 8.1.

8.2 Ordinary Differential Equations

An equation of the form $y^{(n)} = f(x, y, y', ..., y^{(n-1)})$ is called ordinary differential equation of the order n. It can be reorganized into a system of n coupled differential equations of 1^{st} order [332]. As an example, the differential equation of 2^{nd} order:

$$\frac{\mathrm{d}^2 y}{\mathrm{d}x} + q(x)\frac{\mathrm{d}y}{\mathrm{d}x} = r(x)$$

can be transformed in two differential equations of 1^{st} order:

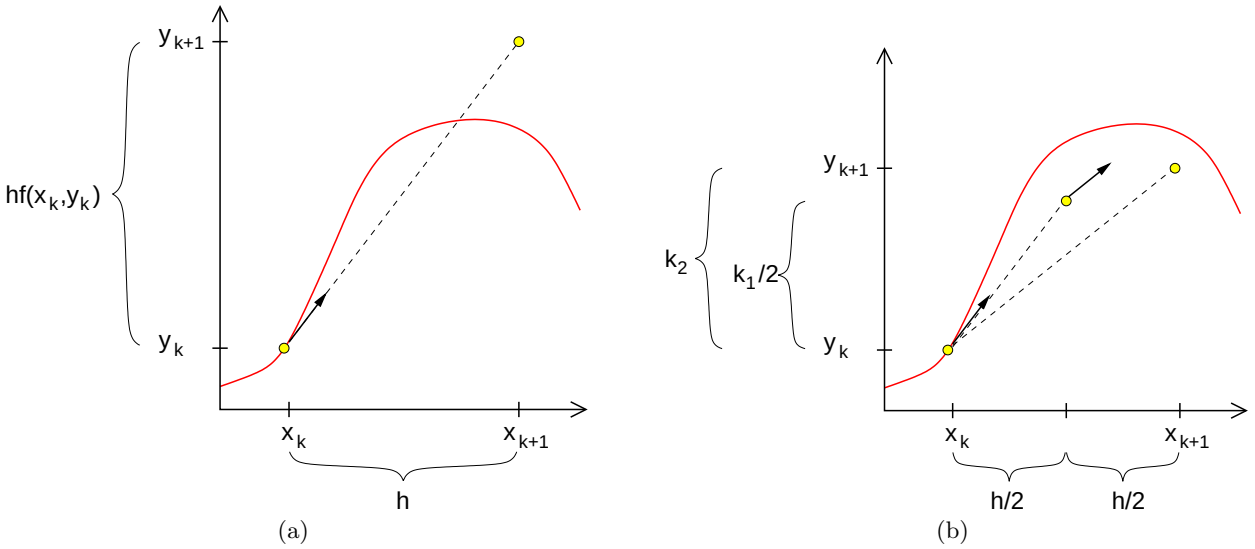

Fig. 8.2. Euler and 2^{nd} order Runge-Kutta method. (a) Euler method. The first derivative at the initial value and the initial value itself is used to approximate the point at the end of the interval. (b) 2^{nd} order Runge-Kutta method. The derivatives and the values at the beginning of the interval and in the middle are considered.

$$\frac{\mathrm{d}y}{\mathrm{d}x} = z(x)$$
$$\frac{\mathrm{d}z}{\mathrm{d}x} = r(x) - q(x)z(x)$$

A system of coupled differential equations often has no analytical solution. The system of 1^{st} order equations can be solved numerically if the initial values

$$y(x_0) = b_0, y'(x_0) = b_1, ..., y^{(n-1)}(x_0) = b_{n-1}$$

are known. Such numerical methods are e.g. the Euler and the Runge-Kutta method. For these methods, the continuous functions have to be discretized. The interval $[x_0, x]$ of the continuous function is subdivided into m discrete points with the constant step-size h

$$h = \frac{x - x_0}{m}$$

The approximations of the function values y_i at the discrete points $x_i = x_0 + ih$ are calculated with aid of the previous values $y_0, ..., y_{i-1}$.

8.2.1 Euler Method

Based on the differential equation

$$\frac{\mathrm{d}y}{\mathrm{d}x} = f(x, y)$$

its differential quotient is replaced using the Euler method by the differences quotient (fig. 8.2a) [333]:

$$\frac{\mathrm{d}y}{\mathrm{d}x} = \frac{y(x+h) - y(x)}{h}$$

Thus, the continuous function is approximated segment-wise by straight lines. The iteration function of the Euler method is defined by:

$$y_{i+1} = y_i + hf(x_i, y(x_i))$$

Compared to a Taylor series expansion, the Euler method neglects derivatives of the order greater than one. The approximation thus has a 1^{st} order error term $O(h^2)$. The Euler method is only useful if the function is close to a straight line in the interval h. This can be achieved e.g. by reducing the step-size h. The integration of the function using the Euler method has a non-symmetric solution because of only considering information about the derivative at the beginning of the interval.

8.2.2 Runge-Kutta Methods

The Runge-Kutta methods are approximations of higher order compared to the Euler method and have a symmetric solution [333]. Not only the derivatives at the beginning of the interval are considered for the Runge-Kutta methods, but also further approximated derivatives of the function f. Commonly the Runge-Kutta methods of 2^{nd} and 4^{th} order are used. Compared to the Euler method, the Runge-Kutta methods deliver more precise results but require more mathematical operations.

2^{nd} order Runge-Kutta method: The interval is separated in two sub-intervals (fig. 8.2b). The derivative at the beginning of both sub-intervals is considered for the calculation of the mean approximated slope of the function f:

$$\begin{aligned} k_1 &= hf(x_k, y_k) \\ k_2 &= hf(x_k + \frac{h}{2}, y_k + \frac{k_1}{2}) \\ y_{k+1} &= y_k + k_2 + O(h^3) \end{aligned}$$

The error term has now the order of two.

4^{th} order Runge-Kutta method: The 4^{th} order Runge-Kutta method demonstrated in fig. 8.3 includes four derivatives at several equidistant points inside the interval. The mean approximated slope of the function f is estimated by the weighted arithmetic mean of the four derivatives:

$$\begin{aligned} k_1 &= hf(x_k, y_k) \\ k_2 &= hf(x_k + \frac{h}{2}, y_k + \frac{k_1}{2}) \\ k_3 &= hf(x_k + \frac{h}{2}, y_k + \frac{k_2}{2}) \\ k_4 &= hf(x_k + h, y_k + k_3) \\ y_{k+1} &= y_k + \frac{1}{6}(k_1 + 2k_2 + 2k_3 + k_4) + O(h^5) \end{aligned}$$

The error term is reduced to the order of 4.

8.2.3 Rush-Larsen Method

In special cases, the ordinary differential equation has the form:

$$\frac{\mathrm{d}y}{\mathrm{d}t} = \frac{y_\infty(u) - y}{\tau_y(u)}$$

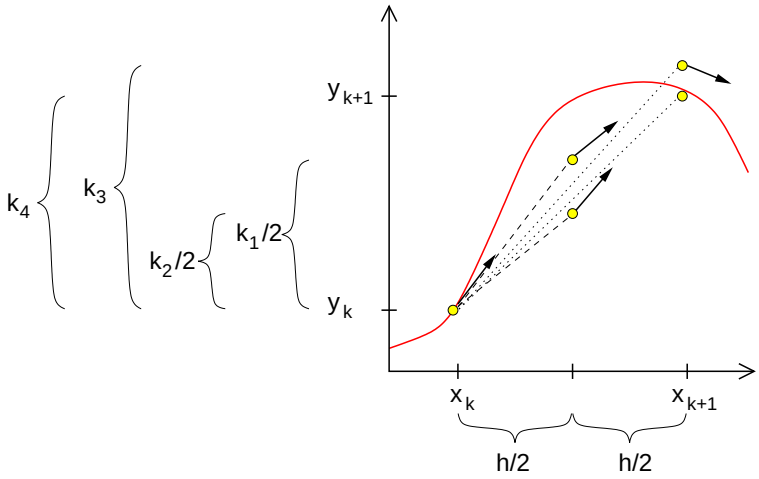

Fig. 8.3. 4^{th} order Runge-Kutta method. Four derivatives and function values are considered.

with the variable y being a function of u, the steady state value y_∞, and the relaxation time constant τ_y. An analytical solution of this differential equation is obtained if the dependence of the variable y on u can be neglected in the time interval $[t, t + \Delta t]$:

$$y(t + \Delta t) = y_\infty + (y(t) - y_\infty) \exp\left[-\frac{\Delta t}{\tau_y}\right]$$

As the gating variables described in section 5.1.1 satisfy the above mentioned form, the calculation of the differential quotient in the $(k+1)$-th step is simplified by the so-called Rush-Larsen scheme [334]:

$$\begin{aligned} y^{(k+1)} &= y_\infty(u^{(k)}) + (y^{(k)} - y_\infty(u^{(k)})) \exp\left[-\frac{\Delta t}{\tau_y(u^{(k)})}\right] \\ &= a_y(u^{(k)}, \Delta t) y^{(k)} + b_y(u^{(k)}, \Delta t) \end{aligned}$$

with the functions

$$a_y(u, \Delta t) = \exp\left[-\frac{\Delta t}{\tau_y(u)}\right] \quad \text{and} \quad b_y(u, \Delta t) = y_\infty(u) \left(1 - \exp\left[-\frac{\Delta t}{\tau_y(u)}\right]\right)$$

The Rush-Larsen method has the advantage that it is more accurate than the Euler method since the function depends only on the variation of u and not on the derivative of y. Furthermore, this method is more efficient as the time increment Δt is often constant and thus lookup tables for a_y and b_y can be created to describe the exponential dependency.

8.3 Theory of Electrical Fields

Modeling of the excitation conduction in the heart and the distribution of electrical potentials in the body is based on solving Poisson's equation. Understanding the mechanisms and the origin of Poisson's equation necessitates the knowledge of electrical field theory. This theory is given by Maxwell's equations describing the electromagnetism in media. The properties of the media can be nonlinear and anisotropic and are mathematically described by tensors. A good understanding of the properties of biological tissue is necessary for the modeling of electrical fields in these media.

The numerical solution of Poisson's equation is based on discretization with the finite element method or the finite difference method (section 8.4). This discretization leads to a linear equation system (section 8.5), which is solved with direct or iterative methods.

8.3.1 Maxwell's Equations

Maxwell's equations are given by:

$$\begin{aligned} \nabla \times \boldsymbol{E} &= -\frac{\partial \boldsymbol{B}}{\partial t} \\ \nabla \times \boldsymbol{H} &= \boldsymbol{J} + \frac{\partial \boldsymbol{D}}{\partial t} \\ \nabla \cdot \boldsymbol{D} &= \rho \\ \nabla \cdot \boldsymbol{B} &= 0 \end{aligned}$$

They describe the interaction between the electrical field $\boldsymbol{E}$, the magnetic flux density $\boldsymbol{B}$, the magnetic field $\boldsymbol{H}$, the electrical free current density $\boldsymbol{J}$, the electrical flux density $\boldsymbol{D}$, and the electrical free charge density ρ. The corresponding material equations are:

$$\boldsymbol{B} = \mu_0(\boldsymbol{H} + \boldsymbol{M}), \qquad \boldsymbol{D} = \epsilon_0 \boldsymbol{E} + \boldsymbol{P}, \qquad \text{and} \qquad \boldsymbol{J} = \sigma \boldsymbol{E} + \boldsymbol{J}_s$$

with the magnetization $\boldsymbol{M}$, the electric polarization $\boldsymbol{P}$, the permeability of vacuum μ_0, the permittivity in vacuum ϵ_0, the electrical conductivity σ, and the electric current density resulting from local sources $\boldsymbol{J}_s$. The material equations describe the interaction of the field and the matter. Maxwell's equations reflect the physical laws.
If the field problem is stationary, Maxwell's equations can be simplified neglecting the temporal derivatives:

$$\nabla \times \boldsymbol{E} = 0, \qquad \nabla \times \boldsymbol{H} = \boldsymbol{J}, \qquad \nabla \cdot \boldsymbol{D} = \rho \quad \text{and} \quad \nabla \cdot \boldsymbol{B} = 0$$

8.3.2 Poisson's Equation for Stationary Electrical Fields

The flow of electrical currents in an electrically conducting medium can be described with Poisson's equation for stationary electrical fields:

$$\nabla \cdot (\sigma \nabla \phi) + f = 0 \tag{8.2}$$

with the source current density f, the electrical conductivity σ, and the scalar electric potential function ϕ. This equation is derived by considering the divergence of the second Maxwell's equation with stationary properties:

$$\nabla \boldsymbol{J} = \nabla \cdot (\nabla \times \boldsymbol{H}) = 0$$

since the divergence of the curl operator is zero. The overall current density $\boldsymbol{J} = \boldsymbol{J}_s + \boldsymbol{J}_o$ is the sum of the electric current density resulting from local sources $\boldsymbol{J}_s$ and the ohmic current density $\boldsymbol{J}_o$. The relation between the electrical field $\boldsymbol{E}$ and the potential function ϕ is given by:

$$\boldsymbol{E} = -\nabla \phi$$

This and $\boldsymbol{J} = \sigma \boldsymbol{E}$ are considered to construct Poisson's equation:

$$\nabla \boldsymbol{J}_s = \nabla \sigma \boldsymbol{E} = -\nabla \cdot (\sigma \nabla \phi) = f$$

The conductivity tensor σ in Poisson's equation is describing the electrical properties of the underlying material. In biological tissue like the heart the conductivity is anisotropic and not homogeneously distributed over the space. This has to be considered when solving Poisson's equation. The construction of the conductivity tensor for local transversal isotropic properties in the global scope is already explained in section 5.6.3.1.
The following sections describe how to handle the partial differential equations given by Poisson's equation numerically to achieve linear equation systems and how these linear equation systems are solved.

8.4 Partial Differential Equation

A partial differential equation (PDE) describes a function f of a set of n independent variables $x_1, x_2, \ldots, x_n$. The order n of partial differential equations is determined by the order of the derivatives of the function. In a two-dimensional space for example, the second order linear PDE describing the function $f = f(x_1, x_2)$ is [335]:

$$\begin{aligned} G(x_1, x_2) = A(x_1, x_2)\frac{\partial^2 f}{\partial x_1^2} + 2\,B(x_1, x_2)\frac{\partial^2 f}{\partial x_1 \partial x_2} + C(x_1, x_2)\frac{\partial^2 f}{\partial x_2^2} \\ + D(x_1, x_2)\frac{\partial f}{\partial x_1} + E(x_1, x_2)\frac{\partial f}{\partial x_2} + F(x_1, x_2) \end{aligned}$$

with the functions A, B, C, D, E, F, and G. Partial differential equations can be classified into three groups under the assumption that $A^2 + B^2 + C^2 \neq 0$:

- Elliptical PDE, if $AC - B^2 > 0$
- Hyperbolical PDE, if $AC - B^2 < 0$
- Parabolical PDE, if $AC - B^2 = 0$

In the electromagnetic field theory, the independent variables of the elliptical PDEs often are spatial coordinates and the unknown function is assumed to be in steady state. For the parabolical PDEs, one variable is time and the others are spatial coordinates. In this case, the function is describing a non-stationary process.
Poisson's equation (eq. 8.2) for example is an elliptical PDE. The elliptical PDE is described in the simplest case with $\boldsymbol{x}$ as an n-dimensional vector by:

$$\nabla f(\boldsymbol{x}) = G(\boldsymbol{x})$$

The second part of the bidomain equation (eq. 5.20) is a parabolic PDE, which can be described by a differential equation of the simplest form:

$$\frac{\partial f(\boldsymbol{x})}{\partial t} = D \nabla f(\boldsymbol{x})$$

Due to the similarity to diffusion processes D is called the diffusion constant. As the parabolic PDE is describing a non-stationary process, the solution depends on initial values.
Furthermore, all partial differential equations need boundary conditions to generate unique solutions [335, 336]. Three different boundary conditions are applicable: Cauchy, Dirichlet, and Neumann conditions.

The Cauchy condition is the general formulation of boundary conditions:

$$\frac{\partial u}{\partial \boldsymbol{n}}(\boldsymbol{x}) + \alpha(\boldsymbol{x})u(\boldsymbol{x}) = \beta(\boldsymbol{x})$$

with the normal direction $\boldsymbol{n}$ and the functions α and β defined at a boundary segment. The Cauchy condition includes the Dirichlet and Neumann conditions as special cases.
The Dirichlet condition defines the values at parts of the boundary with the function ϕ:

$$f(\boldsymbol{x}) = \phi(\boldsymbol{x})$$

The Neumann condition specifies the values of gradients in normal direction $\boldsymbol{n}$ of a boundary segment with the function γ:

$$\frac{\partial f}{\partial \boldsymbol{n}}(\boldsymbol{x}) = \gamma(x)$$

Several technique are available for solving partial differential equations. Analytical methods are commonly not used. Instead, a diversity of numerical approaches exists. The most established of these are the:

- finite element method
- finite differences method
- finite integration method
- boundary element method

As the methods used in this work for the implementation of the bidomain model are the finite element method and the finite differences method, both approaches are described briefly in the following.

8.4.1 Discretization Methods

Partial differential equations can be solved with the finite element method (FEM) and the finite difference method (FDM). Therefore, the space is represented by structured or unstructured meshes. The node points representing these meshes are regularly distributed in the FDM consisting in this work of a rectangular and isotropic grid having the node points at the vertices. In FEM, the problem domain is subdivided into so-called "finite elements". Some typical finite elements are based on linear or quadratic descriptions e.g. lines in 1D, triangles and quads in 2D, and tetrahedrons, hexahedrons, and prisms in 3D. The finite elements can have different size and the resulting mesh can be unstructured.
The idea of FEM and FDM is to discretize the partial differential equations of the problem to get to a linear equation system, which is then solved numerically. The main difference between FEM and FDM is the way of achieving the discretization. The grid regularity in FDM simplifies the discretization of the partial differential equations. In FEM, the solution function is determined in every element by function values at the element nodes and is computed by interpolation in the rest of the space. Typically, linear or quadratic interpolation is used. For both FEM and FDM, the discretization delivers a system of equation for each element. The global equation system is then generated with the equations from the single elements. After the incorporation of the boundary conditions, the global system of linear equations is solved directly or iteratively (section 8.5).
The finite element method and the finite difference method are detailed in e.g. [336, 337, 338, 339]. In addition, both methods are explained for the special case of solving the bidomain equation on cubic volume elements in [340].

8.5 Linear Equation Systems

A system of linear equations is given in matrix formulation by:

$$\boldsymbol{A}x + b = 0 \tag{8.3}$$

with the matrix $\boldsymbol{A} = [a_{ij}]$ and the vectors $x = [x_j]$ and $b = [b_i]$. a_{ij} and b_i are the coefficients of the system and x_j the unknowns. The number of unknowns is N depicting the columns of $\boldsymbol{A}$. The number of equations equivalent to the rank of $\boldsymbol{A}$ is M. This can be written in the component notation:

$$\begin{aligned} a_{11}x_1 + a_{12}x_2 + \cdots + a_{1N}x_N + b_1 &= 0 \\ a_{21}x_1 + a_{22}x_2 + \cdots + a_{2N}x_N + b_2 &= 0 \\ &\vdots \\ a_{M1}x_1 + a_{M2}x_2 + \cdots + a_{MN}x_N + b_M &= 0 \end{aligned}$$

The matrix $\boldsymbol{A}$ is symmetric and positive-definite if:

$$\boldsymbol{A} = \boldsymbol{A}^T, \qquad \text{and} \qquad \boldsymbol{x}^T\boldsymbol{A}\boldsymbol{x} > 0 \quad \forall \boldsymbol{x} \neq 0$$

These linear equation systems are solved using direct and iterative methods. Direct methods uses the successive elimination of unknowns, iterative methods refine iteratively approximated solutions.

8.5.1 Direct Solution Methods

A variety of direct solution method for solving a linear equation system are known e.g. the Gaussian elimination, the Gauß method, and the Cholesky method [336]. Most of these approaches are based on factorization of the symmetric and positive-definite matrix $\boldsymbol{A}$. Exemplary, the Cholesky method is described in this section.

8.5.1.1 Cholesky Method

The matrix $\boldsymbol{A}$ is factorized into the lower triangular matrix $\boldsymbol{L}$ and its transpose $\boldsymbol{L}^T$:

$$\boldsymbol{A} = \boldsymbol{L}\boldsymbol{L}^T$$

The linear equation system $\boldsymbol{A}x+b = 0$ is transformed into $\boldsymbol{L}\boldsymbol{L}^Tx+b = 0$ and can be separated into two steps considering the auxiliary vector y:

$$-\boldsymbol{L}y + b = 0, \quad \text{and} \quad \boldsymbol{L}^Tx + y = 0$$

$\boldsymbol{L}$ is determined by a row-wise calculation. The diagonal elements l_{ii} and the non-diagonal elements l_{ij} are given by:

$$l_{ii} = \left(a_{ii} - \sum_{k=1}^{i-1} l_{ik}^2\right)^{\frac{1}{2}}, \quad \text{and} \quad l_{ij} = \frac{1}{l_{jj}}\left(a_{ij} - \sum_{k=1}^{j-1} l_{ik}l_{jk}\right)$$

The band diagonal properties of the matrix $\boldsymbol{A}$ is preserved using the Cholesky method i.e. the matrix $\boldsymbol{L}$ has the same bandwidth and also the same profile as the matrix $\boldsymbol{A}$.

8.5.2 Iterative Solution Methods

Iterative methods are based on the successive refinement of the approximated solution $x^{(k)}$. The start vector $x^{(0)}$ can be an arbitrary vector. The error vector $e^{(k)}$ of an approximated solution is given by:

$$e^{(k)} = x - x^{(k)}$$

with the exact solution x. An iterative method reduces this error in each iteration step. The iterative method is stopped if the maximum number of iterations is achieved or a stopping criterion is satisfied. The norm of the residuum of an approximated solution $r^{(k)}$ can be one stopping criterion and is defined by:

$$r^{(k)} = \boldsymbol{A}x^{(k)} + b \tag{8.4}$$

Common iterative methods for solving systems of linear equations are [336]:

- Method of steepest descent
- Conjugate gradient method
- Jacobi method
- Gauß-Seidel method

The mathematical descriptions used in this work are the Gauß-Seidel method and the conjugate gradient method. These two approaches are detailed below.

8.5.2.1 Gauß-Seidel Method

The Gauß-Seidel method is performed by decomposition of the matrix $\boldsymbol{A}$ into the sum of the lower triangular matrix $\boldsymbol{L}$, the diagonal matrix $\boldsymbol{D}$, and the upper triangular matrix $\boldsymbol{U}$. The Gauß-Seidel method considers already calculated coefficients in the new solution. This is e.g. one difference between the Jacobi method and the Gauß-Seidel method. The k-th approximated solution $x^{(k)}$ is determined in matrix and component notation by:

$$(L + D)x^{(k)} = -Ux^{(k-1)} + b, \qquad \text{and} \qquad x_i^{(k)} = \frac{-1}{a_{ii}} \left(b_i + \sum_{j=0}^{i-1} a_{ij} x_j^{(k)} + \sum_{j=i+1}^{n-1} a_{ij} x_j^{(k-1)} \right)$$

8.5.2.2 Conjugate Gradient Method

The conjugate gradient method uses the minimization of the quadratic function F:

$$F(x) = \frac{1}{2} x^T \boldsymbol{A} x + b^T x$$

to determine a solution iteratively. The k-th residuum $\mathrm{r}^{(k)}$ of the quadratic function F is determined by the approximated solution $x^{(k)}$:

$$r^{(k)} = \nabla F(x^{(k)}) = \boldsymbol{A}x^{(k)} + b$$

The minimization in the direction of the correction $p^{(k)}$ delivers a new approximate solution $x^{(k+1)}$:

$$x^{(k+1)} = x^{(k)} + \alpha^{(k+1)} p^{(k)}$$

with the scalar factor $\alpha^{(k)}$:

$$\alpha^{(k)} = \frac{r^{(k-1)T} r^{(k-1)}}{p^{(k-1)T} \boldsymbol{A} p^{(k-1)}}$$

The residuum $r^{(k)}$ is given by:

$$r^{(k)} = r^{(k-1)} + \alpha^{(k)} \boldsymbol{A} p^{(k)}$$

and the correction $p^{(k)}$ is:

$$p^{(k)} = -r^{(k-1)} + \beta^{(k-1)} p^{(k-1)}$$

The scalar factor $\beta^{(k)}$ is determined by:

$$\beta^{(k)} = \frac{r^{(k)T} \boldsymbol{A} p^{(k)}}{p^{(k)T} \boldsymbol{A} p^{(k)}}$$

The method creates a sequence of directions, which are pairwise conjugated as well as residuals, which are orthogonal. Thus, the conjugate gradient method reaches an end theoretically after N steps.

8.6 Minimization Techniques

A minimization problem is to find parameters of a function, which cause the function to deliver a minimal value. It can be solved basically in several ways, e.g. with analytical methods. If the problem cannot be solved analytically, numerical methods offer an alternative. Minimization is used in the scope of this work for the adaption of model parameters to measured data. Steady state current-voltage relationships or relaxation time constants of the ionic channel characteristics are mainly given. Also the rate constants of the model describing the tension development have to be adapted to measured data.
The n variables $x_1, x_2, \ldots x_n$ given for a minimization procedure can be represented as a parameter vector $\boldsymbol{x}$:

$$\boldsymbol{x} = [x_1 \; x_2 \; \ldots \; x_n]^T$$

The minimization is performed on a function $f(\boldsymbol{x})$ that is defined by:

$$f(\boldsymbol{x}) = f(x_1, x_2, \ldots x_n)$$

A variety of numerical minimization algorithms exists for multi-dimensional spaces. Methods using only evaluations of the function can be distinguished from methods, which necessitate the calculation of derivatives of the function. Non-derivative methods are e.g. the downhill simplex method, Powell's method, and the simulated annealing method. Approaches necessitating derivatives of the function are e.g. the steepest descent method and the conjugate gradient method. Furthermore, nonlinear minimization techniques exist e.g the Levenberg-Marquardt method [333].

8.6.1 Non-Derivative Methods

These methods require only the function values and not the derivatives of the function. The standard minimization procedures known from the one-dimensional (1D) case [332] can be extended to the multi-dimensional space. As an example for a two dimensional (2D) case, a contour map is shown in fig. 8.4 that defines a long, narrow valley. When using sequentially

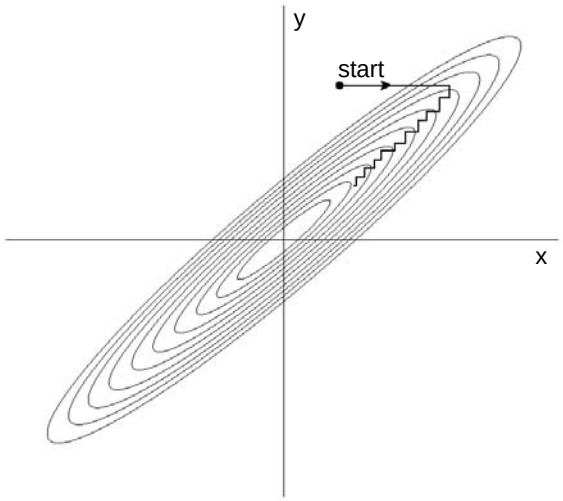

Fig. 8.4. Successive minimizations along coordinate directions in a simple non-derivative minimization method. Unless the function is optimally oriented, this method is inefficient. Fig. adapted from [333].

the 1D methods in 2D, the method will step along the basis vectors at each stage in a series of many tiny steps. More generally, in N dimensions, if the function's second derivatives are much larger in magnitude in some directions than in others, many cycles through all N basis vectors will be required in order to get to the minimum. This problem can be solved with the so-called direction set methods.
All direction set methods consist of prescriptions for updating the set of directions as the method proceeds. They attempt to come up with a set, which either includes some good directions that will take the calculation far along narrow valleys, or includes some number of non-interfering directions. This can avoid endless cycling through the set of directions.

8.6.1.1 Powell's Method

Powell first discovered a direction set method that does produce N mutually conjugate directions [333]. The first step of the Powell's method is to find the minimum along all basis vectors $\boldsymbol{e}_i$. The following sequence of steps will be repeated until the function's minimum is approached:

1. Categorization of the step length α_i by a 1D minimum search along all directions $\boldsymbol{p}_i$ for all $i = 1, \ldots, n$. The end point is $\boldsymbol{x}_i = \boldsymbol{x}_{i-1} + \alpha_i \, \boldsymbol{p}_i$.
2. Construction of the line $\boldsymbol{q} = (\boldsymbol{x}_n - \boldsymbol{x}_0)/\|\boldsymbol{x}_n - \boldsymbol{x}_0\|$ and 1D minimization along $\boldsymbol{q}$ to achieve $\boldsymbol{x}_{n+1} = \boldsymbol{x}_n + \alpha_{n-1} \, \boldsymbol{q}$.
3. Elimination of first search direction $\boldsymbol{p}_1$, shifting of the other search directions ($\boldsymbol{p}_i = \boldsymbol{p}_{i+1}, \; i = 1, \ldots, n-1$), and placing of the new search direction $\boldsymbol{q}$ at the end of the list of search directions ($\boldsymbol{p}_n$=$\boldsymbol{q}$).
4. The starting point for the next iteration is the endpoint of the last: $\boldsymbol{x}_0 = \boldsymbol{x}_{n+1}$.

8.6.2 Derivative Methods

This group of methods consider the gradient vector $\boldsymbol{g}(\boldsymbol{x})$ of the function $f(\boldsymbol{x})$ given by:

$$\boldsymbol{g}(\boldsymbol{x}) = \nabla f(\boldsymbol{x}) = \left[\frac{\partial f}{\partial x_1} \; \frac{\partial f}{\partial x_2} \; \cdots \; \frac{\partial f}{\partial x_n} \right]^T$$

The methods are capable of finding the minimum, if e.g. the elements of the gradient vector $\boldsymbol{g}(\boldsymbol{x})$ are all zero.

8.6.2.1 Steepest Descent Method

The simplest method using derivatives of the function is the steepest descent method, where the direction of search is equivalent to the negative gradient ($\boldsymbol{p}_k = -\boldsymbol{g}_k$). Each search along the gradient of a function will stop at the local minimum. The next gradient of the function is perpendicular to the direction of the previous search (fig. 8.5a). As such, this method has the same disadvantages as the simple approaches, which do not use the gradient information. The method will perform many small steps in going down a long, narrow valley (fig. 8.5b).

8.6.2.2 Conjugate Gradient Method

Compared to the method of steepest descent, the conjugate gradient method is not proceeding down a found gradient, but rather in a direction, which is constructed to be conjugate to the old directions, and, as far as possible, to all previous directions traversed. This method can be applied to any minimization problem. In order to understand the algorithm, we start with the Taylor expansion and include the quadric term:

$$f(\boldsymbol{x} + \Delta\boldsymbol{x}) = f(\boldsymbol{x}) + \sum_{i=1}^{N} \frac{\partial f}{\partial x_i} x_i + \frac{1}{2} \sum_{i,j=1}^{N} \frac{\partial^2 f}{\partial x_i \partial x_j} x_i x_j + \cdots \approx c + b\,\Delta\boldsymbol{x} + \frac{1}{2} \Delta\boldsymbol{x}^T\, \boldsymbol{A}\, \Delta\boldsymbol{x}$$

with $c = f(\boldsymbol{x})$ and $b = \boldsymbol{g}^T(\boldsymbol{x})$. The matrix $\boldsymbol{A}$ is called the Hessian matrix. Its components are the second partial derivative of the function f:

$$[A]_{ij} = \frac{\partial^2 f}{\partial x_i \partial x_j}$$

The change of the gradient can be approximated by:

$$\delta\boldsymbol{g}(\boldsymbol{x}) = \boldsymbol{g}(\boldsymbol{x} + \Delta\boldsymbol{x}) = \boldsymbol{g}(\boldsymbol{x}) + \boldsymbol{A}\,\Delta\boldsymbol{x}$$

Thus, if a minimum is found along the direction $\boldsymbol{u}$ the change of the gradient is zero. For the next step into a new direction $\boldsymbol{v}$, the gradient needs to stay conjugate to $\boldsymbol{u}$. This leads to:

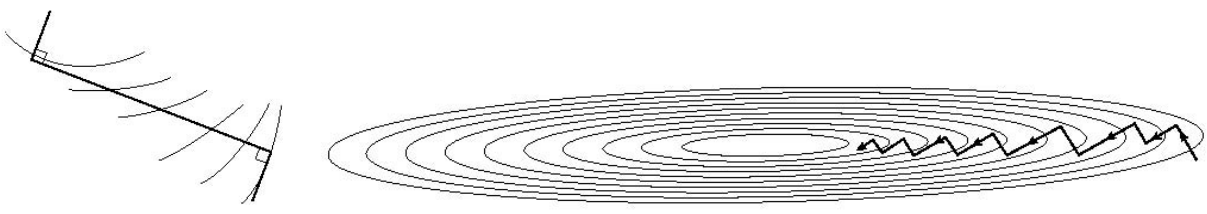

(a) (b)

Fig. 8.5. Derivative numerical minimization: steepest descent (a) This method, in a long, narrow valley, is an inefficient strategy, taking many steps to reach the valley floor. (b) Magnified view of one step: A step starts off in the local gradient direction, perpendicular to the contour lines, and traverses a straight line until a local minimum is reached, where the traverse is parallel to the local contour lines. (Fig. from [333])

$$0 = \boldsymbol{u}\,\delta\boldsymbol{g}(\boldsymbol{x}) = \boldsymbol{u}\,\boldsymbol{A}\,\boldsymbol{v}$$

Thus, the successive line minimization of the function f along the conjugate set of directions lead to a minimum after N steps, with N being the dimension of the problem and the function being perfectly expressed by a quadratic form. The procedure of achieving the minimum iteratively is equivalent to the Powell's method.

8.7 Matrix Diagonalization Method

The matrix diagonalization method is used in this work for finding the three main (principal) axis of an object in a three-dimensional image. In digital image processing this technique is known as Hotelling transformation [69].
A data set $\boldsymbol{x}$ of M coincidental vectors x_i is given in transposed formula by:

$$\boldsymbol{x} = (x_1, x_2, \ldots, x_n)^T$$

The mean vector $\boldsymbol{m_x}$ is given for M coincidental vectors with:

$$\boldsymbol{m_x} = \frac{1}{M}\sum_{i=1}^{M}\boldsymbol{x}_i$$

The covariance matrix $\boldsymbol{C_x}$ has the dimension $n \times n$, if the vector $\boldsymbol{x}$ has a dimension of n. The covariance matrix is given by:

$$\boldsymbol{C_x} = \frac{1}{M}\sum_{i=1}^{M}\boldsymbol{x}_i\boldsymbol{x}_i^T - \boldsymbol{m_x}\boldsymbol{m_x}^T$$

The element c_{ii} of the matrix $\boldsymbol{C_x}$ is the variance of the vector x_i and the elements c_{ij} and c_{ji} are the covariances between x_i and x_j. Thus, the covariance matrix $\boldsymbol{C_x}$ is symmetric and real. This guarantees to find always a set of n orthogonal eigenvectors $\boldsymbol{e}_i$ with the corresponding eigenvalues λ_i. If the eigenvalues are sorted by their size and the corresponding sorted eigenvectors are elements of a matrix $\boldsymbol{A}$, the so-called Hotelling transformation is given by:

$$\boldsymbol{y} = \boldsymbol{A}(\boldsymbol{x} - \boldsymbol{m_x})$$

and the covariance matrix $\boldsymbol{C_x}$ can be transformed into:

$$\boldsymbol{C_y} = \boldsymbol{A}\boldsymbol{C_x}\boldsymbol{A}^T$$

The matrix $\boldsymbol{C_y}$ is a diagonal matrix having as elements the eigenvalues λ_i of $\boldsymbol{C_x}$. Thus, the elements of the vector $\boldsymbol{y}$ are linearly independent. The first three diagonal elements of $\boldsymbol{C_y}$ correspond to the largest eigenvalues. The corresponding eigenvectors of $\boldsymbol{A}$ are the three principal axes of the object.

9

Methodology

In this chapter, the combination of the mathematical approaches, experimental data, and modeling fundamentals of the previous chapters are discussed. They were utilized to develop new models and enhance existing ones. Furthermore, the computational environment is illustrated considering techniques used to implement, optimize, and parallelize the electrophysiological cell models, the excitation conduction, and the tension development models. At the end of this chapter, visualization methods are discussed briefly.

9.1 Developing and Enhancing Models

A focus of this work was directed to development of new and adjustment of existing models describing the heterogeneous electromechanics in the human heart, taking experimental data into account. The electromechanical simulations were performed on geometrical data taken from the Visible Female data set. The methods used to enhance this anatomical model in the atrium are discussed. The design of electrophysiological cell models and tension development models as well as adjustment of parameters of existing models based on experimental data are explained below.

9.1.1 Anatomical Modeling

A foundation of this work was the anatomical model of the entire human heart [341]. This model was derived from the Visible Female data set (section 3.1.2.2). The images were preprocessed to obtain a 3D data set of cubic volume elements. The data set was segmented and classified using different techniques of digital image processing, e.g. region-growing and interactively deformable contours. Figure 9.1 depicts the model consisting of cubic volume elements in a surface-based visualization. It has a spatial resolution of $0.33\,mm$, is differentiated into 19 tissue classes, and has approximatly 76 million cubic volume elements.
This model was the basis for the anatomical data sets presented in section 10.1. For the schematic models, the length and distances were extracted from the Visible Female heart and described as parameters that were used in rule-based methods to generate the schematic models. The model of the left ventricle (section 10.1.2) was directly extracted from the Visible Female heart. The main axes of this ventricular model were identified with the matrix diagonalization method (section 8.7). The model was rotated considering the transformation matrix given by the matrix diagonalization method to determine a cubic lattice with the smallest amount of volume elements. This procedure reduced both the time of computation and the amount of allocated memory by approximately 30 %.

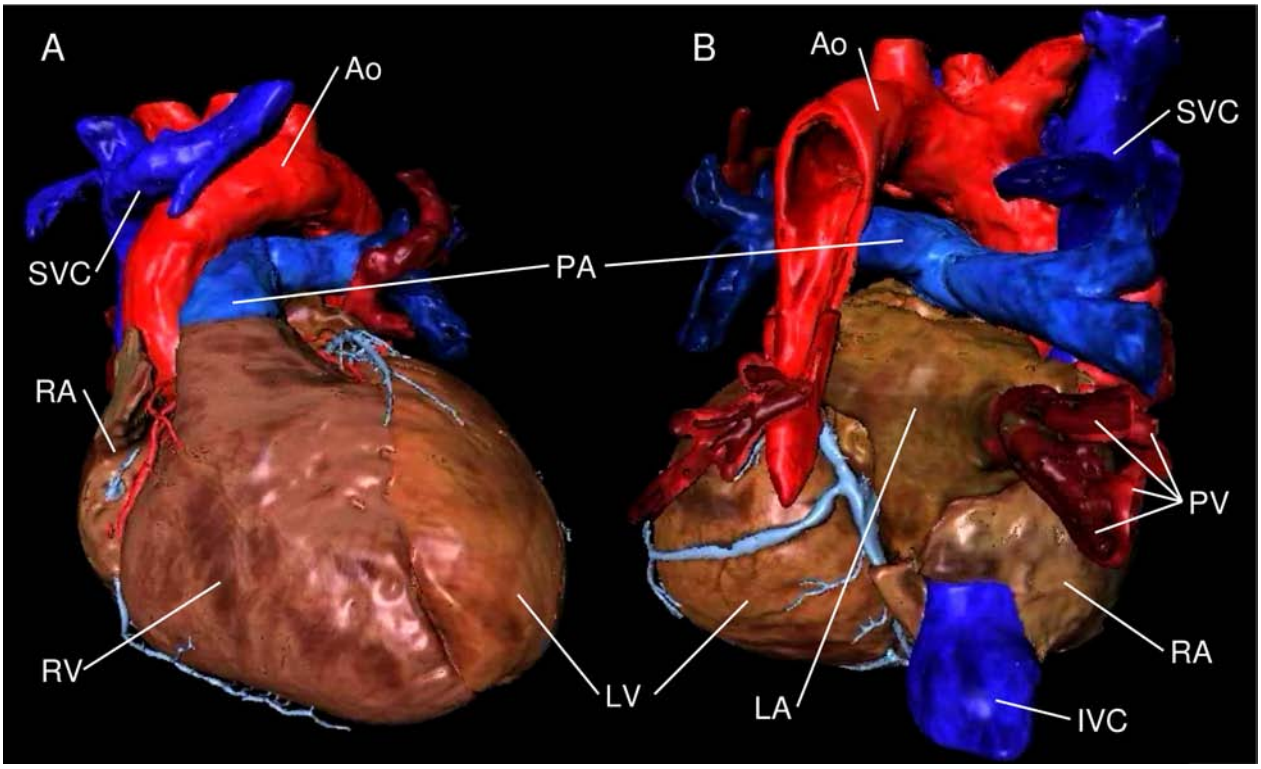

Fig. 9.1. Anatomical heart model from a frontal (A) and dorsal (B) view. RA indicates the right atrium; LA, left atrium; RV, right ventricle; LV, left ventricle; SVC/IVC, superior/inferior vena cava; PV, pulmonary veins; Ao, aorta; and PA, pulmonary artery.

The construction of a 3D anatomical model of the atrium (section 10.1.1) was also based on the Visible Female heart. In addition to the already segmented atrial working myocardium, the sinoatrial node, the crista terminalis, several pectinate muscles, the fossa ovalis in the septum, the Bachmann's bundle, and the right and left atrial appendages were included. In order to achieve this, interactive deformable meshes were used (section 3.2.2). The classification was performed manually using anatomical knowledge. This strategy was necessary since these structures were too fine for automatic segmentation and thus could not be detected even in the detailed photographic images.

9.1.2 Cellular Models

Markov models were used in this work to describe both electrophysiology and tension development mathematically. The electrophysiological models combine the descriptions of membrane proteins, the cell membrane itself, and intra- as well as extracellular compartments. Markov models were used in the tension development models to describe the interaction between the proteins troponin, tropomyosin, actin, and myosin.
The development of a new human sinoatrial node model (section 10.3) and the new hybrid tension development model (section 10.6) were based on existing and new approaches, which were combined into a set of coupled ordinary differential equations. The parameters for these equations were adjusted to measured data as described in 9.1.3.
In principle, there are several ways for designing a human sinoatrial node model. One way is to construct a completely new model based exclusively on using measured data. Another way is using an existing rabbit sinoatrial node model and adapting it to human experimental data. A third way is using a human atrial model of electrophysiology and adapting it to the sinoa-

trial node behavior considering measured data. In this work, the third way was used since experimental data describing the human sinoatrial node is rare. It was assumed that the electrophysiological properties of the human atrial tissue are closer to the human sinoatrial node than the sinoatrial node of a rabbit. Thus, the new human sinoatrial node model [342, 343] was constructed based on the electrophysiological model describing the human atrial electrophysiology designed by Courtemanche, Ramirez, and Nattel (CRN, section 5.5.3). Some additional ion channels were included based on the Zhang et al. rabbit sinoatrial node model (section 5.5.9). These were not reported in human atrial working myocardium and hence are not implemented in the CRN model.
A new hybrid tension development model was created in the course of this work [344, 307, 345, 346] and was based on new findings in cell physiology. The model describes the states of the involved proteins actin, myosin, troponin, and tropomyosin. Basic interrelations of the influences and dependencies of these proteins underlie the development of this approach. The Hybrid Tension Development (HTD) model linked the description of calcium binding to troponin with the subsequent conformation change of tropomyosin and the interaction of actin and myosin (chapter 6). The HTD model was called hybrid model because the components are partly taken from other approaches. The process of calcium binding to troponin C was adopted from the Rice-Winslow-Hunter models [325]. The interaction of actin and myosin was based on the work of Gordon et al. [347], Bers et al. [13], and Spudich [348]. The transformation changes of tropomyosin were integrated on the basis of a new approach.

9.1.3 Model Parameter Adjustment

As explained, Markov models describe the electrophysiology and tension development in the human heart in this work. For the adjustment of rate constants between the states of the Markov models to experimental data, minimization techniques were used (section 8.6). An error function was defined, which quantified the differences between simulation results and the given data. The root mean square error function was the subject of the minimization:

$$E_{RMS}(v_1, \ldots, v_M) = \sqrt{\frac{\sum_{i=1}^{N} d_i(m_i, s_i)^2}{N}} \tag{9.1}$$

with the variables v_i, the distance functions d_i, the given values m_i, and the simulated results s_i. M and N quantify the number of variables and of data, respectively. The distance function $d_i(m_i, s_i)$ is defined as:

$$d_i(m_i, s_i) = s_i - m_i$$

The conjugate gradient as well as Powell's method showed the best performance for the adjustment of model parameters to experimental data [349]. Both methods displayed similar qualities in minimizing the root mean square error function.
The inclusion of pathological parameters was performed in the same way as for physiological data by minimizing eq. 9.1. One difference was the possibility the protein characteristics had changed due to e.g. a genetic defect and thus the descriptions for the rate constants may have changed.

9.1.4 Muscle Fiber Orientation

The new approach of implementing the muscle fiber orientation in the ventricles was based on measurements in the human ventricular tissue [66]. The measurements depict the angle α_1,

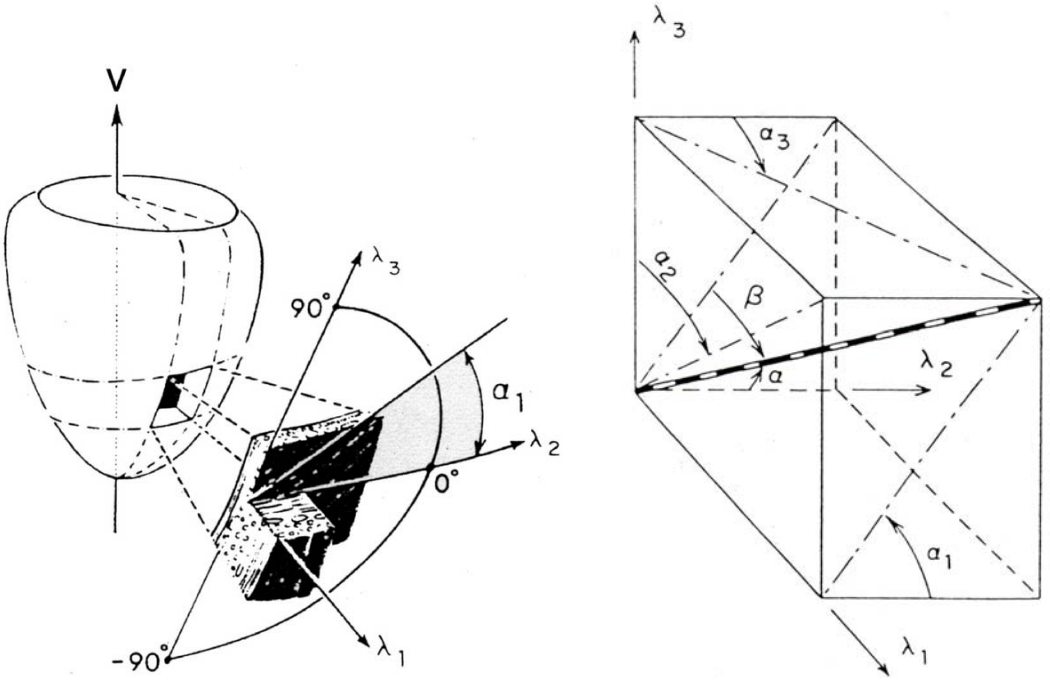

(a) (b)

Fig. 9.2. Measurement of fiber orientation in the ventricular wall. (a) The locally measured coordinate system $(\lambda_1, \lambda_2, \lambda_3)$ is depicted. (b) The fiber angles α_1, α_2, and α_3 are illustrated in relation to λ_1, λ_2, and λ_3 in the block of tissue. Figs. from [66, 350].

α_2, and α_3 in the local coordinate system with respect to the basis vector $\boldsymbol{\lambda} = (\lambda_1, \lambda_2, \lambda_3)^T$ (fig. 9.2). α_1 is the so-called helix angle. $\alpha_1 = 0°$ is determined by the direction λ_2. The angle α_1 is rotating from endocardium (55°) nearly linearly towards epicardium (−75°) with 0° in the midmyocardial layer [66].

9.2 Computational Environment

The computational environment for simulating the single cell electrophysiolgy coupled with the tension development as well as excitation conduction was based on software programmed at the Institute of Biomedical Engineering of the University Karlsruhe (TH). The data structure was based on the kaLattice format representing cubic volume elements [351]. The implemented equations were optimized and parallelized using advanced techniques of software engineering. The achieved results were visualized with volume and surface based methods.
The simulations were performed on parallel computers. The systems used were either Silicon Graphics Inc. (SGI) computers [352] or Apple Computer Inc. Xserves [353]. The network of SGI computers at the Institute of Biomedical Engineering of the University Karlsruhe (TH) consisted of one SGI Origin 2000 with 8 R10000 195 MHz processors interlinked as a shared memory system and three SGI Octane R12000 400 MHz workstations with fast Ethernet access. The parallel Apple computer consisted of 11 Xserve G5 systems with two 2 GHz processors coupled by 1 GBit Ethernet.

9.2.1 Implementation

The cellular models, i.e. electrophysiological as well as tension development models, and the bidomain model were implemented in the software language C++ [354]. Some additional scripts to analyze the data used perl [355]. The cellular models were based on Hodgkin-Huxley like models for describing the gating mechanism of ionic channels or used Markov chain models for depicting the interaction of proteins involved in the force generating units of the myocytes. The coupling of both cellular models was achieved by using the intracellular calcium concentration or the amount of calcium bound to troponin. To implement the bidomain equations, operator splitting techniques were used to reduce the complexity of the numerical problem.

9.2.1.1 Cellular Models

Both electrophysiological and tension development models were cellular models consisting of systems of nonlinear coupled ordinary differential equations. For the electrophysiological models the equations describe intra- and extracellular ion concentrations, ion currents through the cell membrane, states and dynamic changes in ionic channels, and the transmembrane voltage (chapter 5). The equations of the tension development model describe the binding of calcium to troponin, the shifting of tropomyosin, and the cross-bridge interaction of actin and myosin (chapter 7).
These ordinary differential equations were mainly solved using the simplest integration method described in section 8.2, i.e. the Euler method. The necessary temporal increment for the Euler method was found to be $20\,\mu s$ or less in order to adequately integrate the fast gating processes especially of the sodium current I_{Na}. This kind of small time increments allowed to calculate the coupled equations sequentially since it was assumed that the variation of the variables was very small during each time step.

9.2.1.2 Coupling of Electrophysiological and Tension Models

The coupling of electrophysiological models with tension development models was mostly achieved using the free intracellular calcium concentration of the electrophysiological model as a direct input for the tension models where binding of calcium to troponin was described. A problem with this coupling method is that some electrophysiological models also described the binding of calcium to troponin.
To avoid this duality, the software was designed to handle the coupling dynamically. If the electrophysiological model mathematically described troponin, the user can choose between coupling with free intracellular calcium or with the amount of calcium bound to troponin. If the latter method was used, the process of calcium binding to troponin was not executed in the tension model. When using intracellular calcium as coupling mechanism, the troponin buffer was not calculated in the electrophysiological model but in the tension model. In the tension model, the fraction of bound calcium to troponin was then subtracted from the intracellular calcium concentration, which was handled by the electrophysiological model.

9.2.1.3 Bidomain Model

The bidomain equations coupled the cellular models with the description of current flow in the tissue to reconstruct the excitation conduction process (section 5.6.3.1). The computationally

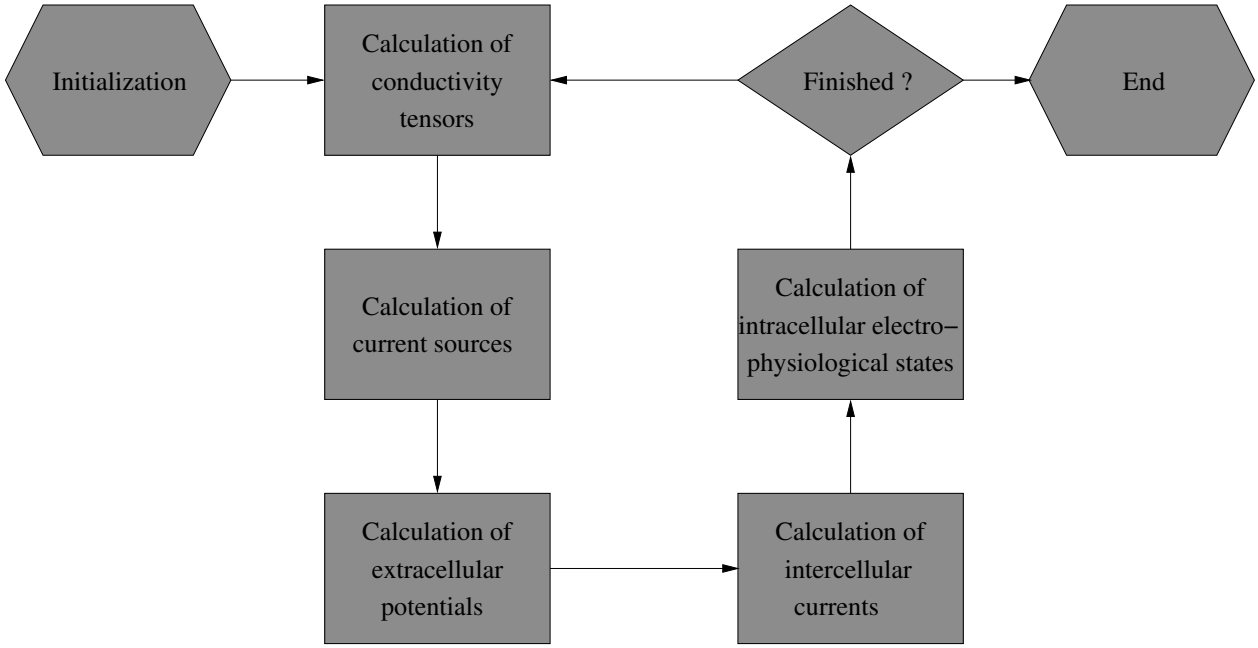

Fig. 9.3. Bidomain modeling of cardiac electrophysiology using operator splitting method. The method consists of determining the intracellular current source density (eq. 9.3), solving eq. 9.4 to get the extracellular potential distribution. Then, the intercellular stimulus current is calculated by eq. 9.5, and this is used as an input to update the membrane kinetics and thus the transmembrane voltage distribution. The procedure is iteratively performed for each time step until the simulation is finished. Fig. from [359].

most expensive part of the simulation environment was the calculation of the extracellular potential distribution.

The bidomain model required solving the elliptical partial differential equation (eq. 5.19) using e.g. an iterative method, then solving the nonlinear parabolic partial differential equation (eq. 5.20) using e.g. an explicit forward Euler method. To achieve a more simple mathematical construction, the two bidomain equations were separated into smaller problems known as the operator splitting method (fig. 9.3) [356, 357, 358]. The two partial differential equations were then described by four systems of differential equations:

$$\frac{\mathrm{d}V_m}{\mathrm{d}t} = -\frac{I_{mem}(V_m,\gamma) - I_{inter}}{C_m}, \qquad \frac{\mathrm{d}\gamma}{\mathrm{d}t} = \alpha_\gamma(1-\gamma) - \beta_\gamma\gamma \tag{9.2}$$

$$\nabla\left(\sigma_i \nabla V_m\right) = -f_m \tag{9.3}$$

$$f_m = \nabla\left(\left(\sigma_i + \sigma_e\right)\nabla\Phi_e\right) \tag{9.4}$$

$$-f_m + \nabla\left(\sigma_i \nabla\Phi_e\right) = \beta I_{inter} \tag{9.5}$$

with the transmembrane voltage V_m, the sum of transmembrane currents I_{mem}, the intercellular stimulus current I_{inter}, the description of the ion channel gating process γ, the rate constants α_γ and β_γ, the intra- and extracellular conductivity tensor σ_i and σ_e, respectively, the source current density f_m, and the extracellular potential Φ_e (section 5.6.3.1).

The first equation (eq. 9.2) is a system of ordinary differential equations describing solely the properties of the electrophysiological model (section 5.1). The second and the last one (eq. 9.3 and 9.5, respectively) are calculations of intracellular and intercellular source current densities, respectively. Equation 9.4 is an elliptical partial differential equation and has to be solved with iterative methods described in section 8.4. In this work, the Gauß-Seidel method was used. The solution of this equation system was the most time consuming part of the

whole computation process since the calculations of the extracellular potential distribution need to be accurate to gain realistic results.
The advantage of the monodomain model (section 5.6.3.2) consists in the direct determination of the intercellular current I_{inter} through the source current density f_m (eq. 9.3). Hence, the elliptical part of the equation system was not computed and the most time consuming part was then the mathematical integration of the electrophysiological properties (eq. 9.2).
One disadvantage of the bidomain model is that the spatial resolution of the underlying geometry needs to be less than $1/3\ mm$ for achieving correct coupling [264]. This led to large grids e.g. with at least approximately 20 million nodes when calculating the excitation conduction in the whole heart.
The conductivity σ was adapted to each selected spatial resolution using numerical experiments with a resolution of $0.1\,mm$ to determine the conduction velocities measured in tissue. The conductivity values for $0.1\,mm$ are taken from Colli Franzone (tab. 5.2).

Determination of the ECG: Transmural electrocardiograms (ECG) were used in this work in order to quantitatively compare the extracellular signals from conduction simulations with measured electrocardiographic data (chapter 11). The determination was achieved by placing the virtual myocardial block of tissue, the so-called wedge preparation, into a virtual bath medium with the conductivity of the extracellular liquid solution. When using the bidomain equations, the extracellular electrical potential was calculated during the excitation conduction simulation for both the myocardium and the bath. The transmural ECG was determined by placing electrodes in the bath on both the endocardial and the epicardial sides of the tissue. The ECG signal is then given by:

$$\Delta\Phi_e = \Phi_{e,epi} - \Phi_{e,endo} \tag{9.6}$$

with the extracellular potential difference $\Delta\Phi_e$, the extracellular potential in the bath near the endocardial border $\Phi_{e,endo}$, and the extracellular potential in the bath near the epicardial border $\Phi_{e,epi}$.

Finite difference approximation of Poisson's equation: When using the bidomain model instead of the monodomain model, the partial differential equation given by eq. 9.4 had to be discretized with e.g. the finite element method or the finite difference method. The discretization of Poisson's equation ($\nabla(\sigma\nabla\phi) + f = 0$) with the finite differences method for example led to an equation with first and second order derivatives of the electrical potential ϕ and first order derivatives of the conductivity σ. In the finite difference method, the partial differential equation was discretized node-wise in order to determine the node equations. This discretization led to discrete approximations of the differential terms. Thus, the node variable, which is describing the unknown function, depends on the node variables of neighboring elements. In the two-dimensional case for example, the central first order derivatives are approximated in rectangular, equidistant meshes at the node point $\boldsymbol{x}_{i,j}$ by:

$$\frac{\partial g}{\partial x_1}(\boldsymbol{x}_{i,j}) \approx \frac{g_{i+1,j} - g_{i-1,j}}{2\Delta x_1}$$
$$\frac{\partial g}{\partial x_2}(\boldsymbol{x}_{i,j}) \approx \frac{g_{i,j+1} - g_{i,j-1}}{2\Delta x_2}$$

with g being either the potential ϕ or the conductivity tensor σ, and the distance between the node points Δx_1 and Δx_2 in x_1 and x_2 direction, respectively. The node variables $g_{i+1,j}$, $g_{i-1,j}$, $g_{i,j+1}$, and $g_{i,j-1}$ correspond to the node points $\boldsymbol{x_{i+1,j}}$, $\boldsymbol{x_{i-1,j}}$, $\boldsymbol{x_{i,j+1}}$ and $\boldsymbol{x_{i,j-1}}$, respectively.

The second order derivatives are determined by two-fold differences:

$$\frac{\partial^2 g}{\partial x_1^2}(\boldsymbol{x}_{i,j}) \approx \frac{g_{i+1,j} - 2g_{i,j} + g_{i-1,j}}{\Delta x_1^2}$$
$$\frac{\partial^2 g}{\partial x_2^2}(\boldsymbol{x}_{i,j}) \approx \frac{g_{i,j+1} - 2g_{i,j} + g_{i,j-1}}{\Delta x_2^2}$$
$$\frac{\partial^2 g}{\partial x_1 \partial x_2}(\boldsymbol{x}_{i,j}) \approx \frac{g_{i+1,j+1} - g_{i-1,j+1} - g_{i+1,j-1} + g_{i-1,j-1}}{4\Delta x_1 \Delta x_2}$$

9.2.2 Optimization

Since most simulations presented in this work were performed with the monodomain model, most computational time was used for the simulation of the excitation conduction by the electrophysiological models. These have been in special focus for optimization procedures. In this scope, the reduction of the amount of mathematical operations or avoiding time consuming functions like exp() and ln() is meant by optimization.
Several different techniques were implemented for achieving the reduction of operations. These were the pre-calculation of groups of constants coupled by mathematical operators, the construction of lookup tables for processes, which were only depending on one parameter, and the so-called time constant grouping.
Lookup tables were created for the gating variables and other functions solely depending on the transmembrane voltage. Most of the rate constants of the gating mechanism (section 5.1.1) were described by complex mathematical structures. The use of pre-calculated lookup tables reduced these operations to the problem of finding the appropriate transmembrane voltage entry in an array and to an additional multiplication. Furthermore, the reversal potentials (eq. 4.3 or 4.4) were sorted in lookup tables, which were dependent on the concentration of ions. Another method of enhancing the calculation speed was to use the Rush-Larsen scheme presented in section 8.2.3 in conjunction with lookup tables.
Time constant grouping is the procedure of separating the variables, which need to be integrated, e.g. into fast, medium, and slow systems. The gating process of the sodium current I_{Na} for example had fast components. On the other hand, the variation of the slow delayed rectifier potassium current I_{Ks} was described by a slow system. The idea of time constant grouping is to calculate fast processes every time step, and use lower time steps for slower systems.
Using all these methods, the calculation time needed for updating the electrophysiological properties was reduced in some models to approximately 10 % of the not optimized versions.

9.2.3 Parallelization

The massive increase in need for greater computing power mirroring the interest in larger and more detailed modeling cannot be satisfied by conventional single processor architectures. Thus parallel programming is an important topic for large scale simulations like the ones described in this work.
The computers normally utilized were based on the multiple instruction multiple data (MIMD) approach. These architectures use either shared or distributed memory. The memory modules in shared system are directly interconnected by a bus-based architecture. In distributed memory systems, each processor has its own private memory and the interconnecting data is transfered across a network.

The bidomain equations (eqs. 5.19 and 5.20) were parallelized in this work. To achieve this, the two equations were partitioned into smaller problems by a method known as operator splitting. This led to a system of four equation sets as described in section 9.2.1.3. Equation 9.2 is describing the electrophysiological changes in each node of the geometrical net. Since all electrophysiological models are independent from each other, a parallelization was easily achieved. Eqs. 9.3 – 9.5 are partial differential equations and thus the vector-matrix operations for solving $\boldsymbol{A}x + b = 0$ were parallelized.
The increased use of parallel computing is accelerated by the development of standards for programming parallel systems. Two of the most important parallelization methods are OpenMP for shared memory systems and MPI for distributed memory architectures. Both types of parallelization were implemented in the software and are introduced briefly.

9.2.3.1 OpenMP

A simple approach to program parallel systems is the so-called data parallelism. In this approach, a data structure is distributed among the processes and the individual processes execute the same instructions on their part of the data structure.
OpenMP is a specification for a set of compiler directives and library routines that can be used to specify shared memory parallelism in Fortran and C/C++ programs [360, 361]. The advantage of OpenMP is that the regular serial structure of a program needs not to be changed, but a compiler directive has to be added in the right place of the code under consideration of some basic rules. The compiler then automatically replaces the user directive with code that distributes the data and performs the parallel data operations.

9.2.3.2 MPI

The most commonly used method of programming distributed memory MIMD systems is message passing. In basic message passing, the processes coordinate their activities by explicitly sending and receiving messages. The Message Passing Interface (MPI) [362, 363] is the most widely used message passing toolkit since it was designed to permit maximum performance on a wide variety of systems.
MPI is a library that can be called from C/C++ and Fortran programs. Two different types of communications are described for MPI. The first one is the synchronous mode, where two processes are waiting for each other until the communication is finished. The second is called buffered mode, where the software can copy the message into a system-controlled block of memory and can directly continue executing.
The code has to be explicitly adapted to the needs of MPI. The software designer has to define when messages and data have to be transfered to other processes and also needs to care about when to parallelize and to synchronize. The efforts of implementing MPI is thus larger than that of OpenMP. The advantage of MPI is that distributed memory systems on which MPI is running are usually less expensive than shared memory systems.

9.2.4 Visualization

The simulation results of the excitation conduction presented in chapter 11 needed adapted and highly efficient techniques for the visualization due to the high spatial and temporal resolution and the large amount of consumed memory [364, 365]. A good visualization allows to analyze the results more easily.

Surface-based and volume-based techniques were used to visualize the electrical potentials as well as the distribution of the transmembrane voltage and the tension development in conjunction with the anatomical context. In this work, the visualized data was mainly scalar as e.g. the extracellular potential distribution. Also vectorial data like the orientation of myocardial fibers were illustrated. The visualization of the three-dimensional data led to a projection on the two-dimensional screen. To illustrate the temporal behavior of the simulations, animations were generated.
The methods implemented for the visualization were based on existing commercial and non-commercial software packages. The anatomical data formed the basis for visualizing the simulation results on the surface or in the volume of the geometrical representation. Therefore, the Silicon Graphics Inc. visualization toolkit Open Inventor [366] or alternatively its free derivate Coin3D [367] were utilized, which were built on top of OpenGL [368] and defines a standard file format for 3D data interchange.

Surface-based visualization: For the surface-based methods, the rendering of objects is performed on triangular or quadratic surfaces of the volumetric data. Since the models in our framework consist of cubic elements, the visualization of quadratic surfaces is just the transformation of colors and transparencies to displayed surface elements. Triangular surfaces were obtained from the volume data by using the so-called marching cube algorithm [369]. Surface rendering has the advantage that it is fast but a lot of detail is usually lost.

Volume-based visualization: The anatomical and the simulation data are visualized directly by the volume-based techniques. All elements with the joined data are displayed. Thus transparencies need to be defined only for extracting the important data or for getting an inside view of the volumetric object. Volume rendering is usually very slow and in general cannot create realistic images. Thus, a combination of volume and surface-based visualization is performed.

Generation of animations: The sequential visualization of e.g. electrical field quantities at the discrete time interval given by the simulations allows the production of animations of the simulated data. The advantage of this technique is the illustration of temporal processes from different angles. The toolkit QuickTime by Apple Computer, Inc. [370] is used to generate the animations.

10

Results: New Methods and Models

This chapter details the first part of the results of this thesis, in which new or adapted models are presented. In the first section, the anatomical models generated in this work are discussed. These geometrical data sets describe the tissue distribution in atria and ventricles either schematically or anatomically correct. In the second part of the results (chapter 11) these anatomical data forms the geometrical basis for calculating the excitation conduction. In order to determine the fiber orientation of the myocardium, the model for constructing the ventricular fiber orientation on a rule-based method is explained in the next section. The information about fiber orientation is necessary to implement a realistic behavior of anisotropic electrical features in the tissue as discussed in chapter 11.
Sections 10.3 – 10.5 illustrate the models that were developed for describing heterogeneous electrophysiology in the heart. First, the equations and features of the human sinoatrial node model are depicted. This approach is based on a model of the human atrial electrophysiology and was adapted to pacemaker activity. The electrophysiological heterogeneity within the sinoatrial node was reconstructed with this new model. The heterogeneous adjustment of parameters in a human atrial model is described in section 10.4. With the different cell behavior, the varying action potential durations given by measurement data were reconstructed. The last section of this block describes a transmural heterogeneous left ventricular model based on the Priebe-Beuckelmann model. This model was adjusted to recently published human ventricular measurement data and was enhanced by including transmurally varying channel conductivity in order to reflect the heterogeneity measured in the ventricles.
The newly developed tension model is detailed in section 10.6. The underlying equations and the included cooperativity mechanisms are described. The characteristics of this model are compared to other existing tension development models during a variety of numerical experiments with different external conditions. This model is coupled to the adapted ventricular ionic model to investigate heterogeneous cellular electromechanics.
The last section of this chapter addresses the developed pathological models describing single cell dysfunction. In the scope of this work, electrophysiological remodeling in the atria due to permanent atrial fibrillation and genetic defects were investigated. In the group of genetic defects, familial atrial fibrillation and the long QT syndrome were implemented. All pathological models were based on recently published measurement data.

10.1 Anatomical Models

The anatomical models constructed in this work were based on the Visible Female data set. The atrial model was derived by enhancing the existing Visible female atrium by several

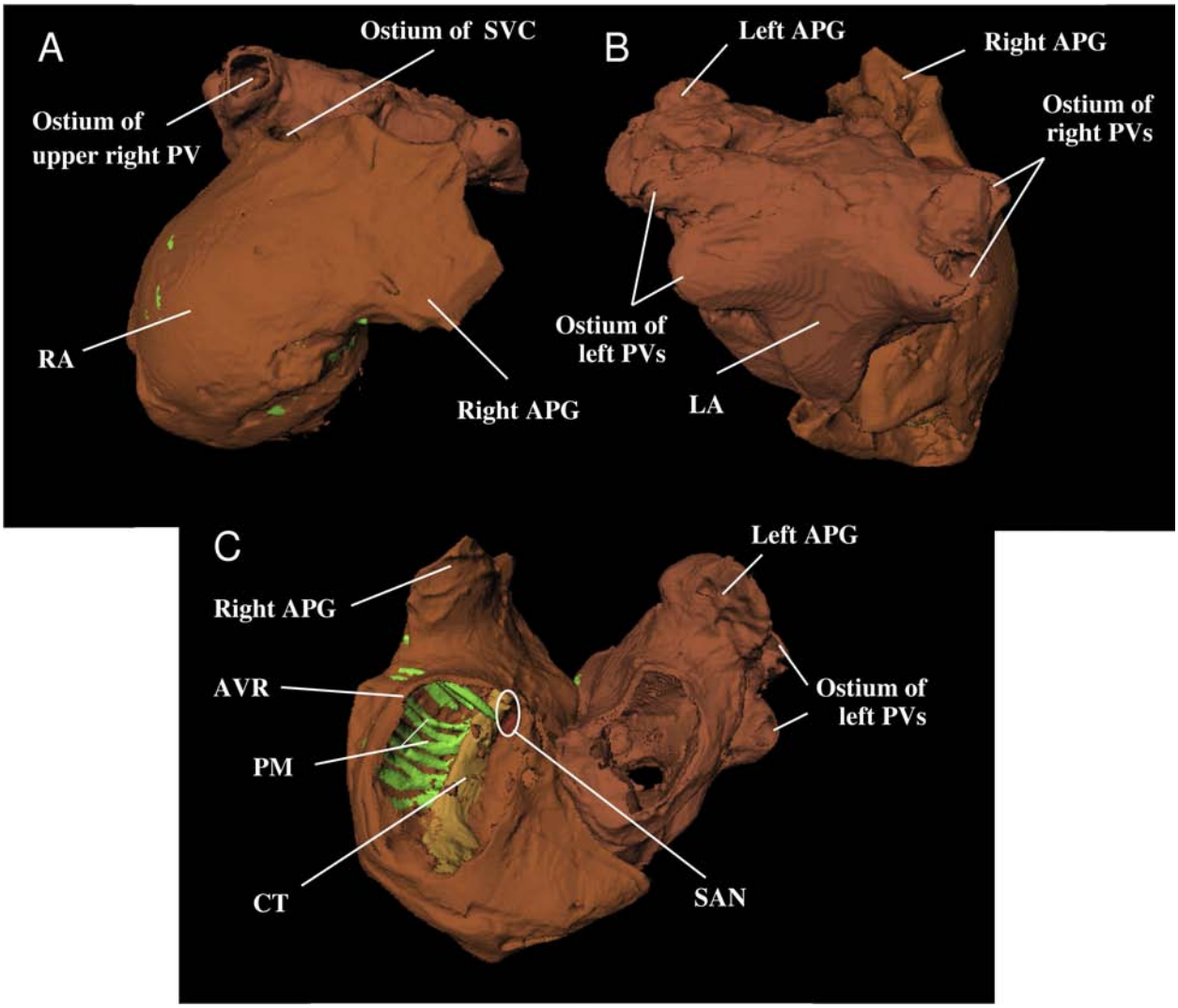

Fig. 10.1. Anatomical model of the atria. A: Right atrium (RA) in a frontal view with its appendage (APG) and the ostium of the superior vena cava (SVC). B: Left atrium (LA) in a dorsal view with the ostium of the pulmonary veins (PVs). C: View through tricuspid and mitral valve. The sinoatrial node (SAN), the crista terminalis (CT), pectinate muscles (PMs), and the atrioventricular ring (AVR) are visible in the RA. Fig. from [343].

tissue classes. Furthermore, fiber orientation was included for the fast conducting bundles in the atrium. The ventricular model was directly extracted from the Visible Female heart. In addition, the fiber orientation was set with a rule-based system described in section 10.2. A group of schematic models are introduced. These were based on the geometrical properties of the Visible Female heart. These schematic models describe the right atrium, a line through the left ventricle, and a virtual wedge preparation of the left ventricular free wall.

10.1.1 Atria

The three-dimensional anatomical model of the human atrium [371, 372, 373, 343] is visualized in fig. 10.1 from different view points. It includes, in addition to the already segmented atrial working myocardium (AWM), the sinoatrial node (SAN), the crista terminalis (CT), ten pectinate muscles (PMs), the fossa ovalis in the septum, the Bachmann's bundle (BB), and the right and left atrial appendage (APG). The methods to achieve this model are detailed in section 9.1.1.

The SAN is located near the ostium of the superior vena cava (SVC). The CT starts next to the SAN and extends towards inferior vena cava (IVC). The PMs are arranged comb-like on the right atrial endocardium starting at the side of CT. BB originates next to SAN and extends into the left atrium towards the left atrial APG.
The SAN is illustrated separately in fig. 10.2. The model was partitioned in seven regions going from central over transitional to peripheral tissue classes. This representation considers the heterogeneous anatomical features presented in section 4.7.1.
In order to set fiber orientation of the conduction pathways, matrix diagonalization methods were used to find the main axis of each segment of the pathways. Fiber orientation was set for CT, PMs, and BB. The resulting orientation was always set parallel to the local main axis of the chosen segment. AWM was set to be isotropic because of conflicting data concerning fiber orientation in human AWM [61, 374, 375]. Furthermore, the resolution of the Visible Female data was too low for automatic detection of fiber orientation in AWM.
The anatomical model of the human atrium consists of 18.8 million cubic voxel including 1.58 million of excitable tissue. The remainder is blood and surrounding tissue. 13 tissue classes were included additionally to the Visible Female heart in this model.

10.1.2 Ventricles

The anatomical model of the ventricles was directly extracted from the Visible Female heart (section 9.1.1). Figure 10.3 A shows the model consisting of cubic voxel in a surface based transparent visualization. The model consists of approximately 18.5 million cubic elements of which approximately 7.8 million are assigned to ventricular myocytes [376, 377].
In order to define transmurally differing electrophysiological properties in this model, different tissue classes were set in this model from endocardium towards epicardium (fig. 10.3 B). This distribution of tissue classes was implemented with a method solving the Poisson's equation. Therefore, the potential was fixed at the epicardium to a value depicting the class number of epicardium and at the endocardium to the endocardial class number. When a solution was calculated for the Poisson's equation iteratively using the Gauß-Seidel method (section 8.5.2.1), the isopotential surfaces depicted the different tissue classes.
The orientation of muscle fibers was included into the model allowing the incorporation of anisotropic electrical and mechanical properties (fig. 10.3 C). The orientation was constructed with a rule-based method that is derived from anatomical studies (section 10.2) [378]. The

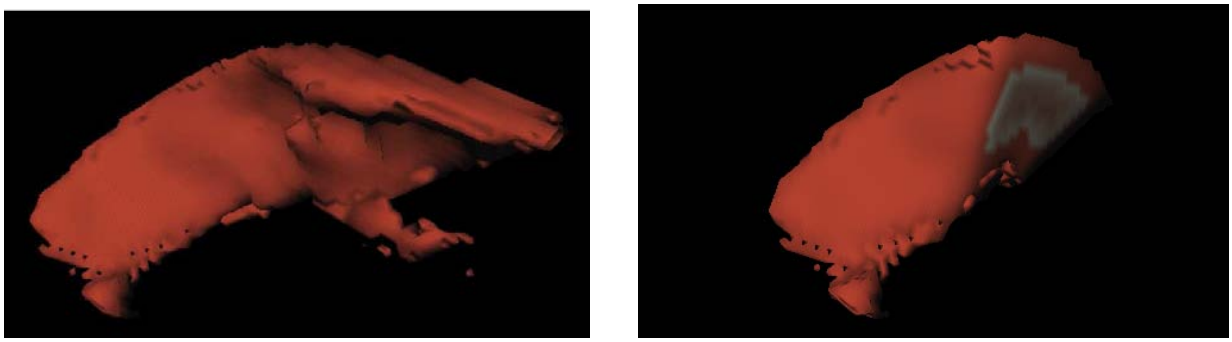

(a) (b)

Fig. 10.2. Heterogeneous human sinoatrial node (SAN) in the anatomical model without surrounding atrial tissue. (a) View of the entire SAN model. (b) Model of the SAN shown sliced in a transversal plane with its smooth transition between central and peripheral cells. Fig. from [371].

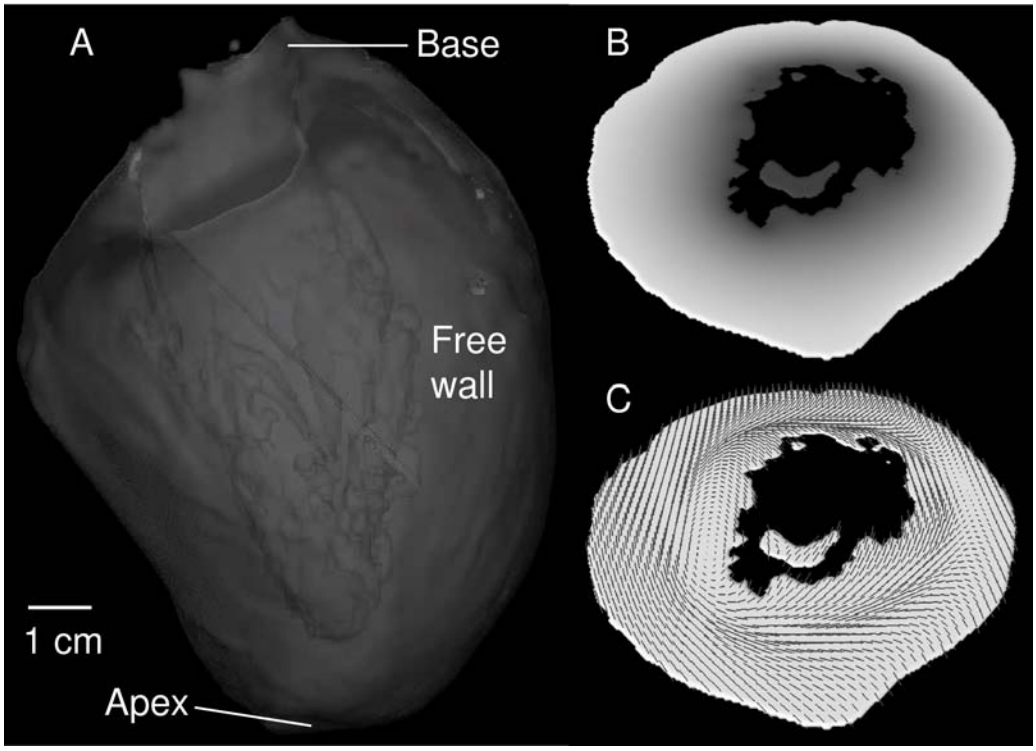

Fig. 10.3. A: Left ventricle of the Visible Female data set in a transparent frontal view. B: Central cross-sectional slice of the model describing the variation of tissue types from endocardium to epicardium with dark gray to white, respectively. C: The vectors are showing the fiber orientation in the same slice. Fig. from [377].

orientation of the fibers varies from subepicardial ($-75°$) via midmyocardial ($0°$) to subendocardial myocardium ($55°$) [66].
The cardiac conduction system was constructed semi-automatically, since these structures were not visible in the cryosection images of the Visible Female data set. Important for application of the ventricular model was the identification of the electrical transition points of the cardiac conduction system to the subendocardial myocardium, i.e. the connection between ventricular myocytes and Purkinje fibers. These points were placed by first identifying the endocardial border of the tissue. The most apical point on the endocardium was selected manually. Starting from this point, a binary method defined the Purkinje fiber ends towards basal regions [270].

10.1.3 Schematic Models

Schematic models were used in this work in order to reduce the complexity of the simulations and to achieve more basic knowledge into the processes. Schematic anatomical models allow to focus mainly on investigating the electrophysiological properties in the tissue without being influenced by the complex geometry.

10.1.3.1 Schematic Right Atrium

The principal behavior of excitation conduction in the right atrium (RA) was qualitatively simulated in a two-dimensional rectangular model shown in fig. 10.4. This anatomical model is a schematic representation of a part of the right atrium. It consists of the heterogeneous

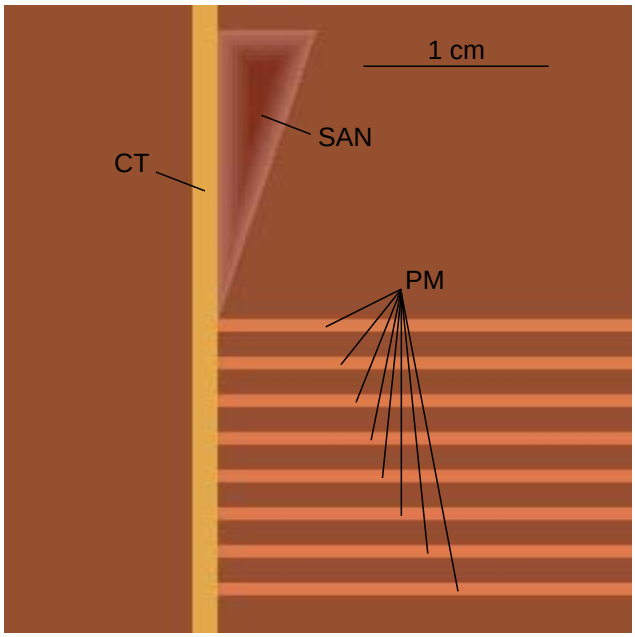

Fig. 10.4. Schematic model of the right atrium including the heterogeneous sinoatrial node (SAN), crista terminalis (CT), and pectinate muscles (PM). The model was derived from principal findings of the anatomically accurate model of the Visible Female data set (fig. 10.1). Fig. adapted from [379, 380].

sinoatrial node (SAN), the crista terminalis (CT) as a longitudinal thick stripe, some pectinate muscles (PM) as parallel horizontal stripes, and the atrial working myocardium (AWM). The heterogeneous characteristics of the sinoatrial node is considered by including seven different tissue classes as a triangle from central over transitional to peripheral regions. This model was designed with a rule-based approach. The rules describing the thickness, shape, and orientation of the implemented structures were extracted from the Visible Female heart. CT and PM are anisotropically fast-conducting bundles, i.e. the fiber orientation was set parallel to the long axis of the cardiac fibers. They form the preferential conduction pathway in the RA. No significant anisotropic conduction was detected in the AWM [375]. Hence, the AWM was assigned to be isotropically conducting.

10.1.3.2 Line through the Left Ventricle

This nearly one-dimensional model is a representation of a transmural line through the left ventricular free wall (fig. 10.5). The model was constructed to investigate transmural electrophysiological heterogeneity without having side-effects from anatomical and anisotropic conditions. Furthermore, the transmural ECG was simulated in this model by measuring the potential difference between the ends of the bath medium (section 9.2.1.3).
The line was segmented in several tissue classes reaching from endocardium to epicardium. Different electrophysiological features were attachable to each tissue class to describe transmural heterogeneity. The model has a diameter of $1\,mm$ and a length of $19.2\,mm$. The model is constructed of $5\,\mathrm{x}\,5\,\mathrm{x}\,96$ voxel each having a side length of $0.2\,mm$. The tissue is embedded in a bath consisting of $25\,\mathrm{x}\,25\,\mathrm{x}\,130$ voxel.

10.1.3.3 Virtual Wedge Preparation

The model of a wedge preparation of the left ventricular free wall was derived from the Visible Female heart (fig. 10.6 a). It is represented by an inhomogeneous and anisotropic

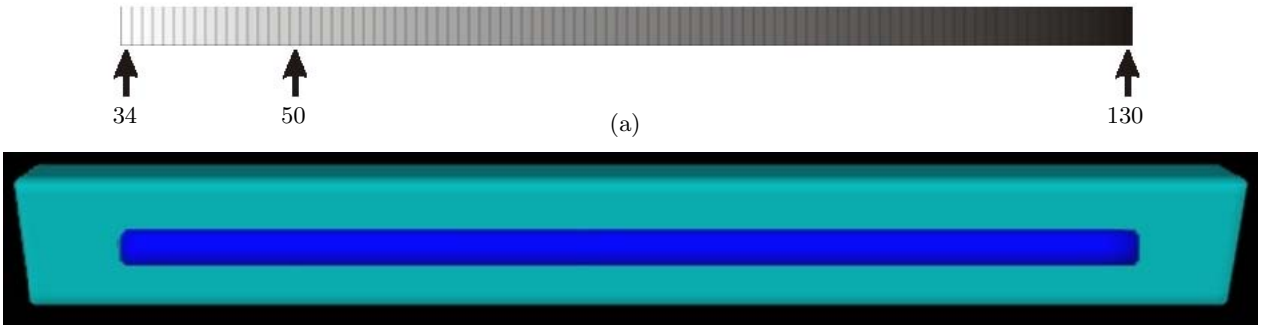

(a)

(b)

Fig. 10.5. One-dimensional heterogeneous model describing a transmural line through the left ventricular free wall. (a) Variation of the tissue classes in the model. The line has 96 different tissue classes and is 19.2 *mm* long. Class 34 is the subendocardium, class 50 is assigned to the M cells and class 130 to subepicardium. (b) Visualization of the transmural line in the surrounding bath medium. Blue is the ventricular tissue and turquoise the bath. Figs. from [381].

three-dimensional segment of an ellipsoid. Transmurally varying tissue classes and twisting fiber orientation were assigned as described in sections 10.1.2 and 10.2, respectively.
The geometry includes 150 x 150 x 125 voxel with a size of 0.2 *mm* x 0.2 *mm* x 0.2 *mm*. Approximately 1.9 million voxel describe myocardial tissue, the remainder is representing surrounding blood. The orientation of the fibers (fig. 10.6 b) varies from subepicardium ($-75°$) via midmyocardium ($0°$) to subendocardium ($55°$) [66].

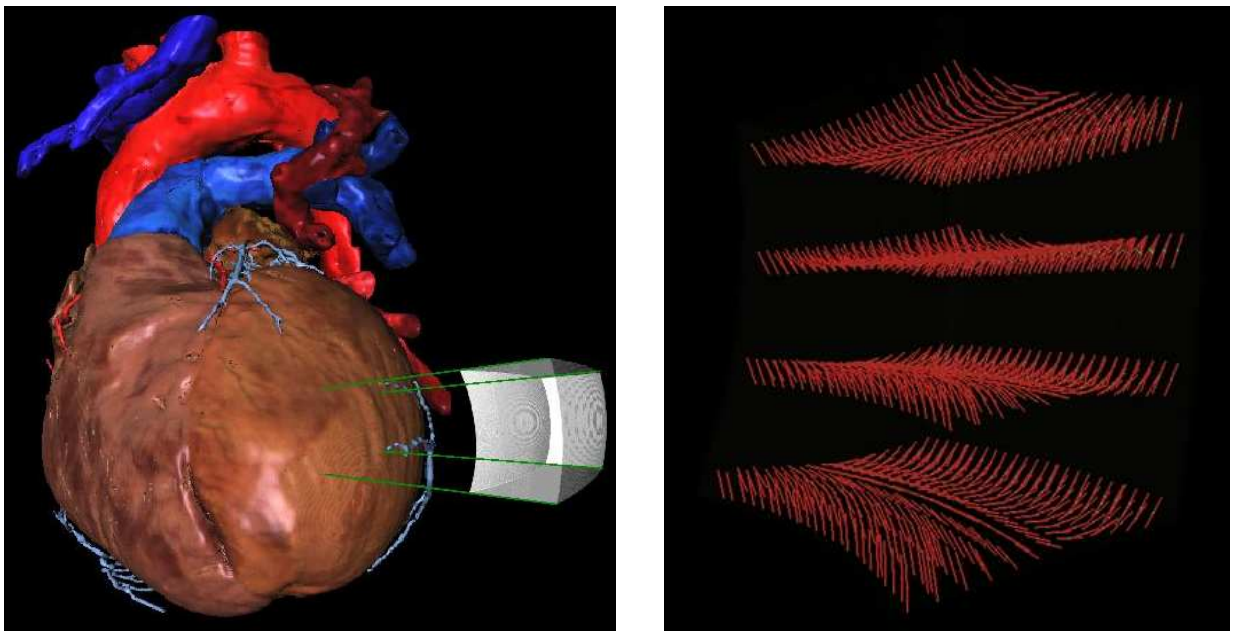

(a) (b)

Fig. 10.6. Schematic model of the left ventricular free wall. (a) Anisotropic and inhomogeneous model of the left ventricular wall in the anatomical context of the Visible Female heart. Fig. from [382]. (b) Red lines indicate the fiber orientation that rotates from the endocardial to the epicardial border. Fig. from [381].

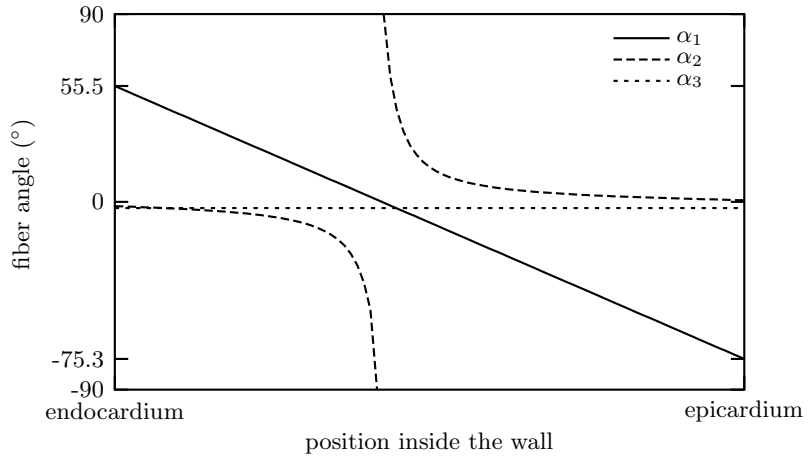

Fig. 10.7. Variation of the fiber angles α_1, α_2, and α_3 from endocardium towards epicardium given by experimantal data [66]. The angle α_1 was set to be linearly varying between 55° for endocardium and $-75.3°$ for epicardium. The angle α_2 was set to a constant value of $-3°$. The variation of α_3 was given by $\tan\alpha_3 = \tan\alpha_1 \cdot \tan\alpha_2$. Fig. from [381].

10.2 Muscle Fiber Orientation

Muscle fiber orientation variation is present in the mammalian ventricles (section 2.3.2) [66]. As described in section 9.1.4, a local coordinate system $\boldsymbol{\lambda} = (\lambda_1, \lambda_2, \lambda_3)^T$ is defined to relate the locally measured fiber angles α_1, α_2, and α_3 to a global coordinate system. An example for these fiber angles is given in fig. 10.7.
The way to set the rotating fiber orientation into a geometry was to find the axis λ_1 in the local coordinate system, which determines the direction from endocardium to epicardium. This direction was found with a method solving the Poisson's equation. Therefore, the potential was fixed at the endocardium to one value and at the epicardium to an other. The normal on the calculated isopotential surfaces defined the axis λ_1. The axis λ_2 was calculated by:

$$\lambda_2 = v \times \lambda_1$$

with v as the first principal axis of the geometry. v is either set manually or calculated with a matrix diagonalization method (section 8.7). The third axis of the local coordinate system is then given by:

$$\lambda_3 = \lambda_1 \times \lambda_2$$

The measured angles α_1 and α_2 are related to λ_1, λ_2, and λ_3 in the local coordinate system. The direction of the fiber in the local coordinate system $\boldsymbol{f_l}$ is constructed by:

$$\boldsymbol{f_l} = \begin{pmatrix} f_{l,1} \\ f_{l,2} \\ f_{l,3} \end{pmatrix} = \begin{pmatrix} \tan\alpha_2 \\ \cot\alpha_1 \\ 1 \end{pmatrix}$$

The transformation of the fiber direction from the local $\boldsymbol{f_l}$ to the global $\boldsymbol{f_g}$ coordinate system is given by:

$$\boldsymbol{f_g} = \begin{pmatrix} f_{g,1} \\ f_{g,2} \\ f_{g,3} \end{pmatrix} = f_{l,1}\,\lambda_1 + f_{l,2}\,\lambda_2 + f_{l,3}\,\lambda_3$$

The bidomain model uses a fiber orientation defined by two angles in spherical coordinates. In order to determine these fiber angles φ and ϑ, the fiber direction $\boldsymbol{f_g}$ in the global coordinate

system had to be transformed. Since only the orientation of the fiber and not the direction was needed to describe anisotropy, the range of the fiber angles φ and ϑ is given by:

$$0 \leq \varphi \leq \pi, \qquad 0 \leq \vartheta \leq \pi$$

The fiber angles φ and ϑ were determined by:

$$\varphi = \arctan \frac{f_{g,2}}{f_{g,1}}, \qquad \forall_{\varphi<0} : \varphi = \varphi + \pi;\ \vartheta = \pi - \vartheta$$

$$\vartheta = \arctan \frac{\sqrt{{f_{g,1}}^2 + {f_{g,2}}^2}}{f_{g,3}}, \qquad \forall_{\vartheta<0} : \vartheta = \vartheta + \pi$$

The reconstruction of the fiber direction $\boldsymbol{f_g}$ in the global coordinate system from the fiber angles φ and ϑ was calculated using:

$$\boldsymbol{f_g} = \begin{pmatrix} f_{g,1} \\ f_{g,2} \\ f_{g,3} \end{pmatrix} = \begin{pmatrix} \sin\vartheta\ \cos\varphi \\ \sin\vartheta\ \sin\varphi \\ \cos\vartheta \end{pmatrix}$$

10.3 Sinoatrial Node Electrophysiology

This project was the first to define an electrophysiological model of human sinoatrial node (SAN) behavior [371, 372, 343]. The ionic model of Courtemanche, Ramirez, and Nattel (CRN, section 5.5.3) [238] was used as a starting point and several rate constants of activation, deactivation, and inactivation and the maximum conductances of ionic channels, exchangers and pumps were adapted to properties of SAN cells. Some additional ion channels were also included, which were not present in the human atrial working myocardium. The Zhang et al. rabbit sinoatrial node (ZRS, section 5.5.9) model [247] was used as reference for the heterogeneous electrophysiological sinoatrial node behavior and was the basis for the inclusion of additional pacemaker specific currents. The differences in the implemented currents between the CRN and the ZRS model are illustrated in tab. 10.1.
The time-independent K^+ outward rectifier current I_{K1} was not implemented in the ZRS model, since this current is not present in SAN cells [127, 383]. The reduction or absence of

Table 10.1. Implemented ionic currents of the human atrial electrophysiological model of Courtemanche et al. [238] and the rabbit sinoatrial node electrophysiological model of Zhang et al. [247].

	Courtemanche et al.	Zhang et al.
I_{Na}	√	√
$I_{Ca,L}$	√	√
$I_{Ca,T}$	—	√
I_{to}	√	√
I_{sus}	—	√
I_{Kr}	√	√
I_{Ks}	√	√
I_f	—	√
$I_{b,Na}$	√	√
$I_{b,Ca}$	√	√
$I_{b,K}$	—	√
I_{NaCa}	√	√
$I_{p,Ca}$	√	√
I_{K1}	√	—
I_{Kur}	√	—
I_{NaK}	√	—

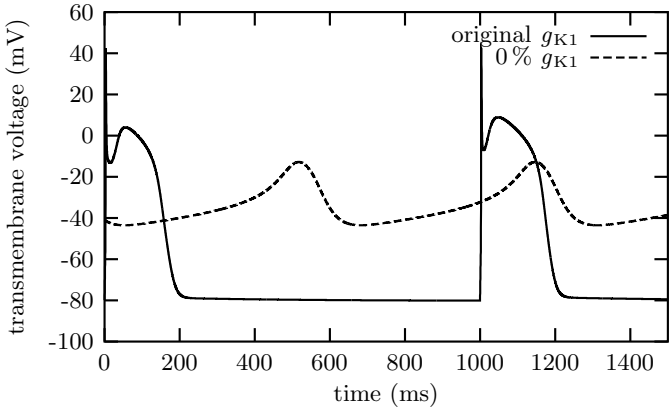

Fig. 10.8. Comparison of the transmembrane voltage course in the CRN model with original $g_{K1,max}$ and block of I_{K1}. The resting voltage is shifting to less negative values and the cell starts with autorhythmic initiation of APs with a block of I_{K1}. An external stimulus was applied for only the original CRN model at $t_1 = 0\,ms$ and $t_2 = 1000\,ms$. Fig. from [371].

I_{K1} is an essential factor in pacemaker cells. I_{K1} is responsible for the stable resting voltage in the working myocardium. If this current is reduced or blocked, the cells starts to depolarize spontaneously as illustrated in fig. 10.8. Thus, $g_{K1,max}$ was set also to 0 % in the human SAN model blocking I_{K1}.
The presence of the T-type Ca^{2+} inward current $I_{Ca,T}$ was shown in cardiac pacemaker cells in experiments [127, 384]. If this current is blocked, a negative chronotropic effect is present in the SAN. $I_{Ca,T}$ was not implemented in the CRN model. The equations of the ZRS model were used to describe the T-type Ca^{2+} channel in the human SAN model. $I_{Ca,T}$ is characterized by:

$$I_{Ca,T} = g_{Ca,T,max}\, d_T\, f_T\, (V_m - E_{Ca,T})$$

with the maximum conductance $g_{Ca,T,max} = 0.214\,nS/pF$ and $E_{Ca,T} = 45\,mV$ as the reversal voltage of the T-type Ca^{2+} current. The rate constants were implemented as in the description of the ZRS model:

$$\alpha_{d_T} = 1.068 \exp\left(\tfrac{V_m+26.3}{30}\right) \qquad \alpha_{f_T} = 15.3 \exp\left(-\tfrac{V_m+71.7}{83.3}\right)$$
$$\beta_{d_T} = 1.068 \exp\left(-\tfrac{V_m+26.3}{30}\right) \qquad \beta_{f_T} = 15 \exp\left(\tfrac{V_m+71.7}{15.38}\right)$$
$$d_{T\infty} = \frac{1}{1+\exp\left(-\frac{V_m+37}{6.8}\right)} \qquad f_{T\infty} = \frac{1}{1+\exp\left(\frac{V_m+71}{9}\right)}$$

The background current $I_{b,K}$ was adopted from the ZRS model, since this current was not implemented in the CRN model:

$$I_{b,K} = g_{b,K,max}\,(V_m - E_K)\,, \qquad \text{with} \qquad g_{b,K,max} = 0.00134\,nS/pF$$

The sustained outward K^+ current I_{sus} was included in the ZRS model in addition the transient outward current I_{to}. Up to now it is not clarified if I_{to} and I_{sus} are two different ion currents or just two different phases of the same [124, 385]. The activation variable o_a of I_{sus} was the same as for I_{to} in the ZRS model. Consequently, the activation characteristics of I_{sus} in the human SAN model was set to the implemented variable of I_{to} of the CRN model. The inactivation variable o_i was only used for I_{to} since I_{sus} has no inactivation:

$$I_{sus} = g_{sus,max}\, o_a^3\,(V_m - E_K)\,, \qquad \text{with} \qquad g_{sus,max} = 0.18\,nS/pF$$

The pacemaker current I_f of the human SAN model, consisting of a Na^+ and a K^+ component, was adopted from the equations of the ZRS model. The characteristics of the activation variable y of I_f is shown in fig. 10.9. The transmembrane voltage $V_{1/2}$, where 50 % of the channels are in the open state during equilibrium, is $-77\,mV$. A $V_{1/2}$ between $-65\,mV$ and $-90\,mV$ was measured in SAN cells [386].
The maximum conductances of some ion currents were adjusted for the human SAN model. $g_{Na,max}$ was reduced to take into account the prominent reduction in the upstroke velocity of the AP in SAN cells compared to atrial working myocardium [160]. The maximum diastolic potential (MDP) of pacemaker cells is determined mainly by the amplitude of I_{Kr}. A MDP of $-62,5 \pm 4,7\,mV$ was measured in human SAN cells [170]. $g_{Kr,max}$ was increased to reach this value. The pacemaker potential, which is the phase where the cells activate slowly towards depolarization, the MDP and thus the frequency is influenced by the current $I_{Ca,L}$. The maximum conductance of this current was adjusted in the human SAN model.
The heterogeneity of the SAN was implemented in the new model following the strategy of Garny et al. [387]. The method uses the parameters of the central and the peripheral cell to determine the characteristics of transitional cells. A scaling factor F_{cell} is calculated by:

$$F_{cell} = \frac{1.0309\, d_{cell}}{1 + 0.7745 \exp\left(-\frac{3d_{cell}-2.05}{0.295}\right)}$$

with the location d_{cell} of cells (d_{cell}=0 central; d_{cell}=1 peripheral). The variation of the maximum conductances in dependance of the position of the cell in the SAN is given by:

$$g_x = g_{x,cent} + F_{cell}\,(g_{x,peri} - g_{x,cent})$$

The maximum conductances of channel type x for central and peripheral cells $g_{x,cent}$ and $g_{x,peri}$, respectively, were set to the same ratio as in the ZRS model:

$$\frac{g_{x,cent}}{g_{x,peri}} = \frac{g_{x,cent,ZRS}}{g_{x,peri,ZRS}}$$

The parameters of central ($F_{\text{cell}} = 0$) and peripheral cells ($F_{\text{cell}} = 1$) are listed in tab. 10.2.
The CRN model considered intracellular Ca^{2+} handling including the sarcoplasmic reticulum (SR). The network SR (NSR) and the junctional SR (JSR) have the so-called uptake (V_{up}) and release volume (V_{rel}), respectively. The volumes of NSR and JSR were changed in the

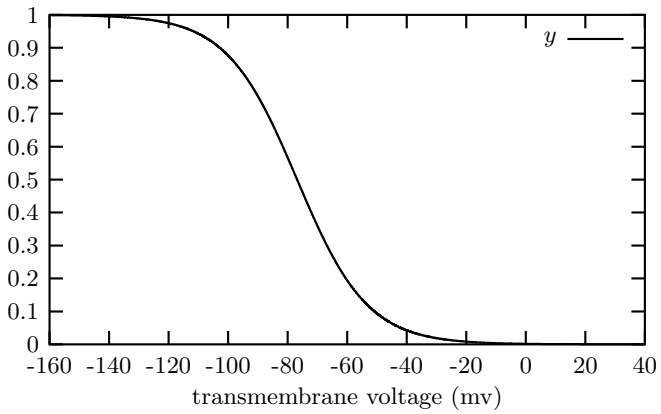

Fig. 10.9. Steady state characteristics of the activation variable y of the pacemaker current I_f in the ZRS model. Fig. from [371].

Table 10.2. Maximum conductances (in nS/pF) of the developed human sinoatrial node model in the center and the periphery.

	central cell	peripheral cell
$g_{Na,max}$	0.000	1. 552
$g_{Ca,L,max}$	0.197	0.510
$g_{Ca,T,max}$	0.214	0.214
$g_{to,max}$	0.144	0.329
$g_{sus,max}$	0.040	0.180
$g_{K,r,max}$	0.101	0.589
$g_{K,s,max}$	0.014	0.129
$g_{f,Na,max}$	0.022	0.105
$g_{f,K,max}$	0.022	0.105
$g_{b,Na,max}$	1.343×10^{-3}	0.341×10^{-3}
$g_{b,Ca,max}$	2.225×10^{-3}	2.248×10^{-3}
$g_{b,K,max}$	1.343×10^{-3}	1.341×10^{-3}

human SAN model compared to the CRN model, because the SR in SAN cells is smaller than in the atrial working myocardium [248]:

$$V_{up} = f_{up}V_{cell}, \qquad V_{rel} = f_{rel}V_{cell}$$

with the volume fraction of uptake and release part f_{up} and f_{rel}, respectively, and the cell volume V_{cell}. f_{up} and f_{rel} were adopted from data by Boyett [248] with $f_{up,cent}$=0.075, $f_{rel,cent}$=0.41, $f_{up,peri}$=0.06, and $f_{rel,peri}$=0.3. The varying volume fraction of cells in-between was considered by the scaling factor F_{cell}.

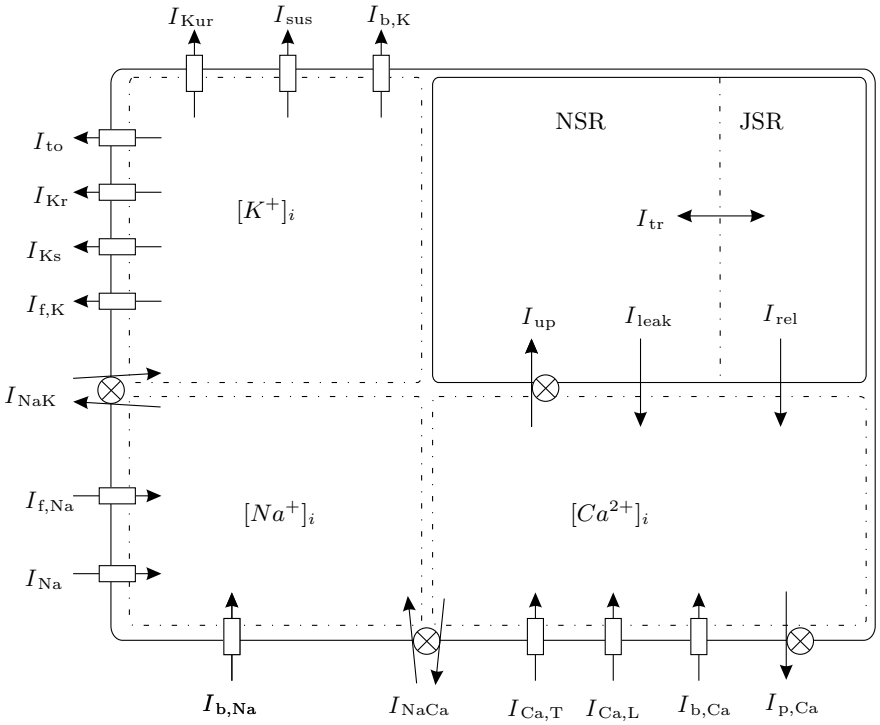

Fig. 10.10. Schematic description of the human SAN model. All implemented ionic currents and the SR with its two domains are shown. The NSR has an uptake and a leakage current I_{up} and I_{leak}, respectively, the JSR the Ca^{2+} induced Ca^{2+} release I_{rel}. Between NSR and JSR flows the translocation current I_{tr}. The arrows illustrate the direction of the ionic flow. The ionic currents are described in the text. Fig. from [371].

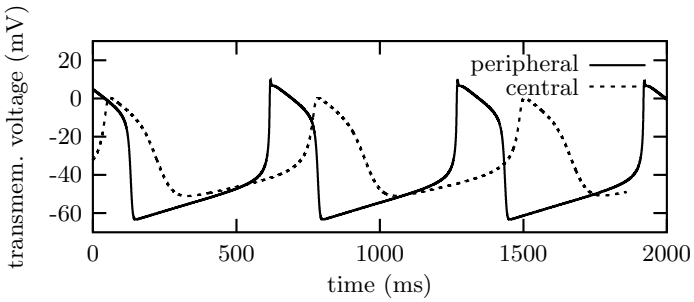

Fig. 10.11. Action potentials of the human sinoatrial node model for central and peripheral cells. Fig. from [371].

A schematic description of the new human SAN model, derived from the CRN model and the ZRS model, is depicted in fig. 10.10. The total membrane current I_{mem} is:

$$I_{mem} = I_f + I_{Na} + I_{to} + I_{sus} + I_{Kur} + I_{Kr} + I_{Ks} + I_{b,K} + I_{Ca,L} \\ + I_{Ca,T} + I_{p,Ca} + I_{b,Ca} + I_{NaK} + I_{NaCa} + I_{b,Na}$$

with I_f = Na^+ and K^+ pacemaker current; I_{Na} = fast Na^+ current; I_{to} = transient outward K^+ current; I_{sus} = sustained outward K^+ current; I_{Kur} = ultra rapid delayed outward K^+ current; I_{Kr} = rapid delayed outward K^+ current; I_{Ks} = slow delayed outward K^+ current; $I_{b,K}$ = background K^+ current; $I_{Ca,L}$ = L-type inward Ca^{2+} current; $I_{Ca,T}$ = T-type inward Ca^{2+} current; $I_{p,Ca}$ = Ca^{2+} pump outward current; $I_{b,Ca}$ = background Ca^{2+} current; I_{NaK} = current through the Na/K pump; I_{NaCa} = current through the Na/Ca exchanger; $I_{b,Na}$ = background Na^+ current.
The mathematical equations characterizing I_{Na}, I_{to}, I_{Kur}, I_{Kr}, I_{Ks}, $I_{Ca,L}$, $I_{p,Ca}$, $I_{b,Ca}$, I_{NaK}, and I_{NaCa} are adopted from the CRN model, the equations for $I_{Ca,T}$, $I_{b,K}$, I_{sus}, and I_f are inserted from the ZRS model. Special focus on the currents I_f, I_{to}, I_{sus}, $I_{Ca,L}$, and $I_{Ca,T}$ is given in section 10.3.1 – 10.3.3 to illustrate the influence of these currents.

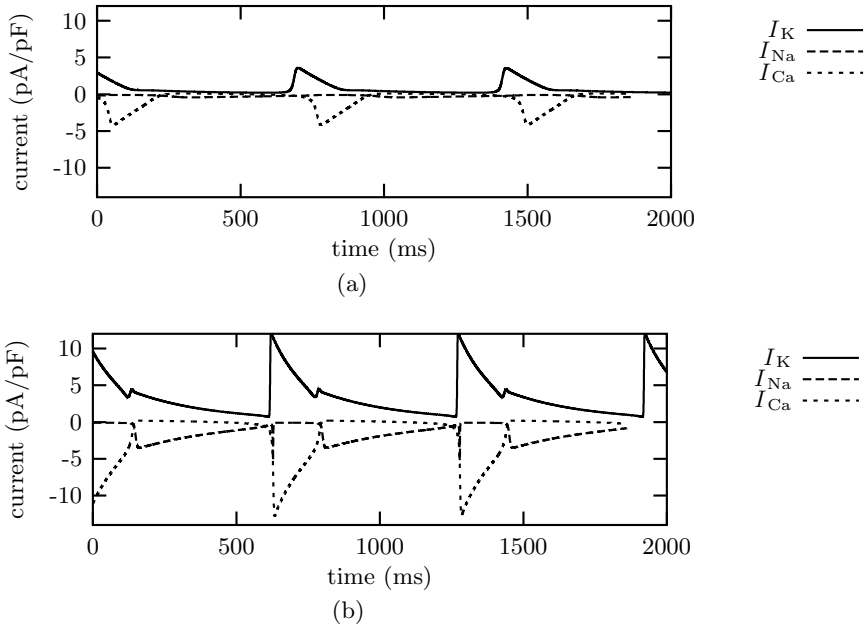

Fig. 10.12. Transmembrane currents of the human sinoatrial node model for (a) central and (b) peripheral cells. Depicted is the sum of all Na^+, the sum of all K^+, and the sum of all Ca^{2+} currents. Figs. from [371].

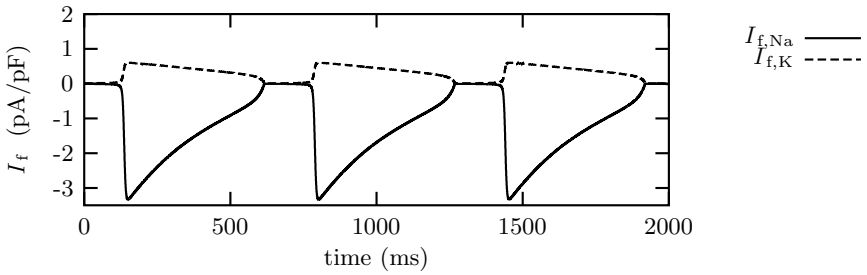

Fig. 10.13. The Na^+ and K^+ component of the pacemaker current I_f with $g_{f,max} = 0.105\,nS/pF$ in a peripheral cell. Fig. from [371].

The simulated transmembrane voltages for central and peripheral cells of human SAN are illustrated in fig. 10.11. The isolated central SAN cell had a lower frequency of auto-rhythmic activation ($1.256\,Hz$) than the peripheral ($1.435\,Hz$). The maximum diastolic potential (MDP) of a central cell is $-51.2\,mV$ and the overshoot $0.3\,mV$. The MDP of a peripheral cell is $-63.3\,mV$ and the overshoot is $9.7\,mV$. The measured values for peripheral cells are MDP $= -62.5 \pm 4.7$ mV and overshoot $= 9.8 \pm 2.7$ mV [170]. Measured values of central cells were not available and estimated by comparing the results with the ZRS model.
The total Na^+, K^+, and Ca^{2+} transmembrane currents for central and peripheral cells are shown in fig. 10.12 a and b, respectively. The amplitude of the ionic currents of central cells were smaller than of peripheral cells.

10.3.1 Characteristics of I_f

I_f is the hyperpolarization activated inward current, which is composed of a Na^+ and a K^+ component (section 4.7.1). Both components of the pacemaker current were calculated with the same gating variable y (fig. 10.9). The maximum conductances $g_{f,Na,max}$ and $g_{f,K,max}$ were also equal since the I_f channel is a protein, which is permeable for both ion types.

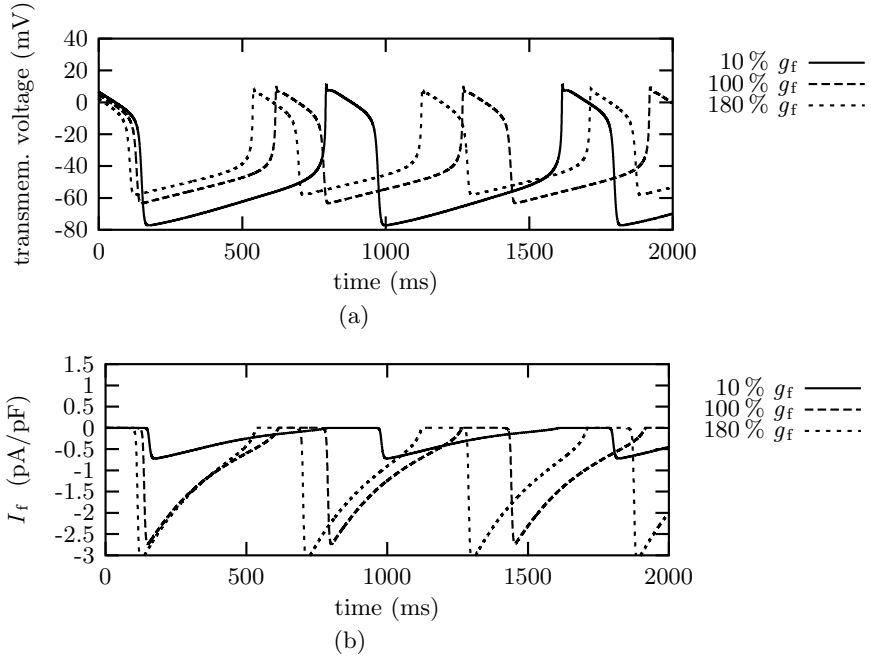

Fig. 10.14. Influence of the variation of I_f by changing the maximum conductance $g_{f,max}$ on (a) the transmembrane voltage V_m of a peripheral cell and (b) the total ionic current I_f. Figs. from [371].

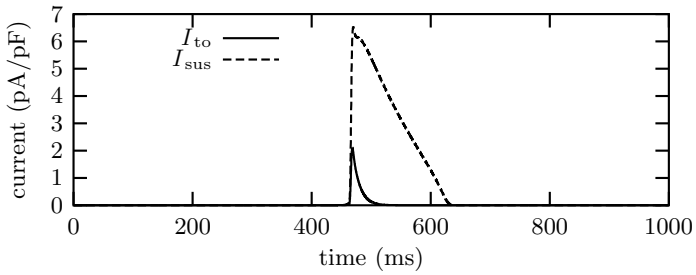

Fig. 10.15. Ionic currents of I_{to} and I_{sus} with $g_{to,max}$ and $g_{sus,max}$ each 100 % in a peripheral cell. Fig. adapted from [371].

The current of the two components of I_f are diplayed in fig. 10.13. The channel for I_f has a larger permeability for Na^+ than for K^+ for negative membrane voltages due to the positive reversal potential of Na^+ and the negative reversal potential of K^+. Therefore, the amplitude of the Na^+ outward current through the pacemaker channel was larger than the inward K^+ component leading to a spontaneous depolarization of the cell.
Varying the total $g_{f,max}$ influences the transmembrane voltage and the pacemaker current I_f itself as illustrated in fig. 10.14. A reduction of the current density of I_f led to a reduction in the frequency of the autorhythmicity and vice versa.

10.3.2 Characteristics of I_{to} and I_{sus}

I_{to} is the transient and I_{sus} the sustained outward K^+ current (section 4.3.1). Both are responsible for the early phase of repolarization. The AP of cells having strong components of these channels show a prominent "spike-and-dome" morphology. The early repolarization characteristics due to I_{to} and I_{sus} was only prominent in peripheral SAN cells (tab. 10.2). I_{to} had a lower amplitude and a shorter duration than I_{sus} (fig. 10.15).

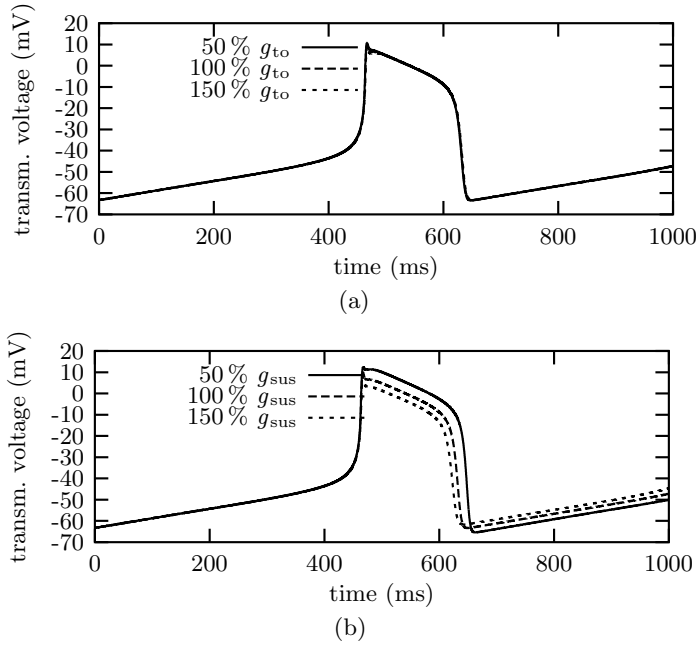

Fig. 10.16. Influence of the variation of the ionic currents I_{to} und I_{sus} by changing the maximum conductance $g_{to,max}$ and $g_{sus,max}$ in a model of a peripheral cell. (a) Transmembrane voltage changes with $g_{to,max}$ variations. (b) Transmembrane voltage changes with $g_{sus,max}$ variations. Figs. from [371].

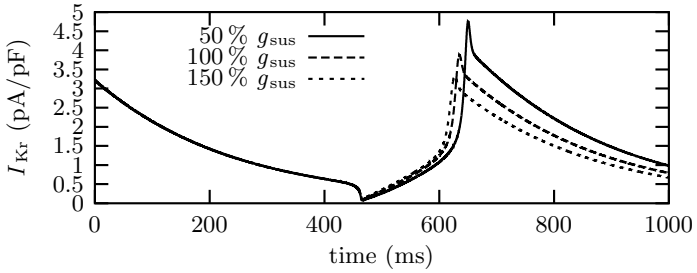

Fig. 10.17. Rapid delayed rectifier K^+ current I_{Kr} during variation of $g_{sus,max}$ in a peripheral human SAN cell. The amplitude of I_{Kr} rises if $g_{sus,max}$ was decreased. Fig. from [371].

The changes in the transmembrane voltage due to a variation in the maximum conductance of $g_{to,max}$ is depicted in fig. 10.16 a for a peripheral SAN cell. The changes of $g_{to,max}$ by $\pm 50\,\%$ had nearly no influence on the AP. The influence of $g_{sus,max}$ is shown in fig. 10.16 b. If $g_{sus,max}$ was reduced by 50 % the overshoot was larger, the early phase of repolarization had a smaller "spike-and-dome" morphology, the MDP was more negative, and the APD was longer. The characteristics were vice versa for increased $g_{sus,max}$.
It was expected that the MDP should be less negative if the outward K^+ current I_{sus} is reduced. This assumption is based on I_{sus} being responsible for phase 1 and 2 of the repolarization but not for phase 3. This phase is mainly influenced by the rapid delayed rectifier K^+ outward current I_{Kr}. If $g_{sus,max}$ was reduced the plateau phase was prolonged. This led to an increase in the amplitude of I_{Kr} (fig. 10.17), and thus to a stronger repolarization phase 3 with a more negative MDP.

10.3.3 Characteristics of $I_{Ca,L}$ und $I_{Ca,T}$

The L-type and T-type Ca^{2+} inward currents influence phase 2 and determine the duration of the AP. The T-type Ca^{2+} current was included with the original equations of the ZRS model

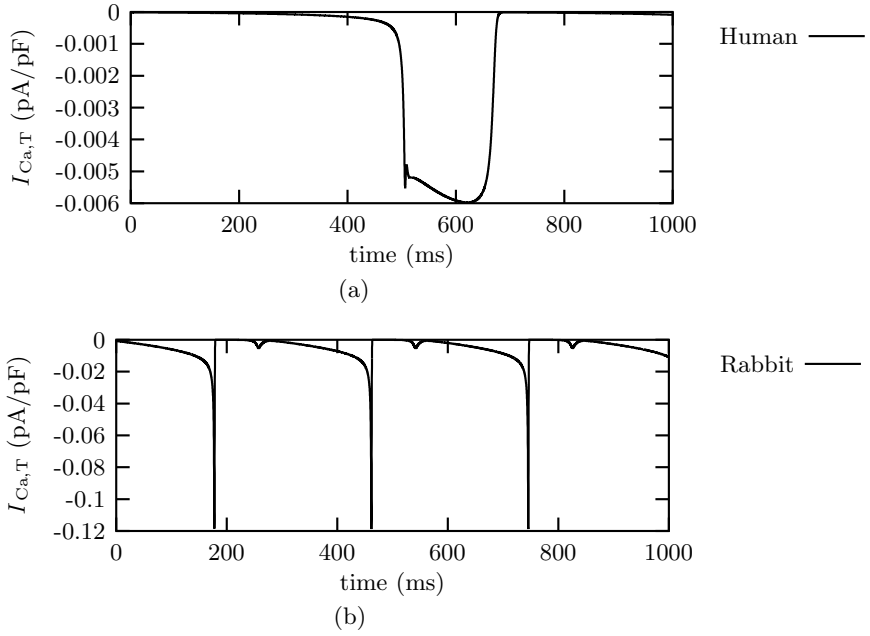

Fig. 10.18. $I_{Ca,T}$ in a peripheral cell of human (a) and rabbit (b) sinoatrial node during an AP. Figs. from [371].

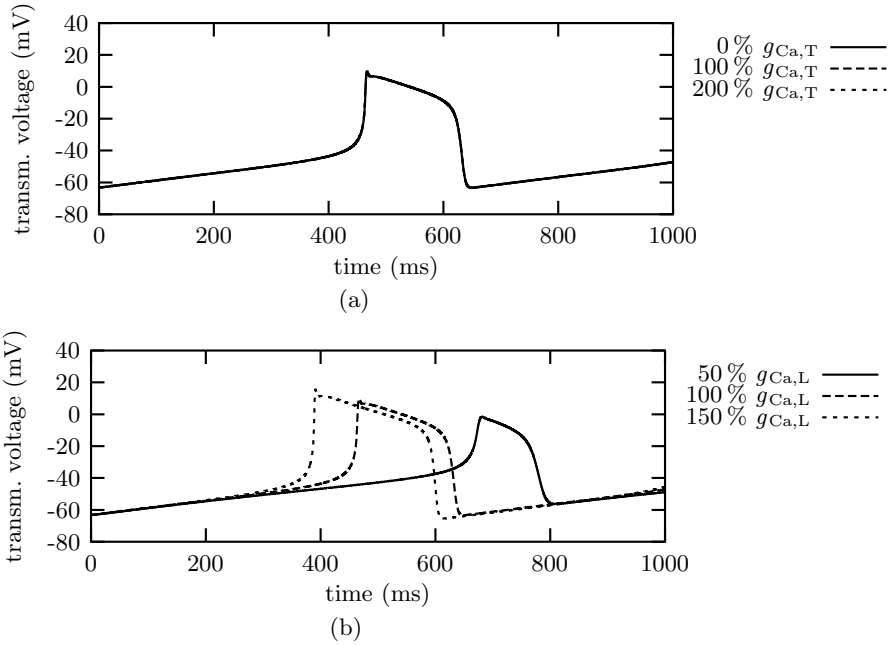

Fig. 10.19. Influence of variation of the ionic currents $I_{Ca,T}$ und $I_{Ca,L}$ of a peripheral cell of a human SAN on the transmembrane voltage by changing $g_{Ca,T,max}$ and $g_{Ca,L,max}$. (a) Variation of $g_{Ca,T,max}$. (b) Variation of $g_{Ca,L,max}$. Figs. from [371].

for rabbit sinoatrial node because of the lack of human $I_{Ca,T}$ measurement data. $I_{Ca,T}$ for human and rabbit peripheral SAN cells is illustrated in fig. 10.18 having the same equations but different characteristics due to the differences in the other ionic currents. The amplitude of $I_{Ca,T}$ in human SAN cells was small compared to the amplitude of rabbit $I_{Ca,T}$ but the duration was much longer.
Large changes in the maximum conductance $g_{Ca,T,max}$ have nearly no influence on the morphology of the AP (fig. 10.19 a). This might be due to the adoption of the parameters of activation and inactivation of the T-type Ca^{2+} channel from rabbit SAN cells.
The influence of $I_{Ca,L}$ on the pacemaker AP is illustrated in fig. 10.19 b. The steepness of the second phase of the pacemaker potential was slightly reduced if $g_{Ca,L,max}$ was reduced by 50 % but the AP was nevertheless triggered later. The APD was shortened compared to a $g_{Ca,L,max}$ of 100 %. The characteristics were vice versa when increasing $g_{Ca,L,max}$.

10.4 Heterogeneous Atrial Electrophysiology

Experimental measurements of atrial tissue from different anatomical regions of canine show electrophysiological differences (section 4.7.2) [174]. The heterogeneity of the atrial working myocardium was implemented in the model of Courtemanche et al. [238] based on these data. In addition, the modeling approach of Ramirez and coworkers [246] reproducing heterogeneous canine electrophysiology was considered. The transmembrane voltages of the differing tissue classes of the measured data and the simulations are depicted in fig. 10.20. The heterogeneity

Table 10.3. Maximum conductance (in nS/pF) of I_{to}, $I_{Ca,L}$ and I_{Kr} for different atrial tissue types.

	PM	CT	APG	AVR
$g_{to,max}$	0.1652	0.2115	0.1123	0.1652
$g_{Ca,L,max}$	0.1238	0.2067	0.1312	0.0829
$g_{Kr,max}$	0.0294	0.0294	0.0294	0.0449

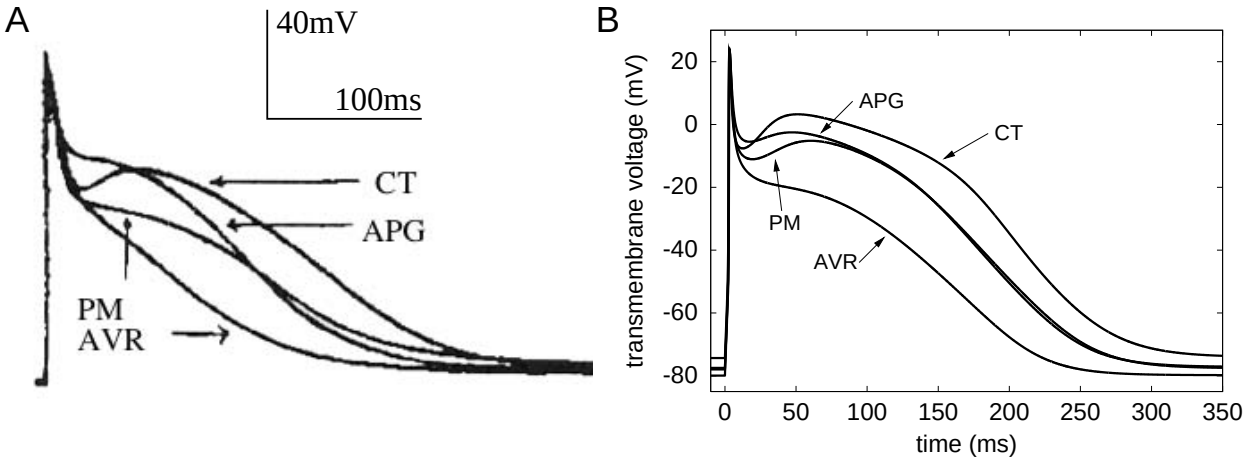

Fig. 10.20. Heterogeneous atrial action potentials of crista terminalis (CT), pectinate muscles (PM), appendage (APG), and atrioventricular ring (AVR). A: Measurement data of Feng et al. [174] from canine atrium. B: Simulated AP heterogeneity by adopting parameters given by Feng et al. [174] to the Courtemanche et al. [238] atrial ionic model of human electrophysiology (parameters see tab. 10.3). Fig. from [343].

of the different APs was reproducible by changing maximum conductances of the currents I_{Kr}, I_{to}, and I_{CaL} (tab. 10.3).
The AP of a cell of the atrioventricular ring had the shortest APD_{90} ($193\,ms$). The APD prolonged from appendage ($231\,ms$) over pectinate muscles ($234\,ms$) to crista terminalis ($265\,ms$). The measurement data of Feng et al. concerning APD is depicted in tab. 4.3. The variation of APD was reproduced in the simulations. The prominent "spike-and-dome" morphology of measured AP in crista terminalis was also present in the simulated data.

10.5 Ventricular Electrophysiology

A model reconstructing transmural heterogeneous electrophysiology in the human left ventricle is described in this section. The description is based on the ionic model of Priebe and Beuckelmann (PB, section 5.5.5) [242]. The parameters of the PB model are describing human ventricular electrophysiology based on measurement data. The disadvantage of the PB model is, that the origin of the employed measurement data within the ventricular wall is either not known or some are from subendocardial and some from subepicardial regions. The aim of designing an adapted PB model was to overcome these disadvantages by implementing the electrophysiological behavior of subendocardial, subepicardial, and M cells based on experimental data from transmurally different regions and including recently published human measurement data.
Most of the rate constants (α_{yi} and β_{yi}) describing the gating mechanism of ionic channels (section 5.1.1) were found in the adopted model by the relationship $\alpha_{yi} = \frac{F_{1\alpha yi}}{F_{2\alpha yi}}$ and $\beta_{yi} = \frac{F_{1\beta yi}}{F_{2\beta yi}}$ [388]. The functions F_i are based on Boltzmann-type equations with the best fit of voltage and time dependencies to experimental data:

$$F_i = a \exp\left[b\,(V_m + c) + d\right] + e \tag{10.1}$$

with the transmembrane voltage V_m, and the parameters a, b, c, d, and e.
Measurement data of the channel kinetics of the currents I_{to}, I_{Ks}, I_{K1}, and I_{Kr} of human myocytes were used to adapt the ionic model of Priebe and Beuckelmann. Furthermore,

Table 10.4. Maximal conductivity of the heterogeneous currents I_{to}, I_{Ks}, I_{K1}, and I_{NaCa} for subendocardial, subepicardial and M cells.

	Subendocardium	M cell	Subepicardium
$g_{to,max}$	0.1301	0.4527	0.5204
$g_{Ks,max}$	0.0382	0.0076	0.0415
$g_{K1,max}$	0.41	0.415	0.5
$k_{NaCa,max}$	720	1080	1000

the presented measurement data concerning heterogeneous density of ion channels were considered in the modifications (section 4.7.3). The results of these reports present differing peak currents due to heterogeneity as well as voltage clamping and voltage step protocols to demonstrate the kinetics and varying density of the ion channels.
The densities and kinetics of ion channels were reconstructed with numerical experiments within the mathematical model. The environmental conditions for the simulations were adopted from the published measurement conditions and described later on. The optimal values for the parameters of the channel characteristics were found using a gradient optimization method to minimize the root mean square error between measured and simulated data as described in section 9.1.3. With this method, the characteristics of the currents I_{to}, I_{Ks}, and I_{K1} were categorized. The current I_{Kr} was also adapted with this method to measurements of human myocytes, but it had no heterogeneous characteristics [117, 178, 179]. The gating parameters for I_{NaCa} were left unchanged, but the maximum conductance g_{NaCa} was adapted regarding the cell type to reflect heterogeneous characteristics (tab. 10.4).

10.5.1 Adaption of I_{to}

The product of two gating variables, r and t, models the fraction of open channels of current I_{to}. The adjustment of the kinetics of I_{to} was based on the measurement data of Näbauer et al. in subendocardial and subepicardial human left ventricular tissue shown in fig. 10.21 [389]. In addition, the measurements show a maximum current that is four times larger in subepicardial cells compared to subendocardial cells.
The measurements as well as the simulations were performed from a holding potential of $-80\,mV$, followed by a $100\,ms$ prepulse at $-60\,mV$. Afterwards, the transmembrane voltage was stepped from –30 to $80\,mV$ for $500\,ms$ [389]. Table 10.5 lists the parameters of the Boltzmann-type function F_i of eq. 10.1 for the gating variables r and t for the optimal fit of simulated to measured data. Figure 10.22 illustrates the time and voltage dependence of the current density for subepicardial, subendocardial and M cells in the simulation. These results corresponded to measured data of subendocardial and subepicardial cells of Näbauer et al. (fig. 10.21) [389].
The root mean square error E_{RMS} for subepicardial cells was smallest ($0.56\,pA/pF$) within this configuration if the maximum conductance was $0.5204\,nS/pF$. The smallest E_{RMS} for subendocardial cells with $0.138\,pA/pF$ was achieved using a maximum conductance of $0.1301\,nS/pF$. The maximum conductance of M cells was set with the help of other experimental data from canine and human right ventricular myocardium [175, 176]. Both measurements show that the maximum conductance of M cells is nearly 87 % of the subepicardial value. Thus, the maximum conductance of M cells was set to $0.4527\,nS/pF$ (tab. 10.4).

10.5.2 Adaptation of I_{Kr} and I_{Ks}

The parameters of the two components of the delayed inward rectifier potassium current I_K were adapted with the help of the measurements of human cardiomyocytes of Li et al.

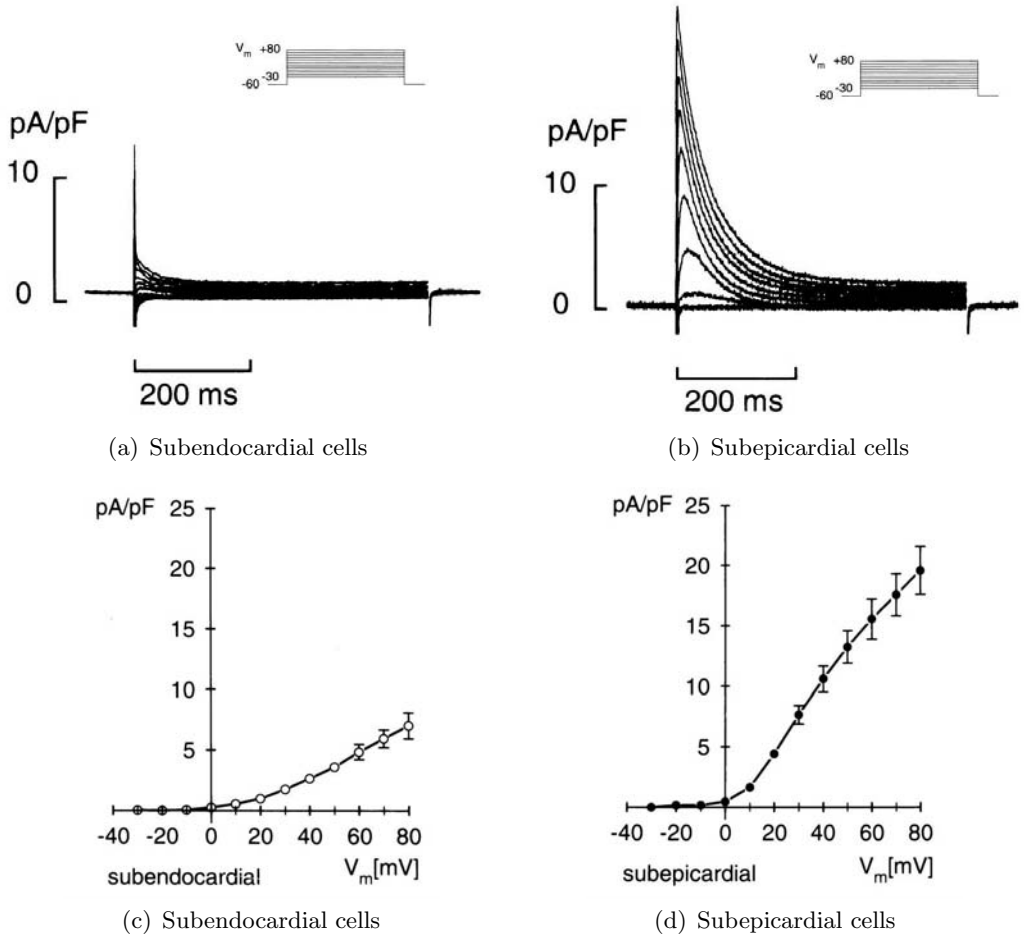

(a) Subendocardial cells

(b) Subepicardial cells

(c) Subendocardial cells

(d) Subepicardial cells

Fig. 10.21. I_{to} measurements of Näbauer et al. to determine the characteristics and ion current density of this heterogeneous distributed channel. The left figures depict the measurements of subendocardial cells, the right ones those of subepicardial myocytes. (a) and (b): Course of current I_{to} during voltage protocol. The maximum peak differs largely between both cell types, but the temporal characteristics are nearly the same. (c) and (d): Maximum peak currents minus the steady state currents at the end of the voltage protocol in dependence on the holding voltage. Figs. from [389].

(fig. 4.15) [175]. The measurement data was assumed to be of midmyocardial cells. The environmental conditions and voltage step protocols identical to the measurements were chosen for the simulations. The initial holding potential was $-60\,mV$. The current I_{Kstep} was elicited during a $3\,s$ lasting voltage step to values between $-40\,mV$ and $+60\,mV$. The subsequent repolarization step to $-30\,mV$ activated the current I_{Ktail}. I_{Kstep} and I_{Ktail} are illustrated in fig. 10.23 A and B for I_{Kr} and I_{Ks}, respectively. The current-voltage relationship of I_{Ktail} in fig. 10.23 C shows agreement of measured and simulated data. Tab. 10.5 lists the parameters of the Boltzmann-type function F_i of eq. 10.1 for the rate constants of I_{Kr} and I_{Ks}, respectively. I_{Kr} was described differently in this model as compared to the original Priebe-Beuckelmann model by:

$$I_{Kr} = g_{Kr}\frac{1}{F_{CIKr}}X_r(V_m - E_K)$$

with the maximum conductance g_{Kr}, additional voltage dependency F_{CIKr} as in eq. 10.1, the gating variable X_r, and the Nernst potential for potassium E_K. The parameters for the additional voltage-dependency F_{CIKr} are listed in tab. 10.5.

The root mean square error E_{RMS} of the adaptation procedure was $0.0132\,pA/pF$ for I_{Ks} and $0.00643\,pA/pF$ for I_{Kr}. For these values, the maximum conductances of I_{Ks} and I_{Kr} were $g_{Ks,max} = 0.0191\,nS/pF$ and $g_{Kr,max} = 0.0159\,nS/pF$, respectively, for midmyocardial cells. Liu and colleagues identified in canine experimentally that I_{Ks} was nearly the same in subendocardial and subepicardial cells but reduced to 50 % in M cells [179]. The selected maximum conductances for subendocardial and subepicardial based on these findings were $g_{Ks,max} = 0.0382\,nS/pF$ in subendocardial and $g_{Ks,max} = 0.0415\,nS/pF$ in subepicardial cells. Liu et al. showed in their experiment that the maximum conductance of I_{Kr} is nearly homogeneously distributed throughout the ventricles. Hence, the maximum conductance from M cells was used to define the corresponding value for the other cell types.

10.5.3 Adaption of I_{K1}

Figure 10.23 D shows the current-voltage relationship of I_{K1}. Wang et al. provided the measured data of human myocytes (fig. 4.5 a) [126]. In the measurements as well as the simulations, the currents were simulated with $300\,ms$ lasting voltage steps from the holding voltage of $-20\,mV$ to between $-140\,mV$ and $+10\,mV$. The exact fit of the parameters to

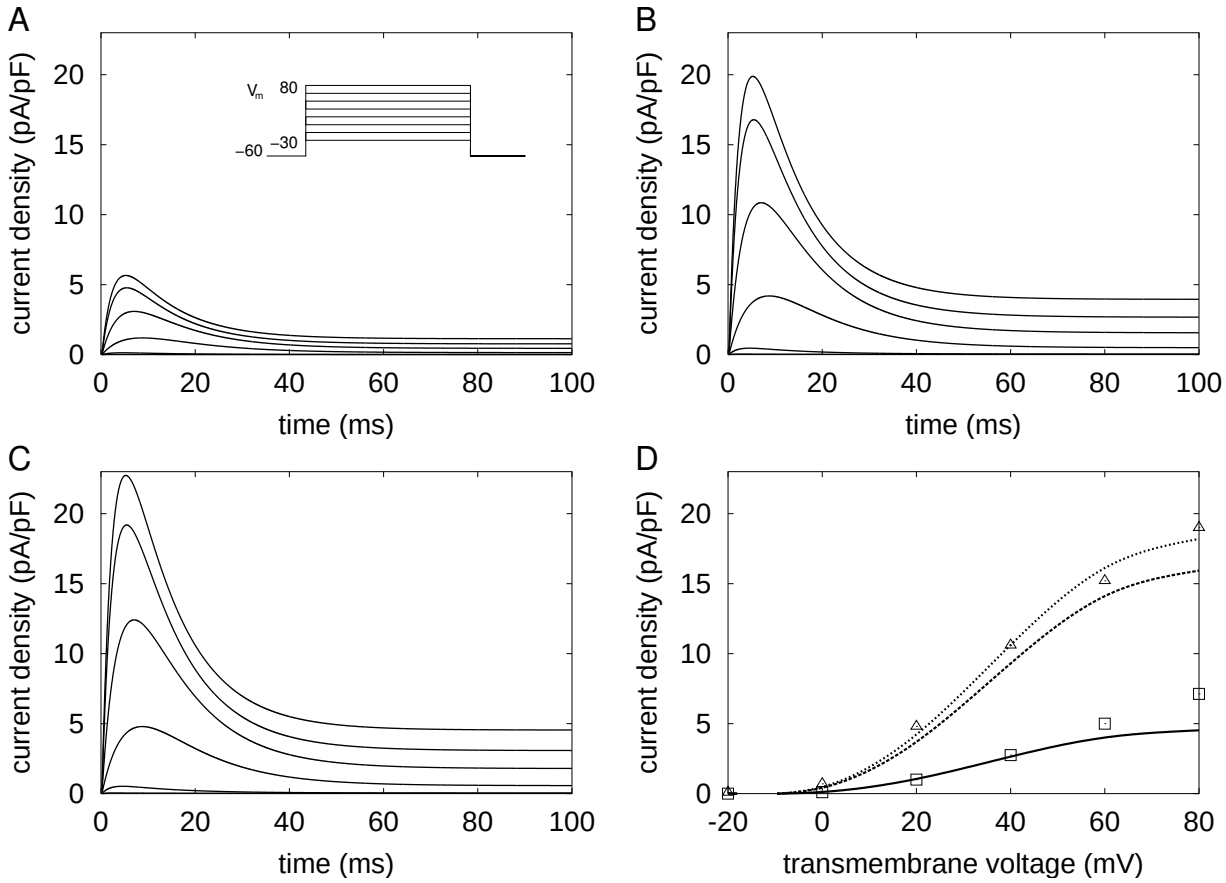

Fig. 10.22. Simulation characteristics of the ionic current I_{to}. A, B, and C demonstrate simulated current data due to the voltage protocol (inset) for subendocardial (A), midmyocardial (B), and subepicardial (C) myocytes. These results correspond to measurement data (fig. 10.21) [389]. D: Measured and simulated current densities depending on voltage and location of the myocyte. The solid line and the boxes illustrate the results of the simulation and the measurement in subendocardial cells, respectively. Simulation data for M cells is presented with the dashed line. No measurement data is available for these cells. The subepicardial data is depicted by a dotted line (simulation) and triangles (measurement). The current is measured as the difference between absolute peak current and steady state value at end of a clamp pulse. Fig. from [390].

Table 10.5. Adjusted rate constants of the gating variables for the currents I_{to} (r and t), I_{Ks} (X_s), and I_{Kr} (X_r) and I_{K1}. The parameters belong to the rate constant relationship in eq. 10.1.

	a	b	c	d	e
$F_{1\alpha r}$	0.5266	–0.01394	–53.2869	0	0
$F_{2\alpha r}$	1	–0.07544	–53.2869	0	1
$F_{1\beta r}$	0.5149	–0.16128	–3.11768	0	$0.00006 \cdot V_m$
$F_{2\beta r}$	1	–0.1348	–0.00006	0	1
$F_{1\alpha t}$	0.0721	–0.13148	26.0324	0	$0.00007 \cdot V_m$
$F_{2\alpha t}$	1	–0.237871	26.0324	0	1
$F_{1\beta t}$	0.0767	$-1.6 \cdot 10^{-9}$	34.0235	0	$0.0001215 \cdot V_m$
$F_{2\beta t}$	1	–0.1604	34.0235	0	1
$F_{1\alpha Xr}$	0.005	0.00044761	2.23685	0	0
$F_{2\alpha Xr}$	1	–0.10727	2.23685	0	0
$F_{1\beta Xr}$	0.016	0.00232	55.811	0	0
$F_{2\beta Xr}$	1	0.066555	55.811	0	0
F_{CIKr}	1	0.023913	29.9	0	1
$F_{1\alpha Xs}$	0	0	0	0	0.003013
$F_{2\alpha Xs}$	1	–0.0593696	13	0.1888755	1
$F_{1\beta Xs}$	0	0	0	0	0.005875
$F_{2\beta Xs}$	1	0.0537295	10	0.3676411	1
$F_{1\alpha K1}$	0	0	0	0	0.3
$F_{2\alpha K1}$	1	0.06	$-206 - E_K$	0	1
$F_{1\beta K1}$	3	0.0002	$94 - E_K$	0	0
$F_{2\beta K1}$	1	0.191	$-16 - E_K$	0	0
$F_{3\beta K1}$	1	–0.5	$4 - E_K$	0	10

reach the measured data produced an APD_{90} of $430\,ms$, which is too long and leads to a non-electrophysiological resting voltage ($-72\,mV$). We decided to adjust the voltage depending parameters by $6\,mV$ after the fitting process. This led to a resting voltage of $-80\,mV$ and a reasonable APD for each of the three main differing cell types. In the adapted Priebe-Beuckelmann model, I_{K1} is described by:

$$I_{K1} = g_{K1}\frac{\alpha_{K1}}{\alpha_{K1} + \beta_{K1}}(V_m - (E_K + V_s))$$

with the maximum conductance g_{K1}, the rate constants α_{K1} and β_{K1}, and the shift voltage V_s of $6\,mV$. Table 10.5 gives the parameters for the rate constants $\alpha_{K1} = \frac{F_{1\alpha K1}}{F_{2\alpha K1}}$ and $\beta_{K1} = \frac{F_{1\beta K1}+F_{2\beta K1}}{F_{3\beta K1}}$.

The minimization procedure delivered a E_{RMS} of $0.3535\,pA/pF$ when using the parameters given in tab. 10.5 in combination with the maximum conductance $g_{K1,max} = 0.5\,nS/pF$. Since the measurement data of Wang and coworkers [126] was from subendocardial myocytes, this value was addressed to the same region in the model. Measurement data showed, that the current density of I_{K1} is 2 % larger in M cells and 22 % larger in subepicardial cells compared to subendocardial myocytes [175]. Hence, the maximum conductance was set to $g_{K1,max} = 0.61\,nS/pF$ for subepicardial and to $g_{K1,max} = 0.51\,nS/pF$ for M cells.

10.5.4 Adaptation of I_{NaCa}

To date, no measurement data depicting the heterogeneous properties of the human Na/Ca exchanger is published. The Priebe-Beuckelmann model uses the description of I_{NaCa} from the Luo-Rudy model (section. 5.5.2), which is describing guinea-pig ventricular electrophysiology. Zygmunt et al. identified recently that the density of Na/Ca exchangers is varying in canine ventricle. The midmyocardial density is increased by 8 % compared to the subepicardium and decreased to 72 % in subendocardial myocardium. These gradients were adopted

in the heterogeneous model by adjusting the scaling factor $k_{NaCa,max}$ of the Na/Ca exchanger. $k_{NaCa,max}$ was set to 1000 for subepicardial cells as well as to 1080 and 720 for M and subendocardial cells, respectively.

10.5.5 Heterogeneous Action Potential Characteristics

Table 10.4 lists the chosen maximum conductances for the currents I_{to}, I_{Ks}, I_{K1} and I_{NaCa} of subendocardial, subepicardial and M cells. These values were set with the help of the presented numerical experiments and led to the measured peak currents presented in tab 4.4. The extracellular potassium concentration $[K^+]_o$ was set to 5.4 mM for the simulations based on the human experimental data reported by Rasmusson et al. [391]. Preliminary calculations of at least 100 cycles with the given basic cycle length (BCL) were performed prior to the start of the experiments to achieve appropriate initial values for the different models.
With this configuration, the results of the simulations were not yet consistent with measured data where the APD was investigated concerning BCL. The APD_{90} remained constant at a

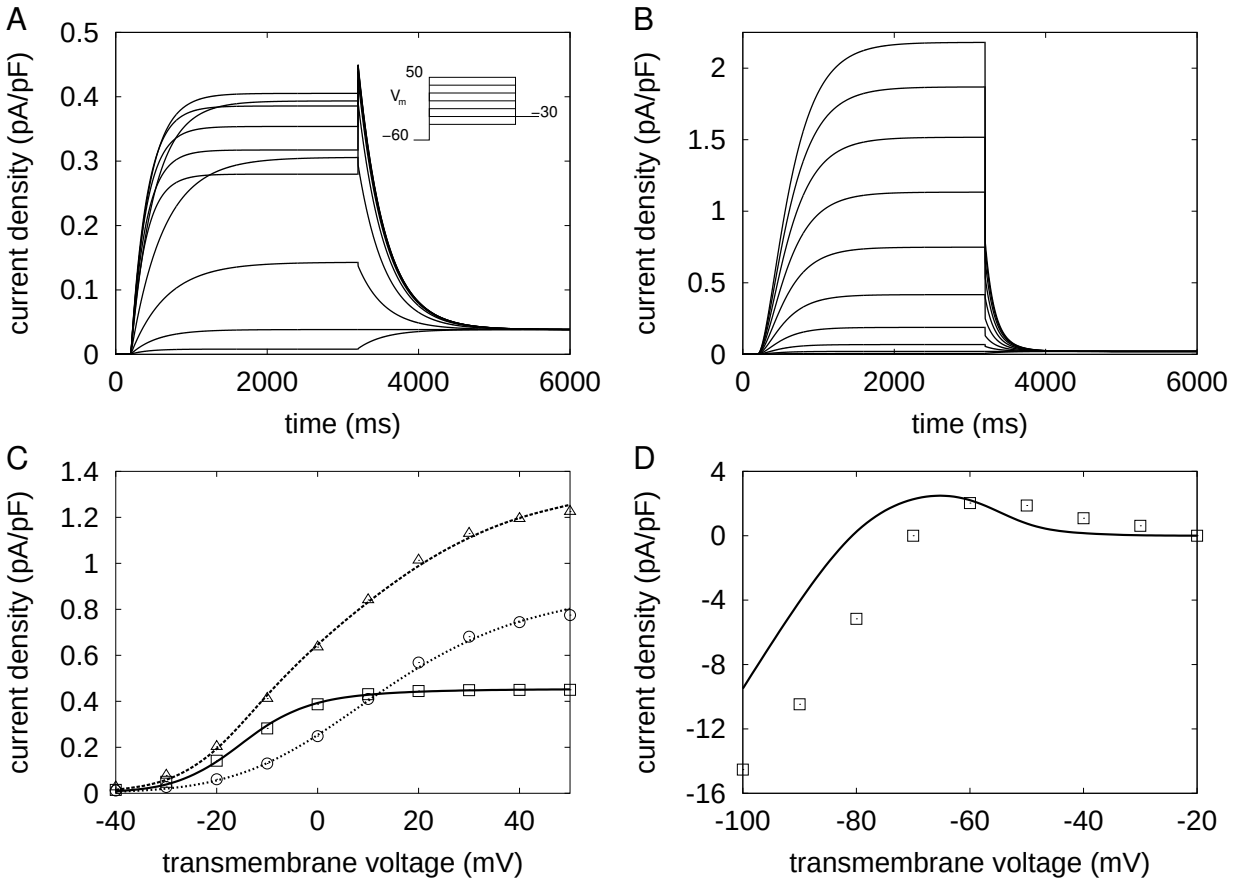

Fig. 10.23. Voltage step simulations of the currents I_{Kr}, I_{Ks}, and I_{K1}. A and B show the voltage dependency of I_{Kr} (A) and I_{Ks} (B) due to the voltage protocol demonstrated in the inset. The first phase of each figure illustrates the time dependency of the current I_{Kstep}, the second phase that of I_{Ktail}. C: Current-voltage relationship for I_{Ktail}. Solid lines and boxes represent the simulated and measured data for I_{Kr}, respectively. The dotted line and the circles are the equivalent values for I_{Ks}. The dashed line and the triangles are the sum of both components, hence I_K. Measurement data is taken from Li et al. [175]. D: Current-voltage relationship of I_{K1} for measured (boxes) and simulated (solid line) data. Wang et al. acquired the measurement data [126]. For the explanation of the differences between measured and simulated data, see text. Fig. from [390].

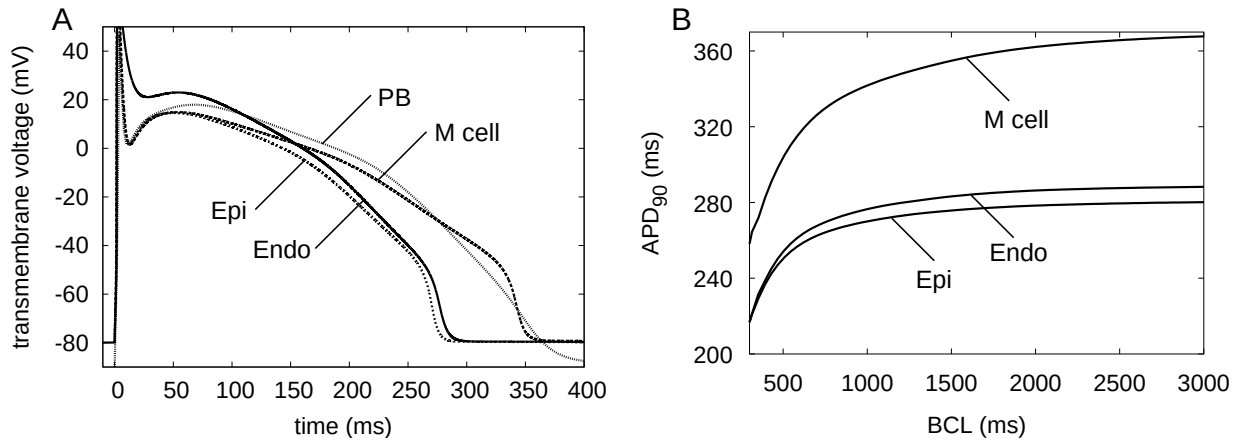

Fig. 10.24. AP characteristics of the three ventricular cell types from subendocardium (Endo), subepicardium (Epi), and midmyocardium (M cell). A: AP of the three cell types in comparison to the original Priebe-Beuckelmann (PB) model. B: Simulated APD restitution for the three different myocytes after X_{S2} gate inclusion.

BCL greater than $500\,ms$, but the APD should increase further when BCL increases. During slow excitation, the APD prolongs more in M cells than in endocardial or epicardial cells.
To avoid the inadequate characteristics of the model concerning BCL the activation process of the slow delayed inward rectifier current I_{Ks} was adopted from the model of Viswanathan et al. [258]. They described the activation process with a fast X_{S1} and a slow X_{S2} component, while X_{S1} is the original gate of I_{Ks}. The time constant of X_{S2} was set to four times the time constant of X_{S1}. The steady state properties for X_{S2} were the same as those of X_{S1}.
In addition, the maximum conductance of the slow delayed rectifier K^+ current I_{Ks} was reduced further by 60 % in the model of midmyocardial cells to achieve the measured APD in these myocytes. Hence, $g_{Ks,max}$ in M cells was set to $0.00764\,nS/pF$.
The action potentials in fig. 10.24 A show the characteristic variation between the three cell types. In order to compare the adopted model with its origin, the Priebe-Beuckelmann model is also illustrated in fig. 10.24 A. The M cells and epicardial cells showed the characteristic notches in repolarization phase 1. When stimulating with a frequency of $1\,Hz$, the action potential duration to 90 % repolarization (APD_{90}) was $272\,ms$ in endocardial, $343\,ms$ in midmyocardial, and $265\,ms$ in epicardial myocytes. The resting voltage was for all three cell types $-80\,mV$. The values of APD_{90} with respect to BCL are shown in fig. 10.24 B. The shape demonstrates the increasing APD_{90} with increasing BCL due to the included X_{S2} gate. The APD_{90} of M cells increased more than that of endocardial or epicardial cells for a BCL $>$ $1000\,ms$.

10.6 Tension Development Model

A hybrid tension development model (HTD) was developed during the course of this work (section 9.1.2) [344, 307, 345, 346]. The model consists of 14 state variables incorporated in three coupled Markov chain models describing the three components troponin, tropomyosin, and actin-myosin interaction. A schematic description of the model is shown in fig. 10.25. The XB–Tn, XB–XB, and Tm–Tm cooperativity mechanisms (section 6.6) were included in the model such that they influence specific transition probabilities between states depending on other states and transitions.

10.6.1 Components

The state variables T and TCa depict the binding process of Ca^{2+} to troponin. T is the fraction of troponin C with no bound Ca^{2+}, TCa with bound Ca^{2+}. The sum of the state variables is defined as one:

$$T + TCa = 1$$

The variation of the binding process was described together with the transition coefficients k_{on} and k_{off} by a system of coupled differential equations of first order:

$$\frac{\mathrm{d}}{\mathrm{d}t}\begin{pmatrix} T \\ TCa \end{pmatrix} = \begin{pmatrix} -k_{on} & k_{off} \\ k_{on} & -k_{off} \end{pmatrix}\begin{pmatrix} T \\ TCa \end{pmatrix}$$

The characteristics of k_{on} are influenced by the concentration of intracellular Ca^{2+}, the amount of cross-bridges XB, and the sarcomere stretch λ.
The configuration of tropomyosin is described by the state variables TM_{off} and TM_{on}. TM_{off} is the fraction of tropomyosin in the non-permissive situation and TM_{on} in the permissive. This process is given by:

$$TM_{on} + TM_{off} = 1$$

If tropomyosin is shifted from its resting position due to the binding of calcium to troponin, tropomyosin is in the permissive ("on") position and the myosin binding sites of actin are available. The process of shifting tropomyosin is controlled by the transition coefficients tm_{on} and tm_{off}. tm_{on} depends on the fraction of bound calcium to troponin TCa and the sarcomere stretch λ. This system is also described by a differential equation:

$$\frac{\mathrm{d}}{\mathrm{d}t}\begin{pmatrix} TM_{on} \\ TM_{off} \end{pmatrix} = \begin{pmatrix} -tm_{on} & tm_{off} \\ tm_{on} & -tm_{off} \end{pmatrix}\begin{pmatrix} TM_{on} \\ TM_{off} \end{pmatrix}$$

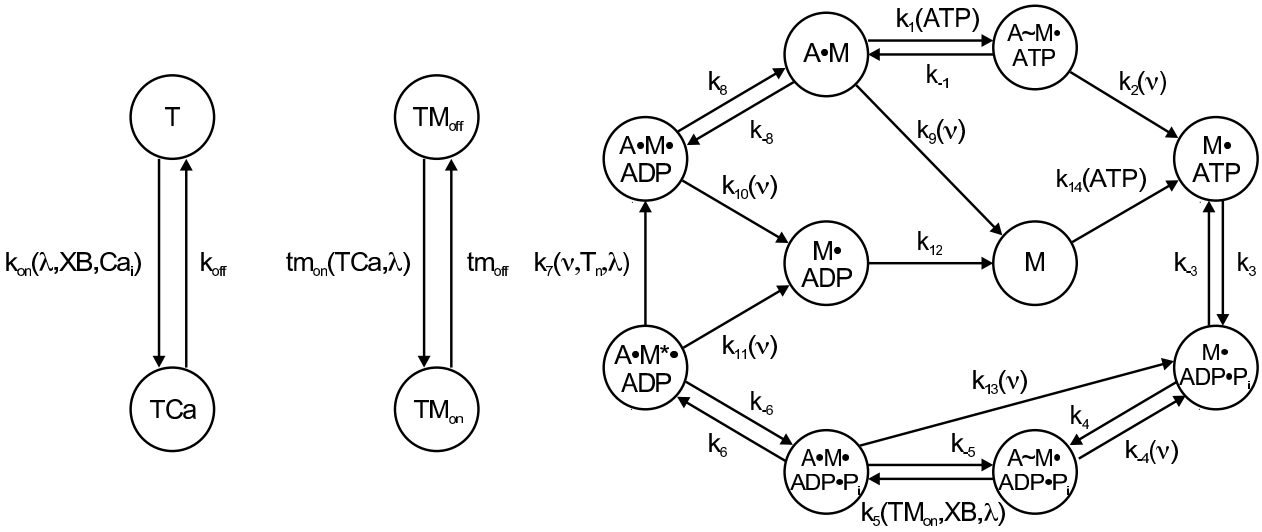

Fig. 10.25. State diagram of the new hybrid tension development (HTD) model. The left Markov chain shows the two states variables T and TCa indicating the binding of calcium to troponin. The middle Markov model depicts the state variables TM_{off} and TM_{on} quantifying the configuration of tropomyosin. The right Markov chain illustrates the cross-bridge cycle including the hydrolysis of ATP with ten state variables. These states represent the interaction of actin A to myosin M and ATP, ADP, and phosphate P_i with strong $\bullet$ and weak $\sim$ bindings. The transition rates depend on the sarcomere stretch λ, the stretch velocity ν, the amount of ATP, the amount of cross-bridges XB, the fraction of shifted tropomyosin TM_{on}, the amount of calcium bound to troponin TCa, the intracellular Ca^{2+} concentration Ca_i, and the normalized tension T_n itself.

If tropomyosin is shifted, actin and troponin interact leading to the cross-bridge cycle. This process is given by ten state variables:

$$M + A \sim M \bullet ATP + M \bullet ATP + M \bullet ADP \bullet P_i + A \sim M \bullet ADP \bullet P_i + A \bullet M \bullet ADP \bullet P_i + A \bullet M^* \bullet ADP + A \bullet M \bullet ADP + A \bullet M + M \bullet ADP = 1$$

with actin A, myosin M, strong binding $\bullet$, and weak binding $\sim$. The hydrolysis of ATP into ADP and phosphate P_i is considered in the system. The interaction of the state variables is given by a system of coupled differential equation of first order:

$$\frac{\mathrm{d}}{\mathrm{d}t}\begin{pmatrix} A \sim M \bullet ATP \\ M \bullet ATP \\ M \bullet ADP \bullet P_i \\ A \sim M \bullet ADP \bullet P_i \\ A \bullet M \bullet ADP \bullet P_i \\ A \bullet M^* \bullet ADP \\ A \bullet M \bullet ADP \\ A \bullet M \\ M \bullet ADP \\ M \end{pmatrix} = \boldsymbol{M} \begin{pmatrix} A \sim M \bullet ATP \\ M \bullet ATP \\ M \bullet ADP \bullet P_i \\ A \sim M \bullet ADP \bullet P_i \\ A \bullet M \bullet ADP \bullet P_i \\ A \bullet M^* \bullet ADP \\ A \bullet M \bullet ADP \\ A \bullet M \\ M \bullet ADP \\ M \end{pmatrix}$$

The 10×10 matrix $\boldsymbol{M}$ consists of the transition coefficients depending on the sarcomere stretch λ, the stretch velocity ν, the amount of ATP, the amount of cross-bridges XB, and the fraction of shifted tropomyosin TM_{on}.

$$\boldsymbol{M} = \begin{pmatrix} -k_{-1} - k_2 & 0 & 0 & 0 & 0 & 0 & 0 & 0 & k_1 & 0 & 0 \\ k_2 & -k_3 & k_{-3} & 0 & 0 & 0 & 0 & 0 & 0 & 0 & k_{14} \\ 0 & k_3 & -k_{-3} - k_4 & k_{-4} & k_{13} & 0 & 0 & 0 & 0 & 0 & 0 \\ 0 & 0 & k_4 & -k_{-4} - k_5 & k_{-5} & 0 & 0 & 0 & 0 & 0 & 0 \\ 0 & 0 & 0 & k_5 & -k_{-5} - k_6 - k_{13} & k_{-6} & 0 & 0 & 0 & 0 & 0 \\ 0 & 0 & 0 & 0 & k_6 & -k_{-6} - k_7 - k_{11} & 0 & 0 & 0 & 0 & 0 \\ 0 & 0 & 0 & 0 & 0 & k_7 & -k_8 - k_{10} & k_{-8} & 0 & 0 & 0 \\ k_{-1} & 0 & 0 & 0 & 0 & 0 & k_8 & -k_{-8} - k_1 - k_9 & 0 & 0 & 0 \\ 0 & 0 & 0 & 0 & 0 & k_{11} & k_{10} & 0 & -k_{12} & 0 & 0 \\ 0 & 0 & 0 & 0 & 0 & 0 & 0 & k_9 & k_{12} & -k_{14} & 0 \end{pmatrix}$$

The sum of the tension developing states T_{AM} is:

$$T_{AM} = A \bullet M^* \bullet ADP + A \bullet M \bullet ADP + A \bullet M$$

The resulting normalized tension T_n is given by:

$$T_n = \frac{\alpha T_{AM}}{T_{max}}$$

with the sarcomere overlap function $\alpha = \alpha(\lambda)$ (eq. 7.4), and the maximum tension T_{max} during resting stretch.
The transition from state $A \bullet M^* \bullet ADP$ to $A \bullet M \bullet ADP$ is the stretch dependent irreversible isomerization. If a large tension acts on the cross-bridges, e.g. during isometric contraction, the transition k_7 was small (3–10 s^{-1}) and the main factor of the cross-bridge cycle [347]. In comparison with this, the value of k_7 was increased up to 500 s^{-1} if a fast shortening of the sarcomere was present (ν large) and the tension on the cross-bridges was low. This correlation is given by:

$$k_7 = k_7^* \frac{k_{7,base} - k_{7,\lambda}\lambda + |\nu|}{1 + k_{7,ten} T_n}$$

with the former value k_7^*, the factors $k_{7,base}$, $k_{7,\lambda}$, and $k_{7,ten}$, and the absolute velocity $|\nu|$.
Experiments showed that the cross-bridges break up during fast length changes [302, 304, 305, 306]. The break up of actin and myosin without bound ATP is described by the states $M \bullet ADP$ and M, which are unlikely to be reached under physiological conditions. The two states were included in the model to investigate and evaluate these characteristics considering velocity dependent transition rates.
The strong as well as the weak bindings between actin and myosin got broken during fast length changes. The transitions k_2, k_{-4}, k_9, k_{10}, k_{11}, k_{13}, and k_{14}, which were dependent on the velocity, were influenced by the velocity dependent factor ν_{factor} described by a Hill equation:

$$\nu_{factor} = \frac{|\nu|^{N_\nu}}{|\nu|^{N_\nu} + \nu_{50}^{N_\nu}}$$

with the absolute velocity $|\nu|$, the velocity ν_{50} at which the half of the maximum velocity is reached, and the transition steepness N_ν.
Measurement data concerning transition times were used for the adjustment of parameters in the model. These data are listed in tab. 10.6.

10.6.2 Cooperativity Mechanisms

The conformation changes of troponin are initiated by the binding of Ca^{2+}. The transition from T to TCa was strongly reduced, if the concentration of intracellular Ca^{2+} was low (tab. 10.7). This transition was increased if the amount of cross-bridges is high enough. This is the XB–Tn cooperativity mechanism (section 6.6), which was included in the model with the equation:

$$k_{on} = k_{on}^*(1 + S_{XB})\lambda^{TCa_\lambda}[Ca^{2+}]_i$$

with the concentration of myosin strongly bound to actin S_{XB}, the sarcomere stretch λ, the intracellular Ca^{2+} concentration $[Ca^{2+}]_i$, the former value k_{on}^*, and the length dependent factor TCa_λ. In the initial length, the sarcomere stretch λ is 1. This is correlating to a sarcomere length of 2 μm. S_{XB} is given by:

$$S_{XB} = A \bullet M \bullet ADP \bullet P_i + A \bullet M^* \bullet ADP + A \bullet M \bullet ADP + A \bullet M$$

The shifting of tropomyosin is regulated by the concentration of calcium bound to troponin C. The Tm–Tm cooperativity mechanism raises the probability of tropomyosin going into the

Table 10.6. Measurements and settings of the transition parameters of the new tension development model. The transitions with * indicate additional parameters influencing this value.

Transition	HTD model	Measurement	Reference
k_1^*	1000	$\sim 1\mu M^{-1} ATP s^{-1}$	[40]
		fast, nearly irreversible	[392]
k_{-1}	10		
k_2	1000	≥ 1000	[347]
k_3	150	$k_3 - k_{-3} = 125 s^{-1}$	[393]
		$k_3 - k_{-3} = 168 s^{-1}$	[394]
k_{-3}	15	$K_3 = \frac{k_3}{k_{-3}} \approx 10$	[347, 392]
k_4	1000	≥ 1000	[347]
k_5^*	25	$k_5 + k_{-5} = 30 - 50 s^{-1}$	[347]
k_{-5}	8	$K_5 = \frac{k_5}{k_{-5}} = 3 - 5$	
k_6	50	$45 s^{-1}$	[395]
		$77 s^{-1}$	[396]
k_{-6}	20	$\sim 20 - 30 s^{-1}$	[347]
k_7^*	30	$3 - 10 s^{-1}$ large tension	[347]
		$\geq 500 s^{-1}$ fast contraction	
k_8	200	$\geq 100 s^{-1}$	[347]
		$200 s^{-1}$	[397]
		$325 s^{-1}$	[395]
k_{-8}	5	$K_8 = \frac{k_8}{k_{-8}} \sim 100$	[347]

permissive state ("on" position) if neighboring tropomyosin proteins were in the permissive state (section 6.6). This mechanism was included in the HTD model by (tab. 10.7):

$$tm_{on} = tm_{on}^*(1 + (TM_{coop} + \lambda)TM_{on})^{TM_{pow}} TCa$$

with the former transition tm_{on}^*, the tropomyosin factors TM_{coop} and TM_{pow}, the sarcomere stretch λ, the concentrations of tropomyosin in the permissive state, and calcium bound to troponin TM_{on} and TCa, respectively.

Actin and myosin interact as long as tropomyosin is shifted and a sufficient concentration of ATP is available. The transitions k_1 and k_{14} are blocked without ATP (tab. 10.7) and myosin cannot detach from actin leading to the so-called rigor complex, which is responsible for the rigor mortis [398].

The support of building cross-bridges by neighboring existing cross-bridges is called the XB–XB cooperativity mechanism (section 6.6). This mechanism was included in transition k_5 in the model (tab. 10.7), which is dependent on the square of S_{XB}:

$$k_5 = k_5^*(k_{5,\lambda}\lambda + 0.4)(1 + k_{5,xb}S_{XB})^2 TM_{on}$$

with k_5^* being the former transition, the length factor $k_{5,\lambda}$, and the cross-bridge factor $k_{5,xb}$. The stretch dependency of transition k_5 is funded on the fact that the increase in stretch of the muscle reduces the diameter of the sarcomere and the distance between actin and myosin. In this case, the probability of building cross-bridges is increased [399].

Table 10.7. Blockage of transitions in the HTD model.

Transition	blocked by	
k_{on}	low intracellular Ca^{2+} concentration	$[Ca^{2+}]_i \rightarrow 0$
tm_{on}	low concentration of Ca^{2+} bound to troponin	$TCa \rightarrow 0$
k_5	Tropomyosin in non-permissive state	$TM_{on} = 0$
k_1, k_{14}	no ATP available	$ATP = 0$

10.6.3 Static Properties

The static properties of the tension development were expressed by the steady state interrelation of calcium and tension (section 6.3). The steady state calcium-tension curves of different tension models are illustrated in fig. 10.26 a–e. Figure 10.26 f shows a measurement result of ter Keurs and Hollander in comparison [400]. The differences in the Hill curve parameters

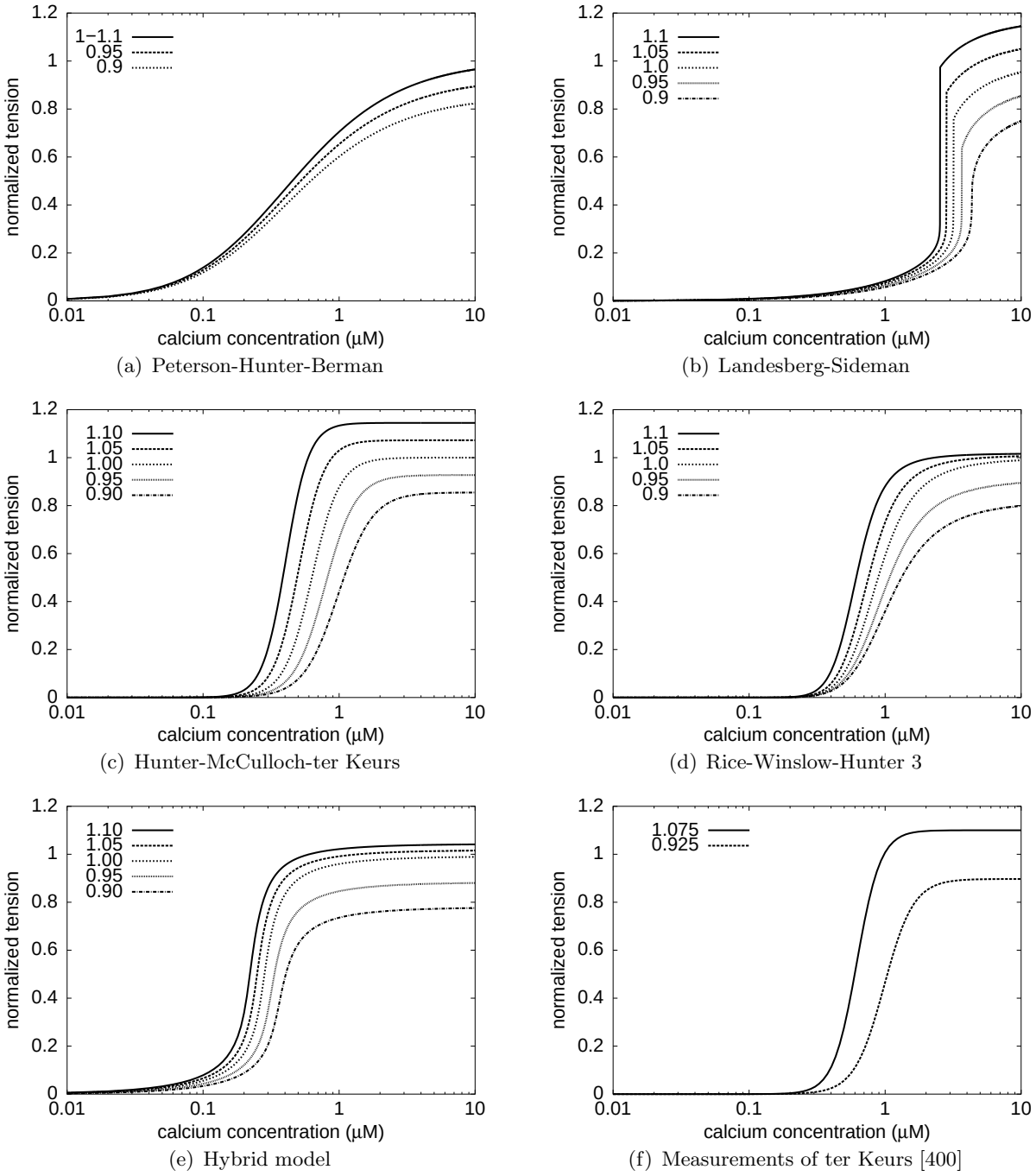

(a) Peterson-Hunter-Berman
(b) Landesberg-Sideman
(c) Hunter-McCulloch-ter Keurs
(d) Rice-Winslow-Hunter 3
(e) Hybrid model
(f) Measurements of ter Keurs [400]

Fig. 10.26. Influence of stretch to the calcium-tension relationship of different tension models and a measurement. The calcium-tension curve describes the stationary tension in relation to varying intracellular calcium concentration. The different curves depending on the sarcomere stretch λ are illustrated. (a–e) Different models. (f) measurement of ter Keurs et al. [400]. Fig. adopted from [307].

Table 10.8. Hill parameters of the various tension development models with varying stretch.

	Stretch	Peterson	Landesberg	Hunter	Rice 3	Rice 4	Rice 5	HTD
N	0.9	1.15	4.627	2.505	2.607	3.603	2.193	3.701
	0.95	1.15	6.635	3.382	2.923	4.207	2.399	3.987
	1.0	1.15	10.627	4.267	3.359	4.885	2.656	4.307
	1.05	1.15	16.287	5.582	3.848	5.521	2.982	4.424
	1.1	1.15	17.323	7.684	4.368	6.230	3.359	4.559
Ca_{50}	0.9	0.46	4.052	1.020	1.132	1.184	1.552	0.360
	0.95	0.46	3.551	0.712	1.021	1.010	1.381	0.318
	1.0	0.46	3.147	0.512	0.895	0.850	1.198	0.283
	1.05	0.46	2.697	0.373	0.765	0.702	1.018	0.254
	1.1	0.46	2.657	0.277	0.625	0.560	0.853	0.225

N and Ca_{50} are quantified in tab. 10.8 for a better comparison between the models and the measurement.
The model of Peterson, Hunter, and Berman (fig. 10.26 a) differed strongly from the measurements. The Hill parameters were not influenced by the stretch and thus the steepness of the Hill curve and the calcium sensitivity during varying sarcomere length were equal. The maximum tension depended linearly on the sarcomere overlap function α.
The Landesberg-Sideman model (fig. 10.26 b) uses a monotonously rising overlap function. The Hill parameters were dependent on the stretch but N was much larger than the measured values or in other models (tab. 10.8) and was strongly dependent on the stretch. Also, the bend in the calcium-tension curve was remarkable.
The model of Hunter, McCulloch, and ter Keurs (fig. 10.26 c) is in good agreement with the measurements. Merely Ca_{50} was shifted towards lower values because the measurements were carried out with skinned myocytes. The dependency of the Hill parameters of this model is directly described by eq. 7.1.
The 3^{rd} model of Rice, Winslow, and Hunter (fig. 10.26 d) is in better agreement with the measurements than the Peterson et al. model, even if both models used the same overlap function. The steeper increase of the curve was mainly due to the implemented Tm–Tm cooperativity mechanism. The stretch dependency of N and Ca_{50} is represented in the tropomyosin transition tm_{on}. The maximum tension was not increasing largely with stretches larger than 1.
Model 4 and 5 of Rice, Winslow, and Hunter (not shown) had a monotonously increasing maximum tension as well as a continuous change of the Hill parameters with increasing stretch. Measurements showed that the maximum tension is increasing again with large stretches [401, 402]. This feature was implemented in all three of the Rice et al. models.
The monotonous increase of maximum tension and calcium sensitivity in the HTD model developed in this work (fig. 10.26 e) is consistent with the measurement data. The HTD model had a lower Ca_{50} value compared to the Rice-Winslow-Hunter models, which led to a more sensitive reaction on lower calcium concentrations. The maximum tension was decreasing and the calcium sensitivity was further increasing with increasing stretch (> 1.1).

10.6.4 Dynamic Properties

In this section, the temporal evolution of the tension development under three different circumstances is illustrated. The tension development was investigated during 1. Constant Ca^{2+} concentration with varying magnitude during which the connection of actin and myosin was broken up by a short but strong length change, 2. Tension development models combined

with ionic electrophysiological models, and 3. Reproduction of the break up experiments considering physiological calcium transients.

10.6.4.1 Tension Development at Constant Calcium Concentration

The tension during constant Ca^{2+} concentration including fast length changes of the sarcomere leading to a break up of the connection between actin and myosin was investigated in this experiment. It was not reproducible with the tension development models, which do not consider velocity dependent transitions. Thus, only the HTD model was able to reproduce these experiments.
A stretch of 8 % for a duration of 3 ms was the setting for the numerical simulation as well as the experiment. Figure 10.27 illustrates the simulated results with the HTD model and the data measured by Baker et al. [304]. After the stretch and the decreased tension, the following tension development is characterized mathematically by (section 6.5):

$$T = T_{max}(1 - e^{-k_{tr}t}) + T_0$$

with the exponential coefficient k_{tr}, the maximum tension T_{max} and the resting tension T_0. The coefficient k_{tr} depicts how fast the tension reaches the original value. The redeveloped tension was slowed down with decreasing calcium concentration, i.e. k_{tr} was smaller with lower maximum tensions.
The transitions k_9, k_{10}, k_{11}, and k_{12} depend on the velocity of the sarcomere in the HTD model (fig. 10.25). Fast length changes led to an increase in the transition rates and an increase in the

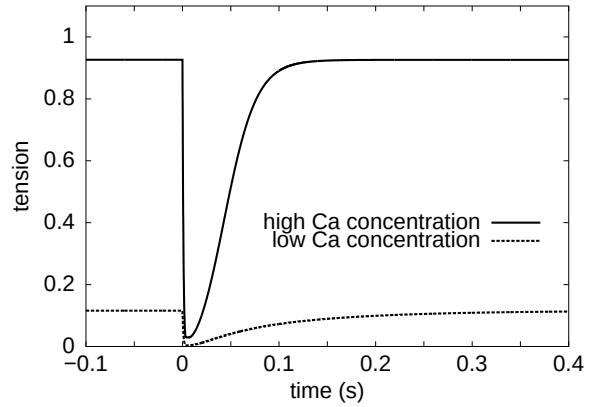

(a) HTD model

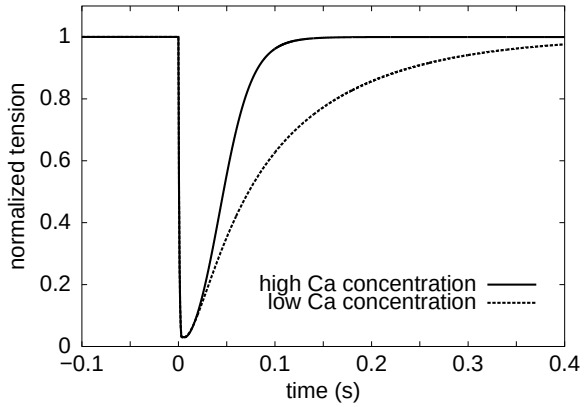

(b) HTD model

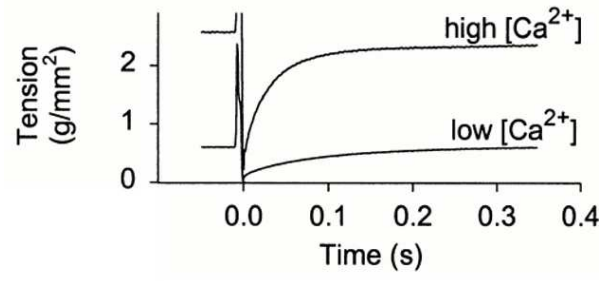

(c) Baker et al.

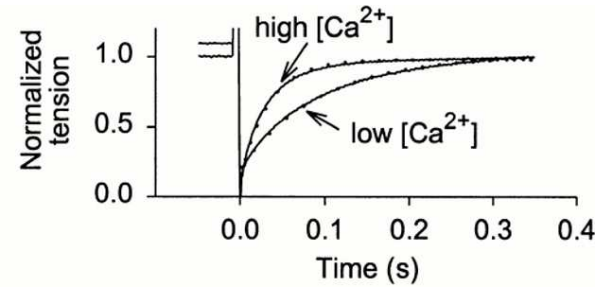

(d) Baker et al.

Fig. 10.27. Influence of calcium concentration on the tension during break up experiments. (a,b) HTD model. (c,d) Experiments of Baker et al. [304]. The left figures show the absolute tension and the right ones the normalized tension. Fig. adopted from [307].

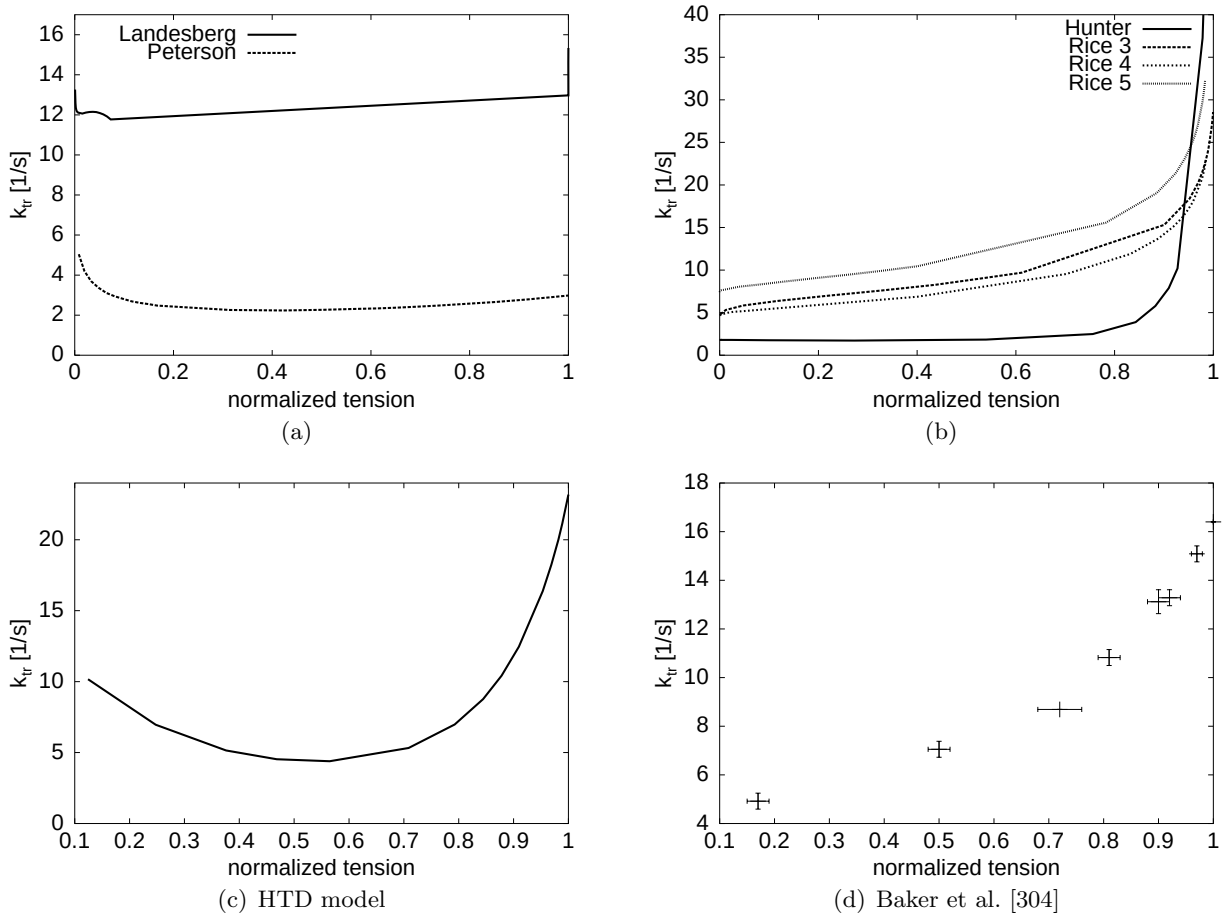

Fig. 10.28. Relationship between k_{tr} and relative tension. The upstroke rate k_{tr} increases with increasing tension during constant $[Ca^{2+}]_i$. (a – c) Various models. (d) Measurement data of Baker et al. [304]. Fig. adopted from [307].

fraction of state $M \bullet ADP$ and M. For the comparison of the tension upstroke velocity with high and low calcium concentrations, the values are presented normalized in fig. 10.27 b,d. The total course of the transition k_{tr} regarding the normalized tension is depicted in fig. 10.28. The course of k_{tr} in the HTD model is in good agreement with the measured data with increasing tension. The model and the measurement differ at small tension.
Figure 10.29 a illustrates the variation of k_{tr} during tension changes with two different TCa values in the 3^{rd} Rice et al. model. A higher concentration of TCa leads to a faster tension development.
The influence of the break up experiment on the amount of calcium bound to troponin in the HTD model is shown in fig. 10.29 b. The simulations confirm the assumption that the breaking of the connections between actin and myosin has no significant influence on the amount of bound calcium.

10.6.4.2 Tension Development Coupled with Electrophysiological Models

The dynamical tension development of the models was investigated by using the calcium output of an electrophysiological model with a realistic transient of the intracellular calcium concentration. The ionic model of Priebe and Beuckelmann [242] was stimulated with a 3 ms lasting external current to exceed the threshold of the activation. The transient of the intracellular Ca^{2+} concentration was the input for the tension development models.

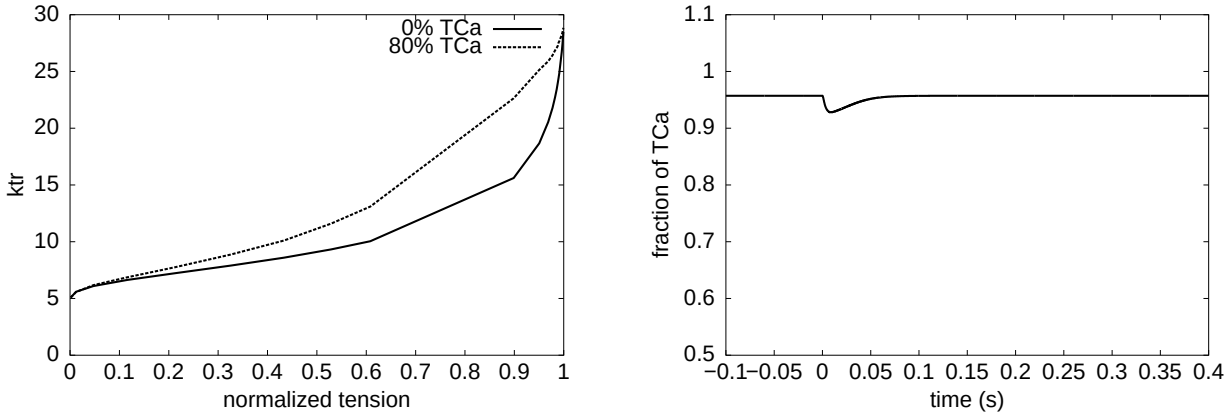

(a) (b)

Fig. 10.29. (a) Differences in k_{tr} depending on the amount of calcium bound to troponin in the 3^{rd} Rice et al. model. The increase of troponin bound calcium leads to a faster tension development. (b) Influence of the break up experiment on the fraction of TCa in the HTD model. Fig. adopted from [307].

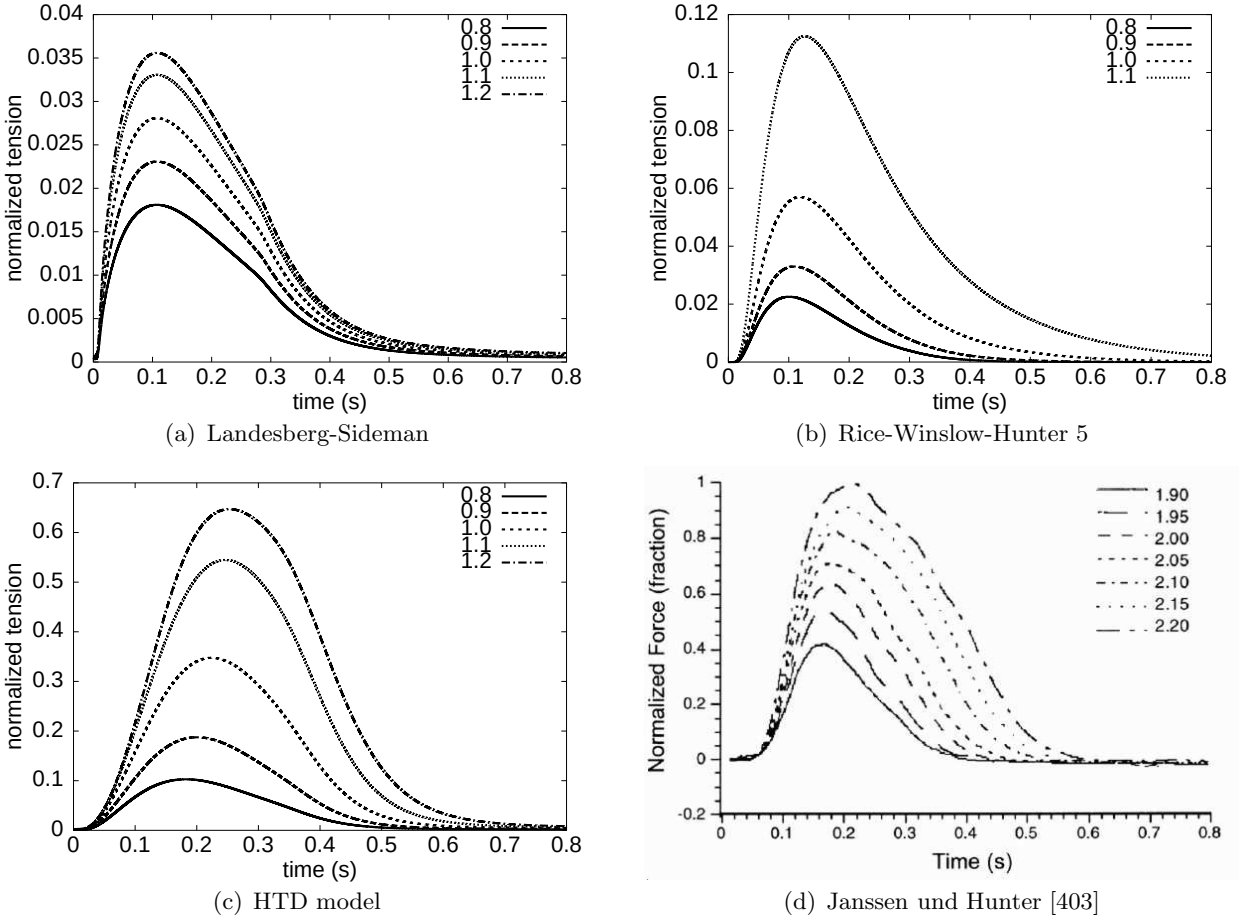

(a) Landesberg-Sideman (b) Rice-Winslow-Hunter 5

(c) HTD model (d) Janssen und Hunter [403]

Fig. 10.30. Simulated and measured course of tension development after electrical excitation with varying stretches of the sarcomere. (a – c) The tension models are coupled with the ionic model of Priebe and Beuckelmann [242]. The stretch is varied between 0.8 and 1.2. (d) Measurement of Janssen and Hunter in a trabeculae of the right ventricle of a rat [403]. The parameter in the plots of the models (a), (b), and (c) is stretch and in the measurement (d) the sarcomere length. Fig. adopted from [307].

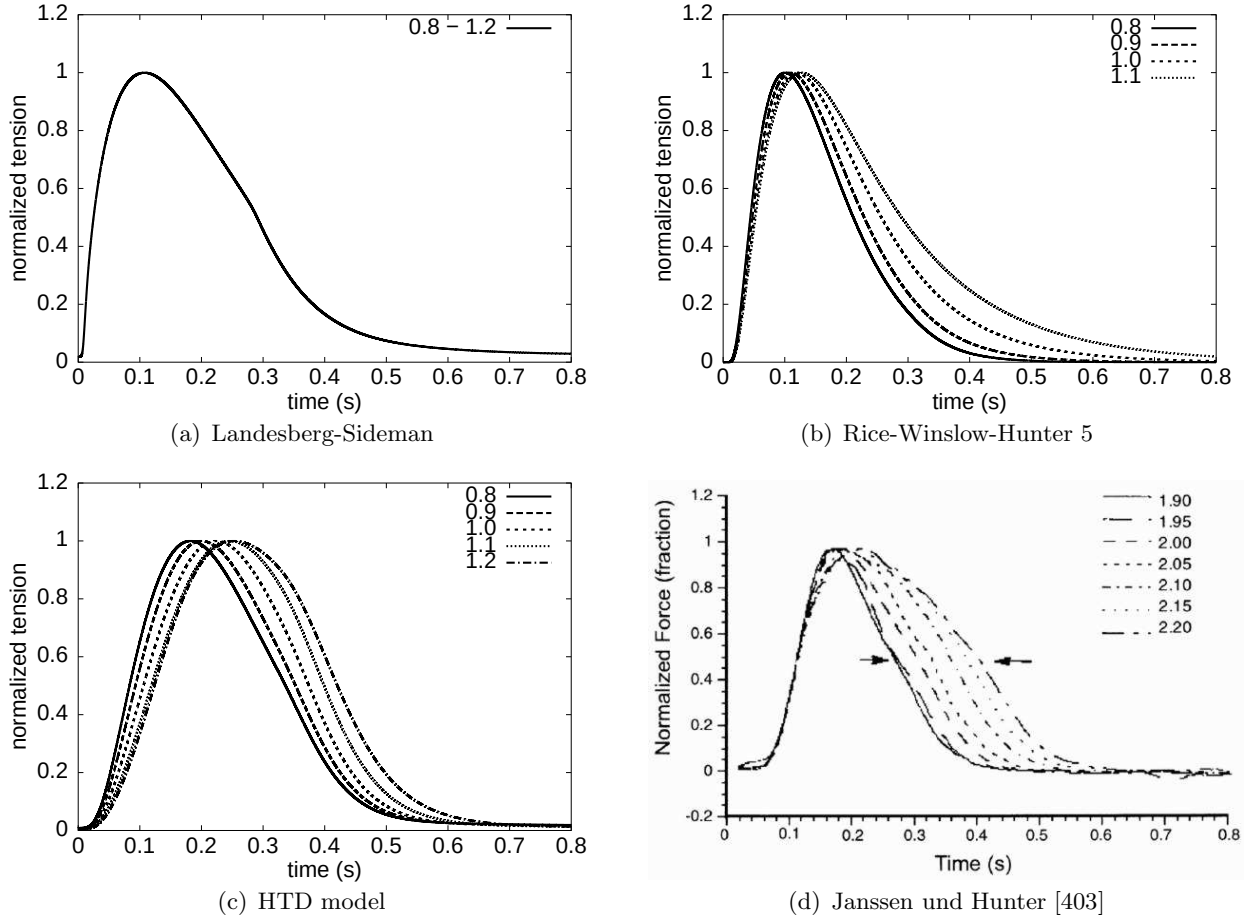

(a) Landesberg-Sideman (b) Rice-Winslow-Hunter 5

(c) HTD model (d) Janssen und Hunter [403]

Fig. 10.31. Scaled courses of the tension development at varying sarcomere length of fig. 10.30. The influence of the stretch on the tension upstroke velocity is clearly visible. Fig. adopted from [307].

Figure 10.30 a–c illustrates the dynamic courses of the tension development in various models depending on the sarcomere stretch. The measurement data of Janssen and Hunter [403] is expressed in fig. 10.30 d in dependence on the sarcomere length. The same data are depicted in fig. 10.31 where the courses are normalized to the maximum tension of each sarcomere length. This allows a better comparison between the upstrokes and the downstrokes of different models and the measurement data.

Several different variations in the course of the tension development are visible with increasing sarcomere length in the measurement data (figs. 10.30 d and 10.31 d). The maximum tension and the time to complete relaxation were increasing. The time to maximum tension is nearly constant with varying sarcomere lengths. Thus, the upstroke velocity increases with increasing sarcomere length. The dynamic behavior of the calcium transient leads to a reduction in the maximum tension of about 50 – 80 % of the maximum tension during simulations without electrophysiological models.

The simulation with the Landesberg-Sideman model showed that consideration of a monotonous increasing overlap function led to a homogeneous increase in the maximum tension with increasing sarcomere length (fig. 10.31 a). The tension development was very low in this model due to the high Ca_{50} value (fig. 10.30 a).

The simulation with the 5^{th} Rice-Winslow-Hunter model showed a homogeneous increase and decrease of the course of the tension development (fig. 10.30 b) also found in the measurement. Only during a stretch of 1 or larger, this model was reacting in a physiological way to

the calcium transient. A significant prolongation of the time to complete relaxation was present with increasing sarcomere length, which results from the additional cross-bridge states compared to the 3^{rd} model (section 7.5). The dynamically developed maximum tensions were relatively small in this model.
The courses of the HTD model are presented in figs. 10.30 c and 10.31 c. The increase and decrease of the tension curve was homogeneous and in good agreement with measurement data. The maximum tension was increasing with raising sarcomere length and between 50 and 80 % of the values reached in the constant calcium simulations. The prolongation of the time to complete relaxation was comparable to data of Janssen and Hunter [403]. The prolongation of the time to maximum tension with increasing sarcomere length in the HTD model was not reproduced in the measurement.
The variation of the maximum tension in the different models was mainly due to their different sensitivity for $[Ca^{2+}]_i$. The $[Ca^{2+}]_i$ sensitivity is determined by the Hill's coefficient Ca_{50}. Ca_{50} is mainly given by the quotient of the calcium binding and unbinding of troponin $\frac{k_{on}}{k_{off}}$. Ca_{50} is increasing with an increasing quotient. The models were adjusted by changing k_{on} and k_{off} to different calcium sensitivities given by different electrophysiological models.

10.6.4.3 Fast Length Changes during Excitation Contraction Coupling

Peterson and co-workers [302] performed a myofilament break up measurement in an electrically excited intact cell. Figure 10.32 b shows the result of the experiment where the cell was stretched for 20 ms to an extent of 4.6 % and was relaxed afterwards. As described in section 10.6.4.1, the existing models were not able to reconstruct the break up experiments since they have not included velocity dependent transition rates.
Figure 10.32 a depicts the break up experiment with the HTD model coupled to the Priebe-Beuckelmann electrophysiological model. The fast length change led to a break up of the cross-bridge bindings. Actin and myosin detach from each other in the states $A\bullet M$, $A\bullet M^*\bullet ADP$, or $A\bullet M\bullet ADP$ in this situation and the states $M\bullet ADP$ and M were occupied (fig. 10.25). This led to the course of the tension development that is comparable to the measured experiment.

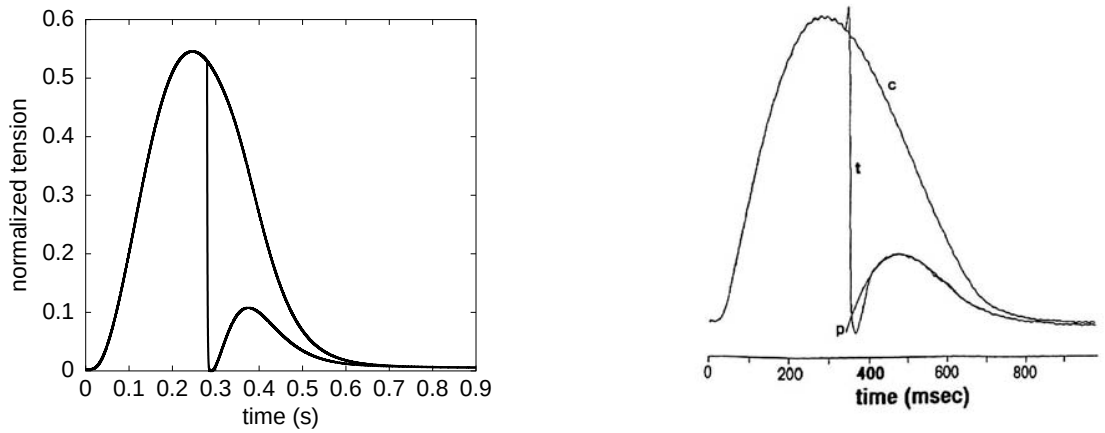

(a) HTD model (b) Peterson et al. [302]

Fig. 10.32. Normalized tension during fast length changes achieved in intact cells that were electrically stimulated. The cells were stretched for 20 ms to an extent of 4.6 % and were relaxed afterwards. Simulation with the HTD model (a) and measured data (b). Fig. adopted from [307].

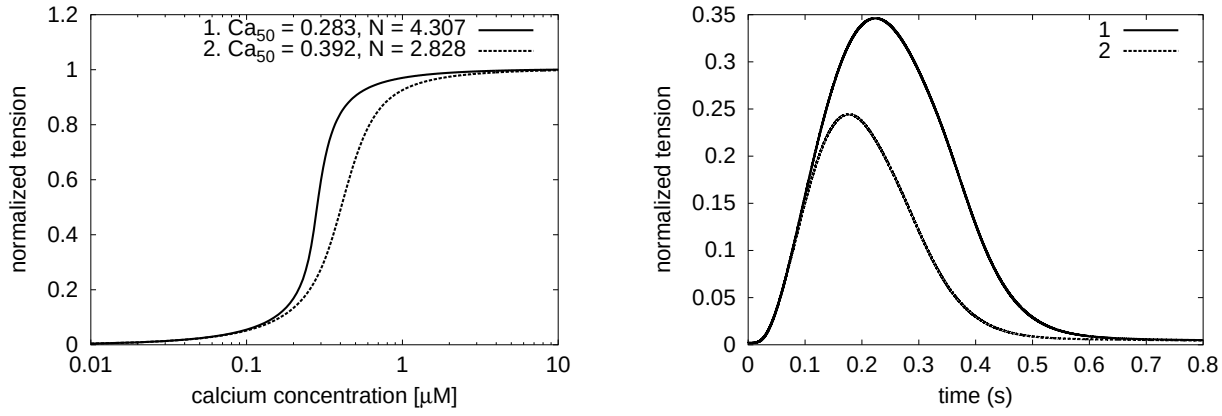

(a) (b)

Fig. 10.33. Influence of XB–Tn cooperativity in the HTD model. The graphs illustrate the properties of the model with the XB–Tn cooperativity mechanism (curve 1) and without (curve 2). (a) Steady state Hill curve. (b) Dynamical tension development coupled to the Priebe-Beuckelmann model. Fig. from [307].

10.6.5 Evaluation of Cooperativity Mechanisms

The cooperativity mechanisms (section 6.6) influence tension development. Several variables affecting the cooperativity lead to this influence i.e. the Hill's parameters Ca_{50} and N, the coefficient k_{tr}, and the maximum tension during static calcium concentration. There is no specific rule how the cooperativity mechanisms influence the changes of the tension since different implementations of the same cooperativity mechanisms show different effects.
The XB–Tn cooperativity mechanism was mainly influencing the calcium sensitivity. Without this feedback, Ca_{50} was increased and N is decreased (fig. 10.33 a). The reduced calcium sensitivity led to a smaller amplitude of maximum tension when the XB-Tn cooperativity was lacking (fig. 10.33 b). Considering this mechanism, the time constants of the tension upstroke during dynamical tension development were reduced. This led to a right shift of the dynamical tension curves with increasing sarcomere length. An influence of the velocity on the tension development with constant Ca^{2+} concentration was not observed.

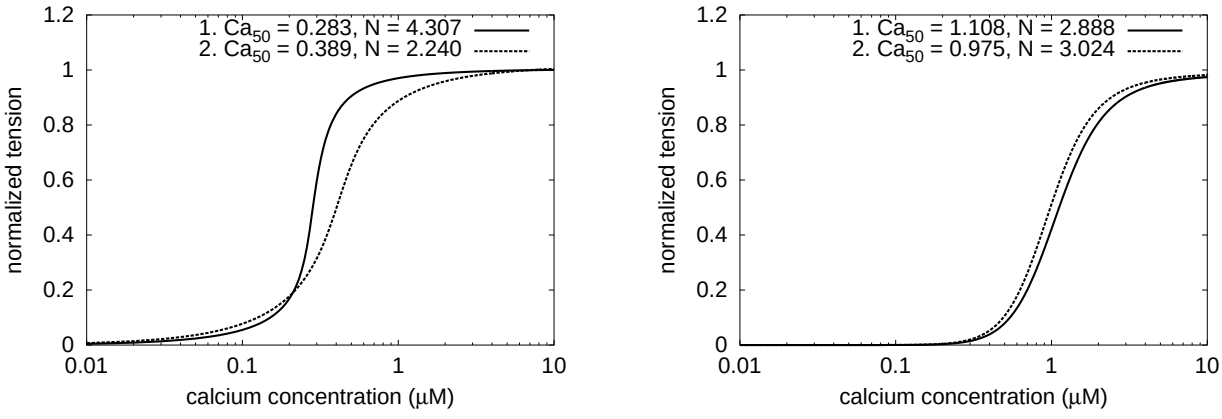

(a) HTD model (b) Rice et al.

Fig. 10.34. Influence of XB–XB cooperativity on tension development. The resulting effects on the steady state calcium-tension relationship is dependent on the different implementation of this cooperativity mechanism. (a) The transition k_5 is increased in the HTD model during increased fraction of cross-bridge bindings. (b) The XB–XB cooperativity mechanism is realized with two additional states P2 and P3 in the 5^{th} Rice-Winslow-Hunter model. Fig. from [307].

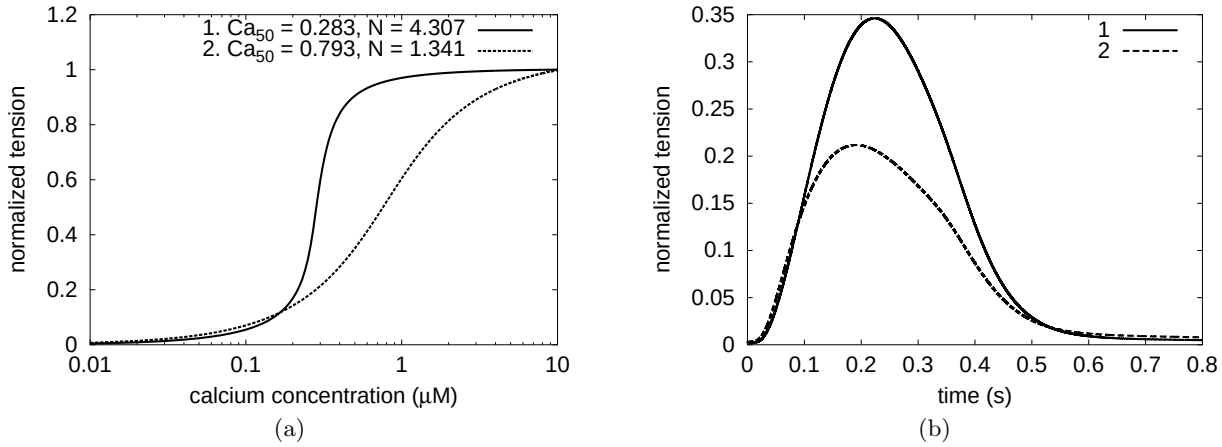

(a) (b)

Fig. 10.35. Influence of Tm–Tm cooperativity mechanism on the HTD model. The graphs illustrate the properties of the model with the Tm–Tm cooperativity mechanism (curve 1) and without (curve 2). (a) Strong influence on the steady state calcium-tension relationship. (b) The changes in the dynamic tension development are due to differences in Ca_{50}. Fig. from [307].

The XB–XB cooperativity mechanism was included in the 4^{th} and 5^{th} model of Rice et al. with two additional states P2 and P3. This feedback mechanism was included in the HTD model by a cross-bridge fraction dependent change in the transition k_5. Figure 10.34 illustrates the differences resulting from both implementations. The HTD model shows large differences in the Hill curves when changing between considering and neglecting the XB–XB cooperativity mechanism. The courses of the HTD model were in agreement with experimental findings [303, 308]. The fraction of cross-bridges was increased in both models with the XB–XB cooperativity mechanism by a factor of two, but the relaxation time constants were slower in the Rice-Winslow-Hunter models considering constant calcium environments. The inclusion of the XB–XB cooperativity mechanism in the Rice et al. models also led to a reduction in the tension upstroke coefficient k_{tr}, which was not effected in the HTD model.
The Tm–Tm cooperativity mechanism was mainly influencing the calcium sensitivity of the stationary calcium-tension relationship (fig. 10.35). The strong increase in the Hill coefficient N when including this mechanism illustrates the characteristics of the troponin complex preferring the position of neighboring troponin molecules. The Tm–Tm cooperativity mechanism had strong influence on the dynamical tension development. The reduced maximum tension was due to the higher Ca_{50} value when the mechanism was neglected.

10.7 Heterogeneous Cellular Electromechanics

To investigate the heterogeneous electromechanical properties on the cellular level a single cell environment was built of the electrophysiological model presented in section 10.5 and the hybrid tension development model of section 10.6. The simulations were performed with three different cell types: subendocardial, midmyocardial (M), and subepicardial myocytes. With decreasing basic cycle length (BCL) the model started to alternate at about a BCL of $300\,ms$. Therefore, results below a BCL of $300\,ms$ were not presented.
Several exemplary simulations with the electromechanical model were performed with varying BCL. A simulation with a BCL of $1000\,ms$ reconstructed the course of transmembrane voltage V_m, of intracellular calcium concentration $[Ca^{2+}]_i$, and of normalized tension (fig. 10.36 A–C) with a simulated sarcomere length of $2.2\,\mu m$.

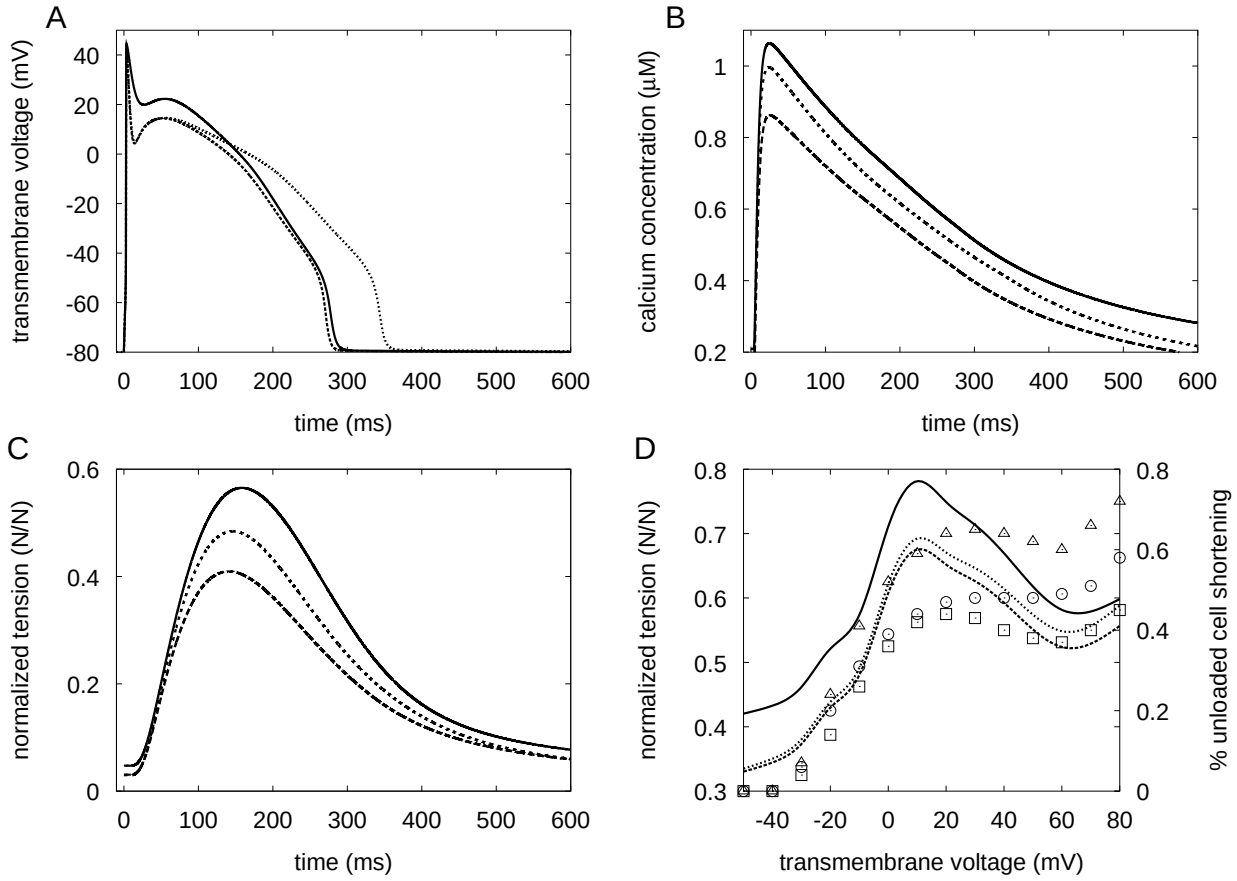

Fig. 10.36. Results of the three different cell types calculated with the electromechanical model. Endocardial myocytes are illustrated with solid lines, M cells with dotted lines, and epicardial cells with dashed lines. Plots in A–C are simulated with a BCL of 1000 ms. A: Action potential of the three cell types. B: Course of intracellular calcium concentration $[Ca^{2+}]_i$. C: Course of normalized tension. The differences in peak tension follow those of peak-$[Ca^{2+}]_i$. D: Peak tension-voltage relationship for simulated data and cell shortening-voltage relationship for measured data. Wallis et al. provided the measurement data [181]. Data of subepicardial cells are depicted by triangles, subepicardial ones by circles and M cells by boxes. Fig. from [390].

The action potential in fig. 10.36 A shows the characteristic notches in repolarization phase 1 for M cells and epicardial cells. Action potential duration of 90 % repolarization (APD_{90}) was 272 ms in endocardial, 336 ms in midmyocardial, and 265 ms in epicardial myocytes. The values of APD_{90} with respect to BCL are shown in fig. 10.37 A. The shape demonstrates the increasing APD_{90} with increasing BCL. The APD_{90} of M cells increased more than that of endocardial or epicardial cells for BCL $>$ 1000 ms.

Figure 10.36 B shows the course of $[Ca^{2+}]_i$. The peak-$[Ca^{2+}]_i$ was largest in endocardial cells (1.052 μM), decreased in M cells (0.996 μM) and smallest in epicardial cells (0.858 μM). Figure 10.37 B illustrates peak-$[Ca^{2+}]_i$ with respect to BCL. Large peak-$[Ca^{2+}]_i$ were found for all three cell types at about a BCL of 800 ms.

The course of the developed tensions at a BCL of 1000 ms is shown in fig. 10.36 C. The largest amplitude was located in endocardial myocytes (55.6 % of maximal tension); it was reduced to 47.4 % in M cells and to 40.3 % in epicardial cells. The relationship between peak tension and BCL is illustrated in fig. 10.37 C. The largest values were found near the BCL of about 750 ms for all three cell types. The peak value of the normalized tension decreased for both increasing and decreasing BCLs. When investigating the difference between peak tension and

resting tension during one excitation, the transient shown in fig. 10.37 D is present. These values depict the effective tension for the contraction. The effective tension decreased faster than the peak tension shown in fig. 10.37 C for BCL $< 800\,ms$ because of the raising resting tension.
Figure 10.36 D illustrates the tension-voltage relationship. The same principal transient of this relationship as compared to the measurements reported by Wallis et al. [181] was reconstructed. They measured percentage of cell shortening which we expected to be in a nearly linear relationship with the developed simulated tension. The simulation yielded the largest values for endocardial myocytes and the lowest for epicardial cells, whereas in the measurement they were largest in epicardial and lowest in M cells.

Discussion: The simulated calcium-BCL and tension-BCL relationship may not reflect the electrophysiology in detail for BCLs $< 500\,ms$. This insufficient feature was due to the simplified description of calcium handling in the Priebe-Beuckelmann model. Calcium handling must be revised for subsequent studies. Because the aim of this section was to reconstruct heterogeneity in the electrophysiological model at BCL $= 1000\,ms$, the inaccuracy of the model at BCLs $< 500\,ms$ does not have much influence on the presented results.
At presence, only two experimental study have been performed exploring the heterogeneity of tensions [181, 183]. Consequently, the model was used to make predictions. The results were

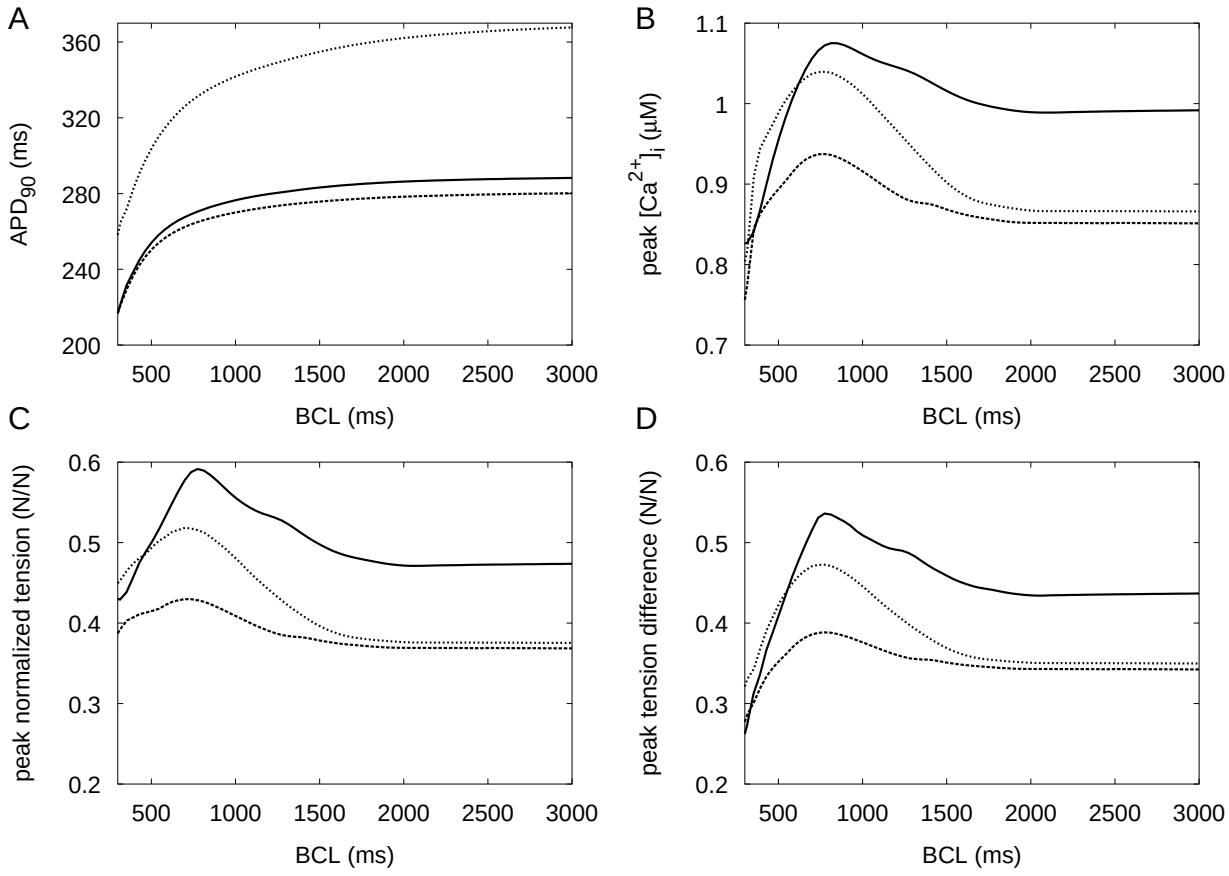

Fig. 10.37. Features of the electromechanical model with respect to the basic cycle length (BCL). Endocardial myocytes are presented with solid lines, M cells with dotted lines, and epicardial with dashed lines. A: Action potential duration at 90 % repolarization (APD_{90}). B: Peak of intracellular calcium concentration $[Ca^{2+}]_i$. C: Maximum peak of normalized tension. D: Difference between maximum peak trension and resting tension of the matching BCL. Fig. from [390].

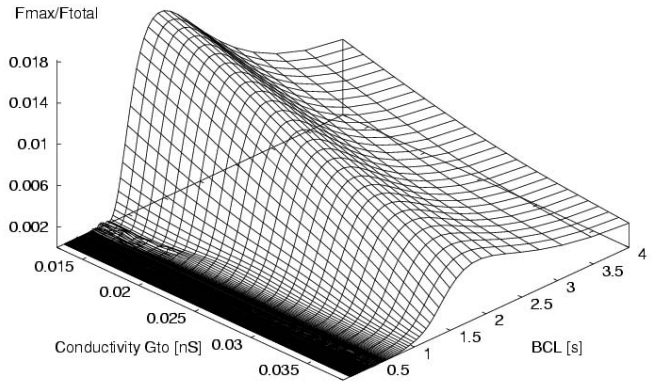

Fig. 10.38. Three dimensional plot of maximum tension depending on BCL and conductivity g_{to}. The conductivity variation reflects the transmural heterogeneity. Small values depict more endocardial cells and large more epicardial myocytes. The utilized electrophysiological approach is the guinea-pig model of Noble et al. [241]. The tension development is described by the 3^{rd} model of Rice et al. [325]. Fig. from [382].

consistent with our previous model (fig. 10.38) [382] using the electrophysiological guinea-pig model of Noble et al. [241] and the 3^{rd} model of Rice et al. [325], which describes tension development. Specifically, the tension was largest in subendocardial myocytes and lowest in subepicardial myocytes. The peak tension differences between the three cell types, however, were larger in the study of the guinea-pig model than in the study of the human model. This may be a consequence of the inaccuracy in modeling the heterogeneity in the guinea-pig model study, which was based on varying only the channel density of current I_{to}.

10.8 Pathological Models

Additionally to the models reconstructing the physiological case presented in this chapter so far, pathological models have been developed in the course of this work. A main focus was set to those pathologies, which have arrhythmogenic character. To achieve this, already existing electrophysiological models were adapted to measured data to determine the mechanisms of these pathologies. This section presents two unphysiological representations of single atrial myocytes and three from ventricular cells. The pathological models were further investigated coupled in tissue in section 11.2.

10.8.1 Electrophysiological Remodeling

In recent years, it has been established that "atrial fibrillation begets atrial fibrillation" by inducing electrophysiological changes in the atrial myocardium (section 4.8.1.2) [202]. This pathological adaptation of the atrial electrophysiological properties from the sinus rhythm to the fibrillatory rhythm is termed electrophysiological remodeling (section 4.8.1.2) [404].
The experimental data of atrial fibrillation (AF) induced variations in ionic channel conductance and kinetics of human atrial myocytes reported in [200] consists of several electrophysiological changes. These changes were incorporated in the Courtemanche-Ramirez-Nattel (CRN) [238] model to reproduce the behavior of human atrial myocytes for patients with chronic AF [380]. To investigate the role of each individual electrophysiological change on the

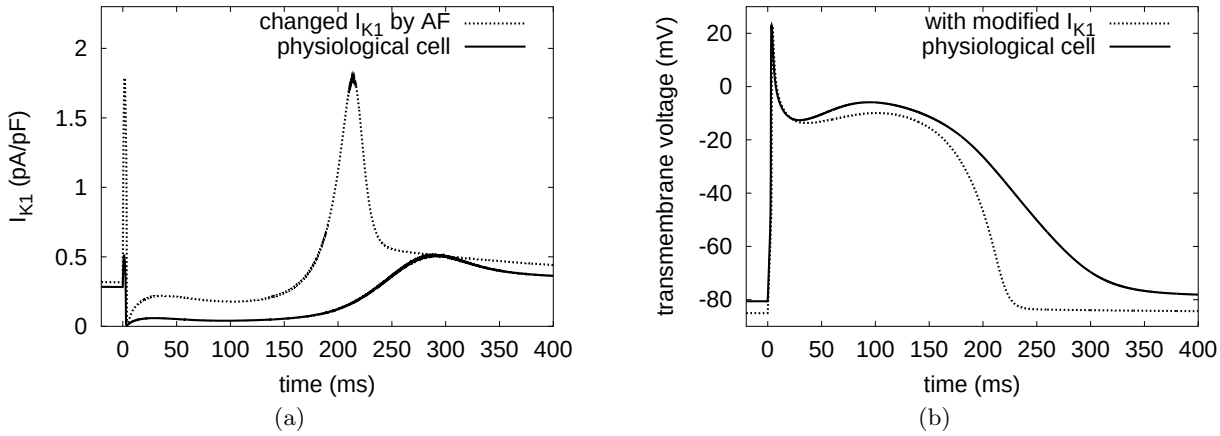

(a) (b)

Fig. 10.39. (a) Variation of I_{K1} by increased g_{K1}. (b) Course of transmembrane voltage with modified I_{K1} induced by chronic AF compared with the physiological AP. Fig. from [380].

remodeling effect, only one modification was incorporated for each stage. Then, the resulting action potential (AP) was compared with the physiological AP.

Change of I_{K1}: The conductance of I_{K1} was increased by 250 % in the cells from the patients in chronic AF [200]. The ionic current and AP computed from the normal model were superimposed with those computed from the remodeling case (fig. 10.39). The dashed curve in fig. 10.39 a illustrates the altered I_{K1} with the increased density. Figure 10.39 b shows the original AP and the AP obtained from the CRN model with only involving the altered g_{K1}. I_{K1} plays a fundamental role in determining the resting potential as well as the final phase of repolarization in the AP [187]. Figure 10.39 depicts that the up regulation of I_{K1} led to an accelerating late repolarization, thus to a reduced APD, and a more negative resting potential. The same effects induced by variated I_{K1} are reported in [200, 405, 406].

Change of I_{CaL}: The abnormality in I_{CaL} includes that the channel conductance g_{CaL} is decreased by 74 % and the time constant of the fast inactivation variable $\tau_{f(Ca)}$ is increased by 62 % [200]. The dashed curve in fig. 10.40 a illustrates the altered I_{CaL} with the modifications. Figure 10.40 b shows the AP obtained from the CRN model with only including the alteration of g_{CaL} and $\tau_{f(Ca)}$. A remarkably shortened activation-time of I_{CaL}, a much lower plateau

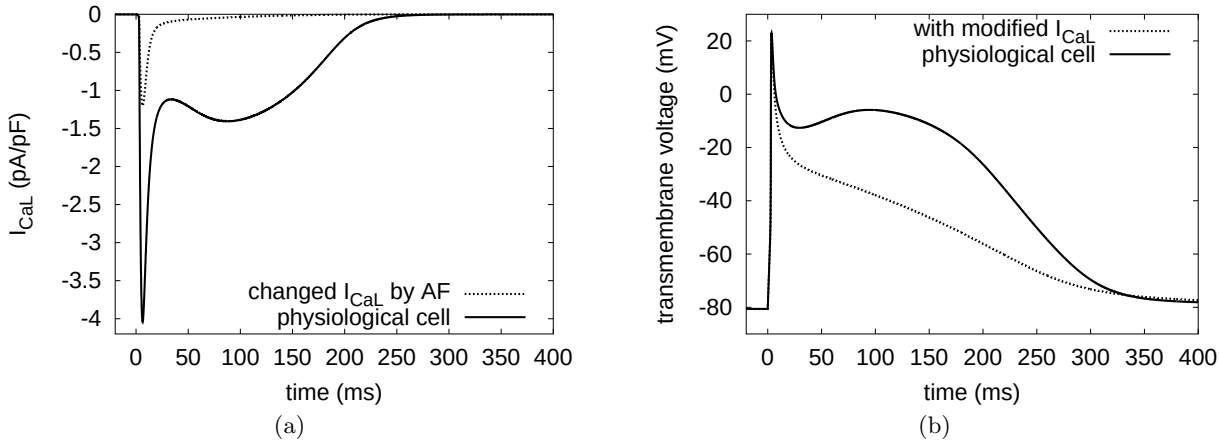

(a) (b)

Fig. 10.40. (a) Variation of $I_{Ca,L}$ by decreased $g_{Ca,L}$ and increased $\tau_{f(Ca)}$. (b) AP with modified I_{CaL} induced by chronic AF compared with the physiological AP. Fig. from [380].

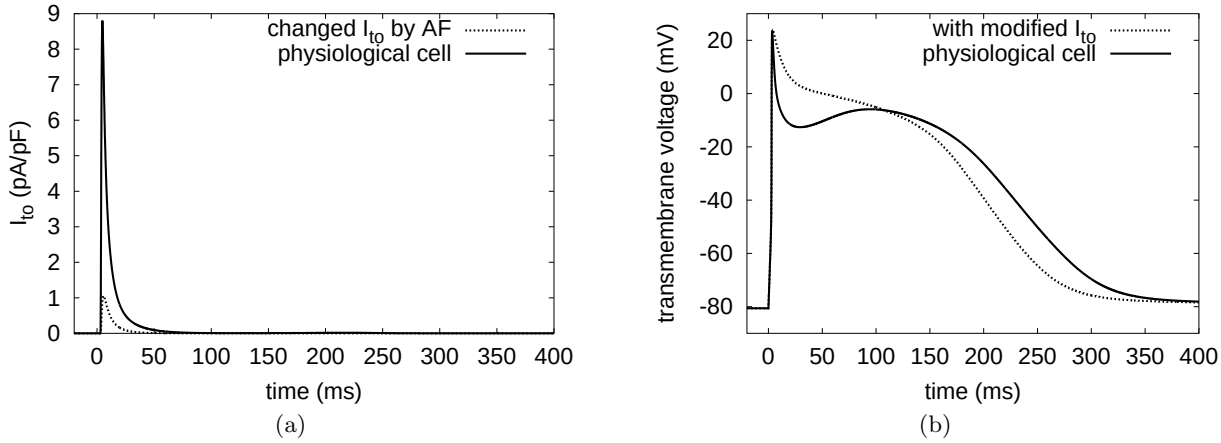

(a) (b)

Fig. 10.41. (a) Variation of I_{to} by decreased g_{to} and elevated o_a. (b) Course of transmembrane voltage with modified I_{to} induced by chronic AF compared with the physiological AP. Fig. from [380].

phase, and an abbreviated APD was observed. These effects are also reported by [199, 200, 404, 407]. The loss of plateau phase was explained by the influence of I_{CaL} on phase 2. The increased calcium permeability sustains the positive membrane voltage by the sodium influx, producing the plateau phase of AP [408]. The balance between plateau inward Ca^{2+} and outward K^+ currents determines the APD. A decreased inward Ca^{2+} current reduces the APD [189, 406].

Change of I_{to}: The channel conductance g_{to} is decreased by 85 % and the activation curve of o_a is shifted by $+16\,mV$ induced by chronic AF [200]. The dashed curve in fig. 10.41 a illustrates the altered I_{to} with the decreased density and shifted o_a. Figure 10.41 b shows the AP with only involving the alteration of g_{to} and o_a. The shift of the activation curve led to the effect that the magnitude of opened K^+ channels decreased during positive transmembrane voltages and the decreased g_{to} caused further reduction of I_{to}. As a consequence, the notch in phase 1 was attenuated in the AP (fig. 10.41 b). The APD was also reduced because of the decreased Ca^{2+} release from the sarcoplasmic reticulum. These findings were consistent with experimental data when inhibiting I_{to} by 90 % [238, 407].

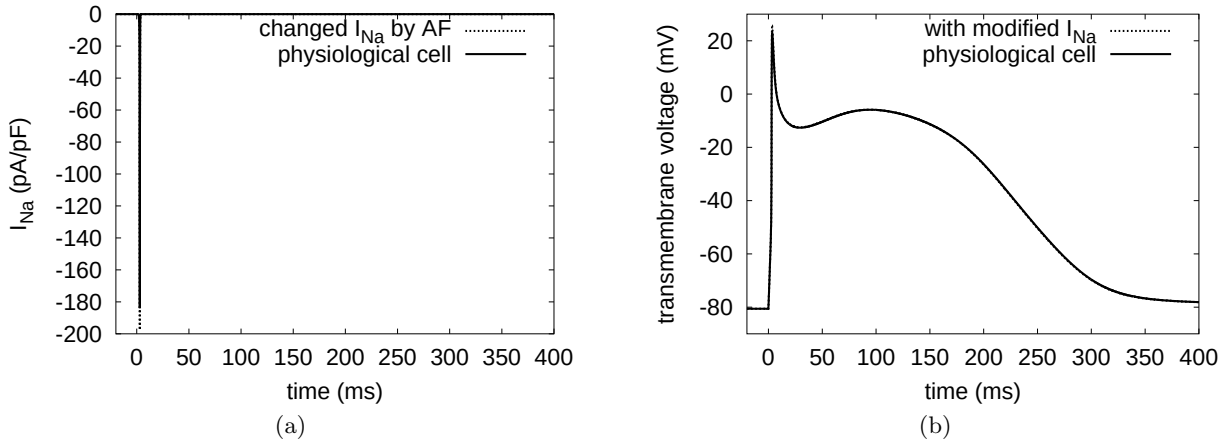

(a) (b)

Fig. 10.42. (a) Variation of I_{Na} by shifting the inactivation variable of I_{Na}. (b) AP with modified I_{Na} induced by chronic AF compared with the physiological AP. The differences in both figures are so small that they cannot be observed in these figures. Fig. from [380].

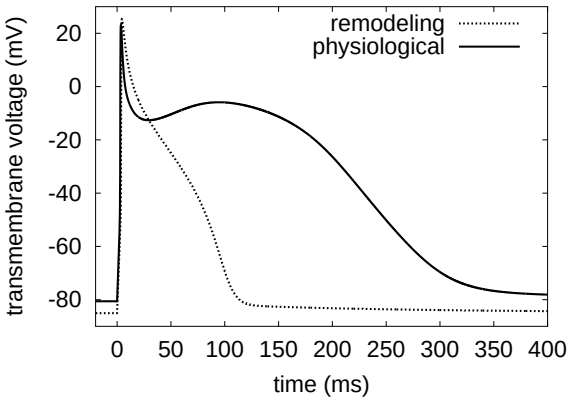

Fig. 10.43. Simulated APs of remodeled and physiological cell. Fig. from [380].

Change of I_{Na}: A shift of the inactivation curve of I_{Na} by $+1.6\,mV$ is reported in electrophysiological remodeling [200]. The equation for I_{Na} contains two inactivation variables: the fast inactivation gating variable h and the slow inactivation gating variable j. The experiment of Bosch et al. [199] revealed that only the voltage dependent inactivation h was shifted to a more positive voltage in AF cells. Figure 10.42 a illustrates the altered I_{Na} with shifted h. In fig. 10.42 b the AP with only the alteration of h is shown. The shift of inactivation led to an increased magnitude of open Na^+ channels during positive transmembrane voltages. The shift of h by only $+1.6\,mV$ caused little alteration of AP (fig. 10.42 b).

AP of Remodeled Cell: All changes described were incorporated in the CRN model of atrial myocytes. The dashed line in fig. 10.43 depicts the AP arosen from the synergetic interaction of all abnormal currents. The simultaneous reduction in atrial I_{to}, I_{CaL} and increase in I_{K1} fully accounted for the marked abbreviation of APD by $250\,ms$ and acceleration of late repolarization. The lower plateau was due to the reduction in I_{CaL}. The enhanced I_{K1} contributed to the decrease of the resting potential from $-80\,mV$ to $-85\,mV$. The attenuated notch in the remodeling case was caused by the reduced I_{to}. The experimental recording of

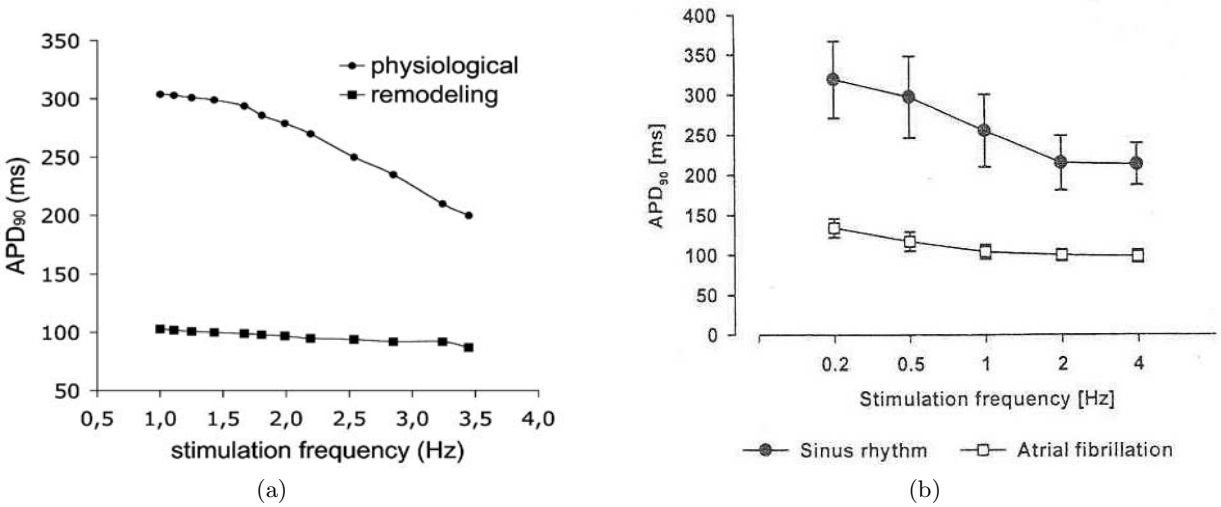

Fig. 10.44. APD_{90} in dependence on stimulation frequency in physiological and remodeled cell. (a) APD_{90} of the model in physiological and remodeled cell. (b) APD_{90} restitution from 10 cells in sinus rhythm and 8 cells of the AF group [199]. Fig. from [380].

AP in case of sinus rhythm and remodeling is shown in fig. 4.17, in which the reduction of APD from 350 ms to 120 ms is consistent with the simulated result.
APD restitution is an important aspect to understand perpetuation of AF. APD_{90} is defined as the APD to 90% repolarization. The normal rate adaptation curve of AP showed a gradual and nearly linear decrease with increasing stimulation frequency. By contrast, patients with AF have nearly flat rate adaptation curves (fig. 10.44 b). The simulated APD restitution in fig. 10.44 a is similar to the clinical report.
This electrophysiologically changed model was incorporated in section 11.2.4 in a schematic model of the right atrium including the human sinoatrial node model (section 10.3) to investigate the effects of electrophysiological remodeling in the tissue.

10.8.2 Genetic Defects

Four different types of genetic defects were modeled in the scope of this work. These were the mutation leading to the familial type of atrial fibrillation [379] and the three first long QT syndromes (LQT1, LQT2, and LQT3) [409].

10.8.2.1 Familial Atrial Fibrillation

A recent study identified a familial type of atrial fibrillation (FAF) based on a mutation influencing the cardiac I_{Ks} channel. The mutant channel is characterized by a gain-of-function and a nearly linear current-voltage relationship (section 4.8.2.1) [204]. The Courtemanche, Ramirez, and Nattel (CRN) ionic model of human atrial cardiomyocytes [238] was utilized to reconstruct the measured mutant characteristics.
Measurement data of Chen et al. [204] in COS-7 cells were used to modify channel kinetics and density of I_{Ks} in the CRN model by numerical minimization. The environmental conditions for the simulation were adopted from the measurement conditions: Temperature was set for the equations of the reversal potential to 22 °C and intracellular and extracellular potassium concentration were set to 5 nM and 150 nM, respectively. The current-voltage relationship was simulated by a step protocol. Starting from the holding potential of $-80\,mV$, the potential was stepped for each 3 seconds between $-130\,mV$ and $50\,mV$ in a $10\,mV$ increment. Figure 10.45 b shows the measured steady state current-voltage relationship at the end of the 3 second voltage step.
The mathematical description of I_{Ks} in the CRN model was left unchanged, only parameters of rate constants and the maximum conductance of the I_{Ks} channel were modified. The optimal values for the parameters of the channel characteristics were found using a gradient optimization method (section 9.1.3) to minimize the mean square error between measured and simulated maximum current for each voltage step [349].
The best fit of simulated mutant characteristics to the measured data is given by:

$$I_{Ks} = g_{Ks} X_s^2 \left(V_m - E_K\right), \qquad \frac{dX_s}{dt} = \frac{X_{s_\infty} - X_s}{\tau_{Xs}}$$

$$\alpha_{Xs} = 1.2 \cdot 10^{-5} \frac{V_m + 30}{1 - \exp\left(-\frac{V_m+30}{10}\right)}, \qquad \beta_{Xs} = 1.1 \cdot 10^{-4} \frac{V_m + 30}{\exp\left(\frac{V_m+30}{8.5}\right) - 1}$$

$$X_{s_\infty} = \left[1 + \exp\left(-\frac{V_m + 30}{22}\right)\right]^{-\frac{1}{2}}, \qquad \tau_{Xs} = \frac{1}{2}\left[\alpha_{Xs} + \beta_{Xs}\right]^{-1}$$

with $g_{Ks} = 1\,nS/pF$ as the maximum conductance of the COS-7 cell, the gating variable X_s, the transmembrane voltage V_m, the Nernst voltage of potassium E_K, the rate constants α_{Xs}

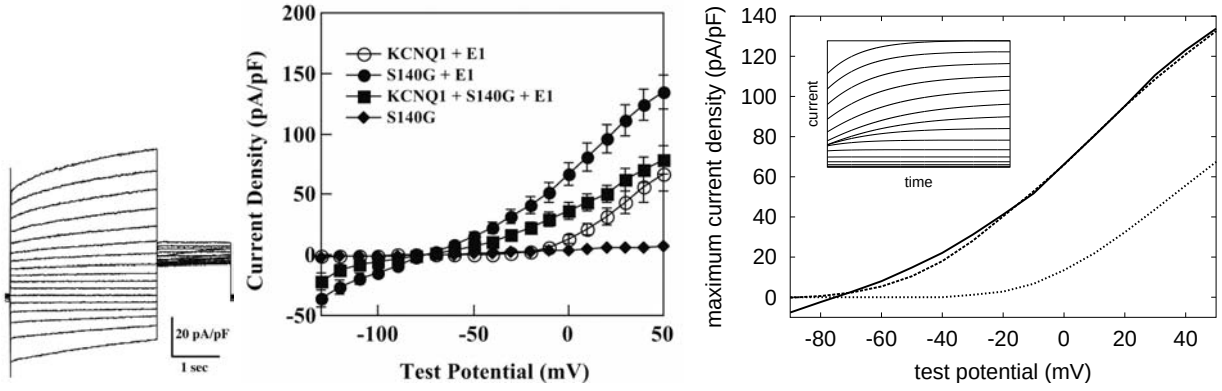

(a) (b) (c)

Fig. 10.45. The S140G mutation alters the KCNQ1-KCNE1 (I_{Ks}) current. (a) Representative current traces recorded from COS-7 cells transfected with S140G-KCNQ1 and KCNE1 [204]. (b) Steady state current density is plotted versus voltage for the indicated transfection combination [204]. (c) Steady state current-voltage relationship of the measured (solid) and simulated (dashed) mutant I_{Ks} channel. The inset shows the simulated current traces. The physiological current-voltage relationship measured by Chen et al. is displayed as dotted line. Fig. from [379].

and β_{Xs}, the steady state constant X_{s_∞}, and the relaxation time constant τ_{Xs}. This solution had a root mean square error (eq. 9.1) of $2.92\,pA/pF$. Fig. 10.45 b,c shows the measured and simulated steady state current-voltage relationship of the mutant channel as well as the normal channel in COS-7 cells [204].

This mutant I_{Ks} channel was incorporated into the CRN model. The maximum conductance g_{Ks} was set for the simulations with the ionic atrial model to the original value of $0.129\,nS/pF$ used in [238]. The normal and the mutant action potentials (AP) are displayed in fig. 10.46 a for different basic cycle lengths (BCL). The APD of the mutant cells was always shorter than the physiological one, but had a lower APD-BCL relationship. The physiological APD_{90} was $302\,ms$ at 1 Hz. The mutant one was reduced to $105\,ms$. Figure 10.46 b illustrates the I_{Ks} current for both physiological and mutant case at $1\,Hz$. The rectifier characteristic of the physiological channel switches to a current, which acts comparable to a very large background current due to the nearly linear current-voltage relationship. This is visible in fig. 10.46 b by

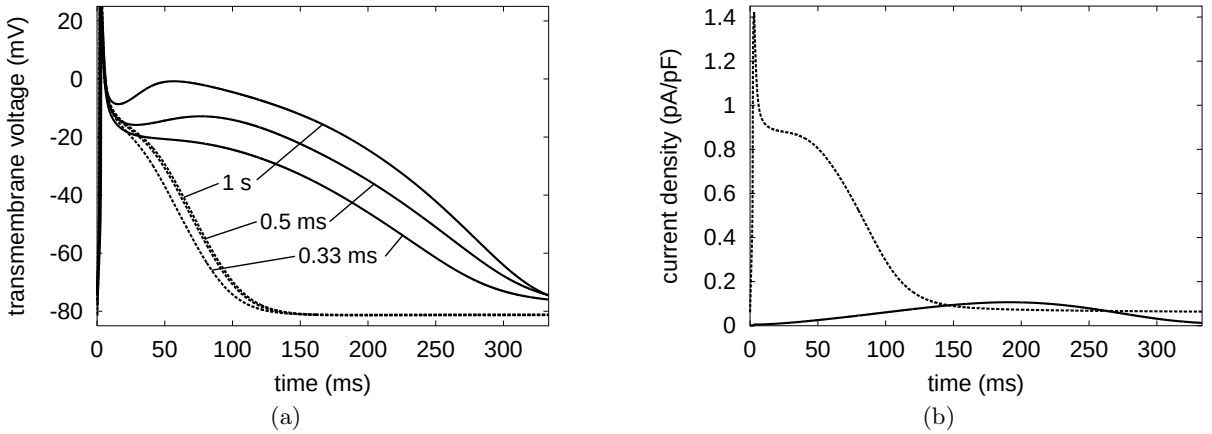

(a) (b)

Fig. 10.46. Characteristics of the FAF mutation. (a) AP of physiological (solid) and mutant (dashed) cells of the CRN model at different basic cycle lengths. (b) Current I_{Ks} for the physiological (solid) and mutant (dashed) cell during the AP presented in (a) at a stimulus frequency of 1 Hz. Figs. from [379].

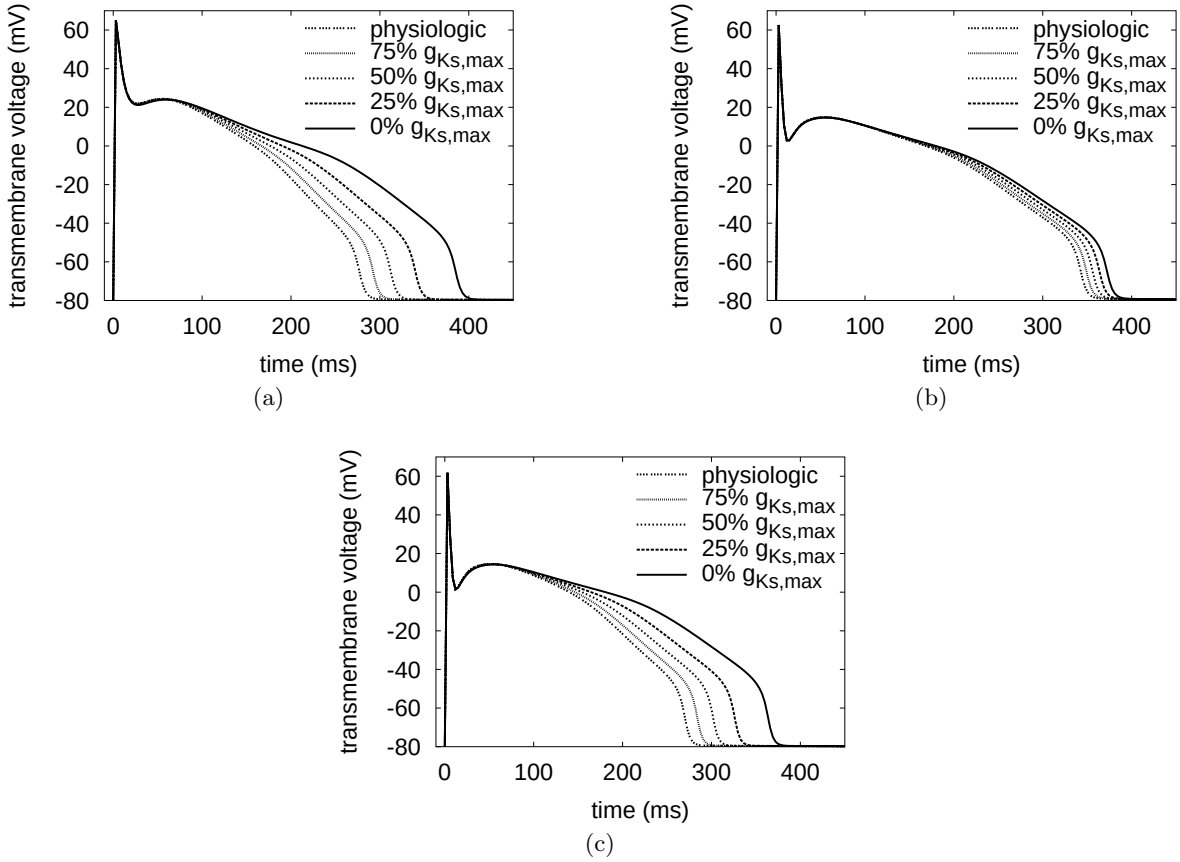

Fig. 10.47. Action potentials of the LQT1 syndrome model. Changes of the transmembrane voltage under consideration of the changes of $g_{Ks,max}$ are shown for (a) endocardial, (b) M, and (c) epicardial cells. Figs. from [409].

the AP-like shape of the mutant I_{Ks}. Thus, the larger current during the plateau phase was responsible for the shortening of the APD in the mutant cell.

Discussion: The differences between simulated and measured current-voltage relationship were not significant. There was no quantitative information about the temporal behavior of the mutant channel. But simulated current traces were in good agreement with measured ones. The main difference between physiological and mutant channel characteristics was a voltage shift in the rate constants of the gating variable.
The measurement was performed at room temperature. We considered the temperature drift of E_K, but not the temperature variation of the rate constants. The simulated APs showed significant reduction of duration. The APs could not be validated by experimental values due to missing data. Thus, the model might not be able to reconstruct the changes in mutant APs absolute correctly. The effects of this mutation in a schematic tissue model of the right atrium are compared to physiological simulations in section 11.2.3.

10.8.2.2 Long QT Syndrome

The aim of this simulation was to investigate the mechanisms and effects of the three first types of the long-QT syndrome (section 4.8.2.2) by assessing single cell simulations and transmural ECGs of coupled cells (section 11.2.7) using a detailed modeling of the electrophysiology. The transmurally heterogeneous ventricular electrophysiological model (section 10.5) was utilized to describe the different cell types.

LQT1, LQT2, and LQT3 were incorporated into this electrophysiological heterogeneous model by changing the ion channel properties of the currents I_{Ks}, I_{Kr}, and $I_{Na,L}$, respectively [208]. The maximum conductances $g_{Ks,max}$ and $g_{Kr,max}$ of I_{Ks} and I_{Kr} were reduced to characterize LQT1 and LQT2, respectively. A Markov model of I_{Na}, which describes a mutation in the C terminus of the channel called 1795insD (fig. 5.14) [286], was incorporated to describe LQT3.

The effects of the LQT1 syndrome on AP are shown in fig. 10.47. The reduction of $g_{Ks,max}$ led to a prolongation of APD in all three cell types. Other than in measurement data [212], the APD of the M cells was not increased in the same way as of endo- or epicardial cells. This was provoked by the homogeneously distributed I_{Kr} as the remaining repolarization current. This is the reason why the APD of all three cell types is nearly the same for complete loss of I_{Ks} function. The reason for the differences between experimental and simulated results could be that a genetic defect of I_{Ks} might also influence the properties of I_{Kr} or that the physiologically existing late component of the fast Na^+ current $I_{Na,L}$ is prolonging the APD during the plateau phase. Both effects were not considered in this approach.

The reduction of I_{Kr} channel density as mechanism for the LQT2 syndrome led in the uncoupled single cell simulations to a prolongation of the APD in all of the three cell types but mostly in M cells (fig. 10.48). This was provoked by the heterogeneously distributed density of I_{Ks} as the remaining repolarization current (tab. 10.4).

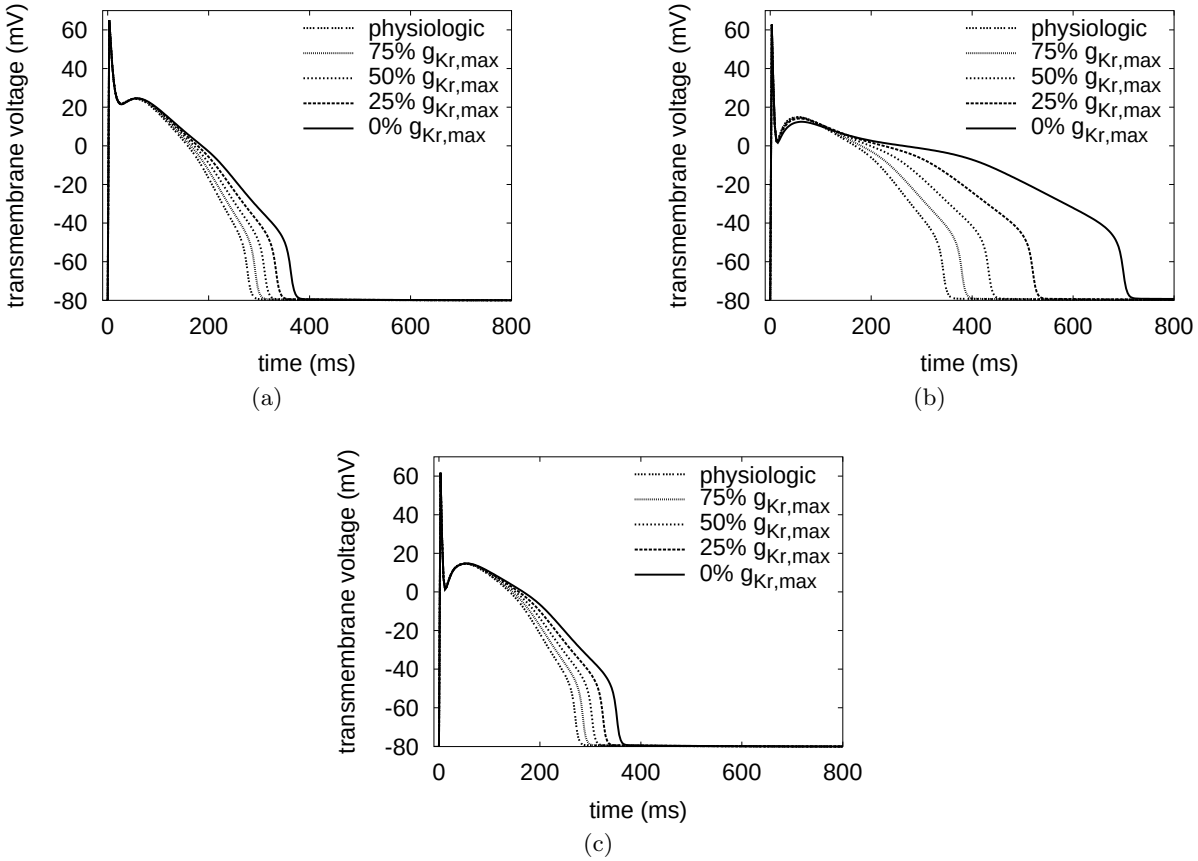

Fig. 10.48. Action potentials of the LQT2 syndrome model. The variation of the transmembrane voltage for (a) endocardial, (b) M, and (c) epicardial cells during the change of $g_{Kr,max}$, respectively is shown. Figs. from [409].

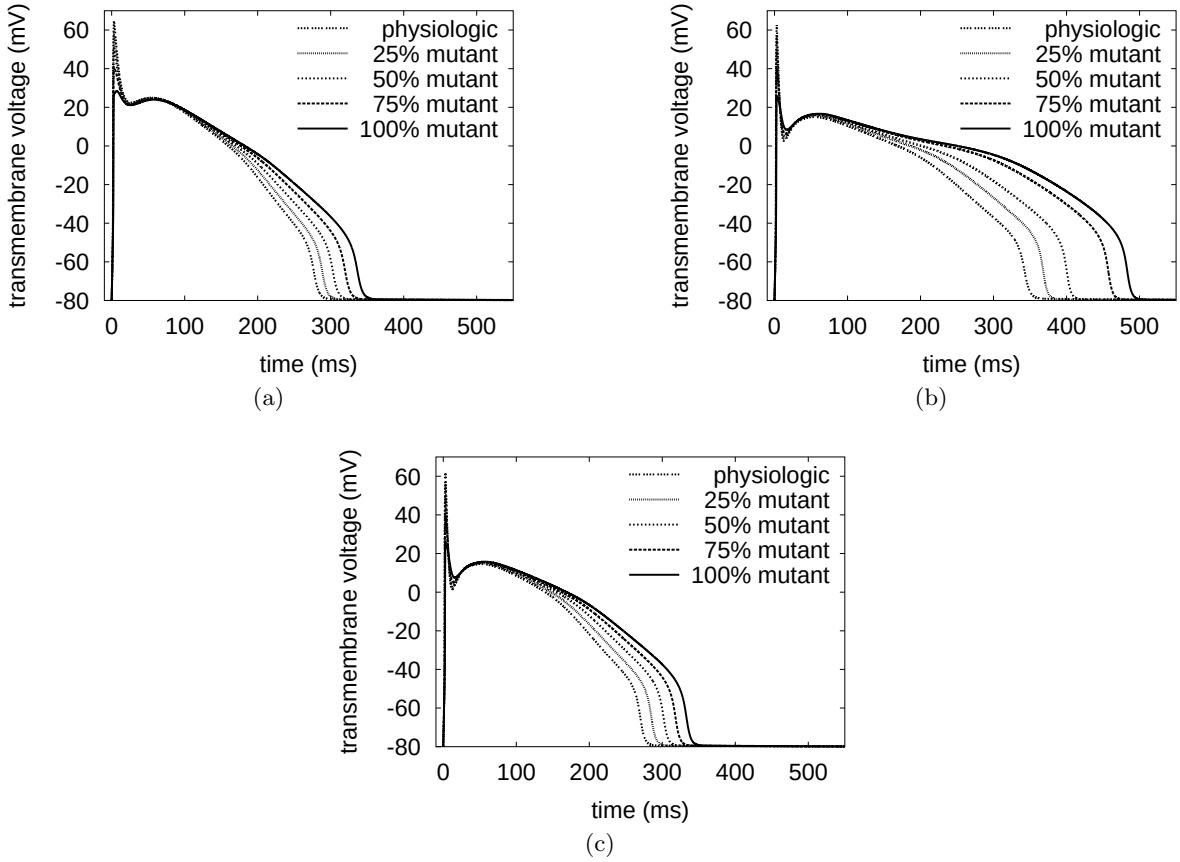

Fig. 10.49. Action potentials of the LQT3 syndrome model. The transmembrane voltage variation of (a) endocardial, (b) M, and (c) epicardial cells due to the inclusion of mutant late I_{Na}. Figs. from [409].

The LQT3 syndrome was described by the inclusion of the presented mutation of I_{Na} channels leading to an unphysiological late component during the plateau phase. The APD prolongation in the single cell simulations was most dominant in mid-myocardial cells (fig. 10.49). This effect happened because the APD of M cells was already longer than in endo- or epicardial cells in the physiological case, which led to a larger component of the inward $I_{Na,L}$ in M cells, which prolongs the plateau phase.
Altogether, the three types of long QT syndrome were reconstructed correctly with the mutant heterogeneous model and all three of the transmural ECGs show prolongation of the QT interval (section 11.2.7).

11

Results: Electrophysiology and Tension Development in Tissue

The second part of the results of this thesis addresses simulations in tissue using the excitation conduction model in conjunction with the models described in chapter 10. The chapter is divided into two parts. The first part illustrates the electromechanical properties of the tissue in physiological and the second in pathological states.
The physiological models consist of the description of the excitation conduction in anatomically accurate geometries of the sinoatrial node, the entire atrium, and the left ventricle. For the left ventricle, both electrical and mechanical properties are described. Excitation conduction simulations in schematic geometries were performed in the right atrium, a line through the left ventricle, and a virtual left ventricular wedge preparation.
The pathological models comprise descriptions of atrial flutter and fibrillation in a schematic model of the right atrium. Furthermore, the mechanisms and effects of familial atrial fibrillation and atrial electrophysiological remodeling in tissue were expressed in a schematic model. The effects of ventricular tachycardia on electromechanical properties were simulated in the virtual wedge preparation. The last section illustrates results obtained in a model of a line through the left ventricle when simulating the long QT syndrome.

11.1 Physiologic Electromechanics in the Heart

This section illustrates results obtained by simulation where the models presented in chapter 10 were combined to electromechanical models on tissue and organ level including anatomical data and considering excitation conduction using the monodomain or bidomain approaches. All simulations presented in this section illustrate the physiological behavior of the human heart. Simulation results with pathophysiological conditions are presented in section 11.2.
The first part of this section describes the excitation conduction in anatomically accurate geometries. For the second part, schematic models were used to reduce the complexity of the obtained data.

11.1.1 Sinoatrial Node

The sinoatrial node (SAN) model of fig. 10.2 was used in combination with the monodomain approach and the electrophysiological model of the heterogeneous human SAN (section 10.3) in order to gain simulation results of excitation conduction in the human sinoatrial node.
Isolated sinoatrial node cells of the periphery show a higher frequency of autorhythmicity (fig. 10.11). This feature was the same in the model of the entire human SAN, but without

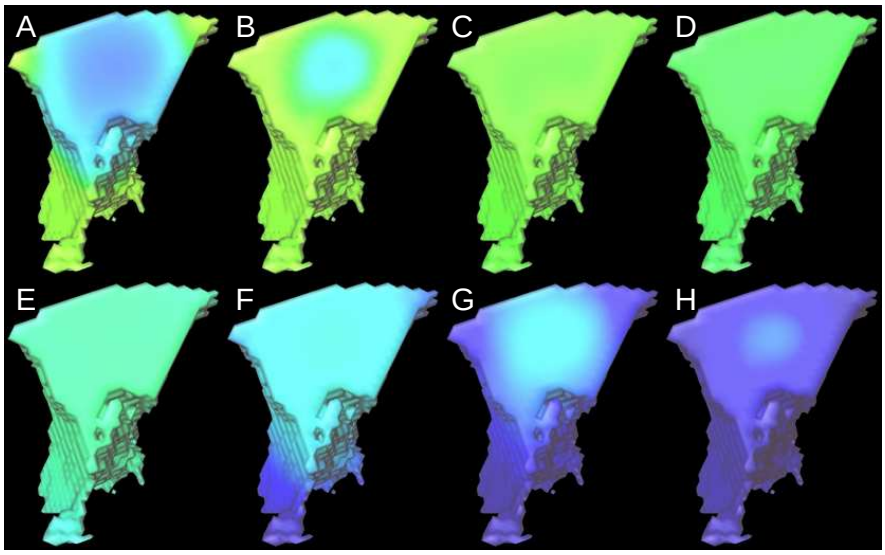

Fig. 11.1. Color coded transmembrane voltages of the isolated human SAN model without coupling to the neighboring atrium. Blue = $-70\,mV$; Yellow = $10\,mV$. The excitation is initiated in peripheral cells due to missing electrotonic effects of surrounding AWM. (A) Activation starts in peripheral cells. (B) Central cells get excited $19\,ms$ after peripheral cells. (C–E) No significant voltage gradient is visible during the plateau phase. (F+G) Cells repolarize from periphery towards center. (H) Activation vanishes finally in central cells. Fig. adapted from [343].

surrounding atrial tissue (fig. 11.1). This electrically coupled model included heterogeneous tissue distribution from central to peripheral cells. The excitation was initiated in peripheral cells (fig. 11.1 A). Afterwards central cells got activated (fig. 11.1 B). The transmembrane voltage distribution was relatively homogeneous during the plateau phase (fig. 11.1 C – E). The repolarization started in peripheral cells (fig. 11.1 F) and propagated afterwards towards central cells (fig. 11.1 G), where final repolarization was recognized (fig. 11.1 H). The autorhythmic frequency of the isolated SAN model was 79 beats per minute (pbm) triggered by peripheral cells.

The sequence of activation changed when the cells were surrounded by atrial working myocardium (AWM) (fig. 11.2). The transmembrane voltage of peripheral cells was shifted towards more negative values due to electrotonic effects of the surrounding atrial cells, which had a resting voltage of approxematly $-80\,mV$. This reduced the autorhythmic frequency of peripheral SAN cells and the final excitation of the SAN started in central cells with 63 bpm (fig. 11.2 A). The central activation was driving the peripheral cells to get excited (fig. 11.2 B). The repolarization sequence of the SAN model coupled to the atrium was comparable to the model without coupling to the AWM, especially during the plateau phase (fig. 11.2 C – H). The repolarization began in peripheral cells due to the longer APD of central cells (fig. 11.2 F,G). Furthermore, the surrounding AWM was already repolarized and shifted peripheral cells towards a more negative voltage.

11.1.2 Visible Female Atrium

For this simulation, the anatomical model of the human atrium (section 10.1.1) was used to describe the excitation conduction. The electrophysiological heterogeneity of the atrial working myocardium was implemented based on [174, 246] (section 10.4) and was set to the different tissue classes that were segmented in the atrial model (fig. 10.1). The excitation conduction in this model was calculated with the monodomain model where the Poisson's

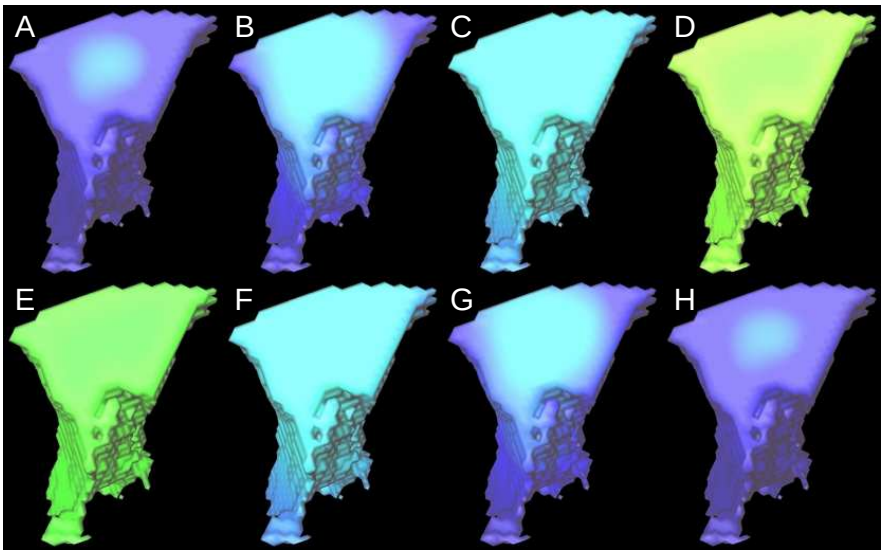

Fig. 11.2. Color coded transmembrane voltages of the human sinoatrial model coupled with surrounding atrial tissue. Only the SAN is illustrated to depict the differences of this model compared with the model of fig. 11.1. Blue indicates $-70\,mV$ and yellow $10\,mV$. The excitation is initiated in central cells due to electrotonic effects. The repolarization sequence is comparable with fig. 11.1. Fig. adapted from [343].

equation was discretized using the finite element method. The simulation was performed on 10 Apple XServe G5 dual 2 GHz processor cluster nodes using multiprocessing techniques (section 9.2.3). The model consists of approximately 18.8 million elements. The simulation required 3.8 GB of main memory and needed 37 hours of calculation time for a $1000\,ms$ interval with a temporal increment for the integration of the ionic models and the calculation of the electric field of $20\,\mu s$. The excitation was initiated by the heterogeneous model of the sinoatrial node (section 11.1.1).

The transmembrane voltage patterns of the computational simulation of the entire atrium including SAN are presented in fig. 11.3 and 11.4. The initiation of the excitation started in the center of the SAN (fig. 11.2 A – C). The excitation spread afterwards to the periphery near to the region where the crista terminalis (CT) is coupled to the SAN. Once the CT was activated, the excitation propagated preferentially towards the atrioventricular region along the CT (fig. 11.3 A – C and 11.4). The excitation spread on the endocardium of the right atrium (RA) along pectinate muscles (PMs) and both CT and PM activated the right AWM (fig. 11.3 B – D and 11.4 D – F). Earliest activation of the left atrium (LA) was found in the region of Bachmann's bundle (BB) and afterwards excitation spread over to the appendage (APG) (fig. 11.3 D – F). The entire left AWM was activated from BB towards atrioventricular region. During the plateau phase, the transmembrane voltage was varying only little within the atrium (fig. 11.3 G). Repolarization started in the area of first activation (fig. 11.3 H) and spread similar to the depolarization but in a more homogeneous manner (fig. 11.3 I).

The atrial model was excited periodically due to the pacemaker with a frequency of 63 bpm. The excitation conduction velocities were $0.6\,m/s$ for AWM, $1.2\,m/s$ for CT, $1.6\,m/s$ for PM, and $1.1\,m/s$ for BB. The time to activation of the right atrium was $5\,ms$ for BB and $21\,ms$ for the septum. In the left atrium, the first activation was found after $24\,ms$ near BB and after $38\,ms$ in septal regions. The endocardial activation times were: $26\,ms$ for BB, $83\,ms$ for the RA, $79\,ms$ for the LA, and $103\,ms$ for the whole atrium. The entire atrium was repolarized after $250\,ms$.

Discussion: The simulation of the entire atrium demonstrates the importance of including realistic anatomical structures and fiber orientation combined with realistic heterogeneous human electrophysiology and anisotropic electrical properties. The importance of BB as a dominant interatrial connection during sinus rhythm was verified.
The conduction velocities of the tissue types were in the range of measured data. Hansson et al. [375] reported $0.68-1.03\,m/s$ for AWM. Boineau et al. [61] measured a velocity in the CT of $0.7-1.3\,m/s$. PMs have been measured yielding a conduction velocity of $1.17-1.54\,m/s$ [410]. Dolber and Spach [411] reported a velocity in BB of $0.92-1.67\,m/s$. The simulated time to activation and total endocardial activation times were equivalent to the measurement data reported by Lemery and coworkers (section 4.7.2) [173].

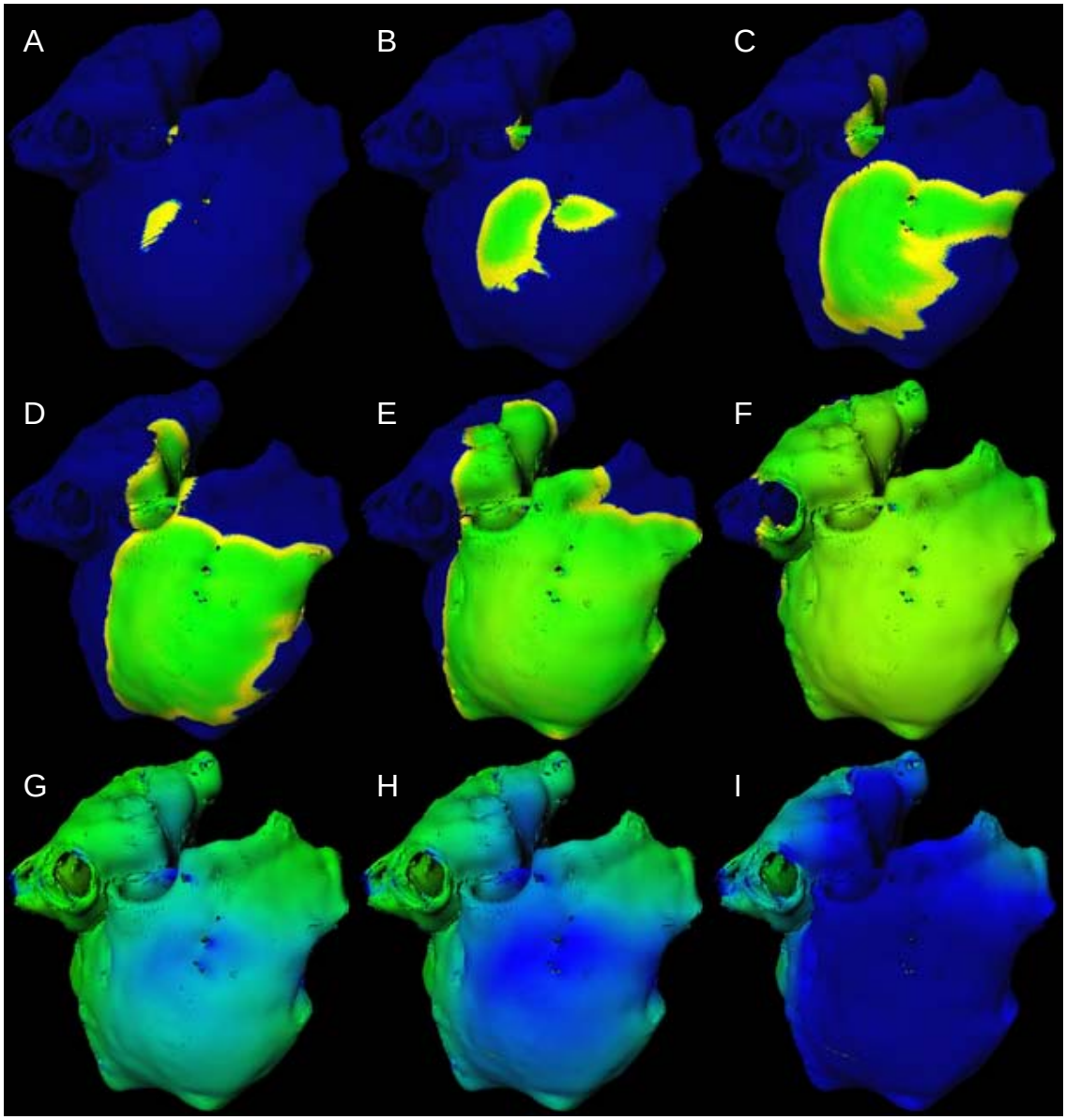

Fig. 11.3. Simulated excitation conduction in the atria in a frontal view. The transmembrane voltage is illustrated color coded from blue $V_m = -70\,mV$ to yellow $V_m = 10\,mV$. The excitation is conducted fastest in the RA along the the CT and PMs. LA is activated in the area along BB. The time instances indicate the temporal offset after the excitation is transmitted from the SAN to surrounding atrial tissue. (A) $10\,ms$, (B) $15\,ms$, (C) $20\,ms$, (D) $25\,ms$, (E) $35\,ms$, (F) $55\,ms$, (G) $200\,ms$, (H) $210\,ms$, (I) $230\,ms$. Fig. adapted from [343].

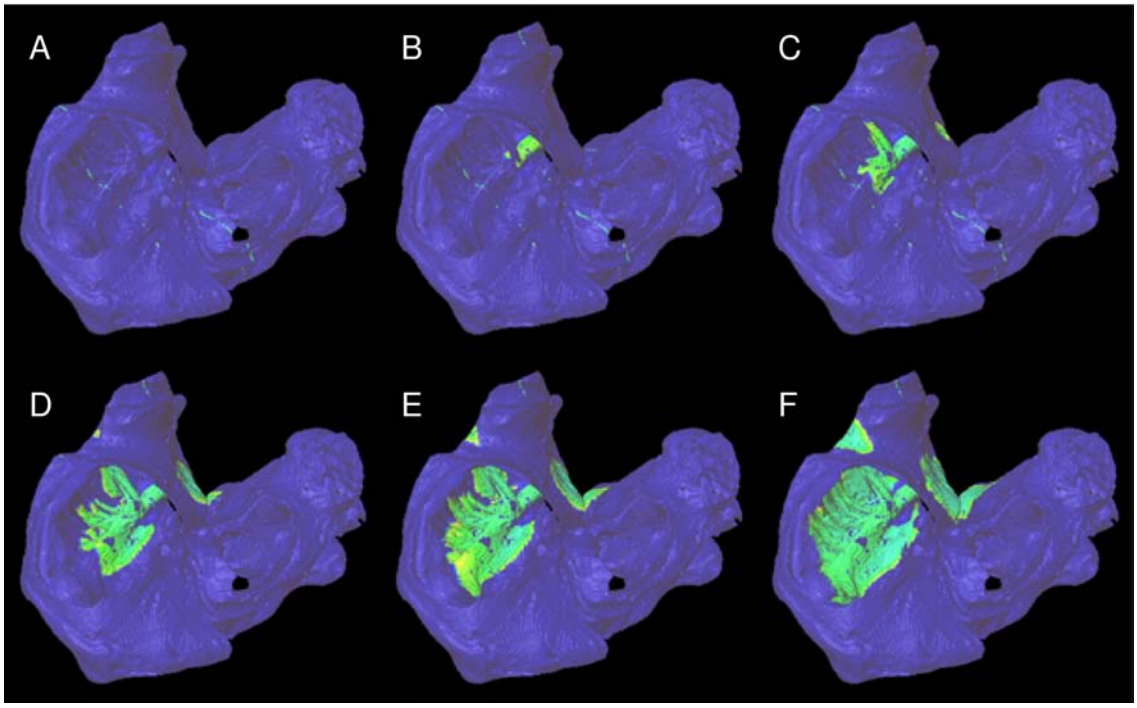

Fig. 11.4. Simulated excitation conduction in the atria in a view through the valve plane. The transmembrane voltage is illustrated color coded from blue $V_m = -70\,mV$ to yellow $V_m = 10\,mV$. The excitation is initiated in the SAN and conducted fastest in RA along CT and PM. The time instances indicate the temporal offset after the excitation is transmitted from SAN to atrium. (A) $1\,ms$, (B) $10\,ms$, (C) $15\,ms$, (D) $20\,ms$, (E) $25\,ms$, (F) $30\,ms$. Fig. adapted from [343, 371].

The first activation of BB was earlier in the model compared to the findings of Lemery and colleagues. This effect can be explained by the fact that transmembrane voltages were traced in this work and Lemery et al. used extracellular potentials. Total endocardial activation time of the entire atrium was shorter in the model. It was longer in the patient study of Lemery et al. possibly due to the effects of reduced atrial gap junction density of patients with AF [412]. Additionally, this can explain the shorter times of first activation in the model.
No measured repolarization data is yet reported. In the model, repolarization was more homogeneous compared to the depolarization because of the heterogeneous APD distribution having longest APD near to the SAN and shortest in distal areas. Repolarization is an interesting topic to investigate since its disturbance due to e.g. pathologies reducing the APD or disturbing the dispersion of repolarization can lead to arrhythmia.
This section showed that detailed anatomical structures combined with fast conducting bundles have to be considered in order to reproduce the normal excitation pattern in the atrium seen experimentally. CT, PM and BB were preferential pathways for atrial conduction. Other groups have also worked on modelling whole human atrial activity [413, 414, 284], but have not included the anatomical and electrophysiological details presented in this work. Furthermore, they stimulated in the SAN region to initiate atrial excitation. The work of Blanc et al. [413] and Zemlin et al. [414] was mainly focused on efficiency for long-time simulations, for which some details were consequently neglected. Blanc and colleagues investigated arrhythmias and their treatment with ablation in a 2D model, but have no fast-conducting bundles. Zemlin et al. included in their 2D model fiber orientation of AWM but neglected BB. Harrild & Henriquez [284] included anatomical structures without heterogeneous electrophysiology. Furthermore, they set slowed conduction in some regions.

11.1.3 Left Ventricle of the Visible Female Data Set

In order to describe the excitation conduction process coupled with the tension development in the human ventricle, several models were combined. The anatomical model of the left ventricle derived from the Visible Female heart formed the geometrical basis (section 10.1.2). The fiber orientation was included in this model using the presented approach in section 10.2. Heterogeneous ventricular electrophysiology was implemented using the adapted heterogeneous Priebe-Beuckelmann model (section 10.5). Tension was described by the hybrid tension development model of section 10.6.
The presented models were combined to an electromechanically coupled heart model [377]. The simulation required 2.6 GB of main memory and needed for a 600 ms interval with a temporal increment of 20 μs seven hours of calculation time. The electrical activation of the tissue was initiated in subendocardial points assigned to Purkinje fiber ends by applying intracellular stimulus currents.
The transmembrane voltage distribution in the left ventricle (LV) is shown in fig. 11.5 at different time steps after the initial activation during one heart cycle. The excitation started at subendocardial, apical points (fig. 11.5 A – B). Afterwards, the depolarization front wandered basally and from endocardial to epicardial regions (fig. 11.5 C – D). No significant transmural gradient of the transmembrane voltage was present during the plateau phase (fig. 11.5 E – F). The repolarization was mainly homogeneous (fig. 11.5 G), but the final repolarization was located in deep subendocardium near the M cells (fig. 11.5 H). These characteristics were also clearly evident in the cross-sectional slice in fig. 11.6 with more quantitative detail.

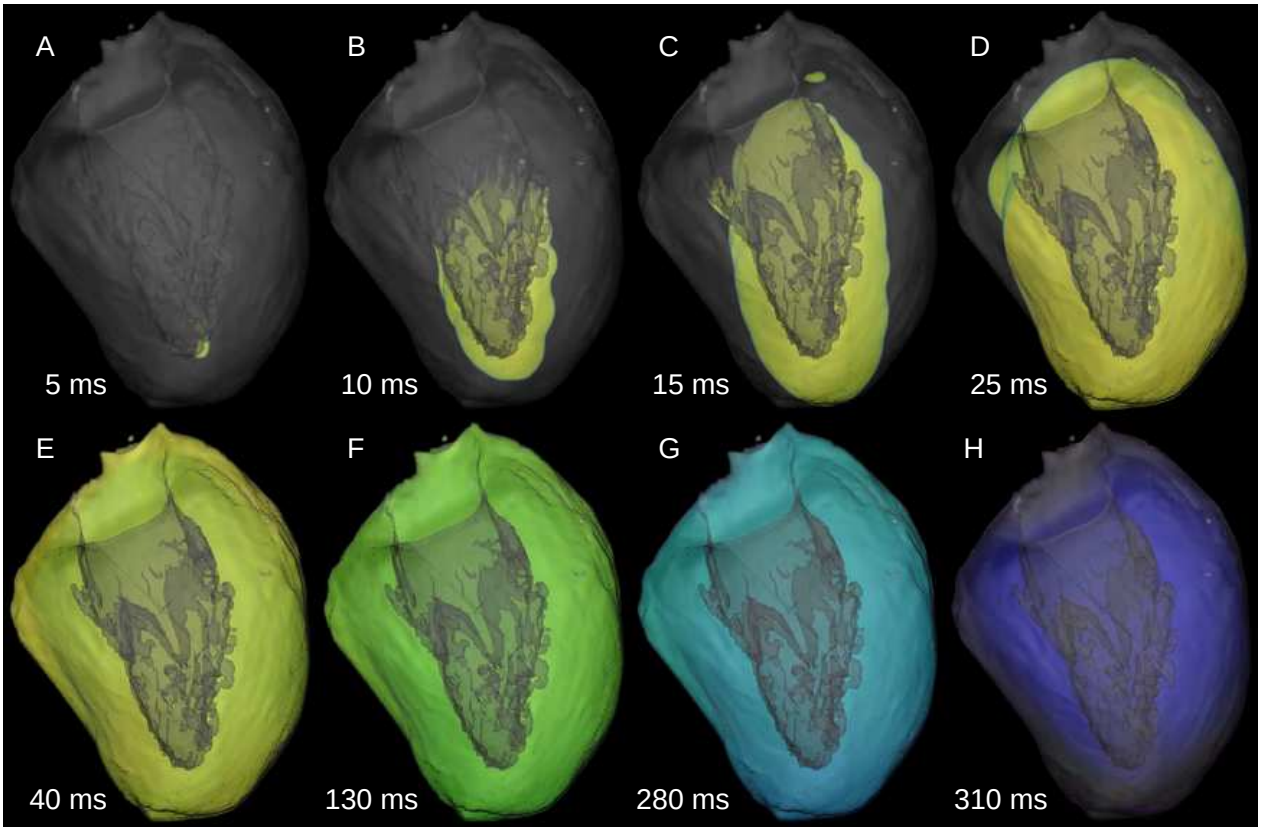

Fig. 11.5. Excitation and repolarization conduction in the Visible Female left ventricle at different time steps after initial activation. The transmembrane voltage distribution is illustrated color coded. Blue is resting (−80 mV) and yellow is activated (10 mV). Fig. adapted from [377].

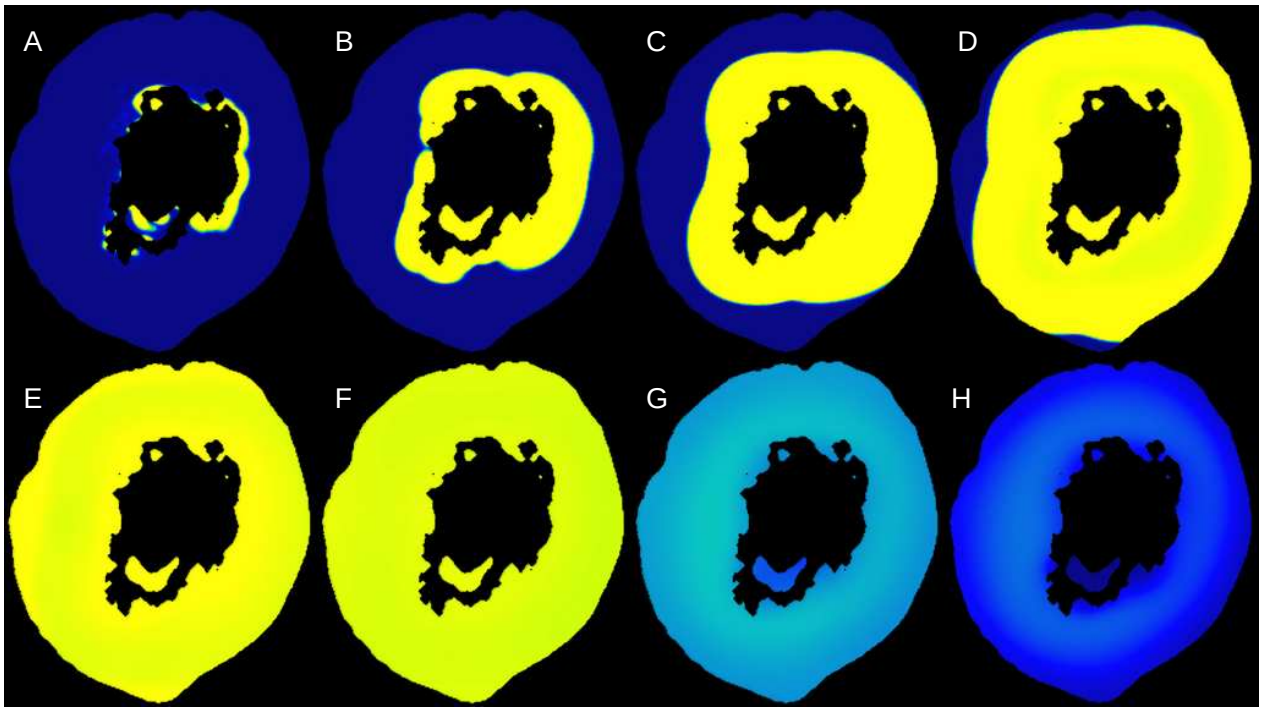

Fig. 11.6. Central cross-sectional slice of the left ventricle. Same information as in fig. 11.5. The action potential heterogeneity is mainly visible during the repolarization phase. Fig. from [377].

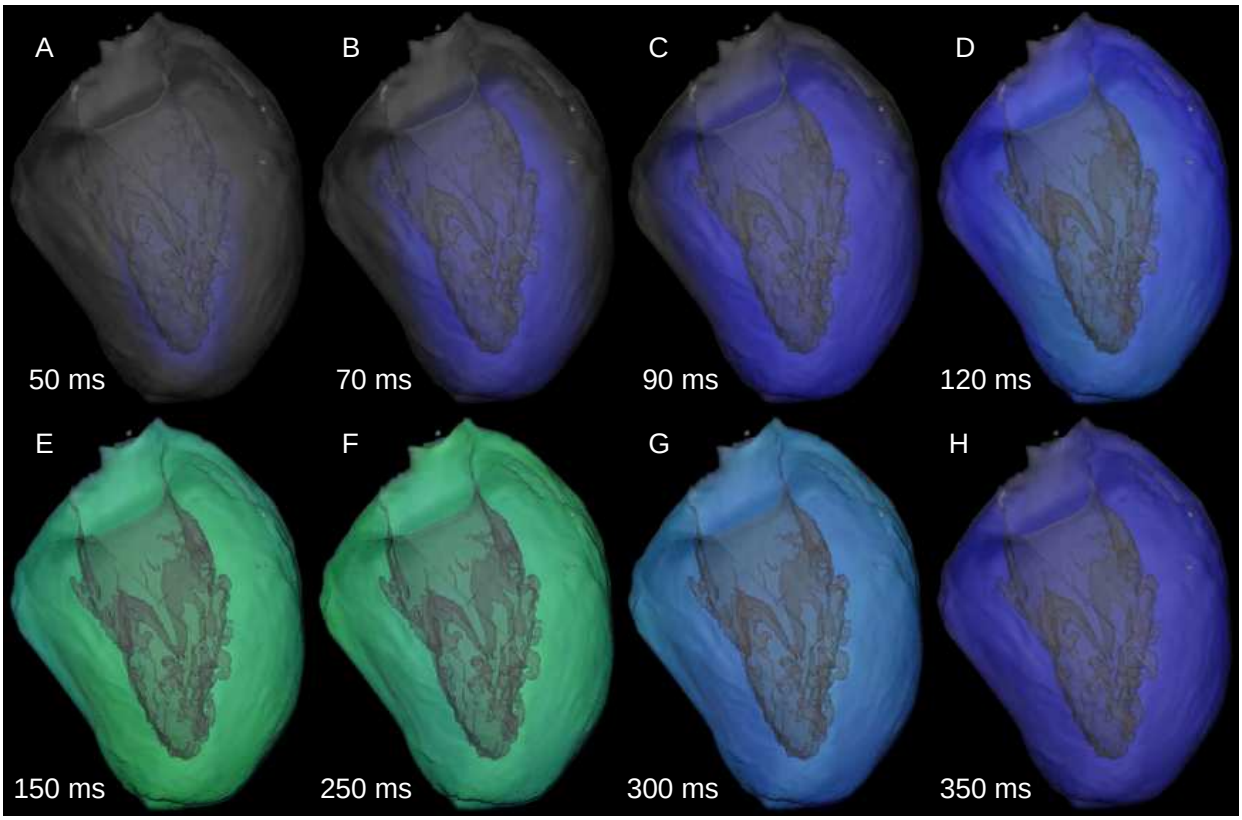

Fig. 11.7. Color coded tension development in the Visible Female left ventricle at different time steps after initial electrical activation. Blue is resting normalized tension (0.2) and yellow maximum (0.7). Fig. adapted from [377].

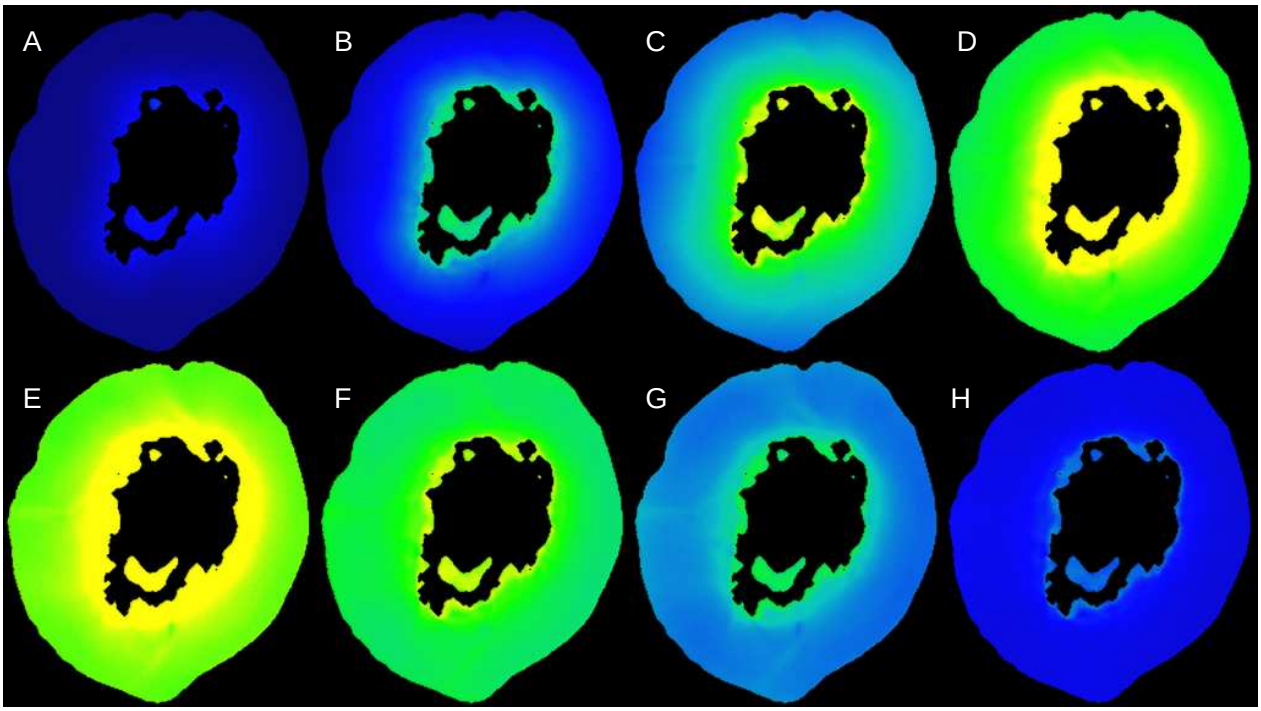

Fig. 11.8. Central cross-sectional slice of the left ventricle. Same information as in fig. 11.7. Fig. from [377].

Figure 11.7 shows the developed tension in the model at different time steps. The onset of tension was more homogeneous than the electrical activation but still started near the endocardium (fig. 11.7 A – D). The maximum tension was also larger in endocardial areas compared to epicardial during the peak of the tension (fig. 11.7 E – F). During relaxation, the tension in endocardium was largest (fig. 11.7 G – H). The same information is shown in a cross-sectional slice in fig. 11.8.

Figure 11.9 demonstrates the distinctions in the electromechanical properties in two different situations: The first results were obtained from simulations with isolated cells of different regions from endo- to epicardium and the others were derived from the heterogeneous and electrically coupled anatomical LV model.

Figure 11.9 A shows that the APD distribution occurring in the simulation with the isolated cells was smoothened in the LV model due to electrotonic interaction. This led to a prolongation of APD mainly in endocardial cells resulting in the vanishing of repolarization in the LV model close to the M cells.

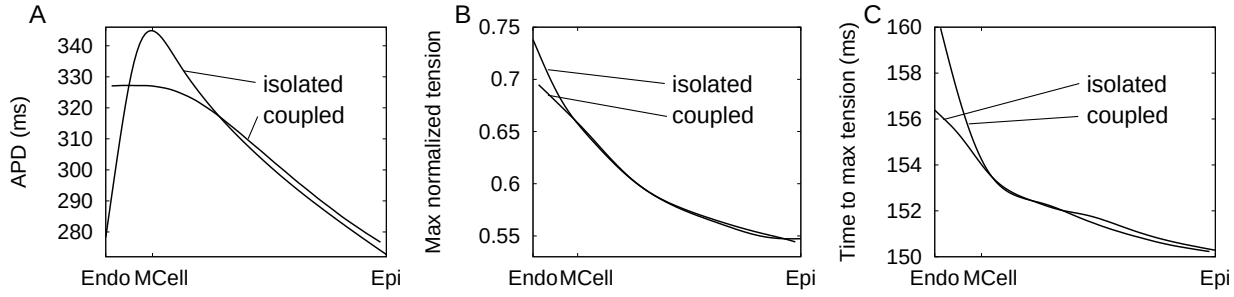

Fig. 11.9. Differences between heterogeneous single cell models and heterogeneous coupled model of the left ventricle. A: Action potential duration B: Normalized maximum peak tension C: Time to maximum peak tension.

The distribution of transmural maximum tension (fig. 11.9 B) was not as much influenced by the electrical coupling as the APD. The reason for this was that the calcium transient was a few milliseconds after the depolarization, but the electrotonic interaction acts mainly on the repolarization phase. The largest differences in transmural direction were visible in the subendocardial area.
The time to peak tension development shown in fig. 11.9 C demonstrates the importance of electrophysiological heterogeneity. The time to peak tension development was longer in subendocardial compared to subepicardial myocytes leading to a homogenization of the tension development. The time to peak for subendocardial cells was more prolonged compared to the isolated cell simulations due to the coupling enhancing the effect of mechanical synchronization.

Discussion: The presented model is suitable to simulate the general effects of the electrophysiologic excitation and the tension. The tension variation induced by heterogeneity is in qualitative agreement with recently published data for canine LV [183]. Both the simulation and the measurements showed that the tension, respectively the deformation in the measurements, was largest in endocardial areas and decreases towards epicardium (fig. 11.9 B). Also, the simulated increasing time to maximum tension from subepicardial to subendocardial cells (fig. 11.9 C) is consistent with the measurements [183]. This results in the synchronization of the tension across the ventricular wall due to the electrophysiological heterogeneity. Further experiments have to be carried out to validate the proposed characteristics.
The calcium handling approach of the electrophysiological model has to be adapted to recent descriptions with new measurement data to reproduce accurately the calcium transient in human ventricular myocytes. Furthermore, the mechano-electrical feedback was neglected in this model. This might reduce the gradient in maximum tension (fig. 11.9 B), because tension is scaled by the deformation due to overlap of actin and myosin.

11.1.4 Schematic Right Atrium

The model of the schematic right atrium (section 10.1.3.1) was used to investigate the interaction of the excitation of the sinoatrial node and the surrounding tissue as well as the excitation conduction in the right atrium considering strong anisotropic tissue like crista terminalis and pectinate muscles. For the crista terminalis (CT) and pectinate muscles (PM), adapted electrophysiological parameters were used to quantify the action potential (AP) shapes and ion channel characteristics of these structures [373] (section 10.4, fig. 10.20, and tab. 10.3). Atrial working myocardium (AWM) was set to isotropic conductivity with an excitation velocity of approximately 0.6 m/s. For CT and PM the conductivity was adapted for anisotropy so that the CT had an excitation velocity in longitudinal direction of approximately 1.2 m/s and PMs of approximately 1.6 m/s as described in [284]. The experimentally measured conduction velocities in the physiological case are presented in tab. 11.1.

Table 11.1. Measured and simulated conduction velocities of atrial working myocardium (AWM), crista terminalis (CT) and pectinate muscles (PM) under physiological conditions [284, 375, 415].

tissue	clinical v (m/s)	simulated v (m/s)
AWM	$0.68 \sim 1.03$	0.6
CT	$1 \sim 1.2$	$1.18 \sim 1.2$
PM	$1.5 \sim 2$	$1.54 \sim 1.58$

The fast longitudinal direction was set to the main axis of each PM and CT by using the matrix diagonalization method (section 8.7). The excitation conduction in this model was calculated with the monodomain model where the Poisson equation was implemented using the finite differences method. The initiation of the excitation conduction in the model was given by the autorhythmic depolarization in the sinoatrial node. The excitation conduction in the schematic model of the right atrium is shown in figure 11.10.
The activation of the SAN was initiated in central cells (fig. 11.10 A – B) and was conducted towards peripheral regions (fig. 11.10 C). The excitation was than preferentially spreading into the crista terminalis (fig. 11.10 D). This was due to the less negative resting potential of the CT compared to other atrial myocytes (fig. 10.20) leading to a less electrotonic gradient between SAN and CT compared to the boundary between SAN and AWM.

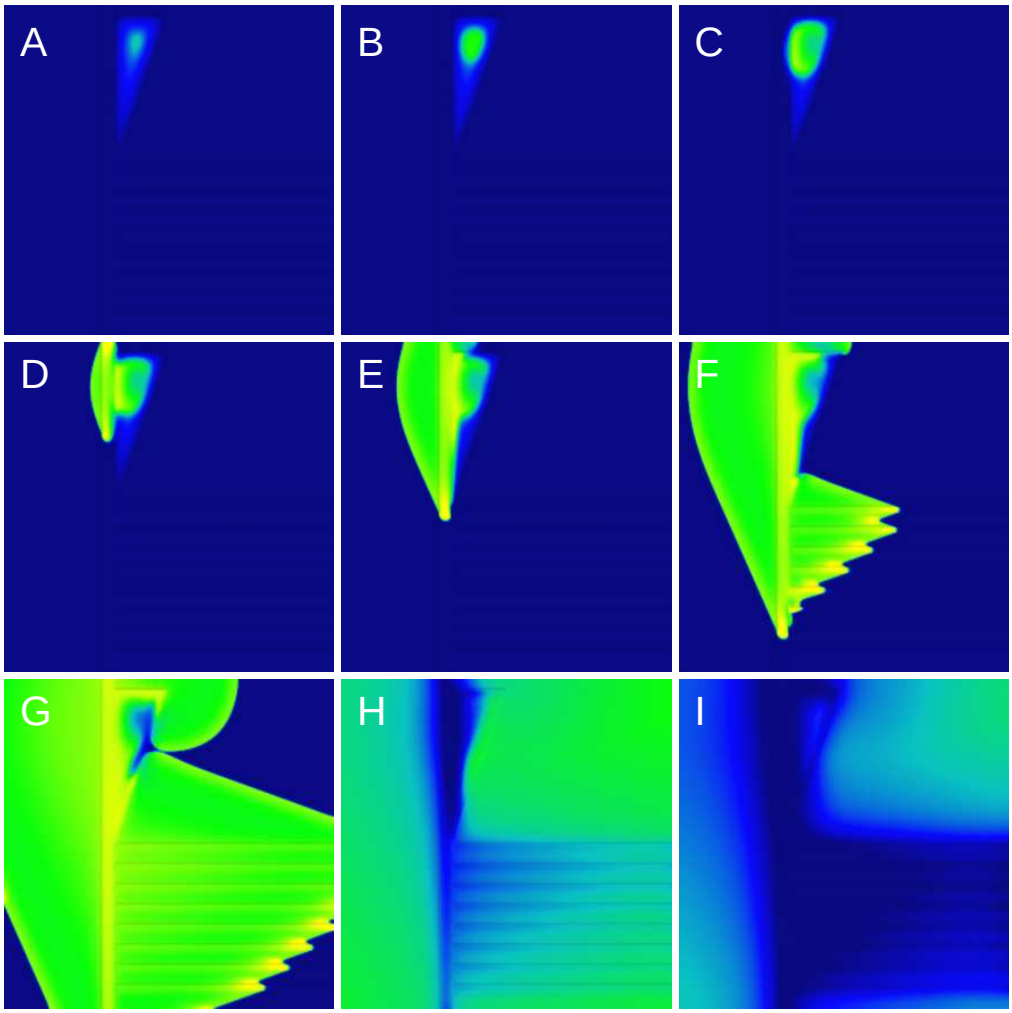

Fig. 11.10. Excitation conduction in the schematic model of the right atrium. The transmembrane voltage is color coded with blue $-70\,mV$ and yellow $20\,mV$. A–B: The center of the sinoatrial node gets activated first. C: The entire SAN is depolarized and the excitation is starting to spread towards the surrounding tissue (tissue activation, ta). D: The CT is the first tissue activated by the SAN (ta+5 ms). E: The excitation propagates fast along the crista terminalis (ta+15 ms). F: The downwards spreading excitation of the CT activates surrounding AWM and the PMs (ta+30 ms). G: The excitation is spreading fast along the PM and the AWM gets completely activated (ta+50 ms). H: The repolarization starts in the cells, which are firstly activated by the SAN (ta+215 ms). I: The repolarization (ta+260 ms) is more homogeneous than the depolarization due to longer APD in CT and PM compared to AWM.

Figures 11.10 D – I illustrate the depolarization and repolarization process of the model at different time steps. After the activation of the tissue by the sinoatrial node (fig. 11.10 D) the excitation spread fast along the CT (fig. 11.10 E). During this time, the AWM arranged along the CT got activated. At the transitions between CT and PMs, the excitation was conducted into the PMs (fig. 11.10 F). The PMs were also fast conducting structures transmitting the activation to the surrounding AWM (fig. 11.10 G). The repolarization started in the area of first activation (fig. 11.10 H). The repolarization was a more homogeneous process compared to the depolarization (fig. 11.10 I) due to the heterogeneous distribution of APD in the atrium (section 10.4).

11.1.5 Line through the Left Ventricle

The electromechanical effects of transmurally varying ion channel characteristics presented in section 10.5 were investigated in a one-dimensional model to verify the necessity of heterogeneous modeling in whole heart simulations [390]. This model described a virtual line of tissue from endocardium to epicardium with surrounding bath medium (fig. 10.5). Electrical coupling of cells was achieved by using the bidomain model, which was discretized with the finite difference method. The stimulation was performed in the subendocardial region modeling myocytes that were stimulated by Purkinje fibers. The heterogeneous distribution of maximum conductances for the currents I_{to}, I_{Ks}, I_{K1}, and I_{NaCa} are depicted in fig 11.11 B. The smoothly varying maximum conductances were achieved by using the values of subendocardial, subepicardial, and M cells as anchor points and interpolating between these points using a spline method.
The transmembrane voltage distribution during depolarization, plateau, and repolarization phase is illustrated in fig. 11.11 A. The depolarization started near the endocardial border and moved towards epicardium. Repolarization first began in subepicardial locations and then in the subendocardial areas. The end of the repolarization vanished near the M cell region because of the prolonged APD in these cardiomyocytes. Figure 11.13 illustrates the same electrophysiological sequence with color-coded transmembrane voltages. In addition, the distribution of the extracellular potential in the surrounding bath medium is shown. In order to compare this heterogeneous model with a commonly used homogeneously approach, the excitation conduction and repolarization was computed in a homogeneous model composed only of myocytes comprising the electrophysiological properties of subepicardial myocytes all along the virtual line of tissue. The sequence of activation and repolarization in this homogeneous model is shown in fig. 11.14 together with the extracellular potential distribution in the bath medium. The depolarization was similar to the heterogeneous model. The repolarization started in subendocardial regions and final repolarization was recognized towards the epicardium.
Figure 11.11 C shows the transmural ECG of the heterogeneous model compared with the homogeneous model. In the heterogeneous model, mainly a monophasic positive T-wave was present, whereas in the homogeneous model, the T-wave had a broadened, negative characteristic. The monophasic positive T-wave has been reported in transmural ECGs of ventricular wedge preparations (fig 11.12) [117]. The negative T-wave in the homogeneous model was produced by the spreading of repolarization in the same direction as the depolarization. The heterogeneous and the homogeneous model generated a J-wave in the transmural ECG. The J-wave is reflecting the electrical influence of subepicardial cells with their characteristic "spike-and-dome" morphology.

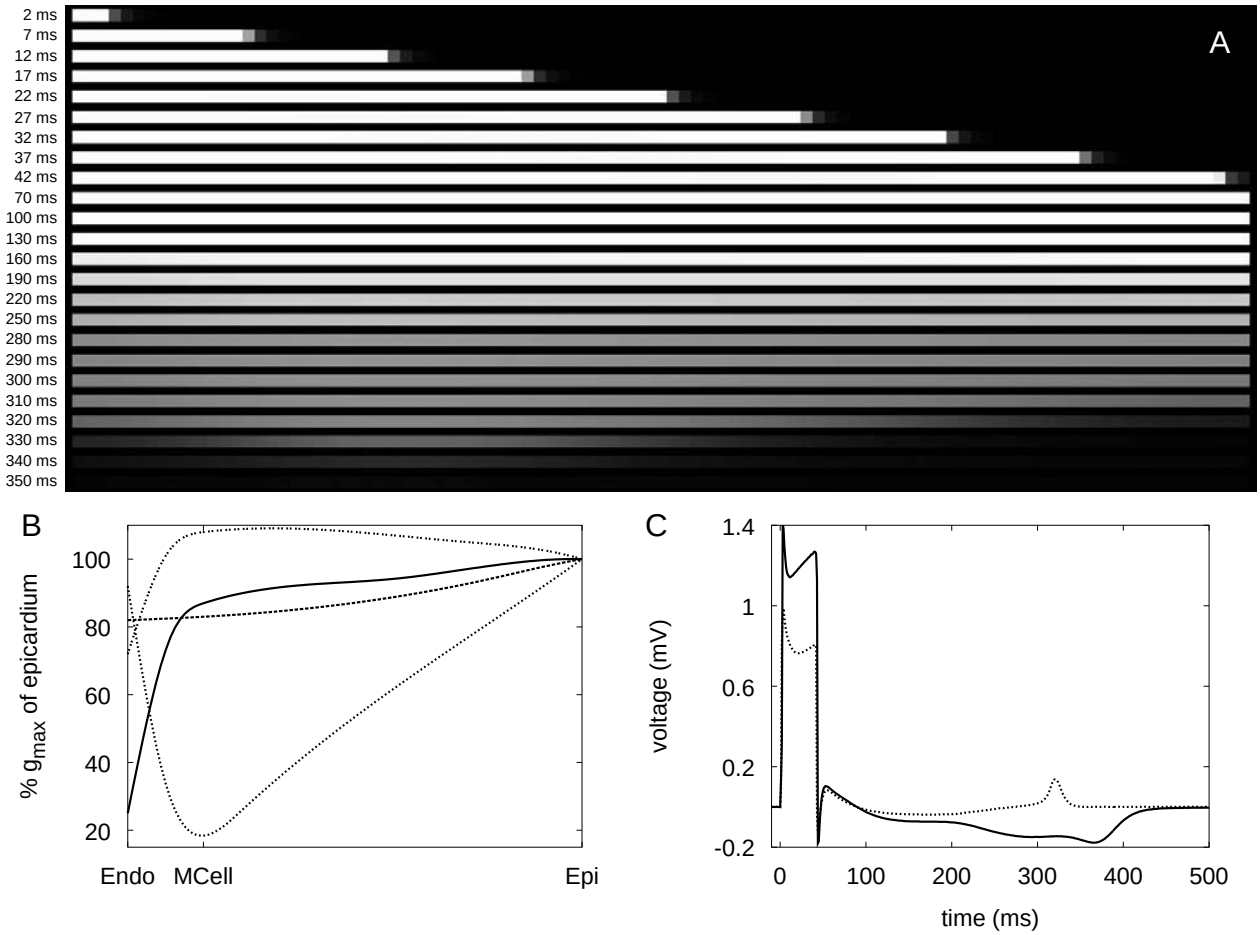

Fig. 11.11. Simulation of a transmural, heterogeneous, one-dimensional line of ventricular tissue. A: Gray-coded transmembrane voltage in the tissue at different time steps. Rows 1–9 depict the depolarization wave. Rows 10–14 show the plateau phase with another temporal resolution because of the minor changes of transmembrane voltage. Rows 15–23 illustrate repolarization phase. B: Distribution of the maximum conductances g_{max} (in percent) with the maximum conductances at the epicardium (tab. 10.4) being 100 %. The location of the M cells in the transmural line is also depicted (g_{to}, solid line; g_{Ks}, dotted line; g_{K1}, wide dotted line; g_{NaCa}, dashed line). C: Transmural ECG of homogeneous (solid line, original Priebe-Beuckelmann) compared to heterogeneous (dashed line, adapted Priebe-Beuckelmann) model. The two electrodes measuring the extracellular potential to calculate the ECG are placed into the bath medium at both ends of the line of virtual tissue. Fig. from [390].

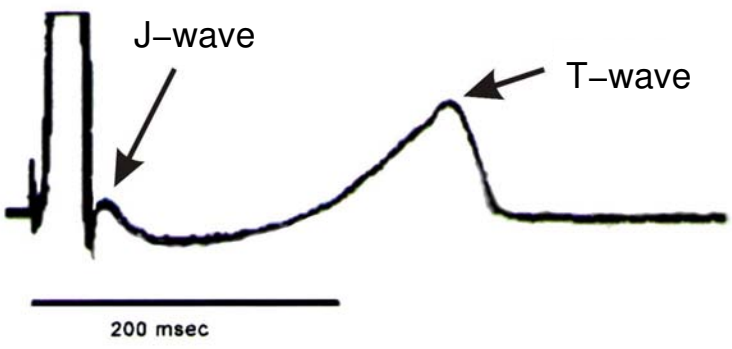

Fig. 11.12. Transmural left ventricular ECG of canine. The electrophysiological heterogeneity of the left ventricular wall determine the J-wave and the upright T-wave in the ECG. Fig. adapted from [212].

Figure 11.15 B illustrates characteristic APD parameters of the three differing cell types in a single cell simulation ("in vitro") compared to the APD of the cells in the multi cell environment ("in vivo"). The coupling of cells smoothened the gradient of APD compared to the uncoupled experiment. The APD was shortened in M cells but was prolonged in subendocardial and subepicardial cells.
In order to calculate the tension development in the heterogeneous model, the model presented in section 10.6 was used. The distribution of normalized tension throughout the ventricular line model at different time steps is illustrated in figure 11.15 A. The tension started at the endocardium approximately 50 ms after the electrical stimulation. The maximum (peak) was reached for every cell in the line after nearly 180 ms. With increasing time, the normalized tension decreased homogeneously within the electrophysiologically heterogeneous model. The distribution of peak values of the normalized tension for the line model is shown in fig. 11.15 C and compared with the simulated values for single cells of the subendocardial, subepicardial, and M cell region. The peak value of the normalized tension differed only in M cells in the two models.

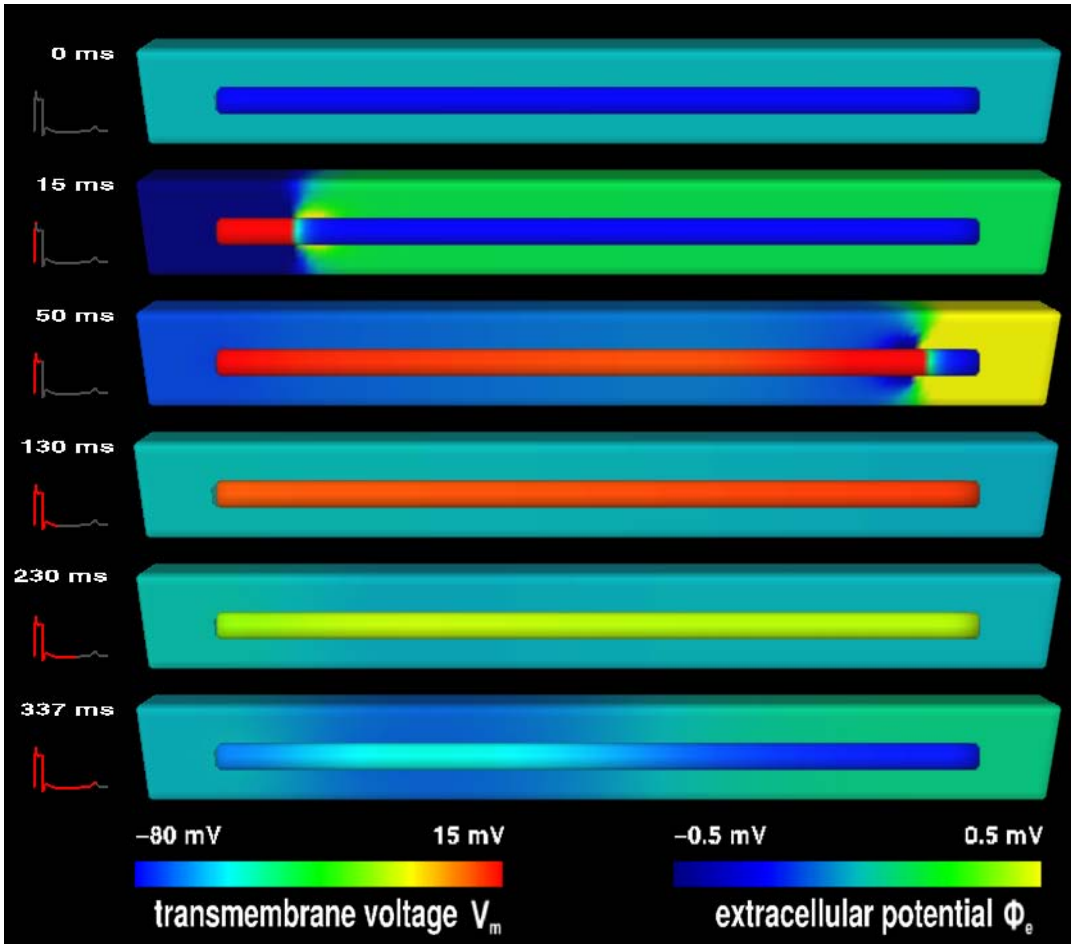

Fig. 11.13. Excitation conduction in a one-dimensional heterogeneous model presented in fig. 10.5 b. The transmembrane voltage and the extracellular potential is depicted color coded. Two electrodes at each end of the bath medium record the transmural ECG presented on the left side. The tissue is activated by an external intracellular stimulus current at the endocardial border of the tissue. The excitation propagates towards epicardium. The repolarization starts at the epicardial area due to the different APDs of the tissue classes and prolonged AP in the subendocardium in the coupled simulation. The repolarization vanishes near the region of M cells. This dispersion of the repolarization generates the positive T-wave in the transmural ECG. Fig. from [381].

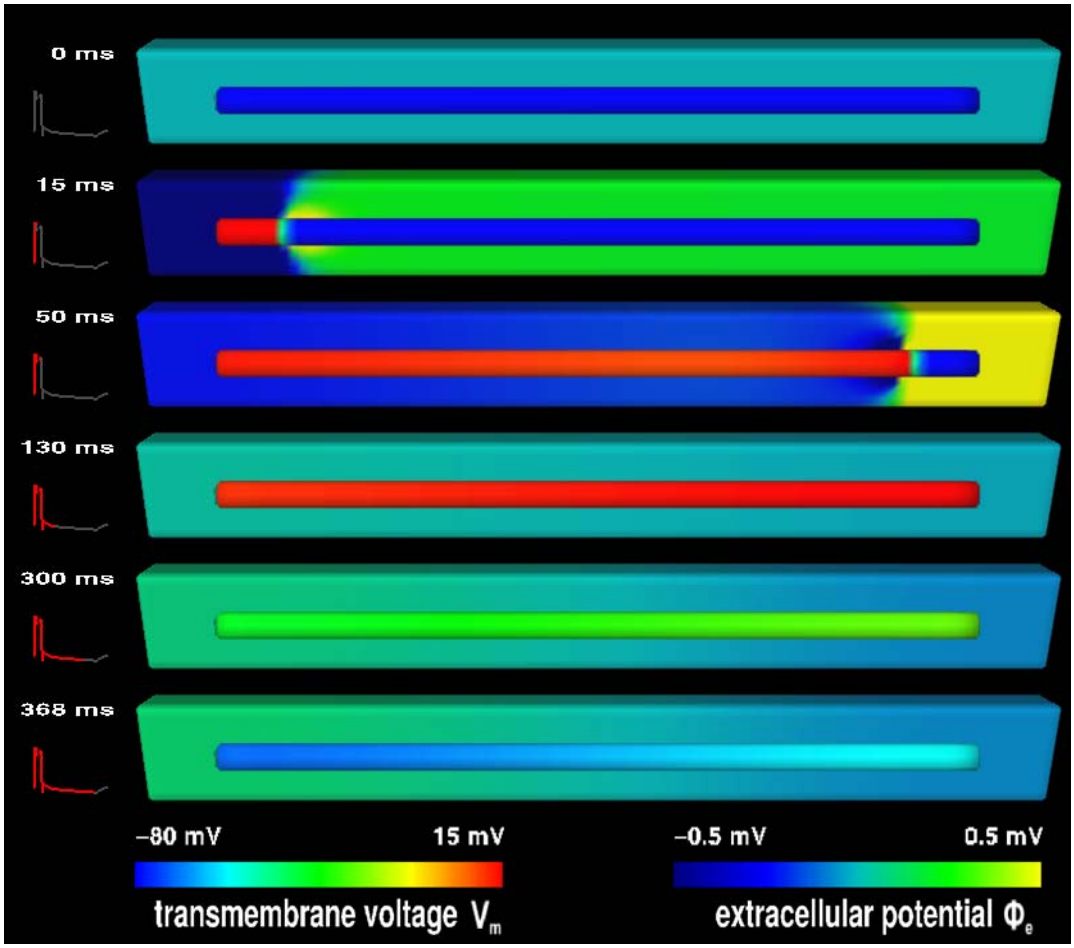

Fig. 11.14. Excitation conduction in a one-dimensional homogeneous model, which is anatomically equivalent to the model presented in fig. 11.13. All tissue classes behave electrophysiologically equal. The depolarization phase is the same as in the heterogeneous model. The repolarization starts at the endocardial border and vanishes at the epicardial since the APD of all tissue classes is the same. This effect leads to a negative T-wave in the transmural ECG (left side). Fig. from [381].

Discussion: The simulations with the one-dimensional line of ventricular tissue illustrated the differences in transmural ECGs of a homogeneous compared to the heterogeneous model. The transmural ECG of the heterogeneous model had a more realistic course of the T wave. Gima and Rudy observed similar results in a computer simulation of a one-dimensional tissue in a guinea-pig model [262].
With the simulations presented in this section, electromechanical properties of subendocardial, midmyocardial, and subepicardial myocytes were predicted that have not been measured yet. In particular, the effects of transmural heterogeneity on the tension development were nearly unexplored until now. The simulation results of this section might support ideas to measure these effects. To obtain more realistic results for the clinical application of these models, further human electrophysiological and tension development measurements will be needed.

11.1.6 Virtual Left Ventricular Wedge Preparation

The transmural heterogeneous one-dimensional model of the previous section was enhanced in this section to a three-dimensional model describing a virtual left ventricular wedge preparation (fig. 10.6). This model considered transmurally varying electrophysiological properties.

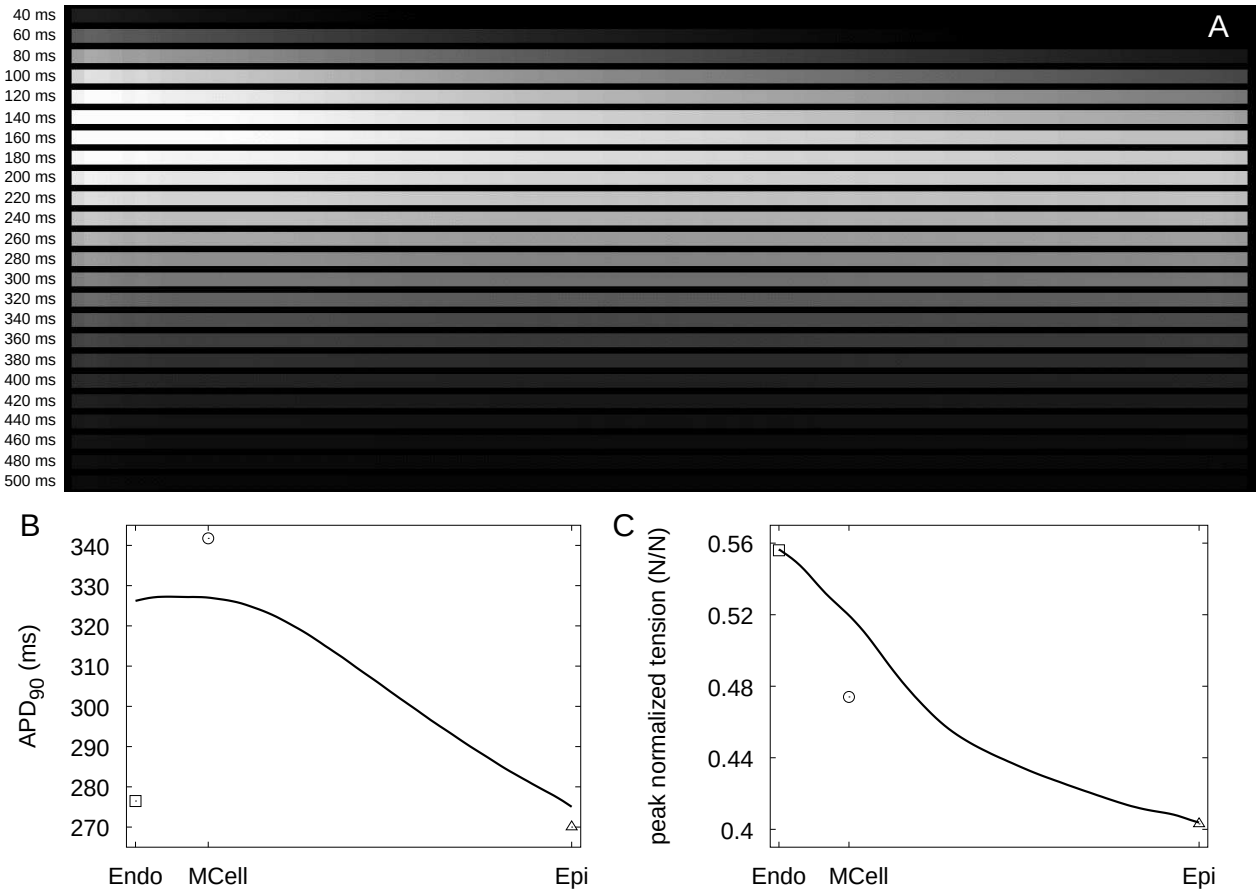

Fig. 11.15. Simulation result of a transmural, heterogeneous, one-dimensional model of ventricular tissue. A: Gray-coded normalized tension at equidistant time steps. B: APD_{90}-distribution of the multicellular heterogeneous model (solid line) compared to the single cell APD_{90} of the subendocardial (box), subepicardial (triangle), and M cell (circle). C: Distribution of the peak value of the normalized tension for the coupled model (solid line) and the values for the uncoupled single cells (subendocardial: box; M cell: circle; subepicardial: triangle). Fig. from [390].

The rotating fiber orientation from endocardium to epicardium was implemented with the approach presented in section 10.2. The excitation conduction was computed with the monodomain model discretized with the finite difference method.

The behavior of depolarization and repolarization in this model shown in fig. 11.16 was comparable to the one-dimensional model. The depolarization wave spread from endocardium to epicardium initiated by virtual Purkinje fiber ends. The sequence of repolarization started in subendocardial areas followed by subepicardial regions. The final repolarization vanished in the midmyocardium near the M cells because these cells had the longest APD. The final repolarization was not directly in M cells due to the influence of the transit time of the depolarization front.

The electrotonic effect of cell coupling via gap junctions shifted the APD measured in single cells from transmurally different regions compared to coupled cells in the virtual wedge preparation. The simulated APD_{90} in M cells was $342\,ms$ in single cells. The surrounding tissue in the wedge model had shorter APDs as compared to the M cells. Hence, the APD_{90} in M cells was reduced to $327\,ms$ in the coupled model. Since the M cell location was closer to the endocardium than the epicardium, the APD_{90} in subepicardial cells was increased from $272\,ms$ in the single cell simulation to $326\,ms$ in the virtual wedge model. The influence of

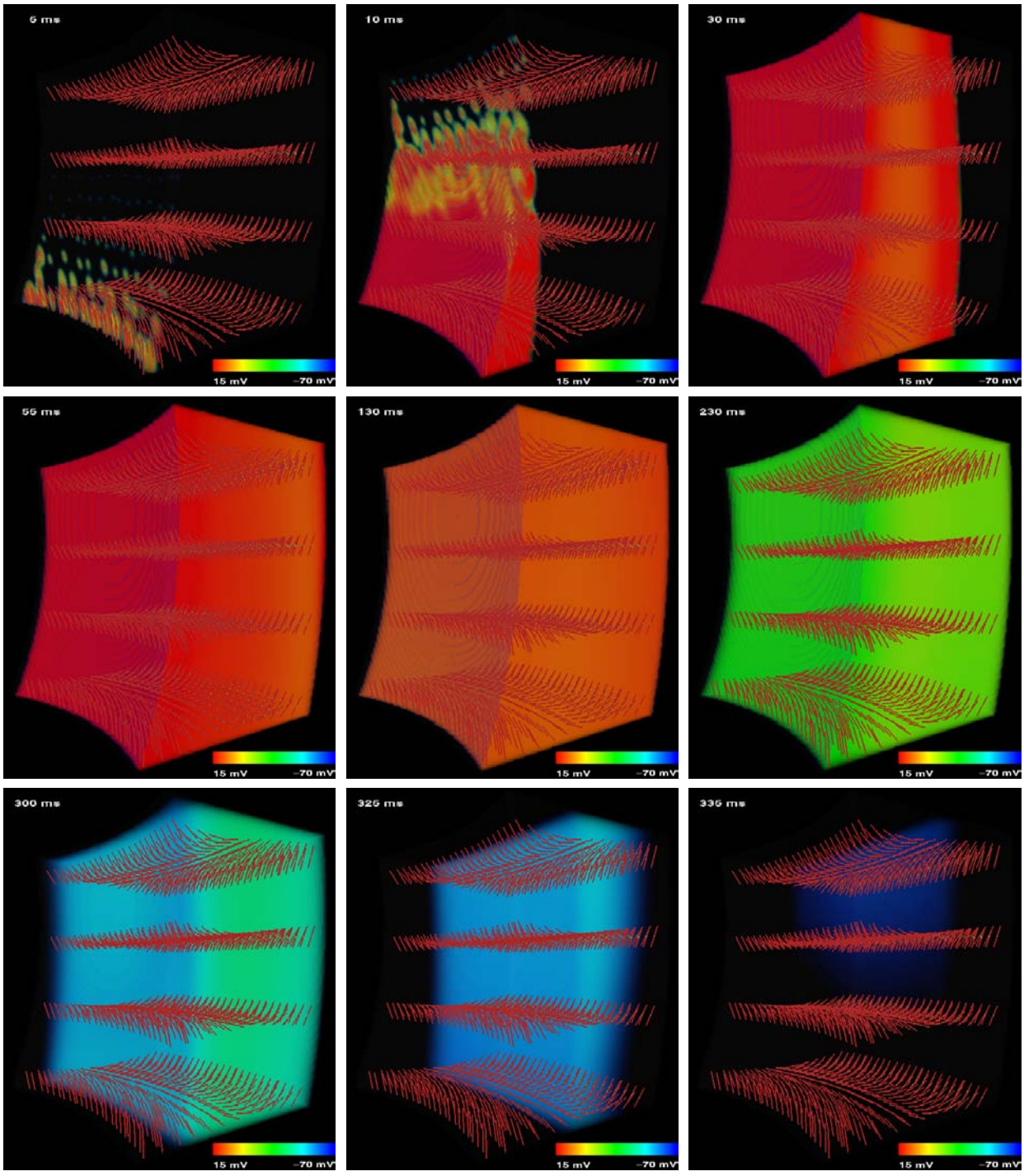

Fig. 11.16. Excitation conduction in the virtual wedge preparation presented in section 10.1.3. The transmembrane voltage is illustrated color coded. The red lines indicate exemplary the fiber orientation. The model is activated by intracellular currents at locations reproducing the transition point between the subendocardial myocardium and Purkinje fibers. The sequence of activation starts in apical endocardial regions of the model and travels in basal epicardial directions. The repolarization starts first in subendocardial regions and then in subepicardial areas. Final repolarization is found in the midmyocardial region due to the longer APD in these cells. Fig. from [381].

M cells on subepicardial cells was smaller. The APD_{90} of these myocytes was $265\,ms$ in the uncoupled model and $275\,ms$ in the coupled simulation.

Discussion: The APD_{90} difference in the physiological simulation of the uncoupled cell types from endocardial, epicardial and midmyocardial regions was approximately $80\,ms$. Li and colleagues measured an APD_{90} gradient in isolated human right ventricular myocytes of approximately $125\,ms$ [175]. Experimental work and simulations from other groups showed that the dispersion of repolarization was reduced in the heterogeneous tissue due to electrotonic effects to a range of $30-45\,ms$ [416, 417, 418]. The simulation with the heterogeneous left ventricular wedge preparation resulted in a dispersion of repolarization of $50\,ms$.
The influence of the fiber orientation on the physiological excitation conduction and repolarization seems to be very small because both depolarization and repolarization always traverse perpendicular to the longitudinal direction of the fibers. The rotating fiber orientation is playing an important role mainly for the mechanical properties of the heart proven by numerical experiments [340]. Furthermore, the fiber orientation variation might influence the excitation conduction during pathological excitation like ventricular tachycardia and arrhythmias.

11.2 Pathophysiological Electrophysiology in the Heart

This section describes the simulations performed during this thesis with the focus directed to the description of pathological cases. For both atria and ventricle, some pathological parameters were inserted in the electrophysiological models to investigate the mechanisms and effects of these pathologies. In the atria, simulations of two types of flutter and a fibrillation are described. Furthermore, the effects of the familial atrial fibrillation model (section 10.8.2.1) and of electrophysiological remodeling (section 10.8.1) in the tissue is investigated. Furthermore, tachycardia and fibrillation is described for ventricular tissue. The last section describes the effects of the three types of long QT syndrome (section 10.8.2.2) on the transmural ECG.

11.2.1 Atrial Flutter

Atrial flutter (section 4.8.1.1) is investigated in this section with two different geometrical models. The first model (fig. 11.17) is a 2D slice of the right atrium. In this model a non-conducting region was included. This region should represent a part of the atrium which is damaged by e.g. radio-frequency ablation. The second geometrical model comprises also a 2D schematic description of the right atrium including a non-conducting zone, which represents an anatomical obstacle e.g. the inferior vena cava. In both models, the tissue was set to isotropic behavior and the utilized electrophysiological description was given by the Courtemanche et al. model of the human atrium (section 5.5.3).
Figure 11.17 shows the effect of a sharp edge in the tissue on the conduction of the excitation. A first depolarization front spread over the tissue. At the edge, the initially planar wave front got curved. This led to a reduction of the excitation conduction velocity after proceeding the edge. When a second planar depolarization front was activated (fig. 11.17 A) it spread into the tail of the first depolarization in the area around the edge, due to the reduced conduction velocity. The second wave front was erased close to the edge (fig. 11.17 B) and only the distal parts traversed into excitable tissue. This led to an initiation of a so-called spiral wave in the tissue (fig. 11.17 C – F), which will continue to rotate if the depolarization is always traveling into an area of excitable tissue.
Figure 11.19 illustrates a simulation with the spiral wave traveling around an anatomical obstacle. The spiral wave was initiated with a S1–S2 protocol. S1 is an initial activation of

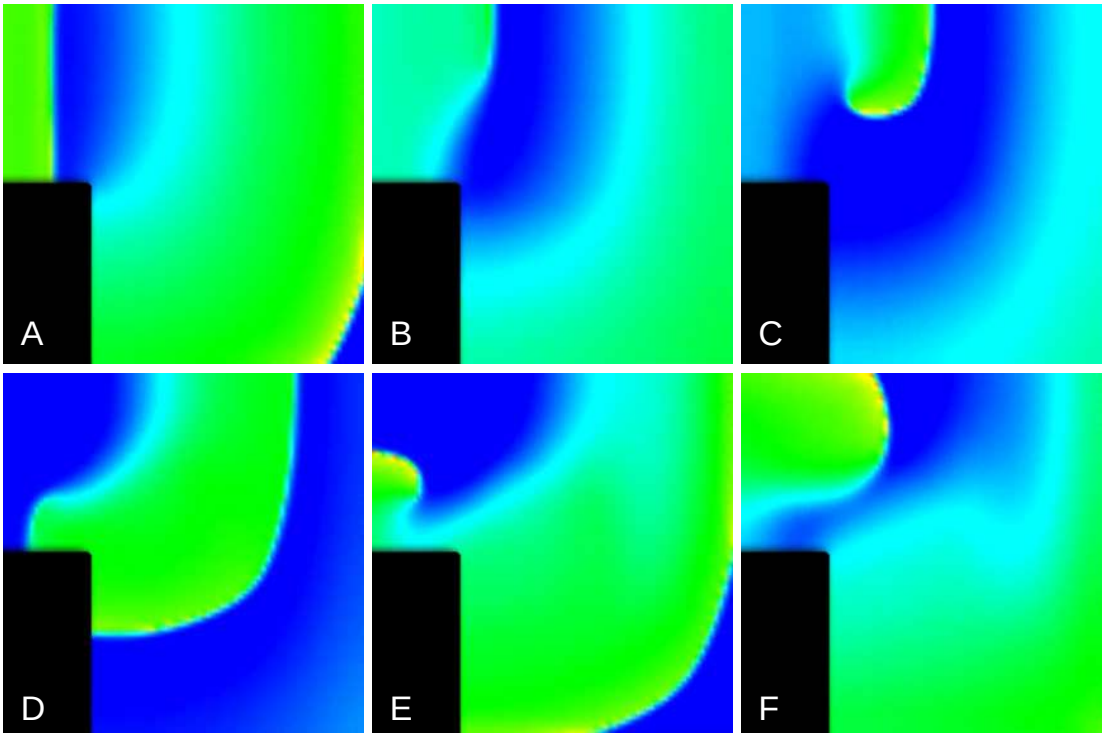

Fig. 11.17. Simulation of the initiation of atrial flutter. The transmembrane voltage is shown color coded. The black area depicts a non-excitable area reproducing a lesion with a sharp edge. A: After an initial depolarization front, a second wave is spreading from the left side into the tissue. Due to the curvature of the wave behind the edge, the first depolarization front is slowed down. B: The initially planar second wave is stopped in the regions of the edge because it is traveling into the tail of the previous wave. Only the distal parts can traverse into excitable tissue. C: This leads to the initiation of a spiral wave. D – E: If the spiral wave always spreads into excitable tissue, the rotation is continued. Figs. adapted from [419].

the tissue in one location (fig. 11.18 A). During the refractory period of the first activation, the second temporally shifted activation S2 was applied to a spatially displaced location compared to the first (fig. 11.18 B). It was located in such a way, that a part of the stimulated volume was in still refractory tissue and another part in again excitable tissue. This produced an unidirectional block of excitation and the rotating electrical wave was traversing around this area (fig. 11.18 C). This rotating wave is also called "figure-of-eight" reentry.

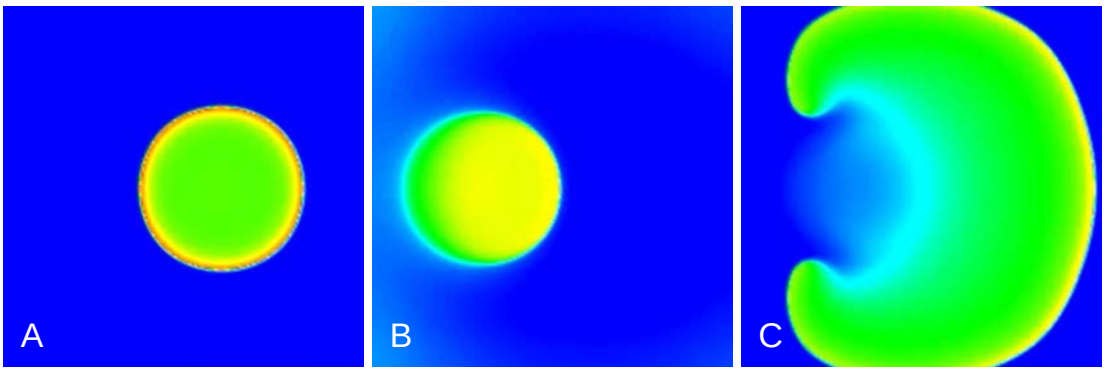

Fig. 11.18. Initiation of flutter by a S1–S2 protocol. A: A first circular wave is initiated called S1. B: A second excitation (S2) is positioned in a different place in a time, when half of the tissue is refractory and the other is excitable. C: This leads to a unidirectional block and the excitation is rotating around two centers. Figs. adapted from [419].

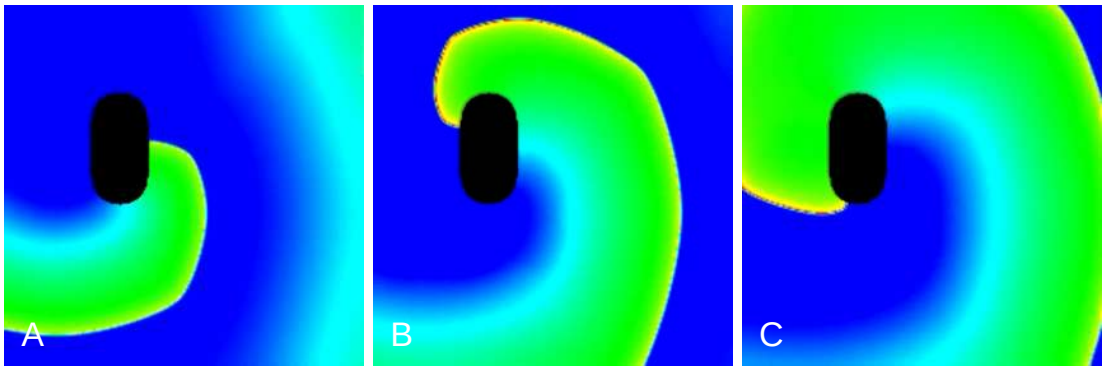

Fig. 11.19. Atrial flutter in a model of the right atrium including a non-excitable area representing an anatomical obstacle e.g. the inferior vena cava. The transmembrane voltage distribution is illustrated color coded. A – C: After initialization of the spiral wave due to a S1–S2 protocol, the wave is continuously traveling around the obstacle. Figs. adapted from [419].

In the 2D atrial model presented in fig. 11.19, such a "figure-of-eight" reentry was not produced because of the boundary of the area. A unidirectional block was induced between the obstacle and the left boundary and the spiral wave was rotating around the anatomical obstacle (fig. 11.19 A – C). This kind of atrial flutter was also reported experimentally [420, 421, 422].

Discussion: Radio-frequency (RF) ablation is clinically used to terminate atrial flutter either by deleting pathways of reentry or by reducing the size of the excitable tissue in which atrial flutter can sustain. The simulation with the model including the edge demonstrated that a lesion due to a RF ablation might trigger again atrial flutter itself when the lesion has a sharp edge. On the other hand, the second simulation demonstrated that atrial flutter due to a rotating wave around an anatomical obstacle can continuously travel. RF ablation might be in this case the only way to stop the atrial flutter.

11.2.2 Atrial Fibrillation

In order to describe the properties of the right atrium during fibrillation, the same model as described in the last section was used. The difference was that the electrical conductivity was reduced to 33 %.
Figure 11.20 shows the distribution of APs during this simulation. The model was initially in the phase presented in fig 11.19 A. Due to the reduced conduction velocity, the rotating wave started to alternate in frequency. This means that the conduction velocity of one rotation was faster than the following one. This effect is given by an action potential with long duration followed by one with short. The alternation of the action potential was increased because the APD restitution curve is steep [423]. At a certain time the rotating wave hits its own tail (fig 11.20 B). In this situation, the wavefront breaked up. Figure 11.20 C illustrates how this break up was producing a local reentry with a higher frequency of rotation than before. For some time this reentry stayed at its position (fig. 11.20 D). Finally the center of the reentry was shifting towards central tissue locations and started to split into three wavefronts (fig. 11.20 E). Figure 11.20 F depicts a situation later in the simulation where a multitude of small wavelets was present at the same time in the tissue. This chaotic excitation is also called multiple circuit reentry [189] and is reported experimentally [424, 425].

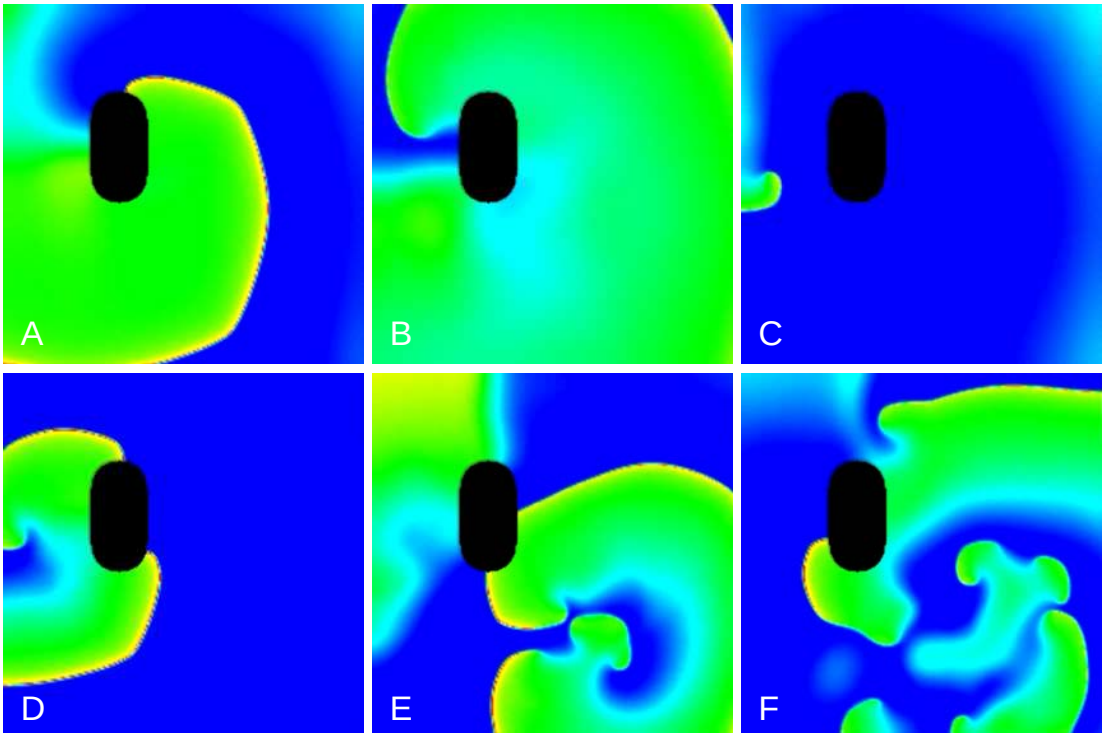

Fig. 11.20. Simulated atrial fibrillation. The model of fig. 11.19 is used and the electrical conductivity is reduced to 33 %. A: For some time, the spiral wave rotates around the anatomical obstacle but starts to alternate in the rotation frequency. B: The wave front hits its own tail and is partly blocked. C: The block leads to a local reentry. D: The local reentry stabilizes. E: The anchor point of the reentry drifts towards the tissue and starts to generate multiple waves. F: The distribution of excitation gets chaotically with a multitude of small wavelets. Figs. adapted from [419].

11.2.3 Familial Atrial Fibrillation

In this section, the multi-cellular environment of the schematic right atrium (fig. 10.1.3.1) was used to determine excitation conduction and the effective refractory period (ERP) in the electrophysiological model of the mutation called familial atrial fibrillation presented in section 10.8.2.1. The anatomical and electrophysiological model was the same as compared to the simulations of section 11.1.4 with the difference that the sinoatrial node was not included in this model and the mutant I_{Ks} derived in section 10.8.2.1 was included in the crista terminalis (CT), pectinate muscles (PMs), and the atrial working myocardium (AWM). The sinoatrial node was removed to reduce the complexity of the simulation and to focus on the mechanisms of the mutation. The excitation conduction in the model was initiated by applying a stimulus current at the upper end of the CT.
The excitation conduction in the schematic model of the right atrium in the mutant case was the same as in physiological model despite the SAN shown in fig. 11.10. The velocity of the excitation was not reduced by the mutation because the mutant I_{Ks} acts mainly in the second and the third phase of repolarization (fig. 10.46). The differences between the physiological and the mutant excitation conduction was only visible during the repolarization process (fig. 11.21). The mutant model started earlier with repolarization (fig. 11.21 a) because the large early I_{Ks} reduces the APD. The physiological model was still in the plateau phase. When the mutant model was nearly repolarized (fig. 11.21 b), the physiological model was at the end of the plateau phase. The repolarization in the physiological simulation (fig. 11.21 c) started approximately 100 ms later than in the mutant model. Final repolarization was even 150 ms

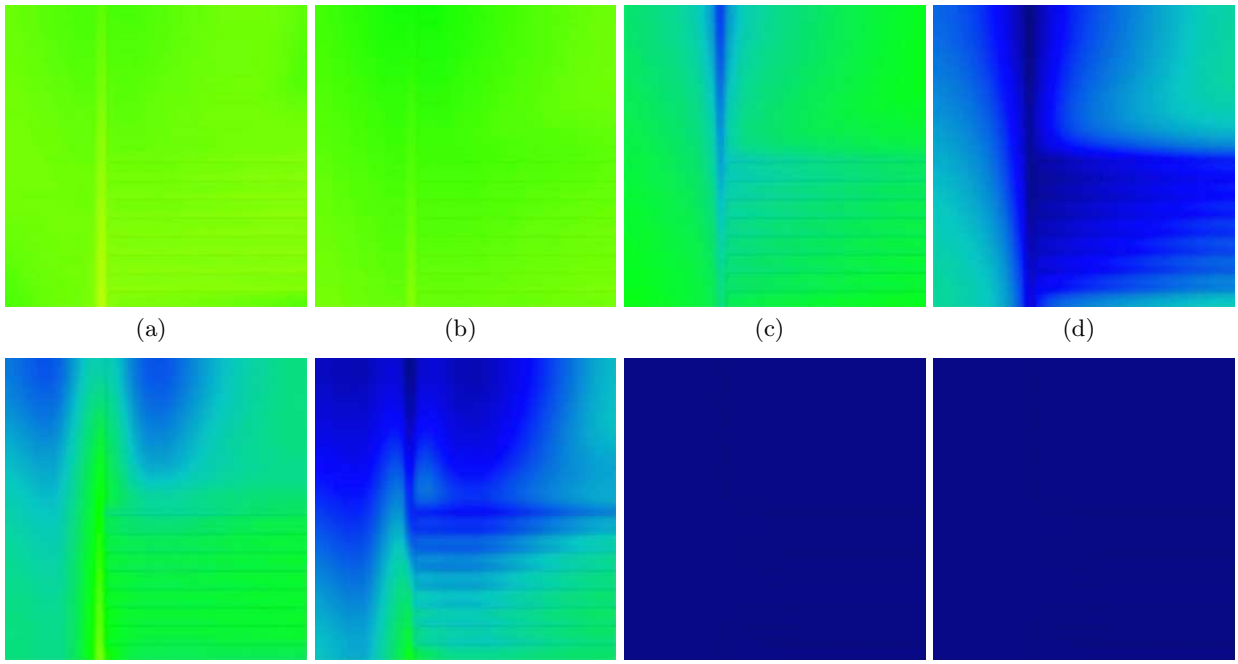

Fig. 11.21. Transmembrane voltage distribution during repolarization in (upper) the physiological and (lower) the mutant model at time steps (a) 100 ms, (b) 125 ms, (c) 200 ms, and (d) 250 ms after the stimulation. Yellow color indicates +10 mV, blue color −80 mV. Figs. adapted from [379].

later in the physiological case (fig. 11.21 d). Hence, the mutation is decreasing the wavelength and thus generates a substrate for the initiation and maintenance of AF (section 4.8.1.2).
The shortest time at which the excitation from the premature beat is able to produce an excitation conduction is called ERP [426, 427]. The ERP was simulated in the schematic right atrial model by applying 5 beats with 1 Hz and then one premature beat followed. For the normal Courtemanche et al. model, the ERP was 324 ms. For the mutant case the simulated ERP was reduced to 148 ms.

Discussion: The measurement of Chen et al. [204] was not performed in cardiac myocytes but in COS-7 cells. Hence, they were able to determine the mutation in the channel but cannot see the effects of the mutation to cardiac cells. With this model, the mutation was incorporated in an atrial cell and the simulations allowed the investigation of the mechanisms of familial atrial fibrillation in tissue. The simulated ERP was reduced in the schematic right atrial model. This is the main reason why the mutation plays an important role in the initiation and maintenance of AF in the familial case.
With this model the electrophysiological findings will be transfered in future to an entire anatomical model of the atria [343] and the initiation and perpetuation of AF based on different mechanisms, e.g. single and multiple wavelet re-entry can be investigated. Also remodeling effects due to sustained AF can be incorporated and investigated [200]. Furthermore, the development of strategies of therapy and design of pharmaceuticals for the treatment of AF can be supported. In addition, the mutant channel can be included into a model of heterogeneous ventricular tissue [409]. There is a necessity to investigate in this model why a large number of patients suffering from familial AF have no significant QT-interval changes [204].

11.2.4 Atrial Electrophysiological Remodeling

The simulation of excitation conduction in the remodeling case was based on the cellular model with the electrophysiological changes described in section 10.8.1. The electrophysiological changes were incorporated in the atrial working myocardium (AWM). The other tissue classes were simulated under physiological conditions. The simulated excitation conduction using the remodeled cellular model was comparable with the first impulse wavefront in chronic atrial fibrillation (AF) patients after cardioversion.
Figure 11.10 shows the activation sequence in the physiological model. The remodeling case was nearly the same (not shown). Therefore, the activation time, which is the time to complete activation of the model was $73\,ms$ in the physiological case and not prolonged in this remodeling simulation. The heart rate was in the physiological and the pathological model 68 bpm.
The quantitative parameters, which are investigated for both remodeling and physiological case in this set of simulations are the conduction velocity, the heart rate, the repolarization and the effective refractory period (ERP).

Conduction Velocity: The slightly decreased conduction velocity shown in tab. 11.2 indicates that changed ionic electrophysiological properties were unessential factors to induce the decreased conduction velocity. This reduced conduction velocity is a characteristic occurring in the patients after cardioversion [428, 429]. I_{Na} determined the steepness of the upstroke in depolarization phase. The altered I_{Na} in the remodeling case had only small influence on the AP (fig. 10.42). The decrease in conduction velocity in the AWM was explained by the more negative resting potential in this simulation. Therefore, it takes longer for the myocytes to reach the threshold and to depolarize. The abnormal electrical coupling between cardiomyocytes through gap junctions were considered as essential factors for the decreased conduction velocity [412, 428]. In several studies the effects of AF on atrial gap junction, which is a major determinant in myocardial conduction, was investigated [199].

Heart Rate: The same heart rate in the physiological and pathological case with 68 bpm was not expected. The frequency of the sinoatrial node (SAN) should decrease due to the coupling to the AWM with more negative resting potential in the remodeling case. This disadvantage of the model can be overcome, if the remodeling condition is incorporated not only in the AWM, but also in the CT and PMs. Since the CT was the first tissue to be activated (fig. 11.10 D) and directly joined with the SAN, the remodeling in CT has a great impact on the frequency of the SAN.

Repolarization: Figure 11.22 shows the significantly abbreviated time to complete repolarization, which reflects the shortening of APD in the remodeled case (fig. 4.8). The physiological right atrium was still in the plateau phase (fig. 11.22 b). The plateau phase was obviously decelerated in the remodeling case. When the physiological right atrium began to repolarize, the entire repolarization process was already proceeded in the remodeling case (fig. 11.22 c).

Table 11.2. Simulated conduction velocity of the atrial working myocardium (AWM), the crista terminalis (CT) and the pectinate muscles (PM) under physiological and remodeling condition.

tissue	physiological $v\,(m/s)$	remodeling $v\,(m/s)$
AWM	0.53	0.5 ∼0.51
CT	1.18 ∼ 1.2	1.16 ∼ 1.18
PM	1.54 ∼ 1.58	1.52 ∼ 1.56

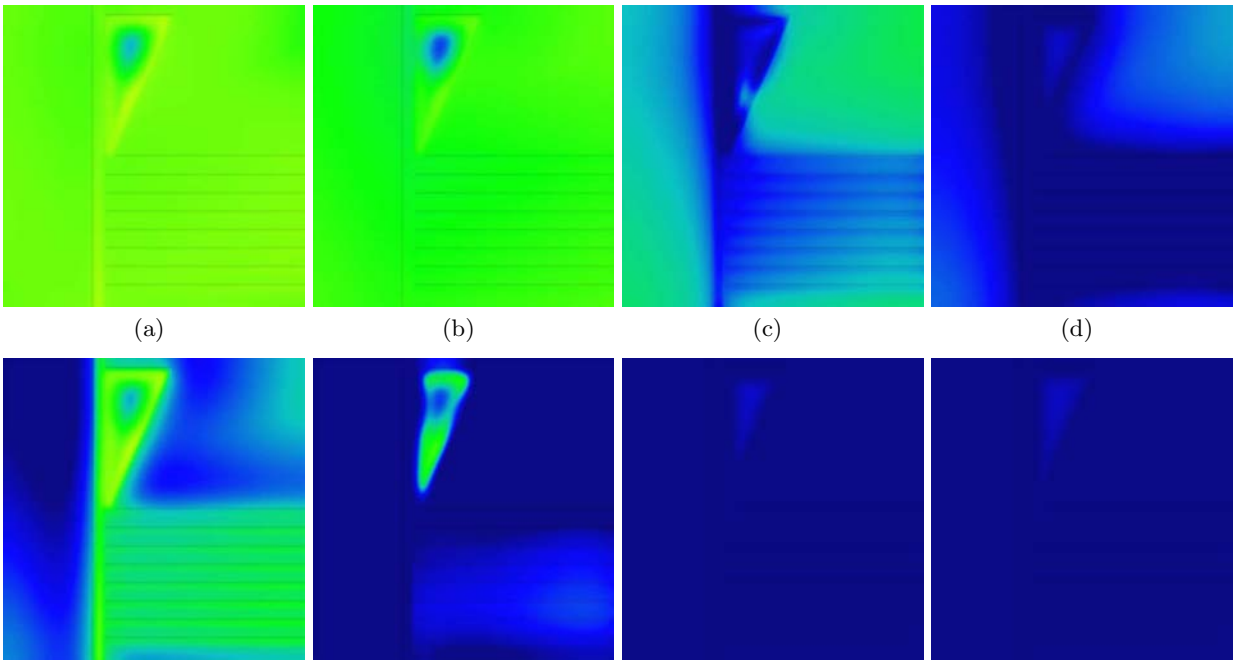

Fig. 11.22. Progression of the repolarization in the physiological right atrium (upper) and in the remodeling right atrium (lower). Gray coded transmembrane voltage distribution at (a) 100 *ms*, (b) 150 *ms*, (c) 225 *ms*, (d) 275 *ms* after activation of the CT. The yellow color indicates the depolarized tissue and the resting tissue is blue. Fig. adapted from [380].

The AWM in the remodeling case was completely repolarized after 145 *ms*. The physiological model repolarized completely after 325 *ms* (fig. 11.22 d).

Effective refractory period: Critical components for patients in chronic AF are the markedly abbreviated ERP and the attenuated ERP rate dependency (fig. 11.23 a), which are also observed in patients after cardioversion [428, 429, 430, 431, 432]. Figure 11.23 b depicts for the simulations the remarkably abbreviated ERP at any cycle length, and the attenuated ERP rate dependency, especially at high frequencies. As the cycle length increases from 200 to 600 *ms*, the slope of ERP restitution in the physiological case is much steeper than in the

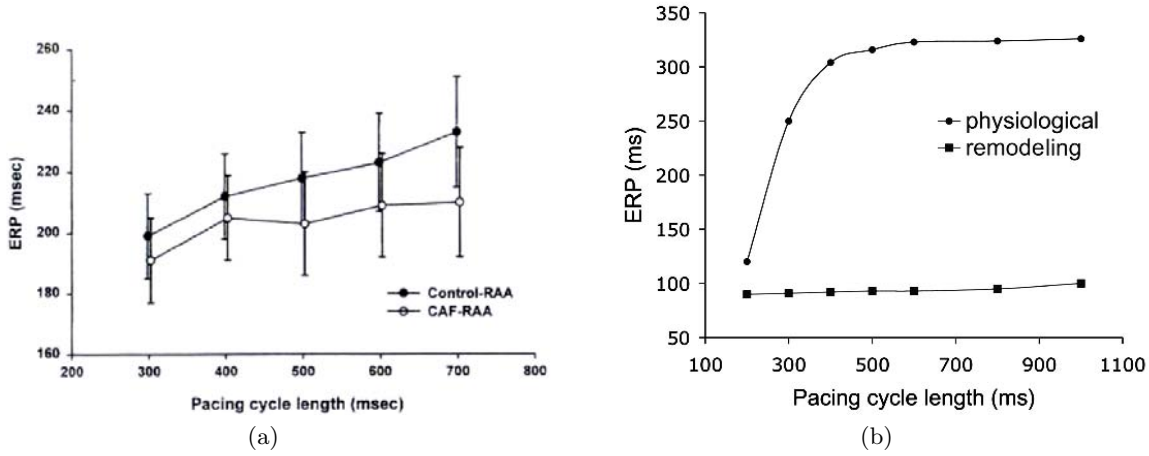

Fig. 11.23. Effective refractory period (ERP) of the right AWM in control (solid symbol) and chronic AF group (open symbol) (a) Measurement data at five pacing cycle length (700, 600, 500, 400, and 300 *ms*) [430]. (b) Simulated ERP plotted against various cycle lengths. Fig. adapted from [380].

remodeling case. The ERP is largely determined by the duration of final repolarization of cells in the pacing site and the electric coupling to surrounding tissue [433]. The simulated ERP in fig. 11.23 b is not concordant with measured data in fig. 11.23 a, which may arise from the heterogeneous APD in various tissue and the adopted cellular models.

Discussion: A short refractory period and its poor adaptation to heart rate are viewed as the electrophysiological milieu for AF recurrence, which results in a shorter wavelength of the atrial impulse. This allows more multiple circuits coexisting in the given tissue, and the vulnerability increases. Therefore, AF recurs in the patients after cardioversion, if the triggers, such as ectopic beats, encounters in the atrium. Chronic AF is associated with the not reversible electrophysiological changes, which induce the pronounced reduction of the ERP. Thus, the decreased wavelength is determined. This alteration facilitates the maintenance and perpetuation of AF. This mechanism of "AF begets AF" could be reconstructed in the simulations.

11.2.5 Ventricular Tachycardia

The anatomical model for simulating ventricular tachycardia is a block of ventricular tissue consisting of a homogeneous and isotropic region of 180 x 180 x 180 voxel and a voxel side length of 0.2 mm. The simulation of the excitation conduction was described by the bidomain approach.
This model was used to demonstrate the unidirectional block as a cause of ventricular tachycardia. The procedure of initiating a rotating wave with a unidirectional block in 3D was the same as in 2D described in section 11.2.1. The unidirectional block was initiated with

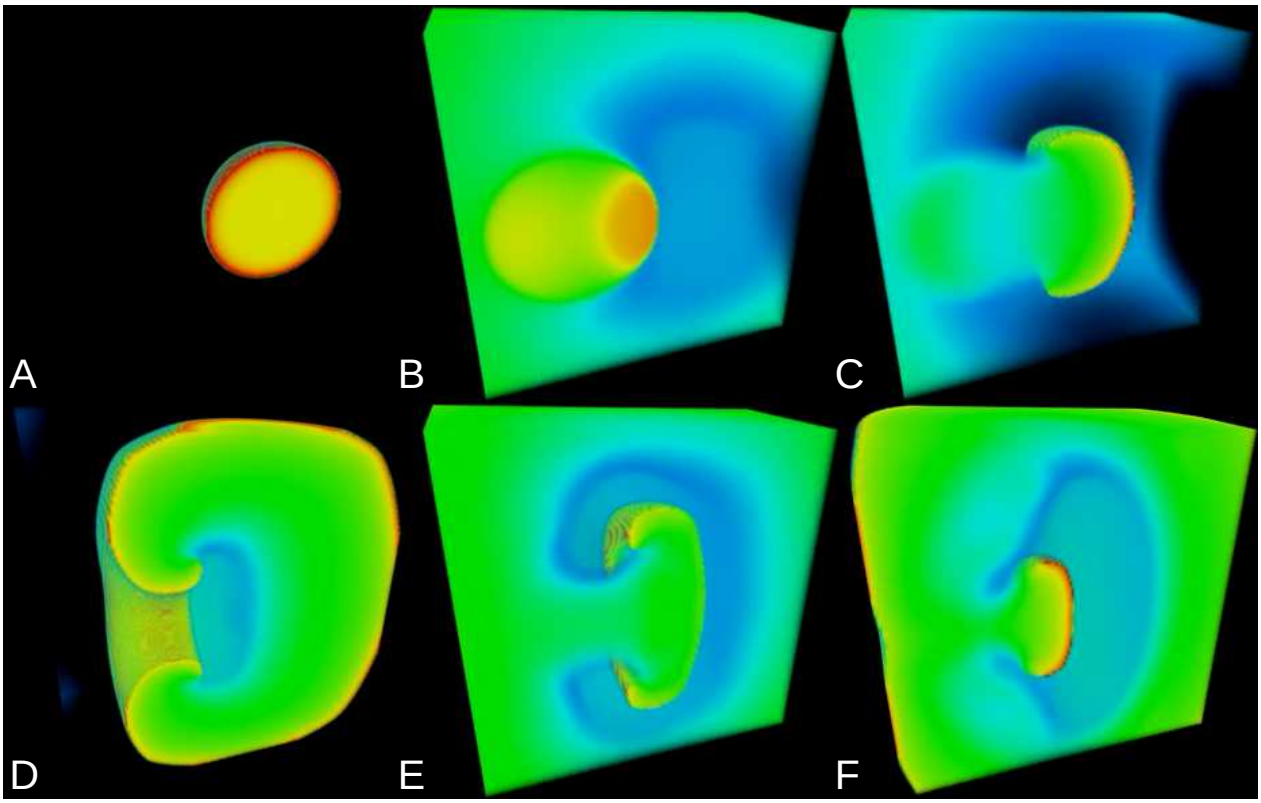

Fig. 11.24. Color coded transmembrane voltage while initiation and perpetuation of a rotating wave in a 3D simulation at different time steps. Two properly spatial and temporal positioned stimulation areas provoke a rotating wave. This kind of reentry is called "figure-of-eight". Fig. adapted from [419, 434].

two spatial and temporal suitably positioned stimulation areas with a radius in this model of 35 voxel [419]. The second stimulation was displaced by 40 voxel and delayed by 245 ms. Figure 11.24 shows the initiation and continuation of the rotating wave. In figs. 11.24 A and B the two stimulations are illustrated. The second one (fig. 11.24 B) led to a unidirectional conduction of the wave (fig. 11.24 C) because of the gradient of refractoriness in the underlying structure. Afterwards, the wave rotated periodically around the area of the second stimulation (figs. 11.24 D – F).
This simulation demonstrated how an ectopic focus in the ventricles caused ventricular tachycardia. The frequency of this rotating wave was approximately 4 Hz. The ventricular tachycardia can initiate ventricular fibrillation if the continuously rotating wave gets splitted or if the frequency of reentry is increased (see next section).

11.2.6 Ventricular Fibrillation

The model to illustrate the electromechanical effects of ventricular fibrillation was the anisotropic and electrophysiologically homogeneous virtual wedge preparation (fig. 10.6). In this case, the electrophysiology was described by the ventricular guinea-pig model of Noble-Varghese-Kohl-Noble [241] and the tension development was given by the third Rice et al. model [325].
In this model shown in fig. 11.25 an area with inhomogeneous conduction properties was placed in the subendocardial layer causing the initiation of fibrillation (fig. 11.25 B) after a normal excitation of the ventricle via Purkinje fibers (fig. 11.25 A). The anisotropic conductivity of the tissue was reduced by 30% in the endocardial area. This led as in the model of ventricular tachycardia of the previous section to a gradient of refractoriness at the endocardial border causing a reentry. After an initial relocation of the center of the spiral wave (fig. 11.25 C,D) the continuation of the fibrillation occurred periodically with a fixed center (fig. 11.25 E,F). The relocation was caused by the complex fiber orientation and the curved surface of the myocardial model.
The reentry shown in fig. 11.25 F was linked to a significant change of the concentration of intracellular calcium $[Ca^{2+}]_i$. The high frequency of re-excitation led to a reduced calcium release of the sarcoplasmic reticulum. This decreased $[Ca^{2+}]_i$ is shown in fig. 11.26 A. As the intracellular calcium transient was reduced, the excitation contraction coupling was nearly stopped. Figure 11.26 B illustrates the nearly vanished developed tension during the ventricular fibrillation.

Discussion: The models of ventricular tachycardia and ventricular fibrillation illustrated the mechanisms of generation and continuation of ventricular rotating waves. In both models only a small shift of the system to abnormal properties was necessary to achieve the presented results. The cycle length of the rotating wave was larger in the model of ventricular tachycardia ($\sim$ 250 ms) than in ventricular fibrillation ($\sim$ 70 ms). In none of both models, wave breakups reported in fibrillating tissue was achieved. Nevertheless, the simulation of ventricular fibrillation showed that the mechanical activity is significantly decreased during fast electrical activity.
A lot of other causes for rotating waves will need to be explored and the models need to be validated by experiments. In addition, the influence of regional electrophysiological heterogeneities on fibrillation mechanisms has to be investigated. These models can be used to investigate the virtual defibrillation process and its mechanisms. Furthermore, the efficiency of various types of treatment can be optimized.

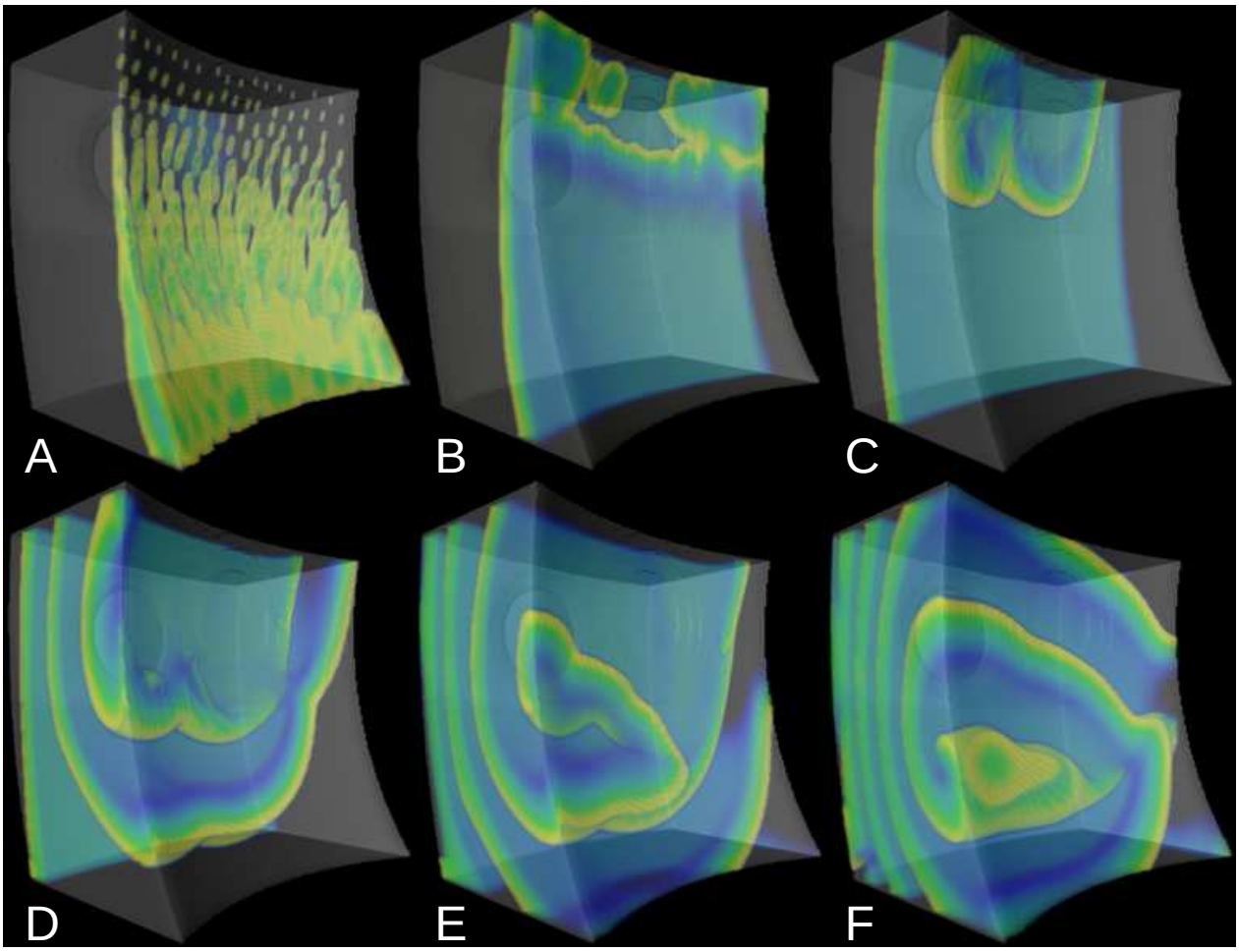

Fig. 11.25. Simulation of fibrillation in a virtual left ventricular wedge preparation at different time steps. The transmembrane voltage is depicted color coded. The fibrillation is initiated by a heterogeneity of the electrical conductivity in the endocardial layer. Fig. adapted from [434].

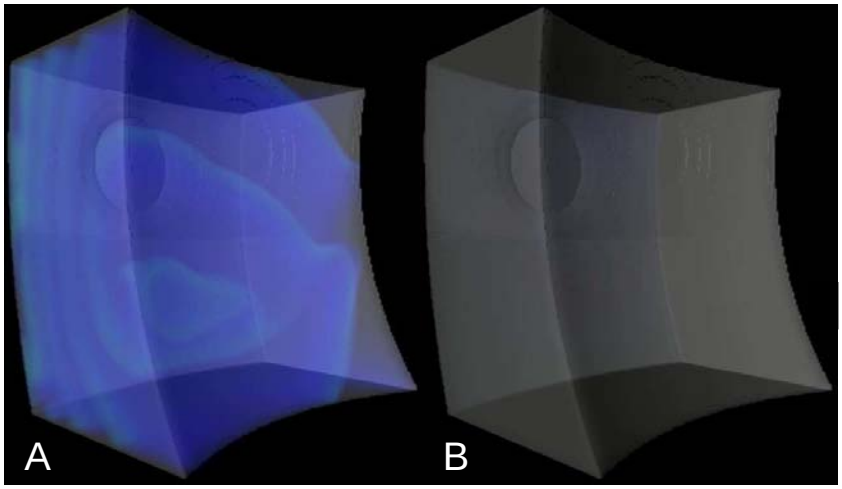

Fig. 11.26. Simulation of ventricular fibrillation. Both figures depict the state of the model given in fig. 11.25 F. A: Intracellular calcium concentration. Blue indicates concentrations of less than $0.1\,\mu M$. B: Tension development. Nearly no tension development is visible. The maximum normalized tension is only 1/100 of the physiological value.

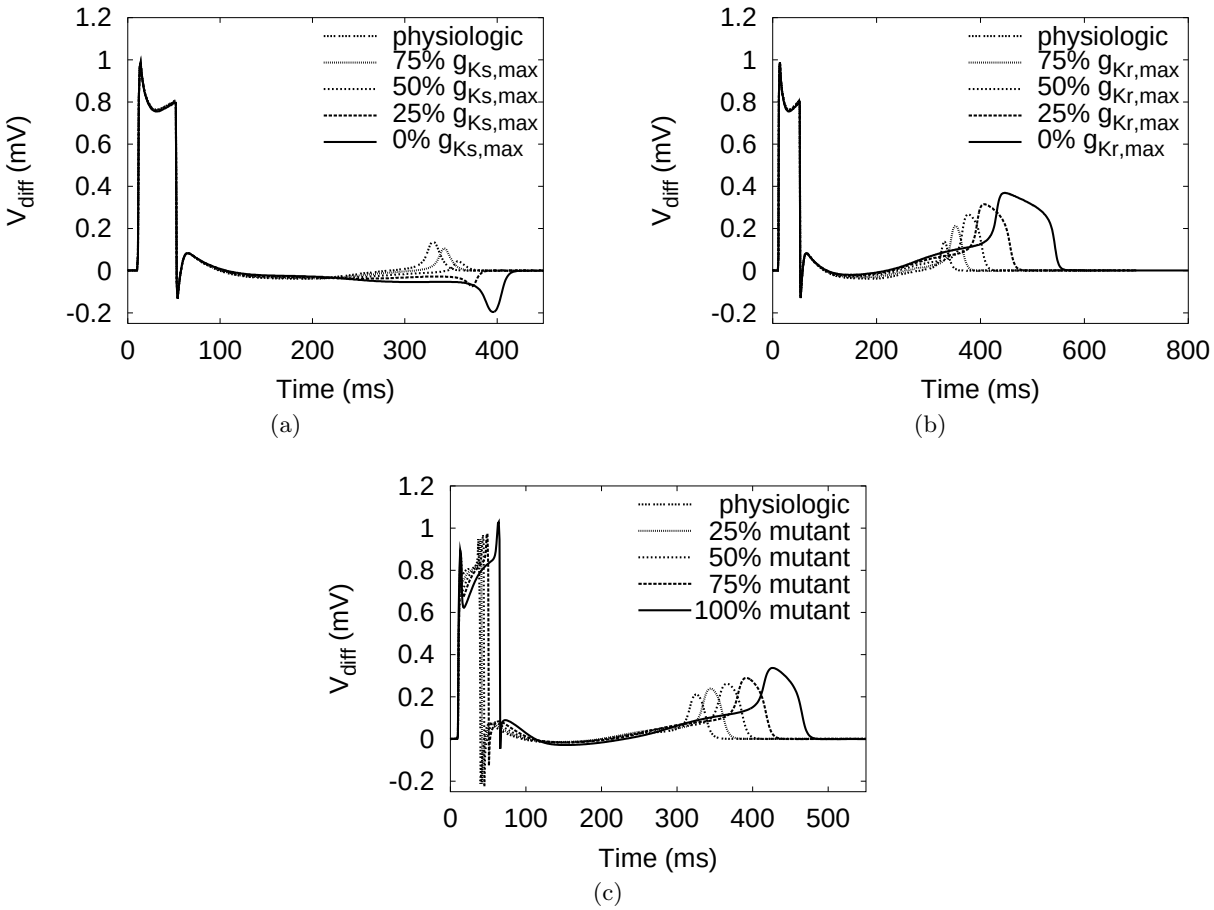

Fig. 11.27. Transmural ECGs of the three long QT syndromes. (a) LQT1. (b) LQT2. (c) LQT3. Figs. adapted from [409].

11.2.7 Long QT Syndrom

In order to investigate the mechanisms of the long QT syndrome in tissue, the presented single cell findings of section 10.8.2.2 were inserted into the three-dimensional model of a virtual wedge preparation of ventricular tissue (fig. 10.6). The model was stimulated at the endocardial side as described in the physiological simulation of section 11.1.6. The excitation conduction was simulated with the bidomain model in order to measure the calculated extracellular potential at the endocardial and epicardial ends of the bath medium.

The effects of the LQT1 syndrome on the transmural ECG are shown in fig. 11.27 a. The reduction of $g_{Ks,max}$ led to a prolongation of the APD in all three cell types (fig. 10.47) but at 100 % mutation the APD of all three cell types was nearly the same for complete loss of I_{Ks} function. This causes a change in polarity of the T-wave in the transmural ECG (fig. 11.27 a) which is not in agreement with the measured transmural ECGs of LQT1 (fig. 4.18 a). In addition to the varying amplitude of the T-wave, an increased duration of the QT interval caused by declining density of I_{Ks} channels and no widening of the T wave morphology was visible.

The reduction of I_{Kr} channel density as mechanism for the LQT2 syndrome led in the uncoupled single cell simulations to a prolongation of the APD in all of the three cell types but mostly in M cells (fig. 10.48). In the transmural ECG (fig. 11.27 b) an extension of the QT interval with an accompanying widening of the T-wave and enlarged amplitude, which was caused by the increased APD in mid-myocardial areas, was visible during decreasing density

of I_{Kr} channels. These simulated properties were the same as compared to the measurement data (fig. 4.18 b)
The LQT3 syndrome was described by the inclusion of the presented mutation of I_{Na} channels leading to a late component during the plateau phase. The APD prolongation in the single cell simulations was most dominant in mid-myocardial cells (fig. 10.49). This led to an amplified dispersion of the repolarization which was maintaining the increased duration of the QT interval as well as the widening and enlargement of the amplitude of the T wave (fig. 11.27 c). The measured transmural ECGs depicted in fig. 4.18 c show the same features. In addition to these effects, the speed of the excitation conduction was reduced during increased inclusion of mutant I_{Na} channels. The reason for this was the reduced speed of the depolarization process due to the mutation. The widening of the signal in the simulated ECG during depolarization is visible in fig. 11.27 c. This widening was not seen experimentally (fig. 4.18 c).

Discussion: The simulation results demonstrated the ionic mechanisms of the three most common long QT syndromes in single cell studies (section 10.8.2.2) and in a model of a human left ventricular wedge preparation. The effects of the long QT syndromes were presented in transmural ECGs. The morphology of the waveforms was comparable to measured data [210, 211]. Only in the case of LQT1, the model does not represent the correct results but still showed prolongation of the QT interval.
Gima and Rudy recently published similar simulations in a one-dimensional model of a guinea-pig with a simplified electrical heterogeneity [262]. The novelty of this work was to characterize the long QT syndromes in a three-dimensional anisotropic heterogeneous human model of the left ventricular myocardium using the bidomain approach.

12

Conclusion

Modeling of the electrophysiology and tension development in the human heart is a promising approach to support the understanding of the complex mechanisms occuring in the cardiovascular system. The knowledge provided in the different space scales from protein to organ obtained are enormous, but the gaps between these scales are yet not bridged. This thesis demonstrates how the findings of different topics of research like biophysics, medicine and engineering can be combined to fill the gaps between the different disciplines and the different space scales.

Modeling of the electromechanical heterogeneity in both the atria and the ventricles and the investigation of the mechanisms and effects of cardiac pathologies are the main topics of this work. In order to achieve this modeling, a wide variety of anatomical and physiological knowledge is necessary to describe the processes involved in electrophysiology and tension development mathematically.

The simulations in the atria revealed the importance of including realistic anatomical structures and fiber orientation combined with realistic heterogeneous human electrophysiology and anisotropic electrical properties in order to reproduce the normal excitation pattern in the atrium seen experimentally. The developed heterogeneous human sinoatrial node model is able to drive the atrial model with a normal heart frequency. The electrophysiological changes due to electrophysiological remodeling caused by atrial fibrillation were reconstructed in the simulations in quantitative good agreement with the experimental data. A genetic defect effecting the ionic current characteristics in the atrium was incorporated in the electrophysiological model and the effects of this mutation on the cell and tissue level were identified by simulations. Simulated atrial flutter and fibrillation has the same characteristics as measurements.

The electromechanical simulations in the ventricle demonstrated the necessity of including electrophysiological heterogeneity in order to reconstruct a homogeneous mechanical process seen experimentally. Both the designed heterogeneous electrophysiological model and the assembled tension development model were in good agreement with measured physiological properties. The inclusion of the fiber orientation in the ventricle by the presented approach is an important extension for the realistic description of the electromechanical processes. The electrocardiograms (ECG) of the three investigated types of long QT syndrome were reconstructed mainly correct. The simulated ventricular arrhythmias demonstrated the risk of the loss of mechanical activity due to high frequency re-excitation.

In the schematic models, the geometrical influences are reduced and the effects of electrophysiological heterogeneity in both atria and ventricles were identified. The electrical interaction of the sinoatrial node with its surrounding tissue was characterized in a model of the right atrium. A model of a line through the left ventricle and a model of a virtual wedge preparation

were used to investigate the effects of electrophysiological heterogeneity on the transmural ECG. A positive T-wave seen experimentally is only reconstructed quantitatively correct when including the transmural electrophysiological heterogeneities.
Different limitations of the models need to be discussed. The anatomical models are mainly based on the Visible Female data set. The heart of this person was not completely healthy and the geometry and shape have changed until the data aquisition. In the presented enhanced atrial model, the structure and fiber orientation of the ostia e.g. of the pulmonary veins have to be included. In the ventricles, the rule-based system to set the fiber orientation needs to be enhanced by a technique to measure this orientation e.g. with diffusion tensor MRI. Furthermore, the influence of ventricular lamination influencing the electromechanical properties was neglected. The calcium handling approach of the electrophysiological models have to be adapted to recent descriptions with new measurement data to reproduce accurately the calcium transient in human myocytes. Moreover, the mechano-electrical feedback was not incorporated in this work.
The methods described in this thesis offer the opportunity to reproduce the interaction of anatomy, electrophysiology, tension development, and contraction more precisely in future work. The methods provide a useful and complementary tool to investigate the dynamical behavior in such a detailed way that cannot be achieved experimentally to date. All parameters during normal and abnormal activity of the heart can be traced and analyzed.
The electromechanical model of the left ventricle can be enhanced by a description of the apico-basal in addition to the transmural heterogeneity. For the atrial model electrophysiological remodeling effects induced by chronic atrial fibrillation can be investigated in the presented model of the entire atrium. The effects of genetic defects on channel properties and the resulting action potentials can be included in the whole atrial or ventricular model to investigate the arrhythmogenic effects of these defects.
To validate the presented models, experimentally recorded ECGs on heart and body surfaces have to be compared to simulated ECGs in physiological, pathological, and pacing cases. Future improvements can incorporate complete electromechanical coupling including the contraction process in the whole heart. Furthermore, a detailed model considering individual human anatomy can gain more information about the influence of varying anatomical architecture on excitation conduction and its role in initiation of arrhythmia.
If computer resources and the availability of measured data will increase like in the past decades, high quality electromechanical models of the whole heart will become standard tools in clinical work in a few years. These models will reconstruct physiological cases of standard humans and pathological cases of individual patients.

List of Figures

List of Tables

References

1. W. Bargmann, "Bau des Herzens," in *Das Herz des Menschen*, W. Bargmann and W. Doerr, Eds., pp. 88–164. Georg Thieme Verlag, Stuttgart, 1963.
2. R. H. Anderson and A. E. Becker, *Anatomie des Herzens*, Georg Thieme Verlag, Stuttgart, 1982.
3. H. Gray and W. H. Lewis, *Anatomy of the human body*, Lea & Febiger, Philadelphia, 20 edition, 1918.
4. J. Sobotta, *Atlas der Anatomie des Menschen*, vol. 2, Urban & Schwarzenberg, 20 edition, 1993.
5. F. H. Netter, "Anatomie," in *Farbatlanten der Medizin*, vol. 1, chapter 1, pp. 2–33. Thieme, Stuttgart; New York, 3 edition, 1990.
6. J. Schrader, "Das Herz," in *Lehrbuch der Physiologie*, R. Klinke and S. Silbernagl, Eds., chapter 7, pp. 109–144. Thieme, Stuttgart, New York, 2001.
7. H. Antoni, "Mechanik der Herzaktion," in *Physiologie des Menschen*, R. F. Schmidt, G. Thews, and F. Lang, Eds., chapter 22, pp. 448–471. Springer, Berlin, Heidelberg, New York, 2000.
8. E. Bauereisen, "Normale Physiologie des Herzens," in *Das Herz des Menschen*, W. Bargmann and W. Doerr, Eds., chapter 7, pp. 313–354. Georg Thieme Verlag, Stuttgart, 1963.
9. R. F. Schmidt, G. Thews, and F. Lang, *Physiologie des Menschen*, Springer, Berlin; Heidelberg; New York, 28 edition, 2000.
10. Wolfgang K¸hnel, *Taschenatlas der Zytologie, Histologie und mikroskopischen Anatomie*, Georg Thieme Verlag, R¸digerstra?e 14, D-70469 Stuttgart, 10 edition, 1999.
11. D. W. Fawcett and N. S. McNutt, "The ultrastructure of cat myocardium. I. ventricular papillary muscle," *Cell Biol.*, vol. 42, pp. 1–45, 1969.
12. J. Dudel, "Grundlagen der Zellphysiologie," in *Physiologie des Menschen*, R. F. Schmidt, G. Thews, and F. Lang, Eds., chapter 1, pp. 3–19. Springer, Berlin, Heidelberg, New York, 2000.
13. D. M. Bers, *Excitation-Contraction Coupling and Cardiac Contractile Force*, Kluwer Academic Publishers, Dordrecht, Netherlands, 1991.
14. E. Marbán, T. Yamagishi, and G. Tomaselli, "Structure and function of voltage-gated sodium channels," *J. Physiol.*, vol. 508, pp. 647–657, 1998.
15. T. J. Kamp and J. W. Hell, "Regulation of cardiac L-type calcium channels by protein kinase A and protein kinase C," *Circ. Res.*, vol. 87, no. 12, pp. 1095–1102, 2000.
16. J. M. Nerbonne, "Molecular basis of functional voltage-gated k^+ channel diversity in the mammalian myocardium," *J. Physiol.*, vol. 525, no. 2, pp. 285–298, 2000.
17. C. W. Balke, E. Marbán, and B. O'Rourke, "Calcium channels: Structure, function, and regulation," in *Cardiac Electrophysiology. From Cell to Bedside*, D. P. Zipes and J. Jalife, Eds., chapter 2, pp. 8–21. W. B. Saunders Company, Philadelphia, 3 edition, 1999.
18. T. J. Kamp, Z. Zhou, S. Zhang, J. C. Makielski, and C. T. January, "Pharmacology of L- and T-type calcium channels in the heart," in *Cardiac Electrophysiology. From Cell to Bedside*, D. P. Zipes and J. Jalife, Eds., chapter 17, pp. 141–156. W. B. Saunders Company, Philadelphia, 3 edition, 1999.
19. D. M. Bers, "Cardiac calcium channels," in *Cardiac Electrophysiology. From Cell to Bedside*, D. P. Zipes and J. Jalife, Eds., chapter 2, pp. 10–18. W. B. Saunders Company, Philadelphia, 4 edition, 2004.
20. X. Chen and S. R. Houser, "Pharmacology of L-type and T-type calcium channels in the heart," in *Cardiac Electrophysiology. From Cell to Bedside*, D. P. Zipes and J. Jalife, Eds., chapter 16, pp. 133–142. W. B. Saunders Company, Philadelphia, 4 edition, 2004.
21. R. L. Rasmusson, "Pharmacology of potassium channels," in *Cardiac Electrophysiology. From Cell to Bedside*, D. P. Zipes and J. Jalife, Eds., chapter 18, pp. 156–167. W. B. Saunders Company, Philadelphia, 3 edition, 1999.
22. G. Y. Oudit, R. J. Ramirez, and P. H. Backx, "Voltage-regulated potassium channels," in *Cardiac Electrophysiology. From Cell to Bedside*, D. P. Zipes and J. Jalife, Eds., chapter 3, pp. 19–32. W. B. Saunders Company, Philadelphia, 4 edition, 2004.
23. M. C. Sanguinetti and M. Tristani-Firouzi, "Gating of cardiac delayed rectifier K^+ channels," in *Cardiac Electrophysiology. From Cell to Bedside*, D. P. Zipes and J. Jalife, Eds., chapter 10, pp. 88–95. W. B. Saunders Company, Philadelphia, 4 edition, 2004.

24. S. J. Carroll, J. Kurokawa, and R. S. Kass, "KCNQ1/KCNE1 macromolecular signaling complex: Channel microdomains and human disease," in *Cardiac Electrophysiology. From Cell to Bedside*, D. P. Zipes and J. Jalife, Eds., chapter 17, pp. 143–150. W. B. Saunders Company, Philadelphia, 4 edition, 2004.
25. M. Dellmar, G. E. Morley, J. F. Ek-Vitorin, D. Francis, N. Homma, K. Stergiopoulos, A. Lau, and S. M. Taffet, "Intracellular regulation of the cardiac gap junction channel connexin43," in *Cardiac Electrophysiology. From Cell to Bedside*, D. P. Zipes and J. Jalife, Eds., chapter 15, pp. 126–132. W. B. Saunders Company, Philadelphia, 3 edition, 1999.
26. M. Delmar, H. S. Duffy, P. L. Sorgen, S. M. Taffet, and D. C. Spray, "Molecular organization and regulation of the cardiac gap junction channel connexin43," in *Cardiac Electrophysiology. From Cell to Bedside*, D. P. Zipes and J. Jalife, Eds., chapter 8, pp. 66–76. W. B. Saunders Company, Philadelphia, 4 edition, 2004.
27. A. P. Moreno, V. Hayrapetyan, G. Zhong, A. D. Martinez, and E. C. Beyer, "Homometric and heterometric gap junctions," in *Cardiac Electrophysiology. From Cell to Bedside*, D. P. Zipes and J. Jalife, Eds., chapter 14, pp. 120–126. W. B. Saunders Company, Philadelphia, 4 edition, 2004.
28. J. W. Kimball, *Biology*, Addison-Wesley, Reading, Massachusetts; Menlo Park, California, 5 edition, 1983.
29. J. E. Saffitz and K. A. Yamada, "Gap junction distribution in the heart," in *Cardiac Electrophysiology. From Cell to Bedside*, D. P. Zipes and J. Jalife, Eds., chapter 21, pp. 271–277. W. B. Saunders Company, Philadelphia, 3 edition, 1999.
30. D. J. Müller, G. M. Hand, A. Engel, and G. E. Sosinsky, "Conformational changes in surface structures of isolated connexin 26 gap junctions," *EMBO J.*, vol. 21, no. 14, pp. 3598–3607, 2002.
31. D. A. Goodenough and D. L. Paul, "Beyond the gap: Functions of unpaired connexon channels," *Nature Reviews Molecular Cell Biology*, vol. 4, pp. 285–295, 2003.
32. V. M. Unger, N. M. Kumar, N. B. Gilula, and M. Yeager, "Three-dimensional structure of a recombinant gap junction membrane channel," *Science*, vol. 283, pp. 1176–1180, 1999.
33. H. J. Jongsma and M. B. Rook, "Biophysics of cardiac gap junction channels," in *Cardiac Electrophysiology. From Cell to Bedside*, D. P. Zipes and J. Jalife, Eds., chapter 14, pp. 119–125. W. B. Saunders Company, Philadelphia, 3 edition, 1999.
34. Mark Yeager, "Molecular biology and structure of cardiac gap junction intercellular channels," in *Cardiac Electrophysiology. From Cell to Bedside*, D. P. Zipes and J. Jalife, Eds., chapter 4, pp. 31–40. W. B. Saunders Company, Philadelphia, 3 edition, 1999.
35. J. E. Saffitz, D. L. Lerner, and K. A. Yamada, "Gap junction distribution and regulation in the heart," in *Cardiac Electrophysiology. From Cell to Bedside*, D. P. Zipes and J. Jalife, Eds., chapter 21, pp. 181–191. W. B. Saunders Company, Philadelphia, 4 edition, 2004.
36. H. Lodish, A. Berk, P. Matsudaira, C. A. Kaiser, M. Krieger, M. P. Scott, S. L. Zipursky, and J. Darnell, *Molecular Cell Biology*, W. H. Freeman and Company, New York, 2003.
37. H. Lodish, A. Berk, S. L. Zipursky, P. Matsudaira, D. Baltimore, and J. Darnell, *Molecular Cell Biology*, W. H. Freeman and Company, New York, 4 edition, 1999.
38. R. Klinke and S. Silbernagl, *Taschenatlas der Physiologie*, Georg Thieme Verlag, Stuttgart; New York, 5 edition, 2001.
39. H. Lodish, A. Berk, S. L. Zipursky, P. Matsudaira, D. Baltimore, and J. Darnell, *Molekulare Zellbiologie*, Spektrum Akademischer Verlag, Heidelberg, Berlin, 2001.
40. A. M. Gordon, E. Homsher, and M. Regnier, "Regulation of contraction in striated muscle," *Physiol. Rev.*, vol. 80, no. 2, pp. 853–924, 2000.
41. H. K. Simmerman and L. R. Jones, "Phospholamban: Protein structure, mechanism of action, and role in cardiac function," *Physiol. Rev.*, vol. 78, no. 4, pp. 921–947, 1998.
42. J. Zhai, A. G. Schmidt, B. D. Hoit, Y. Kimura, D. H. MacLennan, and E. G. Kranias, "Cardiac-specific overexpression of a superinhibitory pentameric phospholamban mutant enhances inhibition of cardiac function in vivo," *J. Biol. Chem.*, vol. 275, no. 14, pp. 10538–10544, 2000.
43. K. Haghighi, A. G. Schmidt, B. D. Hoit, A. G. Brittsan, A. Yatani, J. W. Lester, J. Zhai, Y. Kimura, G. W. Dorn II, D. H. MacLennan, and E. G. Kranias, "Superinhibition of sarcoplasmic reticulum function by phospholamban induces cardiac contractile failure," *J. Biol. Chem.*, vol. 276, no. 26, pp. 24145–24152, 2001.
44. C. Franzini-Armstrong and F. Protasi, "Ryanodine receptors of striated muscles: A complex channel capable of multiple interactions," *Physiol. Rev.*, vol. 77, no. 3, pp. 699–729, 1997.
45. G. Meissner, "Sarcoplasmic reticulum ion channels," in *Cardiac Electrophysiology. From Cell to Bedside*, D. P. Zipes and J. Jalife, Eds., chapter 6, pp. 51–58. W. B. Saunders Company, Philadelphia, 4 edition, 2004.
46. C. Franzini-Armstrong, F. Protasi, and V. Ramesh, "Shape, size, and distribution of Ca^{2+} release units and couplons in skeletal and cardiac muscles," *Biophys. J.*, vol. 77, pp. 1528–1539, 1999.
47. M. D. Stern, G. Pizarro, and E. Ríos, "Local control model of excitation-contraction coupling in skeletal muscle," *J. Gen. Physiol.*, vol. 110, pp. 415–440, 1997.
48. L. Zhang, J. Kelley, G. Schmeisser, Y. M. Kobayashi, and L. R. Jones, "Complex formation between junctin, triadin, calsequestrin, and the ryanodine receptor. proteins of the cardiac junctional sarcoplasmic reticulum membrane.," *J. Biol. Chem.*, vol. 272, no. 37, pp. 23389–23397, 1997.
49. D. W. Shin, Z. Pan, E. K. Kim, J. M. Lee, M. B. Bhat, J. Parness, D. H. Kim, and J. Ma, "A retrograde signal from calsequestrin for the regulation of store-operated ca^{2+} entry in skeletal muscle," *J. Biol. Chem.*, vol. 278, no. 5, pp. 3286–3292, 2003.

50. S. J. Crick, J. Wharton, M. N. Sheppard, D. Royston, M. H. Yacoub, R. H. Anderson, and J. M. Pok, "Innervation of the human cardiac conduction system," *Circ.*, vol. 89, no. 4, pp. 1697–1708, 1994.
51. F. H. Netter, *Atlas der Anatomie des Menschen*, Ciba-Geigy AG, Basel, 1995.
52. L. Wang and R. Patterson, "Multiple sources of the impedance cardiogram based on 3-d finite difference human thorax models," *IEEE Transactions on Biomedical Engineering*, vol. 42, no. 2, pp. 141–148, Feb. 1995.
53. R. H. Anderson and S. Y. Ho, "The architecture of the sinus node, the atrioventricular conduction axis, and the internodal atrial myocardium," *J. Cardiovasc. Electrophysiol.*, vol. 9, pp. 1233–1248, 1998.
54. W. A. McAlpine, *Heart and Coronary Arteries*, Springer, Berlin, 1976.
55. J. Li, H. Dobrzynski, I. D. Greener, V. P. Nikolski, M. Yamamoto, R. Billeter, I. R. Efimov, and M. R. Boyett, "Development of 3-d anatomically-detailed mathematical models of the sinoatrial and atrioventricular nodes," in *Proc. Computers in Cardiology*, 2004, vol. 31, pp. 89–92.
56. R. B. Schuessler, J. P. Boineau, J. E. Saffitz, B. I. Bromberg, and K. F. Kwong, "Cellular mechanisms of sinuatrial activity," in *Cardiac Electrophysiology. From Cell to Bedside*, D. P. Zipes and J. Jalife, Eds., chapter 22, pp. 187–196. W. B. Saunders Company, Philadelphia, 3 edition, 1999.
57. M. D. Rodefeld, S. L. Beau, and R. B. Schuessler, "β-adrenergic and muscarinic chlorinergic receptor densities in the human sinoatrial node: Identification of a high β_2-adrenergic receptor density," *J. Cardiovasc. Electrophysiol..*, vol. 7, pp. 1039–1049, 1996.
58. T. N. James, "Structure and function of the sinus node, AV node and His bundle of the human heart: Part II—function," *Prog. Cardiovasc. Dis.*, vol. 46, no. 1, pp. 327–360, 2003.
59. W. Koch, "Weitere Mitteilungen über den Sinusknoten des Herzens," *Verhandlungen der Dt. Pathologischen Anatomie*, vol. 13, pp. 85–92, 1909.
60. T. N. Mazgalev, D. R. Van Wagoner, and I. R. Efimov, "Mechanisms of AV nodal excitability and propagation," in *Cardiac Electrophysiology. From Cell to Bedside*, D. P. Zipes and J. Jalife, Eds., chapter 23, pp. 196–205. W. B. Saunders Company, Philadelphia, 3 edition, 1999.
61. J. P. Boineau, T. E. Canavan, R. B. Schuessler, M. E. Cain, P. B. Corr, and J. L. Cox, "Demonstration of a widely distributed atrial pacemaker complex in the human heart," *Circ.*, vol. 77, pp. 1221–1237, 1988.
62. A. A. Young, L. J. LeGrice, M. A. Young, and B. H. Smaill, "Extended confocal microscopy of myocardial laminae and collagen network," *J. Microscopy*, vol. 192, pp. 139–150, Nov. 1998.
63. W. Hort, "Untersuchungen ¸ber die Muskelfaserdehnung und das Gef¸ge des Myokards in der rechten Herzkammerwand des Meerschweinchens," *Virchows Arch. Pathol. Anat. Physiol. Klin. Med.*, vol. 359, pp. 694–731, 1957.
64. W. Hort, "Makroskopische und mikrometrische Untersuchungen am Myokard verschieden stark gef¸llter linker Kammern," *Virchows Arch. Pathol. Anat. Physiol. Klin. Med.*, vol. 333, pp. 523–564, 1960.
65. D. D. Streeter, jr. and D. L. Bassett, "An engineering analysis of myocardial fiber orientation in pig's left ventricle in systole," *Anatomical Record*, vol. 155, pp. 503–512, 1966.
66. D. D. Streeter, "Gross morphology and fiber geometry of the heart," in *Handbook of Physiology: The Cardiovascular System*, Berne Bethesda, Ed., vol. I, pp. 61–112. American Physiology Society, 1979.
67. I. J. LeGrice, P. J. Hunter, and B. H. Smaill, "Laminar structure of the heart: A mathematical model," *Am. J. Physiol.*, vol. 272, pp. H2466–H2476, 1997.
68. I. J. LeGrice, B. H. Smaill, L. Z. Chai, S. G. Edgar, J. B. Gavin, and P. J. Hunter, "Laminar structure of the heart: Ventricular myocyte arrangement and connective tissue architecture in the dog," *Am. J. Physiol.*, vol. 269, pp. H571–H582, 1995.
69. R. C. Gonzalez and R. E. Woods, *Digital Image Processing*, Addison-Wesley, Reading, Massachusetts; Menlo Park, California, 1992.
70. M. J. Ackerman, "Viewpoint: The Visible Human Project," *J. Biocommunication*, vol. 18, no. 2, pp. 14, 1991.
71. "Visible Human Project, National Library of Medicine, Bethesda, USA," .
72. H. Morneburg, Siemens Aktiengesellschaft, Ed., *Bildgebende Systeme für die medizinische Diagnostik*, Publicis MCD, Erlangen, 3 edition, 1995.
73. W. A. Kalender and A. Polacin, "Physical performance characteristics of spiral CT scanning," *Med. Phys.*, vol. 18, pp. 910–915, 1991.
74. J. A. Ambrose, "Computerized transverse axial tomography," *Brit. J. Radiol.*, vol. 46, pp. 401, 1973.
75. D. P. Boyd and M. J. Lipton, "Cardiac computed tomography," in *IEEE*, 1983, vol. 71, p. 298.
76. S. Mang, F. B. Sachse, I. H. de Boer, C. D. Werner, and O. Dössel, "Registrierung morphologischer und elektrischer Messwerte am Langendorff-Präparat," in *Biomedizinische Technik*, Sep. 2000, vol. 45-1, pp. 515–516.
77. Y. Shang and O. Dössel, "Construction of cardiac anatomical models using deformable model methods," in *Bildverarbeitung für die Medizin 2004*, Berlin, Germany, Feb. 2004.
78. G. Reinerth, G. Seemann, S. Kewitz, O. Dössel, T. Schmidt, J. Albers, C.-F. Vahl, and S. Hagl, "Simulation of cardiac electrophysiology using mathematical models and computer based processing of digital image data," *Europ. Heart J.*, vol. 24, pp. S285, 2003.
79. A. Abragam, *The principles of nuclear magnetism*, Oxford University Press, Ney York, 1961.
80. D. D. Stark and W. G. Bradley, *Magnetic Resonance Imaging*, Mosby Year Book, St. Louis, 1992.
81. P. B. Roemer, W. A. Edelstein, C. E. Hayes, S. P. Souza, and O. M. Mueller, "The NMR phased array," *Magn. Res. Med.*, vol. 16, pp. 192, 1990.

82. J. J. Wild, "Use of ultrasonic pulses for the measurement of biologic tissue and the detenction of tissue density changes," *Surgery*, vol. 27, pp. 148, 1950.
83. H. Ermert and H.-P. Harjes, *Acoustical Imaging*, vol. 19, Plenum Press, Ney York, London, 1991.
84. L. Hatle and B. Angelsen, *Doppler ultrasound in cardiology. Physical principles and clinical applications*, Lea and Febinger, Philadephia, 1985.
85. F. B. Sachse, C. D. Werner, and G. Seemann, "Simulation of cardiac electrophysiology and electrocardiography," in *Computer Simulation and Experimental Assessment of Cardiac Electrophysiology*, N. Virag, O. Blanc, and L. Kappenberger, Eds., pp. 97–104. Futura Publishing, Armonk, New York, 2001.
86. I. N. Bankman, *Handbook of Medical Imaging Processing and Analysis*, Academic Press, 2002.
87. J. S. Duncan and N. Ayache, "Medical image analysis: Progress over two decades and the challenges ahead," *IEEE Trans. on Patt. Anal. and Mach. Intell.*, vol. 22, pp. 85–106, 2000.
88. B. Jähne, *Digitale Bildverarbeitung*, Springer, Berlin; Heidelberg; New York; London; Paris; Tokyo; Hong Kong; Barcelona; Budapest, 3 edition, 1993.
89. T. Lehmann, W. Oberschelp, E. Pelikan, and R. Repges, *Bildverarbeitung für die Medizin*, Springer, Berlin, Heidelberg, 1997.
90. A. Rosenfeld and A. Kak, *Digital Image Processing*, Academic Press, New York, 1982.
91. J. C. Russ, *The Image Processing Handbook*, CRC Press, Boca Raton; Ann Arbor; London; Tokyo, 2 edition, 1995.
92. N. Arad and D. Reisfeld, "Image warping using few anchor points and radial functions," *Computer Graphics Forum*, vol. 14, no. 1, pp. 35–46, 1995.
93. G. Xingfei and T. Jie, "An automatic active contour model for multiple objects," *IEEE Int. Conf. Pattern Recognition*, pp. 881–884, 2002.
94. D. Terzopoulos, A. Witkin, and M. Kass, "Constraints on deformable models recovering 3D shape and nonrigid motion," *Artificial Intelligence*, vol. 36, pp. 91–123, 1988.
95. R. F. Schmidt and G. Thews, *Physiologie des Menschen*, Springer, Berlin; Heidelberg; New York, 25 edition, 1993.
96. G. Meissner, "Sarcoplasmic reticulum ion channels," in *Cardiac Electrophysiology. From Cell to Bedside*, D. P. Zipes and J. Jalife, Eds., chapter 6, pp. 51–58. W. B. Saunders Company, Philadelphia, 3 edition, 1999.
97. P. Lipp and Martin D. Bootman, "The physiology and molecular biology of cardiac Na/Ca exchange," in *Cardiac Electrophysiology. From Cell to Bedside*, D. P. Zipes and J. Jalife, Eds., chapter 5, pp. 41–51. W. B. Saunders Company, Philadelphia, 3 edition, 1999.
98. D. L. Ypey and L. J. DeFelice, "The patch-clamp technique: A theoretical and practical introduction using simple electrical equivalent circuits," in *Channels, Receptors, and Transporters*, L. J. DeFelice, Ed., chapter 6. Biophysics Textbook On-Line, Biophysical Society, Bethesda, MD, 2000.
99. M. Lindau, "The patch clamp technique: High resolution studies of single proteins," Apr. 2000.
100. J. E. Burnes, B. Taccardi, R. S. MacLeod, and Y. Rudy, "Noninvasive ECG imaging of electrophysiologically abnormal substrates in infarcted hearts: A model study," *Circ.*, vol. 8, pp. 533–540, Feb. 2000.
101. M. R. Franz, "Monophasic action potential recording," in *Cardiac Electrophysiology. From Cell to Bedside*, D. P. Zipes and J. Jalife, Eds., chapter 26, pp. 763–770. W. B. Saunders Company, Philadelphia, 3 edition, 1999.
102. R. J. Schilling, N. S. Peters, and D. W. Davies, "Simultaneous endocardial mapping in the human left ventricle using a noncontact catheter," *Circ.*, vol. 98, pp. 887–898, 1998.
103. F. B. Sachse, B. W. Steadman, J. H. B. Bridge, B. B. Punske, and B. Taccardi, "Conduction velocity in myocardium modulated by strain: Measurement instrumentation and initial results," in *Proc. 26th Conf. IEEE EMBS*, 2004.
104. M.-A. Bray, S.-F. Lin, and J. P. Wikswo, "Three-dimensional surface reconstruction and fluorescent visualization of cardiac activity," *IEEE Trans. Biomed. Engin.*, vol. 47, no. 10, pp. 1382–1391, 2000.
105. S. M. Dillon, T. E. Kerner, J. Hoffman, V. Menz, K. S. Li, and J. J. Michele, "A system for in-vivo cardiac optical mapping," *IEEE Engin. Med. Biol.*, vol. 17, no. 1, pp. 95–108, 1998.
106. S. Silbernagl and A. Despopoulos, "Grundlagen, Zellphysiologie," in *Taschenatlas der Physiologie*, chapter 1, pp. 2–41. Georg Thieme Verlag, Stuttgart, 2001.
107. W. Nernst, "Zur Kinetik der in Lösung befindlichen Körper: Theorie der Diffusion," *Z. Phys. Chem.*, pp. 613–637, 1888.
108. S. Silbernagl and A. Despopoulos, "Nerv und Muskel, Arbeit," in *Taschenatlas der Physiologie*, chapter 2, pp. 42–76. Georg Thieme Verlag, Stuttgart, 2001.
109. P. B. Bennett and H.-G. Shin, "Biophysics of cardiac sodium channels," in *Cardiac Electrophysiology. From Cell to Bedside*, D. P. Zipes and J. Jalife, Eds., chapter 8, pp. 67–78. W. B. Saunders Company, Philadelphia, 3 edition, 1999.
110. M. C. Sanguinetti and M. Tristani-Firouzi, "Delayed and inward rectifier potassium channels," in *Cardiac Electrophysiology. From Cell to Bedside*, D. P. Zipes and J. Jalife, Eds., chapter 9, pp. 79–86. W. B. Saunders Company, Philadelphia, 3 edition, 1999.
111. K. Shivkumar and J. N. Weiss, "Adenosine triphospate-sensitive potassium channels," in *Cardiac Electrophysiology. From Cell to Bedside*, D. P. Zipes and J. Jalife, Eds., chapter 10, pp. 86–93. W. B. Saunders Company, Philadelphia, 3 edition, 1999.

112. M. Vassalle, H. Yu, and I. S. Cohen, "Pacemaker channels and cardiac automaticity," in *Cardiac Electrophysiology. From Cell to Bedside*, D. P. Zipes and J. Jalife, Eds., chapter 11, pp. 94–103. W. B. Saunders Company, Philadelphia, 3 edition, 1999.
113. U. Ravens, "Mechano-electric feedback and arrhythmias," *Prog. Biophys. Mol. Biol.*, vol. 82, no. 1-3, pp. 255–266, 2003.
114. M. J. Ackerman and D. E. Clapham, "G protein and ion channels," in *Cardiac Electrophysiology. From Cell to Bedside*, D. P. Zipes and J. Jalife, Eds., chapter 13, pp. 112–118. W. B. Saunders Company, Philadelphia, 3 edition, 1999.
115. D. Grammig S. Frings, "Vorlesungsskripte Zoophysiologie – Struktur und Funktion von Ionenkanälen," 1998.
116. T. Nagatomo, Z. Fan, B. Ye, G. S. Tonkovich, C. T. January, and J. C. Makielski, "Temperature dependence of early and late currents in human cardiac wild-type and long q-t δKPQ Na^+ channels," *Am. J. Physiol.*, vol. 275, pp. H2016–H2024, 1998.
117. C. Antzelevitch, G. Yan, W. Shimizu, and A. Burashnikov, "Electrical heterogeneity, the ECG, and cardiac arrhythmias," in *Cardiac Electrophysiology. From Cell to Bedside*, D. P. Zipes and J. Jalife, Eds., chapter 26, pp. 222–238. W. B. Saunders Company, Philadelphia, 3 edition, 1999.
118. E. Marbán and G. F. Tomaselli, "Molecular biology of sodium channels," in *Cardiac Electrophysiology. From Cell to Bedside*, D. P. Zipes and J. Jalife, Eds., chapter 1, pp. 1–8. W. B. Saunders Company, Philadelphia, 3 edition, 1999.
119. T. Kiyosue and M. Arita, "Late sodium current and its contribution to action potential configuration in guinea pig ventricular myocytes.," *Circ. Res.*, vol. 64, pp. 389–397, 1989.
120. A. C. Zygmunt, G. T. Eddlestone, G. P. Thomas, V. V. Nesterenko, and C. Antzelevitch, "Larger late sodium conductance in M cells contributes to electrical heterogeneity in canine ventricle," *Am. J. Physiol.*, vol. 281, pp. H689–H697, 2001.
121. G.-R. Li, J. Feng, L. Yue, M. Carrier, and S. Nattel, "Evidence for two components of delayed rectifier K^+ current in human ventricular myocytes," *Circ. Res.*, vol. 78, pp. 689–696, 1996.
122. D. J. Snyders, "Molecular biology of potassium channels," in *Cardiac Electrophysiology. From Cell to Bedside*, D. P. Zipes and J. Jalife, Eds., chapter 3, pp. 21–31. W. B. Saunders Company, Philadelphia, 3 edition, 1999.
123. D. DiFrancesco, "Pacemaker channels and normal automaticity," in *Cardiac Electrophysiology. From Cell to Bedside*, D. P. Zipes and J. Jalife, Eds., chapter 12, pp. 103–111. W. B. Saunders Company, Philadelphia, 4 edition, 2004.
124. H. Honjo, M. Lei, M. R. Boyett, and I. Kodoma, "Heterogeneity of 4-aminopyridine-sensitive current in rabbit sinoatrial node cells," *Am. J. Physiol.*, vol. 276, pp. H1295–H1304, 1999.
125. Z. Wang, B. Fermini, and S. Nattel, "Delayed rectifier current and repolarization in human atrial myocytes," *Circ. Res.*, vol. 73, pp. 276–285, 1993.
126. Z. Wang, L. Yue, M. White, G. Pelletier, and S. Nattel, "Differential distribution of inward rectifier potassium channel transcripts in human atrium versus ventricle," *Circ.*, vol. 98, pp. 2422–2428, 1998.
127. H. Irisawa, H. F. Brown, and W. Giles, "Cardiac pacemaking in the sinoatrial node," *Physiol. Rev.*, vol. 73, no. 1, pp. 197–227, 1993.
128. E.-J. Speckmann, "Allgemeine Neurophysiologie," in *Physiologie*, P. Deetjen and E.-J. Speckmann, Eds., chapter 2, pp. 5–45. Urban & Fischer, München, Stuttgart, Jena, Lübeck, Ulm, 1999.
129. D. C. Gadsby and M. Nakao, "Steady-state current-voltage relationship of the na/k pump in guinea pig ventricular myocytes," *J Gen Physiol.*, vol. 94, no. 3, pp. 511–537, 1989.
130. S. Matsuoka and D. W. Hilgemann, "Steady-state and dynamic properties of cardiac sodium-calcium exchange. Ion and voltage dependencies of the transport cycle," *J Gen Physiol.*, vol. 100, no. 6, pp. 963–1001, 1992.
131. M. G. Vila Petroff, J. Palomeque, and A. R. Mattiazzi, "Na^+-Ca^{2+} exchange function underlying contraction frequency inotropy in the cat myocardium," *J. Physiol.*, vol. 550, no. 3, pp. 801–817, 2003.
132. H. Zhang, A. V. Holden, and M. R. Boyett, "Gradient model versus mosaic model of the sinoatrial node," *Circ.*, vol. 103, pp. 584–588, 2001.
133. D. E. Goldman, "Potential, impedance, and rectification in membranes," *J. Gen. Physiol.*, vol. 27, pp. 37–60, 1943.
134. A. L. Hodgkin and B. Katz, "The effect of sodium ions on the electrical activity of the giant axon of a squid," *J. Physiol.*, vol. 108, pp. 37–77, 1949.
135. J. Dudel, "Informationsvermittlung durch elektrische Erregung," in *Physiologie des Menschen*, R. F. Schmidt, G. Thews, and F. Lang, Eds., chapter 2, pp. 20–42. Springer, Berlin, Heidelberg, New York, 2000.
136. R. F. Schmidt, "Erregungsphysiologie des Herzens," in *Physiologie kompakt*, chapter 23, pp. 197–204. Springer, Berlin, Heidelberg, New York, 1999.
137. E. Cerbai, A. Zaza, and A. Mugelli, "Pharmacology of membrane ion channels in human myocytes," in *Cardiac Electrophysiology. From Cell to Bedside*, D. P. Zipes and J. Jalife, Eds., chapter 19, pp. 167–173. W. B. Saunders Company, Philadelphia, 3 edition, 1999.
138. A. V. Panfilov, "Three-dimensional wave propagation in mathematical models of ventricular fibrillation," in *Cardiac Electrophysiology. From Cell to Bedside*, D. P. Zipes and J. Jalife, Eds., chapter 31, pp. 271–277. W. B. Saunders Company, Philadelphia, 3 edition, 1999.
139. K. Hoshino, J. Anumonwo, M. Delmar, and J. Jalife, "Wenckebach periodicity in single atrioventricular nodal cells from the rabbit heart," *Circ.*, vol. 82, no. 6, pp. 2201–2216, 1990.

140. M. S. Spach, J. F. Heidlage, and P. C. Dolber, "The dual nature of anisotropic discontinous conduction in the heart," in *Cardiac Electrophysiology. From Cell to Bedside*, D. P. Zipes and J. Jalife, Eds., chapter 25, pp. 213–222. W. B. Saunders Company, Philadelphia, 3 edition, 1999.
141. A. G. Kléber, V. G. Fast, and S. Rohr, "Continuous and discontinuous propagation," in *Cardiac Electrophysiology. From Cell to Bedside*, D. P. Zipes and J. Jalife, Eds., chapter 24, pp. 213–222. W. B. Saunders Company, Philadelphia, 3 edition, 1999.
142. S. Verheule, M. J. A. van Kempen, P. H. J. A. te Welscher, B. R. Kwak, and H. J. Jongsma, "Characterization of gap junction channels in adult rabbit atrial and ventricular myocardium," *Circ. Res.*, vol. 80, pp. 673–681, 1997.
143. A. Noma and N. Tsuboi, "Dependence of junctional conductance on proton, calcium and magnesium ions in cardiac paired cells of guinea-pig," *J. Physiol.*, vol. 382, pp. 193–211, 1987.
144. S. P. Thomas, J. P. Kucera, L. Bircher-Lehmann, Y. Rudy, J. E. Saffitz, and A. G. Kléber, "Impulse propagation in synthetic strands of neonatal cardiac myocytes with genetically reduced levels of connexin43," *Circ. Res.*, vol. 92, pp. 1209–1216, 2003.
145. R. H. Hoyt, M. L. Cohen, and J. E. Saffitz, "Distribution and three-dimensional structure of intercellular junctions in canine myocardium," *Circ. Res.*, vol. 64, pp. 563–574, 1989.
146. E. Carafoli, "Calcium signaling: A tale for all seasons," *Proc. Natl. Acad. Sci. USA*, vol. 99, no. 3, pp. 1115–1122, 2002.
147. D. M. Bers, "Cardiac excitation-contraction coupling," *Nature*, vol. 415, pp. 198–205, 2002.
148. S. M.Cibulsky and W. A.Sather, "Control of ion conduction in L-type Ca^{2+} channels by the concerted action of S5-6 regions," *Biophys. J.*, vol. 84, pp. 1709–1719, 2003.
149. N. A. Beard, M. M. Sakowska, A. F. Dulhunty, and D. R. Laver, "Calsequestrin is an inhibitor of skeletal muscle ryanodine receptor calcium release channels," *Biophys. J.*, vol. 82, no. 1, pp. 310–320, 2002.
150. B. K. Chamberlain, C. J. Berenski, C. Y. Jung, and S. Fleischer, "Determination of the oligomeric structure of the Ca^{2+} pump protein in canine cardiac sarcoplasmic reticulum membranes using radiation inactivation analysis," *J. Biol. Chem.*, vol. 258, no. 19, pp. 11997–12001, 1983.
151. C. Nediani, C. Fiorillo, S. Rigacci, F. Magherini, M. Francalanci, G. Liguri, A. Pacini, and P. Nassi, "A novel interaction mechanism accounting for different acylphosphatase effects on cardiac and fast twitch skeletal muscle sarcoplasmic reticulum calcium pumps," *Fed. Europ. Biochem. Soc. Lett.*, vol. 443, pp. 308–31, 1999.
152. K. Haghighi, F. Kolokathis, L. Pater, R. A. Lynch, M. Asahi, A. O. Gramolini, G.-C. Fan, D. Tsiapras, H. S. Hahn, S. Adamopoulos, S. B. Liggett, G. W. Dorn II, D. H. MacLennan, D. T. Kremastinos, and E. G. Kranias, "Human phospholamban null results in lethal dilated cardiomyopathy revealing a critical difference between mouse and human," *J. Clinical Invest.*, vol. 111, no. 6, pp. 869–876, 2003.
153. P. Caroni and E. Carafoli, "The Ca^{2+}-pumping ATPase of heart sarcolemma: Characterization, caldomulin dependence, and partial purification," *J. Biol. Chem.*, vol. 256, no. 7, pp. 3263–3270, 1981.
154. S. Cortassa, M. A. Aon, E. Marbán, R. L. Winslow, and B. O'Rourke, "An integrated model of cardiac mitochondrial energy metabolism and calcium dynamics," *Biophys. J.*, vol. 84, pp. 2734–2755, 2003.
155. A. Fabiato, "Time and calcium dependence of activation and inactivation of calcium-induced release of calcium from the sarcoplasmic reticulum of a skinned canine cardiac purkinje cell," *J. General Physiol.*, vol. 85, pp. 247–289, 1985.
156. J. H. B. Bridge, P. R. Ershler, and M. B. Cannell, "Properties of Ca^{2+} sparks evoked by action potentials in mouse ventricular myocytes," *J. Physiol.*, vol. 518, no. 2, pp. 469–478, 1999.
157. M. Inoue and J. H. B. Bridge, "Ca^{2+} sparks in rabbit ventricular myocytes evoked by action potentials," *Circ. Res.*, vol. 92, pp. 532–538, 2003.
158. J. S. K. Sham, L.-S. Song, Y. Chen, L.-H. Deng, M. D. Stern, E. G. Lakatta, and H. Cheng, "Termination of Ca^{2+} release by a local inactivation of ryanodine receptors in cardiac myocytes," *Proc. Natl. Acad. Sci. USA*, vol. 95, pp. 15096–15101, 1998.
159. S. L. Lipsius, J. Hüser, and L. A. Blatter, "Intracellular Ca^{2+} release sparks atrial pacemaker activity," *News Physiol. Sci.*, vol. 16, pp. 101–106, 2001.
160. I. Kodama, M. R. Nikmaram, M. R. Boyett, R. Suzuki, H. Honjo, and J. M. Owen, "Regional differences in the role of the ca^{2+} and na^{+} currents in pacemaker activity in the sinoatrial node," *Am. J. Physiol.*, vol. 272, pp. H2793–H2806, 1997.
161. A. Noma and H Irisawa, "A time- and voltage-dependent potassium current in rabbit sinoatrial node cell," *Pflügers Arch.*, vol. 366, pp. 251–258, 1976.
162. R. Wilders, H. J. Jongsma, and A. C. E. van Ginneken, "Pacemaker activity of the sinoatrial node: A comparison of mathematical models," *Biophys. J.*, vol. 60, pp. 1202–1216, 1991.
163. A. Moroni, L. Gorza, M. Beltrame, B. Gravante, T. Vaccari, M. E. Bianchi, C. Altomare, R. Longhi, C. Heurteaux, M. Vitadello, A. Malgaroli, and D. DiFrancesco, "Hyperpolarization-activated cyclic nucleotide-gated channel 1 is a molecular determinant of the cardiac pacemaker current I_f," *J. Biol. Chem.*, vol. 276, no. 31, pp. 29233–29241, 2001.
164. A. M. W. Alings and L. N. Bouman, "Electrophysiology of the ageing rabbit and cat sinoatrial node – a comparative study," *Eur. Heart J.*, vol. 14, pp. 1278–1288, 1993.
165. D. DiFrancesco, "Block and activation of the pace-maker channel in calf purkinje fibres," *J. Physiol. (London)*, vol. 329, pp. 485–507, 1982.

166. M. R. Boyett, H. Honjo, M. Yamamoto, M. R. Nikmaram, R. Niwa, and I. Kodama, "Regional differences in effects of 4-aminopyridine within the sinoatrial node," *Am. J. Physiol.*, vol. 275, no. Heart Circ. Physiol. 44, pp. H1158–H1168, 1998.
167. H. Honjo, M. R. Boyett, and I. Kodoma, "Correlation between electrical activity and the size of rabbit sinoatrial node cells," *J. Physiol.*, vol. 496, pp. 795–808, 1996.
168. H. Honjo, M. R. Boyett, S. R. Coppen, Y. Takagishi, T. Opthof, N. J. Severs, and I. Kodoma, "Heterogeneous expression of connexins in rabbit sinoatrial node cells: Correlation between connexin isotype and cell size," *Cardiovasc Res.*, vol. 53, no. 1, pp. 89–96, 2002.
169. M. R. Boyett, H. Honjo, M. Yamamoto, M. R. Nikmaram, R. Niwa, and I. Kodama, "Downward gradient in action potential duration along conduction path in and around the sinoatrial node," *Am. J. Physiol.*, vol. 276, no. Heart Circ. Physiol. 45, pp. H686–H698, 1999.
170. E. Drouin, "Electrophysiologic properties of the adult human sinus node," *J. Cardiovasc. Electrophysiol.*, vol. 8, pp. 254–258, 1997.
171. F. X. Roithinger, J. Cheng, A. S. Groenewegen, R. J. Lee, and L. A. Saxon, "Use of electroanatomic mapping to delineate transseptal atrial conduction in humans," *Circ.*, vol. 100, pp. 1791–1797, 1999.
172. M. Chauvin, D. C. Shah, M. Haissaguerre, L. Marcellin, and C. Brechenmacher, "The anatomic basis of connections between the coronary sinus musculature and the left atrium in humans," *Circ.*, vol. 101, no. 6, pp. 647–652, 2000.
173. R. Lemery, L. Soucie, B. Martin, A. S. L. Tang, M. Green, and J. Healey, "Human study of biatrial electrical coupling: Determinants of endocardial septal activation and conduction over interatrial connections," *Circ.*, vol. 110, no. 15, pp. 2083–2089, 2004.
174. J. Feng, L. Yue, Z. Wang, and S. Nattel, "Ionic mechanisms of regional action potential heterogeneity in the canine right atrium," *Circ. Res.*, vol. 83, pp. 541–551, 1998.
175. G.-R. Li, J. Feng, L. Yue, and M. Carrier, "Transmural heterogeneity of action potentials and I_{to1} in myocytes isolated from the human right ventricle," *Am. J. Physiol.*, vol. 275, pp. H369–H377, 1998.
176. D.-W. Liu, G. A. Gintant, and C. Antzelevitch, "Ionic bases for electrophysiological distinctions among epicardial, midmyocardial, and endocardial myocytes from the free wall of the canine left ventricle," *Circ. Res.*, vol. 72, no. 3, pp. 671–687, 1993.
177. E. Wettwer, G. J. Amos, H. Posival, and U. Ravens, "Transient outward current in human ventricular myocytes of subepicardial and subendocardial origin," *Circ. Res.*, vol. 75, pp. 473–482, 1994.
178. T. Opthof, C. E. Conrath, R. Wilders, P. Taggart, and E. Coronel, "Electrical inhomogeneity in the human ventricle," *J. Physiol.*, vol. 544.P, pp. 1P, 2002.
179. D.-W. Liu and C. Antzelevitch, "Characteristics of the delayed rectifier current (i_{Kr} and i_{Ks}) in canine ventricular epicardial, midmyocardial and endocardial myocytes: a weaker i_{Ks} contributes to the longer action potential of the M cell," *Circ. Res.*, vol. 76, pp. 351–365, 1995.
180. A. C. Zygmunt, R. J. Goodrow, and C. Antzelevitch, "I_{NaCa} contributes to electrical heterogeneity within the canine ventricle," *Am. J. Physiol.*, vol. 278, pp. 1671–1678, 2000.
181. H. L. Wallis, C. Sears, and S. Bryant, "Regional differences in excitation-contraction coupling in the guinea-pig left ventricle," *J. Physiol.*, vol. 544.P, pp. 53P–54P, 2002.
182. C. Antzelevitch, W. Shimuzu, G. X. Yan, S. Sicouri, J. Weissenburger, V. V. Nesterenko, A. Burashnikov, J. M. Di Diego, J. E. Saffitz, and G. P. Thomas, "The M cell: Its contribution the the ECG and to normal and abnormal electrical function of the heart," *J. Cardiovasc. Electrophysiol.*, vol. 10, pp. 1124–1152, 1999.
183. J. M. Cordeiro, L. Greene, C. Heilmann, D. Antzelevitch, and C. Antzelevitch, "Transmural heterogeneity of calcium activity and mechanical function in the canine left ventricle," *Am. J. Physiol.*, vol. 286, no. 4, pp. H1471–H1479, 2003.
184. N. Ueda, D. P. Zipes, and J. Wu, "Functional and transmural modulation of m cell behavior in canine ventricular wall," *Am. J. Physiol.*, vol. 287, no. 6, pp. H2569–2575, 2004.
185. A. Bauer, R. Becker, C. Karle, K. D. Schreiner, J. C. Senges, F. Voss, P. Kraft, W. Kuebler, and W. Schoels, "Effects of the i_{Kr}-blocking agent dofetilide and of the i_{Ks}-blocking agent chromanol 293b on regional disparity of left ventricular repolarization in the intact canine heart," *J. Cardiovasc. Pharmacol.*, vol. 39, no. 3, pp. 460–467, 2002.
186. D. Lin and D. J. Callans, "Sinus rhythm abnormalities," in *Cardiac Electrophysiology. From Cell to Bedside*, D. P. Zipes and J. Jalife, Eds., chapter 52, pp. 479–484. W. B. Saunders Company, Philadelphia, 4 edition, 2004.
187. J. Jalife, "Dynamics and molecular mechanism of ventricular fibrillation in normal heart," in *Cardiac Electrophysiology. From Cell to Bedside*, D. P. Zipes and J. Jalife, Eds., chapter 43, pp. 390–398. W. B. Saunders Company, Philadelphia, 4 edition, 2004.
188. C. J. Meurling, "Non-invasive assessment of atrial fibrillation (AF) cycle length in man: Potential application for studying af," *Ann. Ist. Super.*, vol. 37, pp. 341–349, 2001.
189. S. Nattel, "New ideas about atrial fibrillation 50 years on," *Nature*, vol. 415, pp. 219–226, 2002.
190. G. Thews, E. Mutschler, and P. Vaupel, "Herz," in *Anatomie, Physiologie und Pathophysiologie des Menschen*, chapter 7, pp. 133–170. Wissenschaftliche Verlagsgesellschaft mbH, Stuttgart, 4 edition, 1991.
191. F. H. Netter, "Physiologie und Pathophysiologie," in *Farbatlanten der Medizin*, vol. 1, chapter 2, pp. 35–141. Thieme, Stuttgart; New York, 3 edition, 1990.

192. A. L. Waldo, "Atrial flutter: Mechanisms, clinical features, and management," in *Cardiac Electrophysiology. From Cell to Bedside*, D. P. Zipes and J. Jalife, Eds., chapter 54, pp. 490–499. W. B. Saunders Company, Philadelphia, 4 edition, 2004.
193. J. Wu, J. Wu, and D. P. Zipes, "Mechanisms of initiation of ventricular tachyarrhythmias," in *Cardiac Electrophysiology. From Cell to Bedside*, D. P. Zipes and J. Jalife, Eds., chapter 42, pp. 380–389. W. B. Saunders Company, Philadelphia, 4 edition, 2004.
194. D. J. Callans and M. E. Josephson, "Ventricular tachycardia in patients with coronary artery disease," in *Cardiac Electrophysiology. From Cell to Bedside*, D. P. Zipes and J. Jalife, Eds., chapter 61, pp. 569–574. W. B. Saunders Company, Philadelphia, 4 edition, 2004.
195. J. M. Galvin and J. N. Ruskin, "Ventricular tachycardia in patients with dilated cardiomyopathy," in *Cardiac Electrophysiology. From Cell to Bedside*, D. P. Zipes and J. Jalife, Eds., chapter 62, pp. 575–587. W. B. Saunders Company, Philadelphia, 4 edition, 2004.
196. P. Brugada, R. Brugada, C. Antzelevitch, J. A. Towbin, and J. Brugada, "The brugada syndrome," in *Cardiac Electrophysiology. From Cell to Bedside*, D. P. Zipes and J. Jalife, Eds., chapter 67, pp. 625–632. W. B. Saunders Company, Philadelphia, 4 edition, 2004.
197. J.E.P. Waktare, "Atrial fibrillation," *Circ.*, vol. 106, pp. 14–16, 2002.
198. A. Samuel Lévy, J. Camm, S. Saksena, E. Aliot, and G. Breithardt, "International consensus on nomenclature and classification of atrial fibrillation: A collaborative of the working group on arrhythmias and the work group of cardiac pacing of the european society of cardiology and the north american society of pacing and electrophsiology," *Cardiovasc. Electrophysiol.*, vol. 14, pp. 443–445, 2003.
199. R. F. Bosch, X. R. Zeng, J. B. Grammer, K. Popvic, and C. Mewis, "Ionic mechanisms of electrical remodeling in human atrial fibrillation," *Cardiovasc. Res.*, vol. 44, pp. 121–131, 1999.
200. H. Zhang, J. J. Zhu, G. J. Garratt, and A. V. Holden, "Cellular modelling of electrical remodelling in two different models of human atrial myocytes," in *Proc. Computers in Cardiology*, 2003, vol. 30, pp. 777–780.
201. D. R. van Wagoner, "Electrical remodeling and chronic atrial fibrillation," in *Cardiac Electrophysiology. From Cell to Bedside*, D. P. Zipes and J. Jalife, Eds., chapter 41, pp. 375–379. W. B. Saunders Company, Philadelphia, 4 edition, 2004.
202. M. C. E. F. Wijffels, C. J. H. J. Kirchhof, R. Dorland, and M. A. Allessie, "Atrial fibrillation begets atrial fibrillation," *Circ.*, vol. 92, pp. 1954–1968, 1995.
203. A. E. Epstein, "Ventricular fibrillation," in *Cardiac Electrophysiology. From Cell to Bedside*, D. P. Zipes and J. Jalife, Eds., chapter 76, pp. 705–710. W. B. Saunders Company, Philadelphia, 4 edition, 2004.
204. Y. H. Chen, S. J. Xu, S. Bendahhou, X. L. Wang, Y. Wang, W. Y. Xu, H. W. Jin, H. Sun, X. Y. Su, Q. N. Zhuang, Y. Q. Yang, Y. B. Li, Y. Liu, H. J. Xu, X. F. Li, N. Ma, C. P. Mou, Z. Chen, J. Barhanin, and W. Huang, "KCNQ1 gain-of-function mutation in familial atrial fibrillation," *Science*, vol. 299, pp. 251–254, 2003.
205. P. J. Schwartz and S. G. Priori, "Long qt syndrome – Genotype-phenotype considerations," in *Cardiac Electrophysiology. From Cell to Bedside*, D. P. Zipes and J. Jalife, Eds., chapter 70, pp. 651–659. W. B. Saunders Company, Philadelphia, 4 edition, 2004.
206. N. El-Sherif and G. Turitto, "Torsade de pointes," in *Cardiac Electrophysiology. From Cell to Bedside*, D. P. Zipes and J. Jalife, Eds., chapter 74, pp. 687–699. W. B. Saunders Company, Philadelphia, 4 edition, 2004.
207. C. Antzelevitch, "Electrical Heterogeneity, Cardiac Arrhythmias, and the Sodium Channel," *Circ. Res.*, vol. 87, pp. 964–965, 2000.
208. P. Viswanathan and Y. Rudy, "Cellular arrhythmogenic effects of congenital and acquired long-QT syndrome in the heterogeneous myocardium," *Circ.*, vol. 101, pp. 1192–1198, 2000.
209. L. Zhang, K. W. Timothy, G. M. Vincent, M. H. Lehmann, J. Fox, L. C. Giuli, J. Shen, I. Splawski, S. G. Priori, S. J. Comptom, F. Yanowitz, J. Benhorin, A. J. Moss, P. J. Schwartz, J. L. Robinson, Q. Wang, W. Zareba, M. T. Keating, J. A. Towbin, C. Napolitano, and A. Medina, "Spectrum of ST-T-wave patterns and repolarization parameters in congenital long-QT syndrome – ECG findings identify genotypes," *Circ.*, vol. 102, pp. 2949–2855, 2000.
210. W. Shimizu and C. Antzelevitch, "Cellular basis for the ECG features of the LQT1 form of the long-QT syndrome: Effects of β-adrenergic agonists and antagonists and sodium channel blockers on transmural dispersion of repolarization and torsade de pointes," *Circ.*, vol. 98, pp. 2314–2322, 1998.
211. W. Shimizu and C. Antzelevitch, "Sodium channel block with mexiletine is effective in reducing dispersion of repolarization and preventing torsade de pointes in LQT2 and LQT3 models of the long-QT syndrome," *Circ.*, vol. 96, pp. 2038–2047, 1997.
212. W. Shimizu and C. Antzelevitch, "Effects of a K^+ channel opener to reduce transmural dispersion of repolarization and prevent torsade de pointes in LQT1, LQT2, and LQT3 models of the long-QT syndrome," *Circ.*, vol. 102, pp. 706–712, 2000.
213. S. G. Priori, I. Rivolta, and C. Napolitano, "Genetics of long QT, brugada, and other channelopathies," in *Cardiac Electrophysiology. From Cell to Bedside*, D. P. Zipes and J. Jalife, Eds., chapter 50, pp. 462–470. W. B. Saunders Company, Philadelphia, 4 edition, 2004.
214. A. L. Hodgkin and A. F. Huxley, "A quantitative description of membrane current and its application to conduction and excitation in nerve," *J. Physiol.*, vol. 177, pp. 500–544, 1952.
215. F. Reif, *Fundamentals of Statistical and Thermal Physics*, Series in fundamentals of physics, 1985.

216. L. P. Endresen and J. S. Hoye, "A possible resolution of the gating paradox," *Biophys. J.*, vol. 76, pp. 1918–1921, 1999.
217. J. W. Moore and R. G. Pearson, *Kinetics and Mechanism*, John Wiley, New York, 1981.
218. K. J. Laidler, *Chemical Kinetics*, Harper-Collins, 1987.
219. B. Hille, *Ionic channels of excitable membranes*, Sinauer Associates, 2 edition, 1992.
220. L. D. DeFelice, *Electrical Properties of the Cells. Patch Clamp for Biologists*, Plenum Publishing Corporation, 1997.
221. D. Noble, "A modification of the Hodgkin-Huxley equation applicable to Purkinje fibre action and pacemaker potentials," *J. Physiol.*, vol. 160, pp. 317–352, 1962.
222. R. E. McAllister, D. Noble, and R. W. Tsien, "Reconstruction of the electrical activitity of cardiac purkinje fibres," *J. Physiol.*, vol. 251, pp. 1–59, 1975.
223. G. W. Beeler and H. Reuter, "Reconstruction of the action potential of ventricular myocardial fibres," *J. Physiol.*, vol. 268, pp. 177–210, 1977.
224. K. Yanagihara, A. Noma, and H. Irisawa, "Reconstruction of sinoatrial node pacemaker potential based on the voltage-clamp experiments," *Jpn. J. Physiol.*, vol. 30, pp. 841–857, 1980.
225. D. G. Bristow and J. W. Clark, "A mathematical model of primary pacemaker cell in SA node of the heart," *Am. J. Physiol.*, vol. 243, no. 2, pp. H207–H218, 1982.
226. D. G. Bristow and J. W. Clark, "A mathematical model of the vagally driven primary pacemaker," *Am. J. Physiol.*, vol. 244, no. 1, pp. H150–H161, 1983.
227. D. Noble and S. J. Noble, "A model of sino-atrial node electrical activity based on a modification of the DiFrancesco-Noble (1984) equations," *Proc. R. Soc. Lond. B. Biol. Sci.*, vol. 222, pp. 295–304, 1984.
228. D. DiFrancesco and D. Noble, "A model of cardiac electrical activity incorporating ionic pumps and concentration changes," *Phil. Trans. R. Soc. Lond.*, vol. 307, pp. 353–398, 1985.
229. D. W. Hilgemann and D. Noble, "Excitation-contraction coupling and extracellular calcium transients in rabbit atrium: Reconstruction of basic cellular mechanisms," *Proc. R. Soc. Lond.*, vol. 230, pp. 163–205, 1987.
230. Y. E. Earm and D. Noble, "A model of single atrial cell: Relation between calcium current and calcium release," *Proc. R. Soc. Lond.*, vol. 240, pp. 83–96, 1990.
231. C.-H. Luo and Y. Rudy, "A model of the ventricular cardiac action potential," *Circ. Res.*, vol. 68, no. 6, pp. 1501–1526, 1991.
232. C.-H. Luo and Y. Rudy, "A dynamic model of the ventricular cardiac action potential: I. Simulations of ionic currents and concentration changes," *Circ. Res.*, vol. 74, no. 6, pp. 1071–1096, 1994.
233. C.-H. Luo and Y. Rudy, "A dynamic model of the ventricular cardiac action potential: II. afterdepolarizations, triggered activity, and potentiation," *Circ. Res.*, vol. 74, no. 6, pp. 1097–1113, 1994.
234. S. S. Demir, J. W. Clark, C. R. Murphey, and W. R. Giles, "A mathematical model of a rabbit sinoatrial node cell," *Am. J. Physiol.*, vol. 35, pp. 832–852, 1994.
235. S. Dokos, B. G. Celler, and N. H. Lovell, "Vagal control of sinoatrial rhythm: A mathematical model," *J. Theor. Biol.*, vol. 182, pp. 21–44, Sep. 1996.
236. D. S. Lindblad, C. R. Murphey, J. W. Clark, and W. R. Giles, "A model of the action potential and underlying membrane currents in a rabbit atrial cell," *Am. J. Physiol.*, vol. 271, no. 4 Pt 2, pp. H1666–H1696, 1996.
237. S. S. Demir, B. O'Rourke, G. F. Tomaselli, E. Marbán, and R. L. Winslow, "Action potential variation in canine ventricle: A modeling study," in *Proc. Computers in Cardiology*, 1996, vol. 23, pp. 221–224.
238. M. Courtemanche, R. J. Ramirez, and S. Nattel, "Ionic mechanisms underlying human atrial action potential properties: Insights from a mathematical model," *Am. J. Physiol.*, vol. 275, no. 44, pp. H301–H321, 1998.
239. A. Nygren, C. Fiset, L. Firek, J. W. Clark, D. S. Lindblad, R. B. Clark, and W. R. Giles, "Mathematical model of an adult human atrial cell," *Circ. Res.*, vol. 82, pp. 63–81, 1998.
240. M. S. Jafri, J. J. Rice, and R. L. Winslow, "Cardiac Ca^{2+} dynamics: The roles of ryanodine receptor adapation and sarcoplasmic reticulum load," *Biophysical J.*, vol. 74, pp. 1149–1168, Mar. 1998.
241. D. Noble, A. Varghese, P. Kohl, and P. Noble, "Improved guinea-pig ventricular cell model incorporating a diadic space, I_{Kr} and I_{Ks}, and length- and tension-dependend processes," *Can. J. Cardiol.*, vol. 14, no. 1, pp. 123–134, Jan. 1998.
242. L. Priebe and D. J. Beuckelmann, "Simulation study of cellular electric properties in heart failure," *Circ. Res.*, vol. 82, pp. 1206–1223, 1998.
243. S. S. Demir, J. W. Clark, and W. R. Giles, "Parasympatheticc modulation of sinoatrial node pacemaker activity in rabbit heart: A unifying model," *Am. J. Physiol.*, vol. 276, pp. H2221–H2244, 1999.
244. R. L. Winslow, J. J. Rice, S. Jafri, E. Marbán, and B. O'Rourke, "Mechanisms of altered excitation-contraction coupling in canine tachycardia-induced heart failure, II model studies," *Circ. Res.*, vol. 84, pp. 571–586, 1999.
245. B. O'Rourke, D. A. Kass, G. F. Tomaselli, S. Kaab, R. Tunin, and E. Marbán, "Mechanisms of altered excitation-contraction coupling in canine tachycardia-induced heart groups = cardiac measurement, failure, I experimental studies," *Circ. Res.*, vol. 84(5), pp. 562–570, 1999.
246. R. J. Ramirez, S. Nattel, and M. Courtemanche, "Mathematical analysis of canine atrial action potentials: Rate, regional factors, and electrical remodeling," *Am. J. Physiol.*, vol. 279, pp. H1767–H1785, 2000.
247. H. Zhang, A. V. Holden, I. Kodama, H. Honjo, M. Lei, T. Varghese, and M. R. Boyett, "Mathematical models of action potentials in the periphery and center of the rabbit sinoatrial node," *Am. J. Physiol.*, vol. 279, no. 1, pp. 397–421, 2000.

248. M. R. Boyett, H. Zhang, A. Garny, and A. V. Holden, "Control of the pacemaker activity of the sinoatrial node by intracellular Ca^{2+}. Experiments and modelling," *Phil. Trans. R. Soc. London*, vol. 359, pp. 1091–1110, 2001.
249. S. V. Pandit, R. B. Clark, W. R. Giles, and S. S. Demir, "A mathematical model of action potential heterogeneity in adult left ventricular myocytes," *Biophys. J.*, vol. 81, pp. 3029–3051, 2001.
250. J. L. Puglisi and D. M. Bers, "LabHEART: An interactive computer model of rabbit ventricular myocyte ion channels and Ca transport," *Am. J. Physiol.*, vol. 281, pp. C2049–C2060, 2001.
251. J. Kneller, R. J. Ramirez, D. Chartier, M. Courtemanche, and S. Nattel, "Time-dependent transients in an ionically based mathematical model of the canine atrial action potential," *Am. J. Physiol.*, vol. 282, pp. H1437–H1451, 2002.
252. Y. Kurata, I. Hisatome, S. Imanishi, and T. Shibamoto, "Dynamical description of sinoatrial node pacemaking: Improved mathematical model for primary pacemaking cells," *Am. J. Physiol.*, vol. 283, pp. H2074–H2101, 2002.
253. O. Bernus, R. Wilders, C. W. Zemlin, H. Verschelde, and A. V. Panfilov, "A computationally efficient electrophysiological model of human ventricular cells," *Am. J. Physiol.*, vol. 282, pp. H2296–H2308, 2002.
254. N. H. Lovell, S. L. Cloherty, B. G. Celler, and S. Dokos, "A gradient model of cardiac pacemaking myocytes," *Progress in Biophysics and Molecular Biology*, vol. 85, no. 2-3, pp. 301–323, 2004.
255. K. H. W. J. ten Tusscher, D. Noble, P. J. Noble, and A. V. Panfilov, "A model for human ventricular tissue," *Am. J. Physiol.*, vol. 286, pp. H1573–H1589, 2004.
256. V. Iyer, R. Mazhari, and R. L. Winslow, "A computational model of the human left-ventricular epicardial myocyte," *Biophys. J.*, vol. 87, no. 3, pp. 1507–1525, 2004.
257. J. Zeng, K. R. Laurita, D. S. Rosenbaum, and Y. Rudy, "Two components of the delayed rectifier K^+ current in ventricular myocytes of the guinea pig type: Theoretical formulation and their role in repolarization," *Circ. Res.*, vol. 77, pp. 140–152, 1995.
258. P. Viswanathan, R. M. Shaw, and Y. Rudy, "Effects of Ikr and Iks heterogeneity on action potential duration and its rate - dependence: A simulation study," *Circ.*, vol. 99, pp. 2466–2474, 1999.
259. G. Faber and Y. Rudy, "Action potential and contractility changes in [Na+]i overloaded cardiac myocytes: A simulation study," *Biophys. J.*, vol. 78, 2000.
260. J. Zeng and Y. Rudy, "Early afterdepolarizations in cardiac myocytes: Mechanism and rate dependence," *Biophys. J.*, vol. 68, pp. 949–964, Mar. 1995.
261. R. M. Shaw and Y. Rudy, "Electrophysiologic effects of acute myocardial ischemia," *Circ. Res.*, vol. 80, no. 1, pp. 124–138, 1997.
262. K. Gima and Y. Rudy, "Ionic current basis of electrocardiographic waveforms – A model study," *Circ. Res.*, vol. 90, pp. 889–896, 2002.
263. M. S. Spach and J. F. Heidlage, "The stochastic nature of cardiac propagation at a microscopic level," *Circ. Res.*, vol. 76, no. 3, pp. 118–130, 1995.
264. G. Seemann, "Elektrische Erregungsausbreitung im Herzen ausgehend von elektrophysiologischen Zellmodellen: Erregungsausbreitung im Zellverband, Parametrisierung Zellulärer Automaten," M.S. thesis, Universität Karlsruhe (TH), Institut für Biomedizinische Technik, Aug. 2000, Diploma Thesis.
265. P. Wach, R. Killmann, F. Dienstl, and C. Eichtinger, "A computer model of human ventricular myocardium for simulation of ECG, MCG, and activation sequence including reentry rhythms," *Basic Research in Cardiology*, vol. 84, no. 4, 1989.
266. R. Killmann, P. Wach, and F. Dienstl, "Three-dimensional computer model of the entire human heart for simulation of reentry and tachycardia: Gap phenomenon and Wolff-Parksinson-White syndrome," *Basic Research in Cardiology*, vol. 86, no. 5, pp. 485–501, 1991.
267. B. E. H. Saxberg and R. J. Cohen, "Cellular automata models of cardiac conduction," in *Theory of Heart*, L. Glass, P. Hunter, and A. McCulloch, Eds., pp. 437–476. Springer, Berlin, Heidelberg, New York, 1991.
268. D. Wei, O. Okazaki, K. Harumi, E. Harasawa, and H. Hosaka, "Comparative simulation of excitation and body surface electrocardiogram with isotropic and anisotropic computer heart models," *IEEE Transactions on Biomedical Engineering*, vol. 42, no. 4, pp. 343–357, Apr. 1995.
269. P. Siregar, J. P. Sinteff, N. Julen, and P. Le Beux, "An interactive 3D anisotropic cellular automata model of the heart," *Computers and Biomedical Research*, vol. 31, pp. 323–347, 1998.
270. C. D. Werner, *Simulation der elektrischen Erregungsausbreitung in anatomischen Herzmodellen mit adaptiven zellulären Automaten*, Ph.D. thesis, Universität Karlsruhe (TH), Institut für Biomedizinische Technik, 2001.
271. M. Delorme, "An introduction to cellular automata," in *Cellular Automata*, M. Delorme and J. Mazoyer, Eds., chapter 1, pp. 5–49. Kluwer, Dordrecht, 1999.
272. T. A. Sudkamp, *Languages and Machines*, Addison-Wesley, Reading, Massachusetts; Menlo Park, California, 2 edition, 1997.
273. J. P. Keener and A. V. Panfilov, "The effects of geometry and fibre orientation on propagation and extracellular potentials in myocardium," in *Computational Biology of the Heart*, A. V. Panfilov and A. V. Holden, Eds., pp. 235–258. John Wiley & Sons, Chichester, 1997.
274. J. M. Rogers, "Modeling the cardiac action potential using b-spline surfaces," *IEEE Transactions on Biomedical Engineering*, vol. 47, no. 6, pp. 784–791, June 2000.
275. R. A. FitzHugh, "Impulses and physiological states in theoretical models of nerve membran," *Biophys. J.*, vol. 1, pp. 445–466, 1961.

276. J. M. Rogers and A. D. McCulloch, "A collocation-Galerkin finite element model of cardiac action potential propagation," *IEEE Transactions on Biomedical Engineering*, vol. 41, no. 8, pp. 743–757, Aug. 1994.
277. J. Rogers, M. Courtemanche, and A. McCulloch, "Finite element methods for modelling impulse propagation in the heart," in *Computational Biology of the Heart*, A. Panfilov and A. V. Holden, Eds., chapter 7, pp. 217–234. John Wiley & Sons, Chichester, 1997.
278. R. Plonsey and R. C. Barr, "Mathematical modeling of electrical activity of the heart," *J. Electrocardiol.*, vol. 20, no. 3, pp. 219–226, 1987.
279. C. S. Henriquez and R. Plonsey, "A bidomain model for simulating propagation in multicellular cardiac tissue," in *Proc. of the Annual International Conference of the IEEE Engineering in Medicine and Biology Society*, 1989, vol. 4, p. 1266.
280. N. G. Sepulveda and J. P. Wikswo, "Bipolar stimulation of cardiac tissue using an anisotropic bidomain model," *J. Cardiovasc. Electrophysiol.*, vol. 5, no. 3, pp. 258–267, May 1994.
281. C. S. Henriquez, A. L. Muzikant, and C. K. Smoak, "Anisotropy, fiber curvature and bath loading effects on activation in thin and thick cardiac tissue preparations: Simulations in a three-dimensional bidomain model," *J. Cardiovasc. Electrophysiol.*, vol. 7, no. 5, pp. 424–444, May 1996.
282. K. Simelius, J. Nenonen, and B. M. Horacek, "Modeling cardiac ventricular activation," *Int. J. Bioelectromagnetism*, vol. 3, no. 2, 2001.
283. J. Malmivuo and R. Plonsey, "Bidomain model of multicellular volume conductors," in *Bioelectromagnetism*, chapter 9, pp. 159–168. Oxford University Press, New York; Oxford, 1995.
284. D. M. Harrild and C. S. Henriquez, "A computer model of normal conduction in the human atria," *Circ. Res.*, vol. 87, no. 7, pp. e25–e36, 2000.
285. K. J. Sampson and C. S. Henriquez, "Simulation and prediction of functional block in the presence of structural and ionic heterogeneity," *Am. J. Physiol.*, vol. 281, no. 6, pp. H2597–2603, 2001.
286. C. E. Clancy and Y. Rudy, "Na^+ channel mutation that causes both brugada and long-QT syndrome phenotypes," *Circ.*, vol. 105, pp. 1208–1213, 2002.
287. F. Xie, Z. Qu, J. Yang, A. Baher, J. N. Weiss, and A. Garfinkel, "A simulation study of the effects of cardiac anatomy in ventricular fibrillation," *J. Clin. Invest.*, vol. 113, no. 5, pp. 686–693, 2004.
288. W. Li, P. Kohl, and N. Trayanova, "Induction of ventricular arrhythmias following mechanical impact: A simulation study in 3d," *J. Mol. Histol.*, vol. 35, no. 7, pp. 679–686, 2004.
289. R. H. Clayton and A. V. Holden, "Propagation of normal beats and re-entry in a computational model of ventricular cardiac tissue with regional differences in action potential shape and duration," *Prog. Biophys. Mol. Biol.*, vol. 85, no. 2-3, pp. 473–99, Jun-Jul 2004.
290. G. Tsiavaliaris, S. Fujita-Becker, and D. J. Manstein, "Molecular engineering of a backwards-moving myosin motor," *Nature*, vol. 427, pp. 558 – 561, 2004.
291. T. Noguchi, P. Camp Jr., S. L. Alix, J. A. Gorga, K. J. Begin, B. J. Leavitt, F. P. Ittleman, N. R. Alpert, M. M. LeWinter, and P. VanBuren, "Myosin from failing and non-failing human ventricles exhibit similar contractile properties," *J. Mol. Cell. Cardiol.*, vol. 35, pp. 91–97, 2003.
292. M. R. Wolff, L. F. Whitesell, and R. L. Moss, "Calcium sensitivity of isometric tension is increased in canine experimental heart failure," *Circ. Res.*, vol. 76, no. 5, pp. 781–789, 1995.
293. Dr. Paul Paolini, "Muscle," .
294. W. F. Bluhm, A. D. McCulloch, and W. Y. W. Lew, "Active force in rabbit ventricular myocytes," *J. Biomechanics*, vol. 28, no. 9, pp. 1119–1122, 1995.
295. M. R. Wolff, S. H. Buck, S. W. Stoker, M. L. Greaser, and R. M. Mentzer, "Myofibrillar calcium sensitivity of isometric tension is increased in human dilated cardiomyopathies: Role of altered β-adrenergically mediated protein phosphorylation," *J. Clin. Invest.*, vol. 98, no. 1, pp. 167–176, 1996.
296. V. A. Browne, V. M. Stiffel, W. J. Pearce, L. D. Longo, and R. D. Gilbert, "Activator calcium and myocardial contractility in fetal sheep exposed to long-term high-altitude hypoxia," *Am. J. Physiol.*, vol. 272, no. 3, pp. H1196–H1204, 1997.
297. S. Siedner, M. Krüger, M. Schröter, D. Metzler, W. Röll, B. K. Fleischmann, J. Hescheler, G. Pfitzer, and R. Stehle, "Developmental changes in contractility and sarcomeric proteins from the early embryonic to the adult stage in the mouse heart," *J. Physiol.*, vol. 548, no. 2, pp. 493–505, 2003.
298. Y. Kihara, M. Inoko, and S. Sasayama, "L-Methionine augments mammalian myocardial contraction by sensitizing the myofilament to Ca^{2+}," *Circ. Res.*, vol. 77, no. 1, pp. 80–87, 1995.
299. P. Li, P. A. Hofmann, B. Li, A. Malhotra, W. Cheng, E. H. Sonnenblick, L. G. Meggs, and P. Anversa, "Myocardial infarction alters myofilament calcium sensitivity and mechanical behavior of myocytes," *Am. J. Physiol.*, vol. 272, no. 1, pp. H360–H370, 1997.
300. J. K. Gwathmey and R. J. Hajjar, "Relationship between steady-state force and intracellular $[Ca^{2+}]$ in intact human myocardium," *Circ.*, vol. 82, pp. 1266–1278, 1990.
301. K. Chaisaowong, "Modeling of human cardiac force development: Quantitative description from myofilament to myocardium," M.S. thesis, Universität Karlsruhe (TH), Institut für Biomedizinische Technik, June 2004, Diploma Thesis.
302. J. N. Peterson, W. C. Hunter, and M. R. Berman, "Estimated time course of Ca^{2+} bound to troponin C during relaxation in isolated cardiac muscle," *Am. J. Physiol.*, vol. 260, pp. H1013–H1024, 1991.

303. P.A. Hofmann and F. Fuchs, "Effect of length and cross-bridge attachement on Ca^{2+} binding to cardiac troponin C," *Am. J. Physiol.*, vol. 253, pp. C90–C96, 1987.
304. A. J. Baker, V. M. Figueredo, E. C. Keung, and S. A. Camacho, "Ca^{2+} regulates the kinetics of tension development in intact cardiac muscle," *Am. J. Physiol.*, vol. 275, pp. H744–H750, 1998.
305. S. Palmer and J. C. Kentish, "Role of Ca^{2+} and crossbridge kinetics in determining the maximum rates of Ca^{2+} activation and relaxation in rat and guinea pig skinned trabeculae," *Circ. Res.*, vol. 83, pp. 179–186, 1998.
306. P. W. Brandt, F. Colomo, N. Piroddi, C. Poggesi, and C. Tesi, "Force regulation by Ca^{2+} in skinned single cardiac myocytes of frog," *Biophys. J.*, vol. 74, pp. 1994–2004, 1998.
307. K. Glänzel, "Kraftentwicklung im Sarkomer unter Berücksichtigung elektromechanischer Kopplung," M.S. thesis, Universität Karlsruhe (TH), Institut für Biomedizinische Technik, Sep. 2002, Diploma Thesis.
308. P.A. Hofmann and F. Fuchs, "Evidence for a force-dependent component of calcium binding to cardiac troponin C," *Am. J. Physiol.*, vol. 253, pp. C541–C546, 1987.
309. P. M. L. Janssen and P. P. de Tombe, "Uncontrolled sarcomere shortening increases the intracellular Ca^{2+} transient in rat cardiac trabeculae," *Am. J. Physiol.*, vol. 272, pp. H1892–H1897, 1997.
310. D. G. Allen and J. C. Kentish, "The cellular basis of the length-tension relationship in cardiac muscle," *J. Mol. Cell. Cardiol.*, vol. 17, pp. 812–840, 1985.
311. D. G. Allen and S. Kurihara, "The effects of muscle length on intracellular calcium transients in mammalian cardiac muscle," *J. Physiol.*, vol. 327, pp. 79–94, 1982.
312. A. Belus, S. Calcghan, and E. White, "The response of cardiac muscle to stretch: Role of calcium," *3rd International Workshop on Cardiac Mechano-Eletric Feedback and Arrhythmias*, pp. 33–34, 2002.
313. M. Endo, "Stretch-induced increase in activation of skinned muscle fibres by calcium," *Nature*, vol. 237, pp. 211–213, 1972.
314. H. Nagashima and S. Asakura, "Studies on co-operative properties of tropomyosin-actin and tropomyosin-troponin-actin complexes by use of N-ethylmaleinide-treated and untreated species of myosin subfragment," *J. Mol. Bio.*, vol. 155, pp. 409–428, 1982.
315. L. S. Tobacman, "Thin filament mediated regulation of cardiac contraction," *Ann. Rev. Physiol.*, vol. 58, pp. 447–481, 1996.
316. A. V. Hill, "The heat of shortening and the dynamic constants of muscle," *Proc. R. Soc. Lond.*, vol. B126, pp. 136–195, 1938.
317. A. F. Huxley, "Muscle structures and theories of contraction," *Prog. Biophys. and biophys. Chemistry*, vol. 7, pp. 255–318, 1957.
318. R. B. Panerai, "A model of cardiac muscle mechanics and energetics," *J. Biomechanics*, vol. 13, pp. 929–940, 1980.
319. A. Landesberg and S. Sideman, "Coupling calcium binding to troponin C and cross-bridge cycling in skinned cardiac cells," *Am. J. Physiol.*, vol. 266, pp. H1260–H1271, 1994.
320. A. Landesberg and S. Sideman, "Mechanical regulation of cardiac muscle by coupling calcium kinetics with cross-bridge cycling: A dynamic model," *Am. J. Physiol.*, vol. 267, pp. H779–H795, 1994.
321. A. Landesberg, R. Beyar, and S. Sideman, "Intracellular control of contraction of the cardiac muscle," in *IFAC Modeling and Control in Biomedical Systems*, 1994, pp. 79–80.
322. P. Hunter, M. P. Nash, and G. P. Sands, "Computational electromechanics of the heart," in *Computational Biology of the Heart*, A. V. Panfilov and A. V. Holden, Eds., pp. 345–408. John Wiley & Sons, Chichester, 1997.
323. P. J. Hunter, A. D. McCulloch, and H. E. D. J. ter Keurs, "Modelling the mechanical properties of cardiac muscle," *Prog. Biophys. Mol. Biol.*, vol. 69, pp. 289–331, 1998.
324. J. M. Guccione, I. Motabarzadeh, and G. I. Zahalak, "Finite element stress analysis of left ventricular mechanics in the beating dog heart," *J. Biomechanics*, vol. 31, pp. 1069–1073, 1998.
325. J. J. Rice, R. L. Winslow, and W. C. Hunter, "Comparison of putative cooperative mechanisms in cardiac muscle: Length dependence and dynamic responses," *Am. J. Physiol.*, vol. 276, pp. H1734–H1754, 1999.
326. J. J. Rice, M. S. Jafri, and R. L. Winslow, "Modeling short-term interval-force relations in cardiac muscle," *Am. J. Physiol.*, vol. 278, pp. H913–H931, 2000.
327. M. Mlcek, J. Neumann, O. Kittnar, and V. Novak, "Mathematical model of the electromechanical heart contractile system - Regulatory subsystem physiological considerations," *Physiol. Res.*, vol. 50, pp. 425–432, 2001.
328. D. P. Nickerson, N. P. Smith, and P. J. Hunter, "A model of cardiac cellular electromechanis," *Phil. Trans. R. Soc. Lond.*, vol. 359, pp. 1159–1172, 2001.
329. Y. Bengio, "Markovian models for sequential data," *Neural Computing Surveys*, vol. 2, pp. 129–162, 1999.
330. A. Krogh, M. Brown, I. Mian, K. Sjlander, and D. Haussler, "Hidden markov models in computational biology: Applications to protein modeling," *J. Mol. Biol.*, vol. 235, pp. 1501–1531, 1994.
331. S. V. Vaseghi, *Advanced Digital Signal Processing and Noise Reduction*, John Wiley & Sons, Chichester, 2000.
332. I. N. Bronštejn and K. A. Semendjaev, *Taschenbuch der Mathematik*, B. G. Teubner, Stuttgart; Leipzig, 1996.
333. W. H. Press, S. A. Teukolsky, W. T. Vetterling, and B. P. Flannery, *Numerical Recipes in C*, Cambridge University Press, Cambridge, New York, Melbourne, 2 edition, 1992.
334. S. Rush and H. Larsen, "A practical algorithm for solving dynamic membrane equations," *IEEE Trans. Biomed. Eng.*, vol. 25, no. 4, pp. 389–92, 1978.
335. H. R. Schwarz, *Numerische Mathematik*, Teubner, Stuttgart, 3 edition, 1993.

336. H. R. Schwarz, *Methode der finiten Elemente*, Teubner, Stuttgart, 3 edition, 1991.
337. K.-J. Bathe, *Finite Element Procedures*, Prentice Hall, Upper Saddle River, New Jersey, 1996.
338. H. I. Saleheen and K. T. Ng, "New finite difference formulations for general inhomogeneous anisotropic bioelectric problems," *IEEE Transactions on Biomedical Engineering*, vol. 44, no. 9, Sep. 1997.
339. B.A. Szabó and I. Babuška, *Finite Element Analysis*, John Wiley & Sons, New York, 1991.
340. F. B. Sachse, *Computational Cardiology: Modeling of Anatomy, Electrophysiology, and Mechanics*, LNCS 2966. Springer, Berlin, Heidelberg, New York, 2004.
341. F. B. Sachse, C. D. Werner, M. H. Stenroos, R. F. Schulte, P. Zerfass, and O. Dössel, "Modeling the anatomy of the human heart using the cryosection images of the Visible Female dataset," in *Proc. Third Users Conference of the National Library of Medicine's Visible Human Project*, Bethesda, USA, 2000.
342. G. Seemann, F. B. Sachse, O. Dössel, A. V. Holden, M. R. Boyett, and H. Zhang, "3d anatomical and electrophysiological model of human sinoatrial node and atria," in *J Physiol*, 2004, p. PC26, submitted.
343. G. Seemann, C. Höper, F. B. Sachse, O. Dössel, A. V. Holden, and H. Zhang, "3d anatomical and electrophysiological model of human sinoatrial node and atria," *Phil. Trans. Roy. Soc.*, 2005, submitted.
344. K. Glänzel, F. B. Sachse, G. Seemann, C. Riedel, and O. Dössel, "Modeling force development in the sarcomere in consideration of electromechanical coupling," in *Biomedizinische Technik*, Sep. 2002, vol. 47-1/2, pp. 774–777.
345. F. B. Sachse, K. Glänzel, and G. Seemann, "Modeling of protein interactions involved in cardiac tension development," *Int. J. Bifurc. Chaos*, vol. 13, no. 12, pp. 3561–3578, 2003.
346. F. B. Sachse, K. Glänzel, and G. Seemann, "Modeling of electro-mechanical coupling in cardiac myocytes: Feedback mechanisms and cooperativity," *LNCS 2674*, pp. 62–71, 2003.
347. A. M. Gordon, M. Regnier, and E. Homsher, "Skeletal and cardiac muscle contractile activation: Tropomyosin "rocks and rolls"," *News Physiol. Sci.*, vol. 16, pp. 49–55, 2001.
348. J. A. Spudich, "TIMELINE: The myosin swinging cross-bridge model," *Nature Reviews Molecular Cell Biology*, vol. 2, pp. 387–392, 2001.
349. F. B. Sachse, G. Seemann, K. Chaisaowong, and M. B. Mohr, "Modeling of electro-mechanics of human cardiac myocytes: Parameterization with numerical minimization techniques," in *Proc. 25th Conf. IEEE EMBS*, 2003, pp. 2810–2813.
350. K. D. Costa, Y. Takayama, A. D. McColloch, and J. W. Covell, "Laminar fiber architecture and three-dimensional systolic mechanics in canine ventricular myocardium," *Am. J. Physiol.*, vol. 276, pp. H595–H607, 1999.
351. "kaLattice format," http://www-ibt.etec.uni-karlsruhe.de/software/.
352. "Silicon Graphics, Inc.," http://www.sgi.com.
353. "Apple Computer Inc.," http://www.apple.com.
354. B. Stroustrup, *Die C++ Programmiersprache*, Addison-Wesley, Bonn, 1997.
355. E. Siever, S. Spainhour, and N. Patwardhan, *Perl in a Nutshell*, O'Reilly, Köln, 2000.
356. J. P. Keener and K. Bogar, "A numerical method for the solution of the bidomain equations in cardiac tissue," *Chaos*, vol. 8, no. 1, pp. 234–241, 1998.
357. J. Sundnes, G. T. Lines, and A. Tveito, "Efficient solution of ordinary differential equations modeling electrical activity in cardiac cells," *Math. Biosci.*, vol. 172, no. 2, pp. 55–72, 2001.
358. E. J. Vigmond, F. N. Aguel, and A. Trayanova, "Computational techniques for solving the bidomain equations in three dimensions," *IEEE Trans. Biomed. Eng.*, vol. 49, no. 11, pp. 1260–1269, 2002.
359. F. B. Sachse, G. Seemann, C. Riedel, C. D. Werner, and O. Dössel, "Modeling of the cardiac mechano-electrical feedback," *Int. J. Bioelectromagnetism*, vol. 2, no. 2, 2000.
360. "OpenMP: Simple, portable, scalable SMP programming," http://www.openmp.org.
361. R. Chandra, L. Dagum, and D. Kohr, *Parallel Programming in OpenMP*, Morgan Kaufmann, San Francisco, 2000.
362. "The Message Passing Interface (MPI) standard," http://www-unix.mcs.anl.gov/mpi.
363. P. S. Pacheco, *Parallel Programming with MPI*, Morgan Kaufmann, San Francisco, 1997.
364. F. B. Sachse, C. D. Werner, K. Meyer-Waarden, and O. Dössel, "Applications of the Visible Man dataset in electrocardiology: Calculation and visualization of body surface potential maps of a complete heart cycle," in *Proc. Second Users Conference of the National Library of Medicine's Visible Human Project*, Bethesda, USA, 1998, pp. 47–48.
365. F. B. Sachse, C. D. Werner, and O. Dössel, "Techniken zur Visualisierung der elektrischen Aktivität des Herzens," in *Bildverarbeitung für die Medizin 1999*, H. Evers, G. Glombitza, T. Lehmann, and H.-P. Meinzer, Eds., Berlin Heidelberg New York, 1999, pp. 427–431, Springer.
366. J. Wernecke, *The Inventor Mentor: Programming Object-Oriented 3D Graphics with Open Inventor*, Addison-Wesley Professional, 1 edition, 1994.
367. "Coin3D," http://www.coin3d.org/.
368. D. Shreiner, M. Woo, J. Neider, T. Davis, and D. Shreiner, *OpenGL Programming Guide: The Official Guide to Learning OpenGL*, Addison-Wesley, 4 edition, 2003.
369. W. E. Lorensen and H. E. Cline, "Marching cubes: A high resolution 3D surface construction algorithm," *Computer Graphics*, vol. 21, no. 4, pp. 163–169, 1987.
370. G. Towner, *Discovering QuickTime*, Morgan Kaufmann, 1999.
371. C. Höper, "Modellierung der Anatomie und Elektrophysiologie des menschlichen Vorhofs," M.S. thesis, Universität Karlsruhe (TH), Institut für Biomedizinische Technik, Nov. 2003, Diploma Thesis.

372. C. Höper, G. Seemann, F. B. Sachse, H. Zhang, and O. Dössel, "3D computer model of human atrial anatomy and electrophysiology," in *Biomedizinische Technik*, 2003, vol. 48-1, pp. 2–3.
373. G. Seemann, C. Höper, F. B. Sachse, H. Zhang, and O. Dössel, "A detailed model of human atrium towards simulation of electromechanics in the heart," in *Proc. MEDICON*, 2004, accepted.
374. S. Y. Ho, R. H. Anderson, and D. Sánchez-Quintana, "Atrial structure and fibres: Morphologic bases of atrial conduction," *Cadiovasc. Res.*, vol. 54, pp. 325–336, 2002.
375. A. Hansson, M. Holm, P. Blomstrom, R. Johansson, C. Luhrs, J. Brandt, and S. Olsson, "Right atrial free wall conduction velocity and degree of anisotropy in patients with stable sinus rhythm studied during open heart surgery," *Eur. Heart. J.*, vol. 19, pp. 293–300, 1998.
376. G. Seemann, F. B. Sachse, and O. Dössel, "Excitation propagation and force development in the left ventricle of the visible female data set," in *Biomedizinische Technik*, Sep. 2002, vol. 47-1/1, pp. 221–224.
377. G. Seemann, D. L. Weiß, F. B. Sachse, and O. Dössel, "Electrophysiology and tension development in a transmural heterogeneous model of the visible female left ventricle," in *FIMH05*, 2005, submitted.
378. F. B. Sachse, R. Frech, C. D. Werner, and O. Dössel, "A model based approach to assignment of myocardial fibre orientation," in *Proc. Computers in Cardiology*, Hannover, 1999, vol. 26, pp. 145–148.
379. G. Seemann, D. L. Weiß, F. B. Sachse, and O. Dössel, "Familial atrial fibrillation: Simulation of the mechanisms and effects of a slow rectifier potassium channel mutation in human atrial tissue," in *Proc. Computers in Cardiology*, 2004, vol. 31, pp. 125–128.
380. H. Ying, "Investigation of atrial fibrillation induced remodeling in human right atrium: A simulation study," M.S. thesis, Universität Karlsruhe (TH), Institut für Biomedizinische Technik, Dec. 2004, Student Research Project.
381. D. L. Weiß, "Charakterisierung der Ventrikelwand durch anatomische und elektrophysiologische Modellierung," M.S. thesis, Universität Karlsruhe (TH), Institut für Biomedizinische Technik, Sep. 2003, Diploma Thesis.
382. G. Seemann, F. B. Sachse, C. Riedel, C. D. Werner, and O. Dössel, "Regional and frequency dependencies of force development in the myocardium: A simulation study," in *Proc. Computers in Cardiology*, Sep. 2001, vol. 28, pp. 345–348.
383. Y. Shinagawa, H. Satoh, and A. Noma, "The sustained inward current and inward rectifier K^+ current in pacemaker cells dissociated from rat sinoatrial node," *J. Physiol.*, vol. 523, pp. 593–605, 2000.
384. T. Mitsuiye, Y. Shinagawa, and A. Noma, "Sustained inward current during pacemaker depolarization in mammalian sinoatrial node cells," *Circ. Res.*, vol. 87, pp. 88–91, 2000.
385. D. Escande, A. Coulombe, J. F. Faivre, E. Deraubaix, and E. Coraboeuf, "Two types of transient outward currents in adult human atrial cells," *Am. J. Physiol.*, vol. 252, pp. H142–H148, 1987.
386. A. Ludwig, X. Zong, J. Stieber, R. Hullin, F. Hofmann, and M. Biel, "Two pacemaker channels from human heart with profoundly different activation kinetics," *The EMBO Journal*, vol. 18, no. 9, pp. 2323–2329, 1999.
387. A. Garny, H. Zhang, P. J. Noble, P. Kohl, M. R. Boyett, and D. Noble, "Advanced computational model of central and peripheral rabbit sino-atrial node cells," *Biophys. J.*, vol. 78, no. 1, pp. 2674, 2000.
388. G. C. L. Bett and R. L. Rasmusson, "Computer models of ion channels," in *Quantitative Cardiac Electrophysiology*, C. Cabo and D. S. Rosenbaum, Eds., pp. 1–60. Marcel Dekker, Inc., New York, 2002.
389. M. Näbauer, D. J. Beuckelmann, P. "Uberfuhr, and G. Steinbeck, "Regional differences in current density and rate-dependent properties of the transient outward current in subepicardial and subendocardial myocytes of human left ventricle," *Circ.*, vol. 93, pp. 168–177, 1996.
390. G. Seemann, F. B. Sachse, D. L. Weiß, and O. Dössel, "Quantitative reconstruction of cardiac electromechanics in human myocardium: Regional heterogeneity," *J. Cardiovasc. Electrophysiol.*, vol. 14, no. S10, pp. S219–S228, Oct. 2003.
391. R. L. Rasmusson, J. W. Clark, W. R. Giles, K. Robinson, R. B. Clark, E. F. Shibata, and D. L. Campbell, "A mathematical model of electrophysiological activity in a bullfrog atrial cell," *Am. J. Physiol.*, vol. 259, pp. H370–H389, 1990.
392. M. A. Geeves and K. C. Holmes, "Structural mechanism of muscle contraction," *Ann. Rev. Biochemistry*, vol. 68, pp. 687–728, 1999.
393. J.D. Johnson and E.W. Taylor, "Intermediate states of subfragment 1 and actosubfragment1 ATPase: Reevaluation of the mechanism," *Biochemistry*, vol. 17, pp. 3432–3442, 1978.
394. M. Regnier, D.M. Lee, and E. Homsher, "ATP analogs and muscle contraction: Mechanics and kinetics of nucleoside triphosphate binding and hydrolysis," *Biophys. J.*, vol. 74, pp. 3044–3058, 1998.
395. M. Brune, J. L. Hunter, J. E. Corrie, and M. R. Webb, "Direct, real-time measurement of rapid inorganic phosphate release using a novel fluorescent probe and its application to actomyosin subfragment 1 atpase," *Biochemistry*, vol. 33, pp. 8262–8271, 1994.
396. H.D. White and E.W. Taylor, "Energetics and mechanism of actomyosin adenosine triphosphatease," *Biochemistry*, vol. 15, pp. 5818–5826, 1976.
397. E.W. Taylor, "Mechanism of actomyosin ATPase and the problem of muscle contraction," *CRC Crit. Rev. Biochem.*, vol. 6, pp. 103–164, 1979.
398. J. C. Rüegg, "Muskel," in *Physiologie des Menschen*, R. F. Schmidt, G. Thews, and F. Lang, Eds., chapter 4, pp. 67–87. Springer, Berlin, Heidelberg, New York, 2000.
399. T. C. Irving, J. P. Konhilas, D. Perry, R. Fischetti, and P. P. de Tombe, "Myofilament lattice spacing as a function of sarcomere length in isolated rat myocardium," *Am. J. Physiol.*, vol. 279, pp. H2568–H2573, 2000.

400. H. E. D. J. ter Keurs, E. H. Hollander, and M. H. C. ter Keurs, "The effect of sarcomere length on the force-cytosolic $[Ca^{2+}]$ relationship in intact rat cardiac trabeculae," in *Skeletal muscle mechanics: From Mechanisms to Function*, W. Herzog, Ed., chapter 4, pp. 53–70. John Wiley & Sons, Ltd, Baffins Lane, Chichester, West Sussex P019 1UD, UK, 2000.
401. A. Fabiato and F. Fabiato, "Contractions induced by a calcium-triggered release of calcium for the sarcoplasmic reticulum of single skinned cardiac cells," *J. Physiol. Lond.*, vol. 249, pp. 469–495, 1975.
402. A. Fabiato and F. Fabiato, "Myofilament-generated tension oscillation during partial calcium activation and activation dependence of the sarcomere length-tension relation of skinned cardiac cells," *J. Gan. Physiol.*, vol. 72, pp. 667–699, 1978.
403. P. M. L. Janssen and W. C. Hunter, "Force, not sarcomere length, correlates with prolongation of isosarcometric contaction," *Am. J. Physiol.*, vol. 269, pp. H676–H685, 1995.
404. D. R. Van Wagoner, "Electrophysiological remodeling in human atrial fibrillation," *Pacing Clin. Electrophysiol.*, vol. 26, no. 7-II, pp. 1572–1575, 2003.
405. J. Kneller, H. Sun, and N. Leblanc, "Remodeling of Ca^{2+}-handling by atrial tachycardia: Evidence for a role in loss of rate-adaptation," *Cardiovasc. Res.*, vol. 54, pp. 416–426, 2002.
406. D. R. Van Wagoner, A. L. Pond, and P. M. McCarthy, "Outward K^+ current densities and kv1.5 expression are reduced in chronic human atrial fibrillation," *Circ. Res.*, vol. 80, pp. 772–781, 1997.
407. M. Courtemanche, R. J. Ramirez, and S. Nattel, "Ionic targets for drug therapy and atrial fibrillation-induced electrical remodeling: insights from a mathematical model," *Cardiovasc. Res.*, vol. 42, pp. 477–489, 1999.
408. "Cardiac action potential," http://education.adam.com/products/ipie/igude/Cardiac-Action-Potential.pdf.
409. G. Seemann, D. L. Weiß, F. B. Sachse, and O. Dössel, "Simulation of the long-QT syndrome in a model of human myocardium," in *Proc. Computers in Cardiology*, 2003, vol. 30, pp. 287–290.
410. H. Hayashi, R. L. Lux, R. F. Wyatt, M. J. Burgess, and J. A. Abildskov, "Relation of canine atrial activation sequence to anatomic landmarks," *Am. J. Physiol.*, vol. 242, no. 3, pp. H421–H428, 1982.
411. P. C. Dolber and M. S. Spach, "Thin collagenous septa in cardiac muscle," *Anat. Rec.*, vol. 218, no. 1, pp. 45–55, 1987.
412. H. M. van der Velden and H. J. Jongsma, "Cardiac gap junction and connexins: Their role in atrial fibrillation and potential as therapeutic targets," *Cardiovasc. Res.*, vol. 54, no. 2, pp. 270–279, 2002.
413. O. Blanc, N. Virag, J.-M. Vesin, and L. Kappenberger, "A computer model of human atria with reasonable computation load and realistic anatomical properties," *IEEE Transactions on Biomedical Engineering*, vol. 48, no. 11, pp. 1229–1237, Nov. 2001.
414. C. W. Zemlin, H. Herzel, S. Y. Ho, and A. Panfilow, "A realistic and efficient model of excitation propagation in the human atria," in *Computer Simulation and Experimental Assessment of Cardiac Electrophysiology*, N. Virag, O. Blanc, and L. Kappenberger, Eds., pp. 29–34. Futura, 2001.
415. H. Antoni, "Mechanik der Herzaktion," in *Physiologie des Menschen*, R. F. Schmidt and G. Thews, Eds., chapter 22, pp. 448–471. Springer, Berlin, Heidelberg, New York, 1997.
416. C. Antzelevitch, Z. Q. Sun, Z. Q. Zhang, and G. X. Yan, "Cellular and ionic mechanisms underlying erythromycin-induced long QT intervals and torsades de pointes.," *J. Am. Coll. Cardiol.*, vol. 28, pp. 1836–1848, 1996.
417. G. X. Yan and C. Antzelevitch, "Delayed repolarization of M cells underlies the manifesation of U waves, notched T waves and long QT intervals in the electrogardiogram (ECG)," *Circ.*, vol. 92, pp. I–480, 1995.
418. P. Taggart, P. Sutton, T. Opthof, R. Coronel, and P. Kallis, "Electrotonic cancellation of transmural electrical gradients in the left ventricle in man," *Prog. Biophys. Mol. Biol.*, vol. 82, pp. 243–254, 2003.
419. D. L. Weiß, "Vergleich des Verhaltens eines Elektrophysiologischen Zellmodells mit einem Zellulären Automaten bei Simulierten Atrialen Fibrillationen," M.S. thesis, Universität Karlsruhe (TH), Institut für Biomedizinische Technik, 2002, Student Research Project.
420. D. K. Racker, P. C. Ursell, and B. F. Hoffmann, "Anatomy of the tricuspid annulus: Circumferential myofibers as the structural basis for atrial flutter in a canine model," *Circ.*, vol. 84, pp. 841–851, 1991.
421. R. A. Gray, K. Takkellapati, and J. Jalife, "Dynamics and anatomical correlations of atrial flutter and fibrillation," in *Cardiac Electrophysiology. From Cell to Bedside*, D. P. Zipes and J. Jalife, Eds., chapter 41, pp. 356–263. W. B. Saunders Company, Philadelphia, 3 edition, 1999.
422. M. Horlitz, P. Schley, D. I. Shin, A. Ghouzi, A. Sause, M. Wehner, M. Müller, R. M. Klein, A. Bufe, and H. Gülker, "Identification and ablation of atypical atrial flutter entrainment pacing combined with electroanatomic mapping," *Z. Kardiol.*, vol. 93, no. 6, pp. 463–473, 2004.
423. Z. Qu, A. Garfinkel, P. S. Chen, and J. N. Weiss, "Mechanisms of discordant alternans and induction of reentry in simulated cardiac tissue," *Circ.*, vol. 102, no. 14, pp. 1664–1670, 2000.
424. P. Jais, M. Hocini, R. Weerasoryia, L. Macle, C. Scavee, F. Raybaud, D. C. Shah, J. Clementy, and M. Haissaguerre, "Atypical left atrial flutters," *Card. Electrophysiol. Rev.*, vol. 6, no. 4, pp. 371–377, 2002.
425. A. Bochoeyer, Y. Yang, J. Cheng, R. J. Lee, E. C. Keung, N. F. Marrouche, A. Natale, and M. M. Scheinman, "Surface Electrocardiographic Characteristics of Right and Left Atrial Flutter," *Circ.*, vol. 108, no. 1, pp. 60–66, 2003.
426. H. F. Tse, C. P. Lau, and G. M. Ayers, "Heterogeneous changes in electrophysiologic properties in the paroxysmal and chronically fibrillating human atrium," *J. Cardiovasc. Electrophysiol.*, vol. 10, pp. 125–135, 1999.
427. L. Yue, J. Feng, and R. Gaspo, "Ionic remodeling underlying action potential changes in canine model of atrial fibrillation," *Circ. Res.*, vol. 81, pp. 512–525, 1997.

428. M. H. Raitt, W. Kusumoto, and G. D. Giraud, "Electrophysiologic predictors of the recurrence of persistent atrial fibrillation within 30 days of cardioversion," *Am. J. Cardiol.*, vol. 93, pp. 107–110, 2004.
429. M. A. Allessie, P. A. Boyden, and A. J. Camm, "Pathophysiology and prevention of atrial fibrillation," *Circ.*, vol. 103, pp. 769–777, 2001.
430. W. C. Yu, S. H. Lee, and C. T. Tai, "Reversal of atrial electrical remodeling following cardioversion of long-standing atrial fibrillation in man," *Cardiovasc. Res.*, vol. 42, pp. 470–476, 1999.
431. M. Biffi, G. Boriani, and M. Bartolotti, "Atrial fibrillation recurrence after internal cardioversion: prognostic importance of electrophysiological parameters," *Heart*, vol. 87, pp. 443–448, 2002.
432. M. R. Franz, "Electrical remodeling of the human atrium: Similar effects in patients with chronic atrial fibrillation and atrial flutter," *JACC*, vol. 30, pp. 1785–1792, 1997.
433. A. J. Workman, K. A. Kane, and A. C. Rankin, "The contribution of ionic currents to changes in refractoriness of human atrial myocytes associated with chronic atrial fibrillation," *Cardiovasc. Res.*, vol. 52, pp. 226–235, 2001.
434. G. Seemann, F. B. Sachse, D. L. Weiß, and O. Dössel, "Investigation of fibrillation in human left ventricle with a reaction-diffusion model," in *Biomedizinische Technik*, 2003, vol. 48-1, pp. 226–227.

Danksagung

Diese Arbeit wurde am Institut für Biomedizinische Technik der Universität Karlsruhe (TH) durchgeführt. An dieser Stelle möchte ich mich bei allen Personen herzlich bedanken, die zum Gelingen dieser Arbeit beigetragen haben.
Mein Dank gilt insbesondere Herrn Prof. Dr. rer. nat. Olaf Dössel für das große Interesse an meiner Arbeit und die kompetente Betreuung. Außerdem bedanke ich mich bei ihm für die Übernahme des Hauptreferats und für viele nützliche Diskussionen während der Ausarbeitung der Dissertation.
Herrn Prof. Dr.-Ing. Rüdiger Dillmann möchte ich ebenfalls für das Interesse an der Arbeit, die kritische Durchsicht und für die Übernahme des Korreferats herzlich danken.
Mein Dank gebührt allen Mitarbeitern des Instituts für Biomedizinische Technik, die mit ihrem Beitrag diese Arbeit unterstützt haben. Insbesondere danke ich Herrn Dr. Frank Sachse für die ausgesprochen fruchtbare Zusammenarbeit der letzten sechs Jahre, für die vielen wissenschaftlichen Diskussionen und die kritische Durchsicht des Manuskriptes. Ebenfalls möchte ich mich bei Herrn Daniel Weiß für die bisherige Zusammenarbeit, seinen wissenschaftlichen Beitrag zu dieser Arbeit als Student und für die detaillierte Korrektur der Dissertation bedanken. Beide haben entscheidend zum Gelingen dieser Arbeit beigetragen. Den Herren Matthias Mohr, Dr. Ulrich Müschen und Matthias Reumann danke ich insbesondere für die Korrektur des Dissertation. Weiterhin möchte ich mich bei allen Studienarbeitern und Diplomanden für ihren Beitrag zu dieser Arbeit bedanken, hier im Besonderen Kerstin Glänzel, Christine Höper, Hong Ying und Daniel Weiß. Auch danke ich Rony Nir, der für ein Praktikum vom Technicon aus Israel gekommen ist, für den letzten Korrekturschliff dieser Arbeit.
Nicht zuletzt möchte ich meinen Eltern, Schwiegereltern und Freunden für ihre Unterstützung während der letzten 4 1/2 Jahre danken. Sie haben mir und meiner Familie während dieser Zeit viele Lasten abgenommen.
Ganz besonders möchte ich mich bei meiner Frau Maike und meinen Kindern Anna und Jan für ihre Geduld und den familiären Rückhalt bedanken, ohne den diese Arbeit nicht zustande gekommen wäre.

Curriculum Vitae

Gunnar Seemann

1973	Born in Hamburg, Germany, at october 28.
1979 – 1984	Primary school: Buckhorn, Hamburg, Germany
1984 – 1988	High school: Buckhorn, Hamburg, Germany
1988 – 1990	High school: Karlsbad, Germany
1990 – May 1992	Engineering high school: Ettlingen, Germany, with "Abitur"
Jun. 1992 – Sep. 1992	Practical work experience at Hermes Abrasives, Virginia Beach, USA
Sep. 1992 – Nov. 1993	Civil service: individual seriously disabled care, school for physically handicapped, Karlsbad, Germany
Oct. 1993 – Sep. 2000	Studies of electrical engineering and information technology at the University Karlsruhe (TH), Karlsruhe, Germany Industrial practical work experience at Philips Medical Systems in Hamburg, Germany, in summer 1998. Specialization of the studies: Biomedical Engineering Degree: Diplom-Ingenieur Diploma thesis: "Elektrische Erregungsausbreitung im Herzen ausgehend von elektrophysiologischen Zellmodellen: Erregungsausbreitung im Zellverband, Parametrisierung Zellulärer Automaten" at the Institute of Biomedical Engineering at the University Karlsruhe (TH), Karlsruhe, Germany
since Nov. 2000	Scientific employee at the Institute of Biomedical Engineering at the University Karlsruhe (TH), Karlsruhe, Germany

Publications

Peer-review journals

First Author

- G. Seemann, C. Höper, F. B. Sachse, O. Dössel, A. V. Holden and H. Zhang, "3D anatomical and electrophysiological model of human sinoatrial node and atria," *Phil. Trans. Roy. Soc.*, submitted, 2005.
- G. Seemann, F. B. Sachse, D. L. Weiß, and O. Dössel, "Quantitative reconstruction of cardiac electromechanics in human myocardium: Regional heterogeneity," *J. Cardiovasc. Electrophysiol.*, vol. 14, no. S10, pp. S219–S228, 2003.
- G. Seemann, F. B. Sachse, D. L. Weiß, and O. Dössel, "Investigating heterogeneity in human heart with simulated transmural electrocardiograms," *Int. J. Bioelectromagnetism*, vol. 5, no. 1, 2003.

Co-author

- D. L. Weiß, G. Seemann, F. B. Sachse, and O. Dössel, "Modeling of the short QT syndrome in a heterogeneous model of the human ventricular wall," *Europace*, 2005, in press.
- I. M. Graf, G. Seemann, D. L. Weiß, and O. Dössel, "Influence of electrophysiological heterogeneity in human healthy and failing heart on electrical stimulation," *BMEC*, 2005, submitted.
- I. M. Popp, G. Seemann, and O. Dössel, "A simulation study of biphasic defibrillation shocks," *BMC Cardiovascular Disorders*, vol. 4, no. 1, pp. 9, 2004
- O. Dössel and G. Seemann, "Modeling cardiac electric fields," *Int. J. Bioelectromagnetism*, vol. 5, no. 1, 2003.
- G. Reinerth, G. Seemann, O. Dössel, C.-F. Vahl, and S. Hagl, "Elektrophysiologische Modellierung des Herzens zur Planung von herzchirurgischen und kardiologischen Eingriffen," *Herzschrittmachertherapie und Elektrophysiologie*, vol. 14, no. 1, pp. 742–746, 2003.
- F. B. Sachse, K. Glänzel, and G. Seemann, "Modeling of protein interactions involved in cardiac tension development," *Int. J. Bifurc. Chaos*, vol. 13, no. 12, pp. 3561–3578, 2003.
- F. B. Sachse, G. Seemann, M. B. Mohr, and Arun V. Holden, "Mathematical modeling of cardiac electro-mechanics: From protein to organ," *Int. J. Bifurc. Chaos*, vol. 13, no. 12, pp. 3747–3755, 2003.
- F. B. Sachse, G. Seemann, K. Chaisaowong, and D. Weiß, "Quantitative reconstruction of cardiac electromechanics in human myocardium: Assembly of electrophysiological and tension generation models," *J. Cardiovasc. Electrophysiol.*, vol. 14, no. S10, pp. S210–S218, 2003.
- O. Dössel, F. B. Sachse, G. Seemann, and C. D. Werner, "Computermodelle der elektrophysiologischen Eigenschaften des Herzens," *Biomedizinische Technik*, vol. 9-10, no. 47, pp. 250–257, 2002.
- F. B. Sachse, G. Seemann, and C. D. Werner, "Combining the electrical and mechanical functions of the heart," *Int. J. Bioelectromagnetism*, vol. 3, no. 2, 2001.
- F. B. Sachse, G. Seemann, C. Riedel, C. D. Werner, and O. Dössel, "Modeling of the cardiac mechano-electrical feedback," *Int. J. Bioelectromagnetism*, vol. 2, no. 2, 2000.
- F. B. Sachse, C. D. Werner, and G. Seemann, "Anatomical models of the heart for the simulation of excitation propagation and force development," in *Annals of Biomedical Engineering*, p. 48, 2001

Peer-review Conferences

First Author

- G. Seemann, D. L. Weiß, F. B. Sachse, and O. Dössel, "Electrophysiology and Tension Development in a Transmural Heterogeneous Model of the Visible Female Left Ventricle," in *Proc. FIMH05*, 2005 accepted.
- G. Seemann, D. L. Weiß, F. B. Sachse, and O. Dössel, "Familial atrial fibrillation: Simulation of the mechanisms and effects of a slow rectifier potassium channel mutation in human atrial tissue," in *Proc. Computers in Cardiology*, vol. 31, pp. 125–128, 2004
- G. Seemann, C. Höper, F. B. Sachse, H. Zhang, and O. Dössel, "A detailed model of human atrium towards simulation of electromechanics in the heart," in *Proc. MEDICON*, 2004
- G. Seemann, G. Reinerth, T. Schmidt, M. Reumann, O. Dössel, C. F. Vahl, and S. Hagl, "Simulation of ventricular activity in ventricular pacing using mathematical models in a porcine model based on 3D-echocardiographic images," in *Proc. CURAC03*, 2003.
- G. Seemann, F. B. Sachse, D. L. Weiß, and O. Dössel, "Investigation of fibrillation in human left ventricle with a reaction-diffusion model," in *Biomedizinische Technik*, vol. 48-1, pp. 226–227, 2003.
- G. Seemann, D. L. Weiß, F. B. Sachse, and O. Dössel, "Simulation of the long-QT syndrome in a model of human myocardium," in *Proc. Computers in Cardiology*, vol. 30, pp. 287–290, 2003.
- G. Seemann, G. Reinerth, O. Dössel, and C. F. Vahl, "Elektrophysiologische Modellierung des Herzens als Grundlage therapeutischer Interventionen," in *Biomedizinische Technik*, vol. 47-1/2, pp. 927–929, 2002.

- G. Seemann, F. B. Sachse, and O. Dössel, "Excitation propagation and force development in the left ventricle of the visible female data set," in *Biomedizinische Technik*, vol. 47-1/1, pp. 221–224, 2002.
- G. Seemann, F. B. Sachse, C. D. Werner, and O. Dössel, "Simulation of surgical interventions: Atrial radio frequency ablation with a haptic interface," in *Proc. CARS 2002*, pp. 49–54, 2002.
- G. Seemann, F. B. Sachse, C. Riedel, C. D. Werner, and O. Dössel, "Regional and frequency dependencies of force development in the myocardium: A simulation study," in *Proc. Computers in Cardiology*, vol. 28, pp. 345–348, 2001.
- G. Seemann, F. B. Sachse, C. D. Werner, and O. Dössel, "Simulation der Kraftentwicklung im Myokard bei physiologischer und pathologischer Erregungsausbreitung," in *Biomedizinische Technik*, vol. 46-1, pp. 192–193, 2001.
- G. Seemann, F. B. Sachse, C. D. Werner, and O. Dössel, "Parametrisierung Zellulärer Automaten der Erregungsausbreitung im Herzen ausgehend von elektrophysiologischen Zellmodellen," in *Biomedizinische Technik*, vol. 45-1, pp. 481–482, 2000.
- G. Seemann, C. D. Werner, F. B. Sachse, and O. Dössel, "Simulation of cardiac electrical activity: Interactive user interface to control the simulation process," in *Proc. EMBEC 99*, pp. 1210–1211, 1999.

Co-author

- M. B. Mohr, G. Seemann, F. B. Sachse, and O. Dössel, "Deformation Simulation in an Elastomechanical Ventricular Model," in *Proc. Computers in Cardiology*, vol. 31, pp. 777–780, 2004
- I. M. Graf, G. Seemann, and O. Dössel, "Theoretical Research on the Influence of Defibrillator Paddle Position on the Human Ventricular Myocardium," in *Proc. Computers in Cardiology*, vol. 31, pp. 97–100, 2004
- I. M. Popp, G. Seemann, and O. Dössel, "Computer modeling of virtual electrodes in human ventricular myocardium," in *Proc. IASTED*, 2004
- I. M. Popp, G. Seemann, and O. Dössel, "The influence of heterogeneity of external applied fields on human ventricular myocardium," in *Proc. MEDICON*, 2004
- I. M. Popp, G. Seemann, and O. Dössel, "Investigation of electrical defibrillation of chaotically fibrillating human ventricular myocardium in a computer model," in *Proc. ICE*, 2004
- I. M. Popp, G. Seemann, and O. Dössel, "The reaction of a fibrillating myocardium to electrical shocks of different durations," in *Proc. BMT*, vol. 49, no. 2, pp. 376-377, 2004
- G. Reinerth, M. Reumann, G. Seemann, N. Kayhan, J. Albers, O. Dössel, S. Hagl, and C.-F. Vahl, "Three-dimensional electrophysiological and morphological computer models for individualisation of antiarrhythmic cardiac surgery," in *Proc. CARS*, 2004
- G. Reinerth, M. Reumann, G. Seemann, N. Kayhan, J. Albers, O. Dössel, S. Hagl, and C.-F. Vahl, "A porcine model to evaluate electrophysiological simulations in cardiac tissue," in *Proc. BMT*, vol. 49, no. 2, pp. 388-389, 2004
- G. Reinerth, M. Reumann, G. Seemann, N. Kayhan, J. Albers, O. Dössel, S. Hagl, and C.-F. Vahl, "Electrophysiological computer models and individualisation of antiarrhythmic cardiac surgery," in *Proc. BMT*, vol. 49, no. 2, pp. 368-369, 2004, in press.
- M. Reumann, G. Reinerth, G. Seemann, C. F. Vahl, S. Hagl, and O. Dössel, "Simulating biventricular pacing on an individual heart model with respect to stimuli delay," in *Proc. MEDICON*, 2004
- M. Reumann, G. Reinerth, G. Seemann, C. F. Vahl, S. Hagl, and O. Dössel, "Computer assisted electrode positioning in biventricular pacing," in *Proc. CARS 2004*, 2004
- M. Reumann, G. Reinerth, G. Seemann, C.-F. Vahl, S. Hagl, and O. Dössel, "Modelling intraventricular conduction delay in cardiac resynchronisation therapy," in *Proc. BMT*, vol. 49, no. 2, pp. 358-359, 2004
- F. B. Sachse, G. Seemann, D. L. Weiß, B. Punske and B. Taccardi, "Accuracy of Activation Times Detected in Simulated Extracellular Electrograms," in *Proc. Computers in Cardiology*, vol. 31, pp. 93–96, 2004
- F. B. Sachse, G. Seemann, and M. B. Mohr, "Electro-Mechanics in Biventricular Models," in *Proc. Computers in Cardiology*, vol. 31, pp. 537–540, 2004
- D. L. Weiß, G. Seemann, and O. Dössel, "Conditions for equal polarity of r and t wave in heterogeneous human ventricular tissue," in *Proc. BMT*, vol. 49, no. 2, pp. 364-365, 2004
- H. Ying, G. Seemann, C. Höper, and O. Dössel, "Investigation of atrial fibrillation induced remodeling in human right atrium: A simulation study," in *Proc. BMT*, vol. 49, no. 2, pp. 358-359, 2004
- K. Chaisaowong, F. B. Sachse, G. Seemann, M. Mohr, and O. Dössel, "Modeling of human cardiac force development:quantitative description from myofilament to myocardium," in *Biomedizinische Technik*, vol. 48-1, pp. 466–467, 2003.
- C. Höper, G. Seemann, F. B. Sachse, H. Zhang, and O. Dössel, "3D computer model of human atrial anatomy and electrophysiology," in *Biomedizinische Technik*, vol. 48-1, pp. 2–3, 2003.
- M. B. Mohr, L. G. Blümcke, F. B. Sachse, G. Seemann, and O. Dössel, "Hybrid deformation model of myocardium," in *Proc. CinC*, vol. 30, pp. 319–322, 2003.
- M. B. Mohr, L. G. Blümcke, G. Seemann, F. B. Sachse, and O. Dössel, "Modeling of myocardial deformation with an extended spring mass system," in *Biomedizinische Technik*, vol. 48-1, pp. 6–7, 2003.
- I. M. Popp, G. Seemann, and O. Dössel, "Investigation of the influence of electric fields on human ventricular myocardium including realistic fibre orientation: A simulation study," in *Proc. CinC*, vol. 30, pp. 213–216, 2003.

- G. Reinerth, G. Seemann, T. Schmidt, N. Kayhan, O. Dössel, C.-F. Vahl, and S. Hagl, "Dreidimensionale elektrophysiologische und morphologische Information zur Operationsplanung in der Herzchirurgie," in *Proc. CURAC03*, 2003.
- F. B. Sachse, G. Seemann, K. Chaisaowong, and M. B. Mohr, "Modeling of electro-mechanics of human cardiac myocytes: Parameterization with numerical minimization techniques," in *Proc. 25th Conf. IEEE EMBS*, pp. 2810–2813, 2003.
- D. L. Weiß, G. Seemann, F. B. Sachse, and O. Dössel, "Investigation of electrophysiological heterogeneity and anisotropy across the human ventricular wall," in *Biomedizinische Technik*, vol. 48-1, pp. 228–229, 2003.
- O. Dössel, M. Nalbach, F. Sachse, G. Seemann, O. Skipa, and C. D. Werner, "Modelling and imaging of bioelectric sources in the heart," in *Proc. 12th Nordic Baltic Conference*, 2002.
- K. Glänzel, F. B. Sachse, G. Seemann, C. Riedel, and O. Dössel, "Modeling force development in the sarcomere in consideration of electromechanical coupling," in *Biomedizinische Technik*, vol. 47-1/2, pp. 774–777, 2002.
- J. Häfner, F. B. Sachse, C. Sansour, G. Seemann, and O. Dössel, "Hyperelastic description of elastomechanic properties of the heart: A new material law and its application," in *Biomedizinische Technik*, vol. 47-1/2, pp. 770–773, 2002.
- M. B. Mohr, L. G. Blümcke, F. B. Sachse, G. Seemann, C. D. Werner, and O. Dössel, "Volumenbasierte Modellierung der Deformation im Myokard ausgehend von Modellen der Kraftentwicklung," in *Biomedizinische Technik*, vol. 47-1/2, pp. 225–228, 2002.
- F. B. Sachse, G. Seemann, M. B. Mohr, L. G. Blümcke, and C. D. Werner, "Models of the human heart for simulation of clinical interventions," in *Proc. CARS*, pp. 43–48, 2002.
- F. B. Sachse, G. Seemann, and C. Riedel, "Modeling of cardiac excitation propagation taking deformation into account," in *Proc. BIOMAG*, pp. 839–841, 2002.
- F. B. Sachse, L. G. Blümcke, M. Mohr, K. Glänzel, J. Häfner, C. Riedel, G. Seemann, O. Skipa, C. D. Werner, and O. Dössel, "Comparison of macroscopic models of excitation and force propagation in the heart," in *Biomedizinische Technik*, vol. 47-1/2, pp. 217–220, 2002.
- F. B. Sachse, G. Seemann, and C. D. Werner, "Modeling of force development in the human heart with a cellular automaton parameterized by numerical experiments," in *Proc. 2nd Joint Conference of the IEEE EMBS and BMES*, pp. 1226–1227, 2002.
- F. B. Sachse, G. Seemann, and C. D. Werner, "Modeling of electro-mechanics in left ventricle," in *Proc. Computers in Cardiology*, pp. 705–708, 2002.
- S. Barros, N. Sa Couto, F. B. Sachse, C. D. Werner, and G. Seemann, "Segmentation and tissue-classification of the visible female dataset - thoracic muscles, bones and blood vessels," in *Biomedizinische Technik*, vol. 46-1, pp. 510–511, 2001.
- L. G. Blümcke, F. B. Sachse, G. Seemann, C. D. Werner, and O. Dössel, "Entwicklung eines schnellen Verfahrens zur Deformation im Herzen ausgehend von makroskopischen Modellen der Kraftentwicklung," in *Biomedizinische Technik*, vol. 46-1, pp. 516–517, 2001.
- M. Jösel, F. B. Sachse, G. Seemann, C. D. Werner, and O. Dössel, "Simulation der Katheterisierung und Radio-Frequenz-Ablation in der Kardiologie mit einem haptischen Interface," in *Biomedizinische Technik*, vol. 46-1, pp. 528–529, 2001.
- M. B. Mohr, F. B. Sachse, G. Seemann, C. D. Werner, and O. Dössel, "Vergleich von mikroskopischen und makroskopischen Modellen der Kraftentwicklung und Deformation im Myokard," in *Biomedizinische Technik*, vol. 46-1, pp. 524–525, 2001.
- F. B. Sachse, C. D. Werner, G. Seemann, and O. Dössel, "Elektromechanische Modellierung des menschlichen Herzens," in *Biomedizinische Technik*, vol. 46-1, pp. 190–191, 2001.
- F. B. Sachse, C. Riedel, C. D. Werner, and G. Seemann, "Stretch activated ion channels in myocytes: Parameter estimation, simulations and phenomena," in *Proc. 23rd Conf. IEEE Eng. in Med. and Biol.*, vol. 1, pp. 52–55, 2001.
- F. B. Sachse, C. Henriquez, G. Seemann, C. Riedel, C. D. Werner, R. C. Penland, B. Davis, and E. Hsu, "Modeling of fiber orientation in the ventricular myocardium with MR diffusion imaging," in *Proc. Computers in Cardiology*, vol. 28, pp. 617–620, 2001.
- F. B. Sachse, G. Seemann, C. D. Werner, C. Riedel, and O. Dössel, "Electro-mechanical modeling of the myocardium: Coupling and feedback mechanisms," in *Proc. Computers in Cardiology*, vol. 28, pp. 161–164, 2001.
- N. Sa Couto, S. Barros, F. B. Sachse, C. D. Werner, and G. Seemann, "Segmentation and tissue-classification of the visible female dataset - non cardiac thoracic organs," in *Biomedizinische Technik*, vol. 46-1, pp. 512–513, 2001.
- M. Thüringer, F. B. Sachse, G. Seemann, C. D. Werner, and O. Dössel, "Simulation der Deformation im Myokard ausgehend von mikroskopischen Modellen der Kraftentwicklung und hyperelastischen Materialbeschreibungen," in *Biomedizinische Technik*, vol. 46-1, pp. 526–527, 2001.
- D. L. Weiß, F. B. Sachse, C. D. Werner, G. Seemann, and O. Dössel, "Vergleich elektrophysiologischer Modelle bei simulierten atrialen Fibrillationen," in *Biomedizinische Technik*, vol. 46-1, pp. 514–515, 2001.
- F. B. Sachse, C. Riedel, G. Seemann, C. D. Werner, and O. Dössel, "Simulating the excitation propagation in mechanoelectrical models of myocardial cells," in *Proc. Computers in Cardiology*, vol. 27, pp. 247–251, 2000.

Others

First Author

- G. Seemann, F. B. Sachse, O. Dössel, A. V. Holden, M. R. Boyett, and H. Zhang, "3D anatomical and electrophysiological model of human sinoatrial node and atria," *J. Physiol.*, PC26, submitted, 2004.
- G. Seemann, "Elektromechanische Modellierung des menschlichen Herzens," in *I. Kongress junge Naturwissenschaft und Technik*, pp. 178–179, 2003.
- G. Seemann, "Elektrische Erregungsausbreitung im Herzen ausgehend von elektrophysiologischen Zellmodellen: Erregungsausbreitung im Zellverband, Parametrisierung Zellulärer Automaten," Diploma Thesis, Institut für Biomedizinische Technik, Universität Karlsruhe (TH), Aug. 2000.
- G. Seemann, "Interaktive Bedienoberfläche für die Simulation und Visualisierung der elektrischen Erregung im Herz," Student Research Project, Institut für Biomedizinische Technik, Universität Karlsruhe (TH), Feb. 2000.

Co-author

- G. Reinerth, T. Schmidt, G. Seemann, J. Albers, O. Dössel, S. Hagl, and C.-F. Vahl, "Planning of surgical antiarrhythmic interventions based on simulations of cardiac electrophysiology," *The Thoracic and Cardiovascular Surgeon*, vol. 52-S1, 2004.
- G. Reinerth, T. Schmidt, G. Seemann, J. Albers, O. Dössel, S. Hagl, and C.-F. Vahl, "Simulation of biventricular activity in ventricular pacing on 3D-echocardiographic images using the cellular automaton in a porcine model," *The Thoracic and Cardiovascular Surgeon*, vol. 52-S1, 2004.
- G. Reinerth, G. Seemann, M. Reumann, T. Schmidt, O. Dössel, and C.-F. Vahl, "Simulation der elektrischen Aktivität der Ventrikel bei biventrikulärer Stimulation," *Z. Kardiologie*, 2004, in press.
- M. B. Mohr, L. G. Blümcke, G. Seemann, F. B. Sachse, and O. Dössel, "Volume modeling of myocard deformation using a spring mass system," *LNCS 2673*, pp. 332–339, 2003.
- G. Reinerth, G. Seemann, S. Kewitz, O. Dössel, T. Schmidt, J. Albers, C.-F. Vahl, and S. Hagl, "Simulation of cardiac electrophysiology using mathematical models and computer based processing of digital image data," *Europ. Heart J.*, vol. 24, pp. S285, 2003.
- F. B. Sachse, K. Glänzel, and G. Seemann, "Modeling of electro-mechanical coupling in cardiac myocytes: Feedback mechanisms and cooperativity," *LNCS 2674*, pp. 62–71, 2003.
- F. B. Sachse and G. Seemann, "Modeling of cardiac electro-mechanics in a truncated ellipsoid model of left ventricle," *LNCS 2673*, pp. 253–260, 2003.
- F. B. Sachse, G. Seemann, and R. Mayer, "Modelling of electro-mechanics in the heart: Mathematical and numerical aspects," in *High Performance Scientific Computing*, W. Juling, Ed., pp. 36–37. Scientific Supercomputing Center Karlsruhe, 2003.
- F. B. Sachse, C. D. Werner, and G. Seemann, "Simulation of cardiac electrophysiology and electrocardiography," in *Computer Simulation and Experimental Assessment of Cardiac Electrophysiology*, N. Virag, O. Blanc, and L. Kappenberger, Eds., pp. 97–104. Futura Publishing, Armonk, New York, 2001.

Supervised diploma theses and student research projects

- H. Ying, "Investigation of Atrial Fibrillation Induced Remodeling in Human Right Atrium: A Simulation Study," Student Research Project, Institut für Biomedizinische Technik, Universität Karlsruhe (TH), Dec. 2004.
- K. Chaisaowong, "Modeling of human cardiac force development:quantitative description from myofilament to myocardium," Diploma Thesis, Institut für Biomedizinische Technik, Universität Karlsruhe (TH), Jun. 2004.
- R. Müller, "Schnelle volumenbasierte Visualisierung unter Berücksichtigung von lokalen Verschiebungen," Student Research Project, Institut für Biomedizinische Technik, Universität Karlsruhe (TH), Mar. 2004.
- F. Toth, "Vergleich zweier Verfahren zur Segmentation von medizinischen Bilddaten mittels topologisch veränderbarer Aktiver Konturen," Student Research Project, Institut für Biomedizinische Technik, Universität Karlsruhe (TH), Feb. 2004.
- C. Höper, "Modellierung der Anatomie und Elektrophysiologie des menschlichen Vorhofs," Diploma Thesis, Institut für Biomedizinische Technik, Universität Karlsruhe (TH), Nov. 2003.
- D. L. Weiß, "Charakterisierung der Ventrikelwand durch anatomische und elektrophysiologische Modellierung," Diploma Thesis, Institut für Biomedizinische Technik, Universität Karlsruhe (TH), Sep. 2003.
- K. Glänzel, "Kraftentwicklung im Sarkomer unter Berücksichtigung elektromechanischer Kopplung," Diploma Thesis, Institut für Biomedizinische Technik, Universität Karlsruhe (TH), Sep. 2002.
- J. Häfner, "Hyperelastische Beschreibung der elastomechanischen Eigenschaften des Myokards: Ein neues Materialgesetz und dessen Anwendung," Diploma Thesis, Institut für Biomedizinische Technik, Universität Karlsruhe (TH), Sep. 2002.

- D. L. Weiß, "Vergleich des Verhaltens eines Elektrophysiologischen Zellmodells mit einem Zellulären Automaten bei Simulierten Atrialen Fibrillationen," Student Research Project, Institut für Biomedizinische Technik, Universität Karlsruhe (TH), Sep. 2002.
- S. Barros, "Visible female thorax segmentation," Student Research Project, Institut für Biomedizinische Technik, Universität Karlsruhe (TH), Jun. 2001.
- M. Jösel, "Simulation der Katheterisierung und Radio-Frequnz-Ablation in der Kardiologie mit einem Haptischen Interface," Diploma Thesis, Institut für Biomedizinische Technik, Universität Karlsruhe (TH), Nov. 2001.
- L. G. Blümcke, "Entwicklung eines schnellen Verfahrens zur Berechnung der Deformation im Herzen ausgehend von makroskopischen Modellen der Kraftentwicklung," Diploma Thesis, Institut für Biomedizinische Technik, Universität Karlsruhe (TH), Sep. 2001.
- M. Mohr, "Vergleich von mikroskopischen und makroskopischen Modellen der Deformation im Myokard," Diploma Thesis, Institut für Biomedizinische Technik, Universität Karlsruhe (TH), Sep. 2001.
- N. Sá Couto, "Visible female thorax segmentation," Student Research Project, Institut für Biomedizinische Technik, Universität Karlsruhe (TH), Jun. 2001.

Prices

Own work

- 2004: Physiological Society award at the retirement meeting of Denis Noble in Oxford in October:
  G. Seemann, F. B. Sachse, O. Dössel, A. V. Holden, M. R. Boyett, and H. Zhang, "3D anatomical and electrophysiological model of human sinoatrial node and atria," *J. Physiol.*, PC26, submitted, 2004.
- 2001: Best poster award at the congress Computers in Cardiologie in Rotterdam:
  G. Seemann, F. B. Sachse, C. Riedel, C. D. Werner, and O. Dössel. "Regional and frequency dependencies of force development in the myocardium: A simulation study". In *Proc. Computers in Cardiology*, vol. 28, pp. 345-348, 2001.
- 2001: Siemens diploma thesis award:
  G. Seemann, "Elektrische Erregungsausbreitung im Herzen ausgehend von elektrophysiologischen Zellmodellen: Erregungsausbreitung im Zellverband, Parametrisierung Zellulärer Automaten," Diploma Thesis, Institut für Biomedizinische Technik, Universität Karlsruhe (TH), Aug. 2000.
- 2000: At the 34. Annual Congress of the German Society of Biomedical Engineering (DGBMT) Gunnar Seemann won the 1. price at the students competition with the paper:
  G. Seemann, F. B. Sachse, C. D. Werner, and O. Dössel. "Parametrisierung Zellulärer Automaten der Erregungsausbreitung im Herzen ausgehend von elektrophysiologischen Zellmodellen," in *Biomedizinische Technik*, vol. 45-1, pages 481-482, Sep. 2000.

Supervised work

2003: At the 37. Annual Congress of the German Society of Biomedical Engineering (DGBMT) the following students won a price at the students competition with the paper:

- 1. rank: D. L. Weiß, G. Seemann, F. B. Sachse, and O. Dössel, "Investigation of electrophysiological heterogeneity and anisotropy across the human ventricular wall," in *Biomedizinische Technik*, vol. 48-1, pp. 228–229, 2003.
- 2. rank: C. Höper, G. Seemann, F. B. Sachse, H. Zhang, and O. Dössel, "3D computer model of human atrial anatomy and electrophysiology," in *Biomedizinische Technik*, vol. 48-1, pp. 2–3, 2003.

2001: At the 35. Annual Congress of the German Society of Biomedical Engineering (DGBMT) the following students won a price at the students competition with the paper:

- 1. rank: L. G. Blümcke, F. B. Sachse, G. Seemann, C. D. Werner, and O. Dössel, "Entwicklung eines schnellen Verfahrens zur Deformation im Herzen ausgehend von makroskopischen Modellen der Kraftentwicklung," in *Biomedizinische Technik*, vol. 46-1, pp. 516–517, 2001.
- 2. rank: D. L. Weiß, F. B. Sachse, C. D. Werner, G. Seemann, and O. Dössel, "Vergleich elektrophysiologischer Modelle bei simulierten atrialen Fibrillationen," in *Biomedizinische Technik*, vol. 46-1, pp. 514–515, 2001.
- 2. rank: M. Jösel, F. B. Sachse, G. Seemann, C. D. Werner, and O. Dössel, "Simulation der Katheterisierung und Radio-Frequenz-Ablation in der Kardiologie mit einem haptischen Interface," in *Biomedizinische Technik*, vol. 46-1, pp. 528–529, 2001.

Administrative work at the Institute of Biomedical Engineering

Teaching assistance

- Bildgebende Verfahren in der Medizin
- Anatomische, physikalische und funktionelle Modelle des menschlichen Körpers
- Computational Biology
- Anatomie und Physiologie

Others

- Systemadministrator: Unix, MacOSX, Software, WWW
- Researcher and contact person of the SFB414 "Rechner- und sensorgestützte Chirurgie" of the german research foundation (DFG)
- Organizer of the Conference "Biomedizinische Technik" with approximately 330 presentations and 600 participants
- Guest reviewer for the Journal of Electrocardiology